The Use of Generalized Beam Theory, Finite Elements and Experimental Testing to Investigate the Stability of Light Gauge Steel Sections Subject to Axial Load

By: Jawad Abd Matooq

Supervised by:

Dr. Lawrence Weekes (Supervisor)

Dr. Philp Leech (Co-supervisor)

Directorate of Civil Engineering
School of Computing, Science and Engineering,
University of Salford
UK

Submitted in partial fulfilment of the requirements of

Degree of Doctor of Philosophy, March 2017

Abstract

The aim of the project is to study and investigate the buckling behaviour of unbranched open cold-formed steel sections. First the advantages and disadvantages of cold-formed steel when compared to hot-rolled steel are demonstrated. Thin-wall steel members have lower stiffness which may lead to increased instability and buckling issues for this kind of member. Buckling issues such as Euler buckling, buckling load factors, linear and non-linear analysis, buckling modes (global, distortional and local buckling) and buckling analysis methods (finite element method, finite strip method and generalized beam theory) are addressed. The literature review is concerned with computer software applications, theoretical analyses and experimental tests which can predict buckling loads and related mode shapes for light gauge steel sections. The study focuses on the Generalized Beam Theory (*GBT*) using the Finite Difference method for solution with a view to developing models using *MATLAB* to predict buckling loads, buckling mode shapes and non-linear yielding loads of members subjected to axial load for different boundary conditions. Some applications (beam subjected to concentrated load), linear analysis of buckling problems (Eigen value problems) and non-linear analysis (Imperfect Problems) have been addressed. Also, the finite element method (*ANSYS*) was used to predict the linear eigen-buckling loads and related mode shapes, and the non-linear material and geometric analyses with the post-buckling and initial imperfection effects were addressed. Finally, for validation purposes, a set of *36* cold-formed steel samples (lipped *C*-section and *Zed*-section) members with different boundary conditions (pinned and fixed end conditions) were tested in the laboratory to obtain the actual failure loads and failure shape and compare them with the two analytical methods. Good agreement between the analytical methods and the experimental data was evident, and recommendations for development of the *GBT* analysis are made.

List of Content

List of Figures

List of Tables

Acknowledgements

I would like to thank the following people and organisations for supporting me in numerous ways throughout my PhD. First and foremost, I am indebted to my supervisor ***Dr. Lawrence Weekes*** for his continuous support and guidance throughout the PhD process. Lawrence, I am so lucky to have you as my supervisor and I would have never completed my PhD without your knowledge, advice and most importantly your encouragement! I would also like to extend my gratitude to my co-supervisor ***Dr. Philip Leech*** for his guidance during the PhD. Philip, I am really appreciated your help and support throughout all the difficult times that I faced before finishing my PhD. Deep thanks from my heart.

I would like to take this opportunity to thank the ***Iraqi ministry of higher education and scientific research,*** their representative ***Iraqi cultural attaché*** and the ***University of Basra/ Collage of engineering*** for offer me this opportunity to finish my PhD here in the UK. Also, I would like to thank the ***School of Computing, Science and Engineering*** for their help and support during my PhD journey. I am grateful to the academic and support staff from the ***School of Computing, Science and Engineering*** for their efficient service and support.

Special thanks to the civil engineering laboratory staff, ***Philip Letham, Antony Burrage & Mark Avis***. Without their support, I would not have completed the PhD as expected. I would also like to thank all my friends especially ***Ammar Dakhil & Osamah Salim*** for their help and support.

My gratitude goes to my wife Salwa for her continuous support and the strength she has given to me throughout my personal life and especially during the final stage of my PhD when I needed her the most. Without her support, I would have never completed the PhD as planned. My family and friends are also thanked for their love and support.

Dedication

I dedicate this piece of research to my mother, brothers, sisters, wife and my lovely kids Hasan, Yzen, and Maria.

Declaration

This thesis is submitted to the University of Salford rules and regulations for the award of a PhD degree by research. While the research was in progress, some research findings were published in refereed journals and conference papers prior to this submission (refer to Appendix G).

The researcher declares that no portion of the work referred to in this thesis has been submitted in support of an application for another degree of qualification of this, or any other university or institution of learning.

Jawad Abd Matooq

CHAPTER ONE

INTRODUCTION

CHAPTER ONE

INTRODUCTION

1.1 General

There are two types of steel members in production, namely hot rolled steel members that are rolled in specialised factories with high temperatures and cold formed steel members that are formed at normal atmospheric temperatures. Hot rolled sections are thicker gauge, provide increased strength and stiffness over cold rolled steel, and are used in general domestic and commercial building construction. Light gauge steel tends to be used for building projects that require less weight to be supported i.e. small portal frames and storage racking. The use of light gauge cold formed steel is increasing rapidly due to its structural characteristics and economy. This type of steel has been used widely in residential, industrial and commercial buildings, bridges, storage racks, grain bins, car bodies, railway coaches, highway products, transmission towers, transmission poles and drainage facilities.

1.2 Manufacturing methods of cold-formed steel

There are two methods used in the manufacture of cold formed steel sections:

1.2.1 Cold roll forming machines

The cold-forming process consists of feeding continuous steel strips through a series of opposing rolls to deform the steel sections plastically and form the desired shapes. The process involved in cold forming C-sections is illustrated in Figure (1-1). A sample section may be produced by as few as six pairs of rollers but a complex section may require as many as 15 sets of rollers,W.-W. Yu (2000).

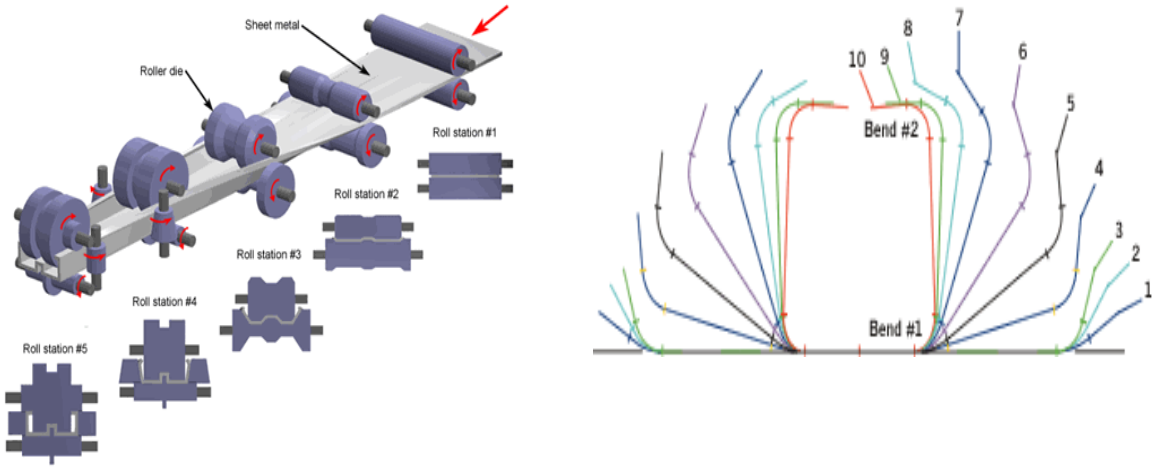

Figure (1-1) Cold-formed C-section sequences (www.custompartnet.com 27th, March 2014)

1.2.2 Press braking

The equipment used in press breaking operations essentially consists of a moving top beam (punch) and a stationary bottom bed (die) that produce one complete fold at a time along the full length of the beam, figure (1-2).

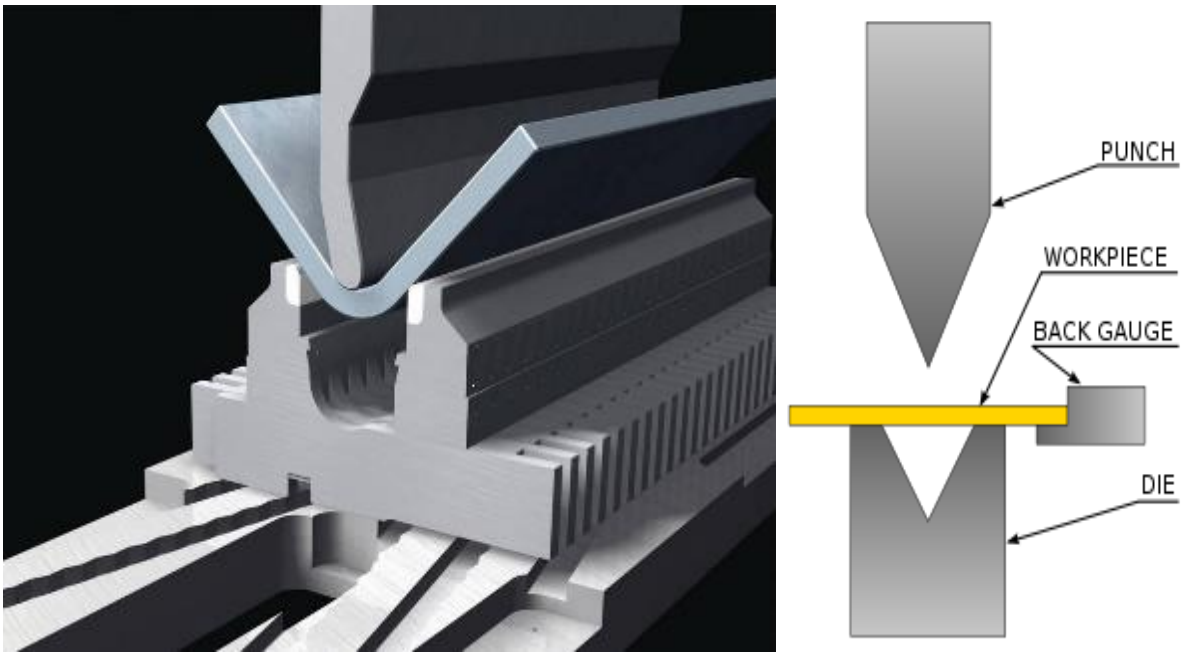

Figure (1-2) Press braking C-section sequences (news.thomasnet.com, 27th March 2014)

The press-braking operation is normally used to produce small quantities of various shaped sections. The initial cost of cold roll forming is higher than the press-breaking method;

however, it is economical to mass produce one particular shape of section. Figure 1.3 shows a range of typical sections which are commonly used for light gauge steel members.

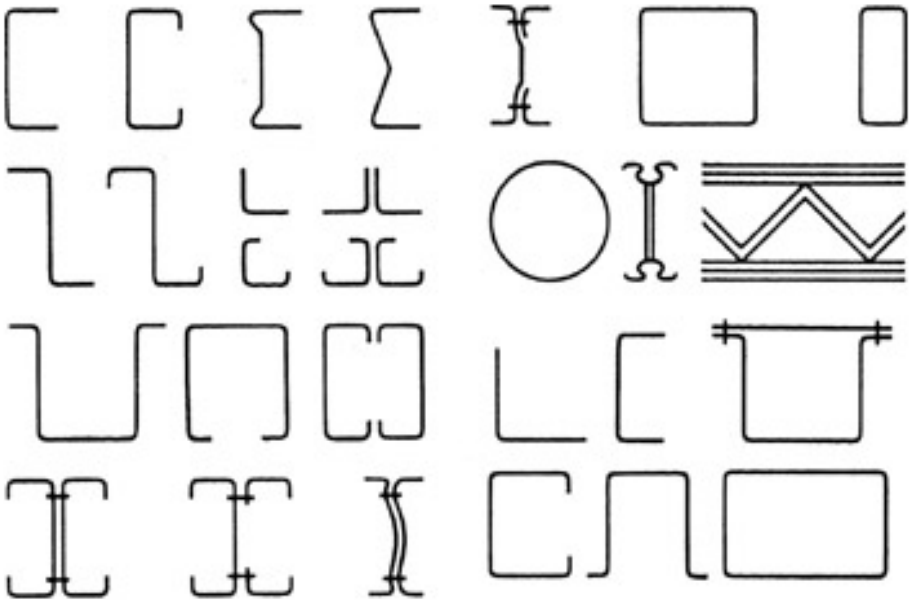

Figure (1-3) Typical cold-formed steel members (Yu, 2000)

Most of the recent research demonstrates that cold formed steel sections are more economical than hot-rolled steel sections; light gauge cold-formed steel sections have the following advantages:

- Ease of manufacturing and mass production.
- Uniformity and high quality control.
- Low self-weight.
- Ease and economy of transportation and handling.
- Fast and simple erection or installation.
- Improved technology of manufacture and corrosion protection.
- Non-shrinking and non-creeping at ambient temperature.
- Improved production of complex shapes (since modern rolling lines are computer controlled, highly complex sections can be produced).

The issues with cold-formed members are that the stiffness tends to be less when compared to hot rolled members, so there may be more displacement in the member and also at the connections. Increased displacements tend to mean that elastic instability is more of an issue with cold-formed members. Light gauge cold-formed steel sheets have thicknesses ranging from 0.4 to 6.4 mm, Yu (2000). Referring to figure (1-4), the nominal yield strength of available cold-formed steel ranges from *250 to 550 N/mm^2*, Yu (2000). The yield strength of

cold-formed steel is determined based on 0.2% proof stress and he modulus of elasticity is determined from the slope of the graph (approximately *200,000 N/mm^2),* Yu (2000).

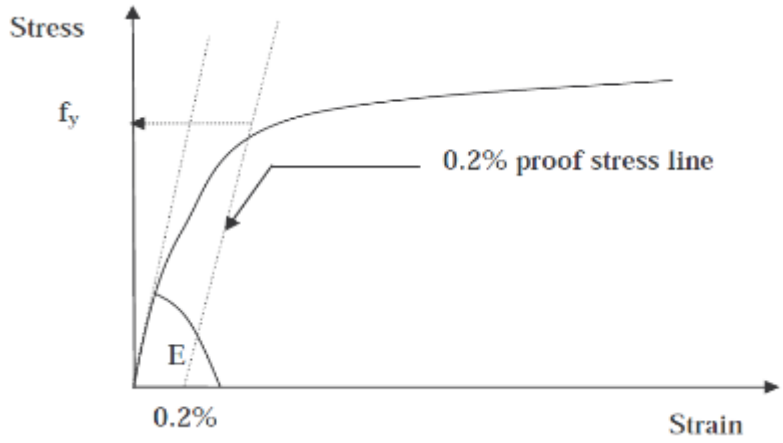

Figure (1-4) Stress strain curve of cold-formed steel (Yu, 2000)

1.3 Buckling terminology

To address the buckling phenomena in light gauge cold formed steel sections the following terms require clarification.

The radius of gyration, *r*, is the units of length that describes the way in which the area of a cross section is distributed around its centroidal axis.

$$r = \sqrt{\frac{I}{A}} \qquad (1-1)$$

Where *I* and *A* are the area moment of inertia, and area of the cross section respectively.

Slenderness is a geometric concept of a two-dimensional area that is quantified by the length of a particular member divided by its ratio of the radius of gyration, $\lambda = \frac{L_E}{r}$.

Stiffness is a structural property, which is proportional to the elastic modulus *E* (*Young's modulus*) and the section geometry in the equation:

$$Axial\ Stiffness = \frac{EA}{L} \qquad (1-2)$$

Where: *A* is the cross section area of the section and *L* is the length of the member.

1.3.1 Euler buckling

Slender or thin walled components under compressive stress are susceptible to buckling. Most people have observed what is called Euler buckling where a long slender member subject to a compressive force moves laterally to the direction of that force, as illustrated in Figure (1-5). Euler buckling is a purely theoretical instability problem and tends to provide an upper bound to real physical buckling which accounts for plasticity/nonlinearity in the material. The force, F, necessary to cause such a buckling motion will vary by a factor depending only on how the two ends are restrained. (i.e. for a pin ended member), as summarised in Megson (2005).

1.3.2 Buckling load factor

The buckling load factor (BLF) is an indicator of the factor of safety against theoretical buckling or the ratio of the buckling loads to the currently applied loads.

Table (1-1) 'Interpretation of the Buckling Load Factor (BLF)' illustrates the interpretation of possible BLF values.

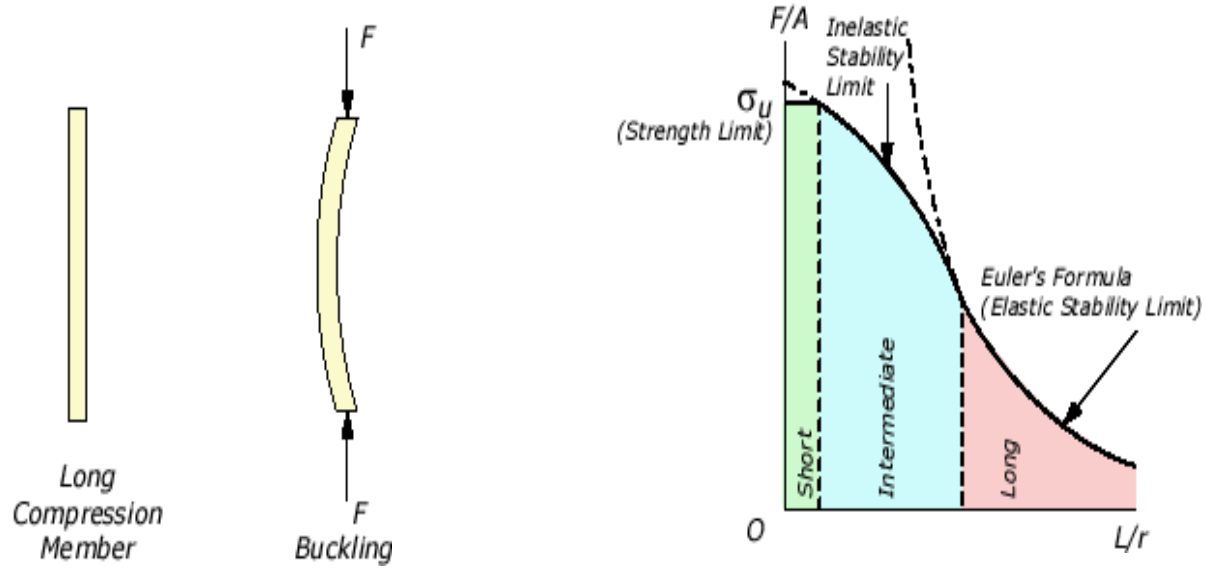

Figure (1-5) Failure of long columns due to instability, (Akin, 2009)

Table (1-1) Interpretation of the buckling load factor (BLF) (Akin (2009)

BLF	Value Buckling	Status Remarks
>1	Buckling not predicted	The applied loads are less than the estimated critical loads.
= 1	Buckling predicted	The applied loads are exactly equal to the critical loads. Buckling is expected.
< 1	Buckling predicted	The applied loads exceed the estimated critical loads. Buckling will occur.
-1 < BLF < 0	Buckling possible	Buckling is predicted if you reverse the load directions.
-1	Buckling possible	Buckling is expected if you reverse the load directions.
< -1	Buckling not predicted	The applied loads are less than the estimated critical loads, even if you reverse their directions.

1.4 Buckling analysis

Buckling analysis is a technique used to determine theoretical buckling loads (critical loads) at which a structure becomes unstable and buckled mode shapes, i.e. the characteristic shapes associated with a structure's buckled response.

1.4.1 Linear buckling analysis (eigenvalue problem)

The solution of second order differential buckling equations leads to a series of eigenvalues which represent critical loads, and eigenvectors which represent the associated buckled mode shape. Referring to figure (1-6) for instance, an eigenvalue buckling analysis of a pin ended column will match the classical Euler solution (eq. (1-3). However, imperfections and nonlinearities in both material and section geometry prevent most real-world structures

from achieving their theoretical elastic buckling strength. Thus, the eigenvalue buckling analysis tends to envelope the failure load, and is usually modified accounting for nonlinearities to provide design load capacities.

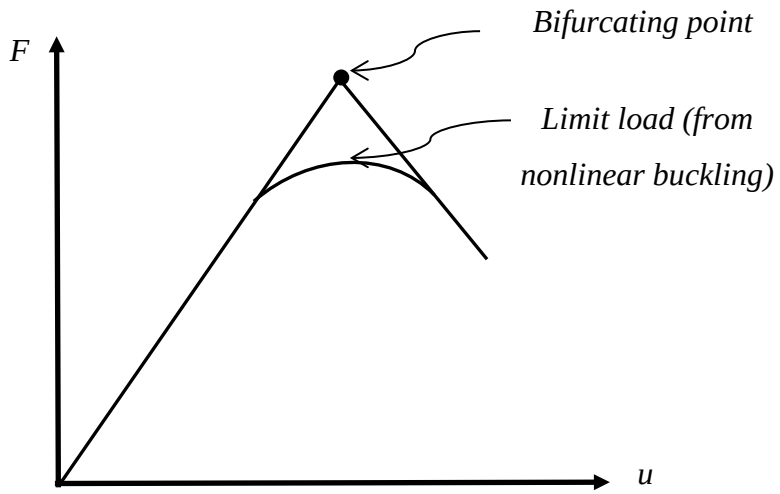

Figure (1-6) Linear (eigenvalue) buckling curve (Kurowski, 2011)

Linear eigen-buckling analyses provide theoretical buckling load magnitudes and associated buckling modes. FEA programs provide calculations of a large number of buckling modes and the associated buckling load factors (BLF) through eigenvalue calculations, Kurowski (2011).

The BLF is expressed as a number by which the applied load must be multiplied (or divided depending on the particular FEA package) to obtain the buckling load magnitude.

The buckling mode illustrates the shape the structure assumes when it buckles in a particular mode, but does not represent numerical values of the displacements or stresses mainly because the analysis is not one which is loaded. The numerical values can be displayed, but are merely relative. Also in the linear (Eigenvalue) buckling, the member may be shown to have buckled in the opposite direction to that predicted. This is not an error; merely the linear buckling analysis only predicts the buckled shape (mode) and not the direction of buckling.

Linear buckling critical load analysis overestimates the real buckling load and provides non-conservative results when compared to actual physical critical loads due to the effects of

initial imperfections. *BLFs* are also overestimated because of modelling uncertainty. *FE* models should represent the actual geometry of the beam.

The well-known buckling load for a pin-ended column is:

$$P_E = \frac{n^2\pi^2 EI}{L^2} \qquad (1-3)$$

Where n = 1, 2, 3, …..

Figure (1-7) shows the higher values of buckling load correspond to more complex buckling mode shapes which can be formed by introducing intermediate restraints along the member length (at the points of contraflexure).

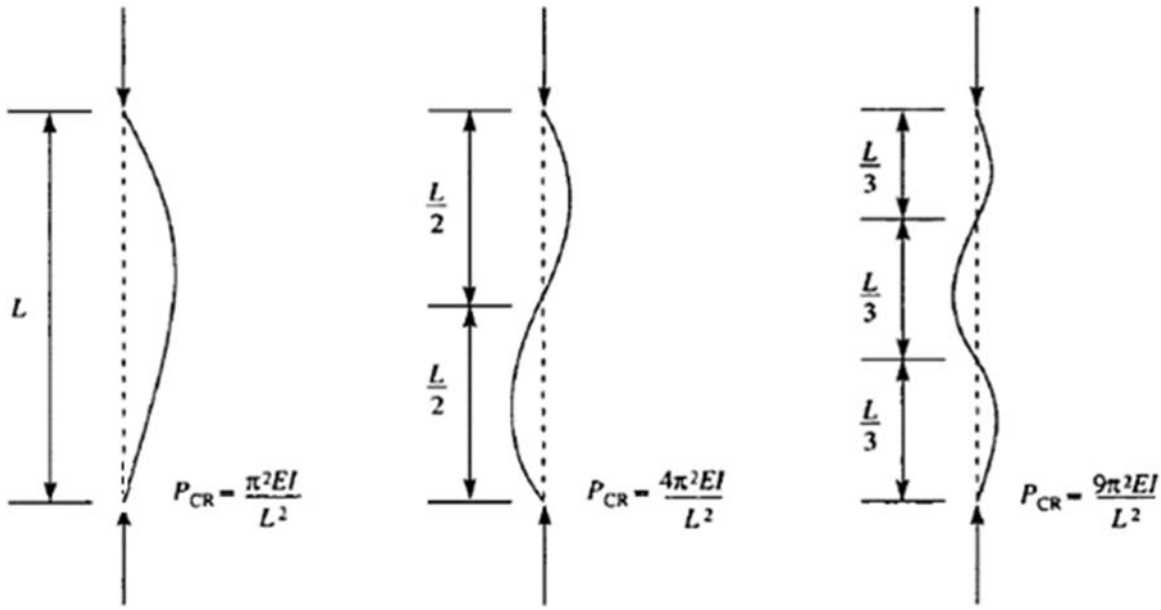

Figure (1-7) Pin-ended column buckling modes, (Megson (2005)

For use in design the Perry-Robertson formula is used which accounts for material nonlinearity and geometric tolerances. This provides design values of axial failure load which account for buckling in long slender beams and is the basis for the design adopted in, Code (2007). The formula in question can be expressed in the following form:

$$\sigma_m = \frac{1}{2}(f_y + \sigma_e(1+\theta) - \sqrt{\left(f_y + \sigma_e(1+\theta)\right)^2 - 4f_y\sigma_e} \qquad (1-4)$$

with

$$\theta = \frac{w_{o,1} C}{i^2}$$

Where:

- σ_m is the average longitudinal stress in the beam's cross-section.
- f_y is the material's elastic limit.
- σ_e is the average tension measured in the cross section which corresponds to the beam's Euler load.
- $w_{o,1}$ the amplitude of the initial geometrical imperfection.
- c is the distance from the cross section's centroid to the section's most stressed fibre.
- i the section's radius of gyration.

1.4.2 Nonlinear analysis

Nonlinear analysis incorporating both material and geometric nonlinearity provides more realistic behaviour and is therefore recommended for design or evaluation of actual structures. This technique employs a nonlinear static analysis with gradually increasing loads to seek the load level at which the structure becomes unstable.

Using the nonlinear approach, the model can include features such as initial imperfections, plastic behaviour, gaps, and large deflection response. In addition, using deflection-controlled loading, it can track the post-buckled performance of the structure (which can be useful in cases where the structure continues to carry load past the theoretical critical load i.e. local and distortional buckling modes).

1.5 Buckling analysis methods

A number of researchers have conducted both numerical and experimental analyses, and have recommended analysis methods for light gauge steel members to predict the buckling loads, modes, and to predict how these structures will perform when subject to axial or flexural loads. Consequently, various alternative methods of analysis have been introduced and here are some of them.

- Generalized Beam Theory (GBT).
- Finite Element Method (FEM).
- Finite Strip Method (FSM).

1.6 Aims and objectives

The above methods (which will be described in detail in the following chapters) have already been written into computer codes to predict the theoretical buckling modes and capacities of various light gauge steel open sections.

So far GBT has been implemented using the finite difference solution technique P Leach and Davies (1996), and the finite element method (Bebiano et al. (2008)). The aim will be to extend the GBT method (currently only employed for providing linear buckling loading and modes solved using FD methods) to incorporate nonlinear geometry effects and provide a prediction of real behaviour up to the onset of material yield.

This will be achieved by reproducing the GBT code in MATLAB, firstly verified against the other available codes, then extending this to nonlinear finite element analyses. The results will be supported by findings from experimental axial tests on a number of light gauge steel sections

In addition, this will also inform the efficiency and suitability of sections, including boundary conditions for various structural usage.

In order to reach these goals, the research will be divided into four steps, namely a literature study, modelling, applications and verification.

Firstly, a literature review will be performed regarding the concept of modelling cold formed steel sections in order to collect important information as well as documenting the development of modelling methods from their beginnings until the present date.

Later, conduct comparative studies of the buckling behaviour of light gauge cold-formed steel compression members with respect to pin-ended and fixed-ended conditions, using the finite strip method (CUFSM) software and generalized beam theory (GBTUL) software.

To develop finite element models capable of simulating the elastic buckling and nonlinear ultimate strength behaviour of light gauge cold-formed steel compression members using the finite element program (ANSYS) and validate them using experimental results.

To develop non-linear finite difference modelling of generalized beam theory for the thin-walled open cross section (initial imperfection effects) using (MATLAB) routines. The acquired results were then compared to those of a commercial FE-software (ANSYS) in order to verify the validity of the application.

To study the effects of initial imperfection on the actual buckling loads (initial imperfection-actual buckling load relation) with different boundary conditions.

Finally, develop suitable experimental tests including evaluation of material properties, test sections, end support conditions, and loading rig set-up. The buckling tests for light gauge cold-formed steel compression members will validate the results of the numerical models including buckling behaviour and capacities for global, local and distortional buckling modes.

1.7 Contents of the thesis

The prediction of actual buckling loads and its mode shapes of cold-formed steel beams was investigated based on generalized beam theory, experimental tests and extensive finite element analyses have been developed in this thesis. This thesis contains eight chapters and the contents of each chapter (except this one) are briefly described as follows:

- ***Chapter Two***, literature review, provides the background concerning research on column buckling behaviour as applied to light gauge steel sections and some of the analysis methods employed to understand it.
- ***Chapter Three***, formulation of the generalized beam theory, describes the behaviour of an open section beam under applied load with several corresponding modes of behaviour according to specific warping displacement functions.
- ***Chapter Four***, applications of the generalized beam theory, presents the applications of the first and second order generalized beam theory using the *Matlab* code in both linear and non-linear analysis to find the theoretical buckling and failure loads of open-section cold-form steel sections.
- ***Chapter Five***, the finite element analysis, presents the linear eigenbuckling and non-linear material and geometric analyses
- ***Chapter Six***, the experimental investigations of cold-formed steel members subjected to axial loads, presents the experimental testing of 36 cold-formed steel (lipped C-section and Zed-section) columns with different boundary conditions. The tests comprised lipped channel & Zed sections full-scale cold-formed steel columns of nine different lengths (two specimens for each length) subjected to axial loading for both pinned and fixed end conditions.
- ***Chapter Seven***, results and the discussion, the results of experimental tests present the actual buckling loads, mode shapes and load-displacement history with the lab representations of boundary conditions for both pinned and fixed end conditions.

These results were compared with both finite element analysis method (ANSYS) and the Generalized Beam Theory (GBT) using nonlinear analysis with the effects of initial imperfections and post-buckling effects to verify the best numerical analysis method, and also to discuss the features of each analysis method.

- ***Chapter Eight***, general conclusions and the further work.

CHAPTER TWO

LITERATURE REVIEW

CHAPTER TWO

LITERATURE REVIEW

Many researchers have studied the buckling behaviour of cold-form steel sections and most of them have examined channel and Zed cross sections, but there appears to be a lack of research, carried out regarding the actual behaviour of these sections under axial and/or flexural loading. This literature review provides the background concerning research on column buckling behaviour as applied to light gauge steel sections and some of the analysis methods employed to understand it.

2.1 Buckling modes

Unfortunately, the behaviour of light gauge cold-form steel sections subjected to axial compression loading is still not fully understood. The behaviour of these sections exhibits different types of buckling, i.e. local buckling, distortional bucking and global buckling; for example, most lipped C-section short columns subjected to concentric compression loads fail because of a combination of local buckling of thin plate elements and distortional buckling of the edge stiffeners. However, there is a lack of research, which addresses how and where these modes happen and the interaction between them.

2.1.1 Local buckling

Local buckling is the buckling of individual plate elements which are under compression without changing the fold lines of the cross-section as shown in Figure (2-1). In the case of beams, local buckling may occur in the compression flange or part of the web which is under compression. Local buckling is characterised by short half wavelengths compared to the other buckling modes. Further, the half-wave length of local buckling is in the order of the width of the individual plate elements.

Earlier researchers, such as Timoshenko and Gere (1961), Bleich (1952), Bulson (1970) and Bulson and Allen (1980), extensively investigated and summarised the elastic critical stresses for local buckling, Hancock and Rogers (1998). The elastic critical stress for local buckling of plate elements in compression, bending or shear is presented by Hancock and Rogers (1998).

$$f_{cr} = \frac{k\pi^2 E}{12(1-v^2)}\left(\frac{t}{b}\right)^2 \qquad (2-1)$$

Where k is called the plate local buckling coefficient which depends on the support conditions, and (b/t) is the plate aspect ratio in which b is the plate width and t is the plate thickness.

A plate element is said to be slender if the elastic critical local buckling stress (f_{cr}) calculated using the above equation is less than the material yield strength. Therefore, if a particular section is slender, local buckling takes place prior to the stresses reaching the yield strength. This leads to a large reduction of section moment capacity of beams because local buckling and the material yielding are the two failure criteria that govern the section moment capacity. If the elastic critical buckling stress (f_{cr}) exceeds the yield stress, the plate element under compression buckles in the inelastic range (Yu, 2000).

If the beam carries increasing load after the local buckling failure, the beam is said to have post-local buckling capacity. Therefore, even if the local buckling occurs in a plate element prior to yielding it does not necessarily mean that the failure of the section has occurred. Normally the post-buckling reserve is allowed for in the design to achieve an economic solution (Hancock and Rogers 1998).

Figure (2-1) Typical local buckling mode.

2.1.2 Distortional buckling

Distortional buckling is the phrase used to describe the state when a flange rotates at the intersection point of flange and web in members provided with edge stiffeners, and for members which are intermediately stiffened. It occurs when the intermediate stiffener has a displacement normal to the plane of the member, as shown in Figure (2-2).

This type of buckling may occur in thin sections in compression or bending at stresses significantly below the yield stress, especially for high strength steels (Hancock and Rogers 1998). The half wavelength of distortional buckling is generally in between that of local buckling and lateral torsional buckling and typically several times larger than the largest characteristic dimension of the section.

If the sections are composed of high-strength steel, then there may be a significant post-buckling reserve of strength beyond the elastic distortional buckling stress in a similar manner to that which normally occurs for local buckling (Kwon and Hancock, 1992). Distortional buckling has less post-buckling capacity than local buckling modes, according to Schafer and Peköz (1999). This is also observed experimentally by Hancock et al. (1994). Distortional buckling failures occur even when local buckling occurs at a lower critical elastic moment than distortional buckling because of reduced post-buckling strength in the distortional failure mode (Schafer and Peköz, 1999).

Figure (2-2) Distortional buckling mode.

2.1.3 Lateral distortional buckling

Lateral distortional buckling involves transverse bending of the vertical web and is most likely to occur if the tension flange is restrained, figure (2-3). This type of buckling often occurs in hollow flange beams because the tubular flanges of hollow flange beams are very stiff torsional while their webs are comparatively slender and easily undergo web distortion. Even though, when the tension flange is not restrained laterally and flanges are not torsional stiff, cold-formed C-section beams may still fail by lateral distortional buckling if the web is particularly slender (Pi et al. 1998).

Figure (2-3) Lateral distortional buckling mode.

2.1.4 Lateral torsional buckling

Lateral torsional buckling failure is the most complex failure criterion of steel beams. This type of failure is identified by the simultaneous bending and twisting of the entire cross-section without cross-sectional deformation, figure (2-4). If a beam is not restrained laterally, it tends to fail by lateral torsional buckling in cases where lateral stiffness and torsional stiffness are low. It occurs generally if the beam has a higher bending stiffness in the vertical plane compared to the horizontal plane. Because of the geometry of the open cross-section, which gives great flexural rigidity about one axis at the expense of low torsional rigidity and low flexural rigidity about a perpendicular axis, cold-formed steel members are particularly susceptible to lateral-torsional buckling according to Chu et al. (2004). The parameters affecting lateral torsional buckling resistance are the length between lateral restraints, the type and the positions of load, the geometry of cross-sections, the type of end supports, the presence or absence of stiffening devices that restrain warping at critical locations, the material properties, the magnitude and distribution of residual stresses, initial imperfections of geometry and loading, and cross-sectional distortion (Galambos, 1998).

Lateral torsional buckling behaviour is related to buckling resistance and slenderness. There are three different ranges of behaviour namely, elastic buckling, inelastic buckling and plastic behaviour. Elastic lateral torsional buckling occurs in slender beams with low resistance to lateral bending and twisting. As the slenderness decreases, the resistance of a beam to elastic buckling increases and the beam may yield before its elastic buckling moment is reached. Yielding reduces the effective out-of-plane rigidities, and hence, lateral torsional buckling occurs before reaching the elastic buckling moment. This type of buckling of beams having intermediate slenderness is called ‘inelastic lateral torsional buckling’. If the beam is fully or adequately restrained laterally so that the slenderness is low, it achieves the full plastic moment capacity.

The elastic critical buckling moment for lateral torsional buckling of an I-beam subjected to pure bending is given in equation (2-2), (Hill, 1954).

$$M_{cr} = \sqrt{\left(\frac{\pi^2 EI_y}{L^2}\right)\left(GJ + \frac{\pi^2 EI_w}{L^2}\right)} \qquad (2-2)$$

In Equation 2.2, EI_y, GJ and EI_w are the minor axis flexural rigidity, torsional rigidity and warping rigidity, respectively.

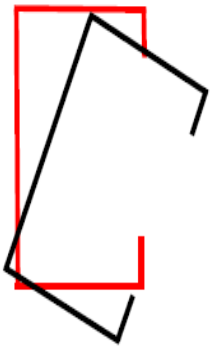

Figure (2-4) Lateral torsional buckling mode.

2.1.5 Lateral (global) buckling

Global buckling describes the state when the cross section of a column remains unchanged while the column itself has either lateral or lateral torsional displacement, figure (2-5) BSI (2014).

Figure (2-5) Lateral (global) buckling mode.

2.2 Experimental investigations

Celebi et al. (1972) conducted tests on two unlipped cold-formed C-section beams loaded eccentrically through the web. Put et al. (1999) conducted approximately 160 tests on lipped and unlipped simply supported cold-formed steel beams loaded above the top flange, either through the web or centroid at the mid-span. The test results showed that the strengths of the beams loaded through the centroid were significantly lower than those loaded through the web. Kavanagh and Ellifritt (1994) reported ten tests of discretely braced cold-formed steel C-section beams loaded at the web centerline and these tests indicated that the strengths generally increased as the amount of bracing increased. Ellifrit et al. (1991) and Winter et al. (1949) have observed the same in their tests conducted on C-section beams.

Young and Rasmussen (1997) conducted an experimental investigation into the behaviour of cold-formed plain and lipped channel columns axially loaded with different boundary conditions such as fixed and pinned ends. It was shown experimentally that local buckling does not occur as a result of overall bending in the case of fixed-ended singly symmetric columns, as it does for pin-ended singly symmetric columns. They found that local buckling has a fundamentally different effect on the behaviour of pin-ended and fixed-ended singly symmetric columns, so a series of tests was performed on plain and lipped channels, brake-pressed from high strength structural steel sheets to examine this fundamentally different effect caused by local buckling, as shown in figure (2-6). Four different cross-section geometries were tested over a range of lengths which involved pure local buckling, distortional buckling as well as overall flexural buckling and flexural-torsional buckling. They also discovered that local buckling influenced the strength of short and intermediate plain channel columns, while for short and intermediate lipped channel columns with fixed-ends distortional buckling was more likely to influence their capacity. Although the local buckling mode does not affect long lengths or some intermediate column lengths significantly, its effects appear to be clearly obvious in short length columns during ultimate loading.

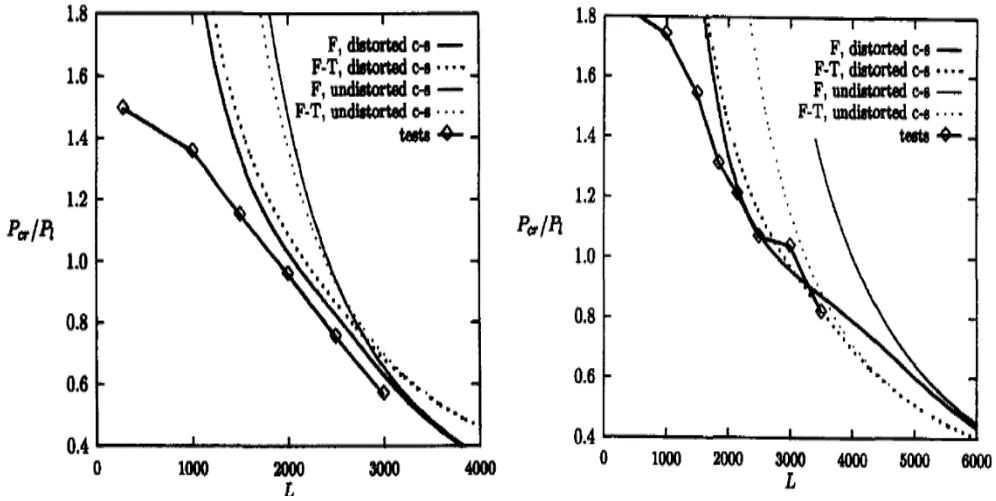

Figure (2-6) Buckling load factor vs length for channel section (Young and Rasmussen, 1997).

Put et al. (1999) performed bending and torsion tests on unbraced simply supported cold-formed steel channel beams loaded eccentrically at the mid-span. The test results showed that the beam strengths decrease as the load eccentricity increases and that the strength is higher when the load acts on the centroid side of the shear centre than when it acts on the side away from the shear centre. They developed simple interaction equations that can be used in the design of eccentrically loaded cold-formed channel beams.

Kesti and Davies (1999) stated that the distortional mode is a critical buckling mode for columns made from cold-formed steel, which depends on the end boundary conditions and the length of the column as well as the effective area of the cross section.

Gotluru et al. (2000) investigated the behaviour of cold-formed steel beams subjected to torsion and bending because the transverse load was not applied at the shear centre. They performed simple geometric nonlinear analyses, finite element analyses and finite strip analyses and compared their results with experimental results. The influence of typical support conditions was studied and they were found to produce partial warping restraints at the ends. Yu (2000) provides numerical methods for calculating torsional properties of thin-walled sections.

Rondal (2000) stated that the distortional buckling mode is a relatively new mode to be considered, also there is a lack of research which compares local and global buckling. However, due to the continual evolution of steels with higher strength formed in thinner sections, distortional buckling could sometimes be considered as a more critical factor than other modes of buckling in more modern structures.

Schafer (2002) found that the distortional buckling stresses in lipped sections are higher than other sections, especially in sections that have lips which are nearly equal in length to the flange width, so these types of sections are better at resisting distortional buckling.

Yu (2000) stated that torsional buckling did not occur in closed sections because of their large torsional rigidity, whereas for open thin-walled sections, flexural buckling and flexural-torsional buckling are both possible. The doubly symmetric sections may fail by pure bending (flexural buckling) and the single symmetric sections may fail either by bending about the weak axis (flexural buckling) or by bending about one axis and twisting about the shear centre (flexural-torsional buckling) depending on factors related to the cross-section properties and the effective length of the column.

Schafer (2002) stated that sections with too wide or too narrow flanges were not good in terms of distortional buckling. He also highlighted another issue, which is the size of the stiffener required to keep the flange in place. In terms of the web's influence on distortional buckling, Schafer (2002) revealed that sections with deeper webs have lower distortional buckling stresses where webs are more flexible when they are deeper, leading to less rotational stiffness at the intersection point of web and flange, which controls the distortional buckling influence on the section.

Hancock (2003) examined the behaviour of members undergoing distortional buckling and the interaction of this mode with other buckling modes. Most of his research looked at simple lipped channel sections.

Narayanan and Mahendran (2003), described the distortional buckling behaviour of a series of innovative cold-formed steel columns. More than 15 laboratory experiments were undertaken on these innovative steel columns of an intermediate length under axial compression. All of these columns failed by distortional buckling with very little post-buckling strength. The section and buckling properties of the columns were determined using the finite strip analysis. The distortional buckling and nonlinear ultimate strength behaviour of the columns was investigated in detail using finite element analyses (ABAQUS). The finite element analyses included relevant geometric imperfections and residual stresses. The deflection and strain results from the experiments compared well with those from the analyses. The ultimate design load capacities were evaluated using the provisions of Australian Cold-formed Steel Structures Standard AS/NZS 4600-1996 and were compared with those from experiments and finite element analyses. A series of parametric studies was also carried out by varying the yield strength, thickness and column length.

de Barros Chodraui et al. (2006) were of the same opinion with the later conclusions of Schafer (2002) about wide flanges. He also studied the behaviour of wide flanges provided with edge stiffeners in cold forms steel sections such as rack, top hat Z, and lipped channels where there are usually wide flanges and lips at the edges. He concluded that these sections are most sensitive to distortional buckling modes rather than others.

Ungermann and Kalameya (2006). conducted fourteen experimental tests on thin-walled channel sections in major axis bending. They had varied parameters such as loading, slenderness ratio, b/t of the local buckling plates (for flanges and the web), global lateral-torsional buckling slenderness ratio of the beams and the type of production process. Five types of channel sections were tested including four welded sections (Grade S355) and one cold-formed section (Grade S235). Beams were tested with simply supported boundary conditions and warping about the minor axis was prevented. The test results showed that the load-carrying behaviour of the specimens depends strongly on the direction of the global lateral imperfections and displacements of the member. According the test results, lateral-imperfections and displacements in the direction of the web (negative y-direction) led to a sudden collapse of the beam with a significant decrease in the load while global imperfections and the increasing

displacements due to lateral-torsional buckling in the direction of the open part of the section led to a ductile failure with no abrupt decline of the load carried. Higher failure moments were observed if the beams failed in the positive direction as compared to those beams with negative imperfections.

Brune and Ungermann (2008) carried out numerical investigations of channel beams subject to coupled instabilities. Numerical models were validated using the test results of Ungermann and Dortmund (2006). They found out that the DSM and EC 3 Part 1.3 overestimate the ultimate loads for thin-walled slender channels in bending.

Kwon et al. (2009) tested a series of cold-formed lipped channels in compression both with and without intermediate stiffeners with fixed ends. The channels were fabricated from 0.6 and 0.8 mm thicknesses of high strength steel plate where the nominal yield stress was 560 N/mm^2. The aim of their research was to study the ultimate strength of columns with intermediate lengths. They discovered that for sections with local buckling as the critical buckling mode, the interaction between the local and distortional buckling modes was observed only in stub columns and an interaction between the local and global buckling modes was the final failure mode in the intermediate and long length columns. However, for sections with distortional buckling as the critical buckling mode, stub and intermediate length columns experienced critical failure mode induced from the interaction between local and distortional buckling modes, and the interaction of local, distortional and global buckling modes occurred in some of the columns' lengths. Finally, it can be said that the existence of the buckling mode interaction within column behaviour in compression depends highly on the cross-section properties and the boundary conditions of the column.

Casafont et al. (2011) examined the interaction of the distortional and the global buckling modes for various lengths of rack columns containing perforations. The range of lengths used was such that the behaviour was between where global buckling was dominant and the length used for columns to examine local buckling strength. They found that the failure mode due to this interaction could be observed in a range of columns' lengths utilised in practice, although they found that the interaction between the distortional and global buckling modes did not affect the column strength significantly, as showed figures (2-7) & (2-8).

Figure (2-7) (A) Test arrangement (B) specimen tested with pinned ends (torsionally restrained) (Casafont et al., 2011).

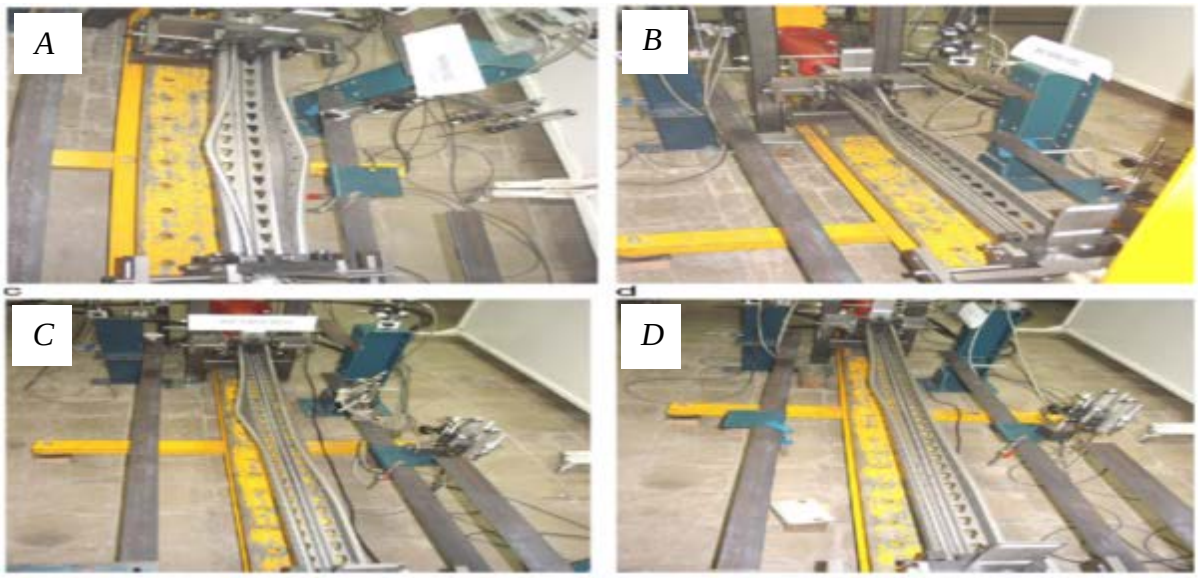

Figure (2-8) Failure of pinned specimens: (A) 800 mm, (B) 1000 mm, (C) 1500 mm and (D) 1800 mm (Casafont et al., 2011).

dos Santos et al. (2012), Silvestre et al. (2012) and Dinis et al. (2007) stated that most open cross section members formed from cold-formed steel have high local and global slenderness, and this makes them oversensitive to geometrical instability phenomena such as local, distortional and global (flexural or flexural-torsional) buckling. Many factors affect the failure mode such as the length, shape and dimensions of cross section and the end support conditions of the member.

dos Santos et al. (2012) proved that there is a triple interaction between local, distortional and global buckling in lipped channel column sections. They also identified its influence on their 12 lipped channel test samples, and concluded that the failure mode of the columns was a combination of symmetric distortional and flexural-torsional buckling modes, figure (2-9).

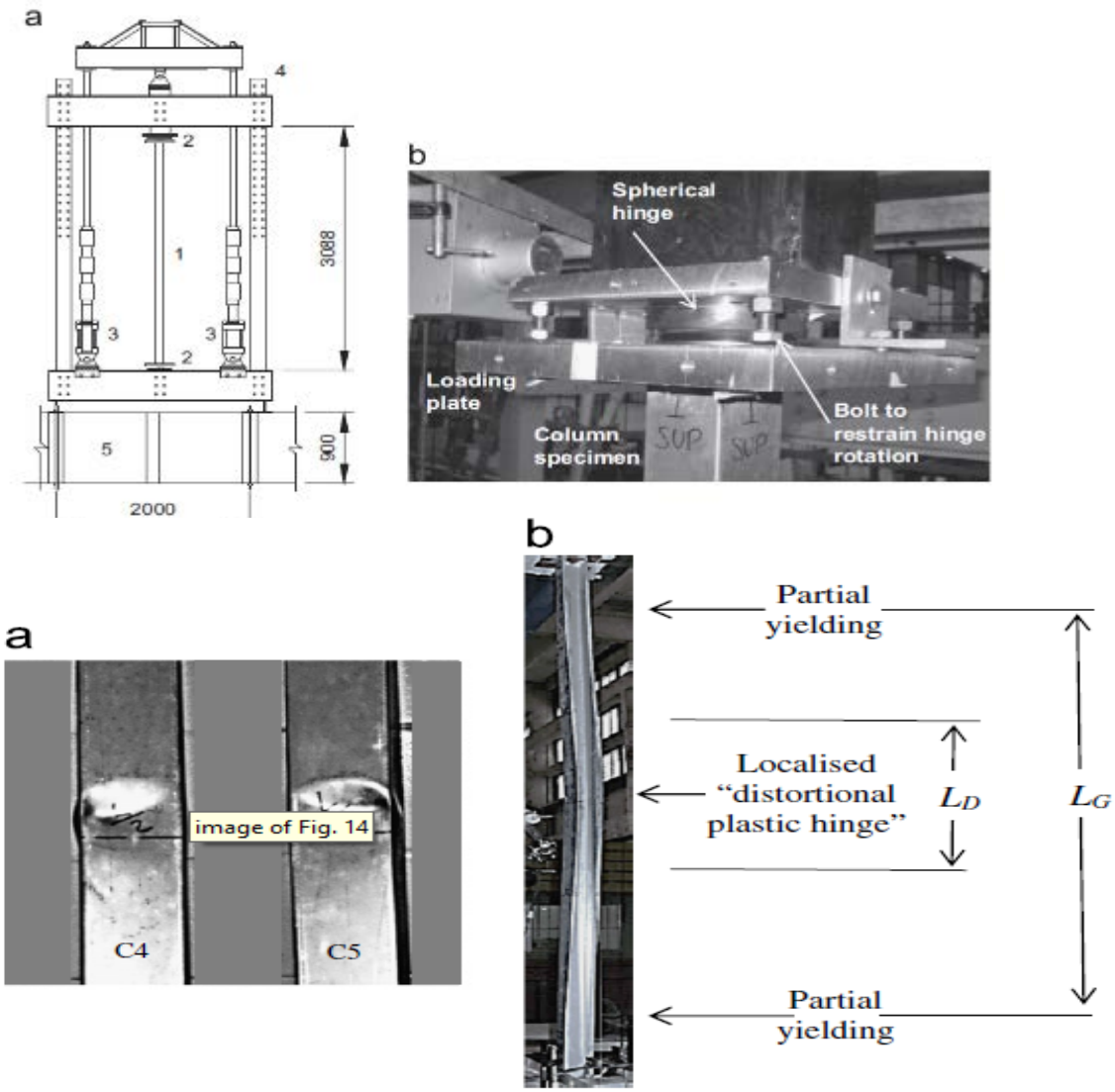

Figure (2-9) Schematic test set-up representation: test specimen, view of the column end support condition (dos Santos et al. (2012).

Godat et al. (2012) investigated in their research the behaviour of the local buckling of tubular polygon columns formed from thin-walled steel, they tested three different cross sections, hexagonal (sixteen-sided), dodecagonal (twelve sided) and octagonal (eight-sided). They concluded that for various thin-walled tubular polygon columns with equal cross section area, it might become advantageous to minimise the plate slenderness ratio (plate width to thickness) due to the increase in local buckling capacity.

Ananthi et al. (2015), presented both the analytical and theoretical investigations on ultimate load carrying capacity and behaviour of CFS unlipped channels with their ends fixed and subjected to axial compression. The numerical studies were carried out in the elastic as well as in the plastic ranges of loading. The slenderness ratio of the channels chosen was 40, 80,100 and 120. Three different web depths (shallow, medium and deep) with five thicknesses were also chosen. In addition to the numerical studies, the comparison was made with the design strengths predicted by using North American Standards for CFS structures. It was observed that the design strength predicted by the specifications were conservative for axially loaded columns. In the present investigation, an attempt is made to study the ultimate load carrying capacity and the mode of failure. Load versus axial shortening behaviour has been studied for various slenderness ratios for a few specimens.

Hansapinyo (2015), presented experimental investigation and finite element analysis on buckling behaviour of irregular section cold-formed steel columns under axially concentric loading. For the experimental study, four different sections of columns were tested to investigate the effect of stiffening and width-to-thickness ratio on buckling behaviour. For each of the sections, three lengths of 230, 950 and 1900 mm were studied representing short, intermediate length and long columns, respectively. Then, nonlinear finite element analyses of the tested columns were performed. The comparisons in terms of load-deformation response and buckling mode show good agreement and hence the FEM models were validated. Parametric study of the stiffening elements and thicknesses of 1.0, 1.15, 1.2, 1.5, 1.6 and 2.0 mm. were analysed. The test results showed that the stiffening effect forms a large contribution to preventing distortional modes of buckling. The increase in wall thickness enhanced buckling stress beyond the yielding strength in short and intermediate columns, but not for the long columns, figure (2-10).

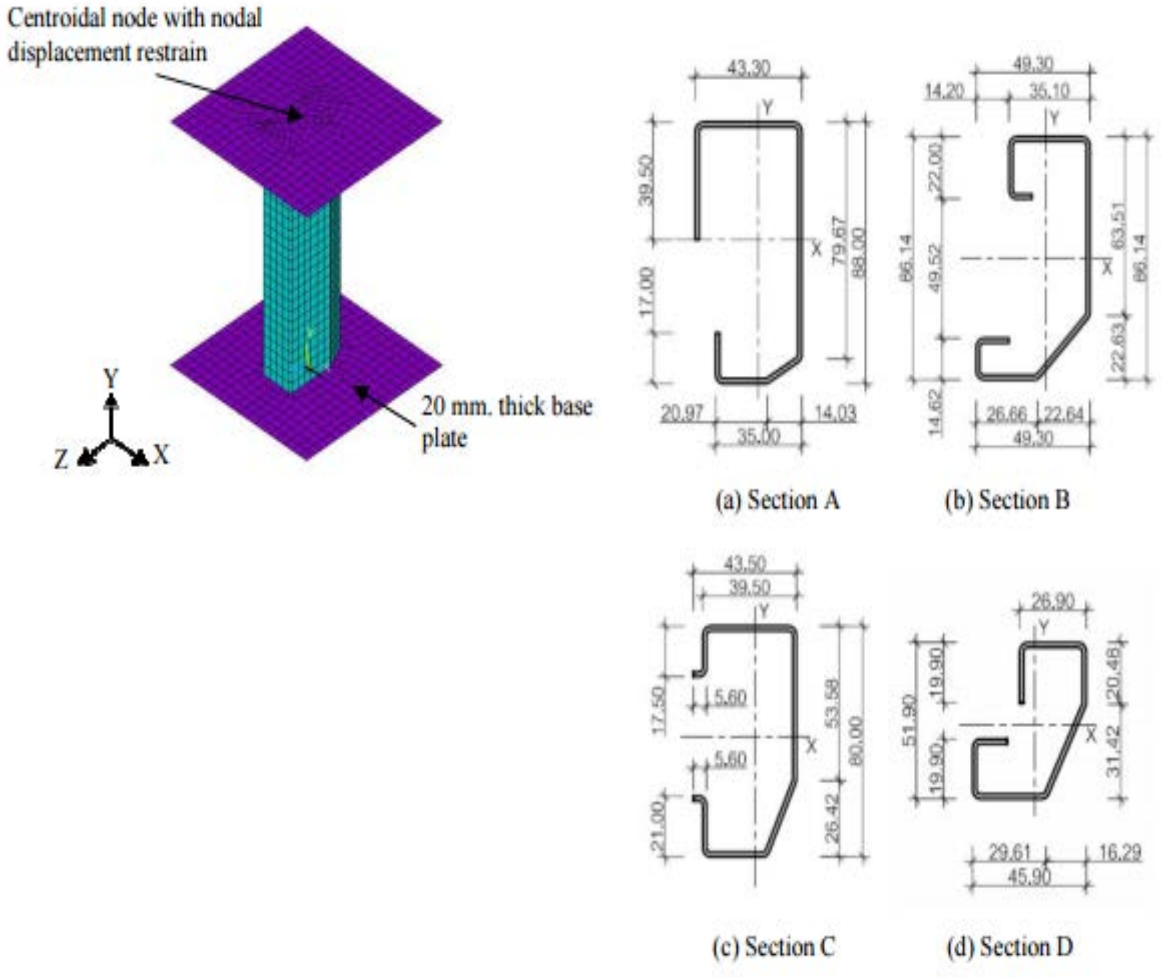

Figure (2-10) 1) Finite element mode. 2) column sections (unit: mm) (Hansapinyo, 2015).

McCann et al. (2016) addressed the Numerical analysis of the local buckling behaviour and ultimate cross-sectional strength of tubular elliptical profiles in compression. After validating the model against previous experimental results, a parametric study comprising a total of 270 elliptical sections was conducted in order to examine the influence of cross-section aspect ratio, geometric imperfections and local slenderness. The obtained ultimate capacities, load–deformation responses and failure modes are discussed in the paper. It was found that for lower cross-section aspect ratios the behaviour of the elliptical hollow sections (EHS) was similar to that of cylindrical shells across a number of metrics; as the aspect ratio increased, more plate-like stable post-buckling behaviour was observed. A design method was proposed for Class 4 EHS members that reflect the reduction in capacity due to local buckling with increasing slenderness, but also recognises the improved post-buckling stability with increasing aspect ratio.

Valarinho et al. (2016), presented results of analytical, experimental and numerical studies on the lateral-torsional buckling (LTB) behaviour of long-span laminated glass beams. The analytical study was mainly focused (1) on the assessment of existing expressions for the determination of the effective flexural and torsional stiffness of 3-layer laminated glass beams and (2) on the determination of the buckling resistance and post-buckling behaviour of long-span laminated glass beams taking into account the influence of changes in the thickness of the glass panes and of the viscoelastic properties of the interlayers. The experimental study comprised a flexural test of a simply supported and unbraced 8.20 m long PVB 3-layer laminated glass fin. Finally, three-dimensional numerical models were also developed in order to simulate the experiments and validate the analytical results. The results obtained showed that the analytical formulae and the numerical tools available are able to accurately predict the LTB behaviour of long-span 3-layer laminated beams. The results also draw attention to the importance of adequately considering the influence of possible thickness reductions on the glass panes and of temperature and loading time effects on the shear behaviour of PVB interlayers.

Craveiro et al. (2016), presented an experimental investigation of the buckling behaviour of compressed single and built-up cold-formed steel columns. Four types of cross-sections were tested, namely, one single, one open built-up and two closed built-up, considering two end support conditions, i.e. pin-ended and fix-ended. The obtained results were compared with the design predictions of EN1993-1-3:2004 and AISI S100-07. For pin-ended lipped channel columns the design predictions were in good agreement with the experimental results, however, for the fixed ended columns, the predictions appeared to be conservative. For built-up columns, it was found that increasing number of different sections may lead to unsafe design predictions, figures (2-11), (2-12) & (2-13).

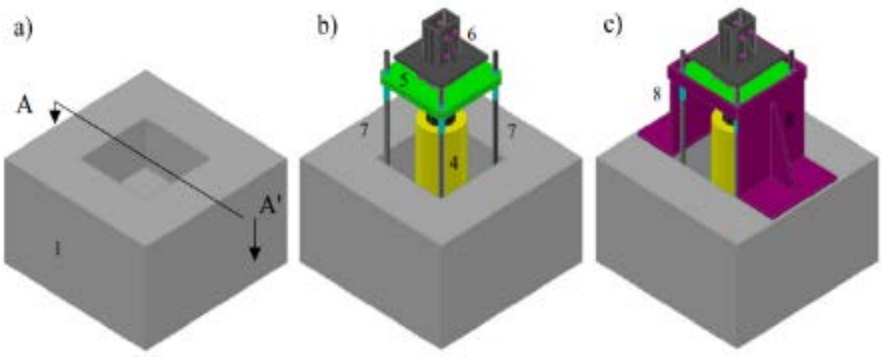

Figure (2-11) Concrete footing schematic view (Craveiro et al. 2016).

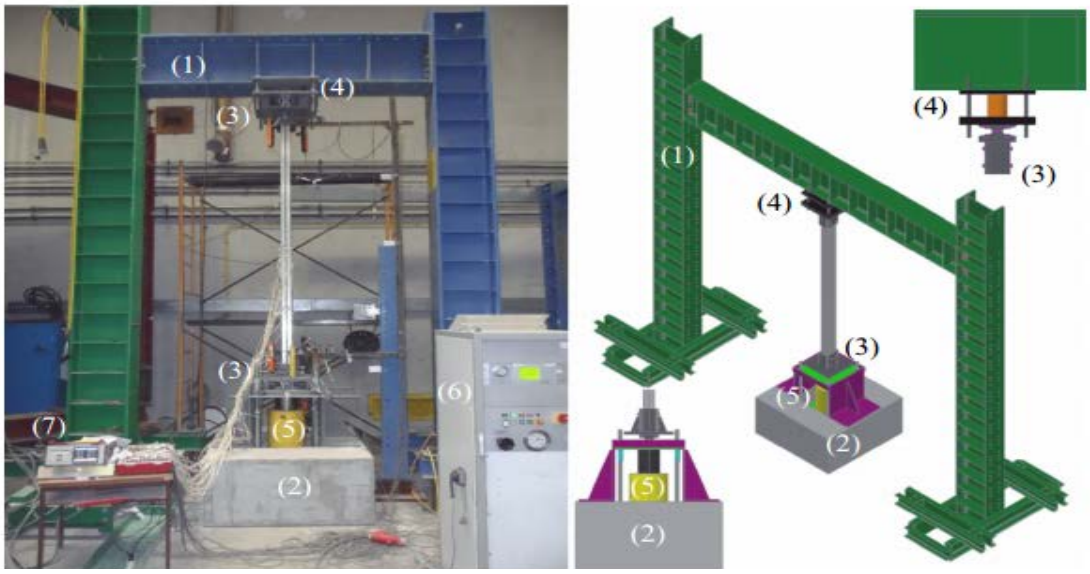

Figure (2-12) Experimental test set-up built for buckling tests (Craveiro et al. 2016).

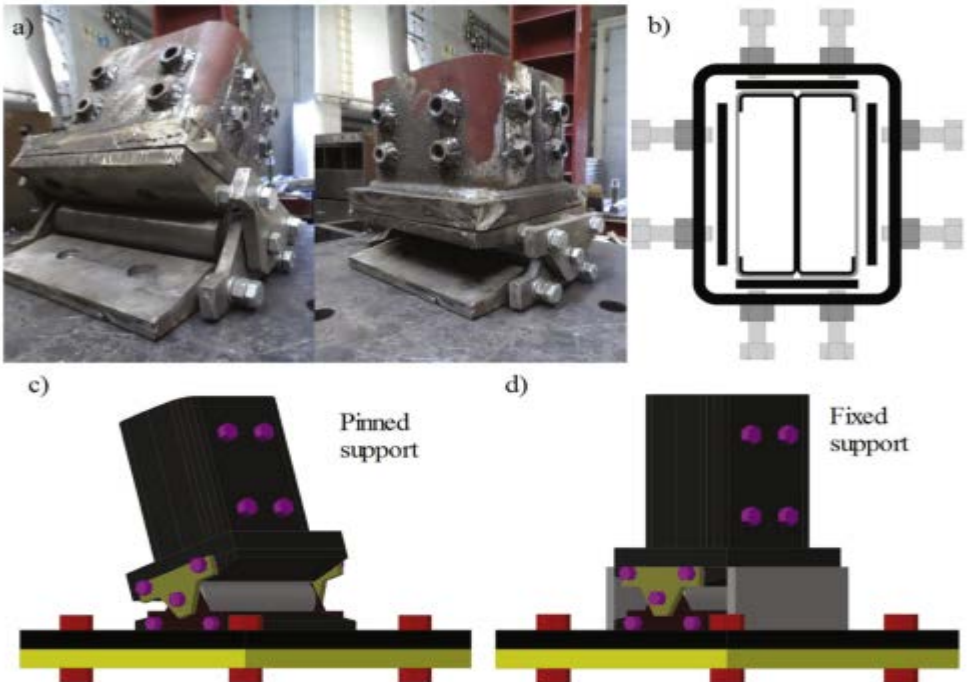

Figure (2-13) End-support devices. (a) general views of the end-support devices. (b) adjustable system adopted to fix each one of tested cross-sections. (c) pin-ended support. (d) fix-ended support (Craveiro et al. 2016).

2.3 Theoretical investigations

A number of researchers have conducted both numerical and theoretical analyses, and have recommended analysis methods for light gauge steel members to predict the buckling loads, modes, and to predict how these structures will behave when subject to axial or flexural

loads. Consequently, various alternative methods of analysis have been introduced and the following section presents these.

2.3.1 Generalized beam theory (*GBT*)

GBT was first presented in the 1960's by a German professor named Richard Schardt. The theory could be interpreted as a combination of the folded plate theory and the Vlasov's theory for thin-walled beams (Simão, 2007).

During the eighties and nineties, several more works on stability analysis using GBT came to light. The first GBT article written in English, contains a brief presentation of GBT for stability analysis and mentions the need to consider a constant shear flow model for closed sections. During the conference where this paper was presented, GBT was introduced to Professor Davies at the University of Salford, (and later of the University of Manchester) – who, by that time, had already realized a vast and very important research work on lightweight steel construction, namely on stressed skin design (Davies and Bryan 1982). Later he would develop several important research avenues regarding the use of GBT, exploring the large potential of this theory to enable a better understanding of the stability behaviour of thin-walled members. So, since the late eighties and under the supervision of Davies, several research works were carried out at Salford and Manchester universities. The first contributions of Davies are associated with Leach (1989) whose PhD thesis contains a detailed description of the GBT procedure for open non-branched sections and an application of GBT to the linear analysis and stability analysis of these sections The finite difference method was used to solve the differential equilibrium equations, exploring to some extent the interaction between the modes of deformation, which correspond to the buckling modes, and benchmarking GBT with other methodologies. As a result of the initial work by Davies and Leach, several strands of research were produced, namely on the first order analysis and stability analysis of open sections submitted to compression and/or bending, exploring the modal interaction between the modes of deformation, containing also some benchmark examples comparing the GBT results with experimental analysis, Leach and Davies (1996). This research ensured that GBT was then spread worldwide. Later, with the collaboration of Jiang, Davies continued applying GBT to study the behaviour of thin-walled members. Jiang (1994) GBT was applied to the stability analysis of purlins. Subsequently, Davies and Jiang continued to apply GBT to explore the distortional behaviour of open sections Davies and Jiang (1996a, 1996b) and the modal interaction of cold-formed members under compression and/or bending Davies and Jiang (1998). More recently, Davies (2000) applied GBT to the study of flange- and web-stiffened

compression members and, in particular, web-perforated sections. Finally, a recent article of (Davies, 2000) is concerned the analysis of thin-walled members with stiffened compression flanges.

2.3.1.1 GBTUL program

Bebiano (2008) GBTUL (an acronym for 'GBT at the University of Lisbon') is a freeware program that performs elastic buckling (bifurcation) and vibration analyses of prismatic thin-walled members. It implements the latest formulations of GBT that (i) accounts for local deformation and (ii) provides an advantageous representation of the deformation field, as a combination of structurally meaningful cross-section deformation modes.

Taking advantage of the GBT model features, the program provides information and visualisation of the member deformation modes. Moreover, it contains tools that make it possible to select the deformation modes to include in the analysis, thus allowing for an in-depth insight into the mechanics of the problem being solved. It is possible to analyse members (i) made of one or several isotropic or orthotropic materials, and (ii) exhibiting various common support conditions (e.g., simple supports, fixed supports or free ends). In the buckling analyses, the user is able to specify any combination of arbitrary axial force, bending moment and bi-moment (longitudinal) diagrams, see Figure (2-14).

Davies and Jiang (1996a), introduced the basic principles of GBT and showed how this theory may be used to analyse cold-form sections in which distortion of the cross-section is significant. The calculation is illustrated by detailed numerical examples.

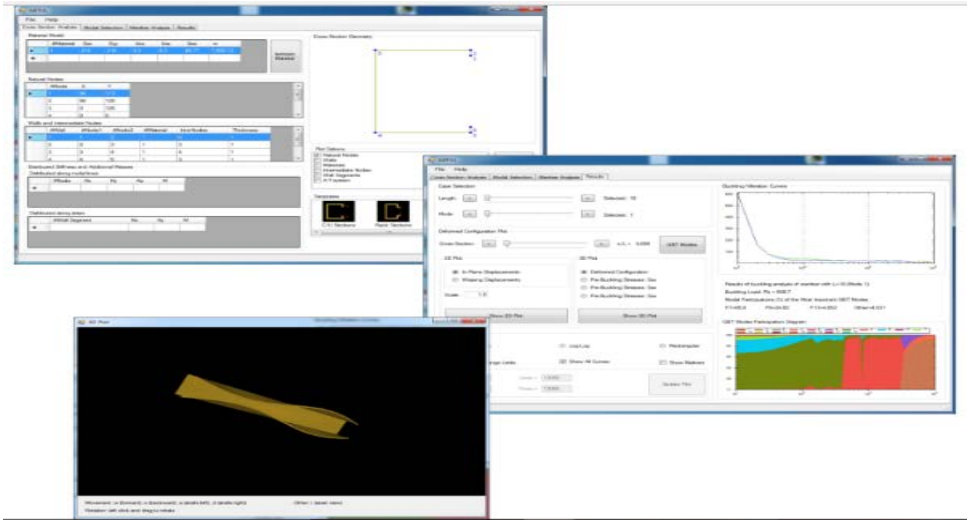

Figure (2-14) GBTUL program views (Bebiano et al, 2008).

Davies and Jiang (1996b) introduced the second order terms associated with geometric non-linearity into the basic equations for the load to cause buckling in individual modes under either axial load or uniform bending moment. Then they showed how the explicit procedure can be extended to consider the interaction between local, distortional and global buckling modes.

The generalized beam theory is applicable to prismatic structural members to take into account the in-plane flexural and distortional cross section deformations and can be used to examine the three generic buckling modes and their interaction (Silvestre, 2007). The second order GBT was developed and introduced as an appropriate method for coupled stability problems by Schardt (1994), and then the GBT method was extensively used for investigating the elastic behaviour for open cross sections fabricated from cold-formed steel (Tomà and Wittemann, 1994). The early formulations of this theory were limited to isotropic thin-walled members to analyse the elastic buckling of unbranched open cross sections. New formulations of GBT were developed by Silvestre and Camotim (2003) to make the theory applicable to open branched and closed cross sections. This was followed by another formulation of the GBT developed by Gonçalves et al. (2009) and this new formulation was more general and capable of dealing with closed and open branched sections, with the applications' domain of the GBT being extended to deal with the curved-wall members by Silvestre (2007).

Silvestre and Camotim (2006) presented GBT formulation for analysing the vibrational behaviour of loaded composite thin-walled members, which accounts for the effects of (i) cross-section in-plane deformation, (ii) shear deformation, (iii) geometric and material coupling, (iv) primary, secondary and non-linear warping, and (v) rotary inertia. Then they used the results to investigate the local and global vibration behaviour of lipped channel columns and beams displaying cross-ply orthotropic. They focused on issues dealing with the variation of the fundamental frequency and the vibration mode in relation to the member length and applied stress level. For validation purposes, they used some GBT-based results to compare with values obtained by means of 4-node shell model constructed using finite element analyses (ABAQUS).

Silva et al. (2008), presented the formulation and illustrated the application of a novel GBT implementation able to handle the influence of localised effects on the buckling behaviour of prismatic thin-walled members (e.g., cold-formed steel profiles). For instance, the formulation accounted for effects stemming from (i) the position of transverse loads (with respect to cross-section shear centres) or (ii) the occurrence of web buckling phenomena (e.g.,

the web crippling). In order to achieve this goal, the GBT formulation traditionally employed in buckling analyses was enhanced by including specifically: (i) non-linear terms and (ii) transverse extension modes. They stated that the GBT formulation/implementation is a very advantageous alternative to shell finite element analyses, the only available method to capture the localised effects rigorously. They presented and discussed numerical results concerning the buckling behaviour of (i) hat and I-section cantilevers acted upon by transverse tip point loads applied at various cross-section points, and (ii) I-section simply supported beams under top-flange distributed and point loads. One also assesses how end support transverse web stiffeners improve the beam buckling behaviour to illustrate the application and capabilities of the proposed GBT formulation-implementation. For validation, the GBT results were compared with previous values reported by ABAQUS shell finite element analyses.

Silvestre et al. (2013) addressed the development and illustrated the application of GBT formulation intended to perform first-order elastic-plastic analyses of thin-walled members comprised of isotropic nonlinear materials exhibiting strain-hardening. Its application is illustrated through the analysis of (i) simply supported Z-section beams and (ii) fixed-ended lipped channel beams. In both cases, a bilinear elastic-plastic material model is adopted. The results presented and discussed consist of equilibrium paths, modal participation diagrams, beam deformed configurations and stress diagrams and contours. For validation purposes, most of the GBT results were compared with values obtained from shell finite element analyses with a few relatively minor exceptions, a very good correlation was found as shown in figure (2-15).

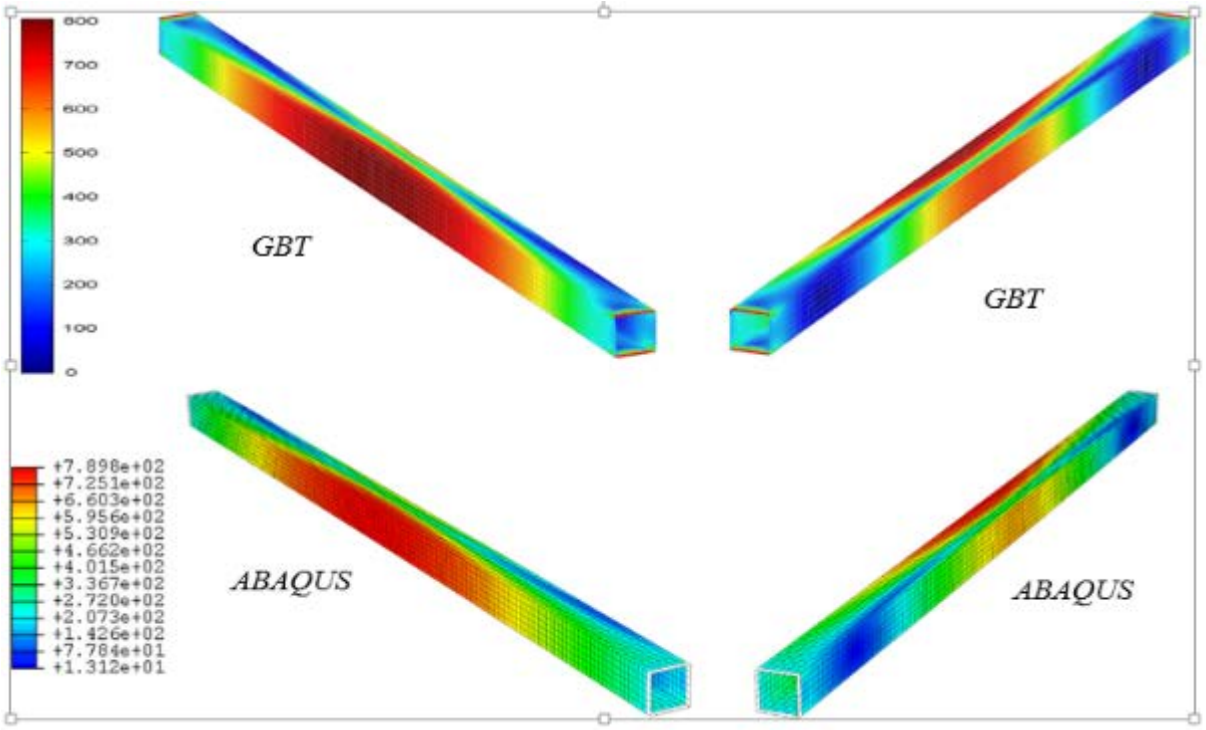

Figure (2-15) Von Mises stress (O_{mises}, N/mm^2) contours at equilibrium state: column sides under (a) compression and (b) tension, (Silvestre et al., 2013)

Abambres et al. (2014), presented a formulation of GBT intended to perform first-order elastic–plastic analyses of thin-walled members experiencing arbitrary deformations and made of non-linear materials exhibiting isotropic hardening. After presenting the GBT fundamental assumptions and kinematic relationships, the member nonlinear equilibrium equations are derived and a non-linear one-dimensional (beam) finite element is formulated. The arc-length control technique is adopted in the numerical solution of the non-linear equations and J2-flow theory is used to model plasticity in conjunction with the Backward Euler return mapping algorithm. In order to show the capabilities and potential of the implemented formulation, a set of numerical illustrative examples are presented and discussed. For validation purposes, most of the GBT results obtained (equilibrium paths, modal participation diagrams, displacement profiles, stress distributions and deformed configurations) are compared with values yielded by ABAQUS shell finite element analyses, figure as shown in (2-16).

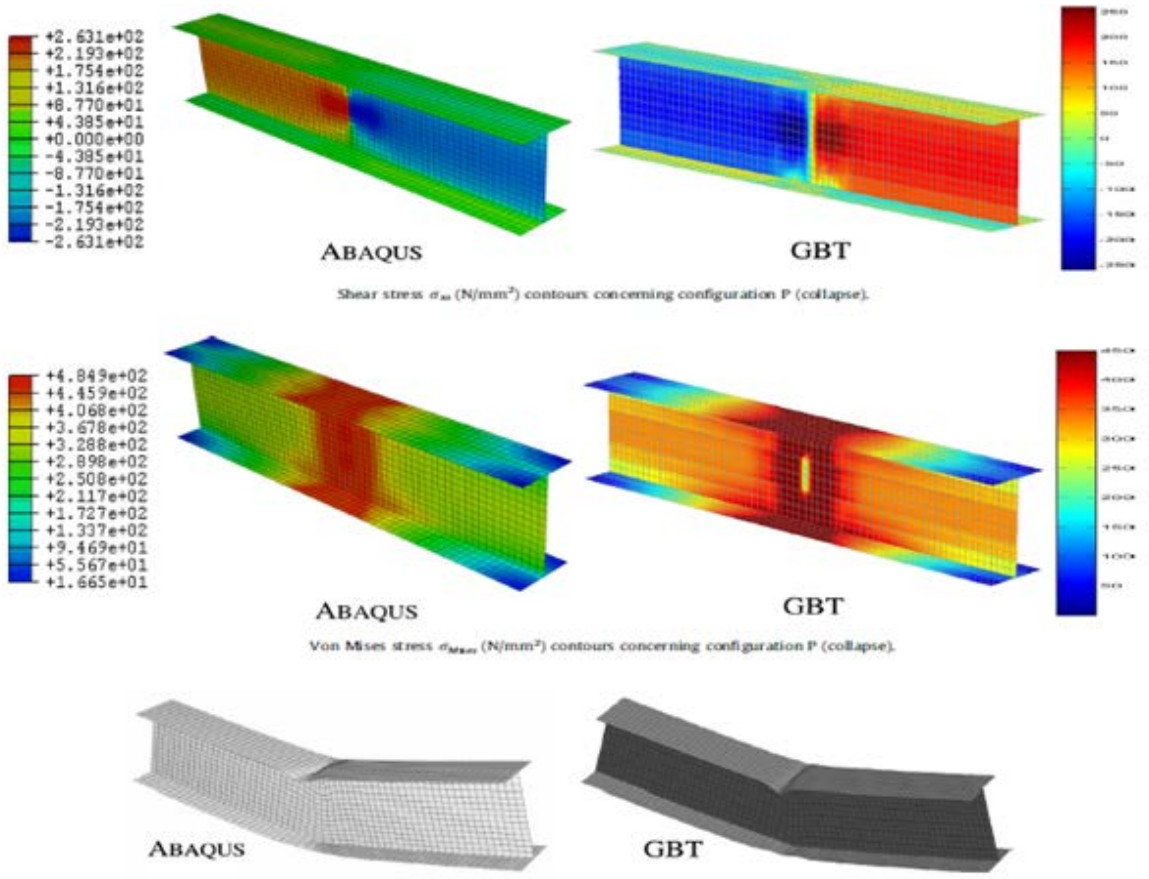

Figure (2-16) Beam deformed shape in both GBT & ABAQUS (Abambres, Camotim and Silvestre, 2013).

Taig and Ranzi (2014), presented an extension to GBT approach to describe the response of prismatic thin-walled members stiffened by means of generic plate arrangements at different cross-sections along their length. Two numerical procedures were implemented to account for the presence of the stiffeners. One approach identified different sets of deformation modes for the unstiffened and stiffened sections, which were then combined for the member analysis. The second procedure relied on the use of constraint equations at the stiffened locations to be included in the member analysis. Two numerical examples were provided to highlight the ease of use of the method of analysis considering open and partially-closed sections, and their results were validated against those obtained with the commercial finite element software ABAQUS.

Abambres et al. (2014), presented the main concepts and procedures involved in the development of a geometrically and materially non-linear GBT formulation and numerical implementation (code), intended to analyse the behaviour and collapse of thin-walled members made of materials with a highly non-linear stress–strain curve (e.g., stainless steel or aluminium). The second objective was to validate and illustrate the application of the proposed

GBT formulation, by comparing its results (equilibrium paths, ultimate loads, deformed configurations, displacement profiles and stress distributions) with those provided by shell finite element analyses of two square hollow section (*SHS*) columns previously investigated, both experimentally and numerically. The stainless steel material behaviour was modelled as non-linear isotropic and the *GBT* analysis included initial geometrical imperfections, but neglected corner strength enhancements and membrane residual stresses. It is also shown that the *GBT* unique modal nature makes it possible to acquire in-depth knowledge concerning the mechanics of the column behaviour, by providing 'structural x-rays' of the (elastic or elastic–plastic) equilibrium configurations: modal participation diagrams showing the quantitative contributions of the global, local, warping shear and transverse extension deformation modes.

Moreover, this feature makes it possible to exclude from future similar *GBT* analyses, those deformation modes found to play a negligible role in the mechanics of the behaviour under scrutiny, thus further reducing the number of degrees of freedom involved in a *GBT* analysis, i.e., increasing its computational efficiency.

Basaglia et al. (2015) reported the results of an investigation on the use of *GBT* to assess the buckling and vibration behaviours of thin-walled members and frames built from cold-formed steel circular hollow section *(CHS)* profiles. Initially, the concepts and procedures involved in performing *GBT* buckling and vibration analyses are presented, paying particular attention to the derivation of the mass tensors that account for the influence of the inertia forces. Then, the formulation, numerical implementation and validation of a GBT-based beam finite element for isolated members are described. Next, the determination of the frame linear stiffness, geometric stiffness and mass matrices, which incorporate the influence of the frame joints, is addressed. Finally, in order to illustrate the application and capabilities of the proposed GBT finite element formulation, numerical results are presented and discussed, they concern the buckling and vibration behaviours of an "L-shaped" frame.

2.3.2 Finite element method (FEM)

The Finite Element Method is one of the numerical methods which is used to solve the differential equations for a structure or structural component through computer software. It is also considered a powerful method of analysis since it can deal with multiphase problems, by utilising the appropriate *FEM* techniques. Applied loads can be positioned on any required member and in any direction. It can provide a huge amount of data concerning the solved structure for a given load such as stresses, strains, deformations and reactions. Non-linear

stress-strain curve relationships can be incorporated into the analysis, as well as non-linear geometry. It can be used to model the contact between connected elements by using links, point-contact elements and compression or tension only members. Complex boundary conditions and perforations can be examined and included within the model for a structure. It is difficult to use *FEM* for practical design, because of the cost and the time consumed in data preparation, so it is generally used as a primary method for research purposes. It should be noted that great care is needed in setting up the required boundary conditions for accurate results meaning that this process may take a significant amount of time and require experienced personnel to use the software.

A series of elastic buckling and nonlinear finite element analyses was carried out using the developed finite element model of simply supported cold-formed steel lipped channel beams subjected to lateral-torsional buckling. Elastic lateral-torsional buckling moments (M_o) and ultimate moment capacities (M_u) were obtained from these analyses. Lateral-torsional buckling of mono-symmetric lipped channel beams is likely to depend on a range of parameters such as beam span, initial geometric imperfections, residual stresses, yield stress, modulus of elasticity, steel thickness, web depth to flange width (d/b) ratio, etc.

At present, finite element analysis programs are extensively used and have greater importance in the field of research. This trend is increasing as the use of finite element analysis programs is relatively inexpensive and time efficient compared with a large number of full-scale tests. The finite element analysis program ANSYS is a very important tool that is widely used in engineering applications. It can be used to solve problems ranging from relatively simple linear analyses to complex nonlinear analyses. Finite element analysis using ANSYS usually consists of three major stages: pre-processing, analysis, and post-processing. In the pre-processing stage, the model of the physical problem is created which includes creating a suitable finite element mesh, assigning appropriate material properties and applying relevant boundary conditions in the form of restraints or loads. In the analysis phase, the numerical problem defined in the model is solved. Once the analysis is completed, results are evaluated in the post-processing stage.

Pi and Trahair (1995) theoretically investigated the lateral buckling strengths of cold-formed steel rectangular hollow sections. Finite element models were developed which used realistic stress-strain curves, residual stresses and initial imperfections. They found that the cross-section shape has a significant effect on the lateral buckling strengths. The comparison of results obtained for RHS beam and I-section beam showed that the capacities of I-section beams are lower than for RHS beams, figure (2-17). The use of a strain-hardening stress-strain curve instead of a trilinear curve for the corners of the RHS was found to be less effect on ultimate moment capacity in the high slenderness region while there is moderate effect at low slenderness. The effects of initial twist were found to be very important while the effects of initial crookedness were less important than for hot-rolled I-sections. A different design equation to that used for hot-rolled I-sections was developed for RHS beams

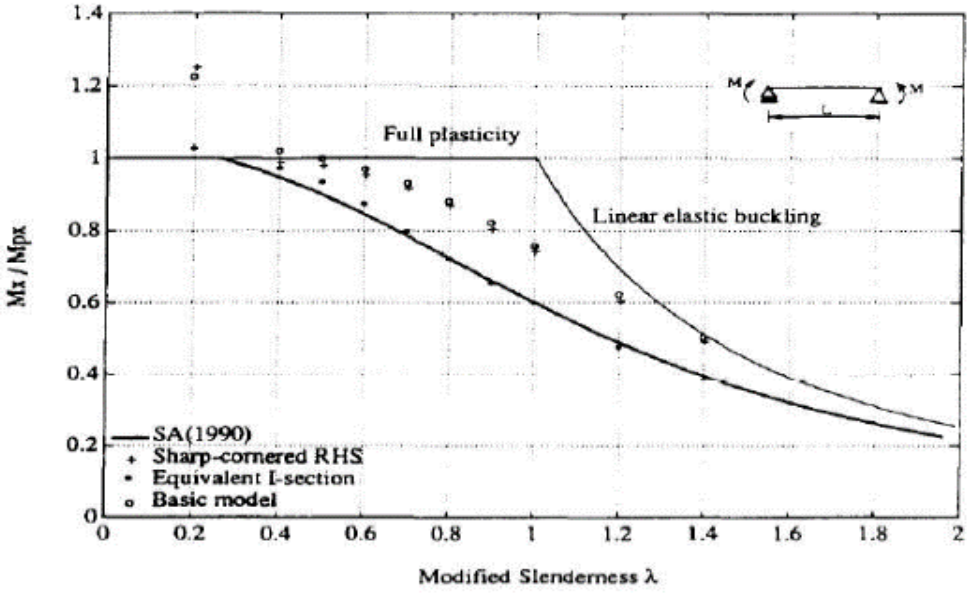

Figure (2-17) Comparison of lateral-torsional buckling strengths of RHS and I-section beams (Pi and Trahair, 1995).

Davies and Jiang (1996b), presented non-linear finite element analysis of cold-formed steel using ABAQUS version 5.4, In this study, the eigenvectors from linear Eigen solutions were introduced as the imperfections in non-linear finite element analyses. However, in the opinion of the authors, this may not have been sufficiently accurate because the patterns of linear buckling and nonlinear buckling could be different due to nonlinear behaviour.

Bailey et al. (1996) conducted finite element analysis of restrained and unrestrained simply supported beams subjected to loading at the shear centre of the cross-section under uniform elevated temperature conditions. The finite element software they used was based on

a non-linear spread-of-yield, the program was originally written by (El-Zanaty and Murray (1983) to study the two-dimensional behaviour of steel frames at ambient temperature. This software was later modified, firstly by Saab and Nethercot (1991) to include elevated temperature effects and more recently extensively reformulated by Najjar (1994) and Najjar and Burgess (1996) to analyse three-dimensional frame behaviour including warping behaviour in fire conditions. This program used two noded one-dimensional line elements with eight degrees of freedom in local coordinates. In the finite element analysis facilities have been provided to incorporate geometric non-linearity together with variation in cross-sectional properties. This software was further modified by Bailey et al.(1996) to include flexural shear stresses to enhance the accurate prediction of lateral torsional buckling effects for loads placed at any level on a cross-section. The ability of software to predict lateral torsional buckling has been checked at ambient temperature with theoretical bifurcation solutions in the elastic range and with experimental and computational results in the inelastic range. They used the results of full-scale tests carried out by Kitipornchai andTrahair (1975) to validate the model for inelastic lateral torsional buckling.

A FEM for stainless steel compressed columns of lipped channel cross sections with short to medium lengths was verified by Macdonald and Rhodes (2005) with experimental results. The finite element analysis showed a good agreement with the experimental results of the load capacity.

Young and Yan (2000), presented a numerical investigation into the behaviour and strengths of cold-formed plain and lipped channel columns using FEA. A non-linear finite element model was developed and verified against the fixed-ended channel column tests conducted by Young and Rasmussen (1998a, 1998b and 1998c). Geometric and material non-linearity were included in the finite element model. It was demonstrated that the finite element model closely predicted the ultimate loads and the behaviour of the tested cold-formed channel columns. Hence, the model was then used for an extensive parametric study of cross-section geometries. Furthermore, the results of the numerical investigation were compared with the design column strengths calculated using the Australian and New Zealand Standard (1996), Amercan (Schafer (1998)) and European (Yu (2000)) specifications for cold-formed steel structures. It was shown that the design column strength (Mahaarachchi and Mahendran, 2005) calculated from the three specifications are generally conservative for plain and lipped channels having a maximum plate thickness of 6.0 mm.

Mahaarachchi and Mahendran (2005), developed a finite element model to investigate the lateral distortional buckling behaviour of Light Steel Beam (LSB) sections. The model accounted for all significant behavioural effects including material inelasticity, local buckling and lateral distortional buckling deformations, member instability, web distortion, residual stresses, and geometric imperfections. They modelled half of the beam taking advantage of symmetry. The S4R5 elements which are thin, shear flexible, isoperimetric quadrilateral shell with four nodes and five degrees of freedom per node. The analysis utilised reduced integration and bilinear interpolation schemes.

Lecce and Rasmussen (2006) made an assessment for the distortional buckling rules in current design guidelines for lipped channels formed from stainless steel undergoing compression loading. The effect of intermediate stiffeners was discussed in this study. They tested two groups of channels: with and without intermediate stiffeners, using experimental data and a simulation using the finite element analysis model. The tests showed that the distortional buckling mode was the critical failure mode for most samples, and an interaction of local and distortional buckling was observed in one shorter length channel.

Yu and Schafer (2006), developed a nonlinear finite element (FE) model to simulate two series of flexural tests, previously conducted by the authors, on industry standard C and Z-section cold-formed steel members. The first test series focused on local buckling failures and the second on distortional buckling failures, see figure (2-18). The objectives of this paper were to (i) validate the developed FE model, (ii) apply this model in a parametric study outside the bounds of the original tests with a particular focus on yield stress, and (iii) study the influence of moment gradient on distortional buckling failures. The predicted ultimate strengths from the developed FE model showed good agreement with the test data. Extension of the tested sections to cover yield stresses from 33.0 to 73.4 ksi (228 to 506 Mpa) indicated that the Direct Strength Method (DSM) is applicable over this full range of yield stresses. The FE model was also applied to analyse the effect of moment gradient on distortional buckling. It was proposed and verified that the moment gradient effect on distortional buckling failures could be conservatively accounted for in the DSM by using an elastic buckling moment that properly reflects the increased elastic distortional buckling moment due to the presence of moment gradient. An empirical equation, appropriate for use in design, to predict the increase in the elastic distortional buckling moment due to moment gradient, was provided.

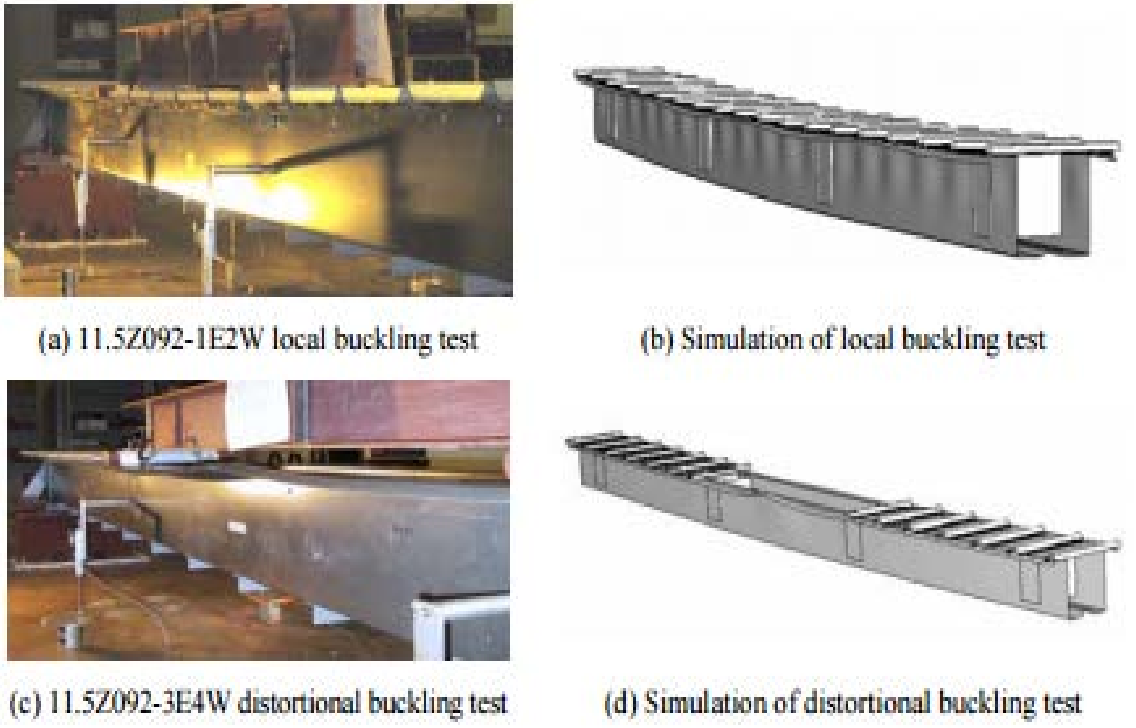

Figure (2-18) General comparison of test and FE models (Yu and Schafer, 2006)

Ben Young and Ellobody (2007), investigated the behaviour and design of unequal angle cold-formed steel columns by using a nonlinear finite element analysis. Sivakumaran and Abdel-Rahman (1998), developed a finite element analysis model to investigate the local and post-local buckling behaviour as well as the capacity of axially compressed members of channel cross-section fabricated from cold-formed steel.

Ali et al. (2011), presented a study on the structural performance of column-base and beam-column connections of cold-formed steel with the use of single-lipped C-sections with bolted moment connections. Experiments were done on two specimens; a column base connection and a beam-column connection and the results showed that section failure caused by flexural buckling was always critical. Managing to attain moment resistances which were close to the results of connected sections, it was proven that the proposed connections were structurally efficient. Finite element models were established with the use of shell elements to model the sections while bar elements were used to model the bolted fastenings for the purpose of examining the structural behaviour of both the column base and the beam-column connections. Incorporation of material non-linearity and comparison between the experimental and numerical results were presented. The proposed analysis method for predicting the

structural behaviour of column-base and beam-column connections with similar connection configuration proved to be adequate.

Thombare et al. (2016), addressed the numerical linear and nonlinear buckling analysis of 2-D cold-formed steel simple cross-aisle storage rack frames. The main focus of the study was to ascertain the stability of 2-D frames of a pallet racking system. With this objective, a pallet racking system with cold-formed steel sections is simulated by three-dimensional models using shell elements in ABAQUS. Linear and nonlinear buckling analyses were carried out on these frames. Results were obtained from finite element analysis of frames with 12 types of column sections. Spacer bars and channel stiffeners were used to improve the torsional strength of original open cross sections. Results show that spacer bars and channel stiffeners are very effective in enhancing the strength of cold-formed steel pallet rack structures, figures (2-19) & (2-20).

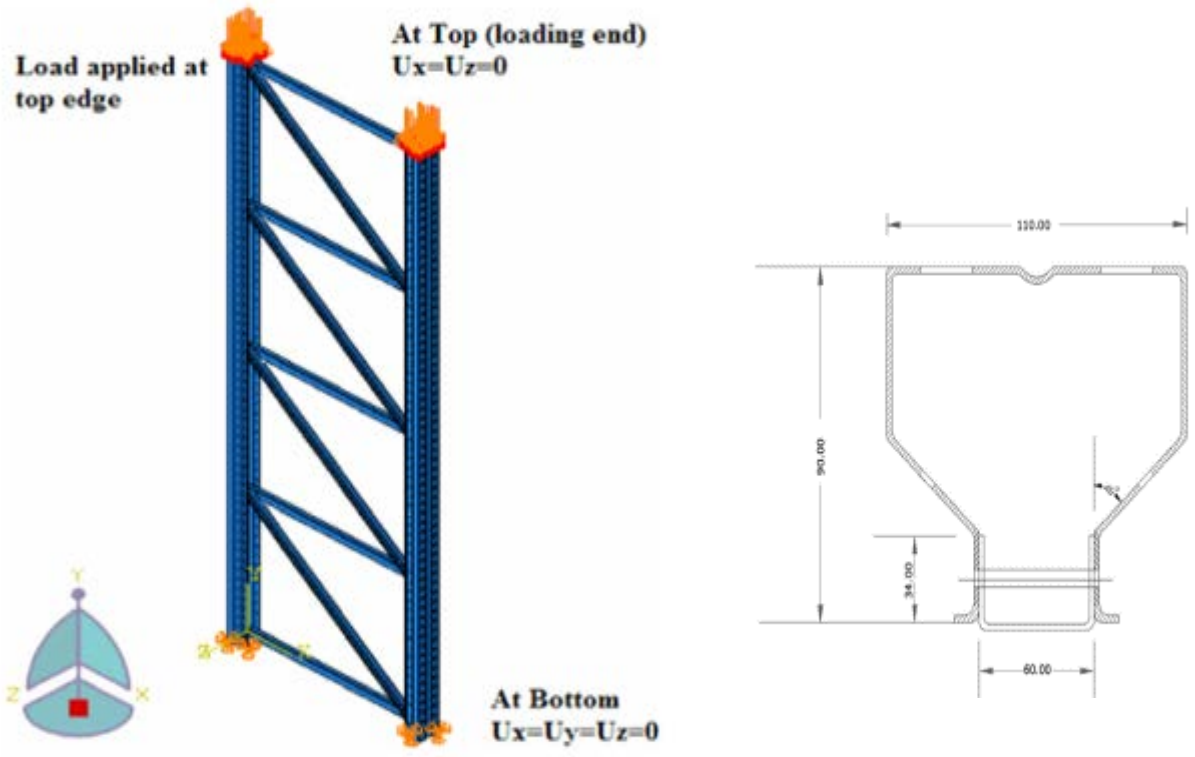

Figure (2-19) Torsional strengthened MW/HW upright section with channel stiffener and its boundary condition rack system (Thombare et al., 2016).

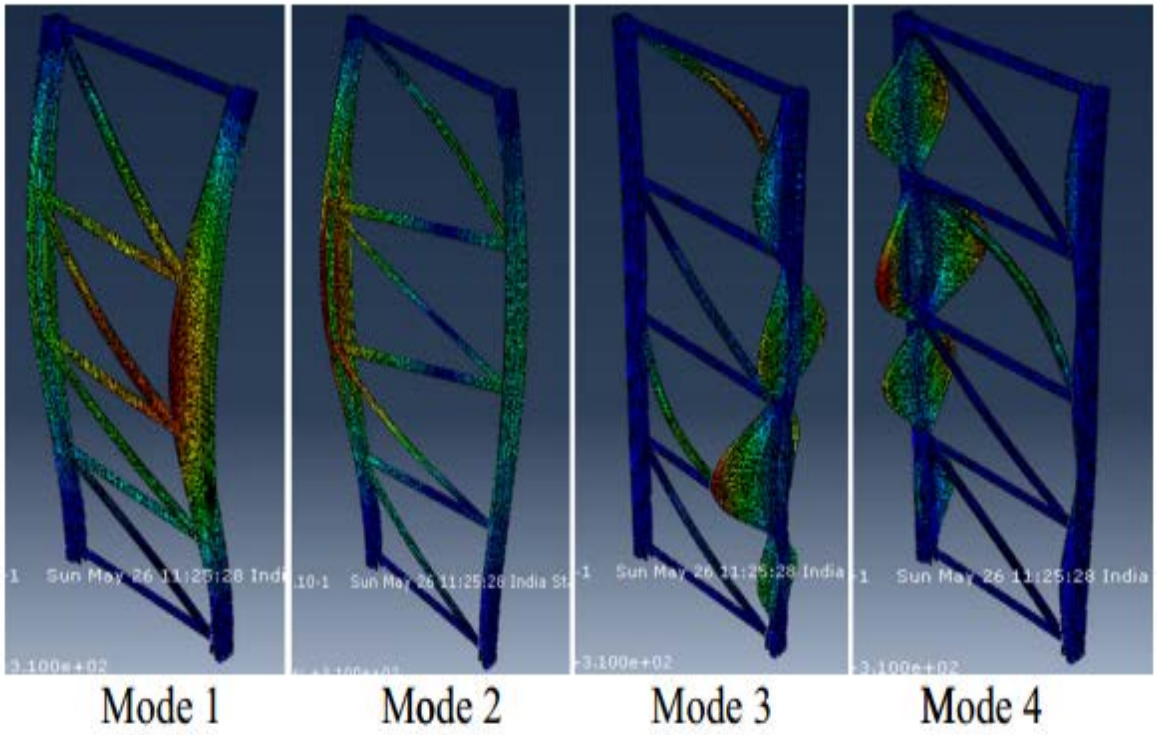

Figure (2-20) Eigen buckling analysis modes for frame MWB2-1.6 mm thickness (Thombare et al., 2016).

2.3.3 Finite strip method

The finite strip method is seen as a semi-numerical, semi-analytical approach. Compared with the finite element method for forming and solving the structural equations, it has the advantage in that it requires less time to build a model and also solves in a shorter time. The finite strip method is considered to be an efficient tool in analysing members with geometrical properties assumed to be constant along the longitudinal axis of the member. It assumes simply pinned end boundary conditions. End conditions other than pinned are difficult to model with this method.

2.3.3.1 CUFSM program

CUFSM is a finite strip analysis program developed by Cornell University researchers, (Schafer, 2006). It provides a convenient and efficient way to determine the elastic buckling stresses and corresponding buckling modes (local, distortional and lateral torsional) of thin-walled structures. However, this analysis can only be performed for simply supported thin-walled members. CUFSM program depicts buckling as a plot of load factor versus half

wavelength of the buckled shape, it also shows the range of half-wave lengths for different buckling modes. The minima points of the curve can be considered to represent the critical buckling loads and buckling modes for a member. The load factor, in the case of bending, is defined as the ratio of elastic buckling moment to the yield moment. The CUFSM program can also be used to calculate the section properties of thin-walled cross-sections, figure (2-21).

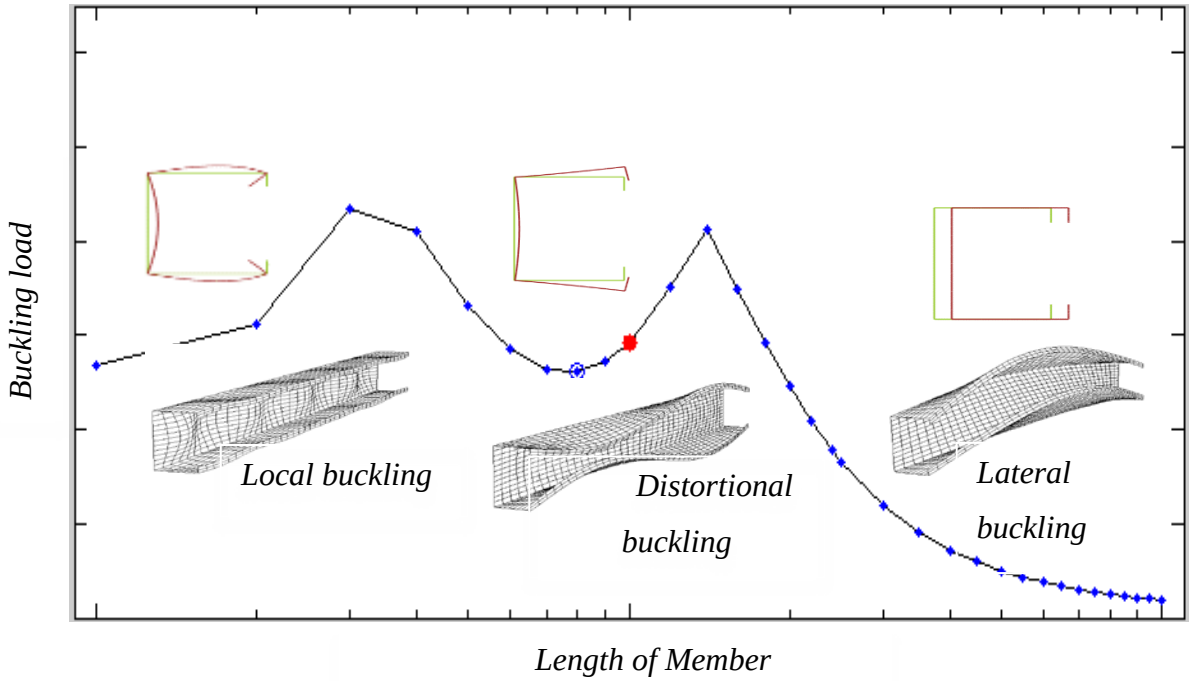

Figure (2-21) Buckling modes vs member length.

adequate edge stiffeners and concluded that for a plane channel, the buckling strength is greatly increased by providing edge stiffeners, and showed that the edge stiffened channels experience a significant amount of post-buckling capacity when they are axially loaded. He was one of the first researchers to use the finite strip method.

Schafer (2002) stated that North American design specifications do not take into account the interaction of the local buckling of cold-formed steel columns; furthermore, there is no explicit check for distortional buckling. The predictions of the three buckling modes were discussed for zed and lipped channels in his study and he considered the interaction of global buckling with local and the distortional buckling modes by the direct strength method that he proposed for column design. Separate strength curves for local and distortional modes are included in this method. This method appears to be easy to apply and provides accurate results for sections examined by Schafer (zed and lipped channel), but for racking columns members

which have perforations and complicated details concerning the restraint conditions, the finite element method may be more accurate.

Key and Hancock (1988) studied large deflection elastic-plastic analysis to calculate the non-linear local buckling behaviour of thin-walled and cold-form steel sections in compression using the finite strip method of structural analysis. The analysis accounts for plate geometric imperfections, the variation of yield stress around a section, the stress-strain characteristics of the material forming the section and complex patterns of residual stress produced by the cold-forming process. Besides that, they made a comparison between the results of plates with a rounded stress-strain curve typical of cold-formed steel and aluminium.

de Barros Chodraui et al. (2006) state that the probability of local buckling is greater than distortional buckling for a member without edge stiffeners. But this is not necessarily the case of racking upright sections as confirmed by (Hancock et al., 1994) where their research was aimed at finding the capacity of unlipped rack upright sections undergoing distortional buckling by using the finite strip method.

2.3.3.2 Direct strength method (*DSM*)

The Direct Strength Method (DSM) is a relatively new design method for CFS members validated for members using the finite strip method results to predict the ultimate strength of a general CFS column or beam with the elastic buckling properties of the member cross section (e.g., plate buckling) and the Euler buckling load (e.g., flexural buckling).

Dawe (2002) stated that Cheung published the first finite strip method paper in 1968 for two opposite simply supported rectangular plates. Since then, thin curved plate finite strips have been used in the analysis of shell structures by a number of researchers. Lau and Hancock (1986) employed this method to study the buckling of flat plate structures with direct and shear stress effects. An elastic finite strip method was developed for plate assemblies by Lengyel and Cusens (1983) to study post-buckling behaviour. Hancock et al. (1994) developed a geometrically non-linear analysis of flat plate structures by utilising this method. Hancock and other well-known researchers such as Pekoz and Rhodes have since prepared computer software programs for this method.

Young et al. (2012), investigated the ultimate strength and design of fixed-ended lipped channel columns experiencing local-distortional buckling mode interaction. First, they reported

the results of an experimental investigation involving a set of 26 columns with several cross-section dimensions and yield stresses that were tested to determine their failure loads and also to provide experimental evidence of the occurrence of local-distortional mode interaction. These results consist of the column geometries, material properties, initial geometric imperfections, nonlinear equilibrium paths, and ultimate strength values. Then, after comparing the experimental column ultimate loads with the estimates provided by the current direct strength method (DSM) design curves against local and distortional failures. However; in the opinion of the authors, it clearly shows that they lead to inaccurate and often very unsafe ultimate strength estimates, the paper presents and assesses the quality of DSM-based design procedures based on approaches providing nominal strengths against local-distortional and distortional-local interactive failures. Next, an in-depth comparison is made between all the experimental ultimate strength results available in the literature and their estimates provided by the preceding DSM design procedures. Finally, the results were close with design considerations and recommendations, motivated by the conclusions drawn from this investigation.

Cava et al. (2016), presented the results of a numerical investigation concerning the relevance and Direct Strength Method (DSM) prediction of the ultimate strength erosion caused by local-distortional-global (LDG) interaction in cold-formed steel fixed-ended lipped channel columns. The geometries of the columns analysed (cross-section dimensions and lengths) were carefully selected to ensure that the three competing critical buckling loads were not more than 20% apart, thus guaranteeing a fairly high level of LDG coupling. In order to cover a wide slenderness range, several yield stresses were considered, falling below, in-between and above the lowest and highest critical buckling stresses. After providing a brief description of the column selection procedure, which is based on buckling analyses performed with (GBT), the methodology adopted to identify the most detrimental initial geometrical imperfection shape (in the sense it minimises the column strength) is addressed. Then, columns containing those initial geometrical imperfections were axially loaded up to failure, by means of ABAQUS shell finite element analyses (SFEA), making it possible to acquire in-depth knowledge of the behaviour of lipped channel columns undergoing LDG interaction and gather considerable failure load data. Finally, they predict failure loads and use the obtained data to assess whether the available design approaches are able to handle adequately the ultimate strength erosion caused by the triple interaction phenomenon under investigation.

2.4 Literature review summary

In this chapter, an extensive literature review was presented, gathering information in the following areas, showing that:

- The use of cold-formed steel in various constructions is increasing because its light weight makes construction easier and more economical compared to hot-rolled steel.
- Several researchers have found that the cold-forming process, particularly by cold-rolled forming, can alter the mechanical properties of cold-formed steel sections due to strain hardening and strain ageing. The design standards allow the use of increased yield strength resulting from cold-working.
- Cold-formed steel flexural members may be subject to complex stability problems because of the thinness of the plate elements. Generally, cold-formed steel beams may undergo four types of buckling modes: local buckling, distortional buckling, lateral distortional buckling and lateral torsional buckling.
- Previous research on cold-formed steel beams regarding experimental investigations of real buckling failures, demonstrate the expected failure bucking mode and simulation of the intended boundary conditions.
- Previous research on cold-formed steel using first and second order Generalized Beam Theory was successfully employed to solve buckling problems.
- Previous research on cold-formed steel using Finite Element Analysis Method, regarding the element type's effects, material properties representations, mesh size effects, perforations effects and boundary conditions was stated. Earlier researchers have used finite element analysis methods to investigate the flexural behaviour of steel beams. They had shown that the behaviour of cold-formed steel flexural members can be accurately studied using finite element analyses provided that the end support and loading conditions, residual stresses, geometric imperfections and mechanical properties are included in the finite element model accurately. Suitable element size and type must be used and the model has to be validated with sufficient experimental results.
- Geometric imperfections in cold-formed steel flexural members cause considerable reduction of the ultimate strength. Therefore, considerations of the geometric imperfections in design capacity calculations and also in finite element analysis are important.

- Previous research on cold-formed steel using the Finite Strip Analysis Method, namely the CUFSM program with its applications and code design method of Direct Strength Method (DSM) was studied.

It appears that there is a lack of research that has been conducted to date, to study the actual buckling loads of cold-formed steel beams with their effect of geometric imperfections by using both the GBT and FE Analysis Methods, and how to represent the right pinned and fixed end conditions in both the analytical methods and experimental tests.

CHAPTER THREE

FORMULATION OF THE GENERALIZED BEAM THEORY

CHAPTER THREE

FORMULATION OF THE GENERALIZED BEAM THEORY

3.1 Introduction

In general, the GBT describes the behaviour of an open section member under applied load with several corresponding modes of behaviour according to specific warping displacement functions; GBT can be divided into two main groups of modes i.e., rigid body beam modes (first four modes) and higher order distortional and local modes. The first four modes correspond to the axial extension, major and minor axis bending and torsion; these modes exactly match the conventional theories (rod-theory, *Euler-Bernoulli beam theory* and non-uniform torsion or *Vlasov torsion theory).*

3.2 Rigid body modes

The conventional theories describe the deformation and stress distribution in a beam assuming that the shape of cross section is maintained. In the other words, the theory allows only rigid body displacement.

To provide a full understanding of rigid body movements of any cross section, four independent and orthogonal displacements and their derivatives are required.

In conventional theories, these displacements are illustrated in figure (3-1)

u - displacement in the z-direction (rod-theory).

v - displacement in the y-direction (Euler-Bernoulli beam theory).

w - displacement in the x-direction (Euler-Bernoulli beam theory).

Θ - displacement in the x-direction (Vlasov torsion theory).

Displacements in any of these directions are results of a warping strain throughout the section, which can be alternatively described by a warping function. So the independent and

orthogonal four warping functions can provide a full description of any rigid body displacement modes of a cross section.

A method of defining these warping functions in a folded plate structure is to define the values of the functions at each of the (n) nodes and assume a warping function distribution between the nodes. For a rigid body, this warping function would be a simple linear distribution between nodes. The rigid body displacement of any folded plate member with (n) nodes can therefore be uniquely described by four warping functions which would each be a column vector with (n) components.

Figure (3-1) shows rigid body warping modes and its warping functions for the 13 nodded cross-section. Each of these modes can be related to rigid body modes using conventional beam theories.

3.3 Higher order distortional and local modes

If a folded plate is described by (n) nodes, however, this plate must have (n) degrees of freedom. There must therefore exist (n) independent orthogonal warping functions to fully describe the displaced state of a folded plate member. It has been shown previously that four of these functions can describe rigid body movements, so the remaining (n-4) functions must describe cross section distortion. The complete behaviour of the member is then described by (n) independent, orthogonal warping vectors, each containing (n) elements. Figure (3-2) shows the additional warping vector which describes the cross section distortion and local modes.

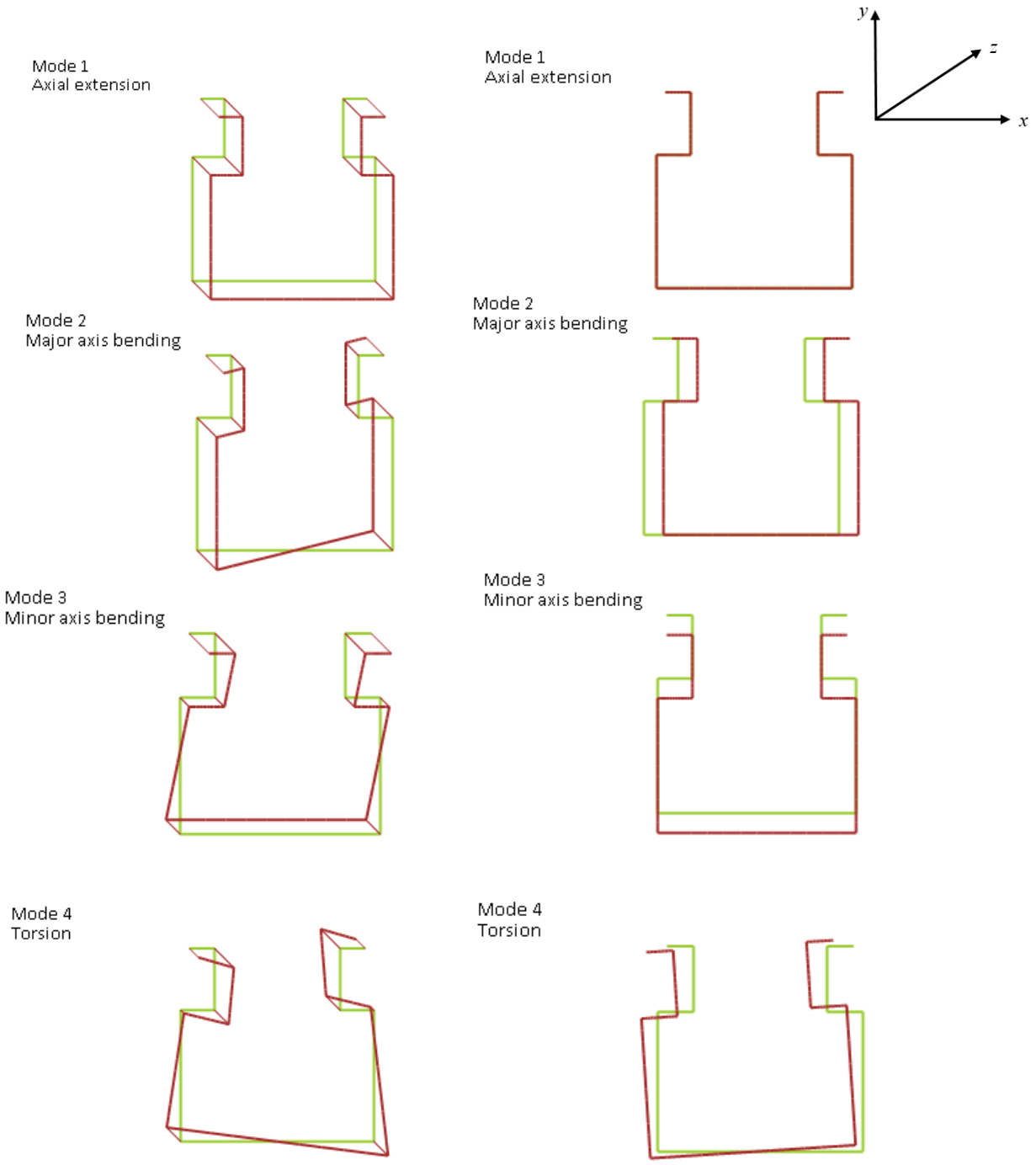

Warping function *Displacement mode shape*

Figure (3-1) Warping function and displacement mode shape rigid body modes (Bebiano et al, 2008).

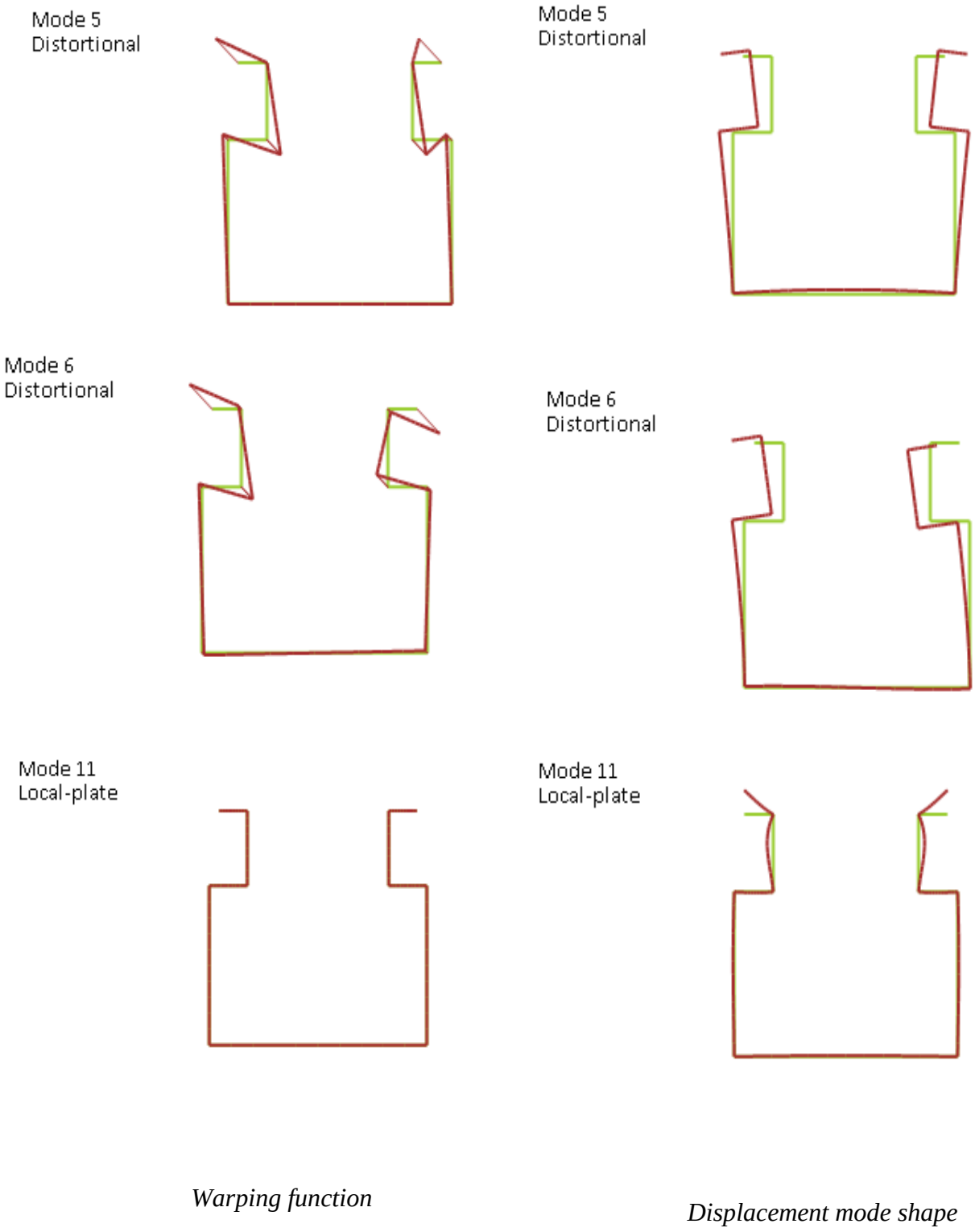

Figure (3-2) Warping function and displacement mode shape of higher order distortional and local modes (Bebiano et al, 2008.

3.4 First order generalized beam theory

First order GBT was addressed by *Schardt (1966)*, to describe the displacement of open thin-walled sections as a folded plate using a warping function vector. He assumed that the shear deformations of the middle surface of the plate were negligible. In this work the warping functions were orthogonalized in such a way that each of first four functions described rigid body displacement, and the remaining (*n-4*) warping functions described cross-section distortional modes.

The first form of *Schardt (1966)* equation is:

$$(C - \lambda B)V = 0 \qquad (3-1)$$

C is the elements of a matrix representing the internal virtual work of the axial stress in the member.

B is the elements of matrix representing the internal virtual work of the transverse bending moment in each plate.

The eigenvector *V* is the warping function related to each mode.

The eigenvalue λ is the ratio of transverse bending stiffness and warping stiffness.

Solution of this equation gives (*n*) eigenvalues, the first four of which are zero. The non-zero eigenvalues produce (*n-4*) eigenvectors which are the warping functions of (*n-4*) cross section distortional modes. The other four eigenvectors are related to rigid body displacement modes. The significance of a zero eigenvalue is that the work of the transverse bending moments is zero in the rigid body modes.

In order to obtain the warping function related to the four rigid body modes, (which could alternatively be obtained by conventional methods), additional eigenvalue problems must be solved, the first of these problems is:

$$(C - \lambda D)V = 0 \qquad (3-2)$$

C is the elements of a matrix represent the internal virtual work of the axial stress in the member as before, except that it has now been orthogonalized to separate the first four body

modes from the other distortional modes, so only the first (*4 x 4*) elements of *C* are inserted in the (*n x n*) matrix, the remaining elements being left as zero.

D is the elements of a matrix representing the internal virtual work of the torsional stresses, similarly orthogonalized and with only the first (4 x 4) elements used in the (n x n) matrix of C. For the solution of this given (n) eigenvalue problem, all of the matrix elements related to rigid body modes will be zero except the eigenvalue of the column related to torsional stresses (twisting about the Z-axis).

The three remaining warping functions are obtained from the following eigenvalue problems:

$$(C - \lambda X)V = 0 \qquad (3-3)$$

C now is the first further orthogonalized matrix representing the virtual work of the axial and bending stresses.

X is the elements of the matrix representing the work done by the second order longitudinal membrane stresses.

Again only the first (3 x 3) matrix elements will be used rather than the higher order modes in matrixes C & X related to three rigid body modes remaining.
Mode 1: displacement along the Z-axis (axial mode).
Mode 2: displacement along the X-axis (major bending mode).
Mode 3: displacement along the Y-axis (manor bending mode).
Having calculated (*n*) warping functions for matrix *C, B & D,* the original definition of these matrices in generalized beam theory related to conventional theory is shown in table (3-1).

Table (3-1) Original definition of section properties.

Deformation Modes	Conventional Theory			Generalized Beam Theory		
1	A	-	-	^{1}C	-	-
2	I_x	-	-	^{2}C	-	-
3	I_y	-	-	^{3}C	-	-
4	r	J	-	^{4}C	^{4}D	-
5	-	-	-	^{k}C	^{5}D	^{k}B

From table (3-1) because the *D* and *B* matrixes are zero in most of the rigid body modes, it can be seen that the C matrix represents the stiffness with regard to direct stress, the D matrix represents the stiffness with regard to torsional stress and the B matrix represents the stiffness with regard to transverse bending stress.

3.4.1 Displacement functions

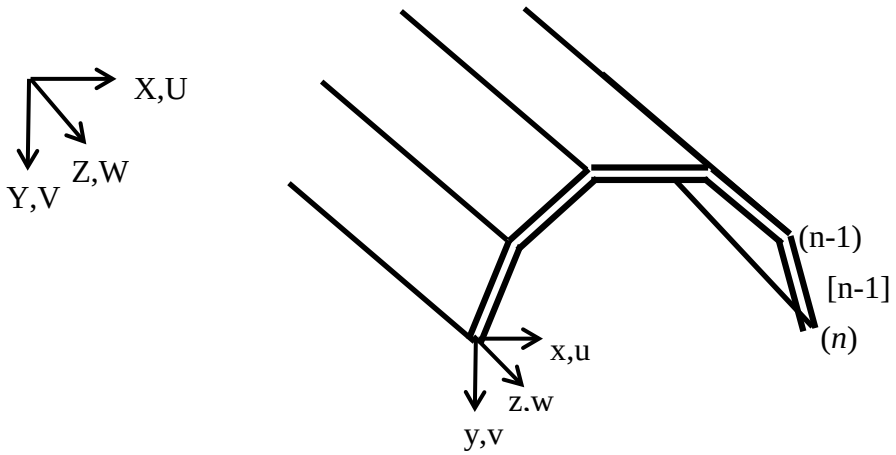

Figure (3-3), Global and local coordinations (Schardt, 1966)

Figure (3-3):

X, Y & Z : Cartesian global coordinate system for member.

x, y & z : Cartesian local coordinate system for each plate.

U, V & W : Displacements in *X, Y & Z* directions respectively.

u, v& w : Displacements in *x, y & z* directions respectively.

σ^{m}_{z} , ε^{m}_{z} : Membrane stress & strain in *z*-direction.

σ^{m}_{x} , ε^{m}_{x} : Membrane stress & strain in *x*-direction.

τm, ϕm : Membrane shear stress & strain.

σ^{b}_{z} , ε^{b}_{z} : Bending stress & strain in *z*-direction.

σ^{b}_{x} , ε^{b}_{x} : Bending stress & strain in *x*-direction.

E : Youngs Modulus.

G : Shear Modulus.

v : Poissons ratio.

Φ_i : Rotation of node (i).

Θ_i : Rotation of plate (i).

The displacement of any node is uniquely defined by nodal values of the vectors w_i , u_i normal to plate (i) and u_{i-1} normal to plate ($i-1$).

Because of compatibility at each node there is a geometrical relationship between these three vectors that must be maintained.

Birman (2011) The basic assumptions of bending theory which were presented by Navier are:

1- The material of the structure is perfectly elastic.
2- Small deflection theory is adopted.
3- The member retains its cross sectional shape while undergoing all deformations during loading.
4- Plane sections remain plane over the entire cross section while undergoing all deformations during loading.
5- The shear deformations of the middle surface can be neglected.

3.4.1.1 Relationship between nodal displacements w_i and u_i

From assumption (5), the membrane shear strain must be zero so:

$$\frac{\delta u}{\delta z} + \frac{\delta w}{\delta x} = 0 \qquad (3-4)$$

Assuming a warping function that is linear between nodes and considering plate (i) this can be rewritten as:

$$\frac{\delta u}{\delta z} = \frac{(w_{(i-1)} - w_i)}{H_i} \qquad (3-5)$$

H_i : the width of plate (i)

3.4.1.2 Relationship between nodal displacements v_i and u_i

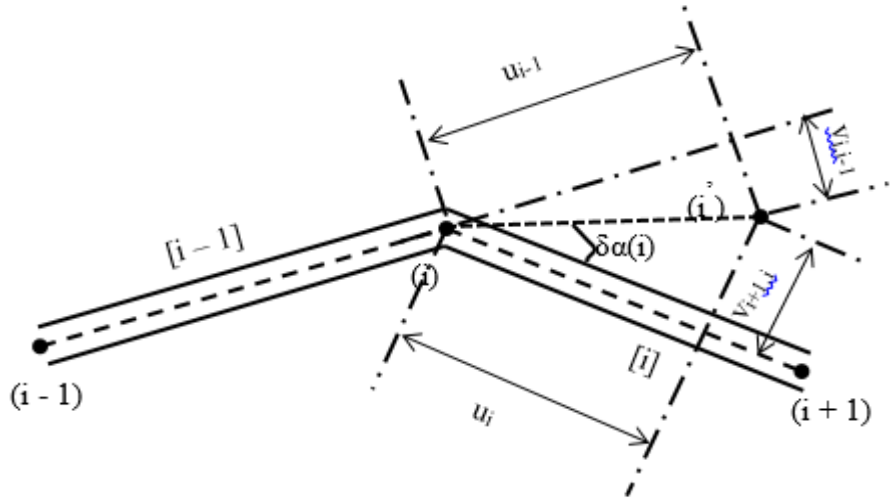

Figure (3-4) Displacement of node, (Schardt, 1966)

From Figure (3-4) the displacement of node (i) to position (i') is:

$$u_{i-1}\cos\delta\alpha(i) + v_{(i,i-1)}\sin\delta\alpha(i) = u_i$$

$$u_{i-1}\sin\delta\alpha(i) - v_{(i,i-1)}\cos\delta\alpha(i) = -v_{(i,i)}$$

Where the double subscript of (v) refers to the plate.

Both these equations must be satisfied for compatibility, so:

$$v_{(i,i-1)} = -\frac{u_{i-1}}{\tan\delta\alpha(i)} + \frac{u_i}{\sin\delta\alpha(i)}$$

$$v_{(i,i)} = -\frac{u_{i-1}}{\sin\delta\alpha(i)} + \frac{u_i}{\tan\delta\alpha(i)}$$

Differentiating with respect to (z) and substitution to equation (3-4), we obtain:

$$\frac{\delta v}{\delta z_{(i,i)}} = [a_{(i,i-1)} \quad a_{(i,i)} \quad a_{(i,i+1)}] * \begin{bmatrix} w_{i-1} \\ w_i \\ w_{i+1} \end{bmatrix} \qquad for\ (2 \le i \le n-1) \qquad (3-6)$$

$$\frac{\delta v}{\delta z_{(i,i-1)}} = [b_{(i-1,i-1)} \quad b_{(i-1,i)} \quad b_{(i-1,i+1)}] * \begin{bmatrix} w_{i-1} \\ w_i \\ w_{i+1} \end{bmatrix} \quad for\ (2 \le i \le n-1)\ (3-7)$$

Where:

$\frac{\delta v}{\delta z_{(i,i-1)}}$ is strain at node (i) normal to plate (i-1).

$\frac{\delta v}{\delta z_{(i,i)}}$ is strain at node (i) normal to plate (i).

$$a_{(i,i-1)} = -\frac{1}{H_{i-1}\, sin\, \delta\alpha(i)}$$

$$a_{(i,i)} = \frac{1}{H_i\, tan\, \delta\alpha(i)} + \frac{1}{H_{(i-1)}\, sin\, \delta\alpha(i)}$$

$$a_{(i,i+1)} = -\frac{1}{H_i\, tan\, \delta\alpha(i)}$$

$$b_{(i-1,i-1)} = -\frac{1}{H_{i-1}\, tan\, \delta\alpha(i)}$$

$$b_{(i-1,i)} = \frac{1}{H_{i-1}\, tan\, \delta\alpha(i)} + \frac{1}{H_{(i)}\, sin\, \delta\alpha(i)}$$

$$b_{(i-1,i+1)} = -\frac{1}{H_i\, sin\, \delta\alpha(i)}$$

Looking at the other end of plate (*i*), the strain at node (*i+1*) normal to plate (*i*) is given by:

$$\frac{\delta v}{\delta z_{(i+1,i)}} = [b_{(i,i)} \quad b_{(i,i+1)} \quad b_{(i,i+2)}] * \begin{bmatrix} w_i \\ w_{i+1} \\ w_{i+2} \end{bmatrix} \qquad for\ (1 \le i \le n-2) \qquad (3-8)$$

3.4.2 Derivation of plate displacements $u^p_{(i)}$ and $v^p_{(i)}$

$u^p_{(i)}$ & $v^p_{(i)}$: Displacements in x & y of centre of plate (i) respectively.

$\frac{\delta \theta}{\delta z_i}$: Rigid body rotational stain.

Using the relationships derived before, the following equations are obtained:

$$\frac{\delta u^p}{\delta z} = \frac{(w_{(i-1)} - w_i)}{H_i} \qquad (3-9)$$

$$\frac{\delta v^p}{\delta z} = \frac{1}{2}\,[\frac{\delta v}{\delta z_{(i+1,i)}} + \frac{\delta v}{\delta z_{(i,,i)}}] \qquad (3-10)$$

$$\frac{\delta v^p}{\delta z} = \frac{1}{2}|a_{(i,i-1)} \quad b_{(i,i)} + a_{(i,i)} \quad b_{(i,i+1)} + a_{(i,i+1)} \quad b_{(i,i+2)}| * \begin{bmatrix} w_{i-1} \\ w_i \\ w_{i+1} \\ w_{i-2} \end{bmatrix} \qquad for\ (1 \le i \le n-2) \qquad (3-11)$$

$$\theta_i = \frac{1}{H_i}\,[\frac{\delta v}{\delta z_{(i+1,i)}} - \frac{\delta v}{\delta z_{(i,,i)}}]$$

$$\theta_i = \frac{1}{H_i}|a_{(i,i-1)} \quad b_{(i,i)} - a_{(i,i)} \quad b_{(i,i+1)} - a_{(i,i+1)} \quad b_{(i,i+2)}| * \begin{bmatrix} w_{i-1} \\ w_i \\ w_{i+1} \\ w_{i-2} \end{bmatrix} \; for\; (1 \leq i \leq n-2) \qquad (3-12)$$

3.4.3 Derivation of plate displacements $w^p_{(i)}$ and $v^p_{(i)}$

Assuming a warping function that is linear between nodes:

$$w_i^p = w_i + [w_i - w_{i+1}] * \beta \qquad (3-13)$$

Where β is a dimensionless coordinate defined by $\beta = \frac{s-s_i}{H_i}$

$$v_i^p = \Omega_O * \frac{\delta v}{\delta z_{(i,i)}} + H_i[\Omega_1 * \theta_i + \Omega_2 * \Phi_i + \Omega_3 * \Phi_{i+1}] \qquad (3-14)$$

Where:

Φ_i is the nodal rotation at node (i).
θ_i is the rigid body rotation of plate (i).

$\Omega_O = 1$
$\Omega_1 = 3\beta^2 + 2\beta^3$
$\Omega_2 = \beta - 2\beta^2 + \beta^3$
$\Omega_3 = -\beta^2 + \beta^3$

3.5 Basic equation of first order generalized beam theory

In order to demonstrate the principles upon which the generalized beam theory is based, the fundamental equations are initially developed according to first order theory. The following simplifications are made:

1- Poisson's ratio is zero (see section 3.13.2)
2- The work done by plate bending terms in the longitudinal direction is neglected.

The three basic deformations of any plate are the functions *u*, *v*, *w*, these deformations are all functions of both the longitudinal (*z*) and circumferential (y) coordinates.

$u = u(x,z)$
$v = v(x,z)$
$w = w(x,z)$
Also it can be rewritten parametrically as:

$u(x,z) = u(x) * V'(z)$

$v(x,z) = v(x) * V(z)$

$w(x,z) = w(x) * V(z)$

Where V(z) is a dimensionless shape function that represents the amplitude of each function along the member length.

From the above relations, the displacement of any section with (n) nodes is uniquely defined by (n) warping ordinates. Hence any section with (n) nodes has (n) degrees of freedom.

It follows that any displacement can be uniquely defined by combining (n) orthogonal warping vectors.

Therefore:

$$u(x,z) = \sum_{k=1}^{n} u_k(x)\, V_k'(z) \qquad (3-15)$$

$$v(x,z) = \sum_{k=1}^{n} v_k(x)\, \mathrm{V}_k'(z) \qquad (3-16)$$

$$w(x,z) = \sum_{k=1}^{n} w_k(x)\, V_k'(z) \qquad (3-17)$$

Where (*k*) is denoted by the mode of each displacement.

3.5.1 Strain displacement relationships

In general, there are three strain components, $\mathcal{E}_x$, $\mathcal{E}_x$ and ϕ_{xz}. These basic components can be further subdivided into:

1- Membrane Components (denoted by superscript (m)).
2- Bending Components (denoted by superscript (b)).

Therefore, there are six components that define the complete strain conditions of any plate, Table (3-2).

Table (3-2) Strain conditions.

Membrane	Bending
ε_x^m	ε_x^b
ε_z^m	ε_x^b
Φ_{xz}^m	Φ_{xz}^b

From conventional theory assumptions in (3.3.1) and (3.4), gives:

$\mathfrak{E}_x^m = 0$

$\Phi_{xz}^m = 0$

Small deflection plate theory gives the following strain displacement relationship:

$$\epsilon_x^b = -yv \qquad (3-18)$$

$$\epsilon_z^b = -yv'' \qquad (3-19)$$

$$\Phi_{xz}^b = -2yv' \qquad (3-20)$$

Also by definition:

$$\varepsilon_z^m = w' \qquad (3-21)$$

3.5.2 Stress-strain relationships

From Hook's Law:

$$\sigma_z^m = E\varepsilon_z^m = Ew' \qquad (3-22)$$

$$\sigma_x^b = E\varepsilon_x^b = Eyv \qquad (3-23)$$

$$\sigma_z^b = E\varepsilon_z^b = Eyv'' \qquad (3-24)$$

$$\tau_{xz}^b = G\Phi_{xz}^b = 2Gyv' \qquad (3-25)$$

3.6 Virtual work of transverse bending moments

The virtual work of the transverse bending stress of the complete section is given by:

$$VW_1 = \iiint_{y\,z\,x} \sigma_x^b \, \delta\epsilon_x^b \, dy\, dz\, dx$$

Using equations (4-15) & (4-25)

$$\sigma_x^b = \sum_{k=1}^{n} -E\, yv_k V_k$$

$$\delta\epsilon_x^b = \sum_{j=1}^{n} -t\delta(v_j\, V_j)$$

Hence:

$$VW_1 = \sum_{k=1}^{n}\sum_{j=1}^{n} \iiint_{y\,z\,x} Ey^2\,(v_k V_k)\delta(v_j V_j)\, dy\, dz\, dx$$

Integrating with respect to (y) between the limits (±t/2), and rewriting $\delta(v_k V_k)$ as $V_k \delta V_k$:

$$VW_1 = \sum_{k=1}^{n}\sum_{j=1}^{n}\frac{Et^3}{12}\iint_{z\,x}(v_k\,v_j)V_k\delta V_j\,dz\,dx$$

Donating $\int_x K(v_k\,v_j)\,dx = B_{kj}$, where $K = \frac{Et^3}{12}$

$$VW_1 = \sum_{k=1}^{n}\sum_{j=1}^{n}\int_z B_{kj}V_k\,\delta V_j\,dz \qquad (3-26)$$

3.7 Virtual work of longitudinal membrane stresses

The virtual work of the longitudinal membrane (warping) stresses of the complete section is given by:

$$VW_2 = \iiint_{y\,z\,x}\sigma_z^m\delta\epsilon_z^m\,dy\,dz\,dx$$

Using equations (4-15) & (4-25):

$$\sigma_z^m = \sum_{k=1}^{n}Ew_k\,V_k''$$

$$\delta\epsilon_z^m = \sum_{j=1}^{n}\delta w_j V_j''$$

Hence:

$$VW_2 = \sum_{k=1}^{n}\sum_{j=1}^{n}\iiint_{y\,z\,x}E(w_k\,w_j)\,V_k''\,\delta\,V_j''\,dy\,dz\,dx$$

Integrating with respect to (y) between the limits (±d/2), and denoting:

$$\int_x (w_j\,w_k)\,dx = C_{kj}^1$$

We obtain:

$$VW_2 = \sum_{k=1}^{n}\sum_{j=1}^{n}E\int_z C_{kj}^1\,V_k''''\delta V_j\,dz \qquad (3-27)$$

3.8 Formulation of the eigenvector problem

If no external load is applied, the virtual work expressions must be constant.

$$VW_1 + VW_2 = Constant$$

Differentiating this expression with respect to (*z*) gives the following equation of static equivalence:

$$VW_1' + VW_2' = 0$$

Substituting equations (3-26) & (3-27) gives:

$$\sum_{k=1}^{n}\sum_{j=1}^{n}(EC_{kj}^{1}\,V_k'''' + B_{kj}V_k)\delta V_j = 0 \qquad (3-28)$$

To continue we now require that equation (4-25) can be split into (*n*) components and that each component equation holds true for some model value of the vector w_k, hence:

$$\sum_{j=1}^{n}(EC_{kj}^{1}\,V_k'''' + B_{kj}V_k)w_k = 0 \qquad (3-29)$$

This is no restriction on the generality of the solution since the vector must, by definition, have (n) degrees of freedom.

Equation (3-27) can be rewritten as

$$\sum_{j=1}^{n}(EC_{kj}^{1} - \lambda B_{kj})w_k = 0 \qquad (3-30)$$

Where $\lambda = -\frac{V_k}{V_k''''}$

Solving the modal equation (3-28) gives (*n*) independent orthogonal warping vectors. Because of their orthogonality, model values of the section properties B_{kj} and C^{1}_{kj} recalculated using these vectors are zero unless $j=k$.

In addition, the solution of equation (3-28) filters out the vectors associated with a zero value of the property B_{kk}. In effect, the solution of (3-28) divides the modal vectors w_k into two categories.

The first category is that in which transverse bending moments occur, giving rise to finite values of B_{kk}. The second category is that in which transverse bending does not occur, leading to zero values of B_{kk}.

These two categories have distinct physical meanings. If the value of B_{kk} is zero, the displacement vectors must be describing rigid body motion, whereas if B_{kk} is non-zero, the cross section must be distorting.

The solution of equation (3-28), therefore, produces four rigid body components and (*n-4*) distortion components. It has therefore divided the problem into precisely the two categories that are required, so that distortional modes can be considered in isolation from rigid body modes and their significance can be assessed.

Rigid body components are recognizable by the fact that the eigenvalue solutions to equation (3-28) are all zero. At this stage the first four modes are therefore mixed together. In order to be of practical use, there is a need to sort these first four modes into the four rigid body displacement modes, which are show in table (3-3).

Table (3-3) Section properties for rigid body modes.

Modes		GBT property	Conventional property
1	Axial	C^1_{11}	A
2	Minor axis bending	C^1_{22}	I_y
3	Major axis bending	C^1_{33}	I_x
4	Torsion	C^1_{44}	J

There are two alternative methods for doing this:

1- Use simple engineering theory to obtain the centroid, principal axes and shear centre of the section, and from these the warping ordinates can be obtained for each mode.
2- Use the Generalized theory to organize the first four modes. To do this some modification to equation (3-28) are required such that the solution to modes (*1-4*) becomes meaningful. This must mean the replacement of B_{kk} for these modes, since $B_{kk}=0$ for rigid body displacement.

3.9 Equilibrium of externally applied loads

The representation of external loads in generalized theory can be resolved as equivalent nodal loads which can then be resolved into forces acting in the planes of plates from which

the section is composed. These forces can be denoted by a vector which has (*n*) components q_1 to q_n. using a similar method to that relating B_{kj} and C_{kj}.

$$q = \sum_{k=1}^{n} q_k \qquad (3-31)$$

Consider the energy of the plate under the influence of these loads:

$$VW_1 + VW_2 - \int_z q\delta \, dz = 0$$

Where: δ is unit displacement.

Differentiating and substituting from equations (3-23), (3-24) & (3-27) gives:

$$\sum_{k=1}^{n} E\, C_{kk}^{1} V_k'''' + \sum_{k=1}^{n} B_{kk}\, V_k - \sum_{k=1}^{n} q_k\, \delta_k = 0 \qquad (3-32)$$

δ_k=unit displacement in mode *k, i.e. 1*.

Hence for each mode:

$$EC_{kk}^{1} V_k''''(z) + B_{kk} V_k(z) = q_k(z) \qquad (3-33)$$

3.10 Equivalent axial loading

Any external loading must be resolved into axial plate forces such that the axial forces are in equilibrium with the sum of the applied loads and the moments caused by the applied loads on the unsupported cross-section.

Note:

1- The effect of leaving the section unsupported is to introduce a pin support (translationally restrained but rotationally free) at nodes (*2*) and (*n-1*) that simulate the restraint given to the section by the first and last plate.
2- The sum of axial loads must be equal to the sum of applied loads.
3- Even if the load is applied to a node in the cross section, if it causes a bending moment through the section it must be treated as described above.

By using virtual work methods, the axial load can be resolved into components as:

$$q_k = \sum_{i=1}^{n} q_k^i \, u^i$$

Where q^i is the axial load in plate (i)

3.11 Individual plate torsional stiffness (distortional stiffness)

When a section is displaced, generally the individual plates undergo, in general, differing rates of twist. This leads to a shear strain through the thickness of the plate denoted by Φ_{xz}^b .The effect of this shear strain must be included in the equation (3-33).

$$VW_3 = \iiint_{y\,z\,x} \Phi_{xz}^b \delta\tau_{xz}^b \, dy \; dz \, dx \qquad (3-34)$$

Using equations (3-16), (3-20) & (3-25)

$$\Phi_{xz}^b = \sum_{k=1}^{n} -2y \, v_k' V_k'$$

$$\delta\tau_{xz}^b = \sum_{j=1}^{n} -2Gy v_k' \, \delta V_k'$$

Hence

$$VW_3 = \sum_{k=1}^{n}\sum_{j=1}^{n} \iiint_{y\,z\,x} 4Gt^2 \, v_k' v_j' V_k' \delta V_j' dy \, dz \, dx$$

Integrating with respect to (y) between the limits $\mp\frac{t}{2}$, will produce:

$$VW_3 = \sum_{k=1}^{n}\sum_{j=1}^{n} \frac{4Gt^3}{12} \iint_{zx} \left(v_k' v_j'\right) V_k'' \delta V_j \, dz \, dx$$

From engineering bending theory, $G = \frac{E}{2(1+\mu)}$, but according to the assumptions before $\mu = 0$.

Take:

$$D_{jk}^1 = \int_x K(v_j' v_k') \, dx$$

$$K = \frac{Et^3}{12}$$

Therefore;

$$VW_3 = \sum_{k=1}^{n}\sum_{j=1}^{n} 2\int_z D_{kj}^1 V_k'' \delta V_j dz \qquad (3-35)$$

This component of work is equivalent to that done by a twisting moment applied to each plate. It therefore enters the equilibrium equation (3-33) in the same sense as the applied load. So equation (3-33) will be rewritten as:

$$EC_{kk}^1 V_k''''(z) + B_{kk}V_k(z) = q_k(z) + VW_3' \qquad (3-36)$$

Differentiating equation (4-33), and substituting it in equation (4-34), we obtain:

$$\sum_{k=1}^{n} EC_{kk}^1 V_k'''' - 2\sum_{k=1}^{n} D_{kk}^1 V_k'' + \sum_{k=1}^{n} B_{kk}V_k = \sum_{k=1}^{n} q_k \qquad (3-37)$$

Hence for each mode:

$$EC_{kk}^1 V_k'''' - 2D_{kk}^1 V_k'' + B_{kk}V_k = q_k \qquad (3-38)$$

This is the basic equilibrium equation of *GBT*

3.12 First order *GBT* section properties evaluation

3.12.1 Evaluation of (C^1_{jk})

$$C_{jk}^1 = \int_x t(w_j\, w_k)dx \qquad (3-39)$$

The function (w) is linear between nodes and discontinues at each node, so the integral (3-39) can be divided into (*n-1*) parts (one for each plate), and the simplified non-linear dimensional function β can be used in place of (*x*), where:

$$\beta = \frac{s - s(i)}{H(i)}$$

Where: *H* is plate width.

Than the equation (3-39) can be rewritten as:

$$C_{jk}^1 = \sum_{i=1}^{n-1} H(i)t(i)\int_0^1 (w_j(i)w_k(i))\, d\beta \qquad (3-40)$$

The term $\left(w_j(i)w_k(i)\right)$ must be evaluated for each mode, but the term ($w(i)$) is a column vector with (*n-1*) components, therefore; this term will become:

$(w_j^T w_k)$

The single function will result from the evaluation of this term related to each plate (i) in each mode (jk). When $j \neq k$, the mixed mode has no physical significance, so the value of C_{jk}^1 will be zero for each $j \neq k$. It can be said that:

$$C_{jk}^1 = 0 \qquad if \quad j \neq k$$

$$C_{jk}^1 \neq 0 \qquad if \quad j = k$$

The general form of the function (w) according to equation (4-15) is:

$$\begin{matrix} plate\ 1 \\ plate\ 2 \\ plate\ 3 \\ \\ \\ \\ plate\ n-2 \\ plate\ n-1 \end{matrix} \begin{bmatrix} 1-\beta & \beta & 0 & 0 & & & & \\ 0 & 1-\beta & \beta & 0 & & & & \\ 0 & 0 & 1-\beta & \beta & & & & \\ & & & & & & & \\ & & & & & & & \\ & & & & & & & \\ & & & 0 & 0 & 1-\beta & \beta & \\ & & & 0 & 0 & 0 & 1-\beta & \beta \end{bmatrix} \begin{bmatrix} w(1) \\ w(2) \\ w(3) \\ \\ \\ \\ w(n-1) \\ w(n) \end{bmatrix}$$

Now the evaluation of terms $w_j(i)$ & $w_k(i)$ can be done, and C_{jk}^1 can be calculated by integrating these functions and summing over all (i) plates.

3.12.2 Evaluation of (B_{jk})

From (section 3.5):

$$B_{jk} = \int_x K(v_k\, v_j)\, dx \qquad (3-41)$$

Dividing the integration above into each plate (i) as before in evaluation of ($C1_{jk}$) in terms of non-dimensions (β) gives:

$$B_{jk} = \sum_{i=1}^{n-1} K(i)H(i) \int_0^1 (v_j v_k)\, d\beta \qquad (3-42)$$

Equation (3-12)

$$v_i^p = \Omega_O * \frac{\partial v}{\partial z}_{(i,i)} + H_i[\Omega_1 * \theta_i + \Omega_2 * \Phi_i + \Omega_3 * \Phi_{i+1}]$$

Each element of term (B_{jk}) is then evaluated in a similar fashion to (C^1_{jk}).

3.12.3 Evaluation of (D^1_{jk})

From (section 3-10):

$$D^1_{jk} = \int_x K\left(\frac{\partial v}{\partial x_j}\frac{\partial v}{\partial x_k}\right) dx$$

$$D^1_{jk} = \sum_{i=1}^{n-1} K(i)H(i) \int_0^1 \left(\frac{\partial v}{\partial x_j}\frac{\partial v}{\partial x_k}\right) d\beta \qquad (3-43)$$

3.13 Basic equation of second order generalized beam theory

It is possible to introduce the generalized beam theory with no simplification; this is termed second order generalized beam theory. So, the basic equation will be developed with inclusion of the effect of Poisson's ratio and the secondary effects of plate bending terms.

3.13.1 Strain displacement relationships

3.13.1.1 Membrane strains

From figure (3-5):

$$\epsilon_z^m = \sqrt{(1-w')^2 + (u')^2 + (v')^2} - 1 \qquad (3-44)$$

Expanding equation (4-44), the following approximation is obtained:

$$\epsilon_z^m = w' + \frac{1}{2}[(u')^2 + (v')^2] \qquad (3-45)$$

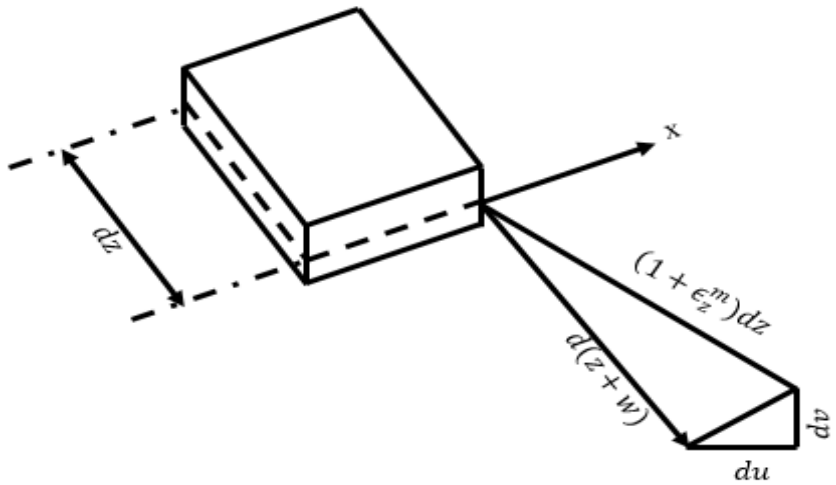

Figure. (3-5) Membrane strain , (Schardt, 1966)

3.13.1.2 Bending strains

For bending strains, equations (3-18), (3-19) & (3-20) will be:

$$\epsilon_x^b = -y\frac{\partial^2 v}{\partial x^2} \qquad (3-46)$$

$$\epsilon_z^b = -y\frac{\partial^2 v}{\partial z^2} \qquad (3-47)$$

$$\Phi_{xz}^b = -y\frac{\partial^2 v}{\partial x \partial z} \qquad (3-48)$$

3.13.2 Stress-strain relationship in presence of poisson's ratio

$$\sigma_x^b = \frac{E}{1-\mu^2}\,(\epsilon_x^b + \mu\epsilon_z^b) \qquad (3-49)$$

$$\sigma_z^b = \frac{E}{1-\mu^2}\,(\epsilon_z^b + \mu\epsilon_x^b) \qquad (3-50)$$

$$\tau_{xz}^b = G\Phi_{xz}^b = \frac{E(1-\mu)\Phi_{xz}^b}{2(1+\mu^2)} \qquad (3-51)$$

$\sigma_z^m = E(\epsilon_z^m + \mu\epsilon_x^m)$

But $\epsilon_x^m = 0$; So:

$$\sigma_z^m = E\epsilon_z^m \qquad (3-52)$$

Substituting equations (3-46), (3-47) & (3-48) in equations (3-49), (3-50), (3-51) & (3-52) gives;

$$\sigma_x^b = \frac{-Et}{1-\mu^2}\left(\frac{\partial^2 v}{\partial z^2} + \mu\frac{\partial^2 v}{\partial x^2}\right) \qquad (3-53)$$

$$\sigma_z^b = \frac{-Et}{1-\mu^2}\left(\frac{\partial^2 v}{\partial x^2} + \mu\frac{\partial^2 v}{\partial z^2}\right) \qquad (3-54)$$

$$\tau_{xz}^b = \frac{-Et}{1+\mu^2}(1-\mu)\left(\frac{\partial^2 v}{\partial x \partial z}\right) \qquad (3-55)$$

$$\epsilon_z^m = E[\frac{\partial w}{\partial x} + \frac{1}{2}\left[\left(\frac{\partial u}{\partial x}\right)^2 + \left(\frac{\partial v}{\partial x}\right)^2\right]] \qquad (3-56)$$

Rewriting the equations (3-53), (3-54), (3-55) & (3-56) using equations (3-15), (3-16) & (3-17) get:

$$\sigma_x^b = \frac{-Et}{1-\mu^2}\sum_{k=1}^{n}\left(\frac{\partial^2 v}{\partial x^2}_k V_k + \mu v_k V_k''\right) \qquad (3-57)$$

$$\sigma_z^b = \frac{-Et}{1-\mu^2}\sum_{k=1}^{n}\left(v_k V_k'' + \mu\frac{\partial^2 v}{\partial x^2}_k V_k\right) \qquad (3-58)$$

$$\tau_{xz}^b = \frac{-Et}{1+\mu^2}(1-\mu)\sum_{k=1}^{n}\left(\frac{\partial v}{\partial x}_k V_k'\right) \qquad (3-59)$$

$$\sigma_z^m = E\sum_{k=1}^{n} w_k V_k'' + \frac{E}{2}\sum_{j=1}^{n}\sum_{k=1}^{n}(u_j u_k + v_j v_k)V_j' V_k'$$

This equation could be rewritten in terms of the warping resultant W_k using the stress relationship of first order theory, so:

$$\sigma_z^m = -\sum_{k=1}^{n}\frac{W_k w_k}{C_{kk}^1}$$

To obtain the complete stress components, the extra second order term must be added, giving:

$$\sigma_z^m = -\sum_{k=1}^{n}\frac{W_k w_k}{C_{kk}^1} - \frac{E}{2}\sum_{i=1}^{n}\sum_{j=1}^{n} v_{ij} V_i' V_j' \qquad (3-60)$$

Where: $v_{ij} = (u_i u_j + v_i v_j)$

3.13.3 Virtual work of transverse bending moment

The equation of virtual work for transverse bending moment is:

$$VW_1 = \iiint_{y\,z\,x} \sigma_x^b\, \delta\epsilon_x^b\, dy\, dz\, dx$$

It can be rewritten using equation (4-57) gives:

$$VW_1 = \sum_{j=1}^{n}\iiint_{y\,z\,x}\frac{Et^2}{1-\mu^2}\left(\frac{\partial^2 v}{\partial x^2}_j V_j + \mu v_j V_j''\right)v_k \delta V_k\, dy\, dz\, dx$$

Integrating with respect to (y) between the limits ($\mp\frac{t}{2}$), will give:

$$VW_1 = \sum_{j=1}^{n}\iint_{z\,x}\left[K\left(\frac{\partial^2 v}{\partial x^2}_j v_k\right)V_j + \mu K(v_j v_k)V_k''\right]\delta V_k dz\, dx$$

Where $K = \frac{Et^3}{12(1-\mu^2)}$ $\quad for\ \mu \neq 0$

But:

$$B_{jk} = \int_x K(v_j v_k)\, dx$$

Defining:

$$D_{jk}^2 = \int_x K\left(\frac{\partial^2 v}{\partial x^2}_j\, v_k\right) dx \qquad (3-61)$$

$$VW_1 = \sum_{j=1}^{n} \int_z (B_{jk} V_j + \mu D_{jk}^2 V_j'')\delta V_k dz \qquad (3-62)$$

3.13.4 Virtual work of longitudinal membrane stress

Virtual work of longitudinal membrane stress is:

$$VW_2 = \iiint_{y\,z\,x} \sigma_z^m\, \delta\epsilon_{zk}^m\, dy\, dz\, dx$$

From equation (3-60) and section (4-2):

$$\delta\epsilon_{zk}^m = w_k \delta_k V_k'' + \sum_{j=1}^{n} v_{kj}\, V_j' \delta V_k'$$

Evaluating the work integral gives:

$$VW_2 = -\iiint_{y\,z\,x} E \sum_{i=1}^{n} \frac{W_i w_i}{C_{ii}^1} w_i w_k V_i'' \delta V_k'' - \sum_{i=1}^{n}\sum_{j=1}^{n} \frac{W_i w_i}{C_{ii}^1} v_{kj} V_j' \delta V_k' - \frac{E}{2} \sum_{i=1}^{n}\sum_{j=1}^{n} w_k\, v_{ij} V_i' \delta V_k''$$
$$+ E \sum_{i=1}^{n}\sum_{j=1}^{n} v_{ij}\, v_{jk} V_i' V_j' V_j' \delta V_k'$$

Ignoring higher order terms, rearranging, and using the substitutions:

$$C_{jk}^1 = \iint_{y\,x} w_k w_j\, dy\, dx$$

$$X_{ijk} = \iint_{y\,x} \frac{w_i v_{ij}}{C_{ii}^1} dy\, dx$$

And

$$(V_j V_i)\delta V_k' = -(V_j V_i)' \delta V_k$$

$$VW_2 = -\sum_{i=1}^{n}\int_z w_i'' \,\delta V_k' dz + \int_z \sum_{i=1}^{n}\sum_{j=1}^{n}\left(W_k X_{ijk} V_j'\right)' \delta V_k dz$$

$$-\frac{E}{2}C_{kk}^1 \int_z \sum_{i=1}^{n}\sum_{j=1}^{n} X_{ijk}(V_i'V_k')''\delta V_k dz \qquad (3-63)$$

The warping moment W_k can be replaced by using the definition:

$$W_k = \iint_{x\,y} \sigma_z^m \, w_k \, dx\, dy$$

Substituting for σ_z^m :

$$W_k = -EC_{kk}^1 V_k'' - \frac{E}{2}C_{kk}^1 \sum_{i=1}^{n}\sum_{j=1}^{n} X_{ijk} V_i' \, V_j'$$

Hence:

$$W_k'' = -EC_{kk}^1 V_k'''' - \frac{E}{2}C_{kk}^1 \sum_{i=1}^{n}\sum_{j=1}^{n} X_{ijk}(V_i'V_j')''$$

Substituting in equation (3-63):

$$VW_2 = \int_z EC_{kk}^1 V_k''''\delta V_k dz + \frac{E}{2}C_{kk}^1 \int_z \sum_{i=1}^{n}\sum_{j=1}^{n} X_{ijk}\,(V_i'V_j')''\delta V_k dz$$

$$+\int_z \sum_{i=1}^{n}\sum_{j=1}^{n}(W_k' X_{ijk} V_j')'\delta V_k dz \; -\frac{E}{2}C_{kk}^1 \int_z \sum_{i=1}^{n}\sum_{j=1}^{n} X_{ijk}\,(V_i'V_j')''\delta V_k dz$$

Hence:

$$VW_2 = \int_z EC_{kk}^1 V_k''''\delta V_k dz + \int_z \sum_{i=1}^{n}\sum_{j=1}^{n} X_{ijk}(W_k V_k')'\delta V_k dz \qquad (3-64)$$

The second term represents the work done by the longitudinal membrane stresses.

3.13.5 Virtual work of longitudinal bending stress

If the second order terms are included in the theory, the virtual work of the longitudinal bending moments must be included in both the initial eigenvector problem and in the equilibrium equation.

For displacement mode (*k*):

$$VW_4 = \iiint_{y\,z\,x} \sigma_z^b \, \delta\epsilon_z^b \, dy\, dz\, dx \qquad (3-65)$$

By using equations (3-16), (3-19) & (3-58), it can be rewritten equation (3-65) as:

$$VW_4 = \sum_{j=1}^{n} \frac{Et^2}{1-\mu^2} \iiint_{y\,z\,x} (v_j\, V_j'' + \mu \frac{\partial^2 v}{\partial x^2}_j \, V_j) v_k \delta V_k'' \, dy\, dz\, dx \qquad (3-66)$$

Integrating with respect to (*y*) and substituting for the plate stiffness *K*:

$$VW_4 = \sum_{j=1}^{n} K \iiint_{y\,z\,x} (v_j\, v_k \delta V_j'''' V_k + \mu \frac{\partial^2 v}{\partial x^2}_j \, v_k \delta V_j'' V_k)\, dy\, dz\, dx \qquad (3-67)$$

Define second order longitudinal stiffness C_{jk}^2 as:

$$C_{jk}^2 = K \int_x v_j\, v_k dx$$

Equation (4- 67) can be rewritten as:

$$VW_4 = \sum_{j=1}^{n} \int_z (C_{jk}^2 V_j'''' \, \delta V_k + \mu D_{jk}^2 V_j'' \delta V_k)\, dz \qquad (3-68)$$

3.13.6 Virtual work of shear stain

Equation (3-36) in absence of Poisson's Ratio:

$$VW_3 = \sum_{k=1}^{n} \sum_{j=1}^{n} 2 \int_z D_{kj}^1 \, V_k'' \delta V_j dz$$

In presence of Poisson's Ratio, it becomes:

$$VW_3 = \sum_{k=1}^{n} \sum_{j=1}^{n} 2(1-\mu) \int_z D_{kj}^1 \, V_k'' \delta V_j dz \qquad (3-69)$$

3.13.7 Virtual work of membrane shear strain

Due to membrane shear strains in the plates, an additional work term arises given by:

$$VW_5 = \iiint_{y\,z\,x} \tau^m \delta^k \, \Phi^m \, dy\, dz\, dx$$

From equation (3-60)

$$\sigma_z^m = -\sum_{k=1}^{n} \frac{W_k w_k}{C_{kk}^1} - \frac{E}{2}\sum_{i=1}^{n}\sum_{j=1}^{n} v_{ij} V_i' V_j'$$

From the relationship between bending moment and shear force:

$$\tau^m t = \int_x (\sigma_z^m)' \, dx$$

This equation can be integrated to give the following expression:

$$\tau^m t = -\sum_{k=1}^{n} \frac{\Pi_k W_k'}{C_{kk}^1} - \frac{E}{2}\sum_{i=1}^{n}\sum_{j=1}^{n} \Pi_{ij} \left(V_i' V_j'\right)' \qquad (3-70)$$

Where:

$$\Pi_k = \int_x t w_k \, dx$$

$$\Pi_{ij} = \int_x t v_{ij} \, dx$$

Using Figure (3-6), the membrane shear deformation is shown to be:

$$\Phi^m = -\frac{\partial v}{\partial z}\delta\left(\frac{\partial v}{\partial x}\right) - \frac{\partial u}{\partial z}\delta\left(\frac{\partial u}{\partial x}\right) - \frac{\partial u}{\partial x}\delta\left(\frac{\partial u}{\partial z}\right) - \frac{\partial v}{\partial x}\delta\left(\frac{\partial v}{\partial z}\right)$$

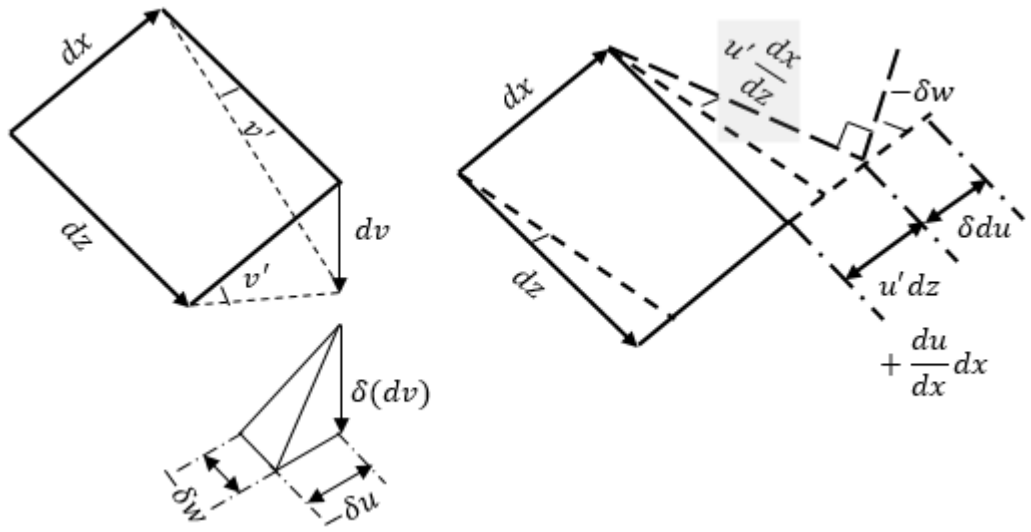

Figure (3-6) Membrane shear deformation , (Schardt, 1966)

This can be expressed in model form as:

$$\delta_k \Phi^m = -\sum_{i=1}^{n} [(v_i \frac{dv}{dx_k} + u_i \frac{du}{dx_k}) V_i' \delta V_k + (\frac{dv}{dx_i} v_k + \frac{du}{dx_i} u_k) V_i \delta V_k']$$

Denoting:

$$\psi a_{ik} = v_i \frac{dv}{dx_k} + u_i \frac{du}{dx_k}$$

$$\psi b_{ik} = \frac{dv}{dx_i} v_k + \frac{du}{dx_i} u_k$$

So it can be rewritten as:

$$\delta_k \Phi^m = -\sum_{i=1}^{n} (\psi a_{ik} V_i' \delta V_k + \psi b_{ik} V_i \delta V_k') \qquad (3-71)$$

So:

$$VW_5 = \iiint_{y\,z\,x} \sum_{j=1}^{n} \sum_{i=1}^{n} \frac{\Pi_j W_k'}{C_{kk}^1} \psi a_{ik} V_i' \delta V_k \, dy \, dz \, dx + \iiint_{y\,z\,x} \sum_{j=1}^{n} \sum_{i=1}^{n} \frac{\Pi_j W_k'}{C_{kk}^1} \psi b_{ik} V_i' \delta V_k \, dy \, dz \, dx$$
$$+ \cdots Higher\ order\ terms$$

$$X_{ijk}^{\tau} = \iint_{y\,x} \frac{\Pi_i \psi a_{ik}}{C_{ii}^1} dx \, dy$$

The first term in the equation becomes:

$$\int_z \sum_{i=1}^{n} \sum_{j=1}^{n} X_{ijk}^{\tau} W_j' V_i' \delta V_k$$

The second term can be rearranged by integrating by parts:

$$[\ i.e. \qquad \Pi_i \psi b_{ik} = \Pi_i \frac{d\psi b_{ik}}{dx} - \Pi_i \psi b_{ik} - \frac{d\Pi_i}{dx} \psi b_{ik}\ ]$$

$$\sum_{i=1}^{n} \sum_{j=1}^{n} \frac{d(\frac{\Pi_j W_k'}{C_{kk}^1})}{dx} - \int_z (X_{ijk} + X_{ijk}^{\tau}) W_i' V_j \delta V_k' \, dz$$

The first term is zero, so the total virtual work expression becomes:

$$VW_5 = \int_z \sum_{i=1}^{n}\sum_{j=1}^{n} X_{ijk}^{\tau} W_j' V_i' \delta V_k dz - \int_z \sum_{i=1}^{n}\sum_{j=1}^{n} X_{ijk} W_i' V_j \delta V_k' dz - \int_z \sum_{i=1}^{n}\sum_{j=1}^{n} X_{ijk}^{\tau} W_i' V_j \delta V_k' dz$$

$$- \int_z \sum_{i=1}^{n}\sum_{j=1}^{n} X_{ijk}^{\tau} W_i' V_j \delta V_k' \qquad (3-72)$$

Substituting $(W_i'V_j)\delta V_k' = -(W_i'V_j)'\delta V_k$, this gives:

$$VW_5 = \int_z \sum_{i=1}^{n}\sum_{j=1}^{n} [X_{ijk}^{\tau}(W_j'V_i') + X_{ijk}^{\tau}(W_i'V_j)' + X_{ijk}(W_i'V_j)']\delta V_k dz \qquad (3-73)$$

This final work term can be expanded if required to become:

$$VW_5 = \int_z \sum_{i=1}^{n}\sum_{j=1}^{n} [X_{ijk}^{\tau}(W_j'V_i' + W_i''V_j + W_i'V_j') + X_{ijk}(W_i''V_j + W_i'V_j')]\delta V_k$$

3.14 Virtual work of membrane shear strain

Equation (3-26) is now modified by the addition an extra term in the first part of equation, the equations then become:

$$\sum_{j=1}^{n}((EC_{kj}^1 + C_{kj}^2)V_k'''' + B_{kj})\delta V_k = 0$$

Let

$$C_{jk} = (EC_{kj}^1 + C_{kj}^2)$$

The equation will be:

$$(C_{jk}V_k'''' + B_{kj})\delta V_k = 0 \qquad (3-74)$$

$$\sum_{j=1}^{n}(C_{kj} - \lambda B_{kj})V_k = 0$$

The solution of this equation gives (*n-4*) model vectors that allow for the second order plate bending effects introduced by C_{kj}^2.

3.15 Virtual work of the external loads

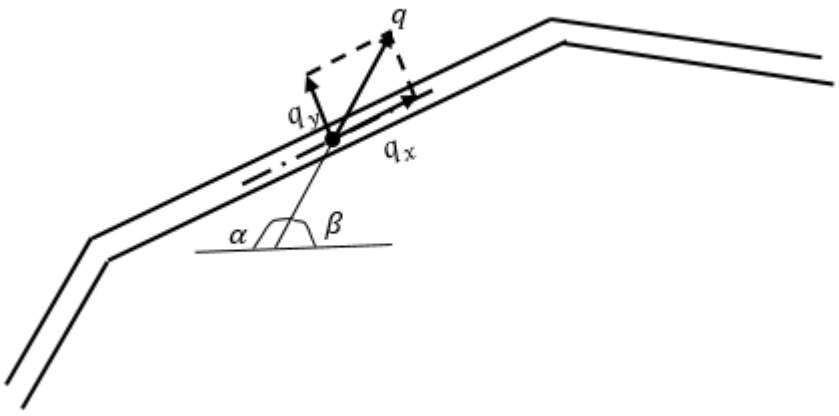

Figure (4-7) Resolution of applied load parallel and normal to a section, (Schardt, 1966)

Any applied load (q) can be written parametrically as:

$$q = q_x Q_z$$

Furthermore, from Figure (4-7), it can be separated into two orthogonal components.

$$q_y = q\,cos(\beta)$$

$$q_x = q\,sin(\beta)$$

The component (q_x) performs work on the displacement δv_k.

The virtual work of the external loads can be written as:

$$VW_e = \iint_{z\,x} (q_y(x)\delta v_k + q_x(x)\delta u_k) Q_z\, V_k dx\, dz$$

This can be rewritten as

$$VW_e = \int_z q_k\, Q_z \delta\, V_k\, dz \qquad (3-75)$$

Where:

$$q_k = \int_x (q_y(x) v_k + q_x(x) u_k$$

3.16 Second order equation of equilibrium

The equilibrium condition is the equality of the virtual work of applied loads to the internal work term. Taking into account the necessary sign differences, the equation for each mode will be:

$$\sum_{j=1}^{n}(B_{jk}V_k + \mu D_{kj}^2 V_k'') + [EC_{kk}^1 V_k'''' + \sum_{i=1}^{n}\sum_{j=1}^{n} X_{ijk}\left(W_i V_j'\right)'] + \sum_{j=1}^{n}(C_{jk}^2 V_k'''' + \mu D_{jk}^2 V_k'')$$
$$- \sum_{j=1}^{n} 2(1-\mu)\left(D_{jk}^1 V_k''\right) + \sum_{i=1}^{n}\sum_{j=1}^{n} X_{ijk}\left(W_i' V_j\right)' + X_{ijk}^{\tau}\left(W_i' V_j\right)' + X_{ijk}^{\tau}\left(W_i' V_j\right)$$
$$= qQ_k$$

This can be rewritten:

$$\sum_{j=1}^{n}[EC_{jk}V_k'''' - GD_{jk}V_k'' + B_{jk}V_k + \sum_{i=1}^{n} X_{ijk}(W_i V_i)'' + X_{ijk}^{\tau}(W_i'' V_j + 2W_i' V_j')]$$
$$= qQ_k \qquad (3-76)$$

Where:

$$C_{jk} = EC_{jk}^1 + C_{jk}^2$$
$$D_{jk} = 2(1-\mu)D_{jk}^1 - \mu(D_{jk}^2 + D_{kj}^2)$$

This equation can be applied to all first and second order problems in order to calculate the stress distribution in a section subject to an arbitrary load, or in order to calculate the bifurcation load of a section when subject to any load (or series of loads).

Appendix A presents the calculations of the GBT section properties as coded with Matlab. For the next steps, the first order GBT is used to solve the flexural and torsional problems for beams subjected to different applied loads. The second order GBT is then used to solve the buckling problems of open-section beam-columns for both linear and non-linear analysis to find the theoretical and actual bucking loads of members with different cross-sections and different boundary conditions.

CHAPTER FOUR

APPLICATIONS OF GENERALIZED BEAM THEORY

CHAPTER FOUR

APPLICATIONS OF GENERALIZED BEAM THEORY

4.1 Introduction

This chapter presents applications of first and second order generalized beam theory using the Matlab code in both linear and non-linear analysis to find eigenvalue buckling and yield loads of open-section cold-form steel section. To implement this the author used the finite difference method to solve the fourth order generalized beam theory differential equation to find the value of (V) displacement function in each mode (k). All theoretical buckling results were compared and verified with examples using the finite strip methods CUFSM and GBT finite element method using GBTUL.

The finite difference is a method of solution which is easier to code than finite elements method. This will be verified in the following sections.

Liner analysis results are verified at this stage with the results of GBTUL & CUFSM. Non-linear analysis results are also addressed and presented and will be verified with experimental and finite element analysis (ANSYS).

4.2 Finite difference analysis of generalized beam theory

The principle of finite difference methods is related to the numerical schemes used to solve ordinary differential equations. It approximates the differential operator by replacing the derivatives in the equation using differential quotients. The domain is partitioned in space and in time and approximations of the solution are computed at space or time points. The error between the numerical solution and the exact solution is determined by the error that is committed by going from a differential operator to a difference operator. This error is called the discretization error or truncation error. The term truncation error reflects the fact that a finite part of a Taylor series is used in the approximation.

In general, the first order GBT equation is:

$$EC_{jk}V_k'''' - GD_{jk}V_k'' + B_{jk}V_k = qQ_k \qquad (4-1)$$

In the finite difference form the second and fourth order derivatives of *V* are:

$$V'' = \frac{V_{i-1} - 2V_i + V_{i+1}}{dx^2}$$

$$V'''' = \frac{V_{i-2} - 4V_{i-1} + 6V_i - 4V_{i+1} + V_{i+2}}{dx^4}$$

So the *GBT* equation for mode (*k*) will be:

$$EC_{jk}\left(\frac{V_{i-2} - 4V_{i-1} + 6V_i - 4V_{i+1} + V_{i+2}}{dx^4}\right) - GD_{jk}\left(\frac{V_{i-1} - 2V_i + V_{i+1}}{dx^2}\right) + B_{jk}V_i = qQ_k \qquad (4-2)$$

If the length of the beam was divided into (*n*) nodes.

The *GBT* equation would become:

$$\left[EC_{jk}\begin{bmatrix} m & -4 & 1 & 0 & 0 & 0 & 0 & 0 \\ -4 & 6 & -4 & 1 & 0 & 0 & 0 & 0 \\ 1 & -4 & 6 & -4 & 1 & 0 & 0 & 0 \\ 0 & 1 & -4 & 6 & -4 & 1 & 0 & 0 \\ 0 & 0 & 1 & -4 & 6 & -4 & 1 & 0 \\ - & - & - & - & - & - & - & - \\ - & - & - & - & - & - & - & - \\ 0 & 0 & 0 & 0 & 0 & 1 & -4 & m \end{bmatrix} - GD_{jk}\begin{bmatrix} -2 & 1 & 0 & 0 & 0 & 0 & 0 & 0 \\ 1 & -2 & 1 & 0 & 0 & 0 & 0 & 0 \\ 0 & 1 & -2 & 1 & 0 & 0 & 0 & 0 \\ 0 & 0 & 1 & -2 & 1 & 0 & 0 & 0 \\ 0 & 0 & 0 & 1 & -2 & 1 & 0 & 0 \\ - & - & - & - & - & - & - & - \\ - & - & - & - & - & - & - & - \\ 0 & 0 & 0 & 0 & 0 & 0 & 1 & -2 \end{bmatrix}$$

$$+ B_{jk}\begin{bmatrix} 1 & 0 & 0 & 0 & 0 & 0 & 0 & 0 \\ 0 & 1 & 0 & 0 & 0 & 0 & 0 & 0 \\ 0 & 0 & 1 & 0 & 0 & 0 & 0 & 0 \\ 0 & 0 & 0 & 1 & 0 & 0 & 0 & 0 \\ 0 & 0 & 0 & 0 & 1 & 0 & 0 & 0 \\ - & - & - & - & - & - & - & - \\ - & - & - & - & - & - & - & - \\ 0 & 0 & 0 & 0 & 0 & 0 & 0 & 1 \end{bmatrix}\Bigg] * \begin{bmatrix} V_1 \\ V_2 \\ V_3 \\ V_4 \\ V_5 \\ - \\ - \\ V_n \end{bmatrix} = \begin{bmatrix} q_1 \\ q_2 \\ q_3 \\ q_4 \\ q_5 \\ - \\ - \\ q_n \end{bmatrix} Q_k \qquad (4-3)$$

m is factor depends on boundary condition type.

m = 5 for fixed end condition.

m = 7 for pinned end condition.

4.2.1 Boundary conditions

As the finite difference equations are formed, at some point the boundary conditions of the structure need to be applied. Any conditions can be applied. At this stage, just two alternatives, pinned and fixed ends will be considered.

Pin end (at node *i*):

$y_i = 0$

$y_{i-1} = - y_{i+1}$

$y_{i-2} = - y_{i+2}$

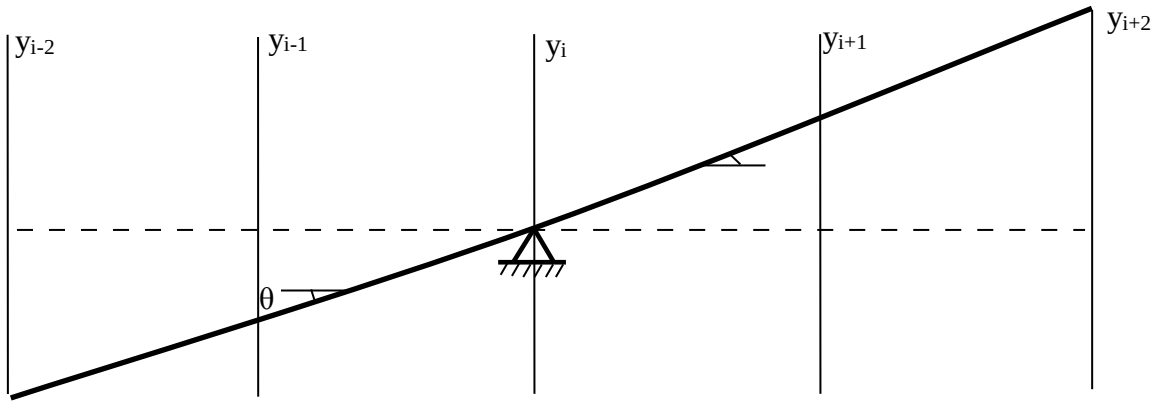

Figure (4-1) Pinned end

Fixed end (at node *i*)

$y_i = 0$

$y_{i-1} = y_{i+1}$

$y_{i-2} = y_{i+2}$

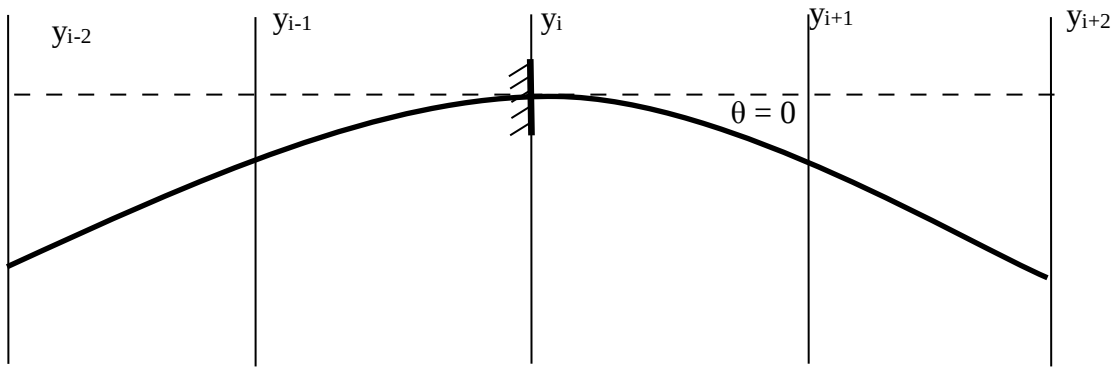

Figure (4-2) Fixed end

4.3 Linear problem using the generalized beam theory (beam subjected to axial load)

The first order basic equation of equilibrium of any member, in *GBT* notation, is:

$$EC_{jk}V_k'''' - GD_{jk}V_k'' + B_{jk}V_k = qQ_k \qquad (4-1)$$

The first four modes (rigid body modes) should be in sequence, the axial, bending about two principle axes and torsion modes in conventional theory.

Table (4-1) Differential equation for rigid body modes.

Mode	Conventional Theory	Generalized Beam Theory
1	$EAu'' = -N$	$EC_1V_1'''' - GD_1V_1'' + B_1V_1 = qQ_1$
2	$EI_{xx}y'''' = q_y$	$EC_2V_2'''' - GD_2V_2'' + B_2V_2 = qQ_2$
3	$EI_{yy}x'''' = q_x$	$EC_3V_3'''' - GD_3V_3'' + B_3V_3 = qQ_3$
4	$E\Gamma\varphi'''' - GJ\varphi'' = m$	$EC_4V_4'''' - GD_4V_4'' + B_4V_4 = qQ_4$

Table (4-2) Compatibility equation for rigid body modes.

Mode	Conventional Theory	Generalized Beam Theory
1	$N = EAu'$	$W_1 = -EC_1V_1''$
2	$M_x = -EI_{xx}y''$	$W_2 = -EC_2V_2''$
3	$M_y = -EI_{yy}x''$	$W_3 = -EC_3V_3''$
4	$B = -E\Gamma\varphi''$	$W_4 = -EC_4V_4''$

Table (4-3) Normal stress for rigid body modes.

Mode	Conventional Theory	Generalized Beam Theory
1	$\sigma = \frac{N}{A}$	$\sigma_1 = \frac{W_1w_1}{C_1}$
2	$\sigma_x = \frac{M_xy}{I_{xx}}$	$\sigma_2 = \frac{W_2w_2}{C_2}$
3	$\sigma_x = \frac{M_yx}{I_{yy}}$	$\sigma_3 = \frac{W_3w_3}{C_3}$
4	$\sigma_\varphi = \frac{B\omega}{\Gamma}$	$\sigma_4 = \frac{W_4w_4}{C_4}$

4.3.1 Equivalent axial loading

To resolve the applied loads at each node into equivalent axial plate forces the loads are applied at a cross-section node in a direction parallel to the web plate and with no component in the direction of any adjoining plates.

The equivalent axial loading for the applied load (*P*) is shown in figure (4-3).

Load case 1, figure (4-3a)

$$q_i = [0 \quad 0 \quad -P \quad 0 \quad 0]$$

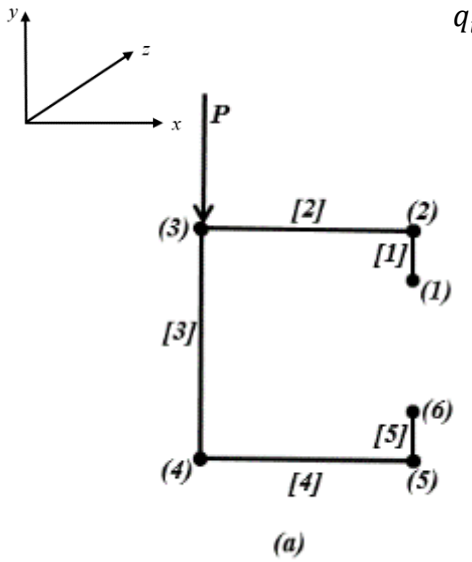

Plate No.	Load
1	0
2	0
3	-P
4	0
5	0

Load case 2, figure (4-3b)

$$q_i = [0 \quad -P \quad 0 \quad P \quad 0]$$

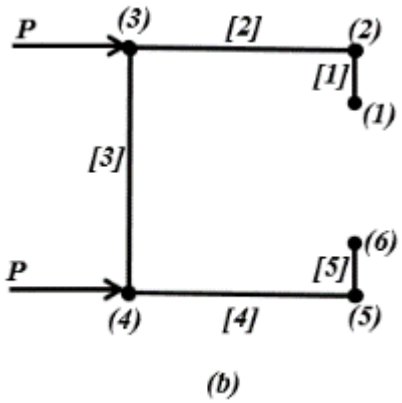

Plate No.	Load
1	0
2	-P
3	0
4	P
5	0

Figure (4-3) Equivalent axial loading.

The equivalent axial loads q_k is:

$$q_k = \sum_{i=1}^{n} q_k\,(i) u^p(i) \qquad (4-4)$$

Appendix B presents the Matlab code used to perform the GBT linear problem solution.

4.3.2 Example

Consider a simply supported beam with the top hat section as shown below in Figure (4-4):

Top hat section properties:

Young's Modulus, E= 21000 kN/cm^2; Poisson's Ratio, ν =0.3 t =0.17 cm
P =2 kN a =200 cm b =400 cm

Plate No.	Length (cm)	inclination (deg)
1	2	0
2	12	90
3	6	0
4	12	-90
5	2	0

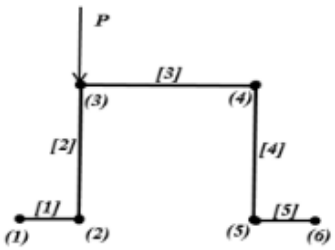

Figure (4-4) Top hat-section

Table (4-4), Figure (4-5) and Figure (4-6) show the relevant *GBT* section properties in the *Matlab* code, *GBTUL* and *CUFSM* respectively:

The GBT section properties of the first four modes (rigid body modes) from the Matlab coding program matched those in the (GBTUL), figure (4-5) and (CUFSM), figure (4-6) which represent cross-section area, moment of inertia about major axis and moment of inertia about manor axis for C_1, C_2 & C_3 in table (4-4) and torsional moment of inertia and torsional constant for C_4 & D_4 in table (4-4).

Table (4-5) shows the displacements of each mode separately through the length of the beam. node No.66 in table (4-5) represents the maximum displacement in mode No.2 which is matched to the maximum bending deflection in the conventional bending theory, equation (4-5). Likewise, the displacement in node No.80 in table (4-5) is matched with the deflection under the point load in the conventional bending theory, equation (4-6).

Table (4-6) demonstrates the stress resultants for each mode individually through the length of the beam. It was noted that the stress resultant of mode No.2 at node No.69 in table (4-6) was matched with the maximum bending moment in the conventional bending theory, equation (4-7).

Table (4-4) GBT section properties in matlab.

Mode	Conventional theories			GBT Section properties		
				C_k	D_k	B_k
1	A	_	_	6.8	0	0
2	I_x	_	_	128.76	0	0
3	I_y	_	_	59.88	0	0
4	Γ	J	_	725.38	0.091	0
5	_	_	_	0.291	0.00021	0.0115
6	_	_	_	0.318	0.00021	0.0159

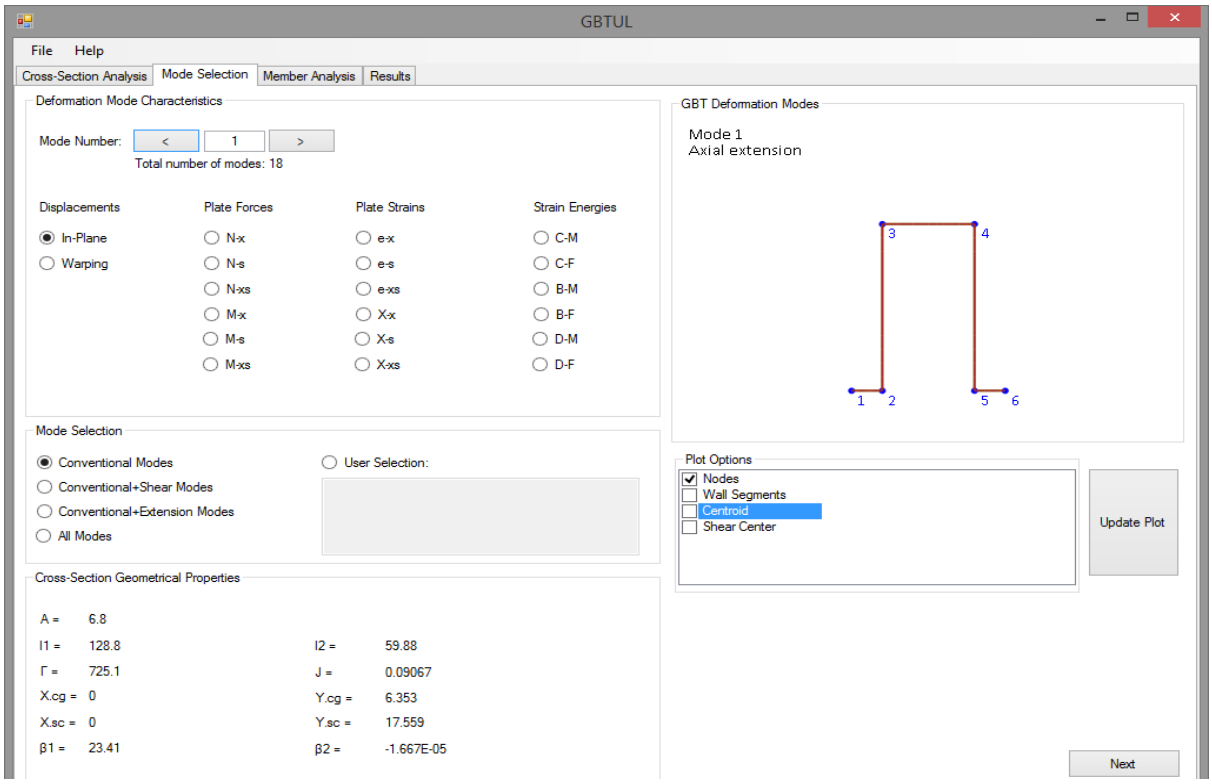

Figure (4-5) GBTUL section properties (Bebiano et al, 2008).

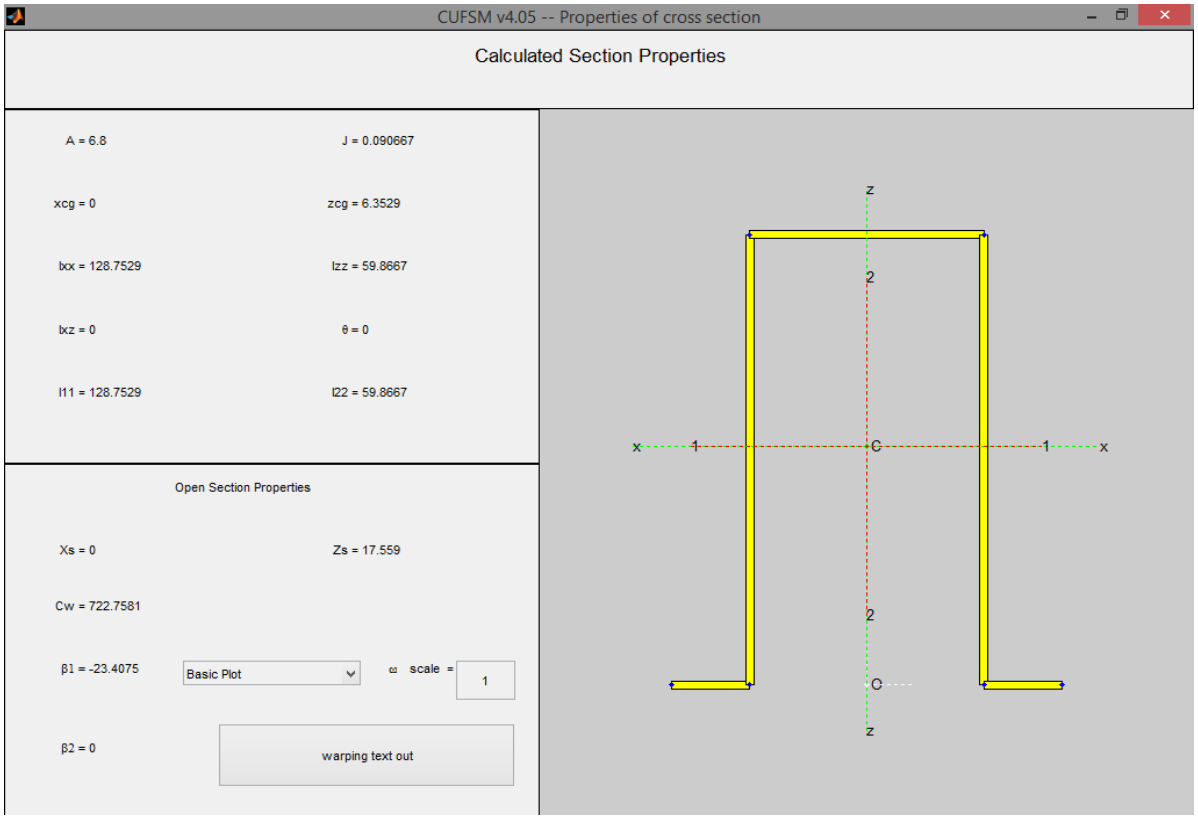

Figure (4-6) CUFSM section properties (Schafer, 2006).

Finite differences can, however, be used to actually find the displacement functions in each mode for any boundary condition. Considering the above problem and dividing the beam into *120* elements, each *50 mm* long, a *119* x *119* matrix is created for each *GBT* mode.

A summary of the results (for selected nodes) is shown in the tables (4-5), (4-6) & (4-7).

Table (4-5) Modal displacement.

Node	Mode 1	Mode 2	Mode 3	Mode 4	Mode 5	Mode 6
	Axial displacemnt	Displacement on major axis	Displacement on minor axis	Torsional displacement	Symmetrical distortional displacement	unsymmetrical distortional displacement
Unit	cm	cm	cm	red	red	red
60	0	-2.82	0	-0.543	0.001	0.000
61	0	-2.84	0	-0.547	0.000	0.000
62	0	-2.85	0	-0.550	0.000	0.000
63	0	-2.85	0	-0.554	-0.001	0.000
64	0	-2.86	0	-0.557	-0.002	0.000
65	0	-2.86	0	-0.559	-0.004	-0.001
66	0	-2.86	0	-0.561	-0.005	-0.001
67	0	-2.86	0	-0.564	-0.007	-0.001
68	0	-2.86	0	-0.565	-0.009	-0.002
69	0	-2.86	0	-0.566	-0.012	-0.003
70	0	-2.85	0	-0.567	-0.015	-0.003
71	0	-2.84	0	-0.567	-0.018	-0.004
72	0	-2.83	0	-0.567	-0.022	-0.005
73	0	-2.82	0	0.566	-0.026	-0.006
74	0	-2.80	0	-0.565	-0.030	-0.008
75	0	-2.78	0	-0.563	-0.034	-0.009
76	0	-2.76	0	-0.561	-0.039	-0.010
77	0	-2.74	0	-0.558	-0.043	-0.011
78	0	-2.72	0	-0.554	-0.047	-0.012
79	0	-2.69	0	-0.551	0.050	-0.013
80	0	-2.66	0	-0.546	-0.052	-0.014
81	0	-2.63	0	-0.541	-0.053	-0.014
82	0	-2.60	0	-0.535	-0.052	-0.014
83	0	-2.56	0	-0.528	0.050	-0.013
84	0	-2.52	0	-0.521	-0.047	-0.012
85	0	-2.48	0	-0.513	-0.043	-0.011

Table (4-6) Stress resultants.

Node	Mode 1	Mode 2	Mode 3	Mode 4	Mode 5	Mode 6
	Axial load	Bending moment on major axis	Bending moment on minor axis	Torsion	Symmetrical distortion	unsymmetrical distortion
Unit	kN	kN.cm	kN.cm	kN.cm	kN.cm	kN.cm
60	0	-196.67	0	-192.62	0.035	0.009
61	0	-200.00	0	-199.65	0.041	0.011
62	0	203.33	0	-206.91	0.048	0.014
63	0	-206.67	0	-214.42	0.055	0.016
64	0	-210.00	0	-222.19	0.062	0.019
65	0	-213.33	0	-230.22	0.069	0.021
66	0	-216.67	0	-238.53	0.076	0.024
67	0	-220.00	0	-247.13	0.081	0.026
68	0	-223.33	0	-256.03	0.085	0.028
69	0	-226.67	0	-265.23	0.087	0.029
70	0	-230.00	0	-274.75	0.086	0.029
71	0	-233.33	0	-284.61	0.081	0.028
72	0	-236.67	0	-294.80	0.071	0.026
73	0	-240.00	0	-305.35	0.056	0.022
74	0	-243.33	0	-316.26	0.034	0.015
75	0	-246.67	0	-327.56	0.003	0.005
76	0	-250.00	0	-339.25	-0.037	-0.008
77	0	-253.33	0	-351.35	-0.088	-0.025
78	0	-256.67	0	-363.87	-0.153	-0.047
79	0	-260.00	0	-376.82	-0.232	-0.074
80	0	-263.33	0	-390.23	-0.327	-0.107
81	0	-266.67	0	-404.11	-0.438	-0.146
82	0	-260.00	0	-388.48	-0.327	-0.107
83	0	-253.33	0	-373.31	-0.232	-0.074
84	0	-246.67	0	-358.59	-0.153	-0.047
85	0	-240.00	0	-344.30	-0.088	-0.025

Table (4-7) Nodal stress.

Node thruogh length	Cross section nodal stress kN/cm^2					
	1	2	3	4	5	6
60	5.61	14.81	13.04	4.20	4.54	14.04
61	5.63	15.16	13.34	4.18	4.51	14.39
62	5.66	15.51	13.66	4.16	4.48	14.74
63	5.67	15.87	13.97	4.13	4.44	15.10
64	5.68	16.24	14.29	4.10	4.39	15.47
65	5.69	16.61	14.62	4.06	4.33	15.84
66	5.69	16.99	14.96	4.02	4.27	16.21
67	5.68	17.38	15.30	3.97	4.20	16.59
68	5.65	17.78	15.65	3.91	4.13	16.97
69	5.62	18.19	16.00	3.84	4.04	17.34
70	5.57	18.61	16.37	3.77	3.95	17.71
71	5.51	19.04	16.74	3.69	3.86	18.07
72	5.43	19.48	17.13	3.60	3.76	18.42
73	5.32	19.94	17.52	3.51	3.66	18.74
74	5.20	20.41	17.92	3.41	3.55	19.05
75	5.04	20.90	18.34	3.29	3.44	19.32
76	4.85	21.40	18.77	3.17	3.32	19.56
77	4.63	21.93	19.22	3.05	3.21	19.76
78	4.37	22.47	19.67	2.91	3.09	19.91
79	4.07	23.04	20.15	2.76	2.98	20.00
80	3.72	23.63	20.64	2.60	2.86	20.03
81	3.32	24.24	21.15	2.44	2.75	19.99
82	3.60	23.42	20.45	2.50	2.74	19.82
83	3.82	22.62	19.78	2.55	2.74	19.59
84	3.99	21.84	19.11	2.59	2.74	19.30
85	4.13	21.08	18.47	2.62	2.74	18.95

From the conventional bending theory, the maximum moment and deflection on the *y*-axis are:

$$\delta_{max} = \frac{Pa(l^2 - a^2)^{\frac{3}{2}}}{9\sqrt{3}lEI_x} = \frac{2 \times 200(600^2 - 200^2)^{\frac{3}{2}}}{9\sqrt{3} \times 600 \times 21000 \times 128.76} = 2.9\ cm \qquad (4-5)$$

$$\delta_{at\ point\ load} = \frac{Pa^2b^2}{3EI_x l} = \frac{2 \times 200^2 \times 400^2}{3 \times 21000 \times 128.76 \times 600} = 2.6\ cm \qquad (4-6)$$

$$M_{max} = \frac{Pab}{l} = \frac{2 \times 400 \times 200}{600} = 266.7\ kN.cm \qquad (4-7)$$

4.4 Buckling problems using generalized beam theory

The basic equation of equilibrium of any member, in GBT notation, is:

$$\sum_{k=1}^{n}[EC_{kk}V_k'''' - GD_{kk}V_k'' + B_{kk}V_k + \sum_{j=1}^{n}\sum_{i=1}^{n} X_{ijk}(W_iV_i)'' + X_{ijk}^{\tau}(W_i''V_j + 2W_i'V_j')] = qQ_k \qquad (4-8)$$

Where:

V is the (unknown) displacement function in each mode. Finite differences can, however, be used to actually find the displacement functions in each mode for any boundary condition.

E, G, are material properties.

C, D, B, x, and x^{τ} are *GBT* section properties.

W is the resultant function of the section (another section property).

q_Q are the applied loads in each mode.

i,j,k are the different possible (coupled) displacement modes.

In the case of open sections, the shear effect is trivial, the term x^{τ} is a second order term related to shear that can usually be ignored.

In the case of buckling problems,

1- The applied load q_Q is zero.

2- The axial load will be represented as a resultant function of mode one; (*k*=1), axial load subjected to beam =W_1. The axial load is constant along the beam so:

$$W_1' = W_1'' = 0$$

The *GBT* equation becomes:

$$\sum_{k=1}^{n}[EC_{kk}V_k'''' - GD_{kk}V_k'' + B_{kk}V_k = -\sum_{k=1}^{n}\sum_{j=1}^{n}X_{1jk}(W_1V_j'') \qquad (4-9$$

4.4.1 Linear analysis of buckling problems (eigen value problems)

4.4.1.1 Buckling in a single mode

Considering a single mode individually, the governing equation is:

$$EC_{kk}V_k'''' - GD_{kk}V_k'' + B_{kk}V_k = -X_{1kk}(W_1V_k'') \qquad (4-10)$$

Finite differences can be used to create an eigenvalue problem where the lowest eigenvalue is the critical load factor and the eigenvector is the buckled mode shape related to this value.

If the length of the beam was divided into (*n*) nodes. The equation (4-10) will be:

$$\left[EC_{kk}\begin{bmatrix} m & -4 & 1 & 0 & 0 & 0 & 0 & 0 \\ -4 & 6 & -4 & 1 & 0 & 0 & 0 & 0 \\ 1 & -4 & 6 & -4 & 1 & 0 & 0 & 0 \\ 0 & 1 & -4 & 6 & -4 & 1 & 0 & 0 \\ 0 & 0 & 1 & -4 & 6 & -4 & 1 & 0 \\ - & - & - & - & - & - & - & - \\ - & - & - & - & - & - & - & - \\ 0 & 0 & 0 & 0 & 0 & 1 & -4 & m \end{bmatrix}\right] -$$

$$GD_{kk}\begin{bmatrix} -2 & 1 & 0 & 0 & 0 & 0 & 0 & 0 \\ 1 & -2 & 1 & 0 & 0 & 0 & 0 & 0 \\ 0 & 1 & -2 & 1 & 0 & 0 & 0 & 0 \\ 0 & 0 & 1 & -2 & 1 & 0 & 0 & 0 \\ 0 & 0 & 0 & 1 & -2 & 1 & 0 & 0 \\ - & - & - & - & - & - & - & - \\ - & - & - & - & - & - & - & - \\ 0 & 0 & 0 & 0 & 0 & 0 & 1 & -2 \end{bmatrix} + B_{kk}\begin{bmatrix} 1 & 0 & 0 & 0 & 0 & 0 & 0 & 0 \\ 0 & 1 & 0 & 0 & 0 & 0 & 0 & 0 \\ 0 & 0 & 1 & 0 & 0 & 0 & 0 & 0 \\ 0 & 0 & 0 & 1 & 0 & 0 & 0 & 0 \\ 0 & 0 & 0 & 0 & 1 & 0 & 0 & 0 \\ - & - & - & - & - & - & - & - \\ - & - & - & - & - & - & - & - \\ 0 & 0 & 0 & 0 & 0 & 0 & 0 & 1 \end{bmatrix} *$$

$$\begin{bmatrix} V_1 \\ V_2 \\ V_3 \\ V_4 \\ V_5 \\ - \\ - \\ V_n \end{bmatrix} = -X_{1kk}W_1\begin{bmatrix} -2 & 1 & 0 & 0 & 0 & 0 & 0 & 0 \\ 1 & -2 & 1 & 0 & 0 & 0 & 0 & 0 \\ 0 & 1 & -2 & 1 & 0 & 0 & 0 & 0 \\ 0 & 0 & 1 & -2 & 1 & 0 & 0 & 0 \\ 0 & 0 & 0 & 1 & -2 & 1 & 0 & 0 \\ - & - & - & - & - & - & - & - \\ - & - & - & - & - & - & - & - \\ 0 & 0 & 0 & 0 & 0 & 0 & 1 & -2 \end{bmatrix} * \begin{bmatrix} V_1 \\ V_2 \\ V_3 \\ V_4 \\ V_5 \\ - \\ - \\ V_n \end{bmatrix}$$

The above equation will be:

$$(A - \lambda B)V = 0 \qquad (4-11)$$

Where:

$$A = EC_{kk}\begin{bmatrix} m & -4 & 1 & 0 & 0 & 0 & 0 & 0 \\ -4 & 6 & -4 & 1 & 0 & 0 & 0 & 0 \\ 1 & -4 & 6 & -4 & 1 & 0 & 0 & 0 \\ 0 & 1 & -4 & 6 & -4 & 1 & 0 & 0 \\ 0 & 0 & 1 & -4 & 6 & -4 & 1 & 0 \\ - & - & - & - & - & - & - & - \\ - & - & - & - & - & - & - & - \\ 0 & 0 & 0 & 0 & 0 & 1 & -4 & m \end{bmatrix}$$

$$- GD_{kk}\begin{bmatrix} -2 & 1 & 0 & 0 & 0 & 0 & 0 & 0 \\ 1 & -2 & 1 & 0 & 0 & 0 & 0 & 0 \\ 0 & 1 & -2 & 1 & 0 & 0 & 0 & 0 \\ 0 & 0 & 1 & -2 & 1 & 0 & 0 & 0 \\ 0 & 0 & 0 & 1 & -2 & 1 & 0 & 0 \\ - & - & - & - & - & - & - & - \\ - & - & - & - & - & - & - & - \\ 0 & 0 & 0 & 0 & 0 & 0 & 1 & -2 \end{bmatrix}$$

$$+ B_{kk}\begin{bmatrix} 1 & 0 & 0 & 0 & 0 & 0 & 0 & 0 \\ 0 & 1 & 0 & 0 & 0 & 0 & 0 & 0 \\ 0 & 0 & 1 & 0 & 0 & 0 & 0 & 0 \\ 0 & 0 & 0 & 1 & 0 & 0 & 0 & 0 \\ 0 & 0 & 0 & 0 & 1 & 0 & 0 & 0 \\ - & - & - & - & - & - & - & - \\ - & - & - & - & - & - & - & - \\ 0 & 0 & 0 & 0 & 0 & 0 & 0 & 1 \end{bmatrix}$$

$$B = -X_{1kk}W_1\begin{bmatrix} -2 & 1 & 0 & 0 & 0 & 0 & 0 & 0 \\ 1 & -2 & 1 & 0 & 0 & 0 & 0 & 0 \\ 0 & 1 & -2 & 1 & 0 & 0 & 0 & 0 \\ 0 & 0 & 1 & -2 & 1 & 0 & 0 & 0 \\ 0 & 0 & 0 & 1 & -2 & 1 & 0 & 0 \\ - & - & - & - & - & - & - & - \\ - & - & - & - & - & - & - & - \\ 0 & 0 & 0 & 0 & 0 & 0 & 1 & -2 \end{bmatrix}$$

After applying boundary conditions, the problem will be an (n-1) x (n-1) eigenvalue problem.

Appendix C presents the Matlab code used to perform the GBT linear analysis of buckling in single mode.

For verification purposes, mode 2 and 3 are the bending modes about two principal axes which must match the Euler buckling about the same axes.

Euler buckling load is:

$$P_{cr} = \frac{\pi^2 EI}{L^2} \qquad (4-12)$$

4.4.1.1.1 Example

Consider the column subjected to an axial load, with the section as shown in Figure (4-7):

The properties of the section are:

Young's Modulus, E=20,000 kN/cm^2; Poisson's Ratio, v =0.3 t =0.167 cm

Nodes	*x*	*y*
1	-4.55	10
2	-3.25	10
3	-3.25	6.8
4	-5	6.8
5	-5	0
6	5	0
7	5	6.8
8	3.25	6.8
9	3.25	10
10	4.55	10

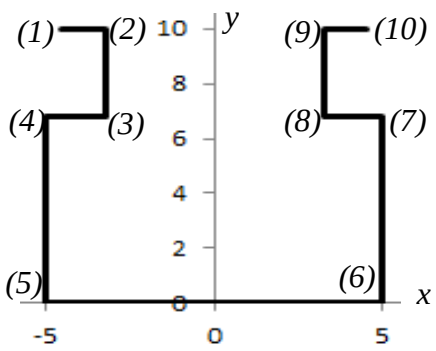

Figure (4-7) Rack column section.

Table (4-12) and figure (4-8) demonstrate the matching between *GBT* second and third modes with Euler buckling loads in same axes along the length of the beam with different boundary conditions. Figure (4-8) at this scale, the results are indistinguishable.

Figures (4-9), (4-10) & (4-11) show the linear buckling load along the length of the member for each mode individually with different boundary conditions.

Table (4-8) GBT & Euler buckling loads (kN)

length (cm)	Pinned-Pinned				Pinned-Fixed				Fixed-Fixed			
	Mode 2		Mode 3		Mode 2		Mode 3		Mode 2		Mode 3	
	GBT	Euler	GBT	Euler	GBT	Euler	GBT	Euler	GBT	Euler	GBT	Euler
10	194917.91	195081.63	153911.94	154050.29	398706.38	390163.27	314828.28	308100.57	779483.09	780326.53	615498.85	616201.14
20	48729.48	48770.41	38477.98	38512.57	99676.60	97540.82	78707.07	77025.14	194870.77	195081.63	153874.71	154050.29
30	21657.55	21675.74	17101.33	17116.70	44300.71	43351.47	34980.92	34233.40	86609.23	86702.95	68388.76	68466.79
40	12182.37	12192.60	9619.50	9628.14	24919.15	24385.20	19676.77	19256.29	48717.69	48770.41	38468.68	38512.57
50	7796.72	7803.27	6156.48	6162.01	15948.26	15606.53	12593.13	12324.02	31179.32	31213.06	24619.95	24648.05
60	5414.39	5418.93	4275.33	4279.17	11075.18	10837.87	8745.23	8558.35	21652.31	21675.74	17097.19	17116.70
70	3977.92	3981.26	3141.06	3143.88	8136.86	7962.52	6425.07	6287.77	15907.82	15925.03	12561.20	12575.53
80	3045.59	3048.15	2404.87	2407.04	6229.79	6096.30	4919.19	4814.07	12179.42	12192.60	9617.17	9628.14
90	2406.39	2408.42	1900.15	1901.86	4922.30	4816.83	3886.77	3803.71	9623.25	9633.66	7598.75	7607.42
100	1949.18	1950.82	1539.12	1540.50	3987.06	3901.63	3148.28	3081.01	7794.83	7803.27	6154.99	6162.01
125	1247.47	1248.52	985.04	985.92	2551.72	2497.04	2014.90	1971.84	4988.69	4994.09	3939.19	3943.69
150	866.30	867.03	684.05	684.67	1772.03	1734.06	1399.24	1369.34	3464.37	3468.12	2735.55	2738.67
175	636.47	637.00	502.57	503.02	1301.90	1274.00	1028.01	1006.04	2545.25	2548.00	2009.79	2012.09
200	487.29	487.70	384.78	385.13	996.77	975.41	787.07	770.25	1948.71	1950.82	1538.75	1540.50
250	311.87	312.13	246.26	246.48	637.93	624.26	503.73	492.96	1247.17	1248.52	984.80	985.92
300	216.58	216.76	171.01	171.17	443.01	433.51	349.81	342.33	866.09	867.03	683.89	684.67
350	159.12	159.25	125.64	125.76	325.47	318.50	257.00	251.51	636.31	637.00	502.45	503.02
400	121.82	121.93	96.19	96.28	249.19	243.85	196.77	192.56	487.18	487.70	384.69	385.13
450	96.26	96.34	76.01	76.07	196.89	192.67	155.47	152.15	384.93	385.35	303.95	304.30
500	77.97	78.03	61.56	61.62	159.48	156.07	125.93	123.24	311.79	312.13	246.20	246.48
550	64.44	64.49	50.88	50.93	131.80	128.98	104.08	101.85	257.68	257.96	203.47	203.70
600	54.14	54.19	42.75	42.79	110.75	108.38	87.45	85.58	216.52	216.76	170.97	171.17
650	46.13	46.17	36.43	36.46	94.37	92.35	74.52	72.92	184.49	184.69	145.68	145.85
700	39.78	39.81	31.41	31.44	81.37	79.63	64.25	62.88	159.08	159.25	125.61	125.76
750	34.65	34.68	27.36	27.39	70.88	69.36	55.97	54.77	138.57	138.72	109.42	109.55
800	30.46	30.48	24.05	24.07	62.30	60.96	49.19	48.14	121.79	121.93	96.17	96.28
850	26.98	27.00	21.30	21.32	55.18	54.00	43.57	42.64	107.89	108.00	85.19	85.29
900	24.06	24.08	19.00	19.02	49.22	48.17	38.87	38.04	96.23	96.34	75.99	76.07
950	21.60	21.62	17.05	17.07	44.18	43.23	34.88	34.14	86.37	86.46	68.20	68.28
1000	19.49	19.51	15.39	15.41	39.87	39.02	31.48	30.81	77.95	78.03	61.55	61.62

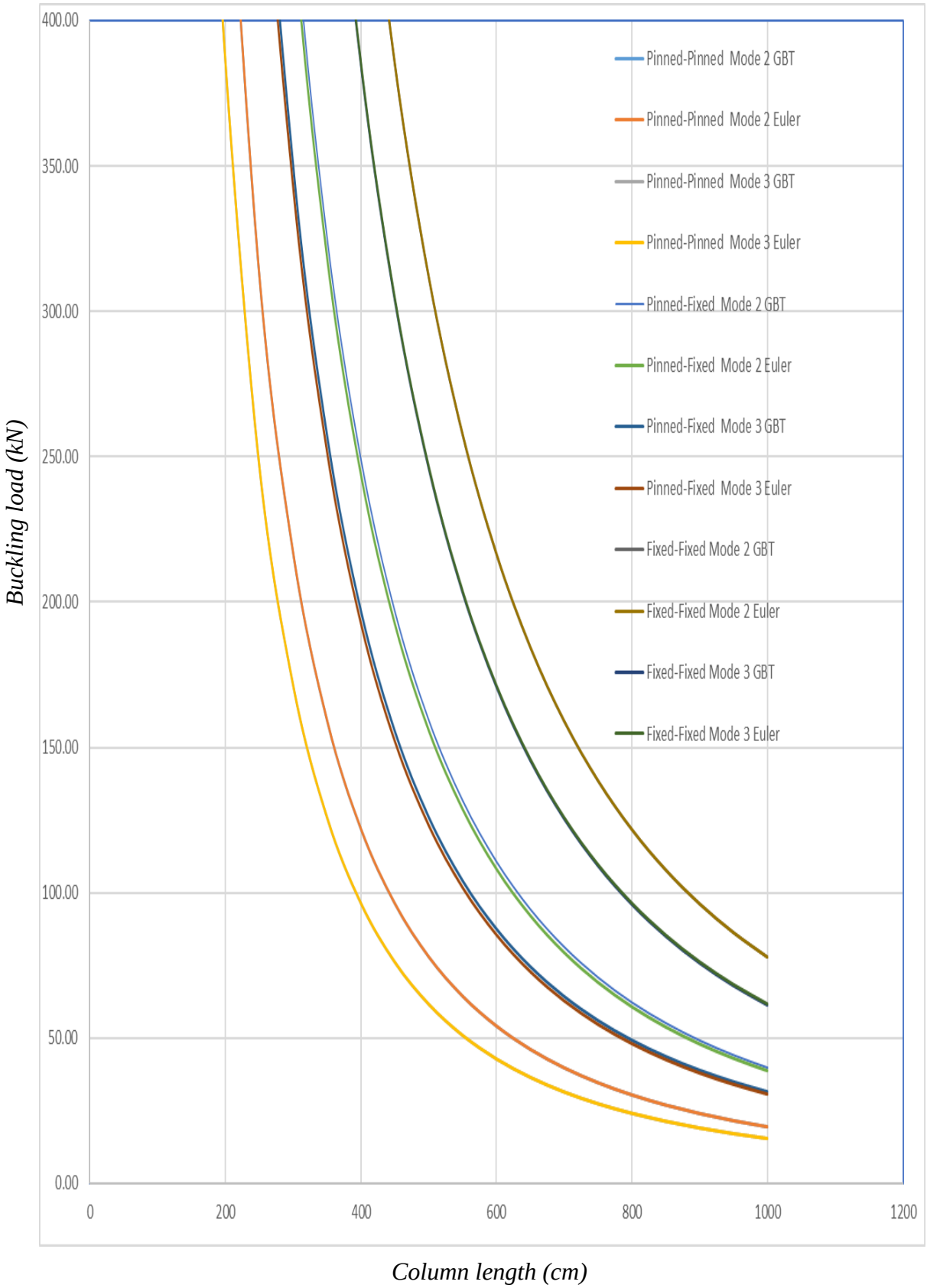

Figure (4-8) GBT & Euler buckling loads.

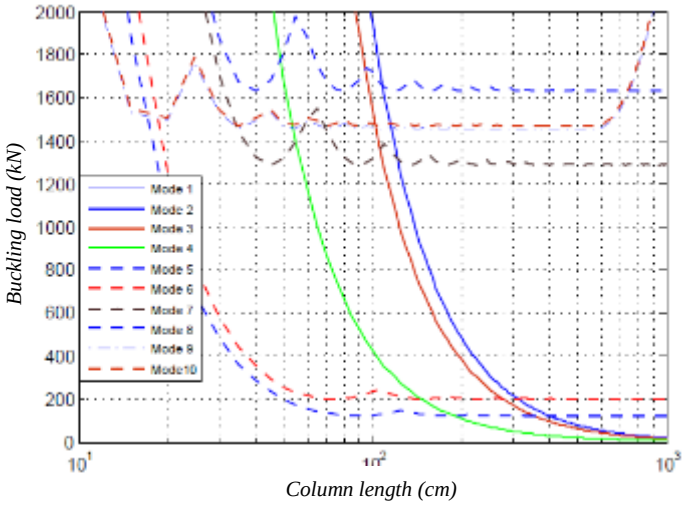

Figure (4-9) Buckling load vs length of column for each mode individually for pinned-pinned ends conditions.

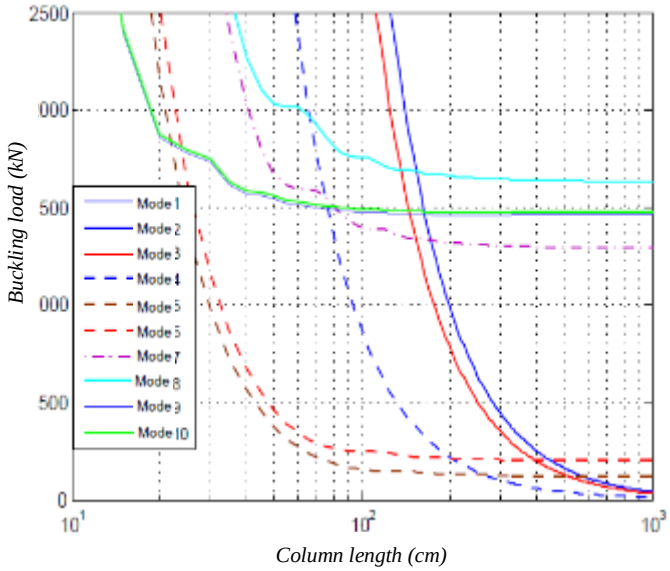

Figure (4-10) Buckling load vs length of column for each mode individually for fixed-pinned ends conditions.

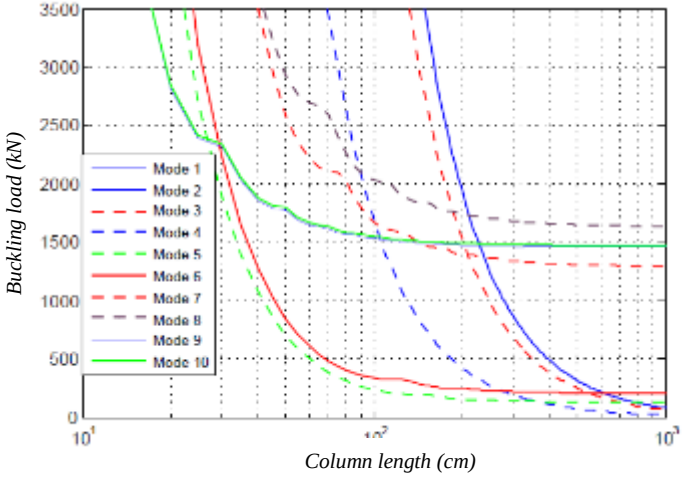

Figure (4-11) Buckling load vs length of column for each mode individually for fixed-fixed ends conditions.

4.4.1.2 Buckling in combined modes

For combined modes, the governing equation is:

$$\sum_{k=1}^{n} EC_{kk}V_k'''' - GD_{kk}V_k'' + B_{kk}V_k = -\sum_{k=1}^{n}\sum_{j=1}^{n} X_{1jk}\left(W_1 V_j''\right) \qquad (4-6)$$

The final buckling problem to consider is that of coupled buckling. The method of solution is again by finite differences.

The eigenvalue problem will be:

$$(C - \lambda D)V = 0 \qquad (4-13)$$

Where:

$$C = \begin{bmatrix} A_1 & 0 & 0 & 0 & 0 & 0 \\ 0 & A_2 & 0 & 0 & 0 & 0 \\ 0 & 0 & A_3 & 0 & 0 & 0 \\ - & - & - & - & - & - \\ - & - & - & - & - & - \\ 0 & 0 & 0 & 0 & 0 & A_k \end{bmatrix}$$

$$D = -\begin{bmatrix} X_{111} & 0 & 0 & 0 & 0 & 0 \\ 0 & X_{122} & 0 & 0 & 0 & 0 \\ 0 & 0 & X_{133} & 0 & 0 & 0 \\ - & - & - & - & - & - \\ - & - & - & - & - & - \\ 0 & 0 & 0 & 0 & 0 & X_{1kk} \end{bmatrix} * W_1$$

$$* \begin{bmatrix} -2 & 1 & 0 & 0 & 0 & 0 & 0 & 0 \\ 1 & -2 & 1 & 0 & 0 & 0 & 0 & 0 \\ 0 & 1 & -2 & 1 & 0 & 0 & 0 & 0 \\ 0 & 0 & 1 & -2 & 1 & 0 & 0 & 0 \\ 0 & 0 & 0 & 1 & -2 & 1 & 0 & 0 \\ - & - & - & - & - & - & - & - \\ - & - & - & - & - & - & - & - \\ 0 & 0 & 0 & 0 & 0 & 0 & 1 & -2 \end{bmatrix}$$

A is the same in single mode eigenvalue problem.

After applying boundary conditions, the problem will be *(n × k-1) x (n × k-1)* eigenvalue problem.

Appendix D presents the Matlab code for GBT linear analysis of buckling in combined modes. The results could be compared with GBTUL and CUFSM for verification purposes.

The figure (4-12) flow chart illustrates procedures to calculate critical buckling loads in both single and combined modes.

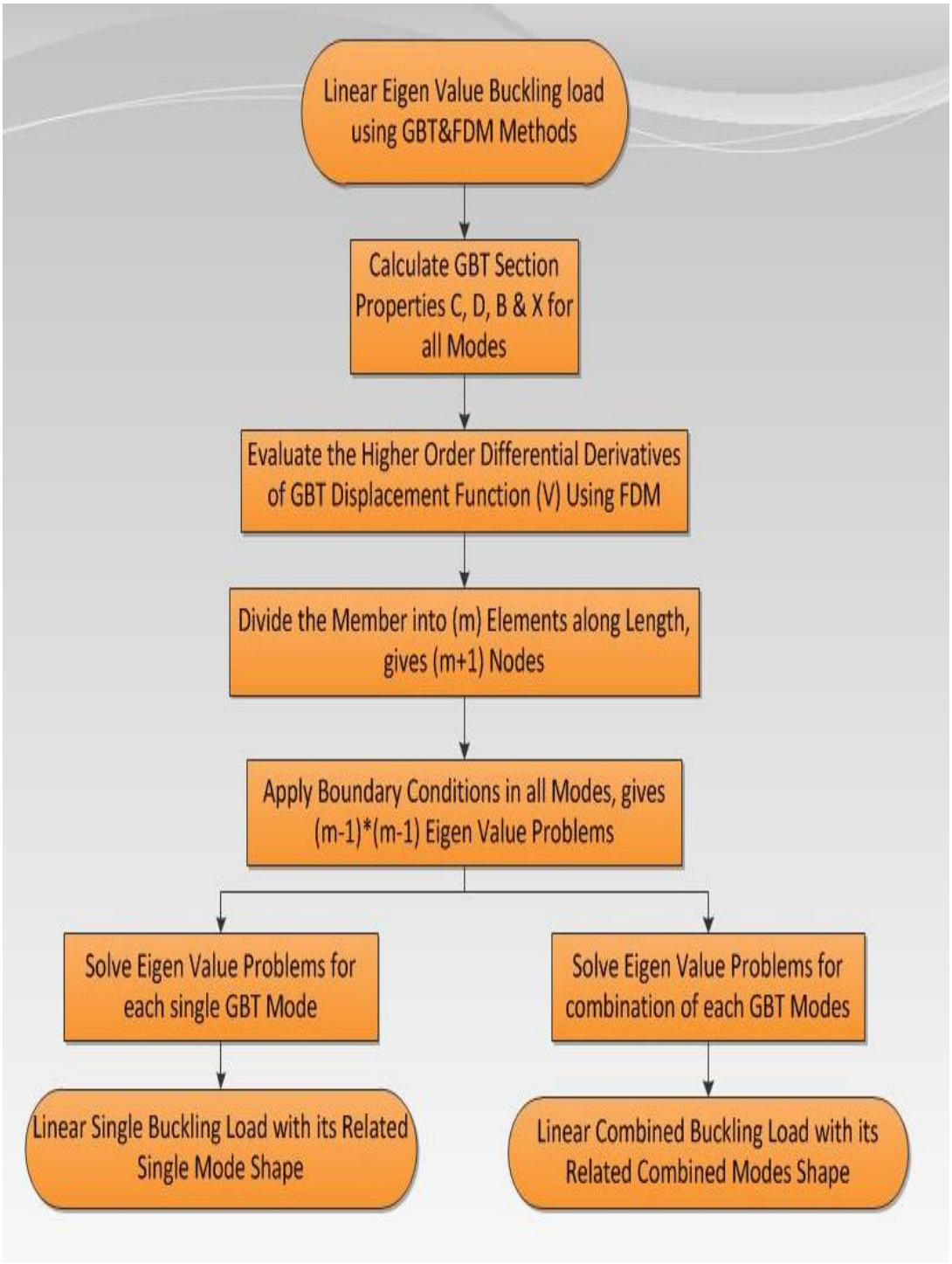

Figure (4-12) Flow chart illustrates procedures to calculate critical buckling loads in both single and combined modes.

4.4.1.2.1 Example

For the cross-section showed in figure (4-7), Figures (4-13) to (4-24) demonstrate the theoretical buckling load through the column length derived from the linear analysis finite difference *Matlab* code, finite element *(GBTUL)* and finite strip method *(CUFSM)* respectively with different boundary conditions.

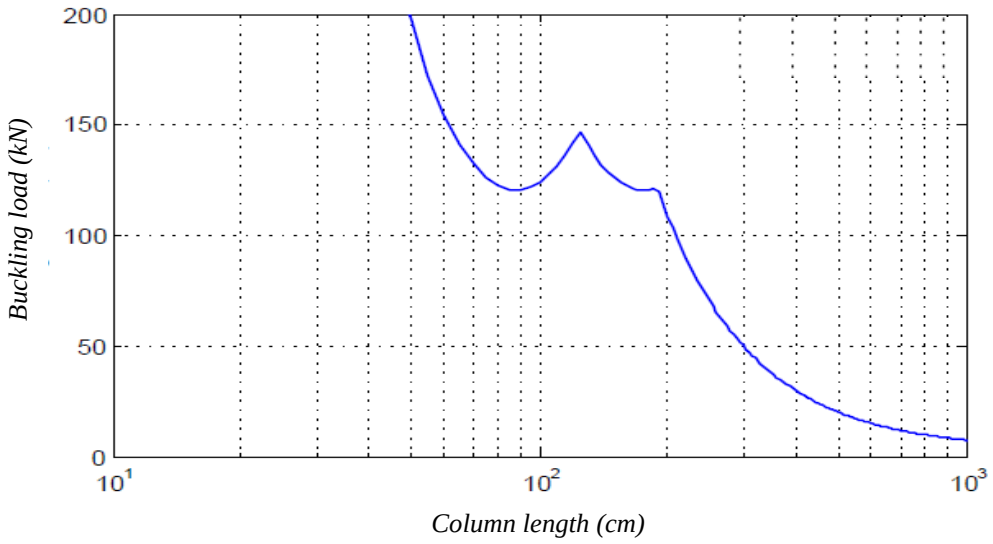

Figure (4-13) Buckling load vs length of column with combined modes in matlab program for pinned-pinned boundary conditions.

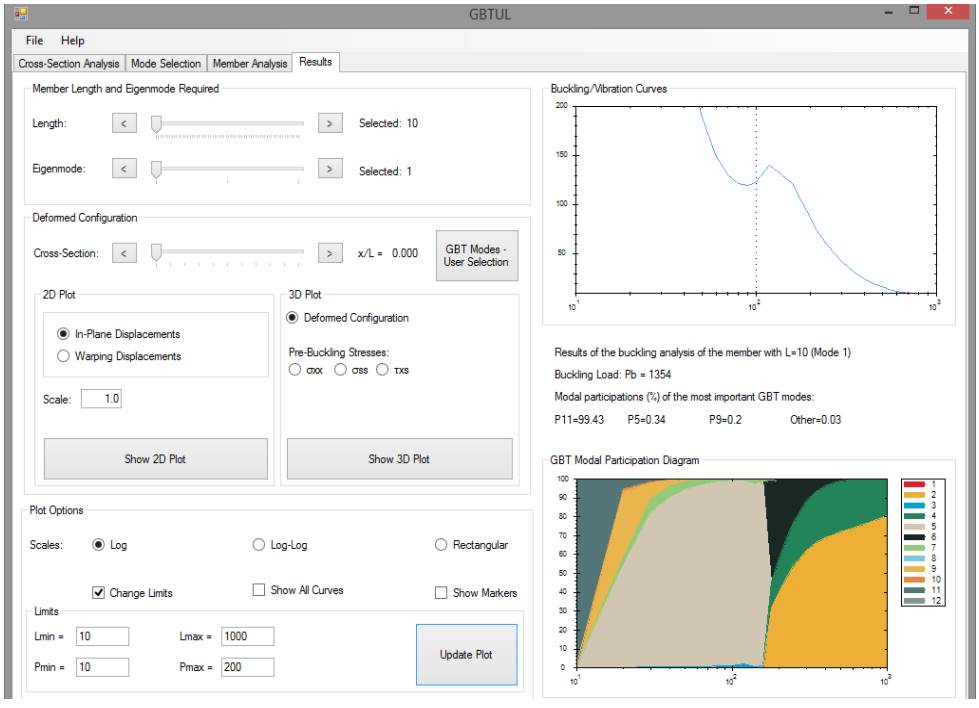

Figure (4-14) Buckling load vs length of column with combined modes in GBTUL for pinned-pinned boundary conditions (Bebiano et al, 2008).

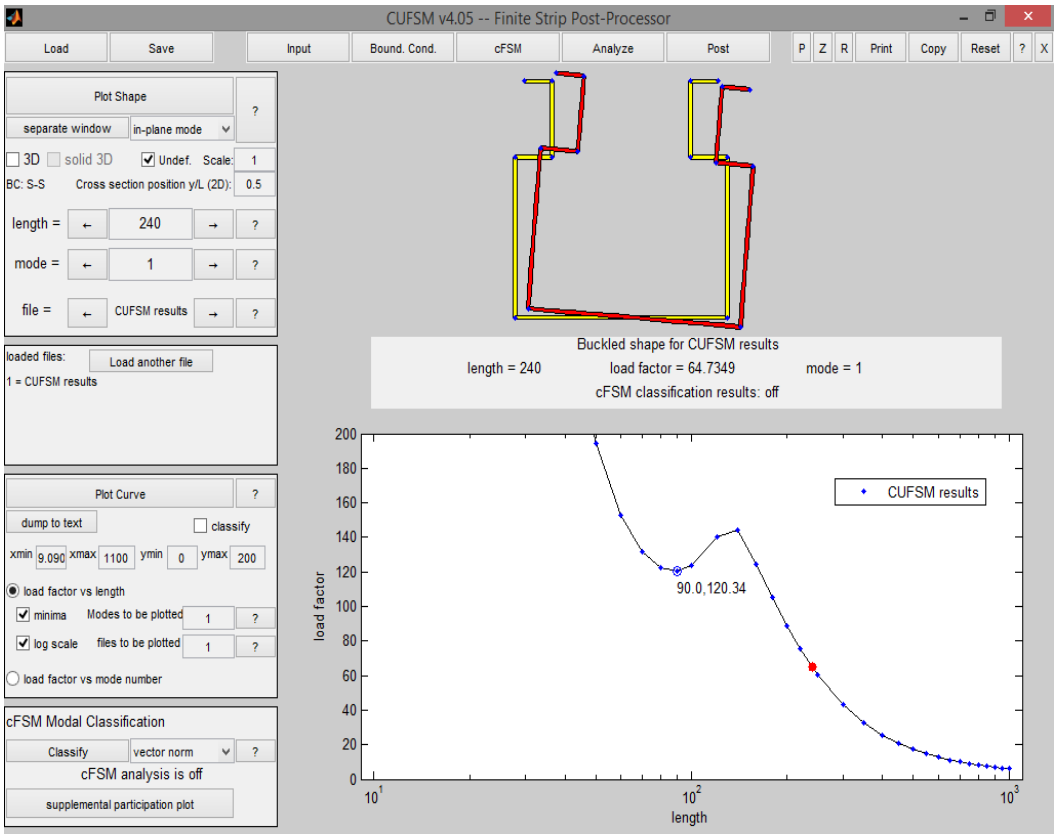

Figure (4-15) Buckling load vs length of column with combined modes in CUFSM for pinned-pinned boundary conditions (Schafer, 2006).

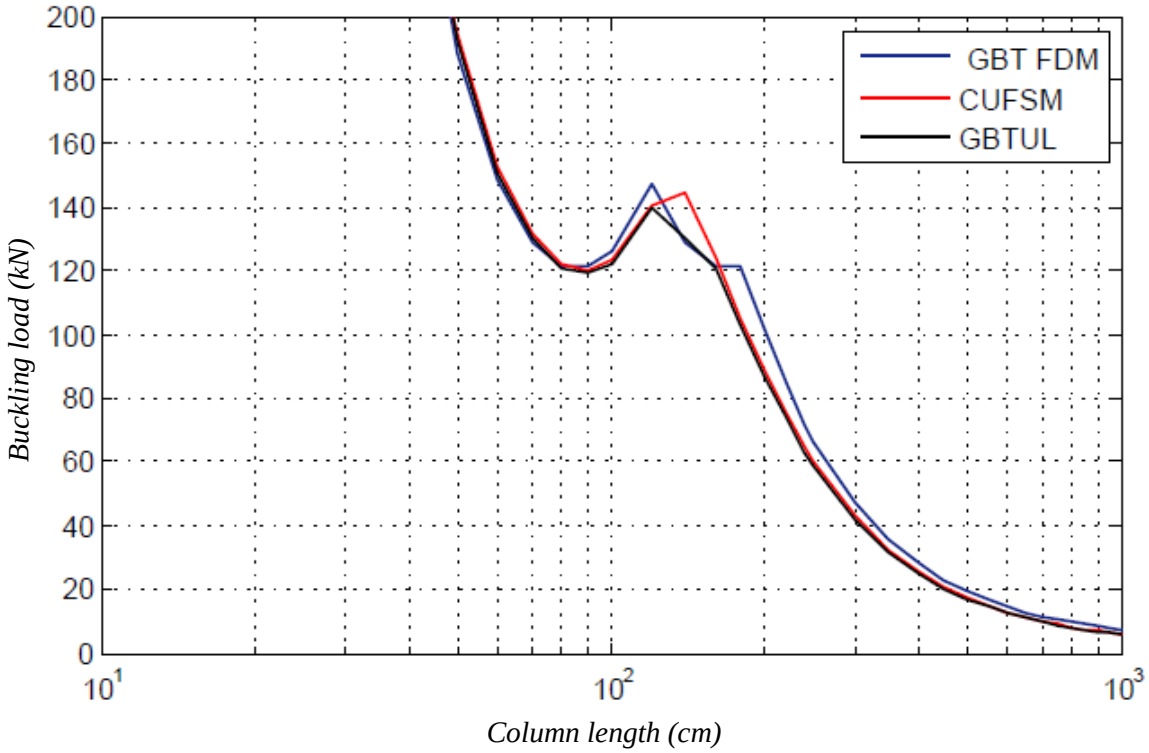

Figure (4-16) Buckling load vs length of column with combined modes for all programs for pinned-pinned boundary conditions.

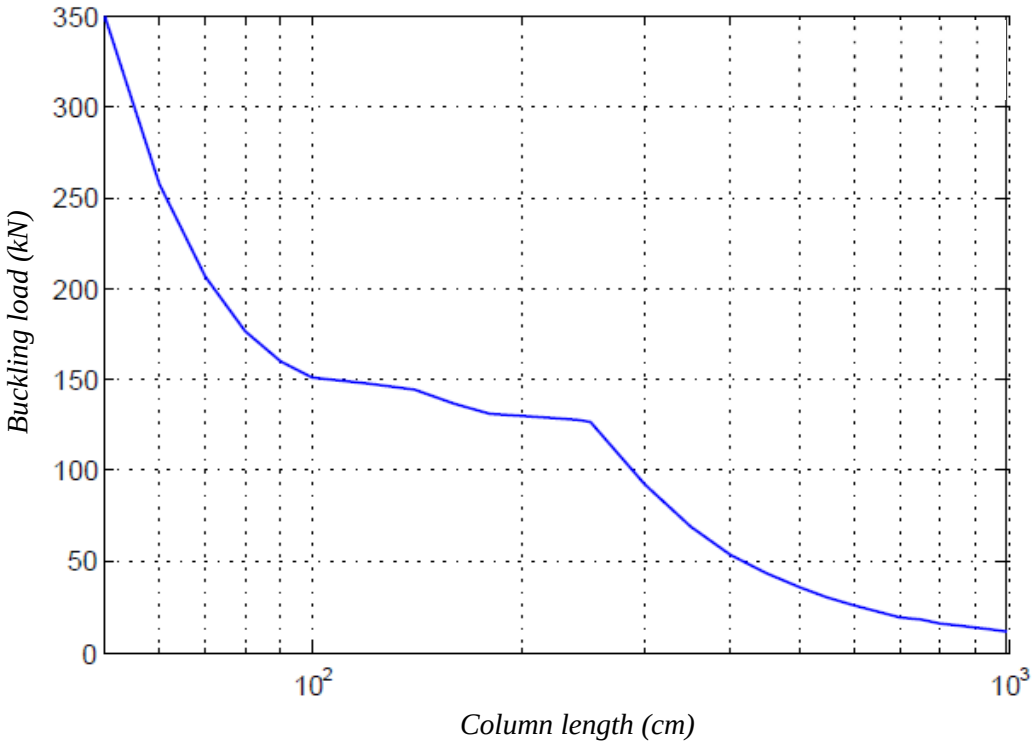

Figure (4-17) Buckling load vs length of column with combined modes in matlab program for pinned-fixed boundary conditions

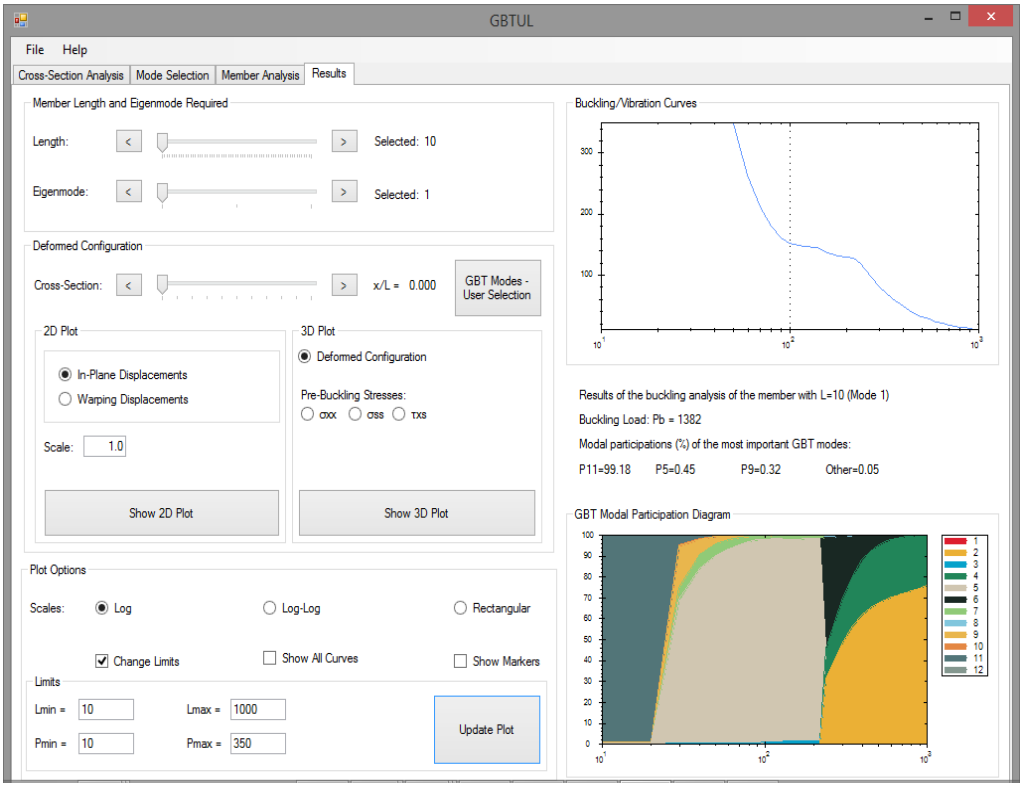

Figure (4-18) Buckling load vs length of column with combined modes in GBTUL for pinned-fixed boundary conditions, (Bebiano et al, 2008)

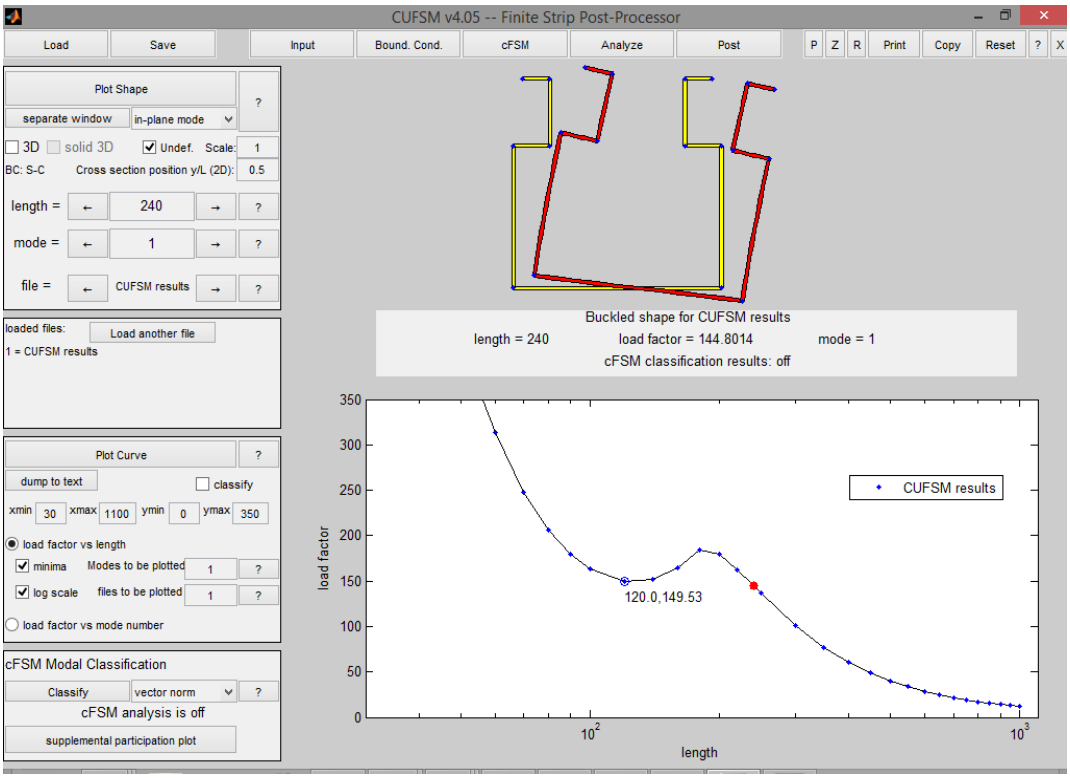

Figure (4-19) Buckling load vs length of column with combined modes in CUFSM for pinned-fixed boundary conditions, (Schafer, 2006)

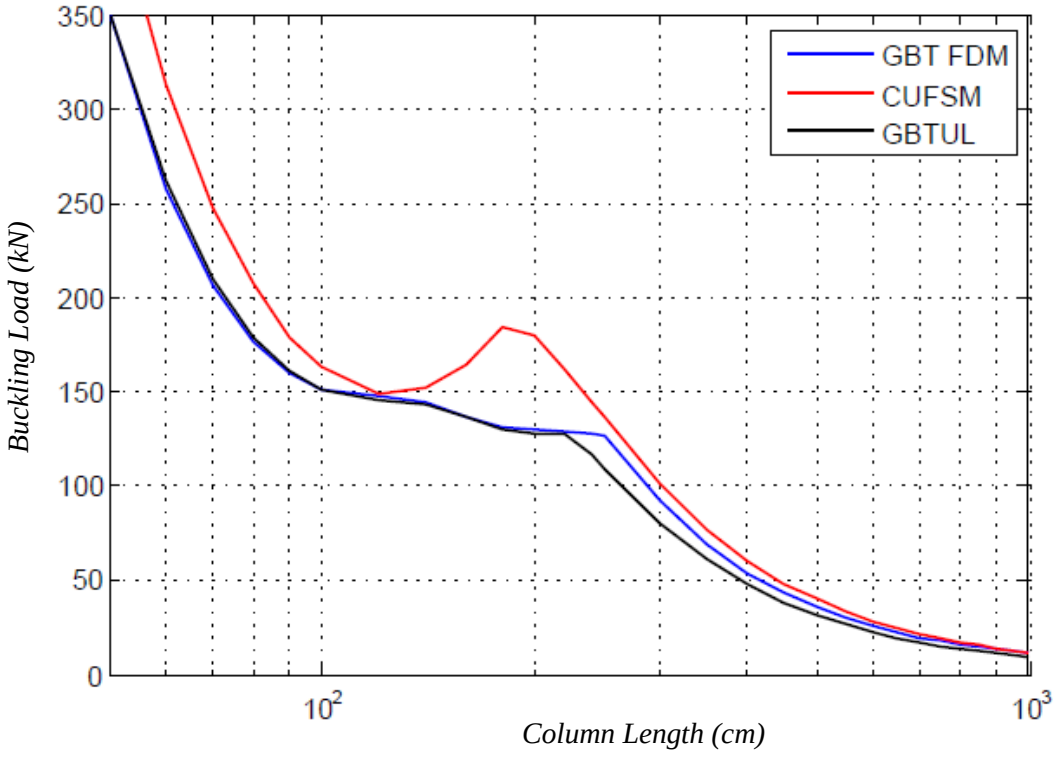

Figure (4-20) Buckling load vs length of column with combined modes in all programs for pinned-fixed boundary conditions

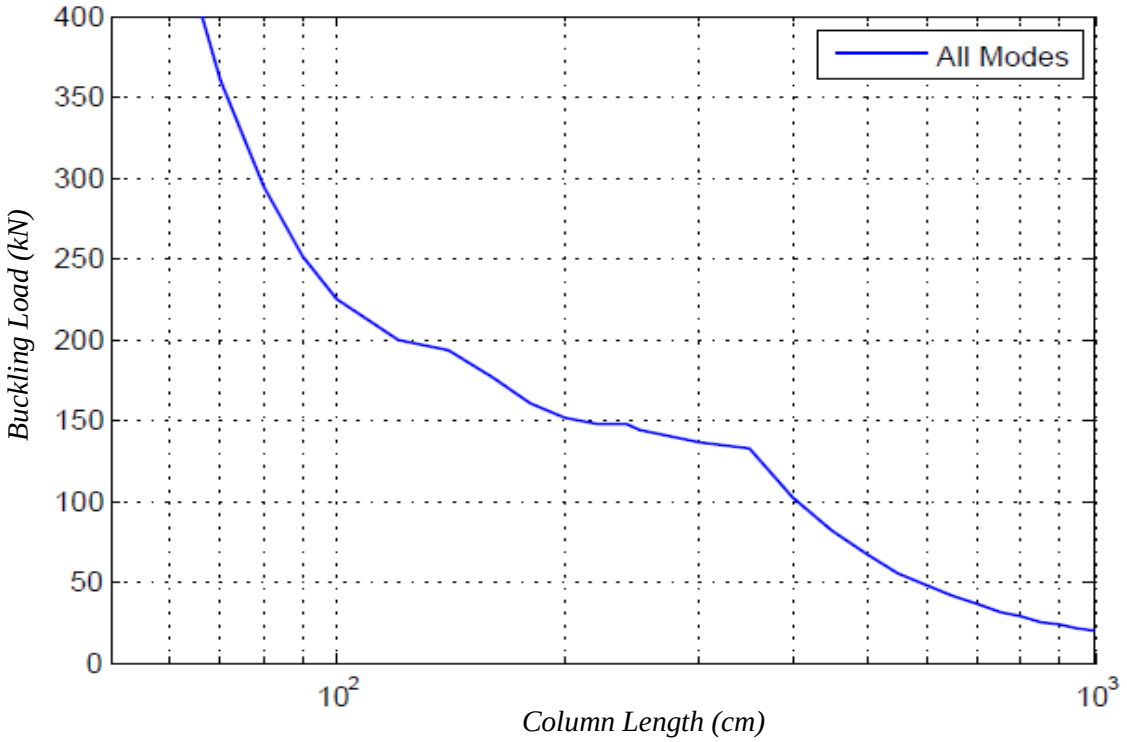

Figure (4-21) Buckling load vs length of column with combined modes in matlab program for fixed-fixed boundary conditions

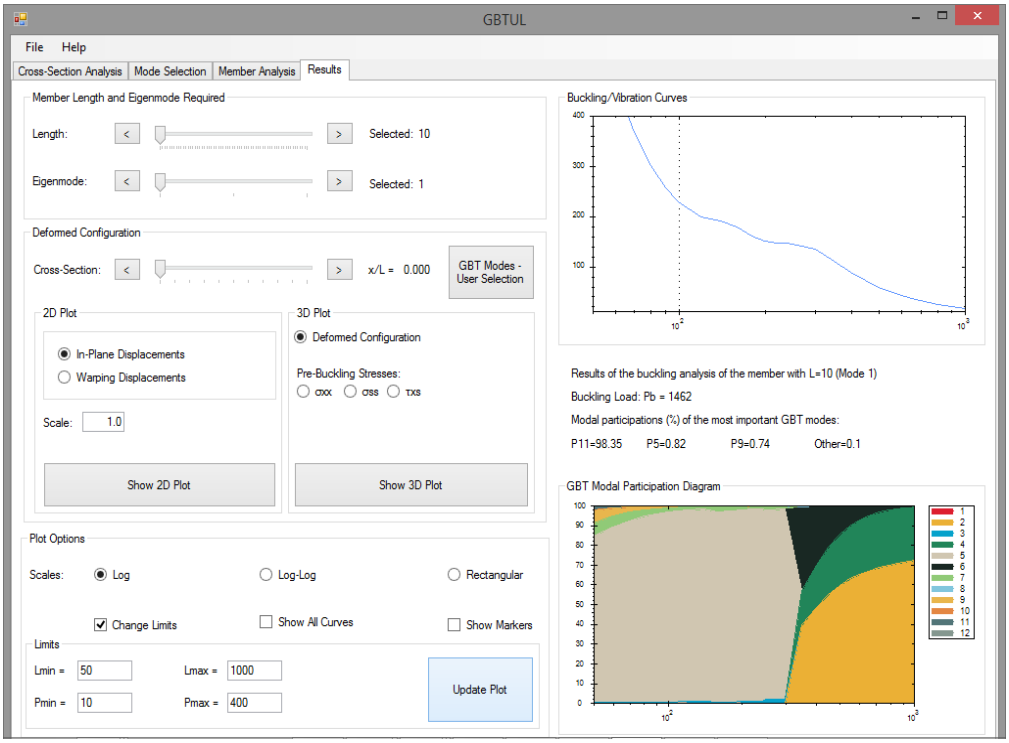

Figure (4-22) Buckling load vs length of column with combined modes in GBTUL for fixed-fixed boundary conditions, (Bebiano et al, 2008)

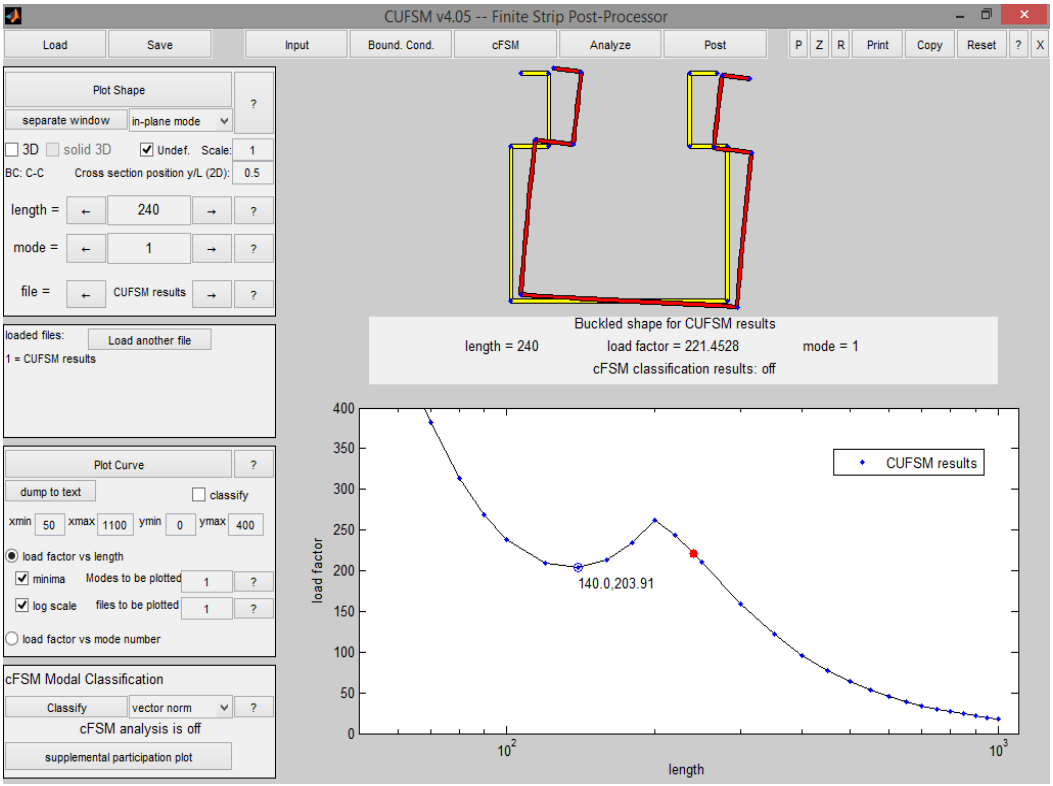

Figure (4-23) Buckling load vs length of column with combined modes in CUFSM for fixed-fixed boundary conditions

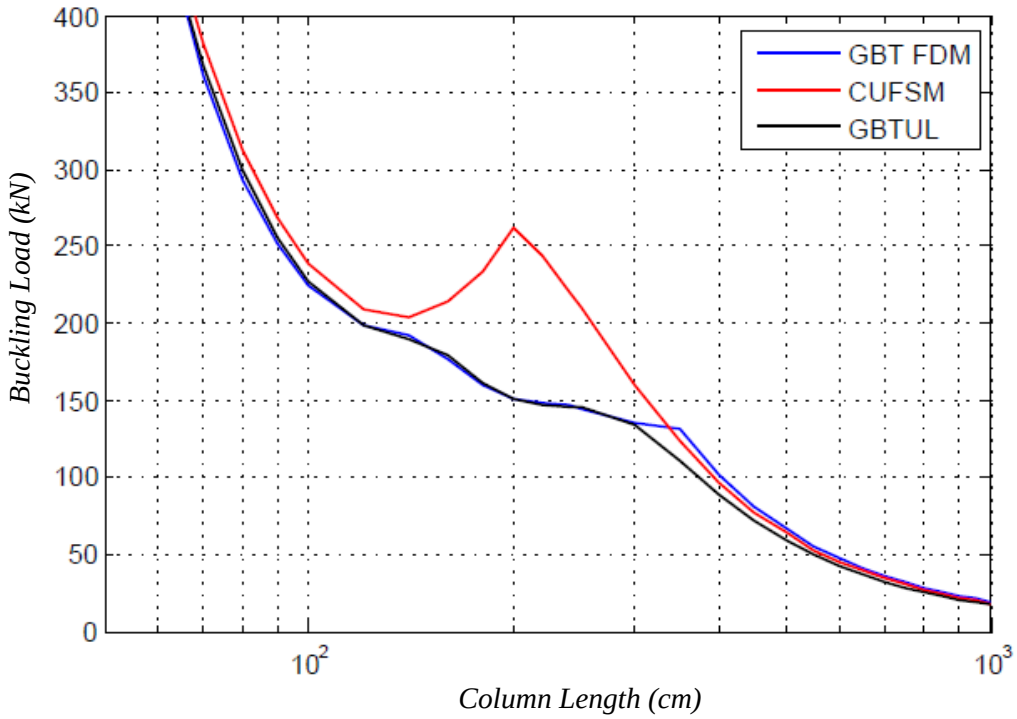

Figure (4-24) Buckling load vs length of column with combined modes in all programs for fixed-fixed boundary conditions

4.4.2 Non-linear analysis of imperfect members

In the real case of buckling failure, there will always be initial imperfections which affect the load at which material yield occurs as the member bends sideways under the effects of axial and /or transverse loading. The load needs to be applied incrementally to update the effects of P-delta until material yield can be identified. Beyond this, conventional theory will break down as the effects of plasticity occur.

This problem considers combined buckling of a member containing initial imperfections. The method of solution is again by finite differences.

The governing equation will be:

$$\sum_{k=1}^{n} EC_{kk}V_k'''' - GD_{kk}V_k'' + B_{kk}V_k = -\sum_{k=1}^{n}\sum_{j=1}^{n} X_{1jk}(W_1V_o'') \qquad (4-14)$$

Where: V_o is an initial imperfection of member.

After evaluating equation above with finite differences it will become:

$$C * V = D * V_o \qquad (4-15)$$

Where:

$C\ and\ D$ are as stated in (4.4.1).

This series of equations can then be solved by applying a small increment of load (W_1) for axial load in presence of initial imperfection V_o and solving for V. This gives a revised set of V_o values for the right hand side in the next load increment. The load is incremented and the equations solved again for these revised values of V_o.

The procedure can then be repeated until the load is such that the value of V does not converge, or until the stress in the section (calculated from the displacements) exceeds the yield stress of the section. For now, the onset of plasticity will be used as a marker for termination of the analysis. The flow chart in figure (4-25) illustrates the iterative operation of this equation.

Appendix E presents the Matlab code of the GBT non-linear analysis.

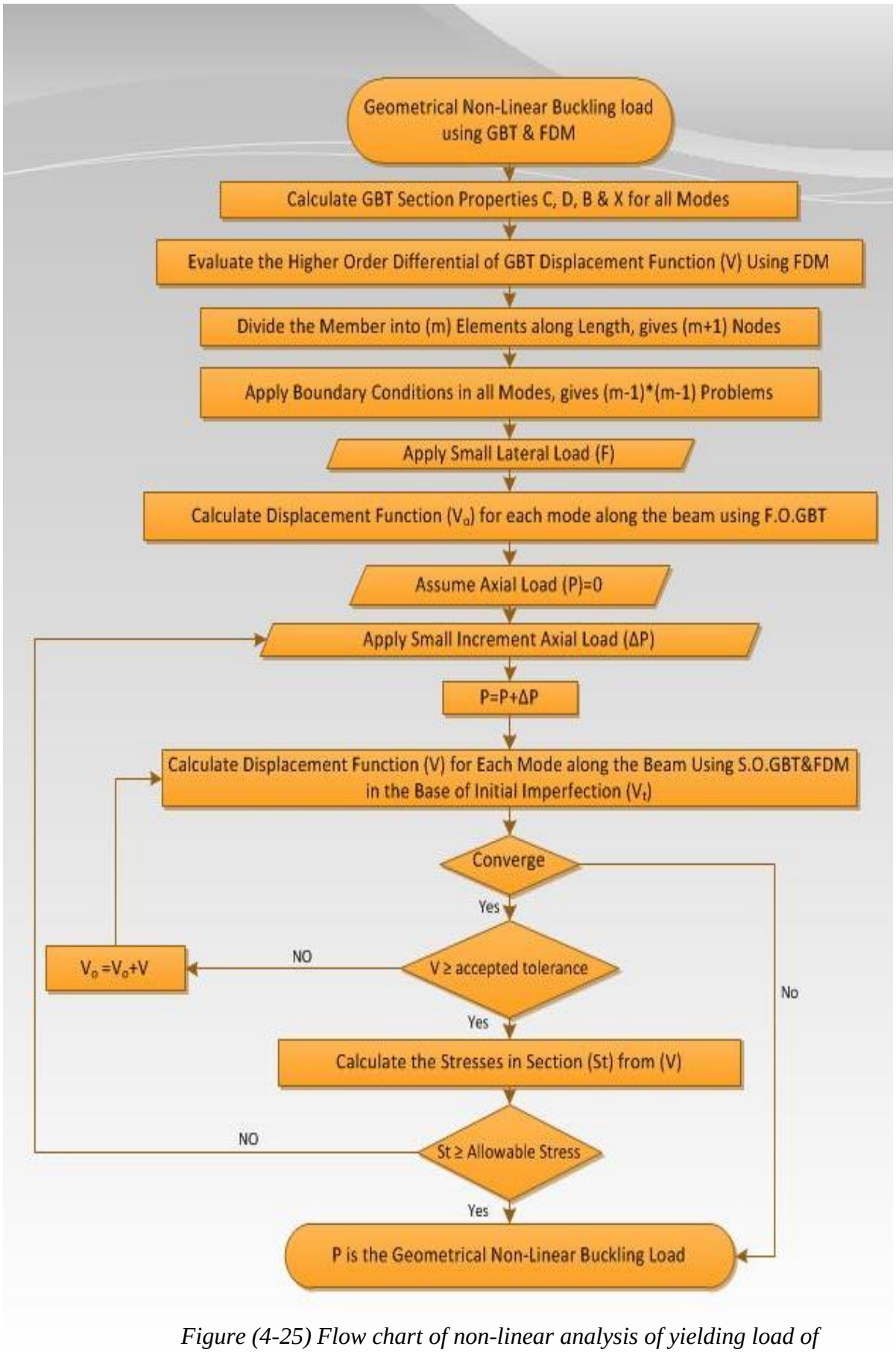

Figure (4-25) Flow chart of non-linear analysis of yielding load of column subjected to an axial load with initial imperfection

4.4.2.1 Example

For the cross-section showed in figure (4-7), f_y = 275 MPa. Figures (4-26) to (4-28) demonstrate the non-linear buckling load compared with linear buckling load in the finite difference Matlab code program with different boundary conditions.

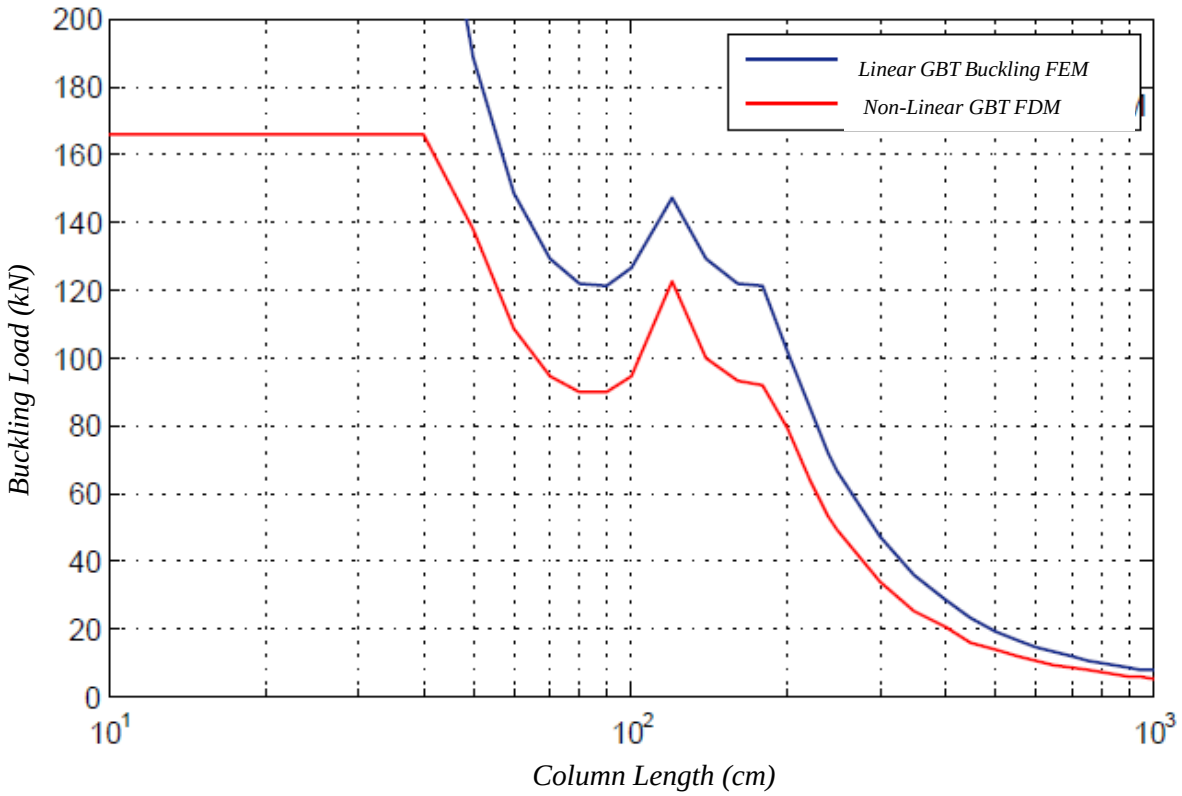

Figure (4-26) Non-linear load vs length of column with pinned-pinned boundary conditions.

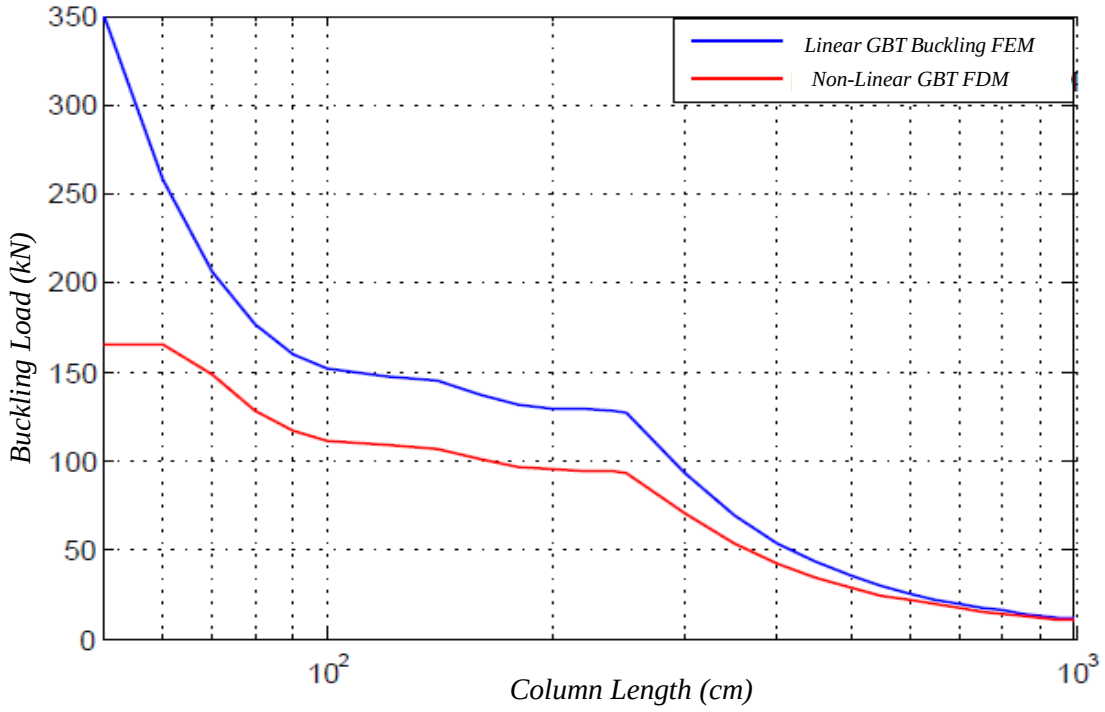

Figure (4-27) Non-linear load vs length of column with pinned-fixed ends boundary conditions

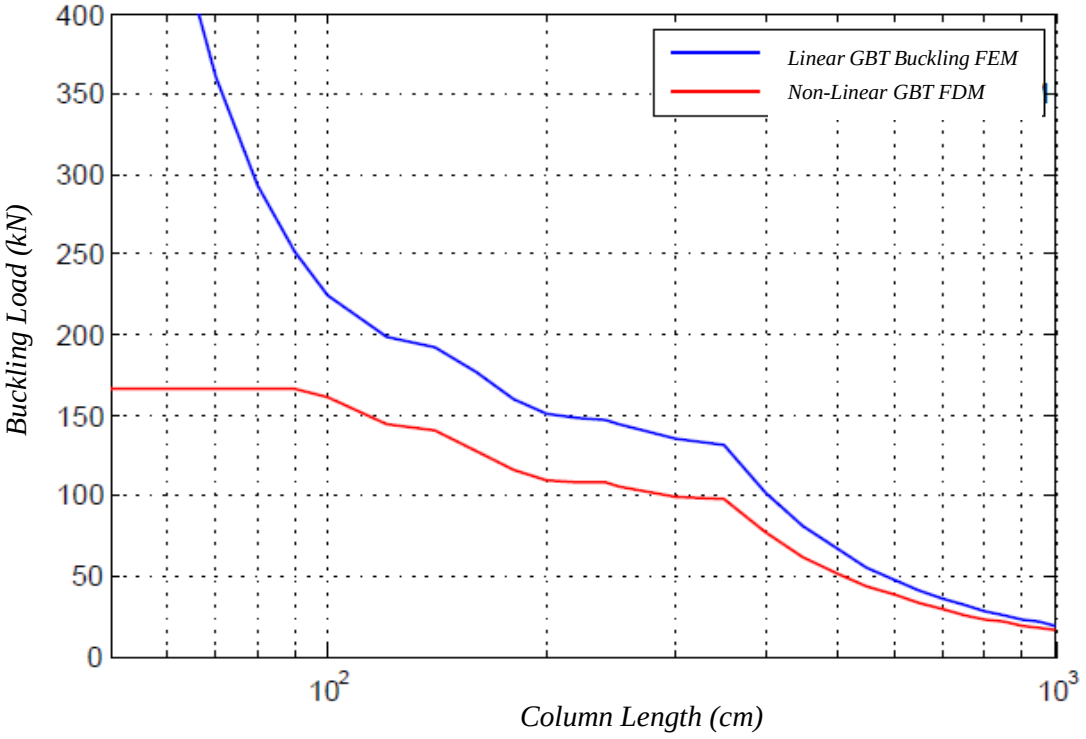

Figure (4-28) Non-linear load vs length of column with fixed-fixed ends boundary conditions

Figures (4-26), (4-27) and (4-28) show that the non-linear load was less than the linear buckling load through the length of the column due to the effect of initial imperfections.

This chapter has addressed the application of generalised beam theory to nonlinear 'real' buckling scenarios. The GBT formulation has been re-coded in Matlab and successfully validated by comparing with Euler buckling loads in second and third rigid body modes for linear eigen-buckling and general beam behaviour for a number of typical section examples which are in close agreement. To verify the nonlinear behaviour, further work through experimentation and finite element analysis will be conducted.

CHAPTER FIVE

FINITE ELEMENT ANALYSIS

CHAPTER FIVE

FINITE ELEMENT ANALYSIS

A set of *ANSYS* modelling guidelines are presented in this chapter to provide a methodology for the finite element studies conducted in this research. Finite element based linear eigenbuckling and non-linear material and geometric analyses are valuable tools for studying the buckling properties of thin-walled structures. The accuracy of these analyses is influenced by decisions made while constructing the finite element models, including the choice of finite element type, geometry, material properties and meshing. Studies are presented here which compare finite element linear eigenbuckling predictions of plate instability problems to known theoretical solutions, whereas nonlinear material and geometric problems relate to actual buckling solutions. Both analyses are performed with the commercial finite element program ANSYS. The accuracy of ANSYS thin shell elements are evaluated, and finite element convergence studies are offered to identify limits on element aspect ratio and meshing. Rules for modelling rounded corners are also provided with both linear and nonlinear buckling studies.

5.1 Element type

ANSYS offers a convenient way to build structural models from any element type, a large library of element types is available for use in many types of analysis. These elements are categorised according to many criteria such as element geometry (i.e. lines, shells/plates and volumes) element characteristics, element degrees of freedom, and perhaps material specific properties (i.e. the ability to crack). These classifications help users to choose the best element type which will provide the most appropriate representation of the problem. The finite element model may be characterised as being 2-D or 3-D, and as being collected of point elements, line elements, area elements, or solid elements. However, the model can be formed from different kinds of elements as necessary (taking care to uphold the appropriate compatibility among degrees of freedom). For example, a stiffened shell structure may be modelled using 3-D shell elements to signify the skin (shell surface) and 3-D beam elements to represent the stiffening ribs. The choice of model dimensionality and element type will often determine which method of model generation will be most practical for the problem at hand. In order to represent a cold-form steel section in finite element analysis an area element has a

triangular or quadrilateral shape and may be a 3-D shell element could choose to achieve the actual behaviour of the thin-walled plate under application of axial loads. In this study, the four node SHELL181 element type has been used to simulate the behaviour of these thin plates because it is suitable for analysing thin to moderately-thick shell structures. It is a four-node element with six degrees of freedom at each node: translations in the x, y, and z directions, and rotations about the x, y, and z-axes. It is also well-suited for linear, large rotation, and/or large strain nonlinear applications. Change in shell thickness is also accounted for in nonlinear analyses. Figure (5-1) shows the geometry, node locations, and the element coordinate system for this element. The element is defined by shell section information and by four nodes (I, J, K, and L).

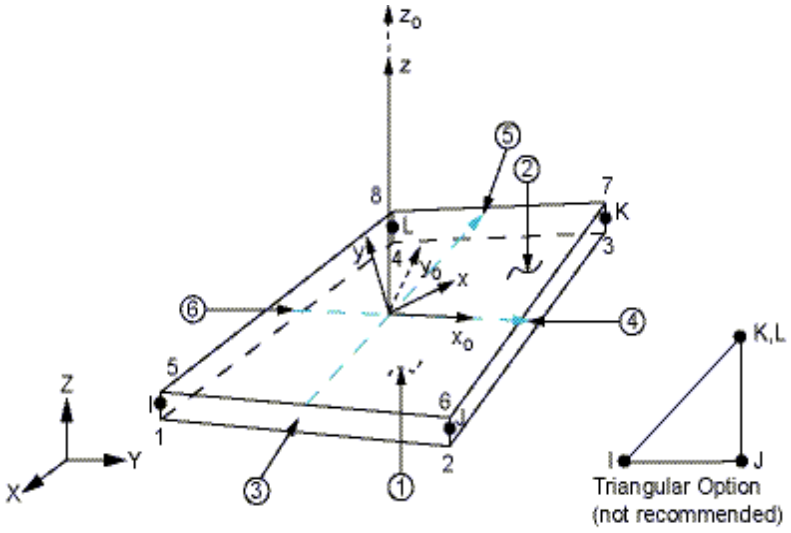

Figure (5-1) Element geometry (Ansys, 2007).

5.2 Material properties

ANSYS allows the input of various material properties. The chosen material properties depend on the type of analysis application, Material properties can be linear or nonlinear as explained in the following sections.

5.2.1 Linear material properties

For elastic response, if the induced stresses are below the material's yield strength, the material can fully recover its original shape upon unloading. From a standpoint of metals this behaviour is due to the stretching but not breaking of bonds between atoms. Because elasticity

is due to this stretching of atomic bonds, it is fully recoverable. Moreover, these elastic strains tend to be trivial. Elastic behaviour of metals is most commonly represented by the stress-strain relationship of Hooke's Law, where stress and strain are linearly related by Young's modulus. Linear material properties can be elastic constant or temperature-dependent, and isotropic (having a physical property which has the same value when measured in different directions), orthotropic (having three mutually perpendicular planes of elastic symmetry at each point) and anisotropic (having a physical property which has a different value when measured in different directions). In this study, because steel is a homogenous material, the linear material properties have been taken as linear elastic isotropic with constant Young's modulus and Poisson's ratio.

5.2.2 Nonlinear material properties

In the case of nonlinear material properties, if a ductile material experiences stress beyond the elastic limit, it will yield, acquiring large permanent deformations. Materials that fail with little plastic deformation are said to be brittle. The ductile response is safer in many respects than is a brittle response, see figure (5-2). There are elastic, inelastic and viscoelastic material properties. To further describe nonlinear material behaviour, it is necessary to review some basics of plasticity by defining pertinent terminology.

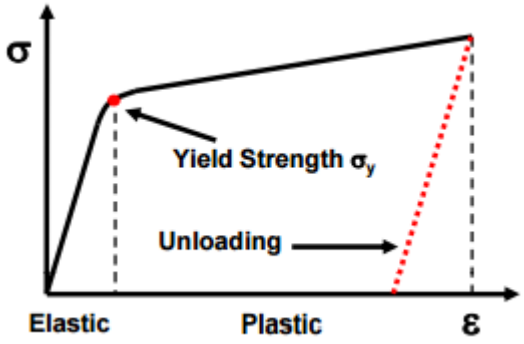

Figure (5-2) Stress-strian curve (Ansys, 2007).

5.2.2.1 Rate-independent material

In this study, the structural behaviour of cold-form steel is not reliant on the rate of loading or deformation, the material is said to be rate –independent. Most metals exhibit rate-independent behaviour at low temperatures (< 1/4 or 1/3 melting temperature) and low strain rates.

5.2.2.2 Isotropic hardening plasticity

Isotropic hardening states that the yield surface expands uniformly during plastic flow. The term 'isotropic' refers to the uniform dilatation of the yield surface and is different from an 'isotropic' yield criterion (i.e., material orientation).

5.2.2.3 Von Mises yield criterion

Tensile testing on specimens provides uniaxial data, which can easily be plotted on one-dimensional stress-strain curves, such as those presented earlier in this chapter, whereas, the actual structure usually exhibits a multiaxial stress state. The yield criterion provides a scalar invariant measure of the stress state of the material which can be compared with the uniaxial case. The von Mises yield criterion predicts that yielding will occur whenever the distortion energy in a unit volume equals the distortion energy in the same volume when uniaxial stressed to the yield strength. When the von Mises equivalent stress exceeds the uniaxial material yield strength, general yielding will occur. In this study, the nonlinear material properties have been taken as inelastic-rate independent-isotropic hardening plasticity- Mises plasticity-bilinear for the cold-formed steel with properties derived from the experimental coupon tests for tensile strength.

5.3 Model geometry

Once the material properties have been defined, the next step in the numerical analysis is to generate a finite element model – i.e. nodes and elements. Cold-form steel beam or column sections have different sectional shapes according to their purpose and position in the frame of a structure. To allow creation of these sections as 2D or 3D finite elements, the ANSYS design modeller has worthy flexible tools required for building any composite model.

When models are created in ANSYS, two important points should be taken into account. First, the model must simulate the actual shape of the sections using full capabilities of the software design modeller. Second, the model must have constricted of element types which are suitable for the analysis in question.

In ANSYS, there are two methods to create the finite element model, direct generation and solid modelling.

5.3.1 Direct generation

In this method, all nodes and elements are input manually. This can be done by defining the location of each node and the connectivity of each element. Several convenient operations, such as copying patterns of existing nodes and elements, symmetry reflection, etc. are available. Figure (5-3) demonstrates how to create a simple model using direct generation method.

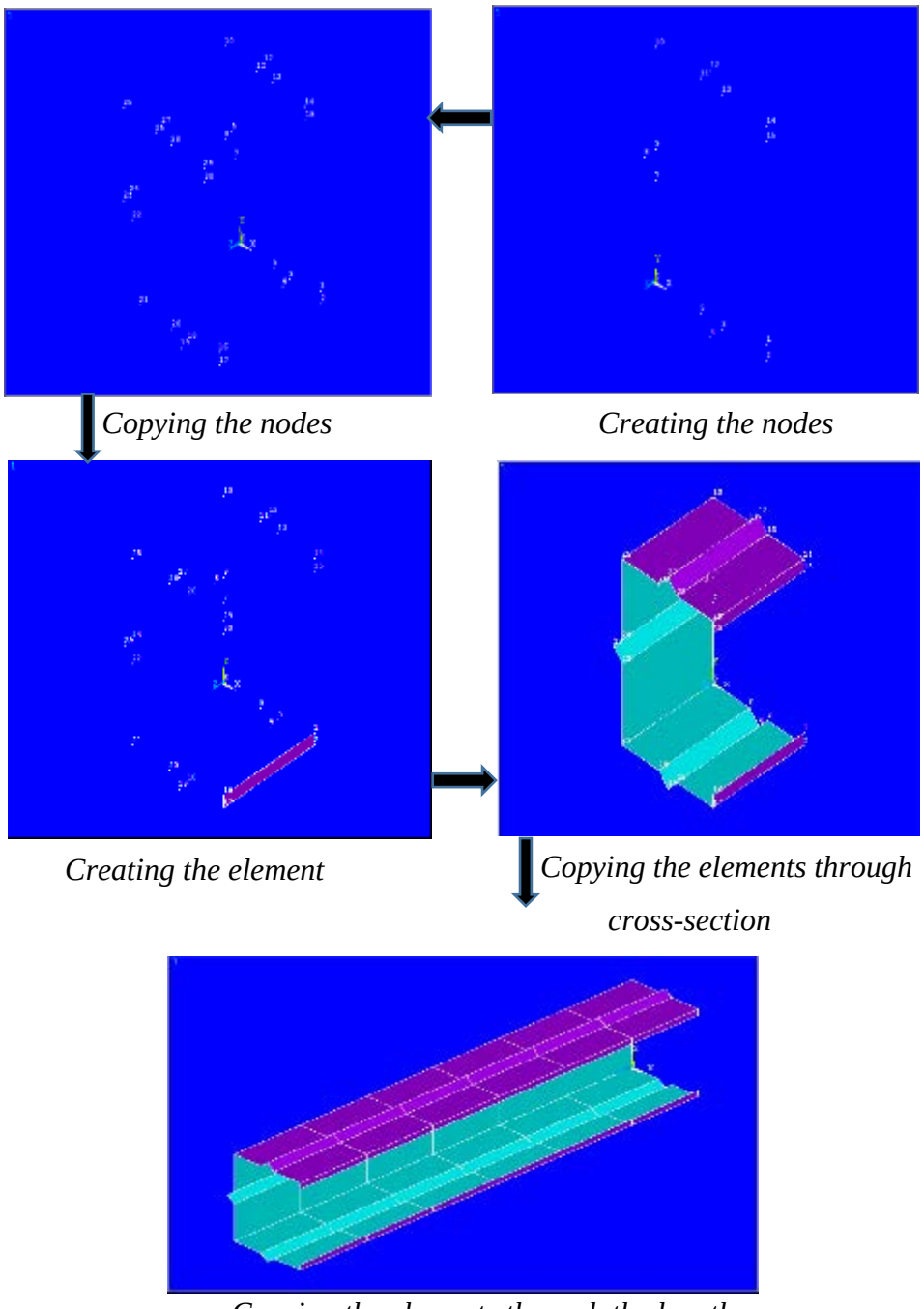

Figure (5-3) Modelling with the direct generation method

➢ The advantages of direct generation are:

- Expedient for small or simple models.
- Provides the user with complete control over the geometry and numbering of every node and every element.

➢ The disadvantages of direct generation are:

- Usually too time-consuming for all but the simplest models; the volume of data the user must work with can become overwhelming.
- Cannot be used with adaptive meshing.
- Can be difficult to modify the mesh (tools such as area mesh refinement, Smart Sizing, etc. cannot be used).
- It is generally more problematical for modelling rounded corners and fillets.

5.3.2 Solid modelling

For the solid modelling method, the input of shape geometry is produced by creating keypoints, lines, areas and volumes. Subsequently operations like copy, add, subtract, intersect, glue, divide, overlap, extrude, etc. can be employed to produce the final desired geometry to simulate the actual shape. The elements chosen to represent the model will dictate the geometry to be created.

➢ The solid modelling method has the following advantages:

- More appropriate for large or complex models, especially 3-D models of solid volumes.
- Allows to work with a relatively small number of data items.
- Allows geometric operations (such as dragging and rotations) that cannot be done with nodes and elements.
- Supports the use of "primitive" areas and volumes (such as polygonal areas and cylindrical volumes) and Boolean operations (intersections, subtractions, etc.) for "top down" construction of your model.
- Supports adaptive meshing. In order to do area, mesh refinement after loads have been applied (solid model loads are also required).
- Readily allows modifications to geometry.
- Facilitates changes to element distribution; you are not bound to one analysis model.
- Improved modelling of rounded corners and fillets.

➢ The disadvantages of solid modelling are:

- May require a large amounts of time in both modelling and solution.
- Can (for small, simple models) sometimes be more cumbersome, requiring more data entries than direct generation.
- Can sometimes fail (the program will not be able to generate the finite element mesh) under certain circumstances.

Figure (5-4) shows how to create complex model using the solid modelling method.

5.3.3 Meshing tools

Meshing is an integral part of the computeraided engineering simulation process. The mesh influences the accuracy, convergence and swiftness of the solution. Furthermore, the time it takes to create and mesh a model is often a weighty portion of the time it takes to obtain results from the solution. Therefore, the better programmed the meshing tools, the faster the solution,

The default mesh controls that ANSYS uses may produce a mesh that is satisfactory for the analysis model. In this case, it is not necessary to specify any mesh controls. Mesh controls allow the user to establish such factors such as the element shape, midsize node placement, and element size to be used in meshing the solid model. This step is one of the most important of the entire analysis, all decisions made at this stage in the modelling process can affect the accuracy and economy of the analysis.

Once the best model is found, meshing technologies from ANSYS provide the flexibility to produce meshes that range in complexity from pure hexagon to highly detailed hybrid; a user can put the right mesh in the right place and ensure that a simulation will accurately validate the physical model. The mesh is usually refined in areas of high stress gradient, or possibly to aid output of results in particular locations. Mesh sensitivity studies are necessary to ensure convergence of results and production of a satisfactory model

For cold-form steel, shell modelling and meshing solutions from ANSYS offer several approaches in providing meshes that best meet the physics. In general, this consists of two approaches that use common tools:

1- 2-D axisymmetric or planar models can be used to simplify 3-D physics in a 2-D fashion. 2-D models can mesh with quad meshes, quaddominant meshes or all-triangle meshes.

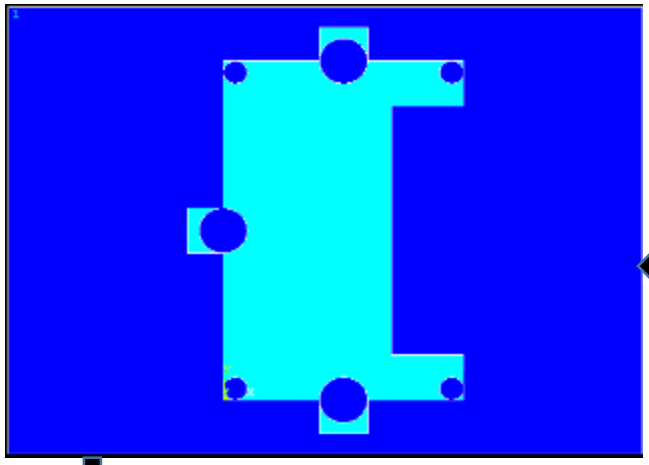

Use ANSYS operations to get the specific shape

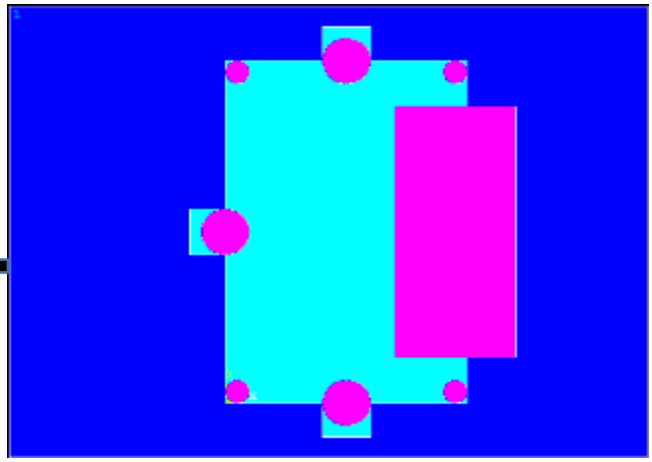

Creating the shapes

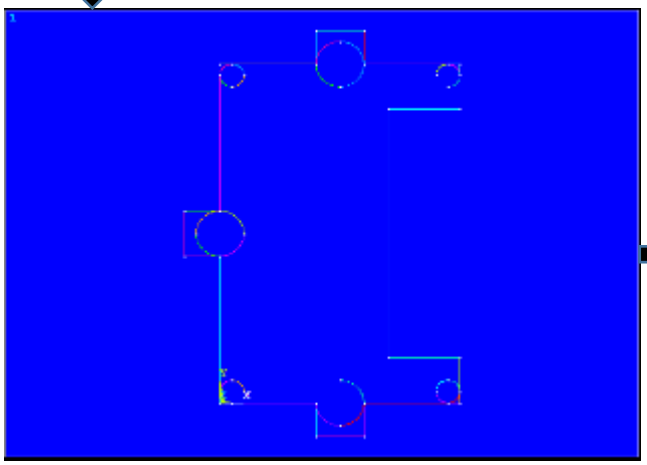

Keep use ANSYS operations to get the specific shape

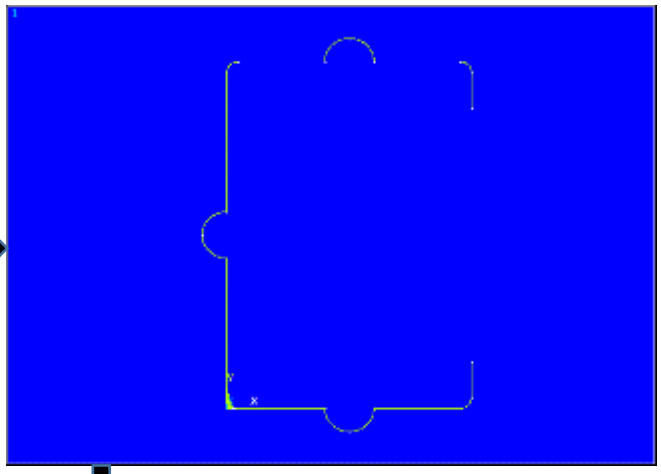

Use ANSYS operations to get the specific shape

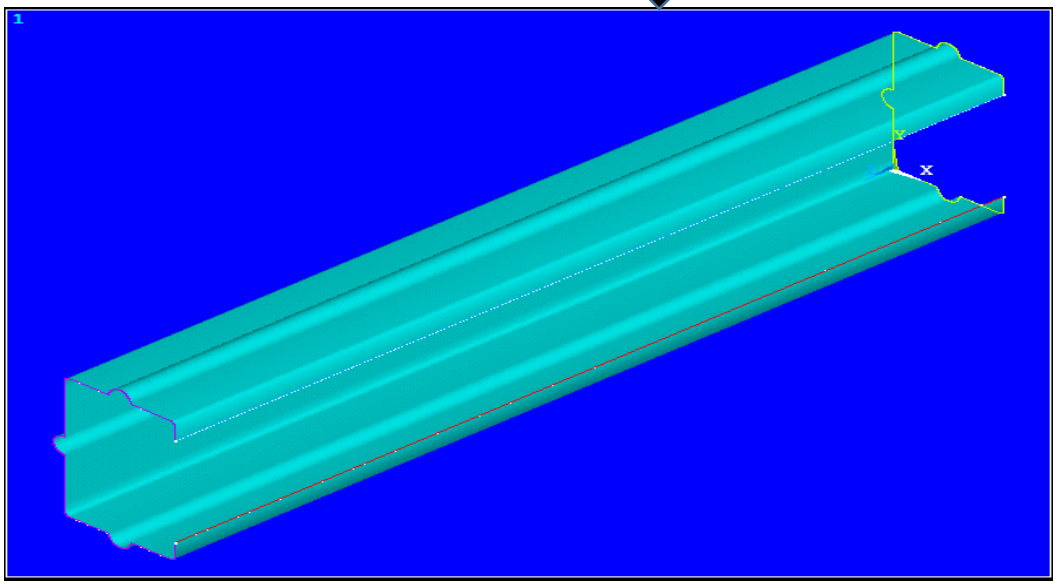

Extrude the final cross section to create the final shape length

Figure (5-4) Modelling with the solid modelling method.

2- Shell models can be used to simplify 3-D models to a set of laminae with a defined thickness exhibiting bending and membrane action. This is particularly useful for modelling sheet metal or thin structural parts. Shell parts can also mesh with quad meshes, quad-dominant meshes or all-triangle meshes. Rectangular element shapes are preferable to triangular element shapes as the element formulation for triangular element become less accurate. Also the aspect ratio of the element can affect the accuracy of the result obtained. Figure (5-5) shows the types of meshing that can be achieved.

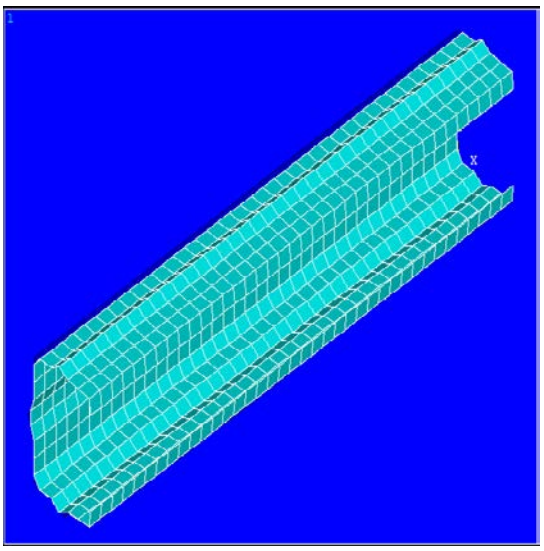

Meshing quad with free

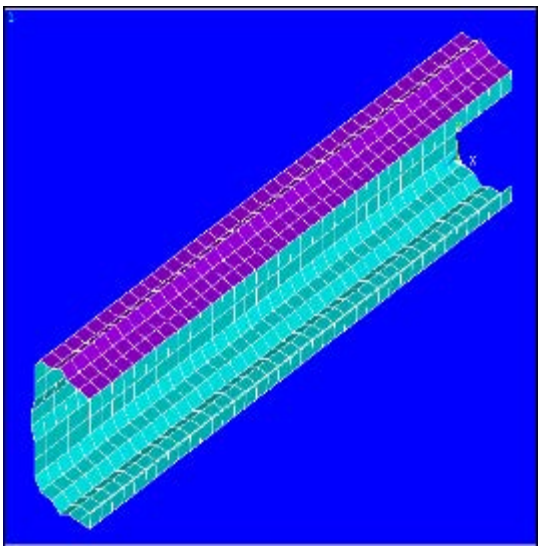

Meshing quad with mapped

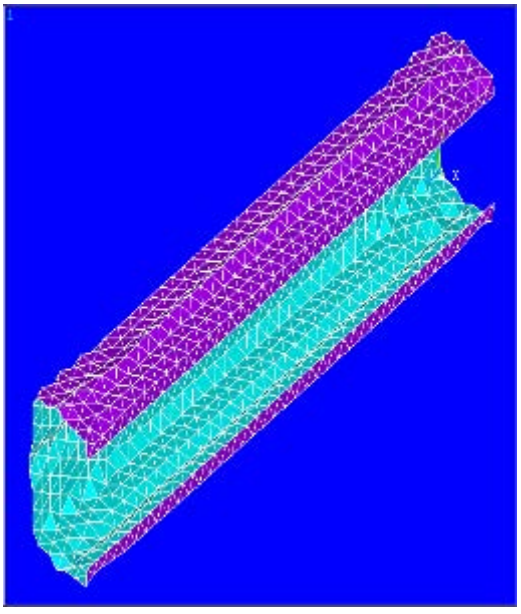

Meshing triangle with free

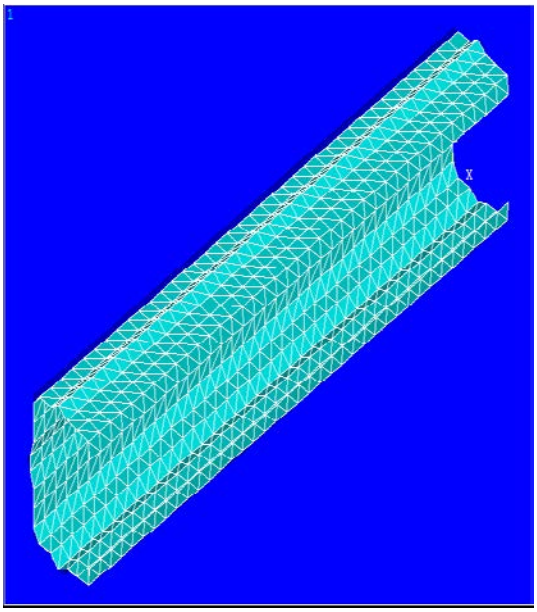

Meshing triangle with mapped

Figure (5-5) Meshing types.

5.3.3.1 Merging of nodes

If two separate entities have the same location, then merging these entities together into a single entity is possible. For example, if two regions that have already been meshed are to be joined it may be desirable to have all the nodes move together in all degrees of freedom. ANSYS has a facility to merge and renumber the nodes according to a set tolerance, the higher numbered node will be deleted and will be replaced with the lower numbered coincident node. Two merged nodes will thus be replaced by a single node. Figure (5-6) demonstrates how to merge nodes.

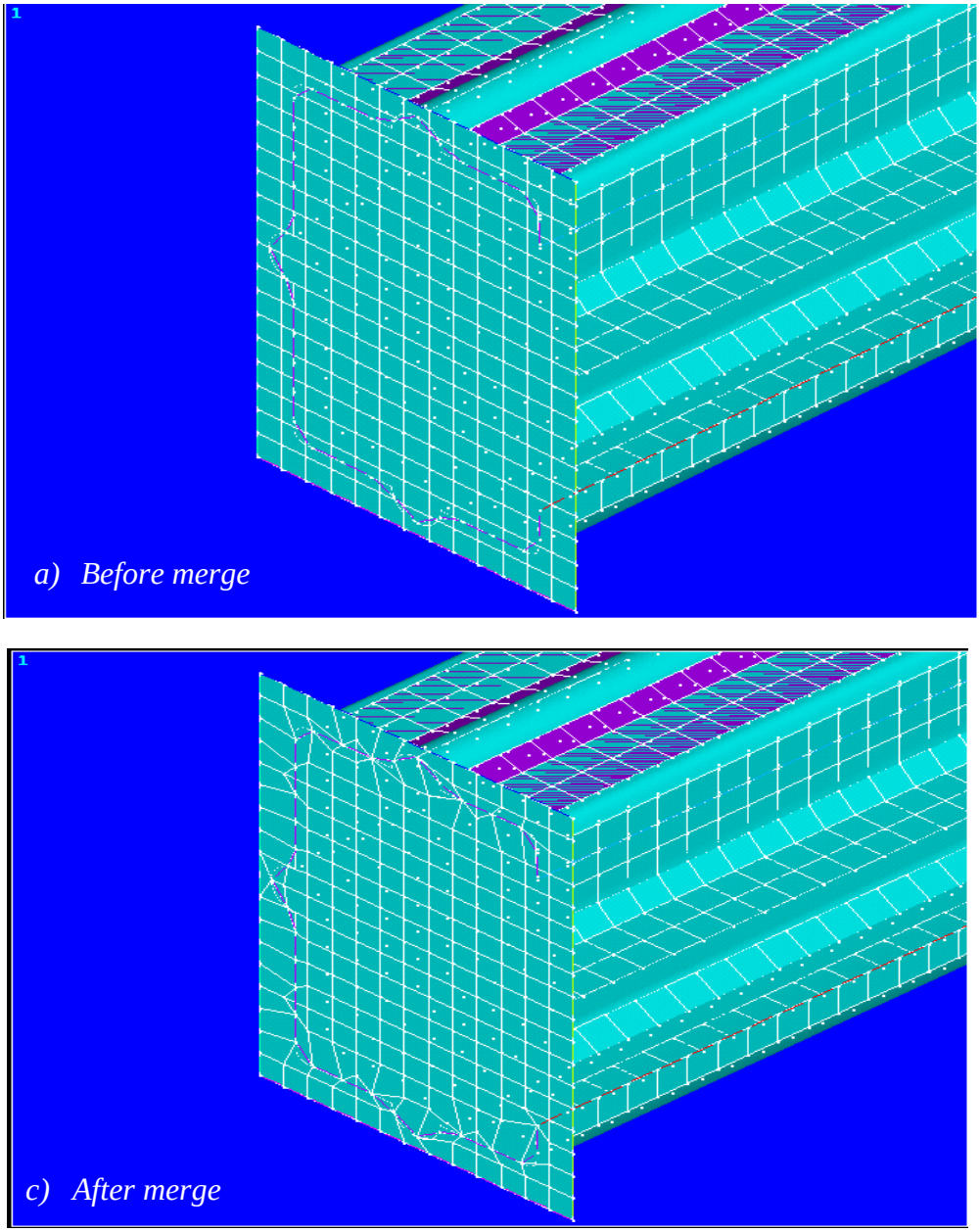

Figure (5-6) Merging in ANSYS FE model.

5.3.3.2 Coupling of nodes

Coupling is a way to ensure a set of nodes have the same DOF's, i.e. producing compatibility between nodes. For example: If nodes 1 and 2 are coupled in the UX direction, the solver will calculate UX for node 1 and simply assign the same UX value to node 2. The solver will calculate the copulated displacements based upon the coupled stiffness of the coupled nodes, figure (5-7).

If pin joints are to be created, coupling can be used to simulate pin joints such as hinges and universal joints. This is done by means of a moment release: coupling translational DOF at a joint and leaving the rotational DOF uncoupled will produce this effect.

Before coupling

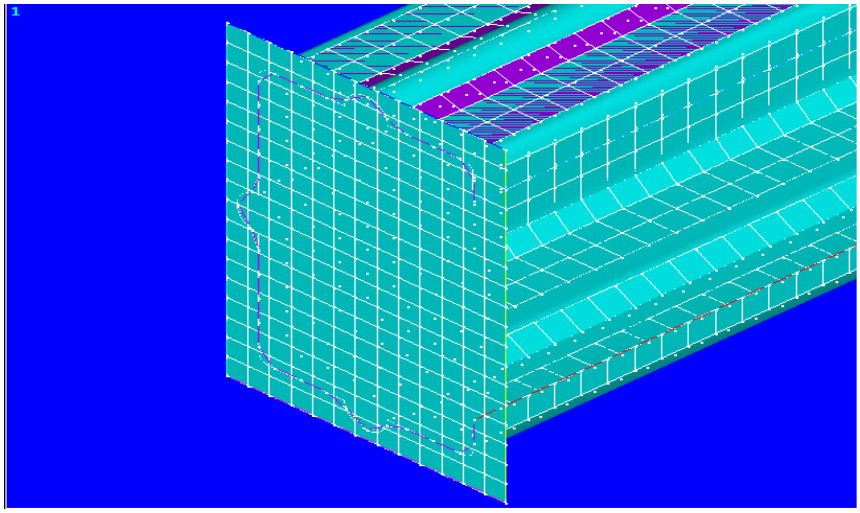

After coupling the displacement in X-direction

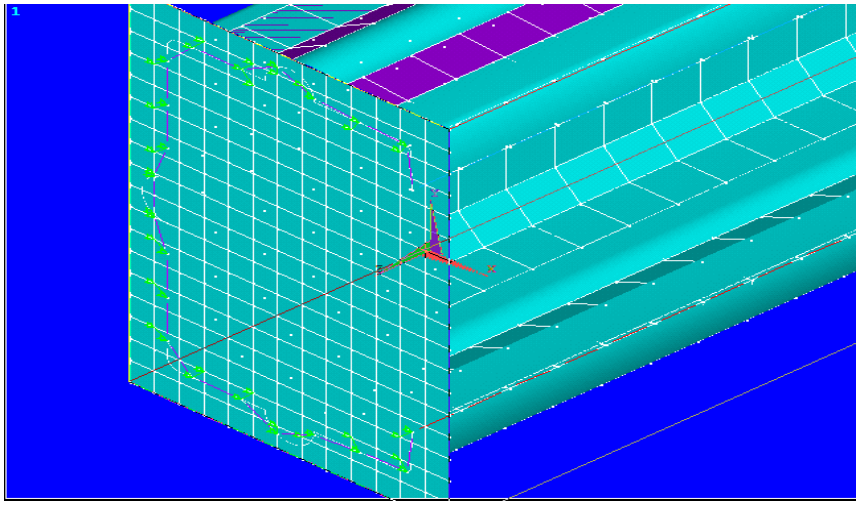

Figure (5-7) Nodes coupling.

5.4 Loads and supports

The structural loads and end supports are the application of a force and/or constraint.

In ANSYS, loads can be applied on either the solid model (on keypoints, lines, and areas) or on the finite element model (on nodes and elements). For example, a load can be specified at a keypoint or a node, but these must then be transferred to the FE model. Similarly, surface loads and pressure can have specified on lines and areas to be subsequently transferred to the finite element model or on nodes and element faces directly. No matter how you specify the loads, the solver expects all loads to be applied to the finite element model. Therefore, for any loads specified on the solid model, the program automatically transfers them to the nodes and elements at the beginning of a solution.

The solid-model loads are independent of the finite element mesh. This means that the element mesh can be altered without the need to alter the position of the applied loads. This allows mesh reforms and mesh sensitivity studies without needing to reapply loads each time. In addition, this usually includes fewer entities than the finite element model. Therefore, selecting solid model entities and applying loads on them is much easier, specifically with graphical picking. Nonetheless, Elements created by meshing commands are in the currently active element coordinate system. Nodes generated by meshing commands use the global Cartesian coordinate system by default. Therefore, the solid model and the finite element model may have different coordinate systems and loading directions. Also the application of keypoint constraints can be tricky, especially when the constraint expansion option is used. The expansion option allows the expansion of a constraint specification to all nodes between two keypoints that are connected by a line.

If loads are applied directly to the FE model, there is no need for concern regarding constraint expansion. All desired nodes can be selected and the applicable constraints specified but any change of the finite element mesh invalidates the loads, requiring deletion of the previous loads and re-application of them on to the new mesh. Also, the application of loads by graphical picking can be problematic, unless only a few nodes or elements are involved or perhaps subsets or entities can be selected.

– **Structural Supports:** These are restraints that prevent movement on certain regions on the FE model for specific degrees of freedom.

In general, there are three types of end supports.

1. Pinned end support: a hinge represents a pin joining to a structural assembly and it does not allow translational movements. It is assumed to be frictionless and to allow rotation of a member with respect to the others.
2. Roller end support: a roller represents a support that permits the attached structural part to rotate freely with respect to the foundation and to translate freely in the direction parallel to the foundation surface. No translational movement in any other direction is allowed.
3. Fixed end support: a fixed support does not allow rotation or translation in any direction.

In this study, the correct simulation of boundary conditions can be complex to represent in all analytical, numerical and practical conditions in cold-formed steel structures. Elastic instability problems are prevalent in these types of members because the stiffness of cold-formed steel tends to be less. So buckling phenomena are the main problem in the behavioural response. Based on this expected behaviour, each of the usual buckling modes (global, torsional, distortional and local) requires explicit boundary conditions to provide the appropriate restraint. Producing the desired conditions are more problematic with pinned end supports as comparing with the others, as it is very difficult to produce a frictionless rotational joint (i.e. there will be some degree of rotational stiffness in practice).

5.4.1 Pinned end support

For this support type, there are three sub-supports which must be applied to restrain the different types of buckling modes which are possible. First, the global single end support at the section centroid is required to restraint the translations in the three directions (*UX, UY and UZ*) and let the rotations (*ROTX, ROTY and ROTZ*) be free. Second, the torsional end support to restrain the rotation in longitudinal *Z*-direction *(ROTZ)* to prevent rigid body motion. Finally, on the periphery of the section the local end support to restrain the translations *(UX, UY)* by friction, constrain the translation *(UZ)* and let the rotations *(ROTX, ROTY and ROTZ)* free in each of the local plates of the section. A better way to apply these constraints in to use a suitable rigid steel plate connected at the ends of the member as shown in figure (4-8). This

representation will also provide the closest simulation to the end conditions provided in the experimental tests.

To simulate axial buckling problems and the pinned end support system, the load is applied as a concentrated axial load (*P*) applied on one of the ends at the centroid of the cross section as shown in figure (5-8). In this case, stresses will concentrate on one node, so the rigid steel plate provided at the end allows for a reduced and more even distribution of these stresses to the end of the member.

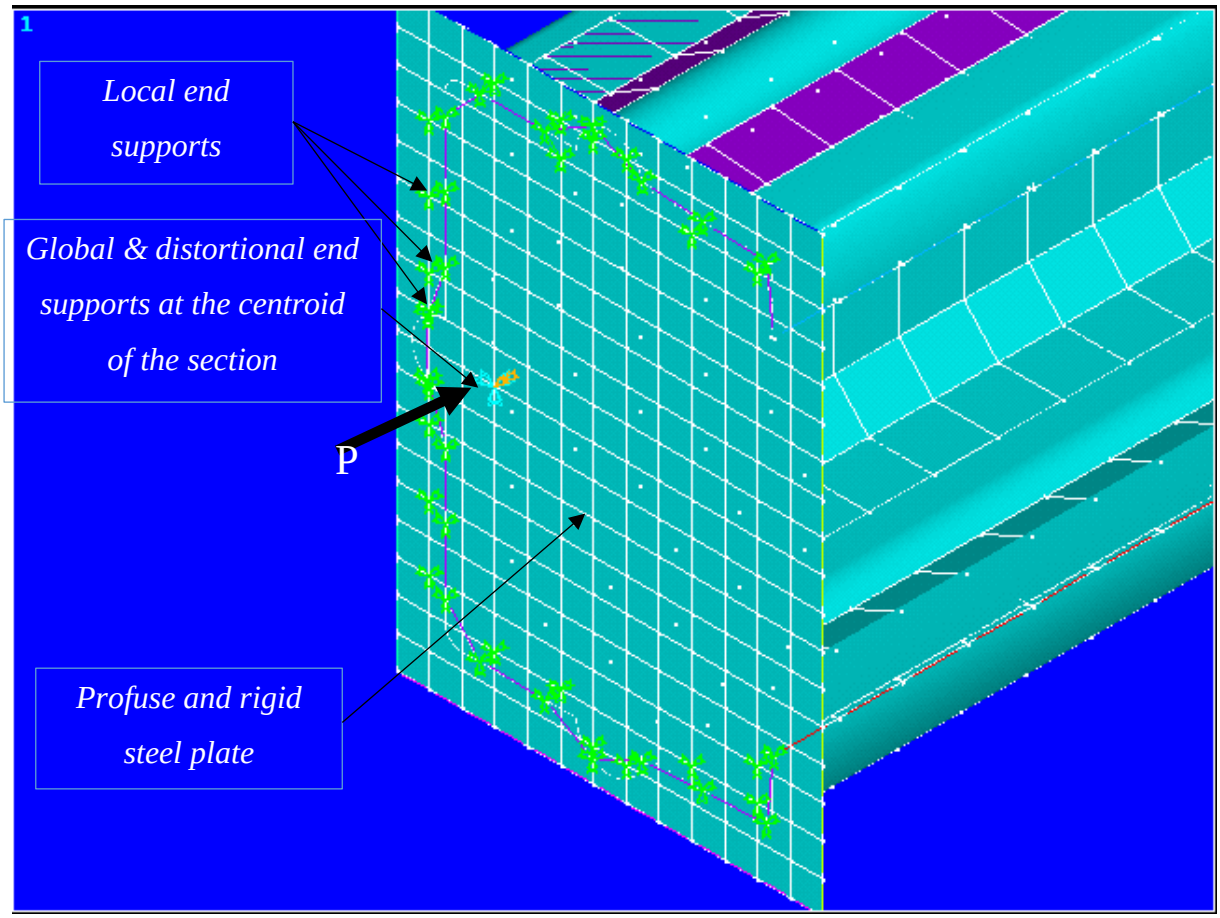

Figure (5-8) Pinned end support modelling.

5.4.2 Fixed end support

A fixed end support is much easier to model than the pinned end support for numerical models but it is more complicated to produce in laboratory tests (see chapter 6). For these supports, all the translations in the three directions *(UX, UY and UZ)* and the rotations *(ROTX,*

ROTY and ROTZ) must be restrained. To produce this effect a suitable length of member beyond the ends is provided and this is restrained in all *DOF's* as shown in figure (5-9).

When the axial load is applied, it is distributed around the periphery of the cross section along support length to prevent stress concentration, as shown in figure (5-9).

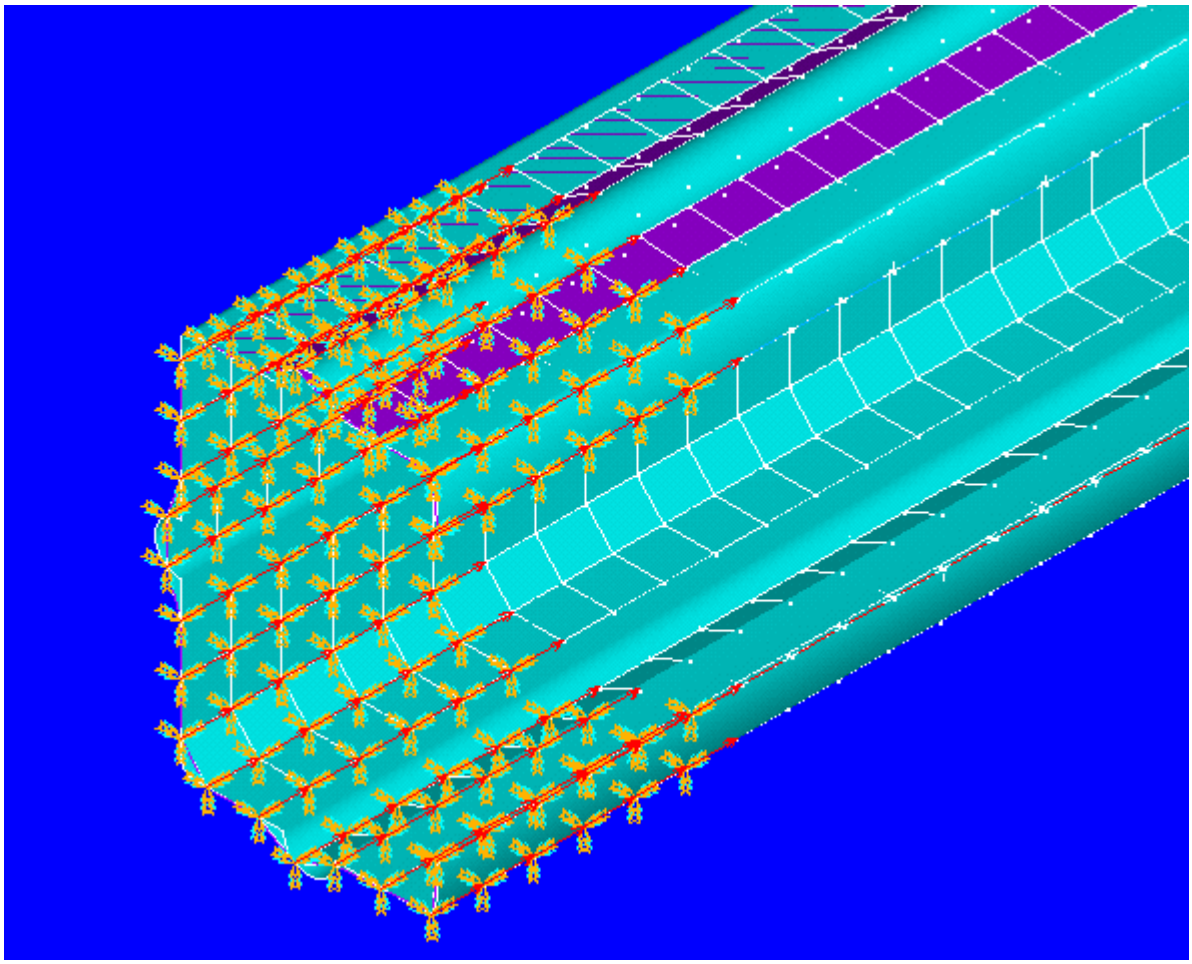

Figure (5-9) Fixed end support

5.5 Buckling analysis

When the applied loading reaches the critical load capacity for the member, structures become elastically unstable. Each load has a related buckled mode shape and this is the shape that the structure assumes in a particular buckled state. Elastic critical loads are theoretically derived instability loads which can be obtained from an eigenvalue extraction. Real failure loads resulting from buckling account for initial imperfections in structure geometry and applied load trajectory, and this coupled with material yield will lead to a realistic prediction of a failure load. Hence there are two primary means to perform a buckling analysis which are addressed in the following two sections.

5.5.1 Linear buckling analysis (eigenvalue buckling)

Eigenvalue buckling analysis calculates the theoretical buckling strength of an ideal elastic structure. It calculates the structural eigenvalues for the given system loading type and restraints. This is generally known as classical Euler buckling analysis. Buckling loads for several common configurations are readily available from closed form solutions. However, in real-life, structural imperfections and nonlinearities prevent most real world structures from reaching their eigenvalue predicted buckling strength. So this analysis over-predicts the expected failure loads. This method is not recommended for design purpose buckling prediction analysis, but is required for use in the calculations of real failure loads using methods such as the *Perry-Robertson formula.*

Referring to the numerical analysis, before the eigen value extraction can be performed, a restressed static analysis must be performed to obtain the stress stiffened stiffness matrix. Stress stiffening effects are prevalent for thin members where the bending stiffness is usually much less than the in-plane stiffness, hence the axial stiffness and bending stiffness have a significant interaction (hence bending and axial effects are coupled in the matrix). This is analogous to activating nonlinear geometry effects within the stiffness matrix.

A static structural analysis determines the displacements, stresses, strains, and forces in structures or components caused by loads that do not induce significant inertia and damping effects. Steady loading and response conditions are assumed; that is, the loads and the structural response are assumed to vary slowly with respect to time.

The results calculated by the linear buckling analysis are buckling load factors that scale the loads applied in the model. Thus for example if a *5 kN* compressive load is applied to a

structure in the pre-stressed static model and the linear buckling analysis subsequently performed calculates a load factor of *150*, then the predicted buckling load is *150* x *5 = 750 kN*. Because of this, it is typical to apply unit loads in the static analysis that precedes the buckling analysis. These factors are applied to all the loads used in the static analysis. Each load factor is related with a different instability mode. Normally, the lowest load factor is of concern, as this will present itself at the lowest applied load in the real physical structure.

Also non-zero displacements can be applied to one or more supports in the static analysis. The load factors calculated in the buckling analysis should also be applied to the associated nonzero reaction values. However, the buckled mode shape associated with this load will show the restraint to have a zero value.

It should be noted that the buckled mode shape provides the engineer with a good understanding of how a part or an assembly deforms when becoming unstable, but does not provide real displacements.

In the analysis results, it is only buckling load factors and corresponding buckling mode shapes that are obtained. The stress and strain results can be extracted from the results file but note that stress results only show the simulated distribution of stress in the structure and are not real stress values.

5.5.2 Nonlinear buckling analysis

Nonlinear buckling analysis is more realistic than eigenvalue analysis because it employs non-linear, large-deflection, static analysis to predict buckling loads. Its mode of operation is very simple: it gradually increases the applied load until a load level is found whereby the structure becomes unstable (i.e. suddenly a very small increase in the load will cause very large deflections), coupled with material yield and eventual failure. The true non-linear nature of this analysis thus permits the modelling of geometric imperfections, load perterbations, material nonlinearities and gaps. For this type of analysis, note that small off-axis loads are necessary to initiate the desired buckling mode. This can be achieved by either introducing small eccentricities on loads or small imperfections in the model geometry to produce a level of antisymmetric. Post-buckled strength which is typically exhibited by structures that present local buckling modes can also be simulated via this analysis.

The implementation of the nonlinear buckling analysis is akin to most other nonlinear analyses with the following additional points:

- A small geometric imperfection is often required to begin buckling. For example, the buckled mode shape from an eigenvalue buckling analysis can be used to produce an initial geometric imperfection. However, the magnitude of the initial imperfection will affect the results of the nonlinear buckling analysis. Therefore, the amplitude of the imperfection (or imperfection generated by the perturbation) should be small relative to the overall dimensions of the structure. In cold-formed steel members, the manufacturing tolerances can be used to estimate the magnitude of the perturbation/imperfection, or using self-weight deflections.
- The applied load should be set to a value somewhat higher (10 to 20%) than the critical load expected by the eigenvalue buckling analysis.
- The analysis must be run with geometric nonlinearities activated.
- Write out results for an appropriate number of intermediate sub-steps so that the load-deflection curve can be reviewed.

To start nonlinear buckling analysis in ANSYS, element type and material properties are selected carefully with nonlinear characteristics (i.e. nonlinear stress-strain curves) see figure (5-10). From the ANSYS results it is possible to predict when buckling begins but the solution may continue to converge if the structure can still carry the load.

Before the solution phase for the nonlinear buckling can be started several solution parameters need to be set, see figure (5-11):

- In the basic solution options tab:

- Allow large static displacements to be invoked (this will include the effects of large deflection in the results, i.e. nonlinear geometry).
- Confirm the automatic time stepping is on. An automatic time stepping lets ANSYS determine suitable sizes for the load steps to achieve convergence. Reducing the step size usually ensures better accuracy, however, this is time-consuming. The automatic time step feature will determine an appropriate balance and uses bisection to adjust load steps as the solution proceeds to ensure convergence.
- If n is the number of sub-steps, then the initial sub-step is set to $1/n^{th}$ of the total load.
- If the maximum number of sub-steps is m this will stop the program if the solution does not converge after m steps.
- The minimum number of sub-steps is 1.

- All solution items are written to a results file. This can result in a large results file size if the model is large so it is possible to write out only selected results of interest if required.
- Write every sub-step frequency to save all sub-step results.

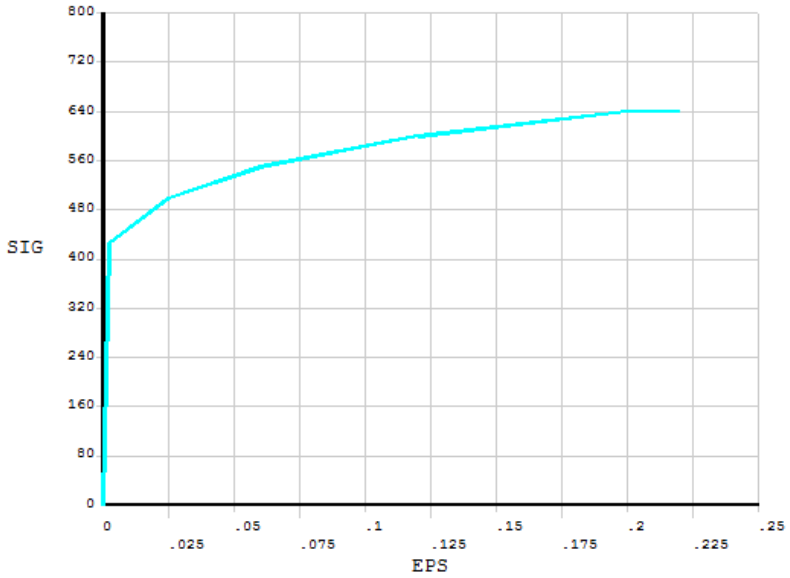

Figure (5-10) Nonlinear stress-strain curves ANSYS modelling.

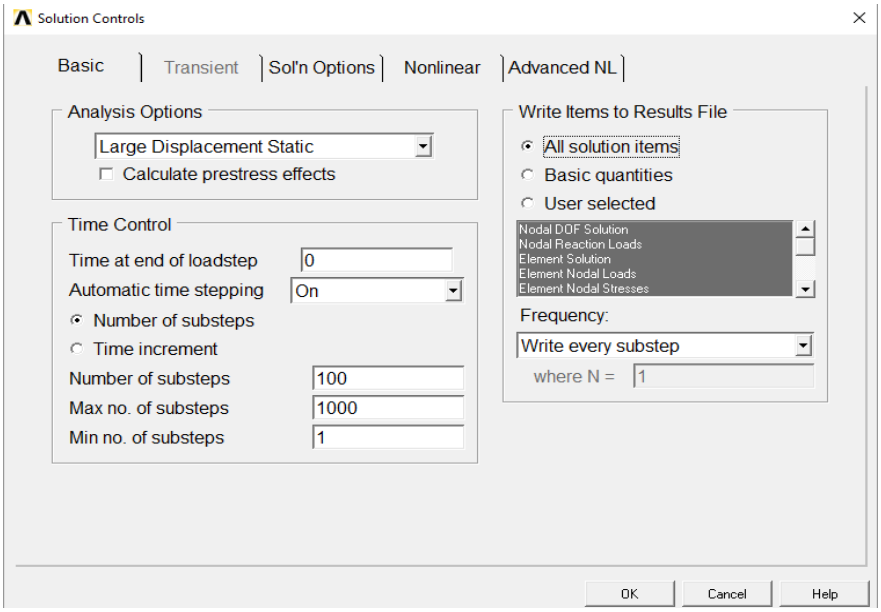

Figure (5-11) Solution control.

➢ In the Non-linear Tab

- Ensure Line Search is 'On'. This option is used to help the Newton-Raphson solver converge.
- Ensure 'Maximum Number of Iterations' is set to the same number as the 'Maximum Number of sub-steps', Figure (5-12).

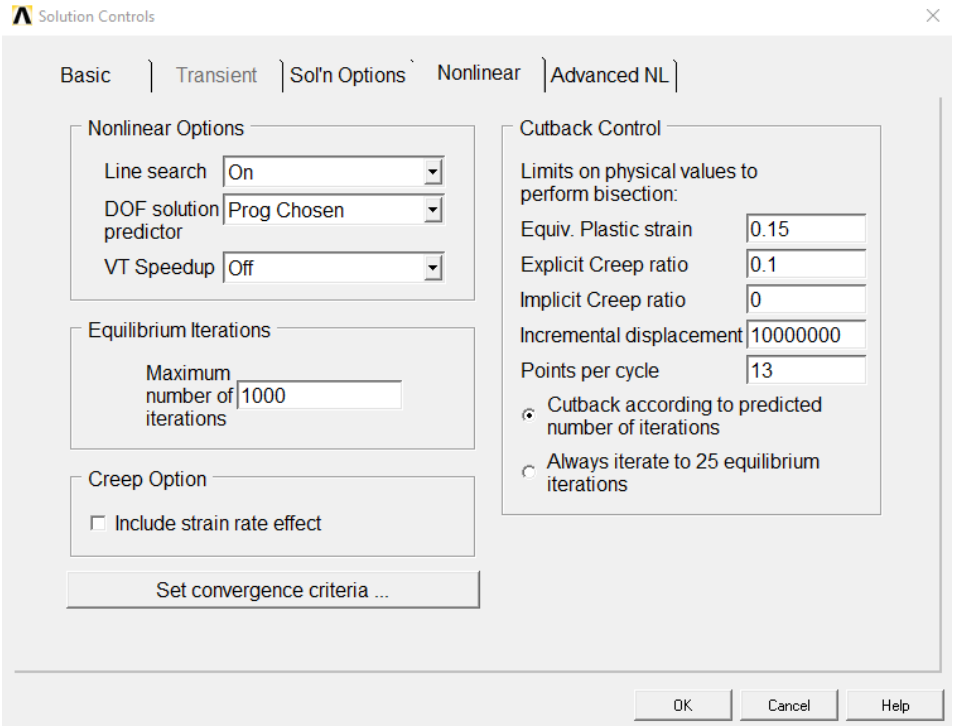

Figure (5-12) Solution control, nonlinear options.

5.6 Finite element modelling of cold-formed cladding section

Plate thickness: 1.6 mm

Modulus of Elasticity: 210000 N/mm^2

Poisson's ratio: 0.3

Yield stress: 415 N/mm^2

Steel density: 7850 Kg/m^3

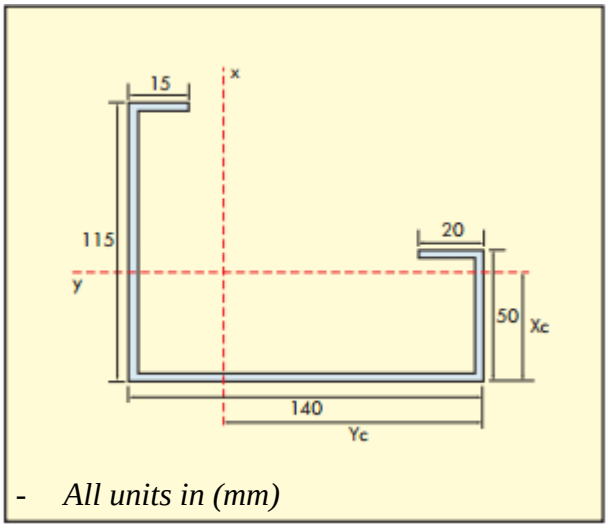

Figure (5-13) Cladding section.

5.6.1 Pinned end support

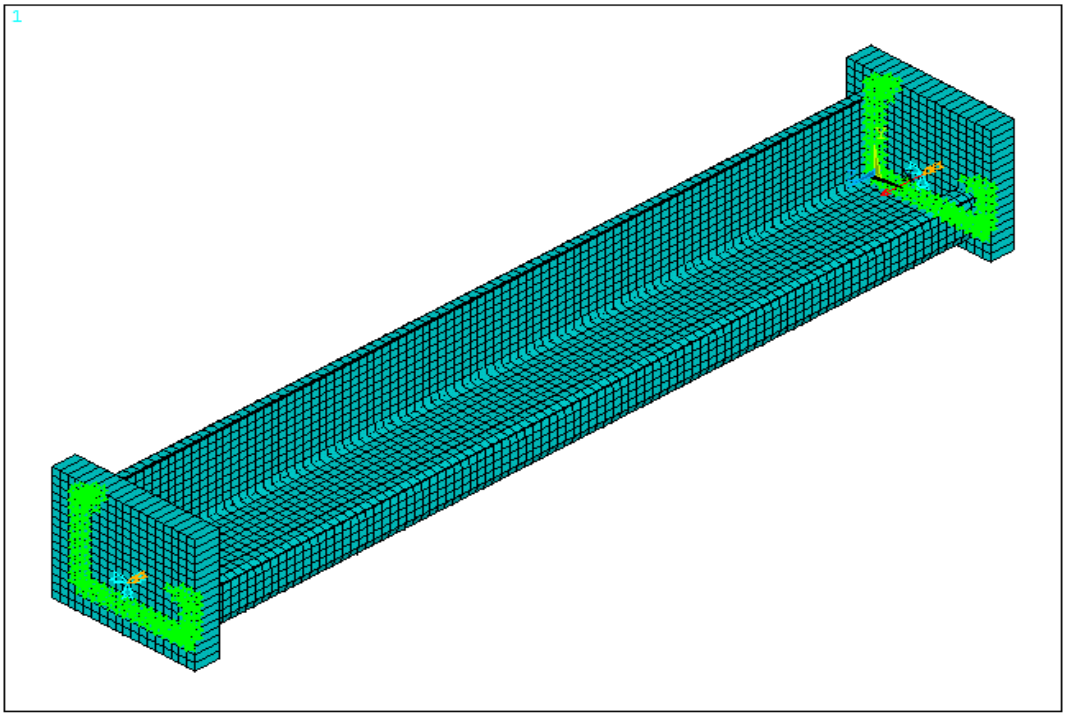

Figure (5-14) Pinned end support (ANSYS model).

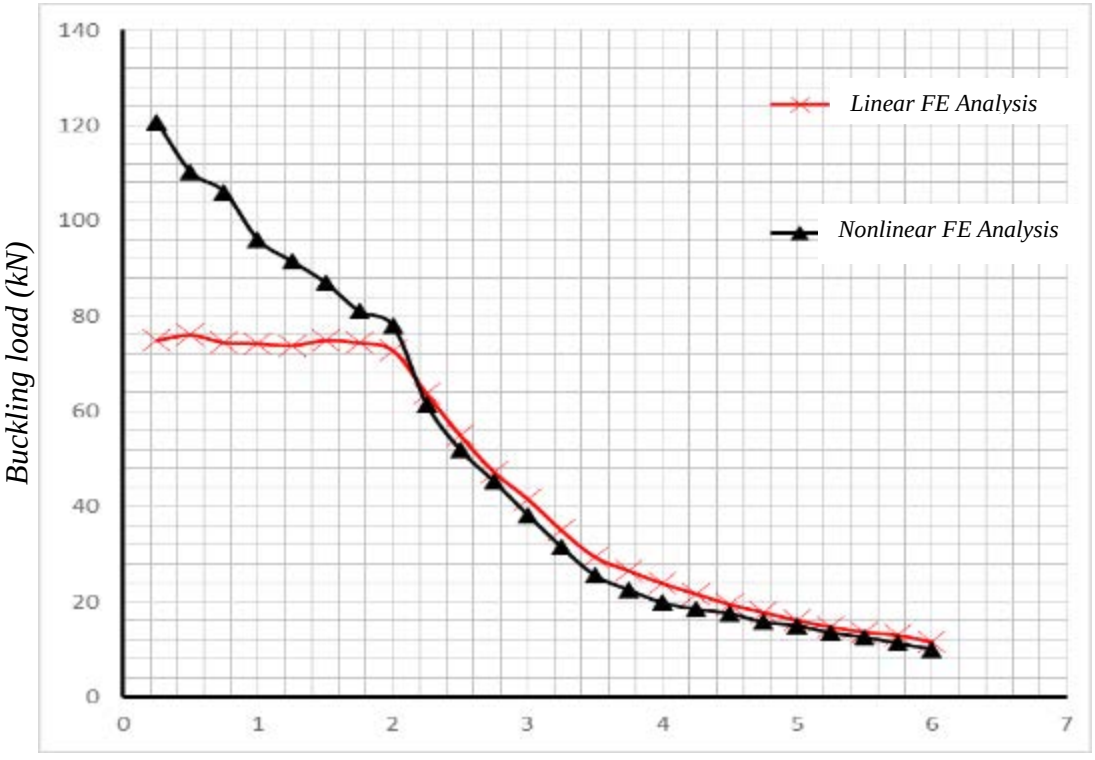

Figure (5-15) Linear and non-linear buckling load versus column length for pinned end support.

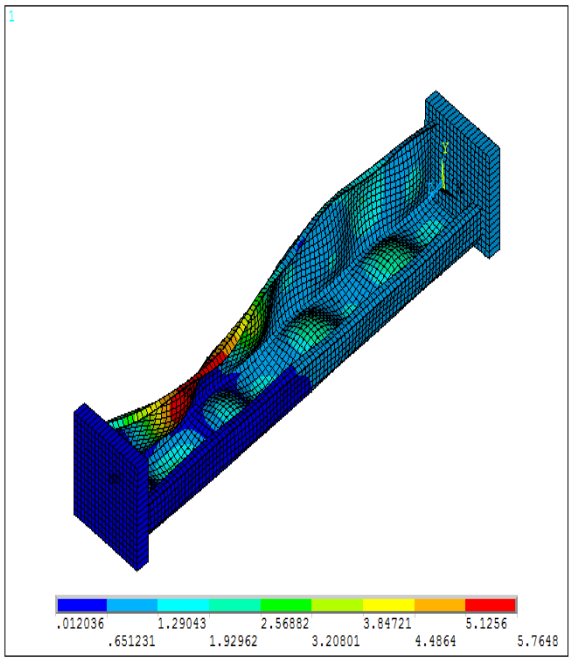

Non-linear mode shape

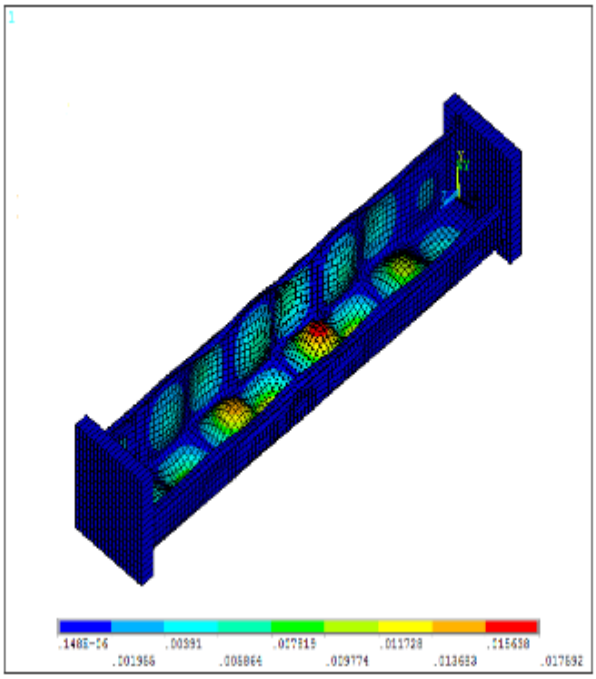

Linear mode shape

Figure (5-16) Linear and non-linear buckling mode shapes for pinned end conditions at a length of 1.0 metre.

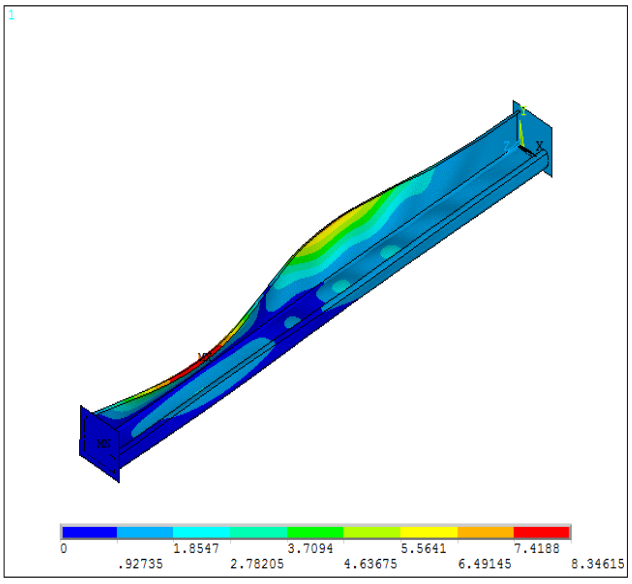

Non-linear mode shape

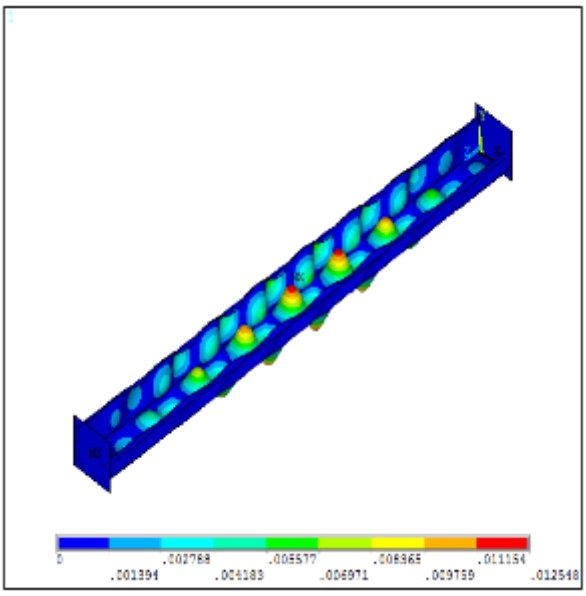

Linear mode shape

Figure (5-17) Linear and non-linear buckling mode shapes for pinned end condition for a length of 2.0 meters

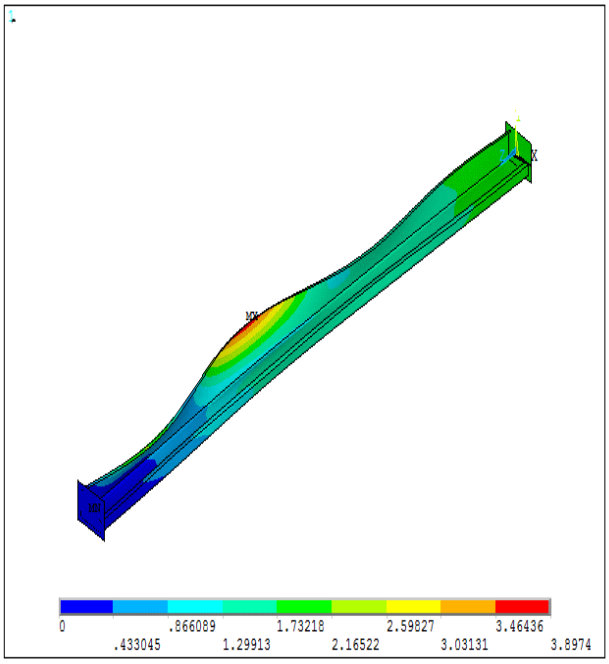

Non-linear mode shape

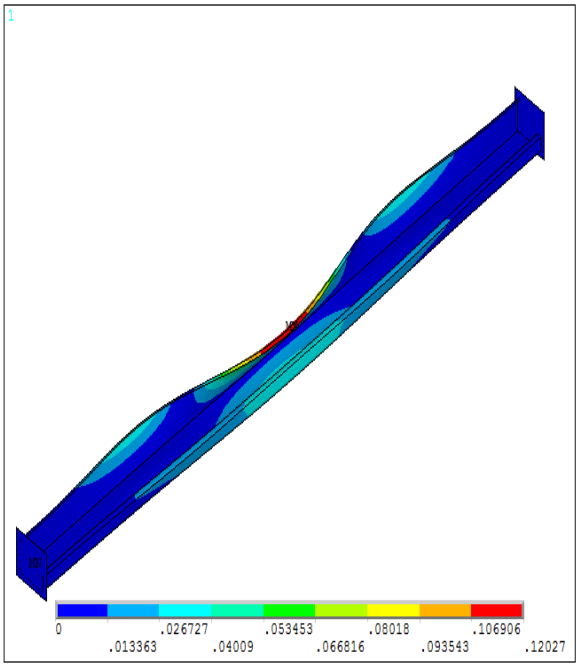

Linear mode shape

Figure (5-18) Linear and non-linear buckling mode shapes for pinned end conditions for a length of 3.0 metres

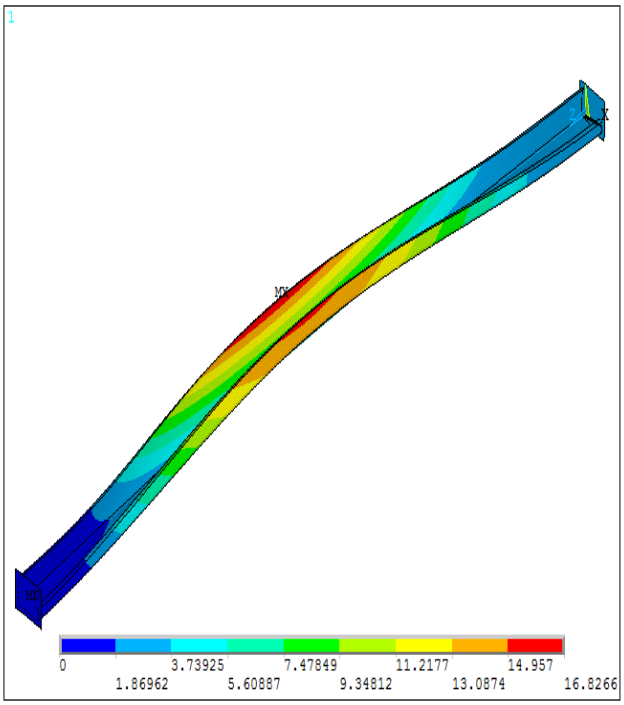

Non-linear mode shape

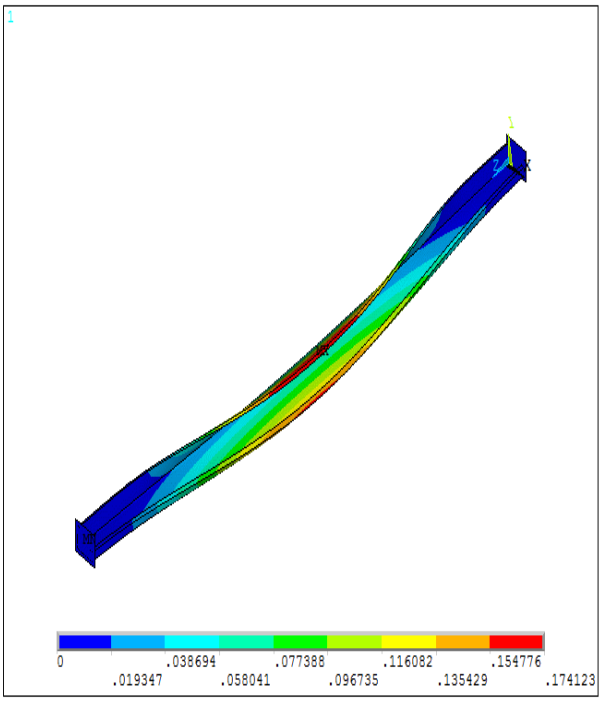

Linear mode shape

Figure (5-19) Linear and non-linear buckling mode shapes for pinned end condition for a length of 4.0 metres.

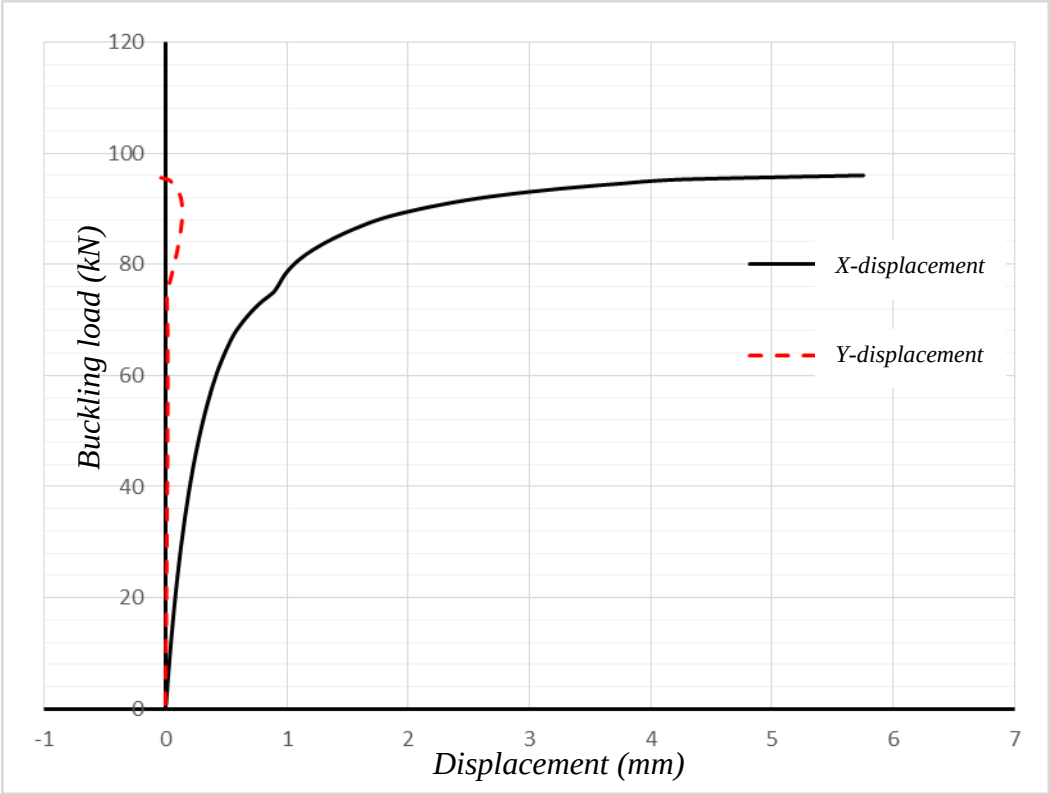

Figure (5-20) Non-linear buckling load versus displacements of max. displacement point for pinned end conditions for a length of 1.0 metre.

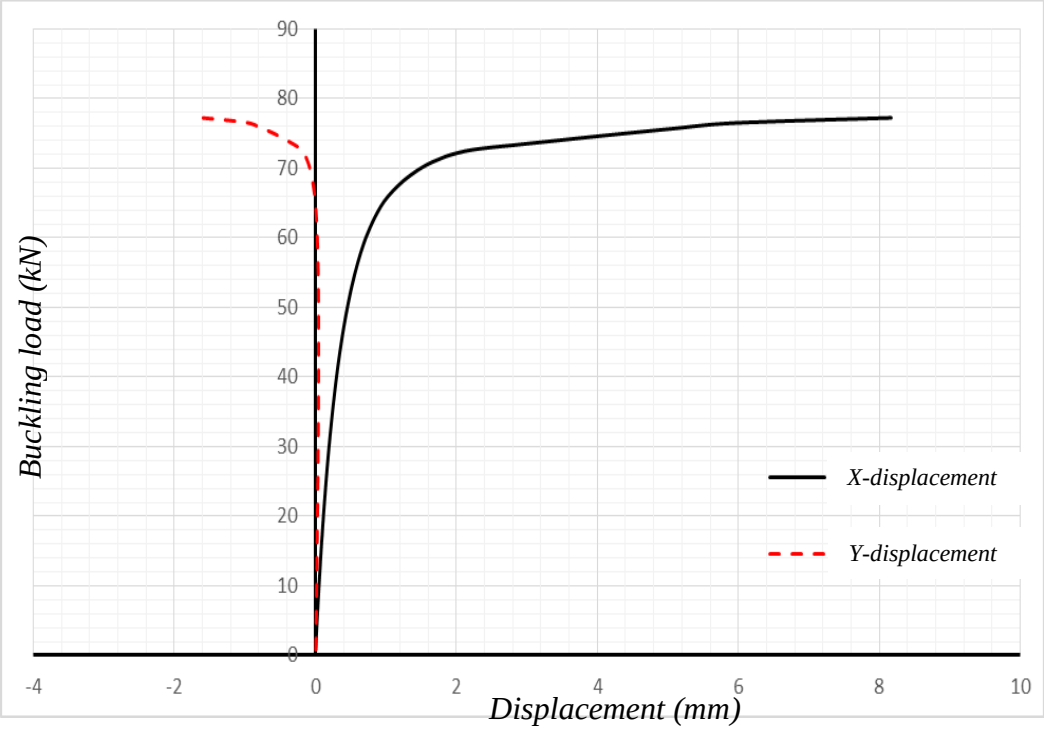

Figure (5-21) Non-linear buckling load versus displacements of max. displacement point for pinned end conditions for a length of 2.0 metres.

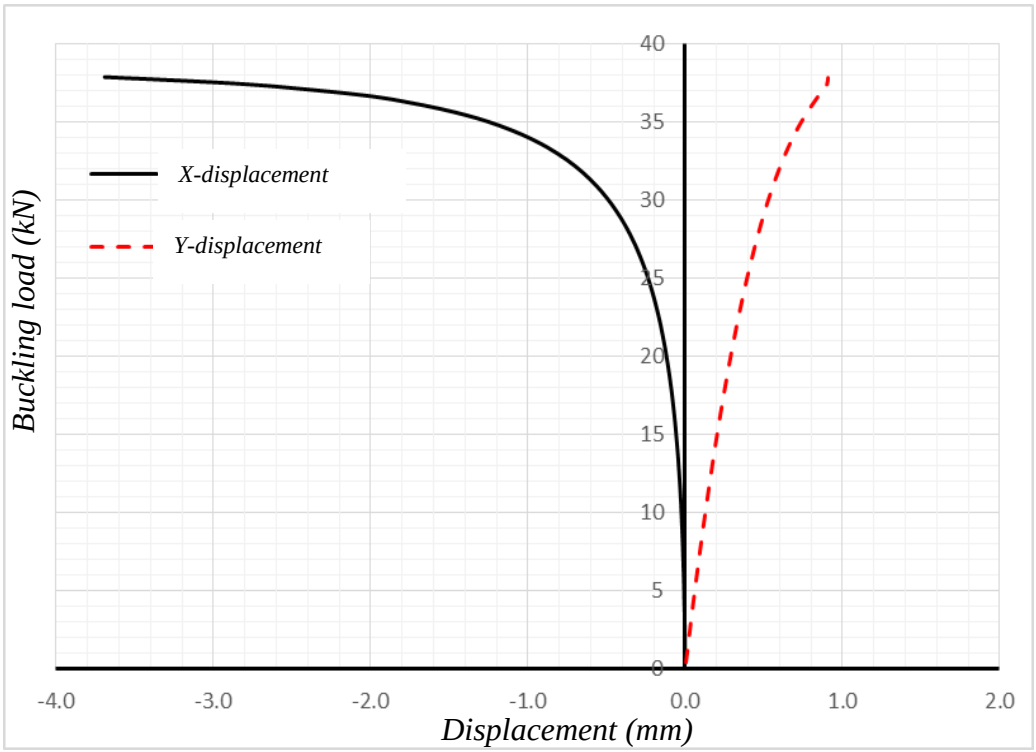

Figure (5-22) Non-linear buckling load versus displacements of max. displacement point for pinned end conditions for a length of 3.0 metres

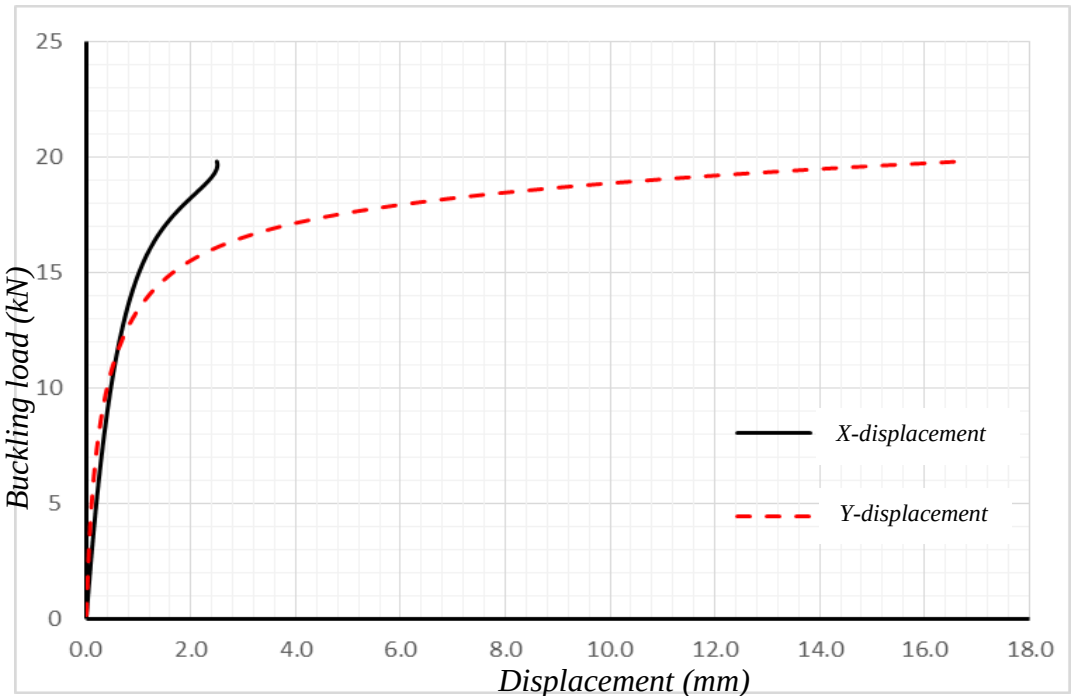

Figure (5-23) Non-linear buckling load versus displacements of max. displacement point for pinned end conditions for a length of 4.0 metres

5.6.2 Fixed end support

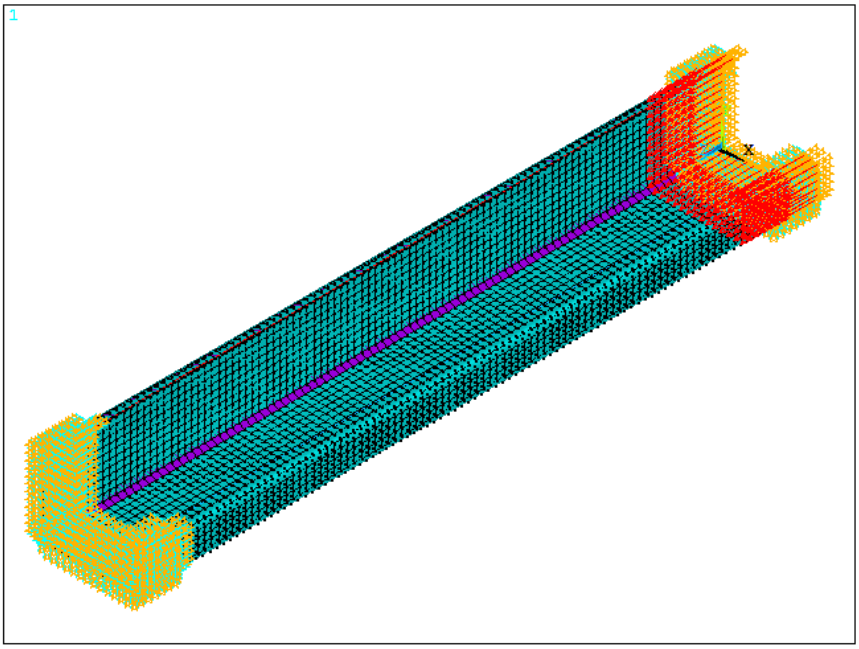

Figure (5-24) Penned end ANSYS modelling

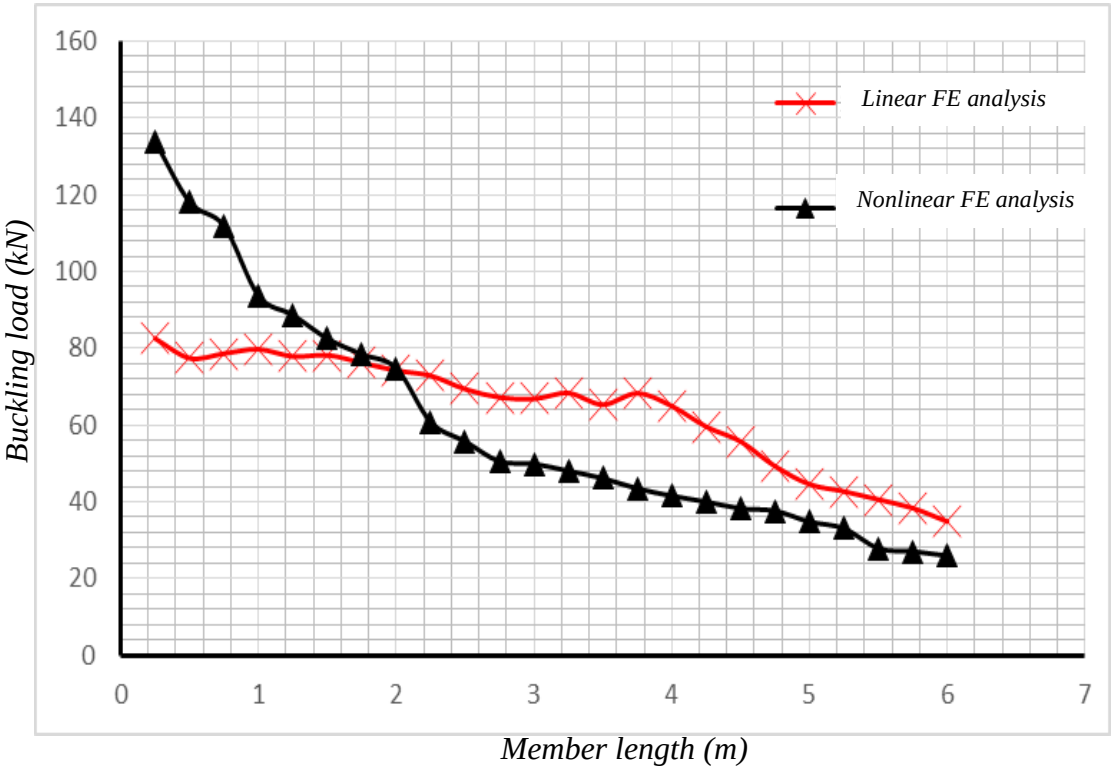

Figure (5-25) Linear and non-linear buckling load versus column length for fixed end support

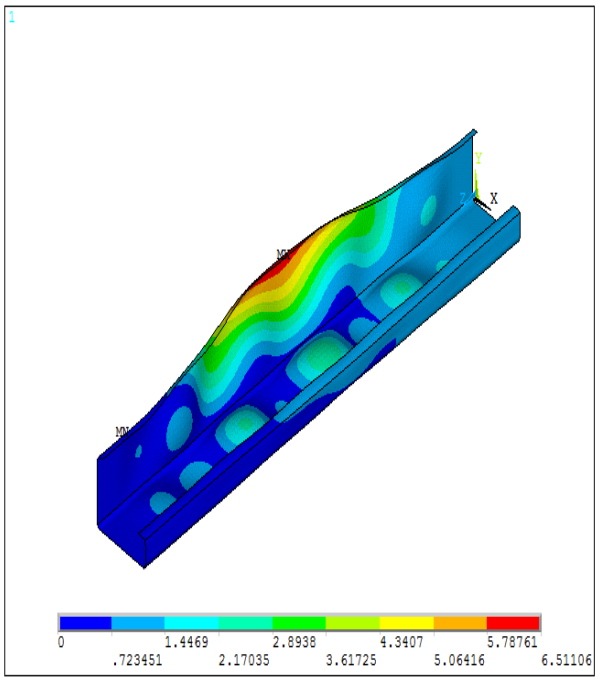

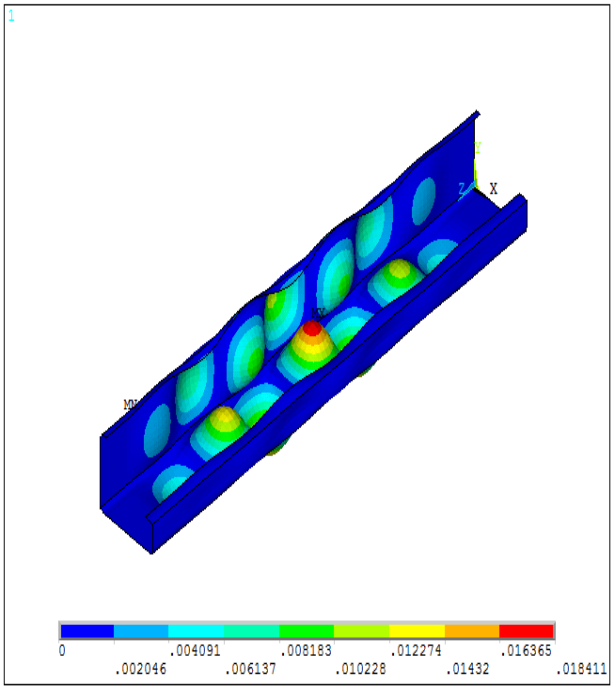

Non-linear mode shape *Linear mode shape*

Figure (5-26) Linear and non-linear buckling mode shapes for fixed end conditions for a length of 1.0 metre

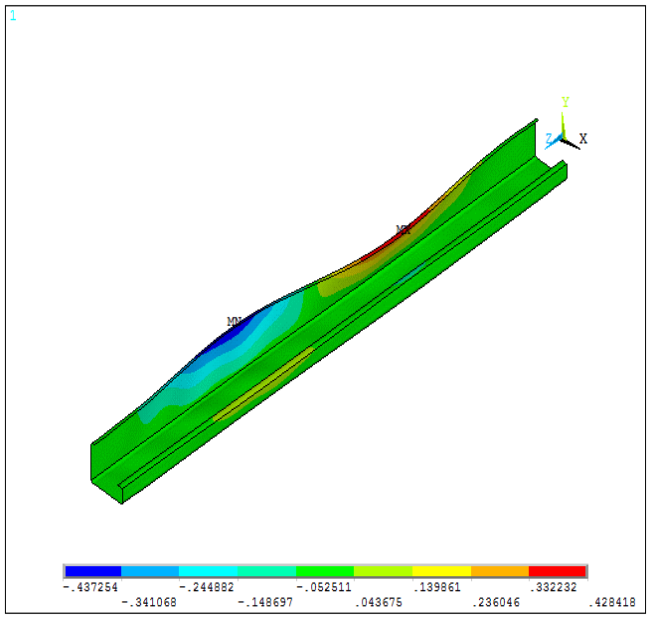

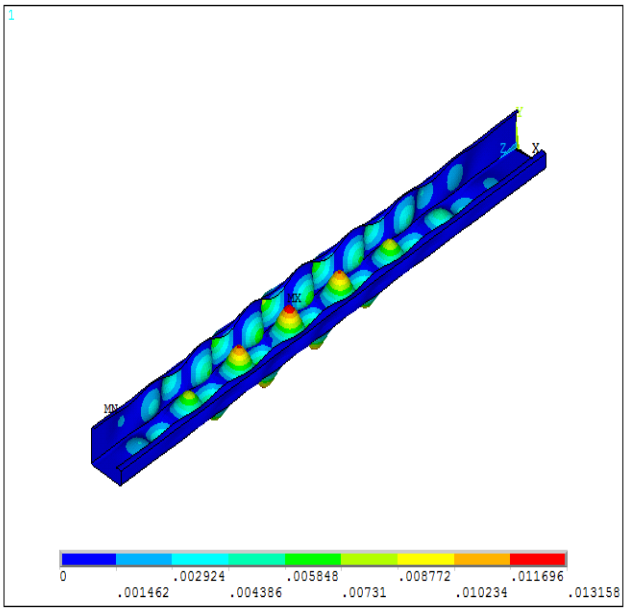

Non-linear mode shape *Linear mode shape*

Figure (5-27) Linear and non-linear buckling mode shapes for fixed end condition for a length of 2.0 metres

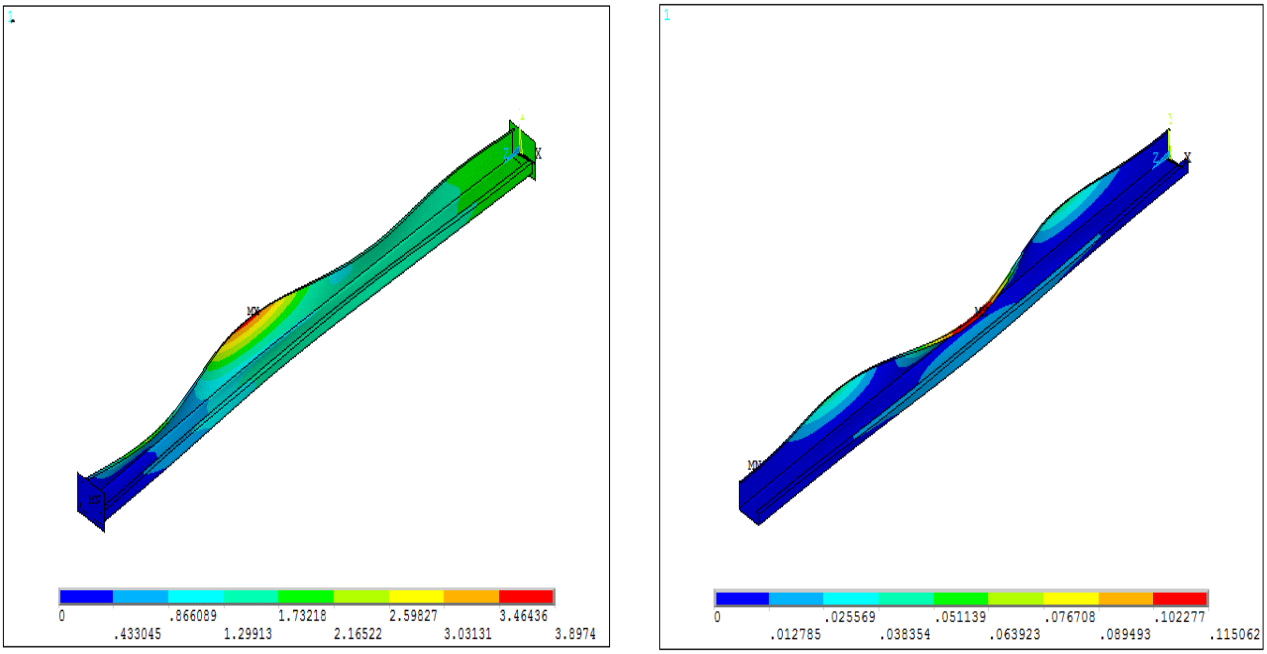

Non-linear mode *Linear mode shape*

Figure (5-28) Linear and non-linear buckling mode shapes for fixed end conditions for a length of 3.0 metres

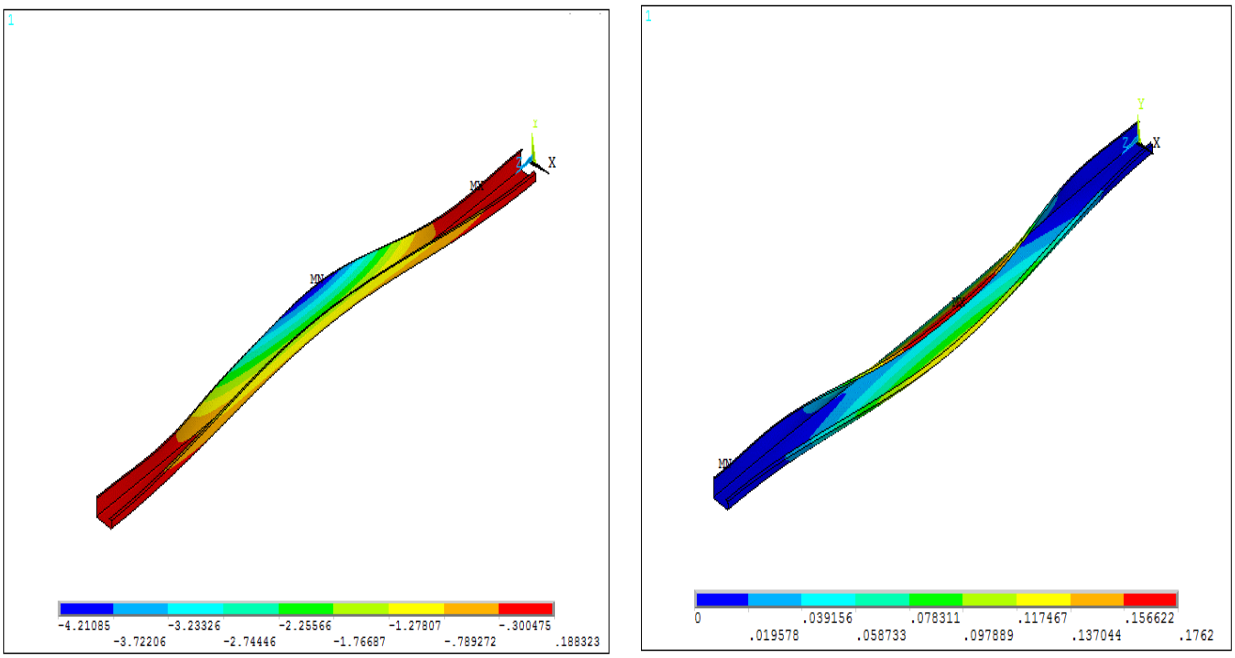

Non-linear mode *Linear mode shape*

Figure (5-29) Linear and non-linear buckling mode shapes for fixed end conditions for a length of 4.0 metres

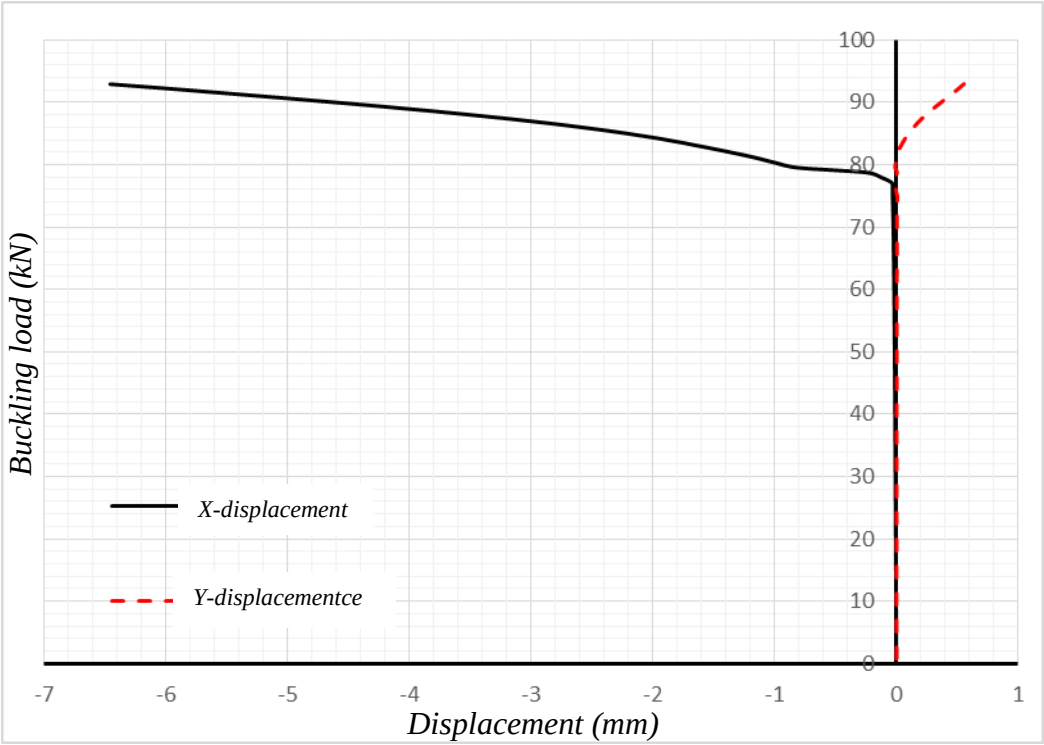

Figure (5-30) Non-linear buckling load versus displacements of max. displacement point for fixed end conditions for a length of 1.0 metre

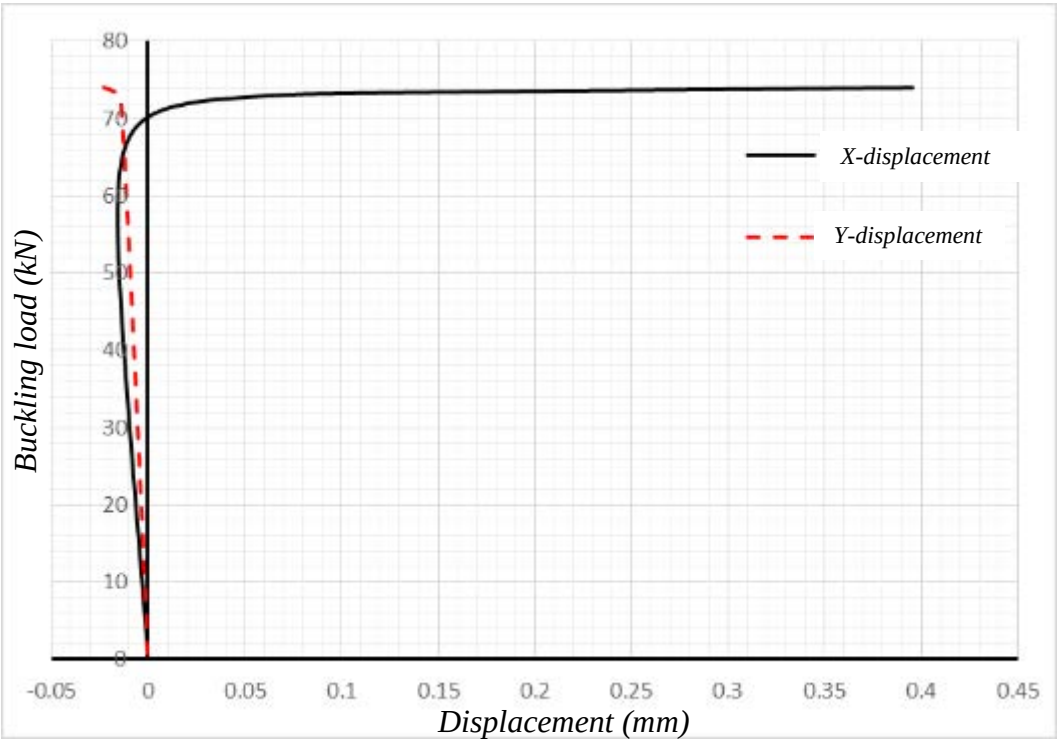

Figure (5-31) Non-linear buckling load versus displacements of max. displacement point for fixed end conditions for a length of 2.0 metres

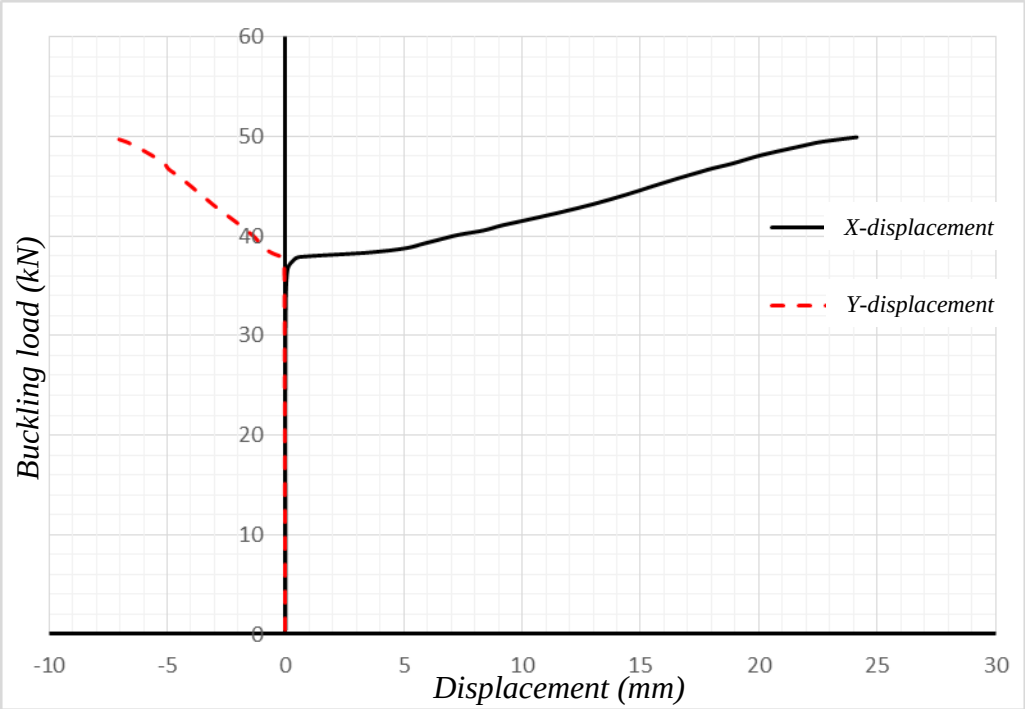

Figure (5-32) Non-linear buckling load versus displacements of max. displacement point for fixed end conditions for a length of 3.0 metres

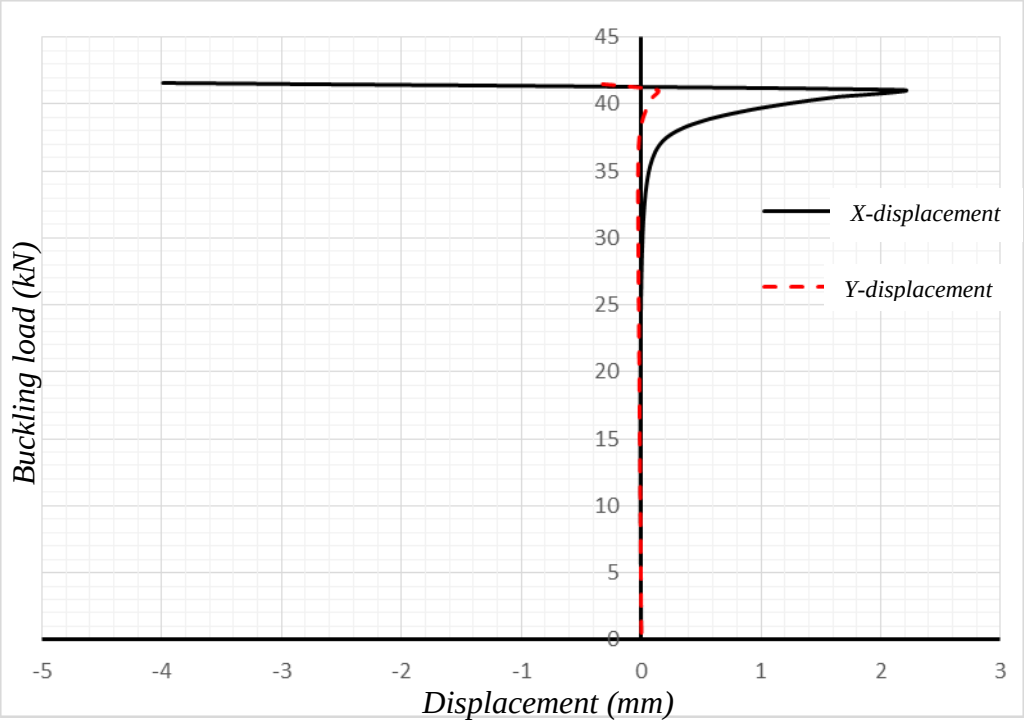

Figure (5-33) Non-linear buckling load versus displacements of max. displacement point for fixed end conditions for a length of 4.0 metres

From the FE modelling summarised in figures (5-10) to (5-33), it can be seen that the finite element modelling in ANSYS gives a good simulation of boundary condition representations for both pinned and fixed end supports. For pinned end supports at the global boundary conditions, it is clear to see that the plate at the end is free to rotate in both X-axis and Y-axis with constraint of rotation in the Z-axis to prevent the rigid body twisting motion, and that the same rigid end plate has been supported against translational displacement in the X-axes, Y-axis and Z-axis at the centroid of section. Also, to ensure that the section plate elements are able to rotate locally, the common nodes between the bearing plate and section elements are coupled in translational degrees of freedom only. The axial load, was applied at the centroid of the section to avoid any effects on axial displacement constraints. While for the fixed end condition the load was applied as a distributed axial load surrounding the cross-section, also the displacements and rotations in all directions were constrained surrounding the cross-section with enough distance beyond the member ends.

From these analysis results, it is obvious that the buckling load decreases with the length of the column in both linear and non-linear analysis, see figures (5-15) & (5-25), but this decrease is not at the same rate as it depends on the type of buckling witnessed. For short length studs, the buckling load has less of a rate of decrease due to local distortional buckling mode shape effects. For medium to long lengths, the buckling load drops rapidly as global buckling dominates the mode shape.

Figures (5-15) & (5-25) demonstrate that linear analysis predicts a smaller load than non-linear analysis due to the fact that it does not take into account post-buckling effects and initial imperfections when calculating the eigenvalue buckling load. For the non-linear static buckling analysis, the effects of post-buckling and initial imperfection increase and decrease the buckling loads through column length depending on mode shape zones respectively. Also nonlinear (yielding) material properties are incorporated into the nonlinear analysis. For local and distortional mode shapes (occurring in the shorter stud lengths), the effects of post-buckling strength mean that the failure loads are higher than the linear (eigenvalue) buckling loads. In comparison, the global and distortional buckling modes which occur in the longer column, the effects of the initial imperfection, serve to decrease the failure loads below linear (eigenvalue) buckling loads. So in general, the non-linear analysis is more representative of the physical behaviour (in terms of buckling and failure) which would occur, than the linear

buckling (eigenvalue) analysis which gives a theoretical estimate of the occurrence of instability in a perfect structure but cannot predict how the structure would actually behave pre or post buckling. Hence the nonlinear analysis (which is path dependent upon the applied loads) is more valuable and verifiable to experimental tests

For mode shape expectations, figures from (5-16) to (5-19) for pinned end condition and (5-26) to (5-29) for fixed end condition illustrate the mode shapes finite element prediction in both linear (eigenvalue) and non-linear analysis for different lengths and different mode shape zones. Likewise, the eigenvalue analysis looks to give poorer predictions in mode shapes as compared to the nonlinear analysis. Figures from (5-20) to (5-23) for pinned end condition and (5-30) to (5-33) for fixed end condition show the nonlinear time-history of out of plane displacements with applied load. These figures give good indications of how the column will buckle during load application, so it will help to predict failure mode shape and compare it with experimental test or other empirical, analytical or numerical analysis solutions.

In general, both linear (eigenvalue) and nonlinear buckling analyses using (ANSYS) have appropriate features to predict the eigen-buckling load or nonlinear failure load and its mode shapes, it also gives a good representation of modelling of boundary conditions in both pinned and fixed end conditions. But, it is time consuming in modelling and solving of each specific case. There are many factors which have an effect on the accuracy of results and the efficiency of solve operations such as element type, element size, element number and element degrees of freedom.

CHAPTER SIX

EXPERIMENTAL

INVESTIGATIONS

CHAPTER SIX

EXPERIMENTAL INVESTIGATIONS

6.1 Introduction

The elastic buckling modes discussed in Chapter 2 and their influence on the load-deformation response of cold-formed steel columns can be readily observed and quantified with experimental testing. This chapter presents the experimental testing of 36 cold-formed steel (lipped C-section and Zed-section) columns with different boundary conditions. The tests comprised Lipped Channel & Zed sections full-scale cold-formed steel columns of nine different lengths (two specimens for each length) subjected to axial loading for both pinned and fixed end conditions. The column lengths and cross-section dimensions were specifically chosen to explore local, distortional, and global buckling behaviour, ultimate strength, and the resulting failure mechanisms. The actual buckling behaviour was evaluated for each specimen using both a finite element nonlinear analysis and nonlinear generalized beam theory, taking care to accurately simulate the tested boundary conditions and measured specimen dimensions. The physical buckling observed through the experimental tests are used to provide a means of understanding the varied deformation response under load. The columns were tested with friction-bearing boundary conditions where the ends of each specimen are milled flat and parallel and bear directly against steel plates. Recommendations are made to advise other researchers on the viability of the friction-bearing boundary conditions when testing short and intermediate length columns. As well as the results of the testing, this chapter presents also, the rig details, material properties tests, boundary conditions simulation, applying load method and measuring device details of this experimental study.

6.2 Section geometry and specimen sizes and lengths

Mono-symmetric lipped channel and non-symmetric Zed sections were selected for the beam tests to provide the desired range of possible buckling mode shapes, see Figure (6-1). Elastic linear eigen-buckling analyses were first carried out on both sections using the well-known generalized beam theory analysis program (GBTUL) with both pinned and fixed end conditions to inform a selection of suitable cross-section sizes and beam spans (this also provides an understanding of buckling loads and mode shapes along the length of the beam.

Figures (6-3) & (6-4) show the results of the generalized beam theory analysis program (GBTUL) using thin-walled sections in a buckling plot format. From these figures, it can be seen at what member lengths the mode shape changes over from local buckling to distortional buckling and to lateral-torsional buckling. At these changeover points, the buckling loads can either increase or decrease depending on the mode shape type. So these ranges of beam lengths require more experimental and validated numerical analysis investigation to understand the behaviour more thoroughly.

The selection of beam spans was made based on the results shown in Figures (6-3) & (6-4) therefore most of the buckling mode shapes would be expected to occur during the tests. The beam span was varied from 1000 mm to 5000 mm for pinned end conditions and from 1000 mm to 4000 mm for fixed end conditions in order to produce a range of beam

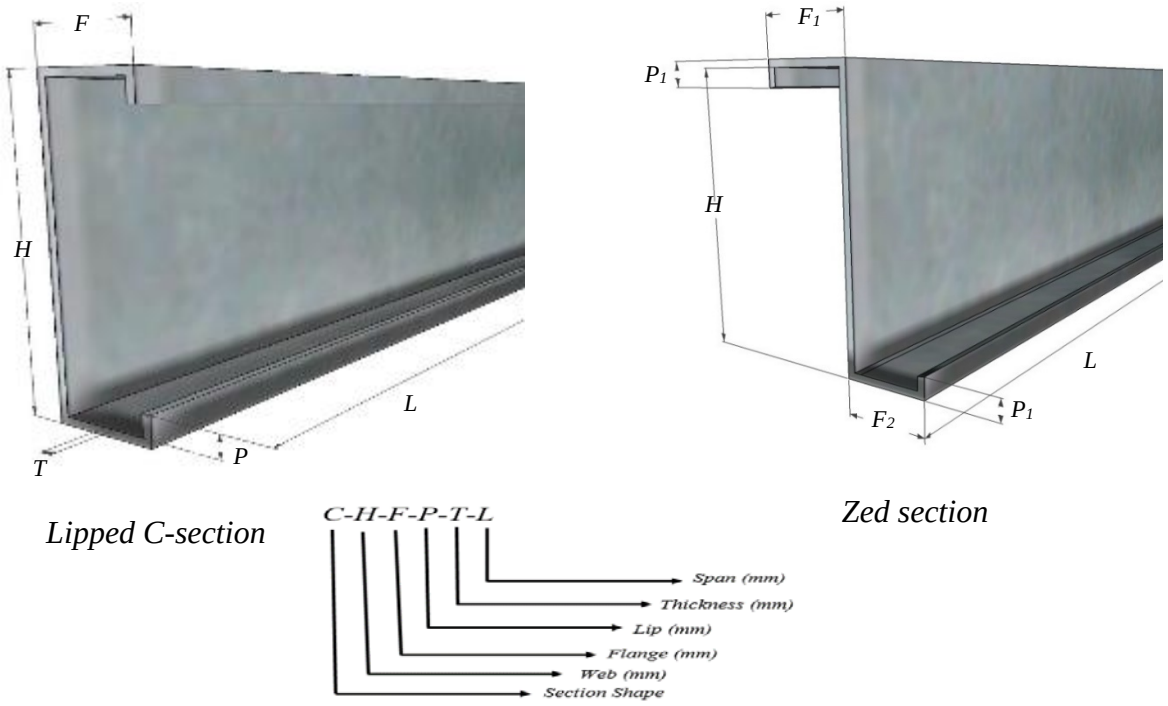

Figure (6-1) Test sections.

Lipped channel section dimensions of 200 mm web depth, 60 mm flange width, 14 mm lip and 1.775 mm thickness and Zed section dimensions of 200 mm web depth, (64&54) mm flange widths, (18&15) mm lips and 2.005 mm thickness were selected. Table (6-1) & Table (6-2) shows the test program for lipped channel and Zed sections beams. All the test specimens were labelled as follows to indicate their cross-section shapes, cross-section dimensions, thickness, and span lengths.

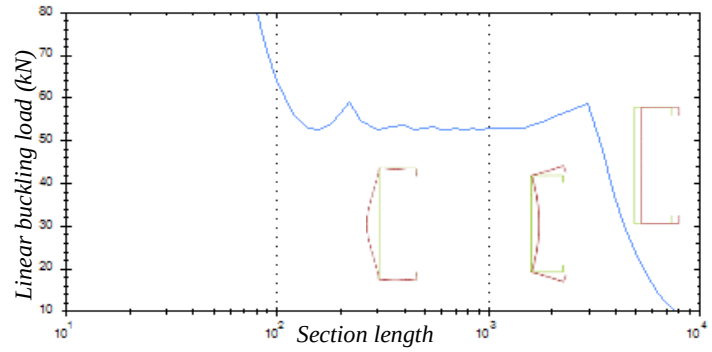

a) Pinned ends condition

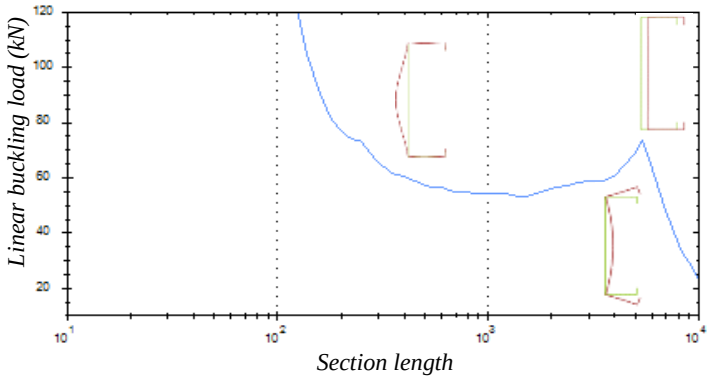

b) Fixed ends condition

Figure (6-2) (GBTUL) eigen-buckling analysis

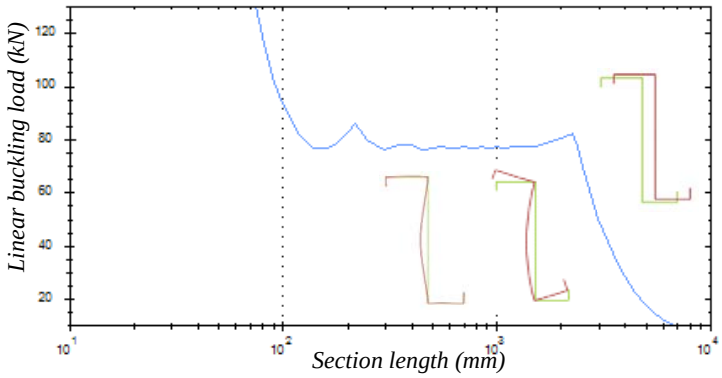

a) Pinned ends condition

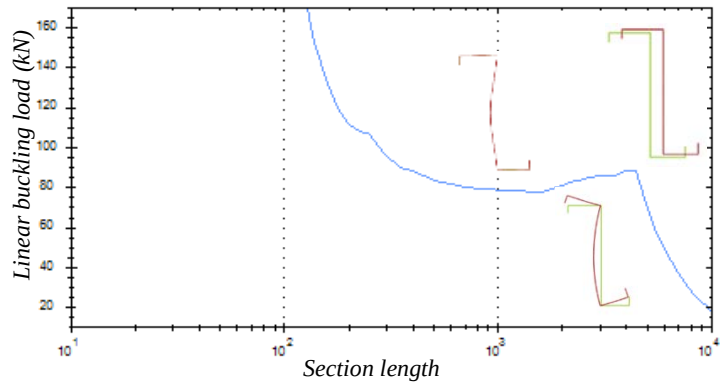

b) Fixed ends condition

Figure (6-3) (GBTUL) eigen-buckling analysis.

Table (6-1) Lipped C-sections details.

Lipped C-Section							
Pinned end condition				Fixed end condition			
Specimen No.	Designation	Grade	Span (mm)	Specimen No.	Designation	Grade	Span (mm)
1	C-200-60-14-1.77	G450	1000	10	C-200-60-14-1.77	G450	1000
2	C-200-60-14-1.77	G450	1300	11	C-200-60-14-1.77	G450	1300
3	C-200-60-14-1.77	G450	1700	12	C-200-60-14-1.77	G450	1700
4	C-200-60-14-1.77	G450	2000	13	C-200-60-14-1.77	G450	2000
5	C-200-60-14-1.77	G450	2300	14	C-200-60-14-1.77	G450	2300
6	C-200-60-14-1.77	G450	2700	15	C-200-60-14-1.77	G450	2700
7	C-200-60-14-1.77	G450	3000	16	C-200-60-14-1.77	G450	3000
8	C-200-60-14-1.77	G450	4000	17	C-200-60-14-1.77	G450	3500
9	C-200-60-14-1.77	G450	5000	18	C-200-60-14-1.77	G450	4000

Table (6-1) Z-sections details

Zed Section							
Pinned end condition				Fixed end condition			
Specimen No.	Designation	Grade	Span (mm)	Specimen No.	Designation	Grade	Span (mm)
19	Z-200-(64-54)-(18-15)-2	G450	1000	28	Z-200-(64-54)-(18-15)-2	G450	1000
20	Z-200-(64-54)-(18-15)-2	G450	1300	29	Z-200-(64-54)-(18-15)-2	G450	1300
21	Z-200-(64-54)-(18-15)-2	G450	1700	30	Z-200-(64-54)-(18-15)-2	G450	1700
22	Z-200-(64-54)-(18-15)-2	G450	2000	31	Z-200-(64-54)-(18-15)-2	G450	2000
23	Z-200-(64-54)-(18-15)-2	G450	2300	32	Z-200-(64-54)-(18-15)-2	G450	2300
24	Z-200-(64-54)-(18-15)-2	G450	2700	33	Z-200-(64-54)-(18-15)-2	G450	2700
25	Z-200-(64-54)-(18-15)-2	G450	3000	34	Z-200-(64-54)-(18-15)-2	G450	3000
26	Z-200-(64-54)-(18-15)-2	G450	4000	35	Z-200-(64-54)-(18-15)-2	G450	3500
27	Z-200-(64-54)-(18-15)-2	G450	5000	36	Z-200-(64-54)-(18-15)-2	G450	4000

All the cross-section dimensions were measured using a Vernier calliper. The uncoated thickness of each beam was measured using a Micrometre Screw Gauge and MikroTest, see figure (6-4). MikroTest is an extremely robust coating thickness gauge, which measures the thickness of non-magnetic coatings on steel substrates on the magnetic attraction principle. The base metal thickness of each steel sample was taken as the average of measured base metal thicknesses (*t*) given in tables (6-1) & (6-2). The centre line dimensions of the cross-section were calculated based on the measured external dimensions are in tables (6-1) & (6-2).

Figure (6-4) Micrometre screw gauge and Mikrotest

6.3 Experimental buckling test rig

For this study, a purpose built test rig was constructed to conduct axial buckling tests of the light gauge steel beams (*LSB*) with different boundary conditions and different section sizes and shapes. The test rig included a specially designed support and loading system that facilitated application of the axial load through the centroid of the section. The schematic and overall views of the test setup are shown in figure (6-5).

The test rig included the main frame which comprised two main beams and two supported sub-beams. The two main beams (Universal Columns 150mm x 30.0kg/m x 6000mm length) shown in figure (6-6) were placed parallel to each other to support the two sub-beam sections of (200 x 100 x 6 RHS) with 1000 mm length which carry the test specimens at both the loading and measuring ends. The sub-beams were positioned horizontally at set locations along the main beams to cover all required lengths of specimens. A support system was provided to prop

the sub-beams at the middle with one end facilitating a hydraulic jack, and the other end facilitating a series of load cells for the measurement of the applied axial load.

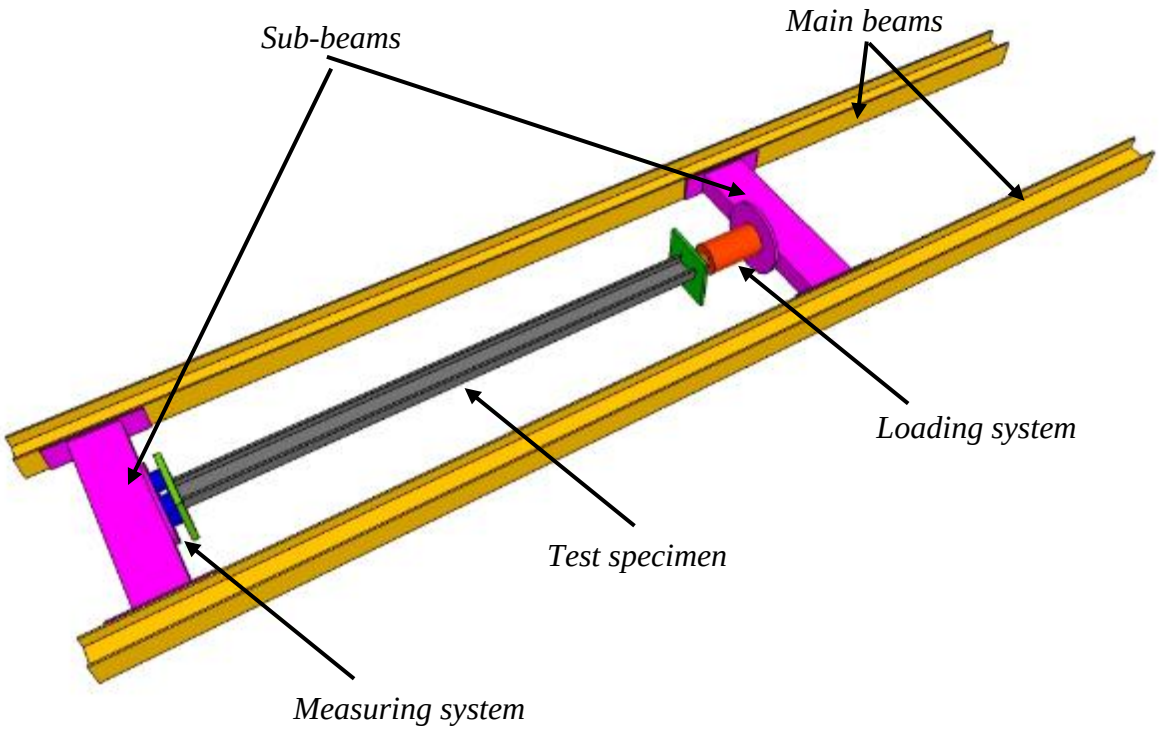

Figure (6-5) Overview of the test set-up

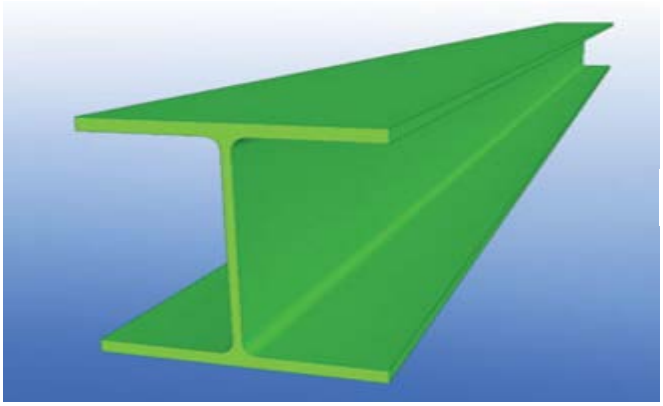

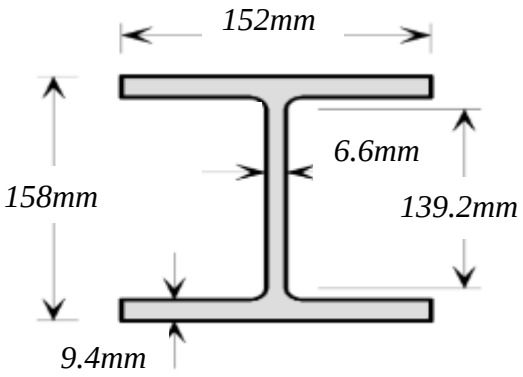

a) Main beam details

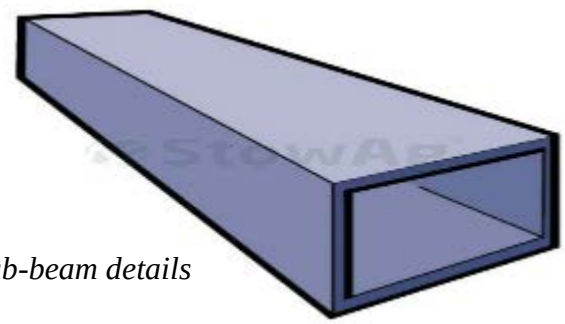

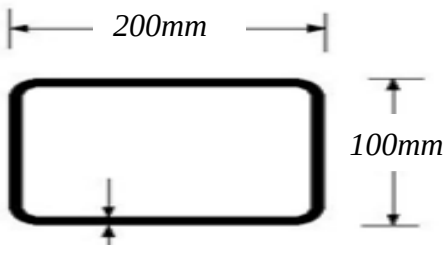

b) Sub-beam details

6-6) Test rig sections.

6.4 Loading system

The cold-form steel test specimen was loaded axially. The loading system employed ensured that the test specimen was loaded through the centroid of the section. It was designed to eliminate the effects of load eccentricity and torsional loading effects. The arrangement of the loading system is shown in Figure (6-7) and (6-8) and is described in the following section.

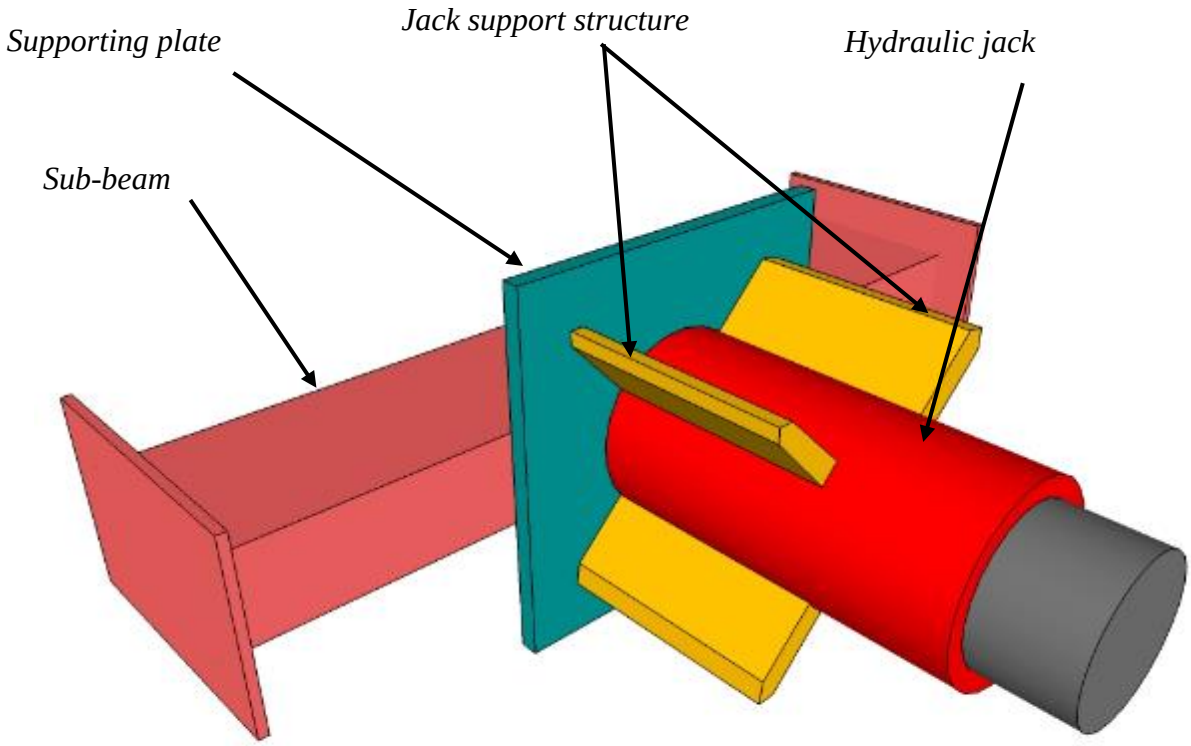

Figure (6-7) Schematic of loading system

The loading system included a hydraulic jack fixed rigidly to one of the sub-beams with no rotations or translational movements to ensure the load was applied axially on the specimens; therefore, this system was able to apply the loads to the test specimen without any restraint to their longitudinal displacements or rotations at the loading points in any direction. The hydraulic jack was operated under load-displacement control using a single hydraulic jack to apply rated loads on the test specimen. The loads were applied horizontally on the sub-beam. The hydraulic jacks were supported on a rail system which had the capability of moving in a parallel direction to the specimen span. Therefore, all the six degrees of freedoms at the loading position of the test beam can be considered as unrestrained.

a) Hydraulic pump

b) Hydraulic jack

Figure (6-8) Loading system.

6.5 Measuring system

In each test the applied loads and the deformations were measured until failure. The *EDCAR (Experimental Data Collection and Recorder)* system was used to record all the measurements automatically.

6.5.1 Loading measuring system

The test specimen was loaded axially using a hydraulic jack, with a 300 kN capacity. To measure the applied loads, three 100 kN capacity load cells were attached to the measuring plate, with the three load cells arranged as an equilateral triangle as shown in Figures (6-9) and (6-10). To prevent any side movements and rotations of the measuring end (in addition to providing accuracy of measurement, all the load cells were linked to a computer-controlled system in which the load and displacement data was graphically displayed, Figure (6-13). All the data was saved automatically for recall at a later time. The three load cells shown in figure (6-10) read different loadings due to eccentricity of the sample, and the end plate was designed to have a large enough stiffness to minimise any effects due to plate bending.

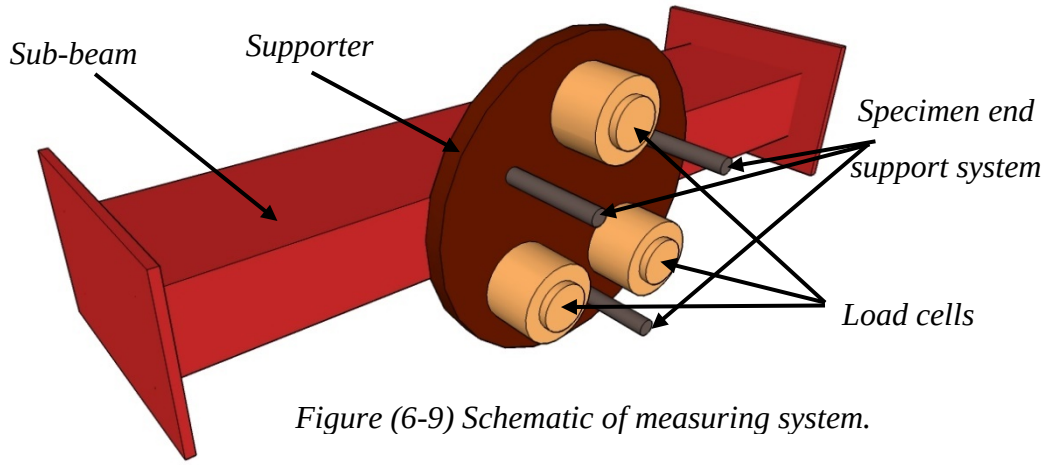

Figure (6-9) Schematic of measuring system.

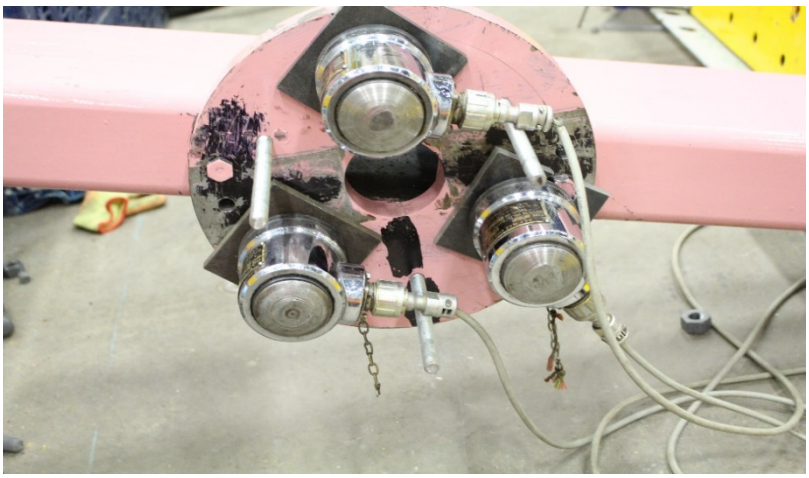

Figure (6-10) Measuring system.

6.5.2 Displacement measuring system

The displacements were measured using linear variable displacement transducers (LVDT's), the LVDT is a type of electrical transformer used for measuring linear displacement positions. The LVDT converts a position or linear displacement from a mechanical reference (zero, or null position) into a proportional electrical signal containing phase (for direction) and amplitude (for distance) information, Figure (6-11). As well as load cells, the LVDT's were linked to a computer-controlled system in which the load and displacement data can be graphically displayed.

6.5.2.1 Vertical displacement measuring system

The vertical displacement was measured using LVDT's positioned at the mid-point of the web of the specimen. This was implemented at three positions along specimen length as shown in figure (6-12), one point in the mid length of the specimen and the other two points at quarter length of the specimen. The LVDT plunger was placed directly on the test specimen, so if the specimen buckled during testing (with a combination of different modes) the movement could possibly cause the LVDT needle to slip from its contact position. To avoid this scenario, the vertical measuring system was connected using tension wires. Overhead stands and tension wires were arranged as shown in figure (6-12) to obtain a more accurate measurement.

The measuring points were arranged to examine a range of possible buckling mode shapes and to log the load-displacement history during the test to enable comparison with the nonlinear finite element and generalized beam theory analyses load-displacement histories for verification purposes.

Figure (6-11) Linear variable displacement transducer (LVDT).

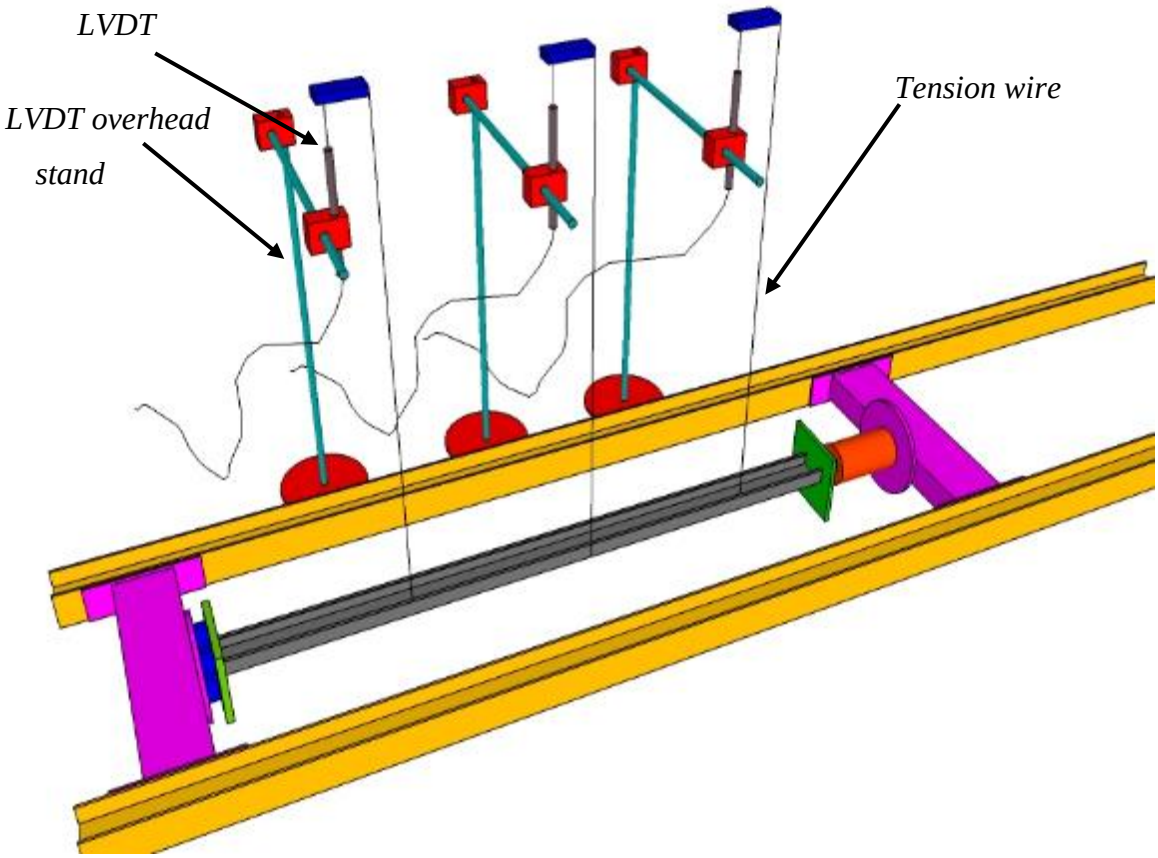

Figure (6-12) Vertical displacement measuring system.

Figure (6-13) Data logger measuring system.

6.5.2.2 Horizontal displacement measuring system

The horizontal displacement measuring system was of a similar arrangement to the vertical displacement measuring system. The the same *LVDT* and data logger measuring system were used to measure the horizontal displacement at the same positions of vertical displacements along the specimen length, see figure (6-15). It was recognized that there was a geometric dependence between the horizontal and vertical displacements. Figure (6-14) shows how these displacements are related, and how the horizontal movement effects the measured vertical displacement. The relationship is simply of triangular form requiring trigonometry to solve. In the experiment the horizontal *LVDT* was placed as far away from the sample as possible to decrease the effects of vertical movement on the recorded horizontal movement. The trigonometry used to then calculate the actual displacements is presented in the following equations:

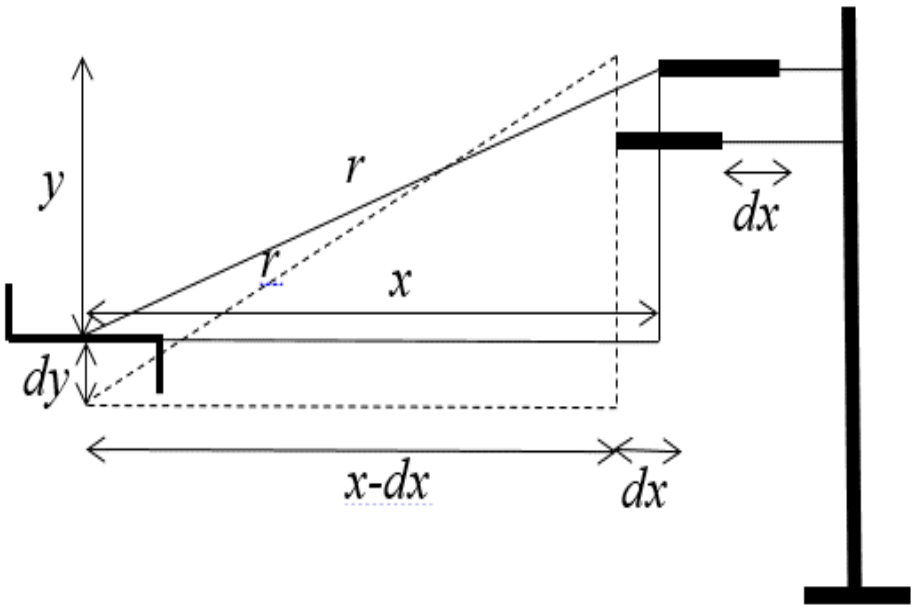

Figure (6-14) Related effect of vertical movement on horizontal movement.

y = the vertical distance between a measuring point and the *LVDT*.

x = the horizontal distance between a measuring point and the *LVDT*.

r = the inclination distance between a measuring point and the *LVDT*.

dy = the vertical movement during the test.

dx = the horizontal movement related to vertical movement during the test.

$$r^2 = x^2 + y^2$$

$$r^2 = (x - dx)^2 + (y + dy)^2$$

$$x^2 + y^2 = (x - dx)^2 + (y + dy)^2$$

$$\cancel{x^2} + \cancel{y^2} = \cancel{x^2} - 2xdx + dx^2 + \cancel{y^2} + 2ydy + dy^2$$

$$dx^2 - 2xdx + (2ydy + dy^2) = 0$$

$$dx = \frac{2x \pm \sqrt{4x^2 - 4(2ydy + dy^2)}}{2} \qquad (6-1)$$

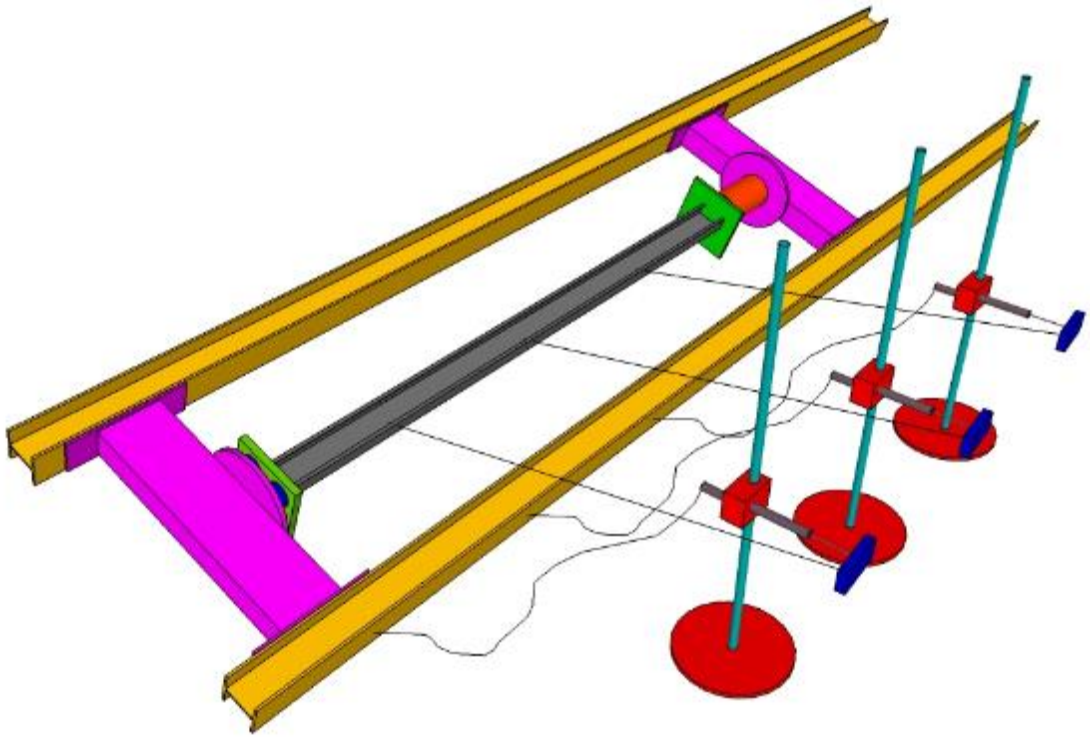

Figure (6-15) Horizontal displacement measuring system.

6.5.2.3 Torsional rotation measuring system

In addition to measuring the lateral displacement, it is also important to measure the rotation about the longitudinal axis to understand how the thin-walled cold-form member behaves under axial loads in torsional, distortional and lateral torsional modes.

The tilting device shown in figure (6-16) was used to measure small inclinations. The sensor was called (Seika), (www.seika.net, 16th August 2017) it is simply placed on the top of test specimens and fixed by means of adhesive glue. All its details are in appendix H.

All data measured by the inclinometer devices were collected using a computerised data logging system with a capability to collect data from 16 channels figure (6-13). For the testing only 10 channels were required, namely 3 channels for horizontal *LVDTs*, 3 channels for vertical *LVDTs*, 1 channel for the tilting device and 3 channels for the load cells.

The computer acquisition software used to collect the data from the data loggers was called DEWESoft, (Manual, 2002).

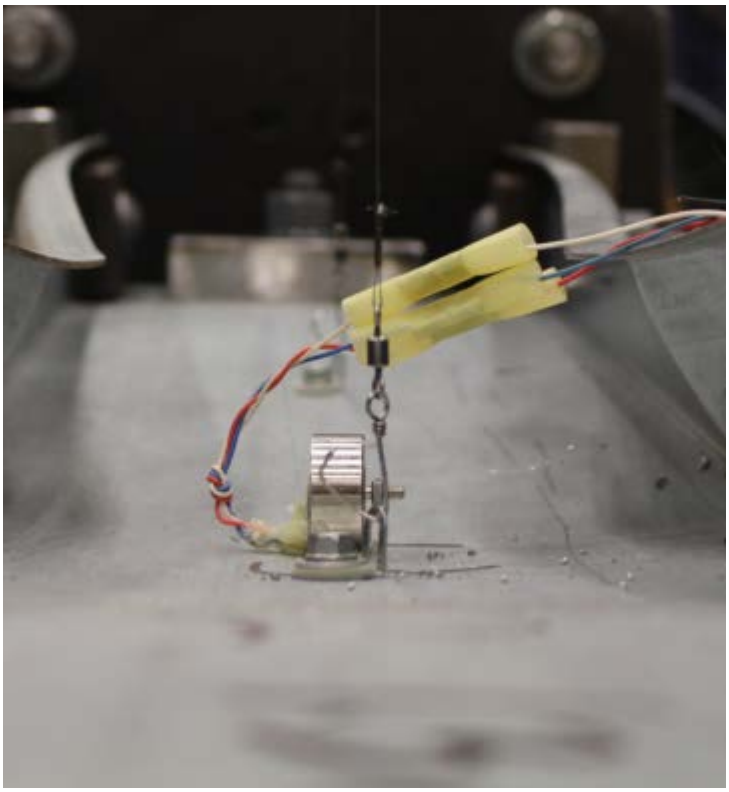

Figure (6-16) Tilting device.

6.6 Material tests for mechanical properties

6.6.1 Uniaxial tensile testing

Uniaxial tensile test is carried out to acquire material parameters such as ultimate strength, yield strength, % elongation, % area reduction and Young's modulus. These important parameters obtained from standard tensile testing are useful for the selection of engineering materials for any application required. These parameters will therefore inform and provide essential information for use in the FE and GBT analyses.

Tensile testing is carried out by applying the longitudinal or axial load at a specific extension rate to a standard tensile specimen with known dimensions (gauge length and cross-sectional area perpendicular to the load direction) until failure. The applied tensile load and extension are recorded during the test for the calculation of the stress and strain relationship for the material.

For cold-form steel, the standard specimen is cut out from a rectangular section plate along the gauge length as shown in figures (6-17), (6-18), in accordance with the requirements of standard. Both ends of the specimens should have sufficient length and a surface condition such that they are firmly gripped during testing in a standard tensile testing machine. The initial gauge length L_o is standardised (in several countries) and varies with the cross-sectional area (A_o) of the specimen as $\left({L_o}/{A_o} = 5.65\right)$. The reason for this is that if the gauge length is too long, the % elongation might be underestimated. Any heat treatments should be applied to the specimen prior to machining to produce the final specimen. This is usually done to prevent surface oxide scales that might act as stress concentration and subsequently affect the final tensile properties, possibly causing premature failure. There are some exceptions, for example, surface hardening or surface coating on the materials. These processes should be employed after specimen machining in order to obtain the tensile property results which include the actual specimen surface conditions.

The equipment used for tensile testing ranges from simple devices to complicated controlled systems. So-called universal tensile and compression testing machines are commonly used, which are driven by hydraulic systems. Figure (6-22a) shows a hydraulic testing machine using the pressure of oil in a piston for load supply. These types of machines can be used not only for tension but also for compression, bending and torsion tests. A more

modernised closed-loop servo-hydraulic machine provides variations of load, strain, or testing machine motion using a combination of the actuator rod and piston. Most of the machines used nowadays are linked to a computer-controlled system in which the load and extension data can be graphically displayed together with the calculations of stress and strain whilst the testing is taking place Figure (6-22b).

General techniques utilised for measuring loads and displacements employ sensors providing electrical signals. Load cells are used for measuring the load applied while strain gauges are used for strain measurement. A change in a linear dimension is proportional to the change in electrical voltage of the strain gauge attached to the specimen.

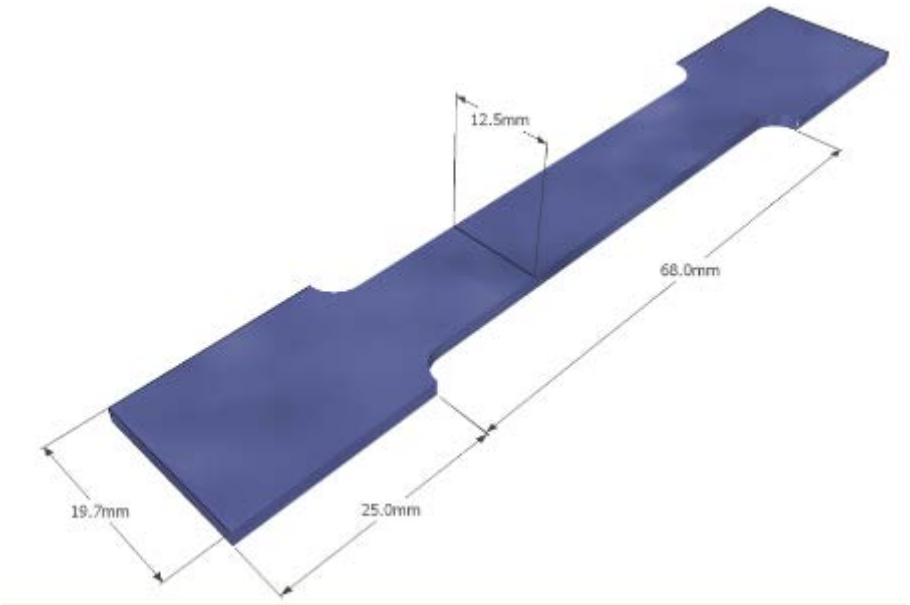

Figure (6-17) Tensile test sheet specimens.

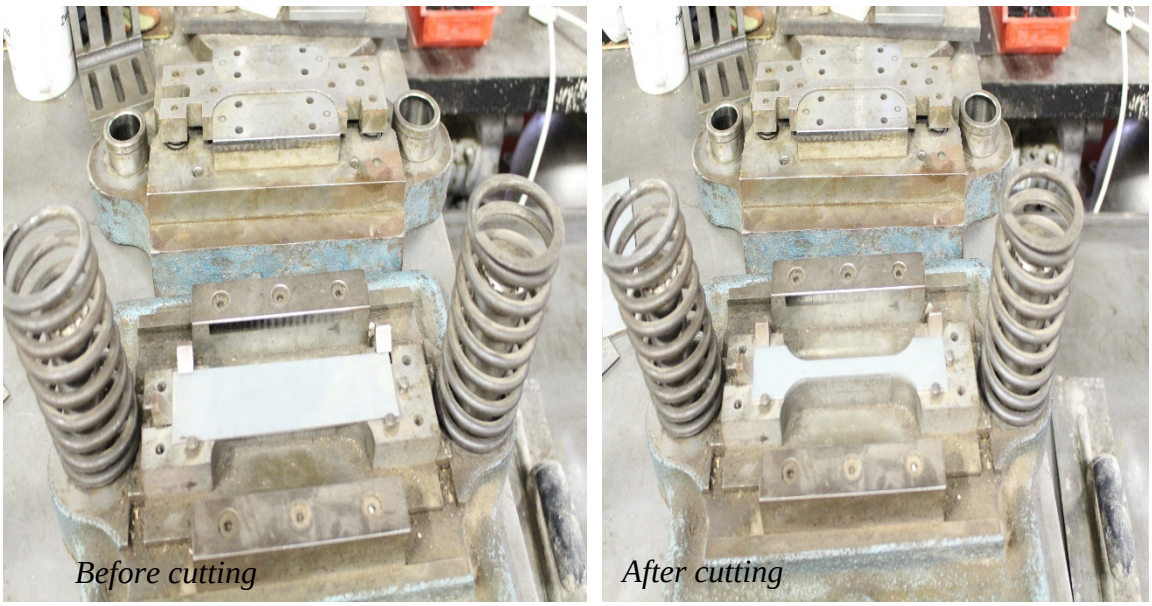

Figure (6-18) Preparing of tensile sheet specimens.

6.6.2 Stress and strain relationship

When a specimen is subjected to an external tensile loading, the metal will undergo elastic and plastic deformation. Initially, the metal will elastically deform giving a linear relationship between load and extension. These two parameters are then used for the calculation of the engineering stress and engineering strain to give the relationship illustrated in figure (6-19) using equations (6-2) and (6-3) as follows:

$$\sigma = \frac{P}{A_o} \qquad (6-2)$$

$$\varepsilon = \frac{L_f - L_o}{L_o} = \frac{\Delta L}{L_o} \qquad (6-3)$$

Where

σ is the engineering stress

ε is the engineering strain

P is the external axial tensile load

A_o is the original cross-sectional area of the specimen

L_o is the original length of the specimen

L_f is the final length of the specimen

6.6.3 Young's modulus, *E*

During elastic deformation, the engineering stress-strain relationship follows the rules of Hook's Law and the slope of the curve indicates Young's modulus (E)

$$E = \frac{\sigma}{\varepsilon} \qquad (6-4)$$

Young's modulus is of importance where the stiffness and deflection of materials is critical for the required engineering application. For example: deflection in structural beams is considered to be crucial for the design of engineering components or structures such as bridges, building, ships, etc. For products such as a tennis racket or a golf club also require specific values of spring constants or Young's modulus values.

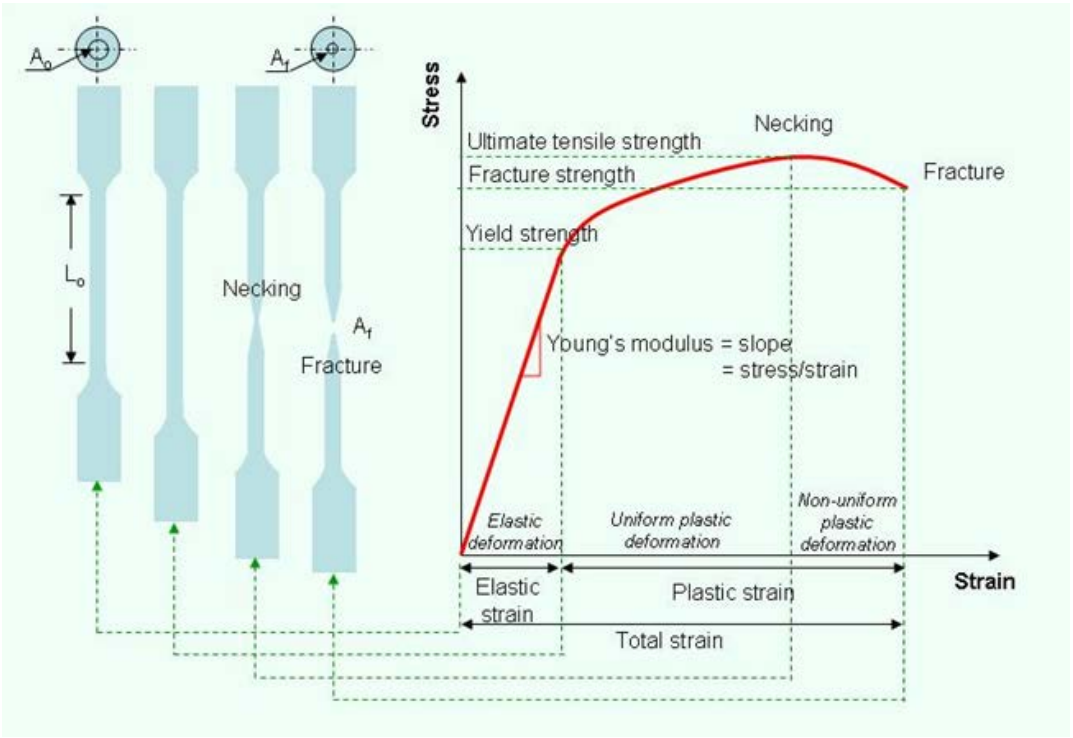

Figure (6-19) Stress-strain relationship under uniaxial tensile loading (Hakim et al., 2015).

6.6.4 Yield strength, σ_y

By considering the stress-strain curve beyond the elastic region, if the tensile loading continues, yielding occurs at the beginning of plastic deformation. The yield stress, σ_y, can be obtained by dividing the load at yielding (P_y) by the original cross-sectional area of the specimen (A_o) as shown in equation (6-4).

$$\sigma_y = \frac{P_y}{A_o} \qquad (6-5)$$

The yield point can be observed directly from the load-extension curve of metals such as iron and steel, and especially low carbon steels. At the yield point elongation, the specimen continues to extend without a significant change in the stress level. As the load is incremented higher this is accompanied by an increasing strain

Cold-formed steel does not show the definite yield point in comparison to those of low carbon steel but shows a smooth engineering stress-strain curve. The yield strength, therefore, has to be calculated from the load at *0.2%* strain divided by the original cross-sectional area.

$$\sigma_{0.2\%y} = \frac{P_{0.2\%}}{A_o} \qquad (6-6)$$

The determination of the yield strength of 0.2% offset or 0.2% strain can be carried out by drawing a straight line parallel to the slope of the stress-strain curve in the linear portion, having an intersection on the x-axis at a strain equal to 0.002. An intersection between the 0.2% offset line and the stress-strain curve represents the yield strength at 0.2% offset or 0.2% strain. However, offset at different values can also be made depending on specific uses.

6.6.5 Tensile ductility

Tensile ductility of the specimen can be represented as % elongation as expressed in the equation (6-7).

$$\%\, Elongation = \frac{\Delta L}{L_o} \times 100 \qquad (6-7)$$

The fracture strain of the specimen can be obtained by drawing a straight line starting at the fracture point of the stress-strain curve parallel to the slope in the linear portion. The interception of the parallel line at the x-axis indicates the fracture strain of the specimen being tested.

6.6.6 Experimental procedure

In this study, three cold-form sections were used, (C-200-60-14-1.770) and (Z-200-(64-54)-(18-15)-2.0) for buckling tests and (C-170-60-14-1.431) for the examination of fixed end boundary condition (this will be explained later in this chapter). Five tensile coupons were tested for each section, so a total of 15 coupons were tested as in figure (6-22c). The coupons were measured and the dimensions recorded in a test sheet. In order to obtain the actual uncoated steel thickness, the Micrometre Screw Gauge and MikroTest, were used, see figure (6-21).

For the strain measurement, an extensometer was used. The extensometer is a device that is used to measure changes in the length of an object. It is useful for stress-strain measurements and tensile tests, see figure (6-20a).

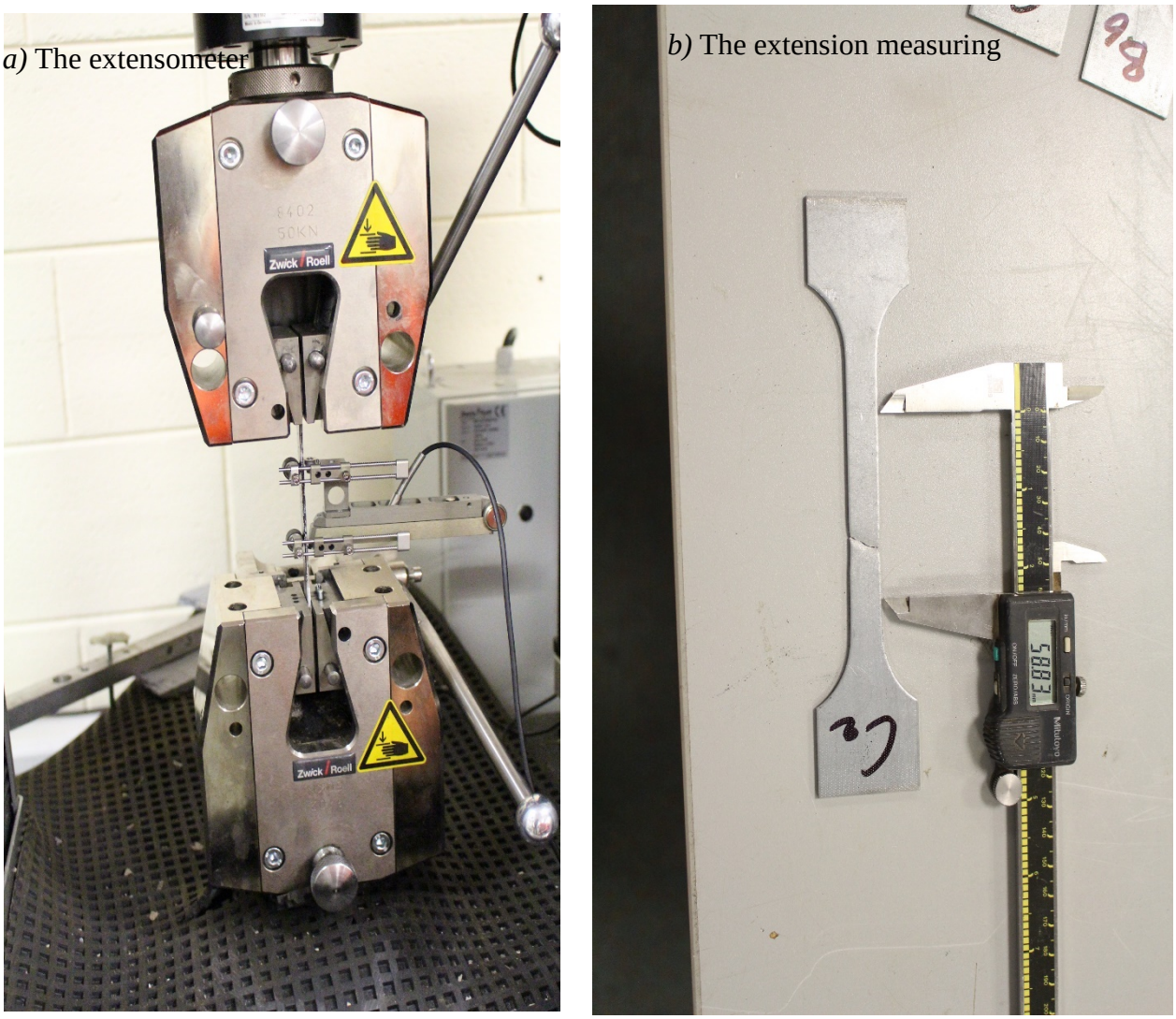

Figure (6-20) The extensometer.

Before mounting the tensile specimen in the universal testing machine, marking the location of the gauge length along the parallel length of each specimen for subsequent observation of necking and strain measurement was done, figures (6-20b). The load and extension for the stress-strain curve was recorded for each tested specimen. From this the Young's modulus was calculated, together with the yield strength, ultimate tensile strength, fracture strain, and % elongation of each specimen. This data is presented in table (6-3). Figures (6-23), (6-24) and (6-25) illustrate the stress-strain relationship of the cold-formed test sections.

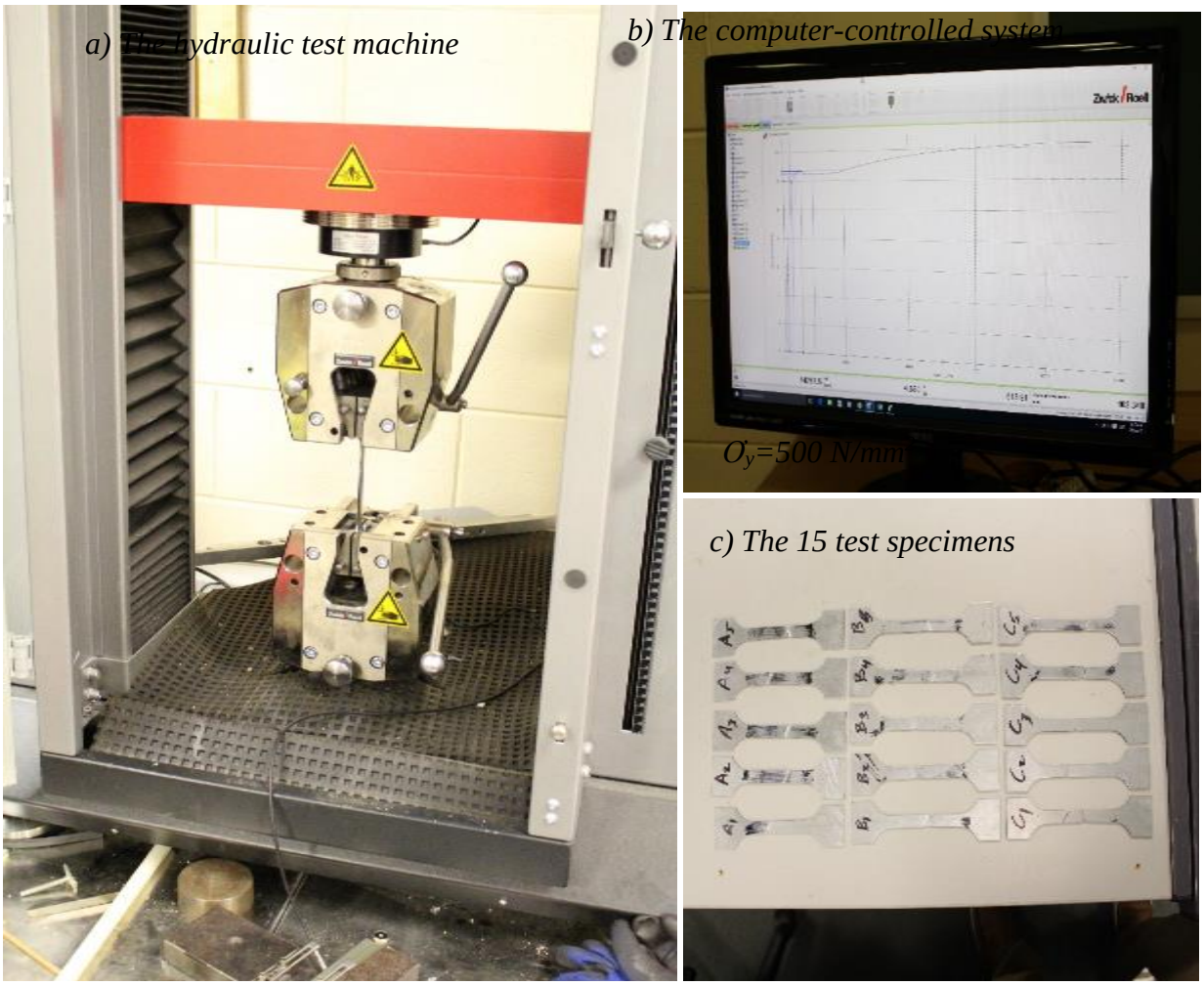

Figure (6-22) The tensile test.

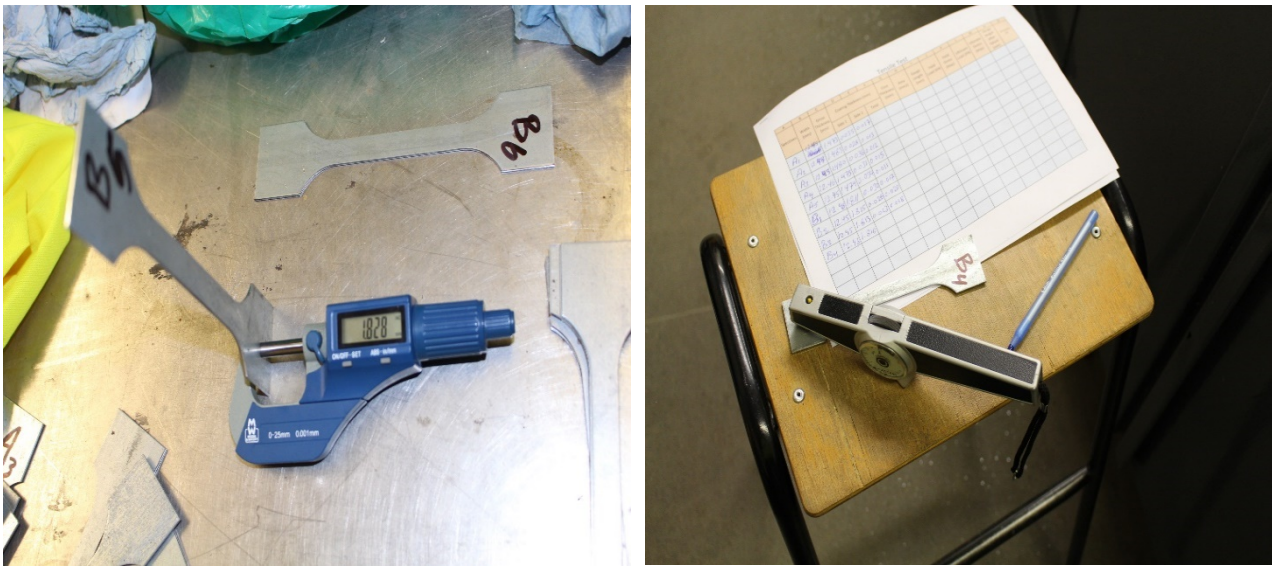

Figure (6-21) Measuring of the tensile sheet coupon.

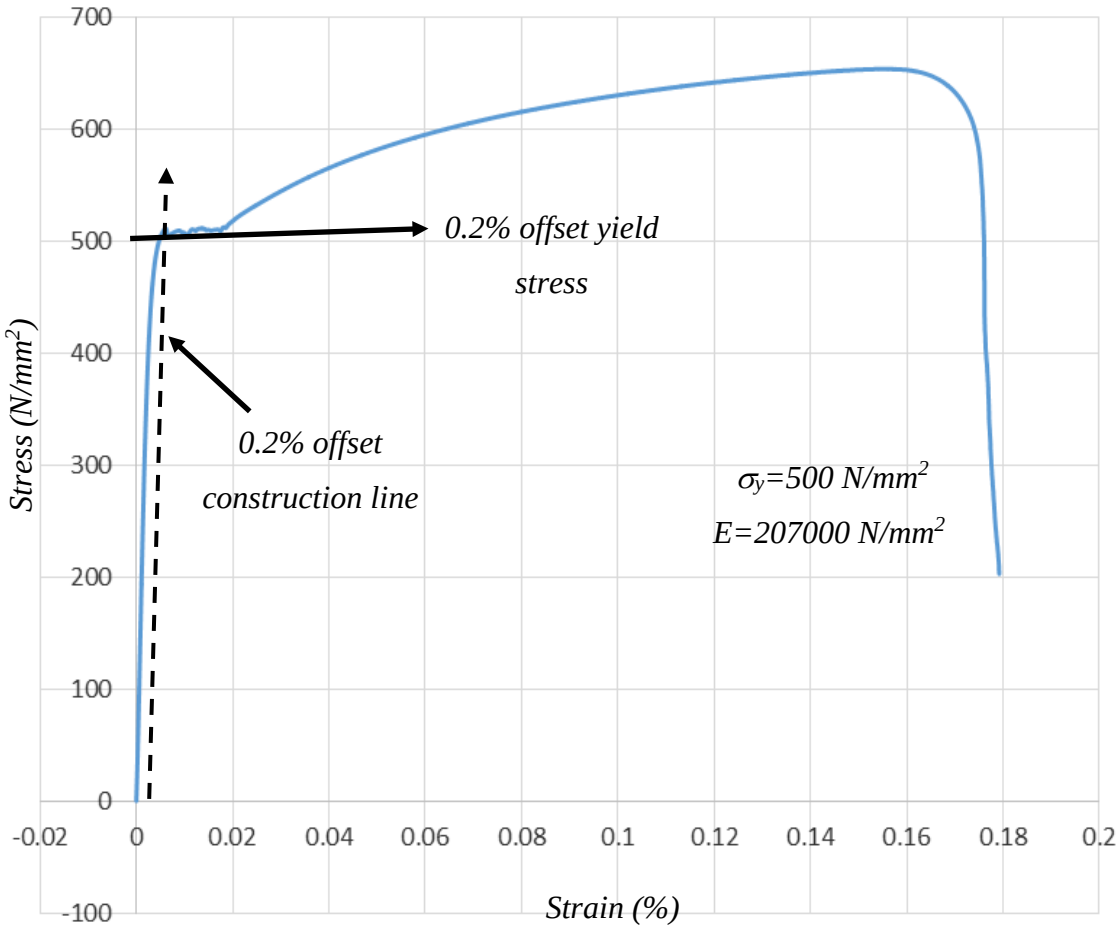

Figure (6-23) Comparative stress-strain relationships of section (Z-200-(64-54) -(18-15)-2.0).

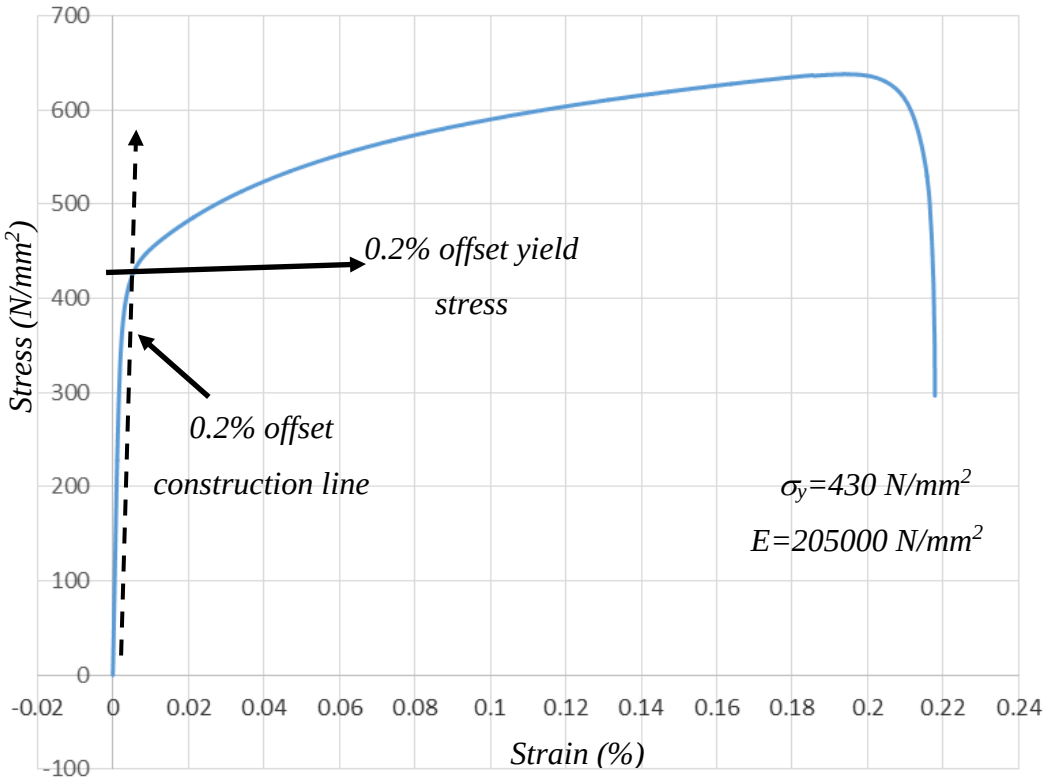

Figure (6-24) Comparative stress-strain relationships of section (C-200-60-14-1.770).

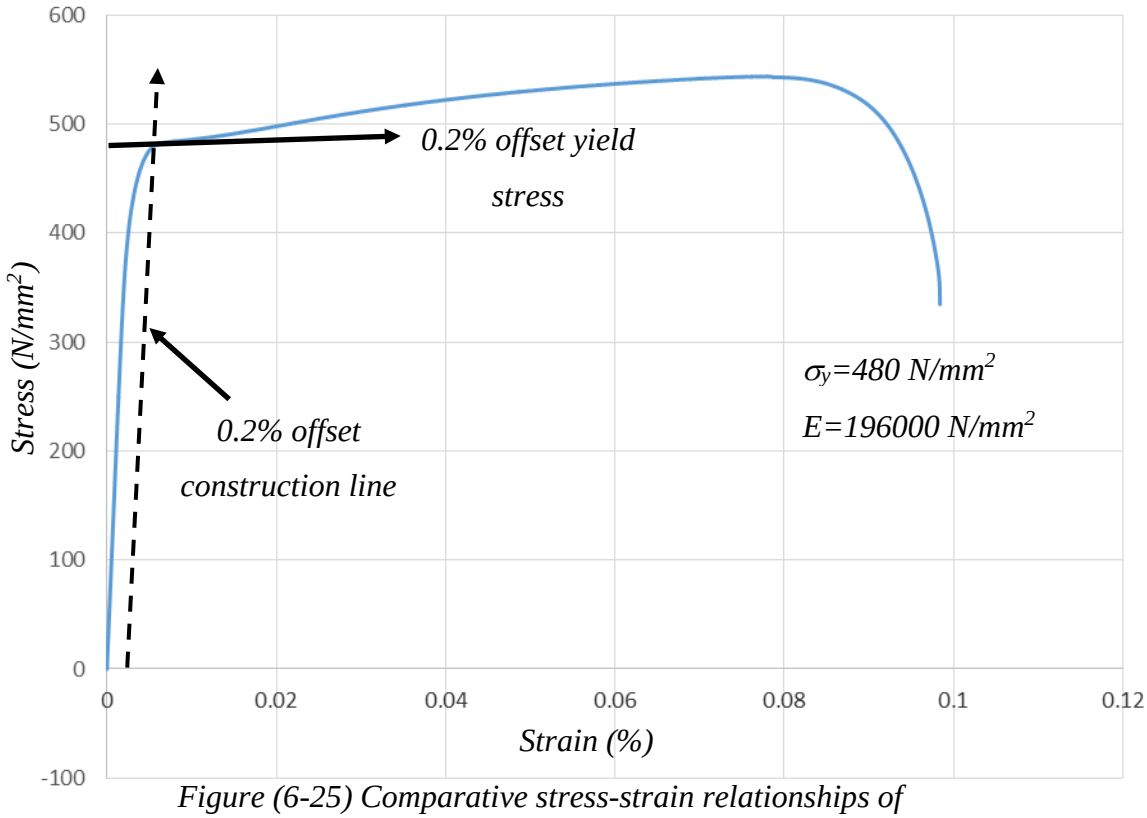

Figure (6-25) Comparative stress-strain relationships of section (C-170-60-14-1.431).

Table (6-3) Tensile test Sheets for provided cold-formed steel sections.

A	B	C	D	E	F	G	H	I	J	K	L	M	N	O
Specimen	*Width (mm)*	*Gross Thickness (mm)*	*Coating Thickness (mm)*			*Core Thickness (mm)*	*Area (mm^2)*	*Gauge Length (mm)*	*Yield Load (kN)*	*Yield Stress (MPa)*	*Ultimate Load (kN)*	*Ultimate Stress (MPa)*	*Gauge length after failure (mm)*	*Elongation (%)*
			Side 1	*Side 2*	*Total*									
C-170-60-14-1.431(1)	12.45	1.473	0.035	0.017	0.052	1.421	17.691	50	8532	482.267	9623	543.935	55.43	0.1086
C-170-60-14-1.431(2)	12.45	1.483	0.028	0.013	0.041	1.442	17.953	50	8469	471.734	9573	533.229	56.34	0.1268
C-170-60-14-1.431(3)	12.45	1.480	0.036	0.012	0.048	1.432	17.828	50	8513	477.497	9784	548.787	55.42	0.1084
C-170-60-14-1.431(4)	12.45	1.475	0.031	0.011	0.042	1.433	17.841	50	8438	472.960	9659	541.398	56.18	0.1236
C-170-60-14-1.431(5)	12.45	1.474	0.034	0.017	0.045	1.429	17.791	50	8386	471.361	9482	532.965	56.51	0.1302
C-200-60-14-1.770 (1)	12.45	1.811	0.030	0.020	0.047	1.764	21.962	50	9257	421.505	14382	654.864	58.64	0.1728
C-200-60-14-1.770 (2)	12.45	1.817	0.026	0.018	0.046	1.771	22.049	50	9354	424.238	14464	655.995	58.23	0.1646
C-200-60-14-1.770 (3)	12.45	1.818	0.023	0.020	0.041	1.777	22.124	50	9420	425.789	14763	667.295	57.83	0.1566
C-200-60-14-1.770 (4)	12.45	1.810	0.028	0.021	0.048	1.762	21.937	50	9295	423.715	14683	669.329	57.26	0.1452
C-200-60-14-1.770 (5)	12.45	1.820	0.023	0.024	0.044	1.776	22.111	50	9327	421.822	14365	649.671	58.45	0.169
Z-200-(64-54)-(18-15)-2.0 (1)	12.45	2.051	0.029	0.027	0.053	1.998	24.875	50	12583	505.847	16458	661.625	57.93	0.1586
Z-200-(64-54)-(18-15)-2.0 (2)	12.45	2.052	0.024	0.024	0.051	2.001	24.912	50	12638	507.297	16249	652.244	58.43	0.1686
Z-200-(64-54)-(18-15)-2.0 (3)	12.45	2.050	0.026	0.024	0.050	2.000	24.900	50	12693	509.759	16396	658.474	57.34	0.1468
Z-200-(64-54)-(18-15)-2.0 (4)	12.45	2.052	0.028	0.026	0.052	2.000	24.900	50	12539	503.574	16173	649.518	58.17	0.1634
Z-200-(64-54)-(18-15)-2.0 (5)	12.45	2.052	0.023	0.025	0.049	2.003	24.937	50	12684	508.635	16298	653.558	58.43	0.1686

6.7 Support system

A compression member with its length considerably larger than its cross-sectional dimension may be defined as a strut. Strut have varying conditions of end restraint, ranging from fixed end conditions to pinned end conditions. Under both types of end conditions, no linear translation of the end of the column occurs relative to the point of load application. The difference between the two extremes of pinned and fixed end conditions is concerned with the provision of restraint against angular rotation. For the fixed-end strut, there is complete restraint against angular rotation at the end of the column. As a result, the slope of the transvers displacement profile of the member at the fixed end is zero. On the other hand, under pinned end conditions, no restraint exists and the column end is free to rotate.

In reality, supports for structures (boundary conditions) have some degree of stiffness associated with them. Pinned and fixed ends are a theoretical construct to represent zero and infinite stiffness respectively. So for this study, in an attempt to produce pinned and fixed support systems the rotational stiffness provided at the supports was maximised and minimised in the two extremes to ensure as close as possible representation was achieved (to within an acceptable uncertainty). In this way, the effects of the boundary conditions with regards instability could be experimentally investigated.

6.7.1 Pinned end support design

A pinned support can resist both vertical, horizontal and axial forces but not a moment. It allows the structural member to rotate, but not to translate in any direction. Practically, many connections are assumed to be pinned connections even though they might resist a small amount of moment. It is also true that a pinned connection could allow rotation in only one directional axis, providing resistance to rotation in any other orthogonal axis direction. The knee can be idealised as a connection which allows rotation in only one direction and provides resistance to lateral movement. The design of a pinned connection is a good example of the idealisation of a real system. The presence of a pinned connection in a structure may mean that the structure needs additional support to ensure stability. To maintain stability in the axially loaded test, rotation about the axial direction at one support at least must be resisted to prevent rigid body motion (i.e. spinning). The representation of a pinned support includes both horizontal and vertical translational.

The pinned-end support test is an important step in the study of column behaviour. Through a knowledge of its behaviour, a basic concept of the strength of columns as affected by such factors as end conditions, residual stresses, initial out-of-straightness, eccentricities of load, and transverse loads may be formulated.

Although the pinned end support is an idealised column not existing in actual structures, an extensive study of its behaviour is relevant to the problem of column design. The pinned end column must be regarded as the basic column since all column specifications throughout the world are defined in terms of such boundary conditions. Until methods for the design of structures as a whole come into use, the design of columns will continue to be based on the strength of the simple pinned-end column.

The analysis of its behaviour represents the most fundamental column instability problem. Each of the factors influencing column strength may be studied separately in the light of their effect on the column strength and structural behaviour.

To attain the ideal pinned condition at the ends, a specially detailed fixture is necessary to provide, first, free rotation of the ends of the column, and second, no relative linear translation between the column ends and the applied load.

The experimental tests on the columns should be able to provide an amount of data which can be used for comparison and validation with the numerical analyses. An evaluation of the results can be made by comparing the experimental value of the maximum load with the theoretical prediction from analysis such as finite element analysis or *GBT* analysis. The occurrence of local buckling or any other phenomena during the test was noted also.

For this study, a pinned end support was designed in the laboratory to simulate the real end support in practice. A 50 mm diameter hardened steel ball, as shown in figure (6-26) with two 25 mm thick parallel bearing plates was used at both the loading and measuring ends to provide the necessary degrees of freedom. To provide the global pinned joint effect, the ball allows rotation in any direction but at the same time the friction between the top of the ball and the bearing plate (due to high axial load) is enough to prevent any displacements in the X, Y & Z directions. For local plate element rotation at the ends of the member the friction between the test specimen and the bearing plate provided resistance to displacement in the X, Y & Z directions and allows free rotation for each plate element of the test specimen individually. The

hardened ball bearing at both ends is coincident (concentric) to the centroid of the test specimen.

Before commencing the test, both ends required temporary supports because there is no axial load to provide a pre-stressed support, so there is not enough frictional force to support the specimen. During the test, when the axial load is applied, the temporary supports were removed to allow the boundary supports to act as pinned ends. Also, at least one of the supports was required to be moment resisting in the longtudinal direction to prevent rigid body spinning as explain before, figures (6-26) & (6-27).

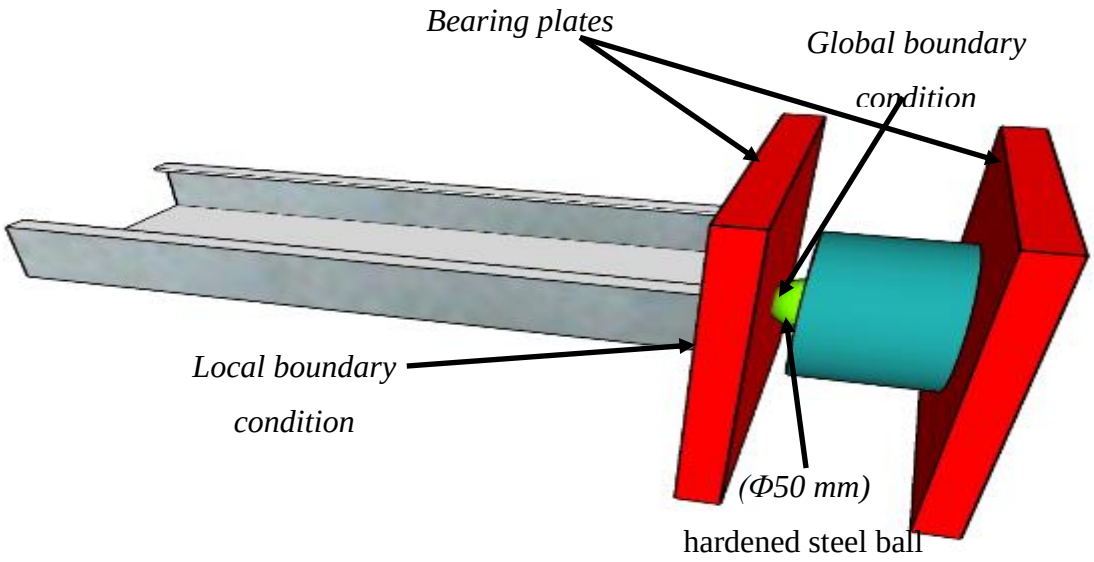

Figure (6-26) Schematic of the pinned end support condition.

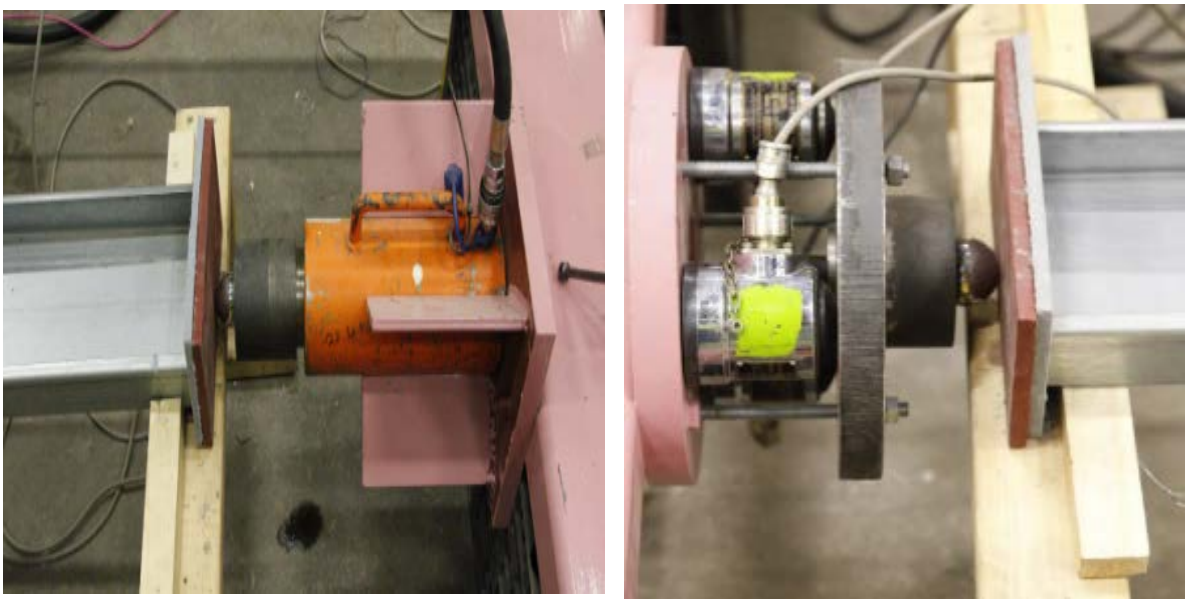

a) Loading end *b) Measuring end*

Figure (6-27) Pinned ends conditions.

6.7.2 Fixed end support

Fixed supports can resist vertical, horizontal and axial forces as well as a moment. Since they restrain both rotation and translation, they are also known as rigid supports. This means that a structure only needs one fixed support in order to be stable. All three equations of equilibrium can be satisfied. The representation of fixed supports always includes three translation forces (horizontal, vertical and axial) and three orthogonal moments.

As discussed for the pinned end support, the fixed-end support is an idealised column which cannot be fully achieved in real structures. In the laboratory, the physical test methods attempt to create a support which is close to a zero-rotation support. All of the observations resulting from the tests which employ these physical boundary conditions were compared with theoretical or numerical analysis methods for verification purposes.

In this study, three experimental methods were examined to choose a nearly zero-rotation for use in the buckling tests, namely concrete blocks, welded plates and bolted/clamped ends were tested with three one-metre length specimens of (C-170-60-14-1.431) cold-formed steel section. A universal hydraulic compression/tension machine was used to test the specimens. The testing machine was provided with an inbuilt computer-controlled system enable plotting the load and displacement data live as it was acquired, figure (6-28).

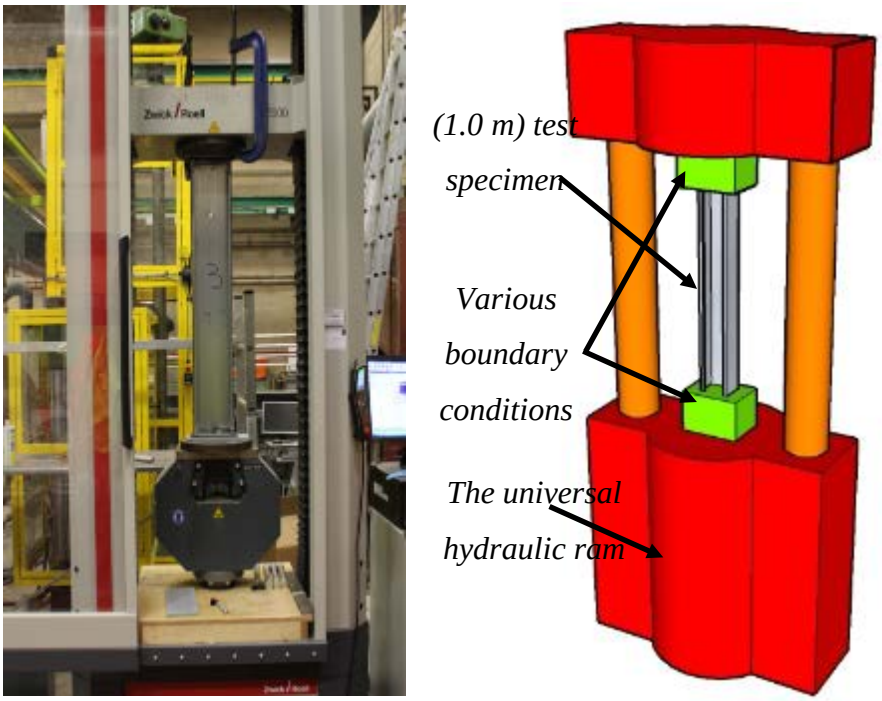

Figure (6-28) Universal hydraulic machine.

All of these methods were compared with nonlinear finite element analysis *(ANSYS)* to select the fixty method, which best-matched one in both nonlinear buckling load and mode shape.

6.7.2.1 Concrete block fixed end support

In this method, concrete blocks were cast at both ends of specimens with 100mm embedment length. The concrete was mixed with (1:1.5:3) ratio of cement, sand and gravel respectively using a mixer, and then the 400 mm diameter blocks were cast at both ends and kept 28 days in wet curing conditions. Next, all the block surfaces were smoothed using epoxy glue to ensure an even bearing surface for the applied load.

a) Concrete block in curing

b) Concrete block after smoothing

c) Concrete block in test machine

Figure (6-29) Concrete block fixed end support

To aid the load distribution a special adhesive glue layer was poured on the top and bottom blocks as shown in figure (6-29c).

The compression testing was carried out on three specimens with an applied load rate of 2 mm/min until a buckling failure occurred. The load-axial displacement relationship was plotted, figure (6-29c).

Figure (6-30) Concrete block fixed end testing.

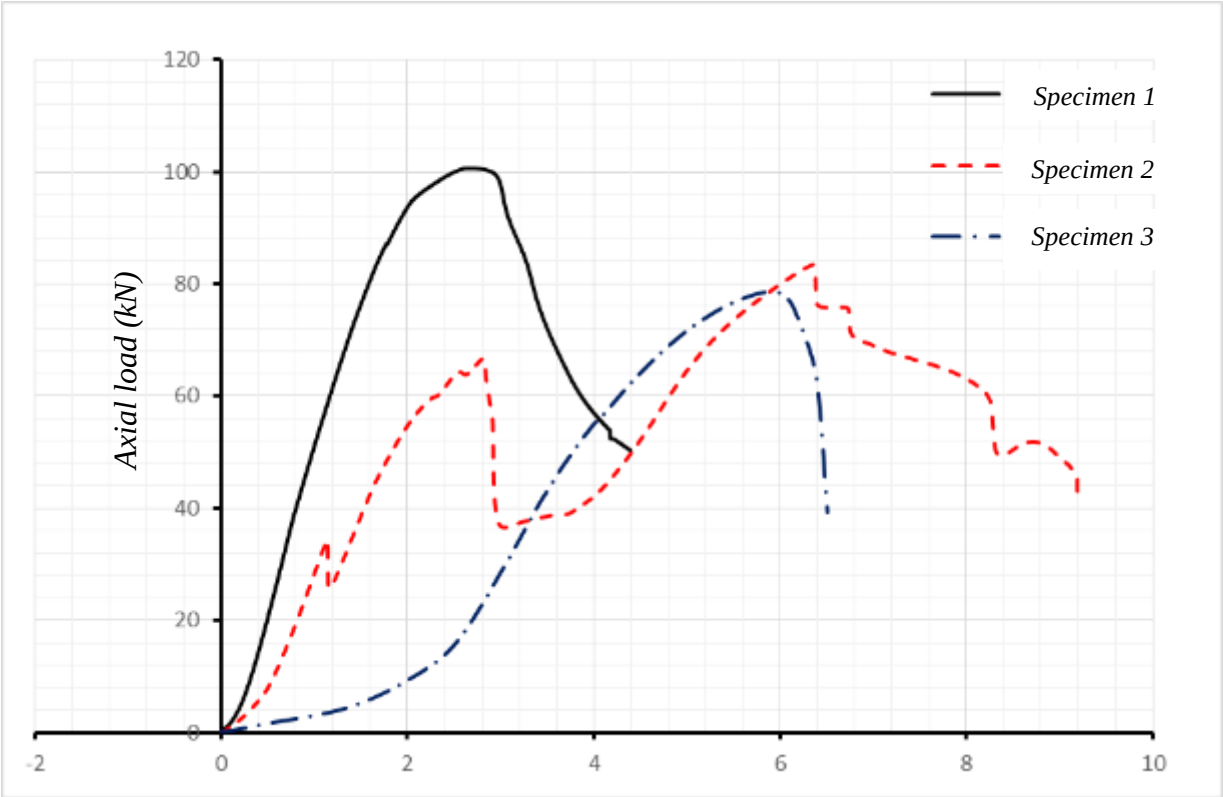

Figure (6-31) Load- axial displacement relationship of specimens with fixed ends represented by concrete blocks.

For the fixed end support represented by concrete blocks, Figures (6-30) & (6-31), it can be observed that:

- It required considerable time to prepare the samples up to the point where they were ready to test (mould preparation, material mixing, concrete pouring and curing time).
- The concrete is not a homogenised material so it is difficult to distribute a uniformly applied load onto its surface.
- The bond between the concrete and steel section plate elements is not enough to prevent end slippage and rotation.
- The concrete can fail before the steel section, and in this case the supports become more representative of pinned-pinned end supports and this results a lower failure load.

6.7.2.2 Welded fixed end support

In this method 300 x 200 x 8 mm bearing plate was welded to the end of specimen as shown in figure (6-32). The intention of the weld was to provide sufficient stiffness to minimise end displacement and rotation. The amount of fixity provided depends on the weld thickness. Before welding, the galvanised coating was removed to ensure that the two sides of steel plate and the specimen will accept the weld.

To ensure that the load was applied uniformly on the end plate, a slice of Medium-density fibreboard (MDF) was used to distribute the load as shown in figure (6-32).

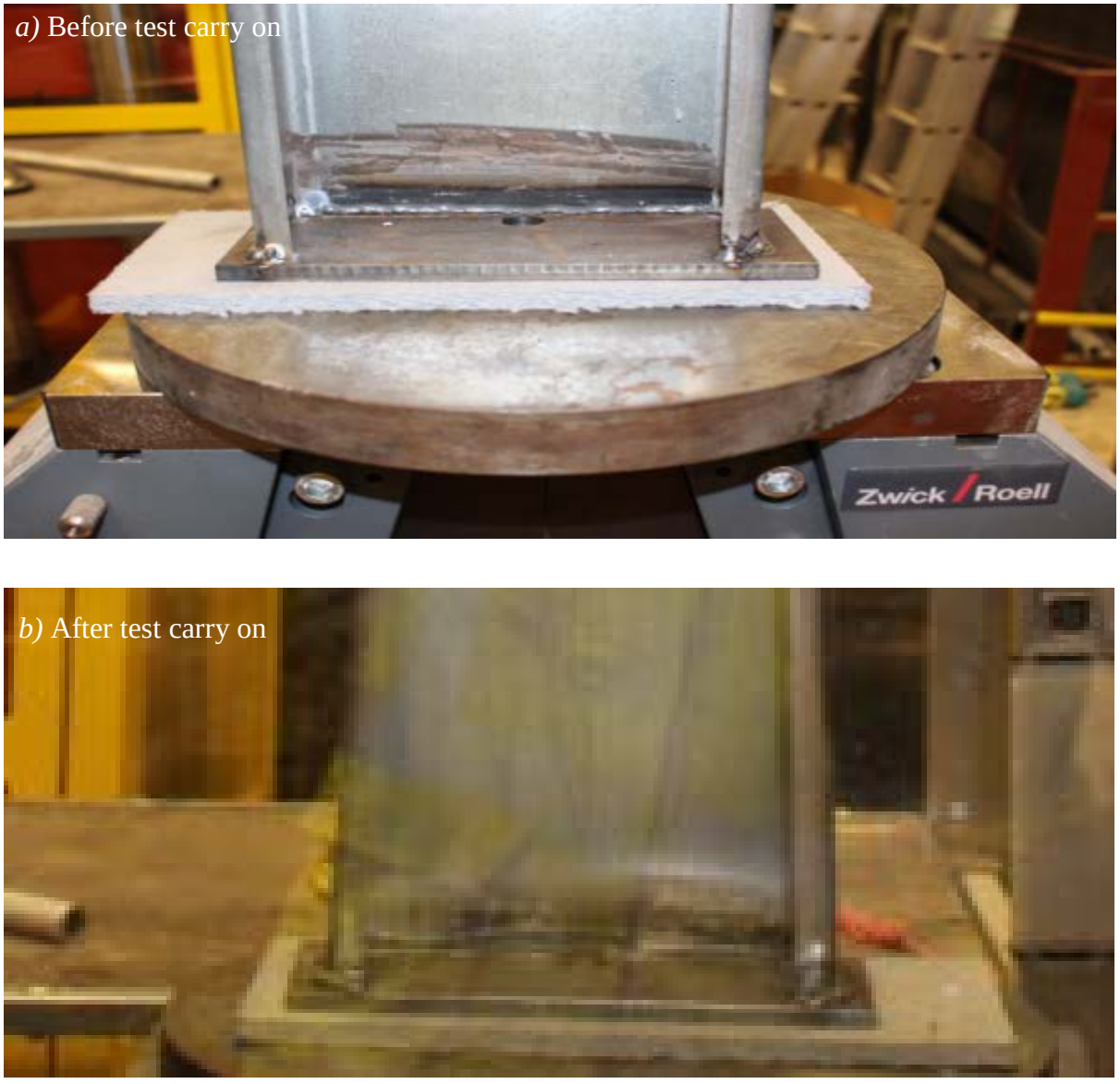

Figure (6-32) Welded fixed end testing.

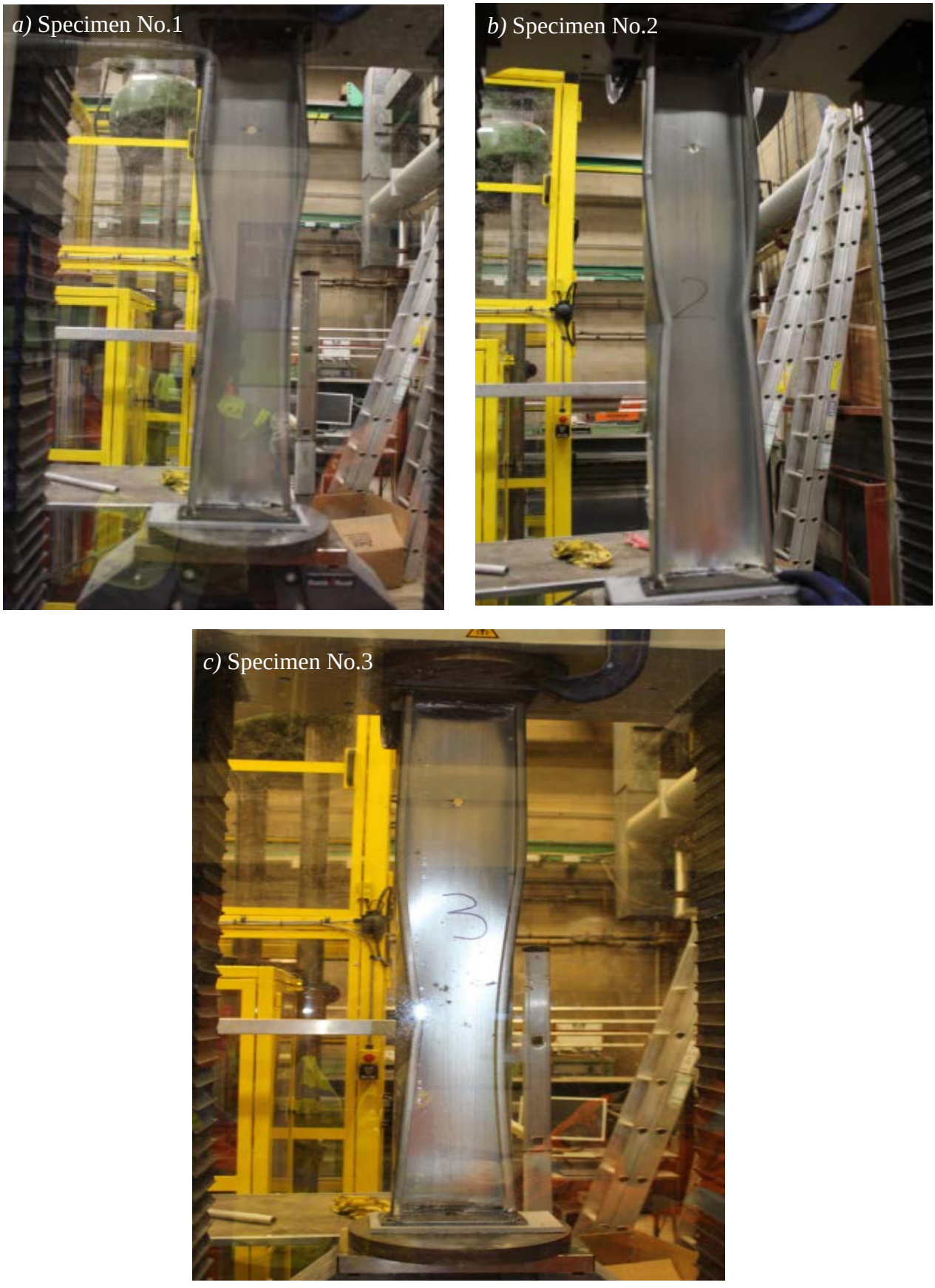

Figure (6-33) Welded fixed end testing.

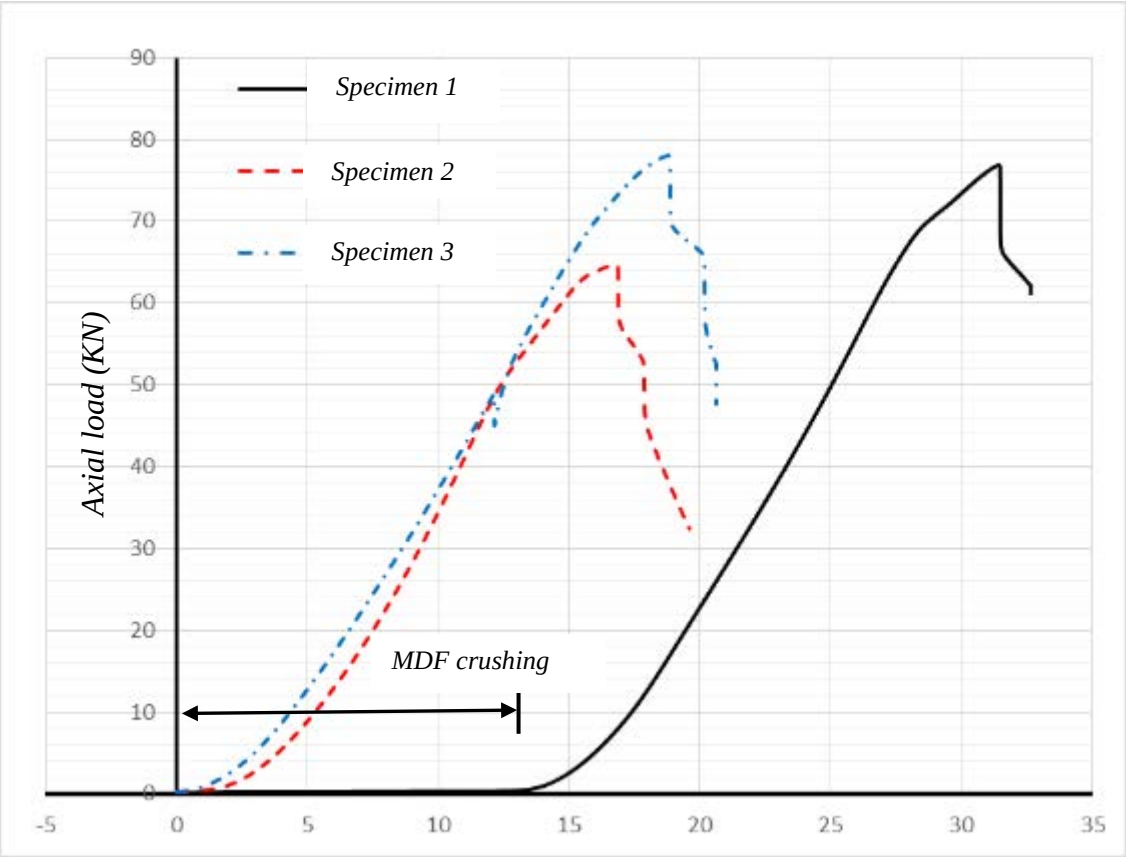

Figure (6-34) Load-axial displacement relationship of welded fixed end support.

From figures (6-33) & (6-34), it can be seen that:

- The weld does not perform as expected as too much rotation occurred at the end support, figure (6-32b).
- Specimen No.1 started in load from 14 mm displacement, which means the MDF was displaced before the specimen was loaded. The interaction between the load-displacement curve of MDF and the steel section specimen means that the displacement would have to be measured from the sample ends rather than the load machine platens.

6.7.2.3 Clamped fixed end support

For this method, the fixed end support was represented with the section plate elements gripped between vice jaws. The jaws are stiff enough to prevent displacement and rotation in the test specimen. The jaws apply the axial load uniformly on the end of the section plate elements through friction between the section element walls and jaws. This friction is sufficient to transfer the axial load from the jaws to the specimen walls, figure (6-35) & (6-36).

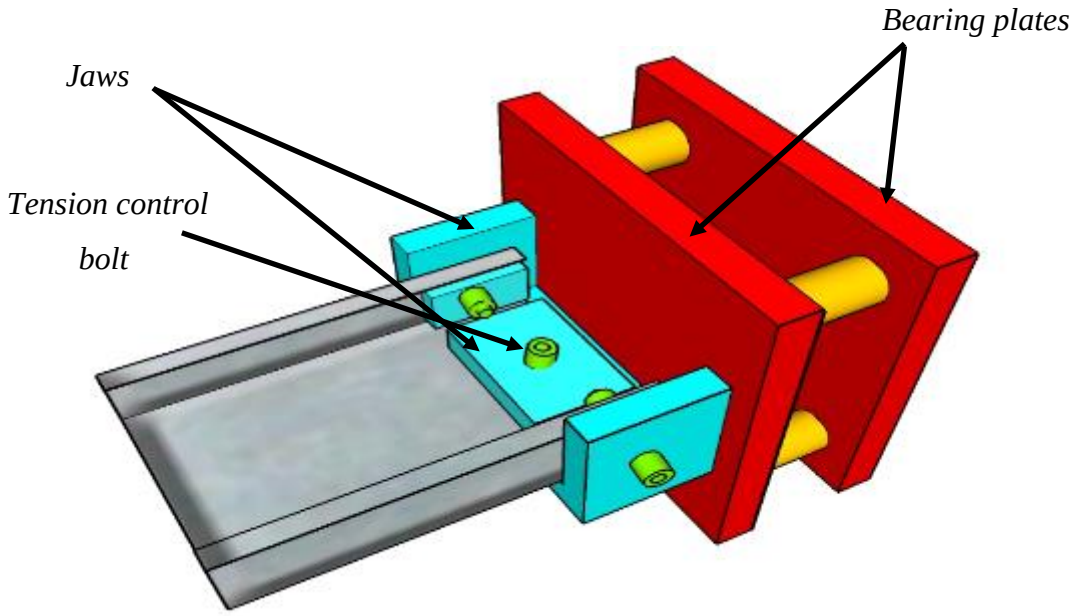

Figure (6-35) Schematic of clamped fixed end condition.

Figure (6-36) Clamped fixed end testing.

To develop an adequate friction between the specimen end and the jaws, tension control bolts (TCBs) were used. The tension control bolts Cosgrove (2004) (TCBs) are a type of high-grade bolt that can be preloaded by torque application that is carried out entirely at the threaded end (i.e. at the nut or spline end) of the bolt. TCBs are usually distinguished by their round head rather than hexagonal head or splines, figure (6-37).

TCB fasteners are high-strength, high-ductility (14%) friction grip bolts for use in structural steelwork connections. Their primary advantage over another type of friction grip bolts is ease of preloading. Preloading is carried out by an electric shear wrench at the threaded end of the bolt (spline end), figure (6-38). When the bolt reaches the required torque, the end spline shears (as the thread and spline counter-rotate). All TCB details are in Appendix F.

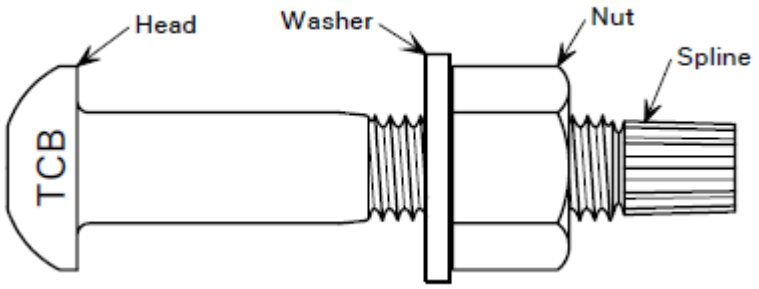

Figure (6-37) Tension control bolts (Cosgrove, 2004).

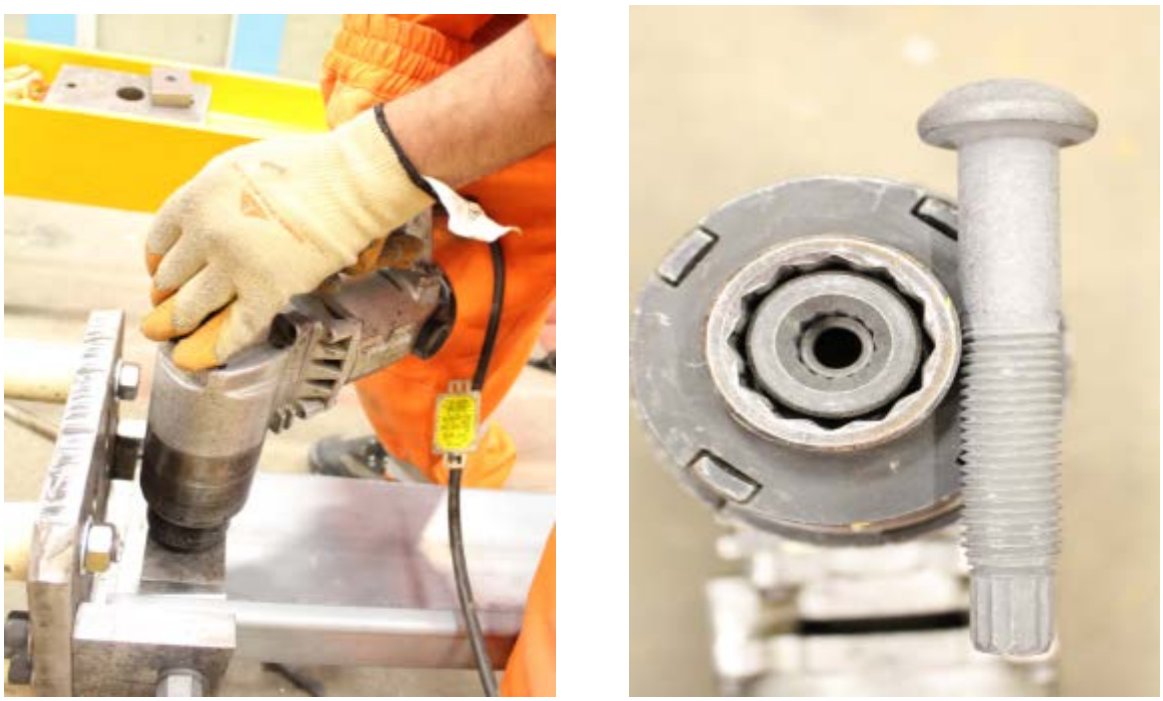

Figure (6-38) Electric shear wrench.

Figure (6-39) Clamped fixed end testing.

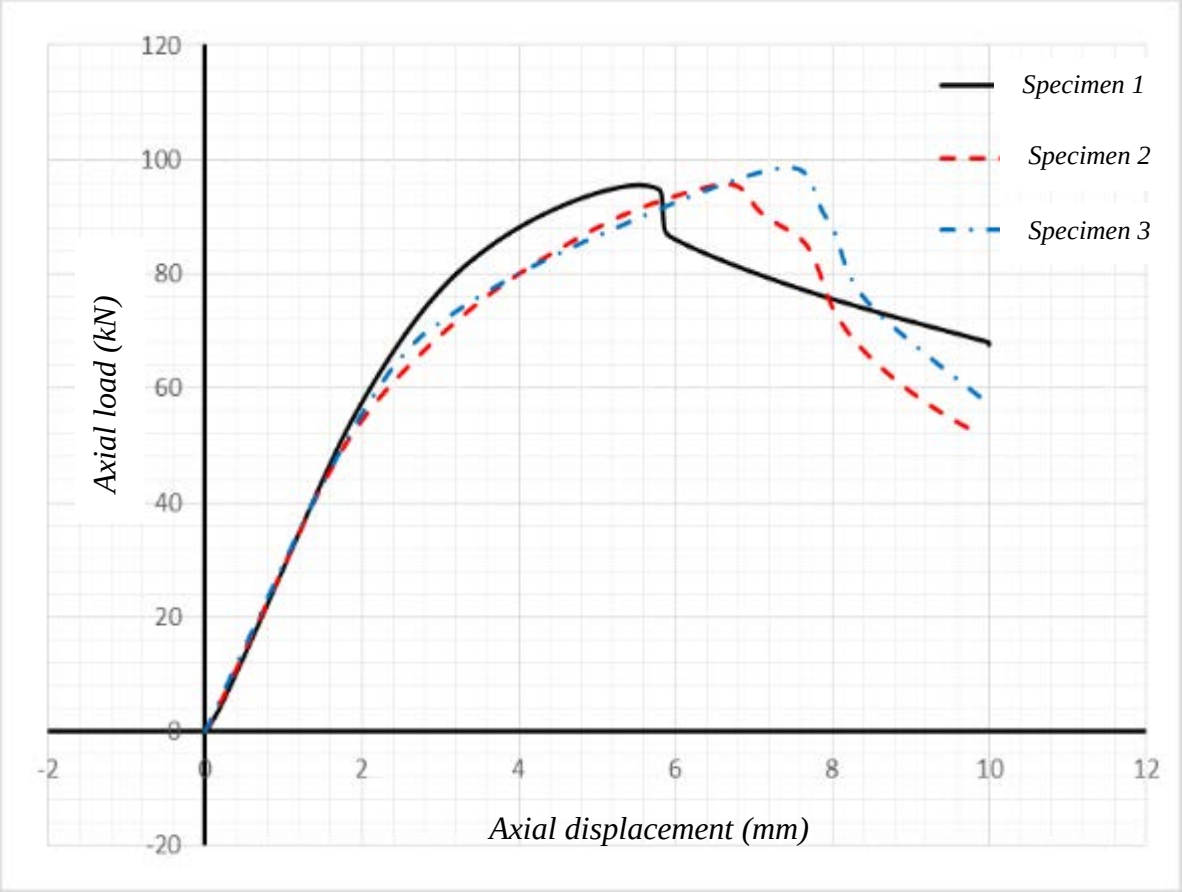

Figure (6-40) Load- axial displacement relationship of clamped fixed end support.

From Figures (6-39) & (6-40), it can be seen that:

- The three specimens appear to buckle in the same mode (local-distortional mode).
- The three specimens appear to buckle symmetrically.
- The rotations at both supports look to be extremely small. This indicates that the jaws are working as expected to prevent any rotation at the support.
- There is no slip between the jaws and specimen wall elements, so the applied load is transferred from the jaws to specimen wall elements uniformly and in the correct manner.

6.7.2.4 Finite element modelling of the fixed end support

Finite element analysis was used to confirm and validate the behaviour of the support. Nine one-metre length specimens of *(C-170-60-14-1.431)* cold-formed steel section column tests were conducted for a typical lipped channel beam with three different fixed end support methods (concrete blocked, welded and clamped) as previously discussed. All the test beams failed by local-distortional buckling mode. The ultimate axial load capacities and axial load versus axial displacement relationships were obtained from these tests. For comparison finite element modelling *(ANSYS)* was verified against the experimental tests.

6.7.2.4.1 Element type

Referring to Chapter 5, the geometry of the cross-section was modelled using the centre line dimensions of the lipped channel beam. A wide range of elements are available in the *ANSYS* element library, which can be used to solve different types of structural problems. Shell elements have been successfully used in studies related to buckling of thin-walled steel beams. In this instance, four noded shell elements were used in the analysis.

6.7.2.4.2 Finite element mesh

The accuracy of finite element analysis results also depends on the mesh size. Use of as many elements as possible increases accuracy. However, to obtain an accurate solution in a reasonable computer runtime, shell elements of 10mm square with an aspect ratio of 1:1 was used to mesh the section wall elements, figure (6-41).

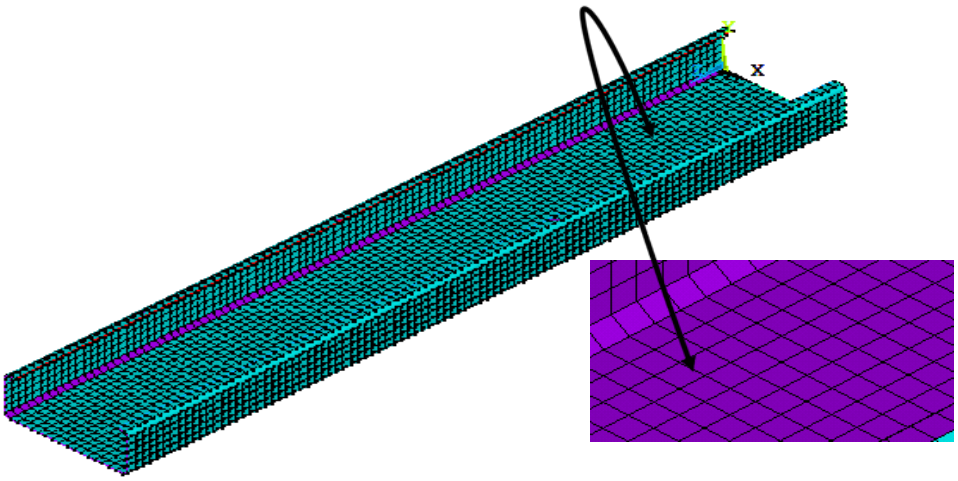

Figure (6-41) Finite element mesh of (10 mm) square shape shell element with aspect ratio constant at 1:1.

6.7.2.4.3 Fixed end support and applied load modelling

Referring to Chapter 5, the ideal model for a fixed end support was developed with restraint at all nodes in both translational displacements and rotation directions over a distance of 50 mm at the ends of the beam. At the end where the axial load was applied the longitudinal displacement restraint was not present.

The axial load was applied as uniform nodal loads of 500 N creating a total load of 115.5 kN, figure (6-42). From figure (6-25), the yield stress is 480 Mpa.

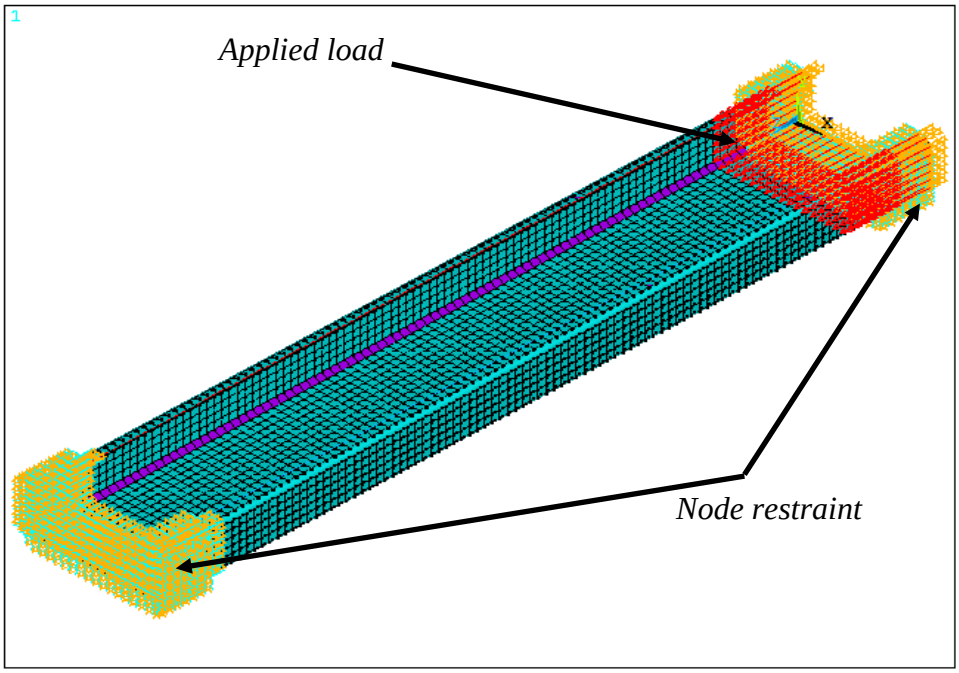

Figure (6-42) Fixed end support and applied load modelling.

6.7.2.4.4 Geometrical initial imperfection

To create the ideal finite element model for lateral-torsional buckling, the fabrication tolerance of L/1000, as recommended by AS4100 (SA, 1998) for flexural members, was used as the overall member imperfection about both section axes.

In this study, the specimen was a short column and the predicted eigenvalue buckling mode shape is the local mode, so the initial imperfection was introduced in the non-linear analysis by solving the model under self-weight only (in the transverse direction. The elastic deformation profile was then used to update the nodal coordinates as a geometric initial imperfection for non-linear analysis. With the shape of the imperfection defined in this way, the magnitude of imperfection to be used was then decided. The largest magnitude of the

imperfection was assigned to the node that has the maximum deformation obtained from the elastic analysis.

6.7.2.4.5 Nonlinear analysis solution and results

Two types of analysis were employed by using the developed finite element model in (ANSYS), elastic linear and nonlinear static analyses. The elastic linear analysis gives the elastic linear curve. The elastic linear curve obtained from the elastic linear analysis was used to input the geometric imperfections in the nonlinear analysis. Non-linear analysis gave the ultimate failure load and simulated the behaviour of lipped channel beams until failure.

In the non-linear analysis, the maximum number of load increments used was 200 with an initial increment size of 0.05 and the automatic increment control was enabled.

The solution terminated at 0.91 times the applied load of 115.5 kN, hence the nonlinear failure load was 0.91 x 115.5 = 105.105 kN.

From figure (6-45), it can be seen that there is significant post buckling capacity (past the theoretical critical load of around 35kN) up to 105kN, as indicated by a decrease in the gradient of the graph.

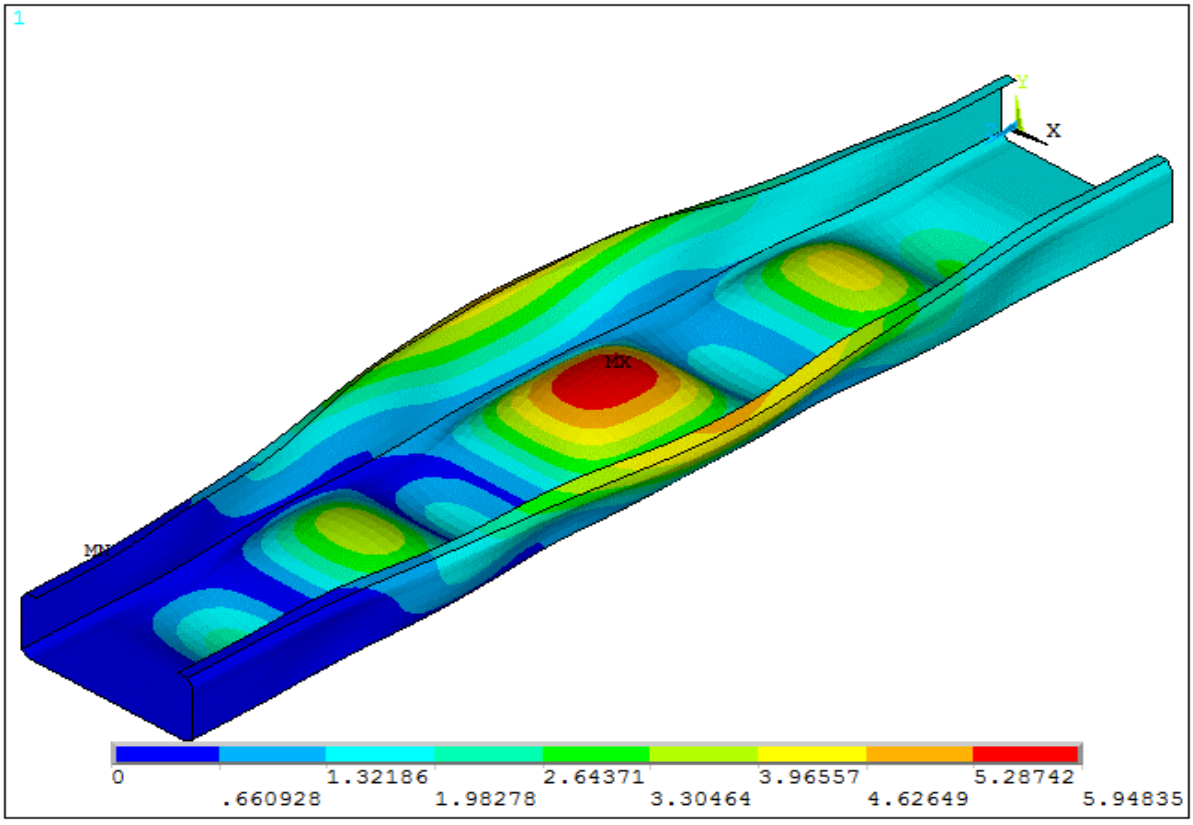

Figure (6-43) Finite element failure mode shape.

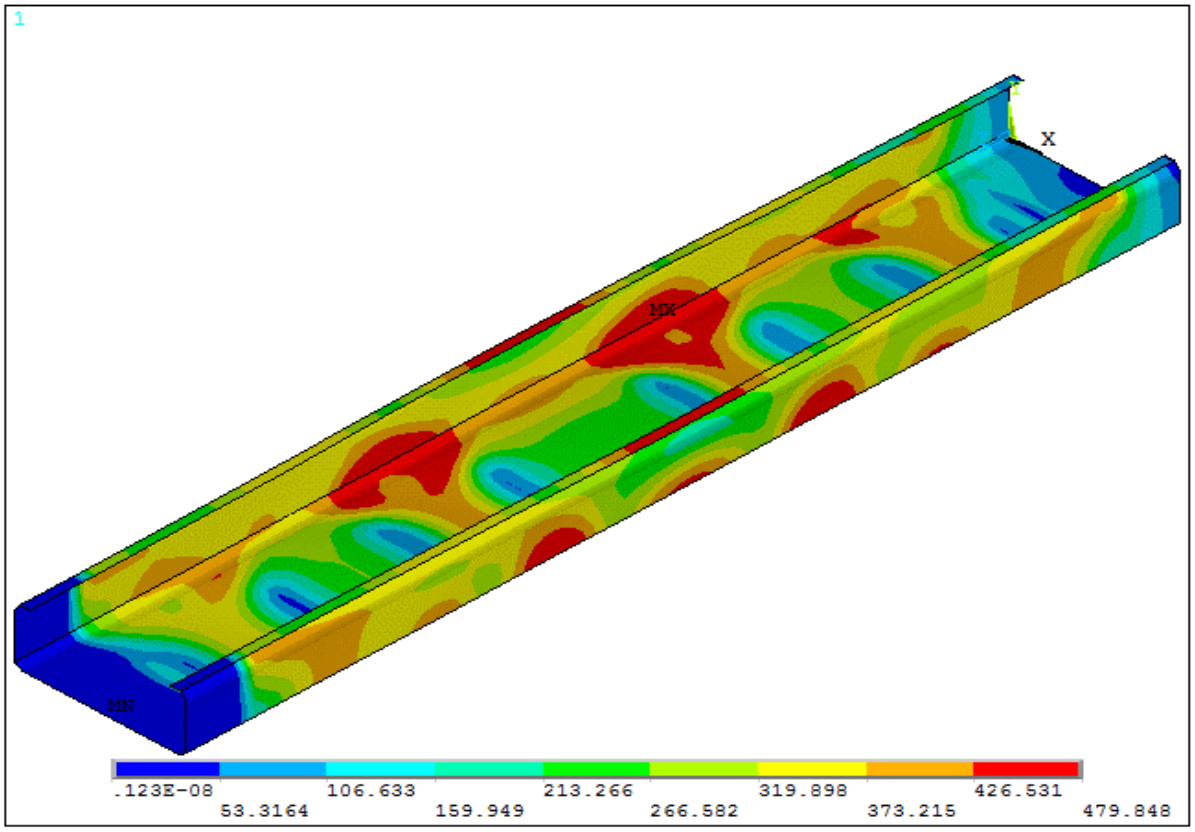

Figure (6-44) Nonlinear failure stress distribution.

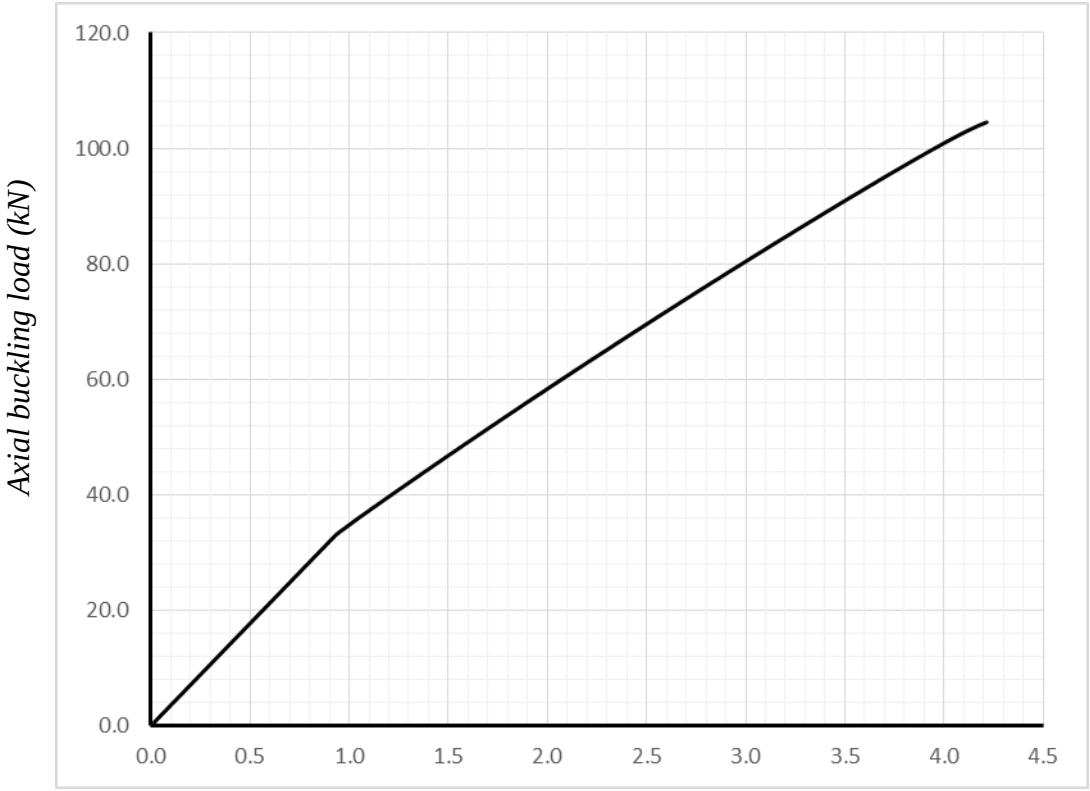

Figure (6-45) Buckling load-axial displacement relationship of nonlinear finite element analysis (ANSYS).

6.7.2.5 Results and discussion

Section 6.7.2 described the experimental tests and finite element model developed for the investigation of appropriate fixed end support conditions for cold-formed steel lipped channel columns subject to local buckling and yielding. A separate finite element model was developed to compare with the three methods investigated in the experimental tests for simulation of a fixed support this was in order to verify and select the best method for a fixed end support to use in the main specimen tests of this study. All the methods were based on one-metre span beams, the finite element model included the following features: shell element, isotropic stress hardening material model, geometric imperfections and non-linear analysis.

The results obtained from the different methods used were compared with the finite element model to propose the best approach to simulate an appropriate and reasonable method of fixed end support, it can be seen that:

- For the concrete block support, Figures (6-30), (6-31), (6-44) & (6-46):
  - Show that there are many irregularities in the load-displacement relationship which means that bond to the concrete may have failed during the test - so the end will work as pinned end condition or one with partial stiffness.
  - The failure mode shape did not appear symmetrical or consistent between the three specimens. Also the same mode predicted by the finite element analysis was not obtained, meaning that at least one of supports does not work to restraint both displacement and rotation.
  - The difference in behaviour between the specimens themselves which have the same conditions when casting, indicates that the concrete is too brittle to prevent both displacement and rotation in the support.
  - Show that the failare load is much smaller when compared with the finite element yield load, so this method does not work properly as a fixed end support.
- Welded end support, Figures (6-33), (6-34), (6-43) & (6-45):
  - Show that there is a clear rotation between the section wall elements and the bearing plate, so the weld cannot stop the rotation at the support.
  - There is a large difference in axial displacement between the specimens due to MDF displacement.

- The load-displacement curve does not compare well with the finite element analysis load-displacement curve in both behaviour and prediction of the failure load, Again the support is acting with partial (and variable) rotational stiffness.

➢ Clamped end support, Figures (6-39), (6-40), (6-43) & (6-45):

- The clamped end support appears rigid and is able to carry loads and stop displacements and rotations at the support.
- Shows a good match in both failure load and failure mode shape with the nonlinear finite element analysis.
- The load-displacement curve is smooth and consistent between all the tested specimens.
- The failure mode shape in all specimens appears symmetrical and matches with the nonlinear finite element analysis.

From the above notes, it can be concluded that the clamped end support is the best method to represent the fixed end support in experimental tests. This method will provide rapid installation and removal of samples as well as providing acceptable support conditions.

To employ this method of fixity, modification was required to ensure it to worked with both lipped channel sections and Zed-sections as showen in figure (6-46).

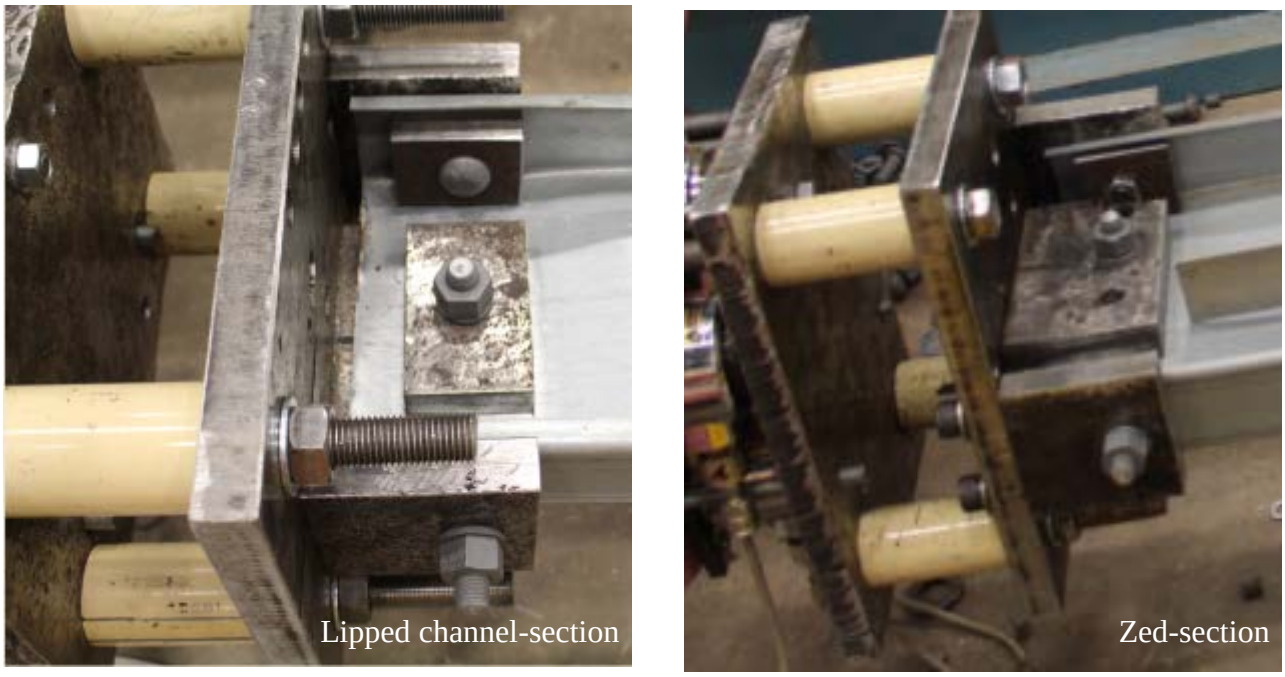

Figure (6-46) Modification of clamped end to work with lipped channel and zed-section.

6.7.2.6 Modification of load system in fixed end support tests

For the pinned end support tests, a two hinge support system was used to support the hydraulic jack end, figure (6-47a). The support was free to rotate in any direction, so small eccentricities in both section directions which are borne from the extension of the hydraulic jack during the test loading, do not affect the support behaviour and actual buckling load results.

For the fixed end support tests, the load system which was used previously for the pinned end support needed modification to apply the axial load on the centroid of the section without any eccentricities in both of the section directions. Hence three locations of rotational articulation (pins) support system was used to support the hydraulic jack end, figure (6-47b). This system keeps the hydraulic jack extension in a straight line during the test loading.

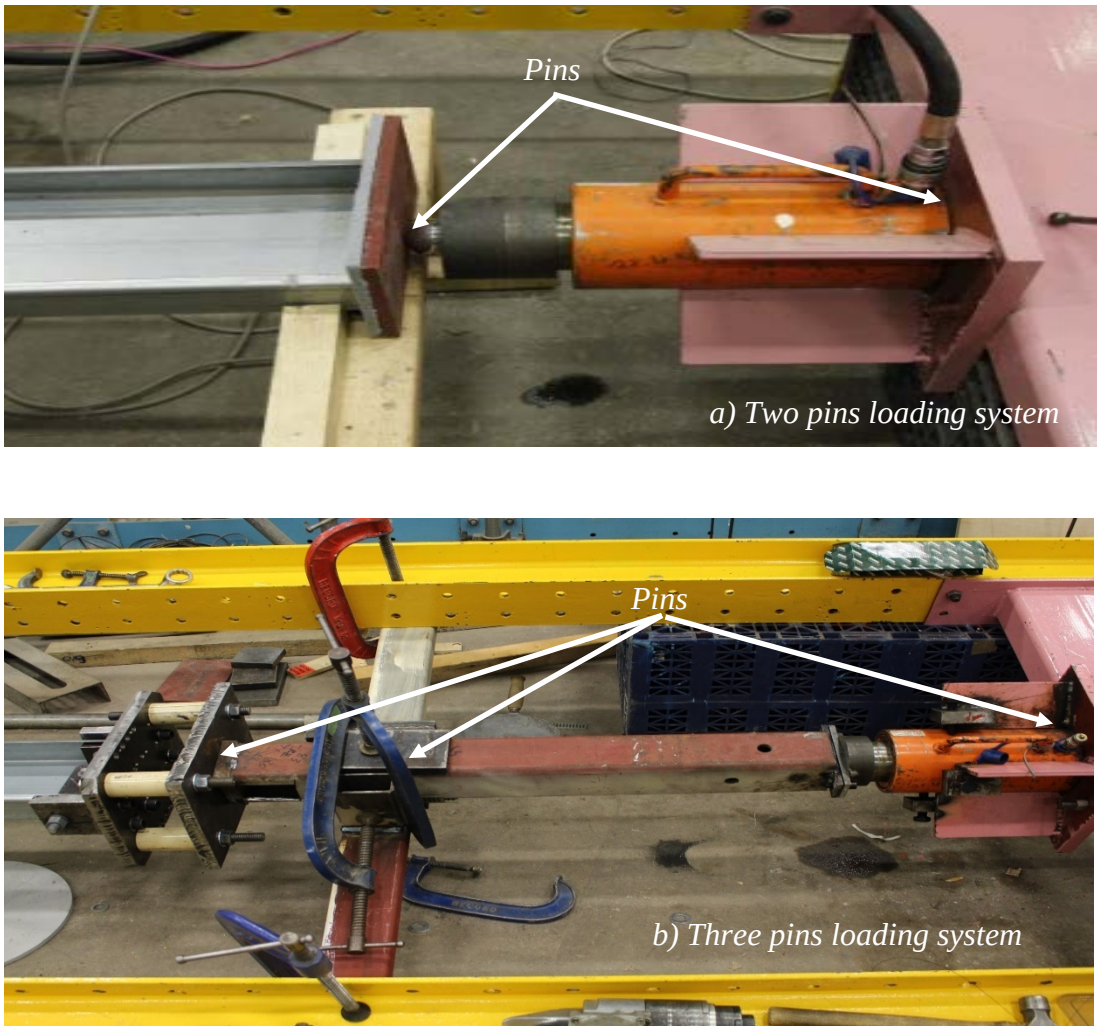

Figure (6-47) Two and three pins loading systems.

6.8 Test procedure

The cross-section dimensions and thickness of each specimen were measured using a Vernier calliper and a Micrometre Screw Gauge, respectively. In the case of a pinned end support, the lengths of specimens are presented in tables (6-1) & (6-2). Deflection and rotation measuring points were marked at the mid-span and quarters points of the specimen. Small screw bolts of 5.0 mm diameter were drilled into the specimen at the required points to attach the tension wires for the displacement transducers (WDTs). The specimen was attached directly to the bearing plate. MDF was placed between the specimen and bearing plate to increase the friction during loading. All loads, displacements and rotations were logged throughout the testing regime.

For the fixed end supports, the test beam length was 50 mm longer than the intended beam span to allow for the connections at each support. Three 10 mm diameter holes were punched (one hole for each section plate element) to accommodate the support assembly, figure (6-48).

Figure (6-48) Punching of section plate elements.

The acquired results were used for verification of the FE and GBT analyses to confirm the application of these numerical methods to predict the actual buckling load and behaviour of cold-formed steel commercial sections under axial load.

CHAPTER SEVEN

RESULTS AND DISCUSSION

CHAPTER SEVEN

RESULTS AND DISCUSSION

Linear buckling analysis methods are usually used to predict buckling loads and associated mode shapes or display the buckling mode shape associated with particular column length ranges. Also the linear results can be used in empirical formula to calculate the actual failure loads and mode shapes. In this chapter, both linear analysis implemented in the finite element analysis method (ANSYS) and GBT were illustrated, together with discussions of advantages and disadvantages of each of the analysis methods.

The results of experiments are presented with regards buckling loads, mode shapes and load-displacement histories with the laboratory representations of boundary conditions for both pinned and fixed end conditions. These results are compared with both FEA and GBT using nonlinear analysis with the effects of initial imperfections and post-buckling effects to verify the best numerical analysis method. The features of each analysis method are also discussed.

7.1 linear buckling behaviour of Cold-Formed Z and C sections

7.1.1 Generalized beam theory *(GBT)*

The cross-sections were divided into natural nodes and intermediate nodes, plate intersection nodes were defined as the natural nodes and the mid-plate nodes were defined as the intermediate nodes, figure (7-1). The generalized beam theory section properties were calculated using the purpose written Matlab Program in Appendix A, as showen in tables (7-1) & (7-2). The program GBTUL was used to obtain the generalized beam theory mode shapes, figures (7-2) & (7-3).

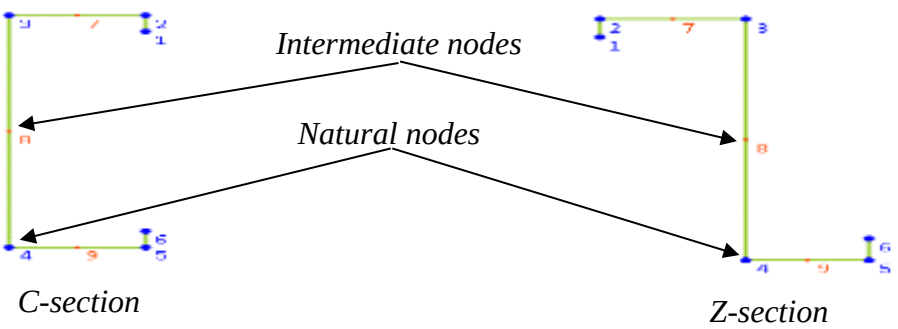

Figure (7-1) Cross-section GBT nodes distribution

Table (7-1) GBT section properties for c-section

Mode	C_k	D_k	B_k
1	615.96	0	0
2	3733514	0	0
3	291616	0	0
4	2.3E+09	643.3	0
5	18.53	9E-04	4E-06
6	19.38	8E-04	1E-05
7	43.35	0.064	0.0017
8	62.02	0.726	0.0592
9	40.63	0.675	0.0662

Table (7-2) GBT section properties for z-section

Mode	C_k	D_k	B_k
1	702	0	0
2	4518050	0	0
3	232693	0	0
4	3.5E+09	936	0
5	15.85	6E-04	2E-06
6	13.37	7E-04	8E-06
7	62.53	0.093	0.0025
8	50.57	0.594	0.0452
9	43.75	0.745	0.0769

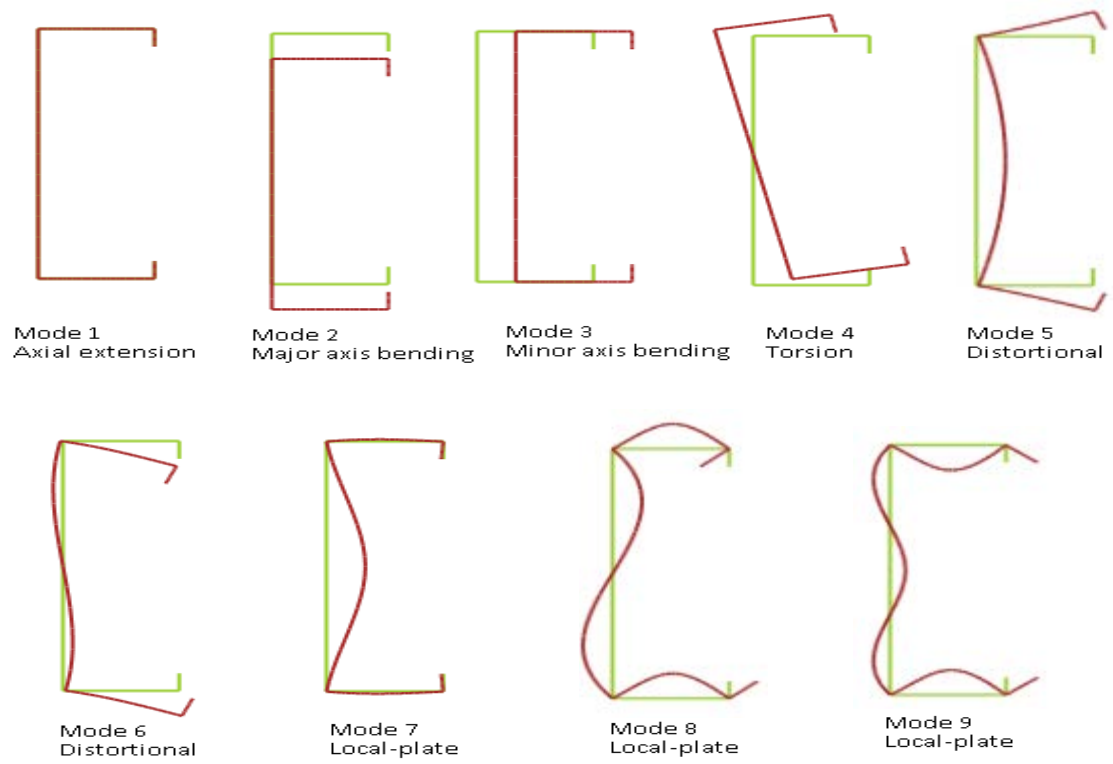

Figure (7-2) GBT C-Section Buckling Modes, (Bebiano et al, 2008), 25th, November 2016

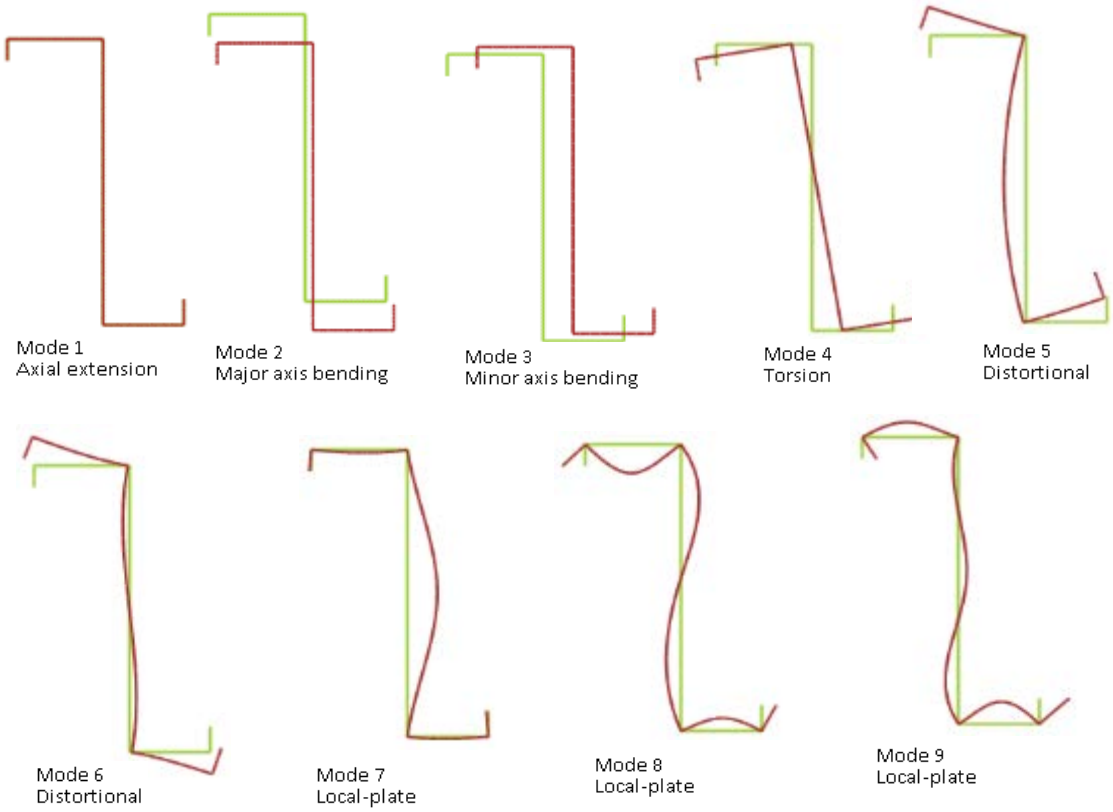

Figure (7-3) GBT Z-section buckling modes, (Bebiano et al, 2008), 25th, November 2016

Considering the GBT buckling analysis for a single mode, this was calculated using the purpose written Matlab Program in Appendix B. The buckling load curves are shown in figures (7-4) & (7-5) for C-sections in pinned and fixed end conditions respectively and figures (7-6) & (7-7) for Z-section in pinned and fixed end conditions respectively using a logarithmic scale for the column length axis.

It is clear that the GBT buckling analysis for a single mode gives a good indication of how the column will buckle in each mode individually. These separate buckled models help to understand the behaviour of any open column section of any length. Figures (7-4) for C-section and (7-6) for Z-section of the pinned end condition show that the column at lengths between 15-340 cm for C-section and 15-245 cm for Z-section buckled in mode No.7, which was a local plate buckling mode with approximately the same buckling loads of 53 kN for C-section and 77 kN for Z-section along the entirety of the load buckling zone., The lengths between 340-1000 cm for the C-section and 245-1000 cm for the Z-section buckled in mode No.3 which was minor axis bending (global) buckling mode with a decrease in buckling load as the length increases. Figure (7-5) for C-section and (7-7) for Z-section with fixed end conditions shows that the column at lengths between 15-680 cm for C-section and 15-485 cm for Z-section buckled in mode No.7 which was a local plate buckling mode with approximately the same buckling loads of 56 kN for C-section and 81 kN for Z-section along the entirety of the load buckling zone, Lengths between 680-1000 cm for C-section and 485-1000 cm for Z-section buckled in mode No.3 which was minor axis bending (global) buckling mode with a decrease in buckling load as the length increases.

The lengths of less than 15 cm for both sections for both boundary conditions have high buckling loads and are expected to fail by direct axial yielding before buckling occurs.

It can be observed that the boundary conditions have a slight effect on the buckling load, but the zone of local plate buckling for the fixed end condition is much longer than the zone for the pinned end condition. This means that the column will bear more buckling load with an extended local plate buckling zone due to the boundary conditions changing from pinned to fixed end.

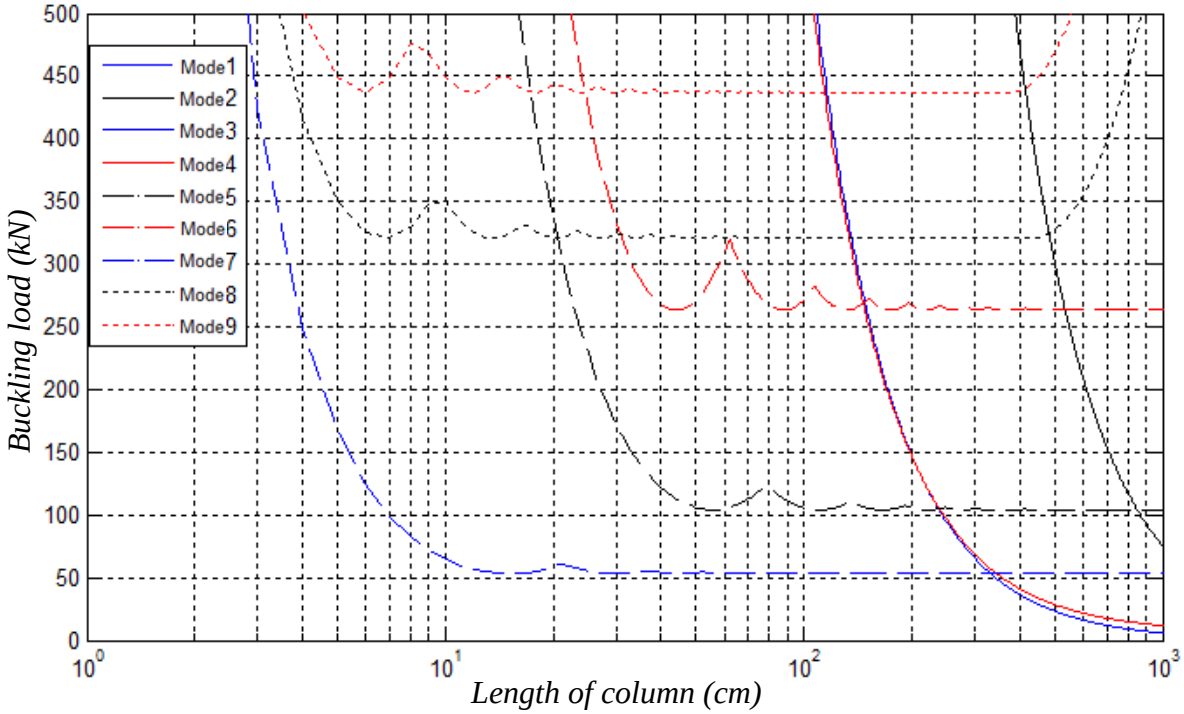

Figure (7-4) Buckling load versus length of the C-section of each single mode with pinned end conditions

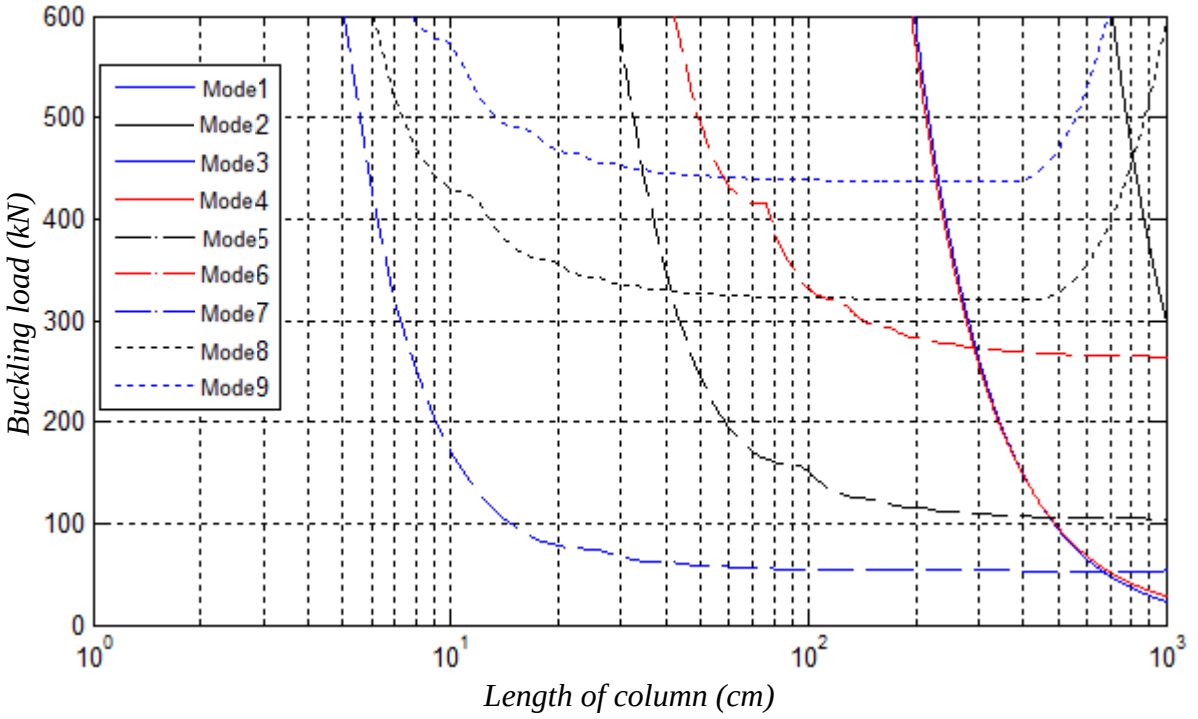

Figure (7-5) buckling load versus length of the C-section of each single mode with fixed end conditions

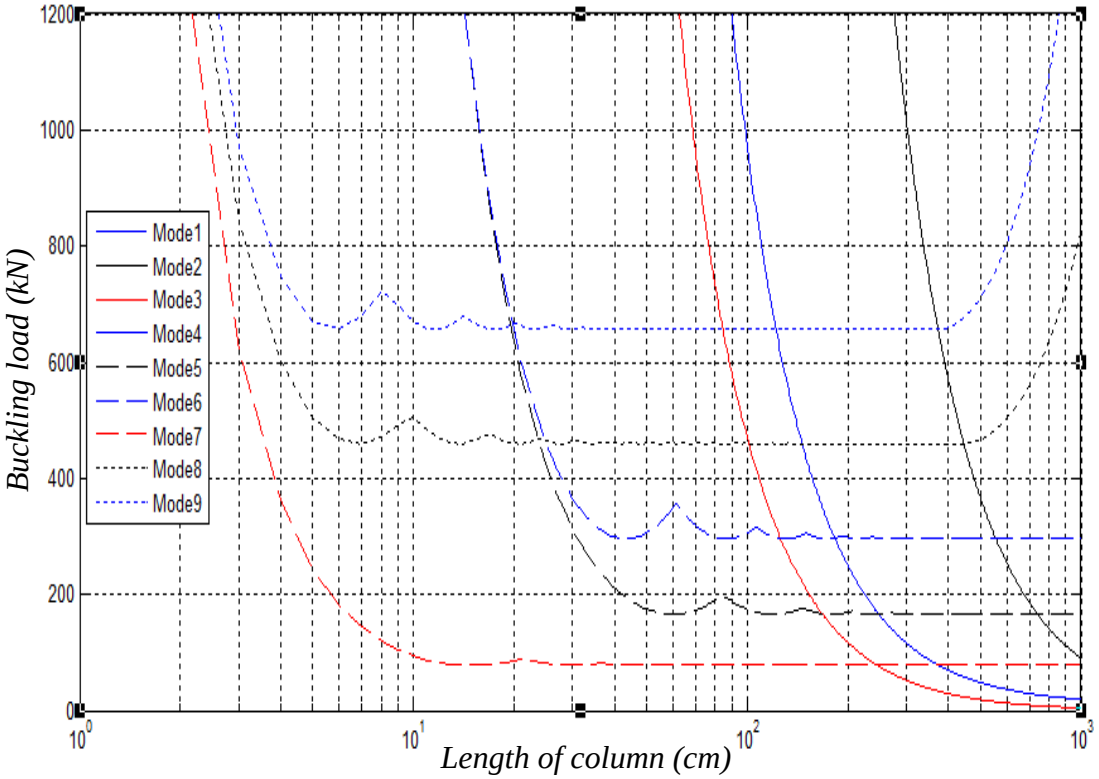

Figure (7-6) buckling load versus length of the Z-section of each single mode with pinned end conditions

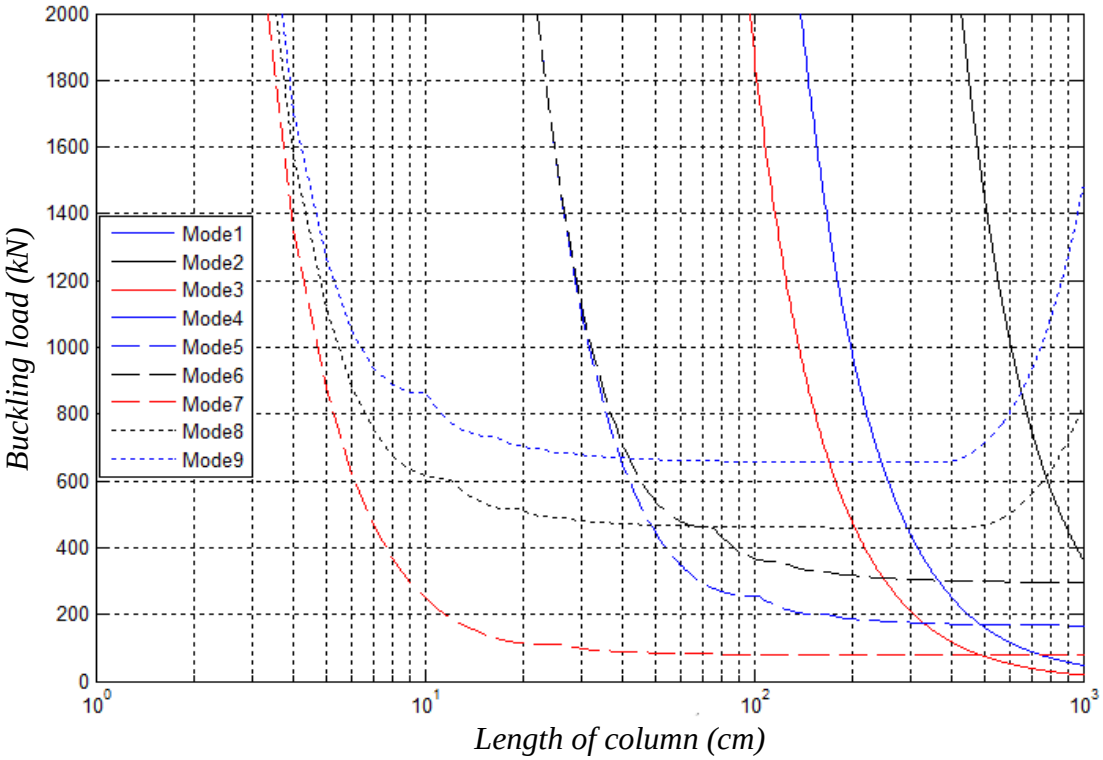

Figure (7-7) Buckling load versus length of the Z-section of each single mode with fixed ends conditions

7.1.2 Finite Element Analysis *(ANSYS)*

The linear Eigen-buckling analysis implemented through the finite element method which yields critical loads provides a good indication which mode the column will buckle in, however it would be tedious to separate the effects of each mode individually, and this aspect is clear in the generalized beam theory analysis. The FE analysis has more flexibility in the representation of boundary conditions for both pinned and fixed end conditions. It is straightforward to split the global boundary conditions and local boundary conditions when compared to the generalized beam theory which requires the representation of the boundary conditions for each mode independently.

The linear buckling analysis of the generalized beam theory (eigenvalue buckling analysis) was implemented using the purpose written Matlab programs in the Appendix B and C.

The first analysis carried out was an eigenvalue linear analysis for determination of the critical buckling load and associated buckling modes. Figures (7-8), (7-11), (7-14) and (7-17) demonstrate the linear buckling behaviour for a range of lengths of the column as predicted by both the linear finite element analysis (ANSYS), the linear finite difference analysis used to solve the GBT and Eurocde design practice (Appendix G), BSI (2014). In these analyses, the load is acting in an ideal state (at the centroid of the cross-sections). The linear FE results are similar to the GBT eigenvalue linear analysis in terms of the critical buckling load. The buckling behaviour for the linear model shows that the column cannot increase its strength beyond bifurcation point because it has zero stiffness after buckling has occurred. Eurocode gives more safety in the case of local and distortional buckling zones, but it matches with both FE and GBT linear analyses in the case of the global buckling zone.

The buckling behaviour of the column can be classified into three main zones, i.e. the local buckling zone which contains all the high-order local buckling modes, the distortional buckling zone which contains the two symmetrical and unsymmetrical distortional buckling modes, and the global buckling zone contains the lateral and torsional buckling modes. Through the local buckling zone, the buckling load was observed to be stable (with only a small decrease or increase as the length increased in both singly symmetrical C-section and unsymmetrical Z-section for both pinned and fixed end conditions. The local web-plate buckling mode (Mode No.7 in GBT) dominated on this zone length. On the global zone, the buckling load dramatically decreased through the length range and the lateral buckling mode

shapes (Modes No.2 & 3 in GBT) were dominated by this zone length. These figures also show that there were not any distortional buckling modes through the length as they were not critical. There was no combination between the buckling mode shape zones.

It can be observed that the local mode shape buckling zone was unchanged in both buckling loads and buckling mode shape type through the length range in each of the cross-section types as compared to the global mode shape zone which is much more sensitive to initial imperfection effects. Hence it is better to use fixed end conditions rather than pinned end conditions to extend the local mode shape buckling zone and provide a long and stable column length. Also, it was observed that the fixed end boundary conditions increased the buckling load through the length range overall.

Figures (7-9), (7-10), (7-12), (7-13), (7-15), (7-16), (7-18) and (7-19) show the eigenvalue buckling mode shapes for both the finite element method and the linear finite difference analysis of GBT for each C & Z-section with different boundary conditions of pinned and fixed ends, the eigen-displacements do not represent the actual displacement. Therefore, these displacement values were ignored and only the buckling mode shapes were taken into account to investigate which mode shape will occur for each length.

It can be seen that the number of half sine waves of local plate buckling mode shape in the local zone for both cross-section shapes with different boundary condition types was exactly the same for both linear analysis methods of the finite element analysis (ANSYS) and the finite difference analysis of GBT, this provided good evidence that both linear analysis methods can predict the correct eigen-buckling mode shape.

For the local buckling zone, both linear analysis methods predicted one-half sine wave in each cross-section shape with different boundary condition types which matched the Euler buckling mode shape.

It can be concluded that the results of either buckling loads or buckling mode shapes have a high degree of similarity in each of the finite element analysis and the GBT. The finite element method (ANSYS) was a much slower process than the GBT due to the extent of modelling and the solution of each length separately. So the GBT provides a quicker analysis method to predict linear buckling loads and mode shapes of thin-walled steel sections considering the relative accuracy of results.

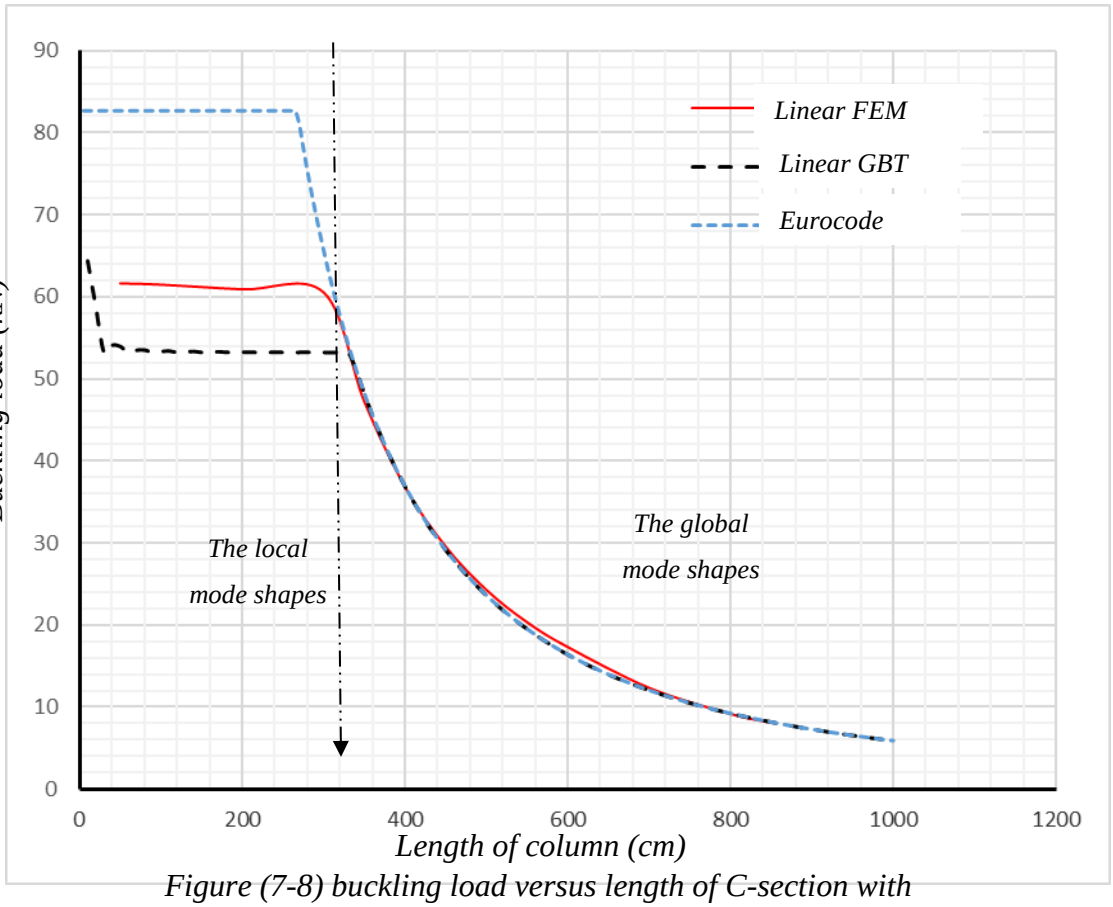

Figure (7-8) buckling load versus length of C-section with pinned end conditions.

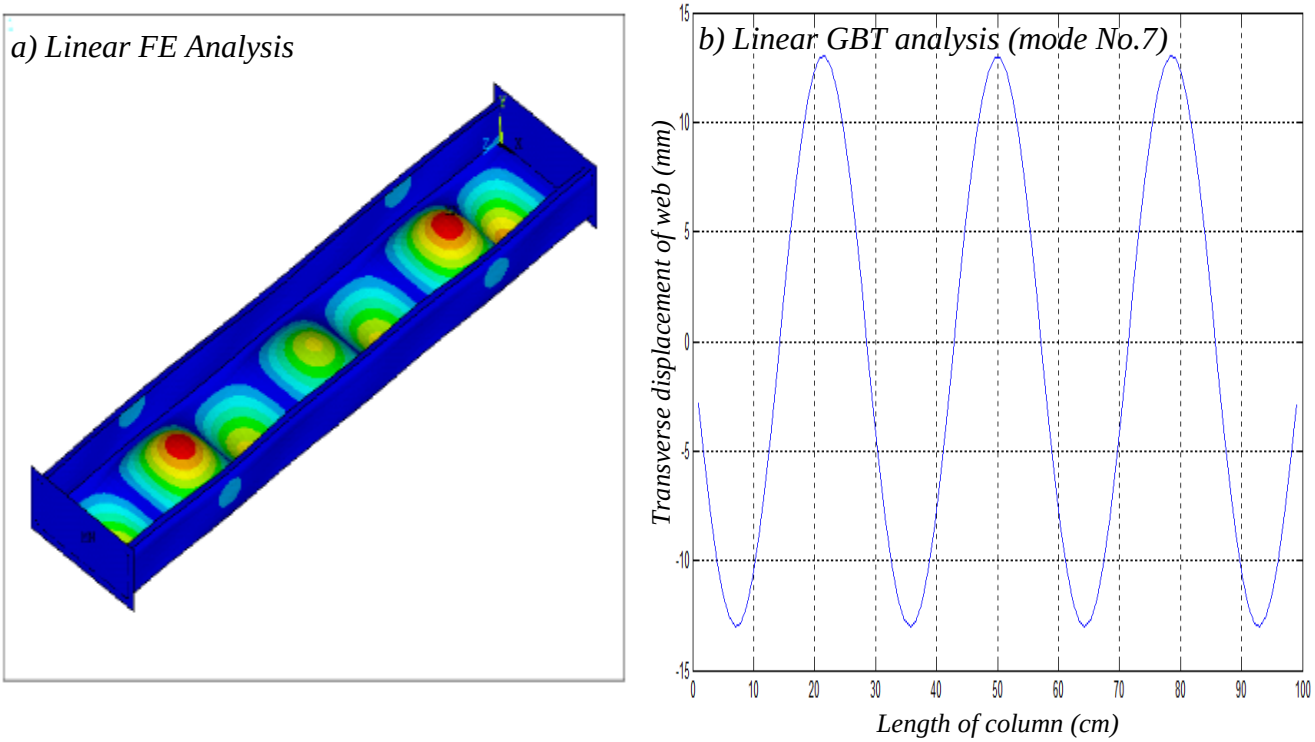

Figure (7-9) Linear buckling mode shapes for 100 cm length for C-section with pinned end conditions.

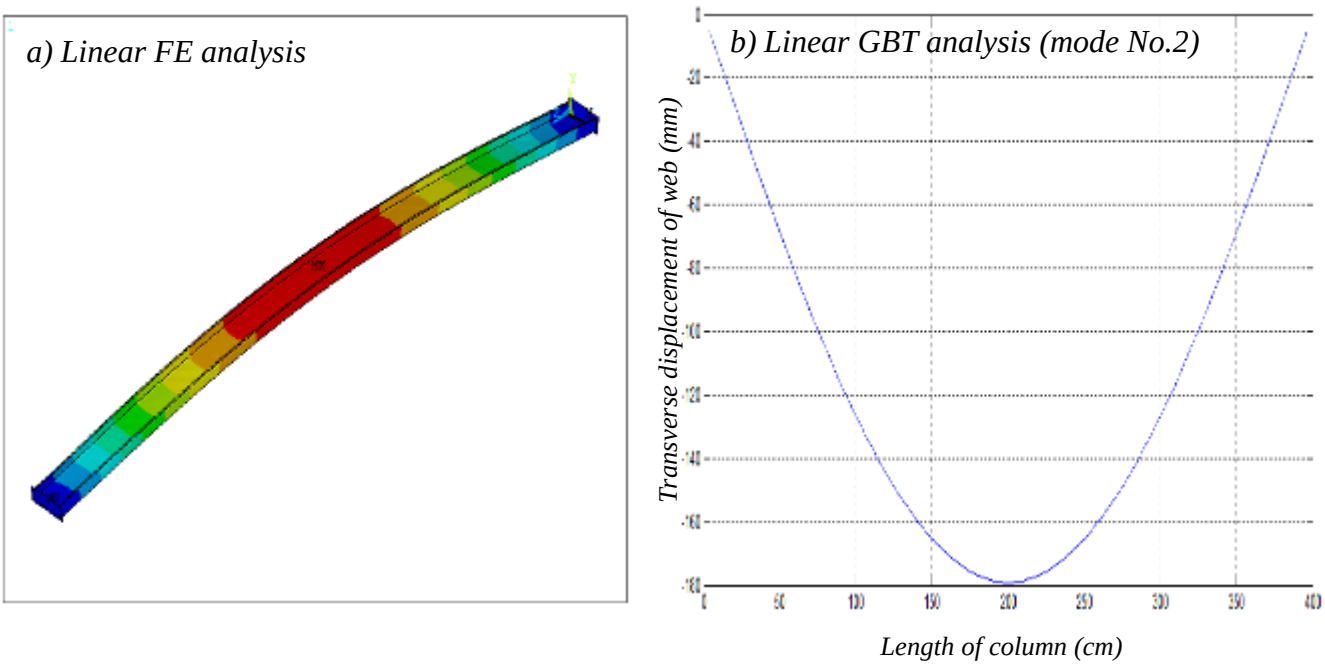

Figure (7-10) Linear buckling mode shapes for400 cm length for C-section with pinned end conditions.

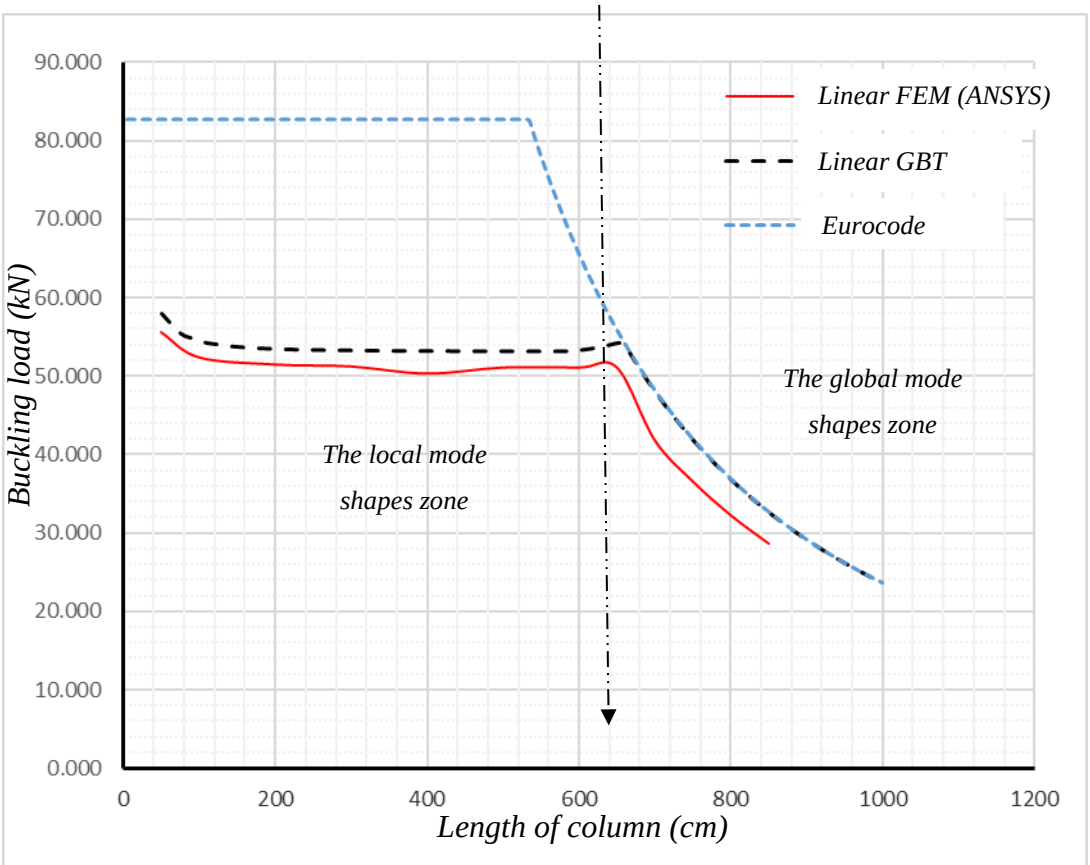

Figure (7-11) Buckling load versus lengths of C-section with fixed end conditions.

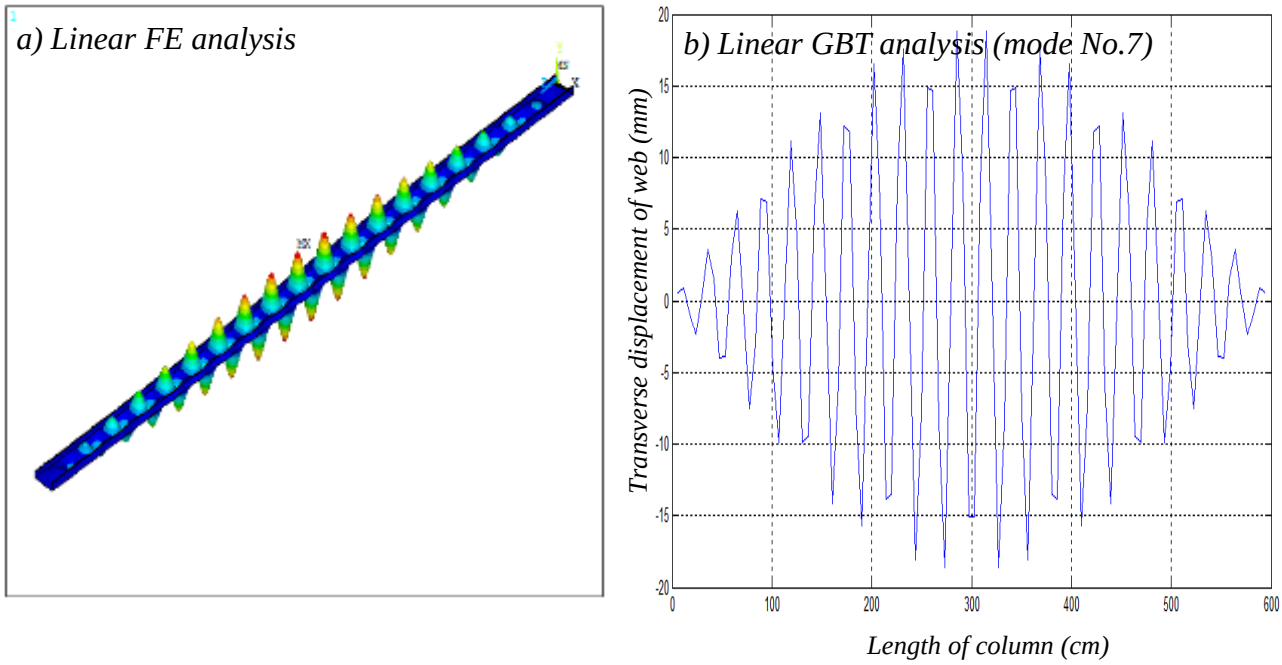

Figure (7-12) Linear buckling mode shapes of 600 cm length for C-section with fixed end conditions.

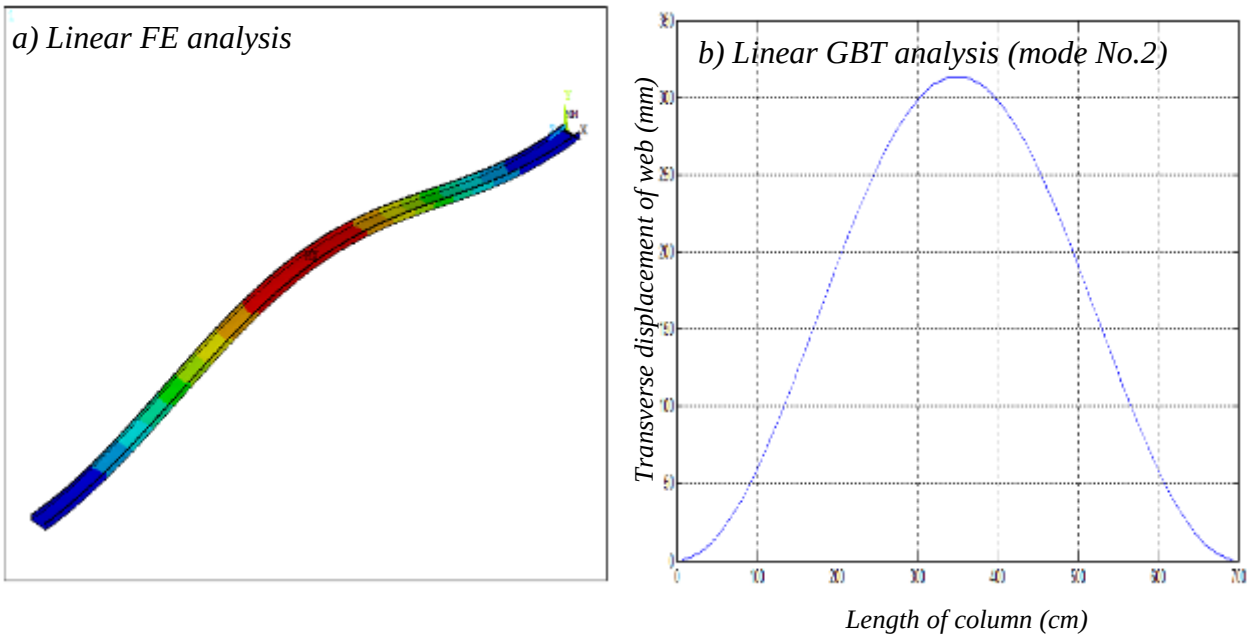

Figure (7-13) Linear buckling mode shapes of 700 cm length for C-section with fixed end conditions.

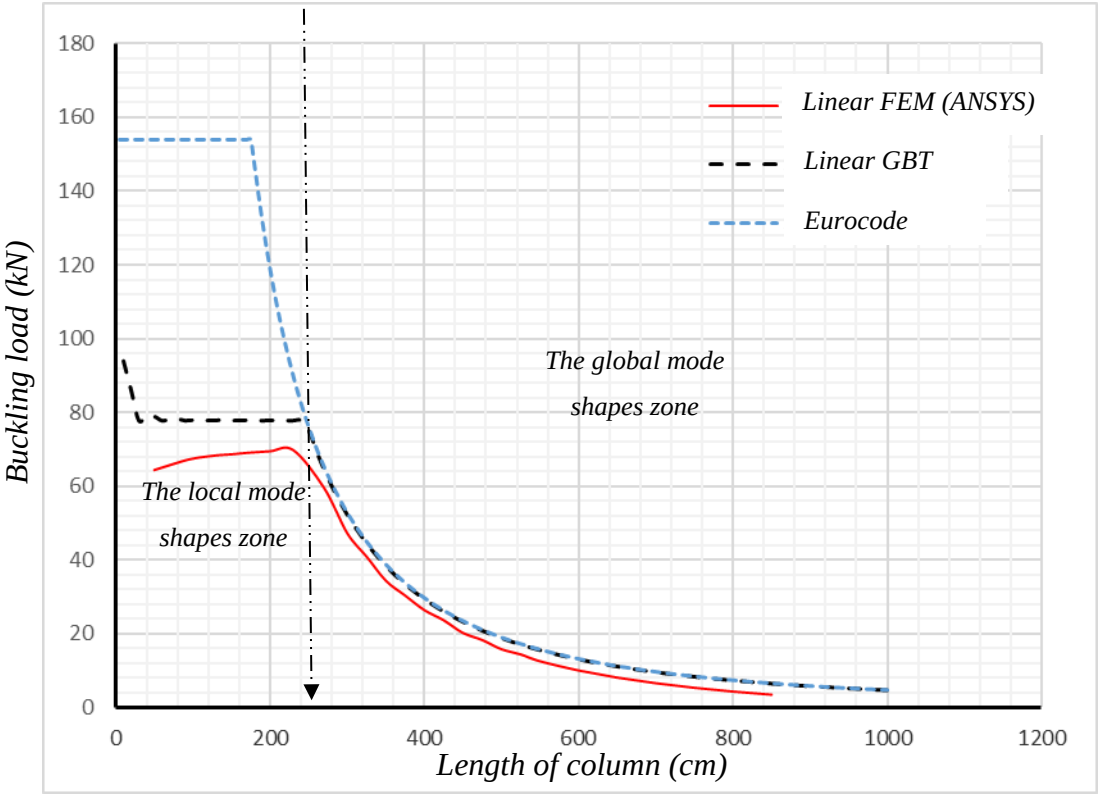

Figure (7-14) Buckling load versus length of Z-section with pinned end conditions.

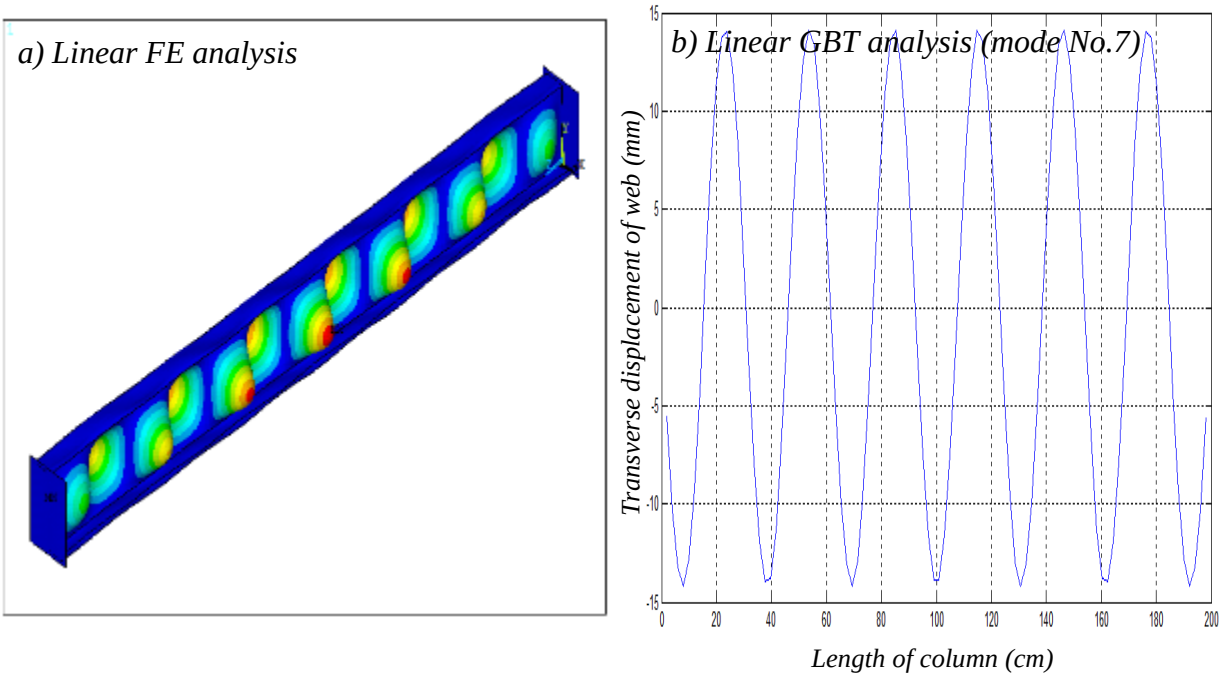

Figure (7-15) Linear buckling mode shapes of 200 cm length for Z-section with pinned end conditions.

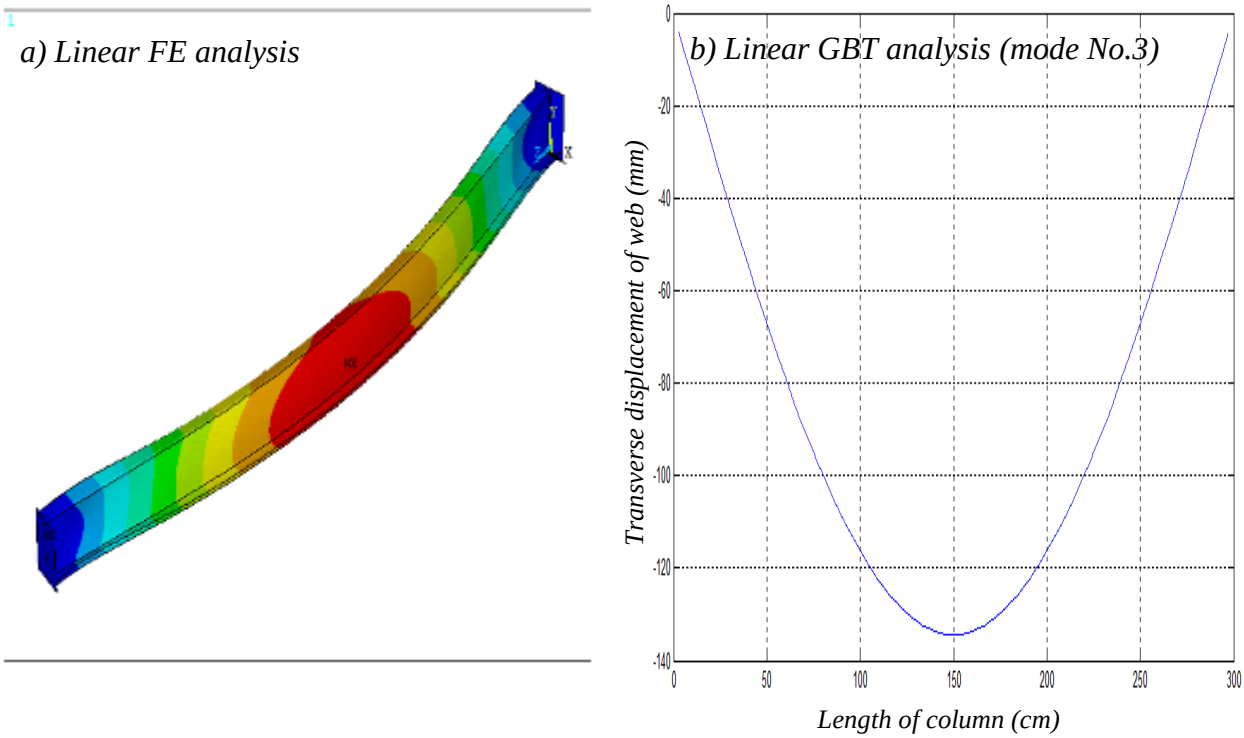

Figure (7-16) Linear buckling mode shapes of 300 cm length for Z-section with pinned end conditions.

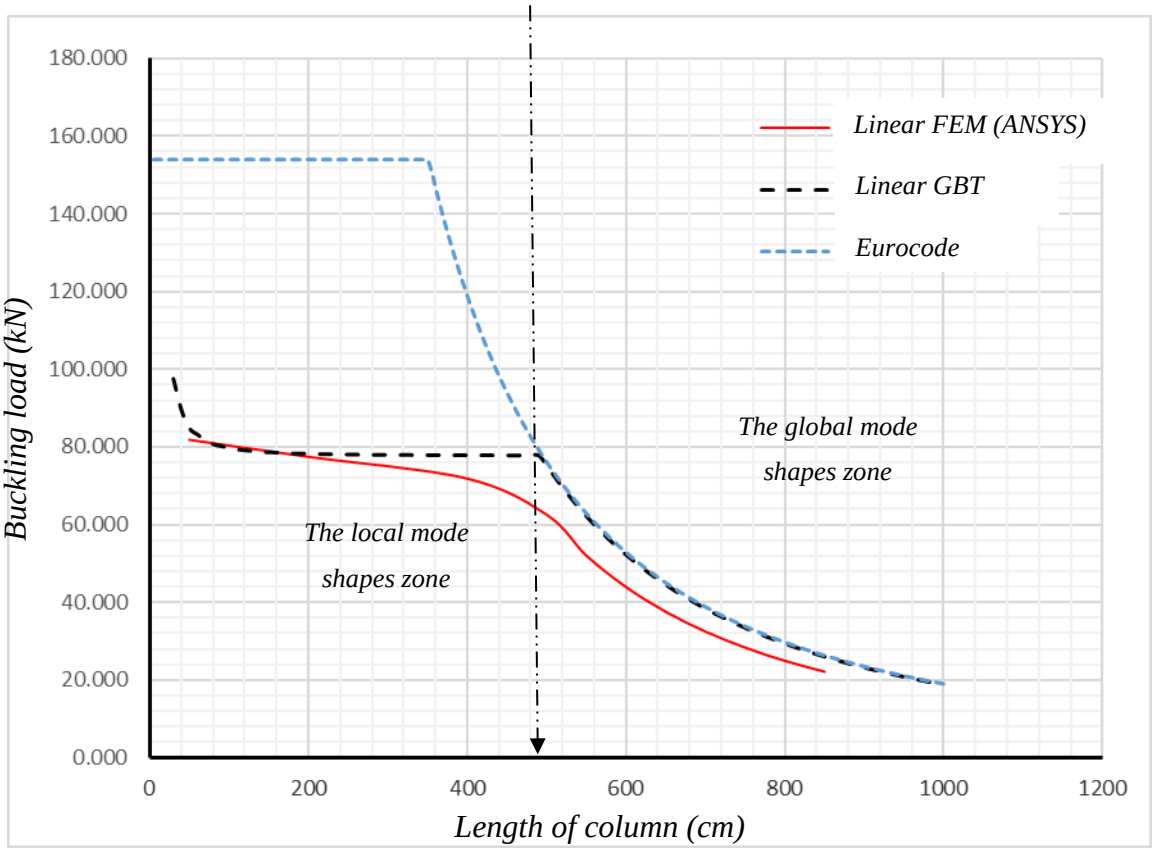

Figure (7-17) Buckling loads for versus lengths of Z-section with fixed end conditions.

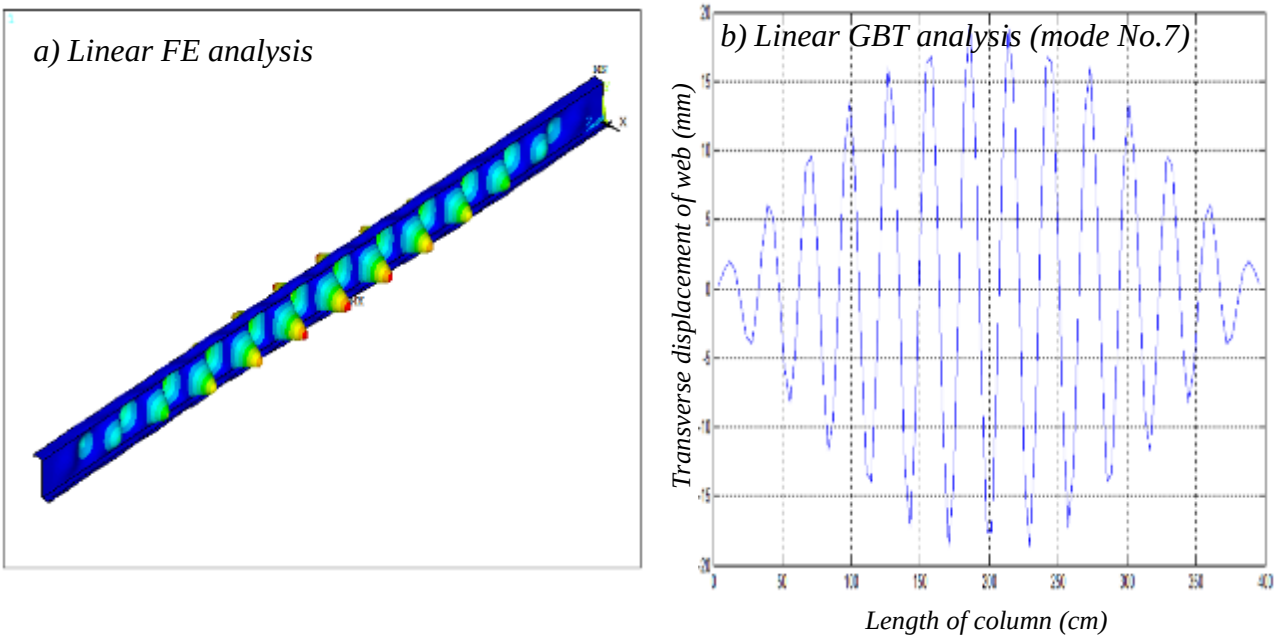

Figure (7-18) Linear buckling mode shapes of 400 cm length for Z-section with fixed end conditions.

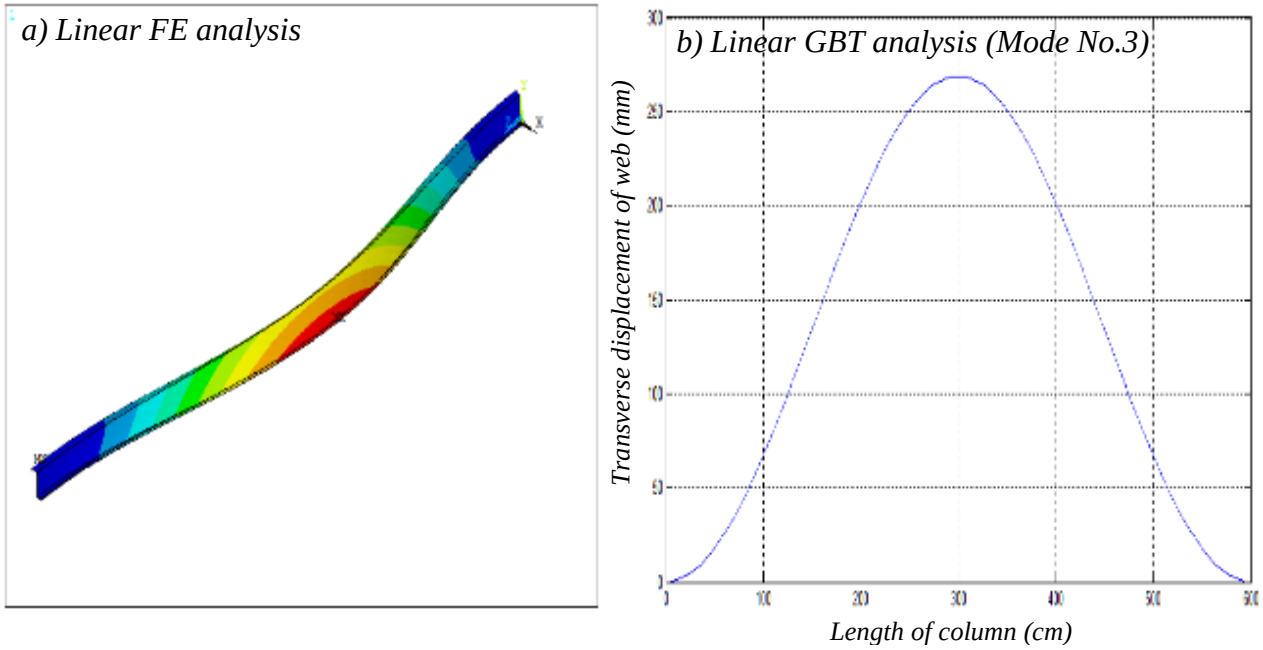

Figure (7-19) Linear buckling mode shapes of 600 cm length for Z-section with fixed end conditions.

7.2 Non-linear analysis and experimental results

7.2.1 Non-linear load results

For non-linear buckling analysis, the effects of initial imperfection and post-buckling effects should be taken into account when examining the failure loads through the length range of the column. Initial imperfections affect the change of cross-section and the length of the column. This was classified into two patterns of local initial imperfection which are an effect of cross-section change and global initial imperfection which is an effect with length change (geometrical non-linearity). The post-buckling affect is incorporated with the cross-section shape and the material non-linear properties.

In this study, the C-section & Z-section cross-sections were measured in the laboratory using calibrated measuring devices (see Chapter 6), and it was found that the differences in the cross-section thickness of these sections were tolerable. So only global initial imperfection was taken into account with length change with the section acting under self-weight, figure (7-20).

The non-linear analysis of the generalized beam theory was implemented the purpose written *Matlab* Programs in Appendix *E*.

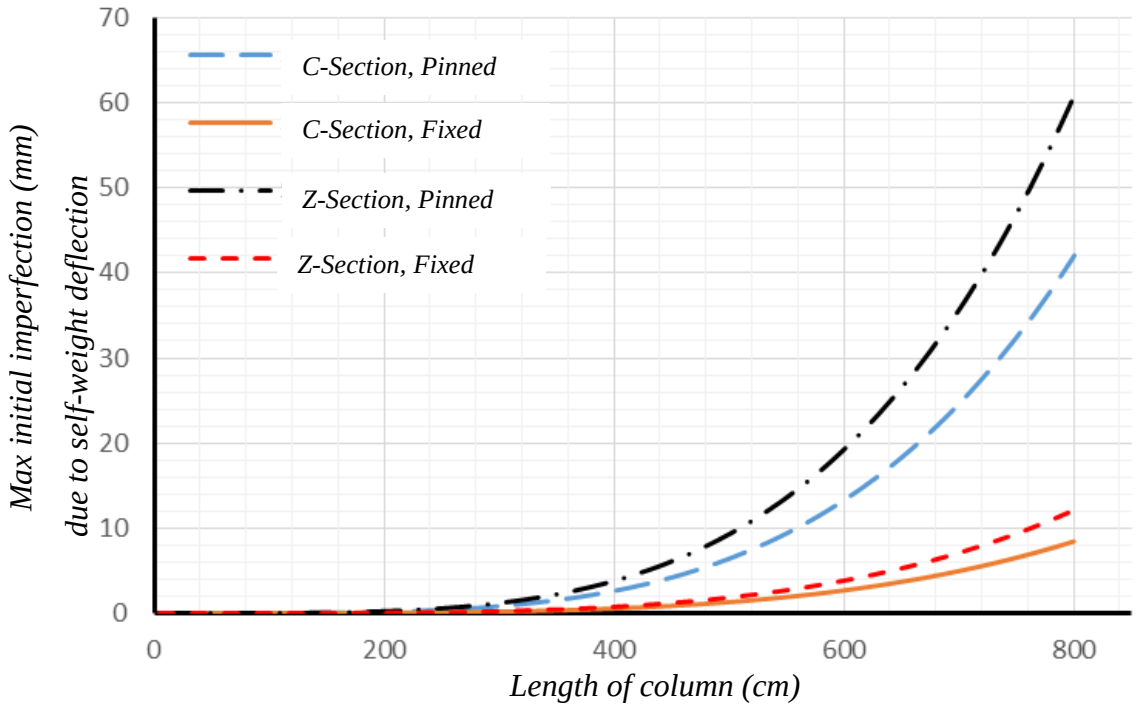

Figure (7-20) Maximum initial imperfection vs length.

For the case with pinned end boundary condition, figures (7-21) & (7-23), when the lengths exceed 300 cm (global buckling zone), it was recognisable that the non-linear failure load decreases as the amount of global initial imperfection increases. This can be seen in both numerical analyses because the global initial imperfection generates extra bending moment aside from axial load which means the column yields at a lower axial load. In this zone, the results demonstrate that the predicted ultimate strength of the C and Z-sections by the non-linear generalized beam theory is in good agreement with the results obtained from the non-linear finite element analysis and experimental test results. For short lengths of less than 100 cm, (local buckling zone), and medium lengths between 100 cm and 300 cm (combination buckling zone), the non-linear finite element analysis can model the effects of post-buckling, whereas the non-linear GBT analysis would require modification to do so. The post-buckling zone clearly shows the difference in failure load between the non-linear finite element analysis and the non-linear generalized beam theory. Therefore, it is clear that for the analysed C and Z-sections, the non-linear finite element analysis provides a higher failure load than can currently be predicted by the non-linear GBT analysis. The experimental test results also show the post buckling effects in these zones, though generally they are enveloped by the FE results to a degree. So in general terms, the post-buckling effect serves to increase the failure load and provides more stability, especially for short columns.

For the fixed end boundary conditions, figures (7-22) & (7-24) show that the post-buckling zone extended to overlap a portion of the global buckling zone in addition to local and distortional buckling zones (which was obviously not the case for pinned end conditions). Also it can be noted from figures (7-21), (7-22), (7-23) & (7-24) that there was no significant differences in the failure loads for both local and distortional buckling zones when comparing between the pinned and fixed end boundary conditions. These zones extend at the expense of the global buckling zone for fixed end boundary conditions, and the failure loads were approximately twice those observed for pin ended boundary conditions in the global buckling zone.

For the experimental test results, it is clear that these are in good agreement with both the non-linear finite element and the non-linear generalized beam theory analyses in the global buckling zone for both pinned and fixed end boundary conditions. But in the local and global buckling zones, the experimental test results are enveloped by the non-linear finite element analysis, due to a combination of the representation of the finite element model boundary conditions as ‘perfect’, and the presence of further imperfections in the member and axial load

paths in the experimental tests. This clearly demonstrates the effect of tolerances and safety factors which must be considered if any prediction of failure is to be based on the output from FE analyses.

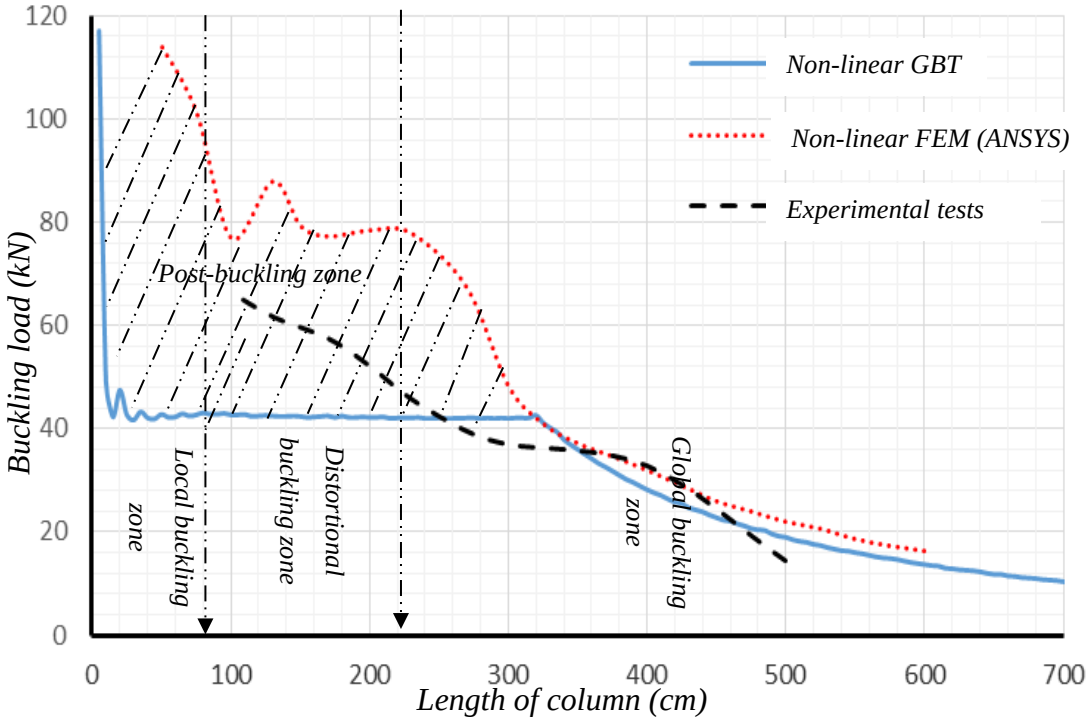

Figure (7-21) Non-linear and experimental buckling load for the length range of the C-section for pinned ends conditions.

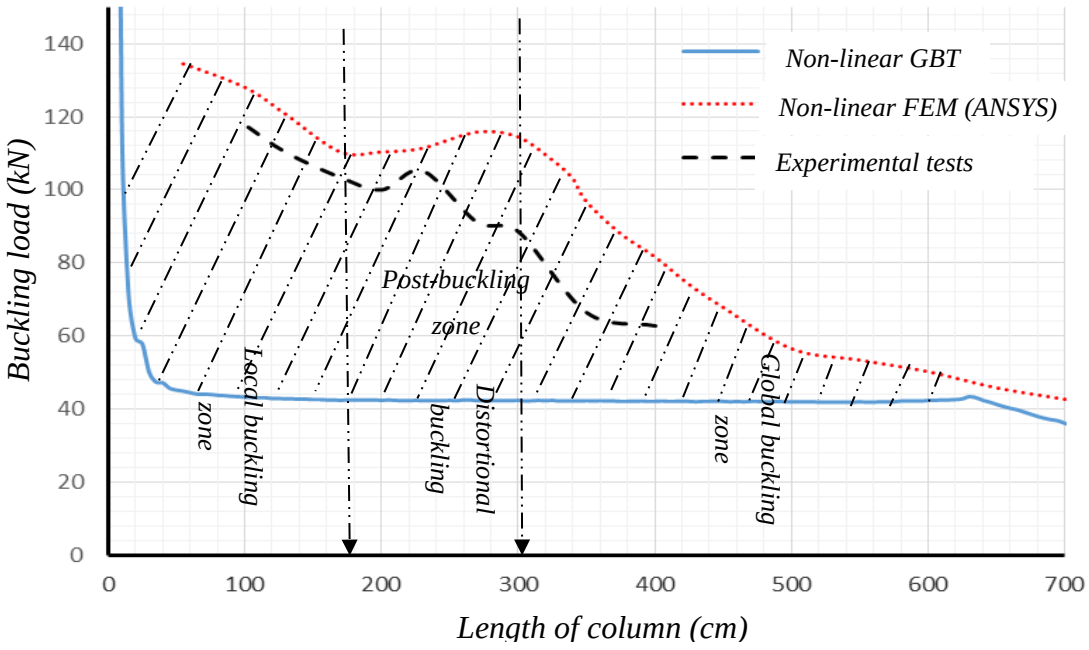

Figure (7-22) Non-linear and experimental buckling load for the length range of the c-section for fixed ends conditions.

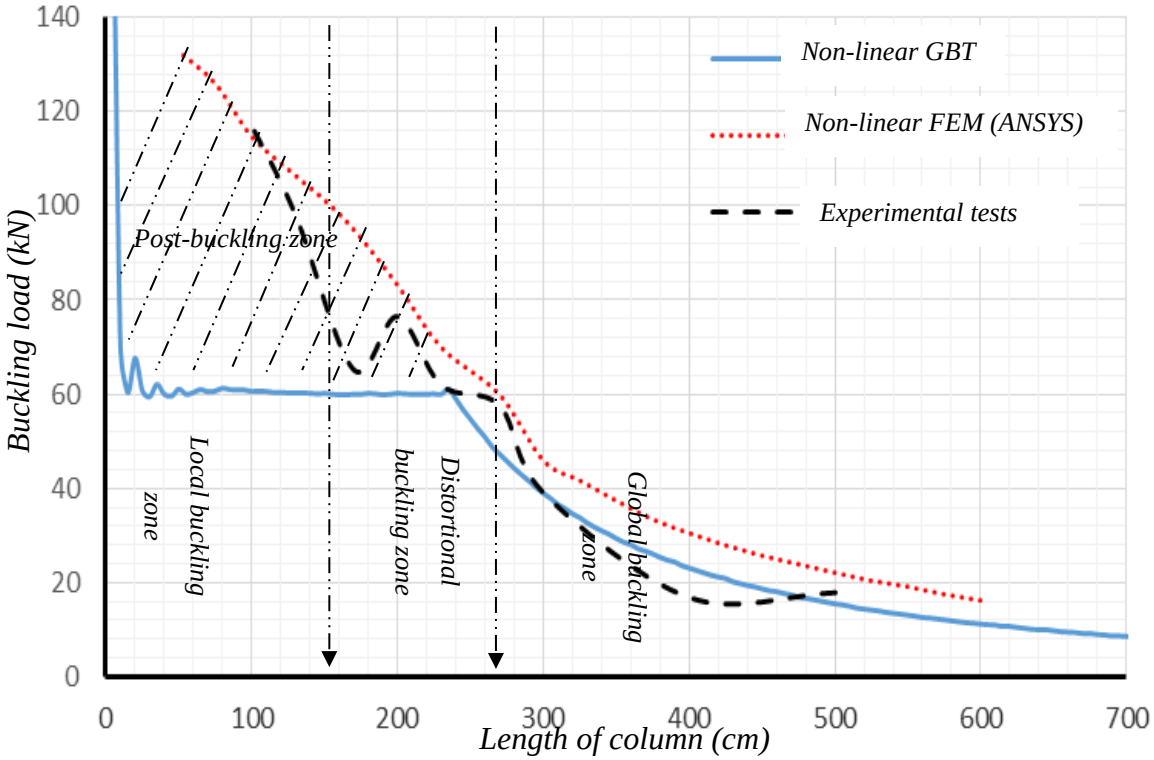

Figure (7-23) Non-linear and experimental buckling load for the length range of the Z-section for pinned ends conditions.

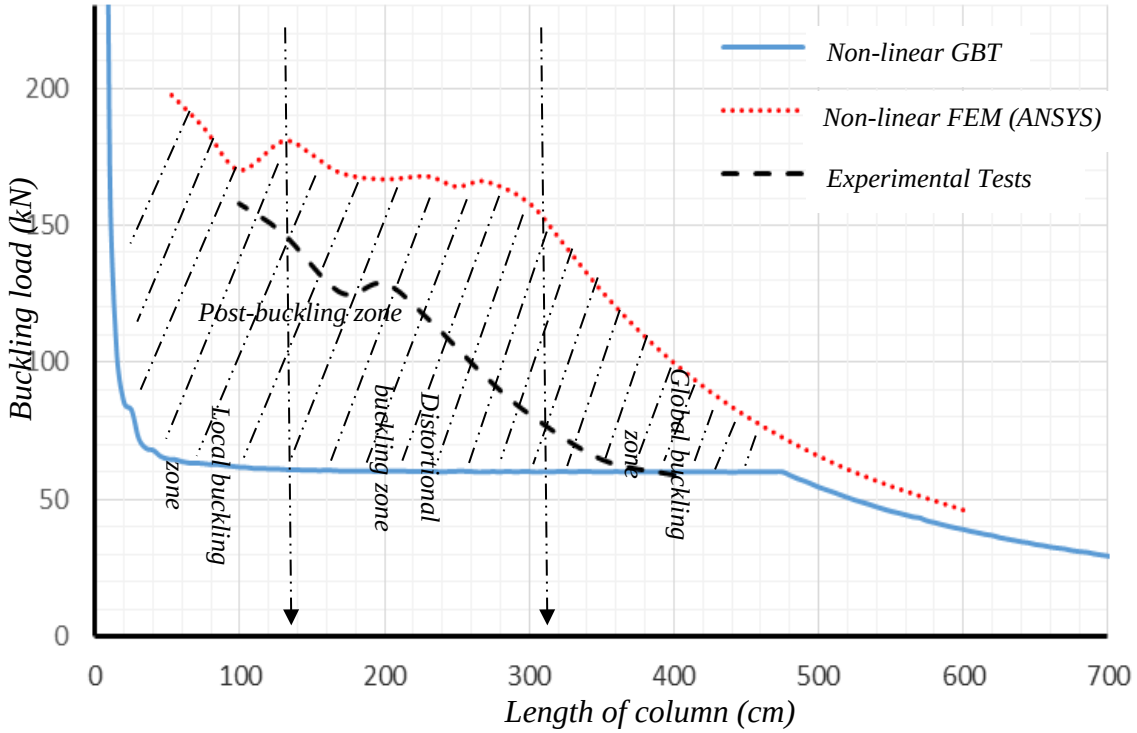

Figure (7-24) Non-linear and experimental buckling load for the length range of the Z-section for fixed ends conditions.

7.2.2 Non-linear mode shape results

From the investigations of the mode shapes obtained from the experimental tests, three lengths of 1.0, 2.3 & 4.0 m were selected to represent the three buckling zones of local, distortional and global buckling. The finite element analysis results of mode shape, transverse load-displacement relation in the two orthogonal section axes, and rotation about the longitudinal axis were compared with the experimental results for verification purposes of the numerical analysis methods for the uniaxial symmetrical C-section and unsymmetrical Z-section cold-formed steel members with both pinned and fixed end boundary conditions.

The results obtained from the different methods were compared with a view to proposing an approach which can provide an appropriate and reasonable method of predicting the actual columns behaviour under axial compression. From figures (7-25) to (7-48), it can be observed that:

- For the uniaxial symmetrical C-section:
  - For short lengths of 1.0 m with pinned end boundary conditions, figure (7-25), it can be seen there were local-distortional failure mode shapes in both the finite element and experimental tests with good agreement between them. From figure (7-26), when the compressive load was high (for this particular length as compared with other lengths of the same cross-section), a small uncontrolled movement of the applied load occurred, moving away from the centroid of section during the test. This movement was likely to have influenced the resulting failure load of 68.44 kN being less than the finite element failure load of 77.33 kN. The failure longitudinal displacements in X and Y-axes (in mm) and rotation about the Z-axis (in degrees) are 0.004, -4.16 and 0.014 respectively in the finite element analysis. These were 0.175, -5.21 and 0.032 respectively in the experimental test, so it can be noted that there was a good agreement in both displacements and rotation between the experimental tests results and nonlinear finite element analysis.
  - For the medium length of 2.3 m with pinned end conditions, figure (7-27), it can be seen that distortional-lateral failure mode shapes presented in both the finite element analysis and the experimental tests with predominance of the lateral mode rather than the distortional mode. Therefore, it can be said that the distortional buckling zone (1.0-

2.3m) was much narrower for this type of boundary condition. From figure (7-28), it can be seen that the finite element and the experimental failure loads were 78.36 kN and 45.13 kN respectively. This relative difference between the experimental and finite element failure load is as a result of the lack of friction between the C-section and the bearing plate during the test. The longitudinal displacements at failure in X and Y directions (in mm) and rotation about Z direction (in degree) are 0.002, -14.37 and 0.033 respectively as predicted by the finite element analysis, whereas for the experiment the displacement were 3.4, -16.13 and 1.02 respectively. These results also showed good agreement between experimental and the numerical method in this length which has acted as a means of verification,

- For the longer length of 4.0 m with pinned end conditions, figure (7-29), it can be observed their lateral failure mode shapes presented in the finite element analysis. For the experimental tests, also a small participation from torsional failure modes was observed. Due to the effect of global initial imperfection and imperfections in the cross-section shape. From figure (7-30), the finite element and the experimental failure loads were 32.08 kN and 31.84 kN respectively, so a very good agreement of failure load was obtained for the longer lengths due to a more appropriate representation of pinned end conditions in practice. The failure longitudinal displacements in X and Y directions (in mm) and rotation about Z direction (in degrees) were -0.04, -63.57 and 0.065 respectively for the finite element (ANSYS) and for the experiment they were -1.03, -34.72 and 6.45 respectively. From these results it was noted that the manufacturing imperfections had more of an effect due to the longer lengths.

- For the short lengths of 1.0 m with fixed end conditions, figure (7-31), due to the high compressive axial load, the fixed end was poorly represented, hence this provides reasoning as to the observed differences between the finite element and experimental mode shape. The local-distortional mode is present in both the experimental and FE analysis. From figure (7-32), the finite element and the experimental failure loads were 128.45 kN and 120.96 kN respectively, so it was clear to see there was a good match in failure load in both cases. The longitudinal displacements at failure in X and Y directions (in mm) and rotation about Z direction (in degrees) were -0.06, 6.34 and 0.052 respectively for the finite element and 1.3, 5.36 and -0.2 respectively for the experimental test. The results compare well between the finite element analysis and experimental tests.

- For the medium lengths of 2.3 m with fixed end conditions, figure (7-33), the similarity between the experimental and FE can be seen. This is an equal amount of local and distortional buckling presented in both. From figure (7-34), the finite element and the experimental failure loads were 111.36 kN and 105.17 kN respectively as before, there is good agreement at this length with a good representation of fixed end boundary conditions. The failure longitudinal displacements in the X and Y directions (in mm) and rotation about Z direction (in degree) are 0.05, 5.52 and 0.063 respectively for the finite element analysis and 3.4, 7.23 and 2.07 respectively for the experimental tests. In this series of tests and analyses the results show confidence in the representation of the boundary condition.

- For the longer lengths of 4.0 m with fixed end conditions, figure (7-35), it can be seen that the column buckled laterally upward in both cases. It can be concluded that the nonlinear finite element analysis has the ability to predict the buckling direction whereas the linear finite element or the linear generalized beam theory analyses cannot. From figure (7-36), the finite element and the experimental failure loads were 81.25 kN and 62.79 kN respectively, this difference in failure load between comes from the global initial imperfection which has a greater effect in longer lengths of columns. The failure longitudinal displacements in section X and Y direction (in mm) and rotation about the longitudinal Z direction (in degrees) are 0.03, 14.23 and 0.071 respectively for the finite element analysis and 4.1, 23.41 and 2.7 respectively for the experimental test, Small differences in displacements and rotations between the two cases may give an indication that the C-section had less imperfections in the cross-section.

▪ For the unsymmetrical Z-section:

- For the short lengths of 1.0 m with pinned end conditions, figure (7-37), shows the comparison between the FE analysis and the experimental test. For the C-section tests with the same length of 1.0 m, movement at the pinned end occurred due to lack of friction between the C-section and the bearing plate. To prevent this for the Z-section tests, a high friction aluminium plate was placed between the bearing surfaces to increase the friction. This resulted in a satisfactory match in the failure mode shapes between the finite element analysis and experimental test. Figure (7-38) shows that the finite element and the experimental failure loads were 116.13 kN and 116.84 kN respectively, so there was excellent agreement in between the two. The longitudinal

displacements in X and Y directions (in mm) and rotation about Z direction (in degree) at failure were 0.73, 3.97 and 0.065 respectively for the finite element analysis and 1.97, 5.76 and -1.82 respectively for the experimental test. This shows were good agreement in the displacement and rotation here.

- For the medium lengths of 2.3 m with pinned end conditions, figure (7-39) shows that the lateral-distortional failure mode shape occurred in both the FE and the experiment, but it was unsymmetrical in the experimental test due to imperfections in the manufacture of the sections. From figure (7-40), the finite element analysis and the experimental failure loads were 72.24 kN and 61.01 kN respectively. The difference between the two results is due to the same cause as previously mentioned, i.e. imperfections of the section. The displacements in the X and Y directions (in mm) and rotation about Z direction (in degree) in failure were 7.1, 27.4 and 0.074 respectively for the finite element analysis and 8.4, 30.75 and 0.23 respectively for the experimental test. These displacements were also in good agreement.

- For the longer lengths of 4.0 m with pinned end conditions, figure (7-41), the mode shape was a pure lateral failure mode shape for both the FE analysis and the experiment. From figure (7-42), the finite element and the experimental failure loads were 30.54 kN and 19.82 kN respectively and the failure longitudinal displacements in the X and Y directions (in mm) and rotation about Z direction (in degree) were 8.5, 26.7 and 0.067 respectively for the finite element analysis and 6.9, 62.4 and 1.96 respectively for the experimental test. This showed a significant difference in failure loads and lateral (Y direction) displacements at these lengths due to the effects of imperfection created whilst mobilizing the samples into position (handling imperfection). This would be presented wherever section an installed in practice.

- For the short lengths of 1.0 m with fixed end conditions, figure (7-43) and figure (7-44), the finite element analysis and the experimental failure loads were 181.6 kN and 157.96 kN respectively. The yield longitudinal displacements in the X and Y directions (in mm) and rotation about Z direction (in degrees) were -0.054, -3.5 and 0.072 respectively for the finite element analysis and -3.76, -3.4 and 1.08 respectively for the experimental test. A reasonable comparison was obtained between each case with the local-distortional failure mode shape presenting in the experimental test, enhanced by the effect of cross-section imperfections.

- For the medium lengths of 2.3 m with fixed end conditions, Figure (7-45) and figure (7-46), the finite element and the experimental yield loads were 168.17 kN and 127.61 kN respectively. The failure longitudinal displacements in the X and Y directions (in mm) and rotation about Z direction (in degrees) were -0.075, 4.4 and 0.055 respectively for the finite element analysis and 5.5, 11.3 and 6.3 respectively for the experimental test. So it is clear to note that the local-distortional failure mode shape was prevalent in the medium lengths with an acceptable comparison for the displacements and rotations.
- For the longer lengths of 4.0 m with fixed end conditions, figures (7-47) and figure (7-48), the finite element analysis and the experimental failure loads were 99.43 kN and 58.88 kN respectively, and the failure longitudinal displacements in the X and Y directions (in mm) and rotation about Z direction (in degrees) were 7.3, 26.2 and 0.041 respectively for the finite element analysis and 7.7, 37.9 and 1.5 respectively for the experimental test. The lateral failure mode shape was prevalent at these lengths with significant differences in the failure load and the displacement in lateral Y direction due to the sensitivity in the global initial imperfections.

In general, it can be seen that there is good agreement between the results of the finite element analysis and experimental results for the short and medium length samples with regards failure loads and mode shapes. The differences become significant at the longer lengths, mainly due to the manufacturing imperfections and handling imperfections as shown in table (7-3).

Table (7-3) Experimental and FEA Buckling loads comparison.

Buckling load (kN)												
Length (m)	C-section						Z-section					
	Pinned			Fixed			Pinned			Fixed		
	Experi-mental	FEA	Error (%)	Experi-mental	FEA	Error (%)	Experi-mental	FEA	Error (%)	Experi-mental	FEA	Error (%)
1.0	68.44	77.33	11.49	120.96	128.45	5.83	116.84	116.13	0.61	157.96	181.60	13.02
2.3	45.13	78.36	42.40	105.17	111.36	5.56	61.01	72.24	15.55	127.61	168.17	24.12
4.0	31.84	32.08	0.75	62.79	81.25	22.72	19.82	30.54	35.10	58.88	99.43	40.78

Overall, it can be said that a good representations of the desired boundary conditions was achieved in the laboratory work for both the pinned and fixed end cases. Modifications were made as the experiments progressed, and these have worked well considering the comparisons of the results of the finite element analysis. All experimental results are contianed in Appendix G.

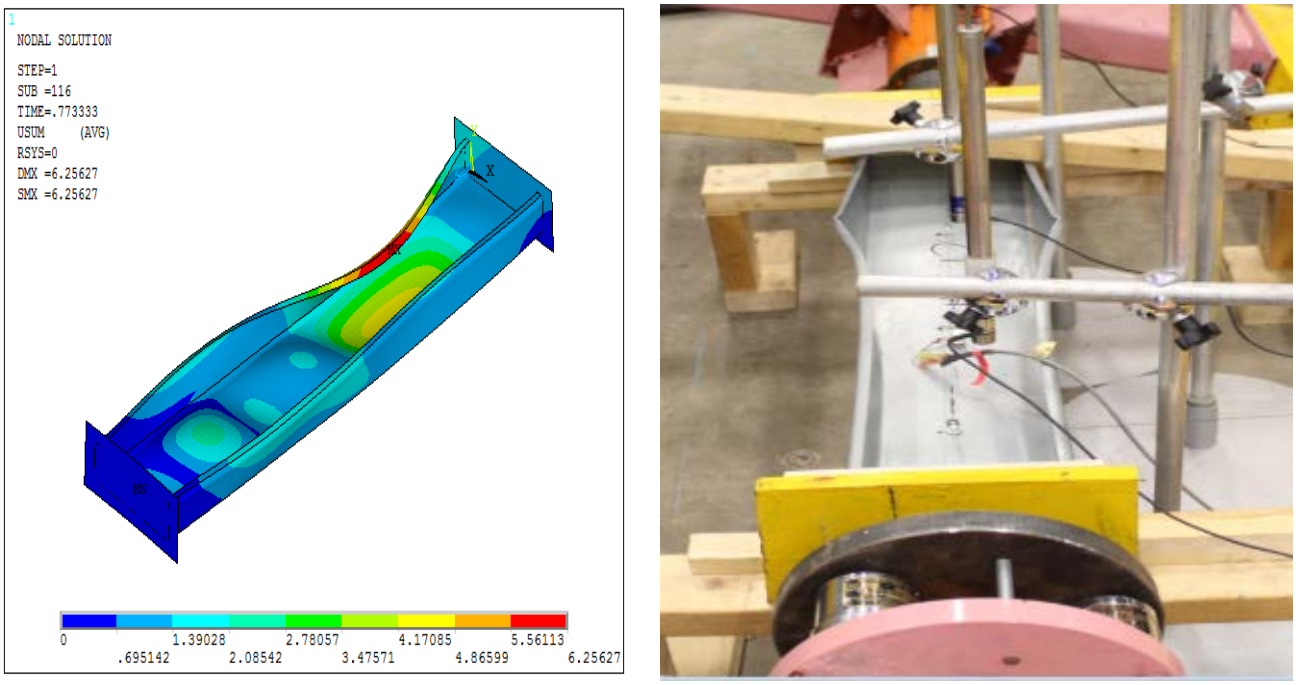

Figure (7-25) FEM and experimental buckling mode shape of 1.0 m length of C-section with pinned end conditions.

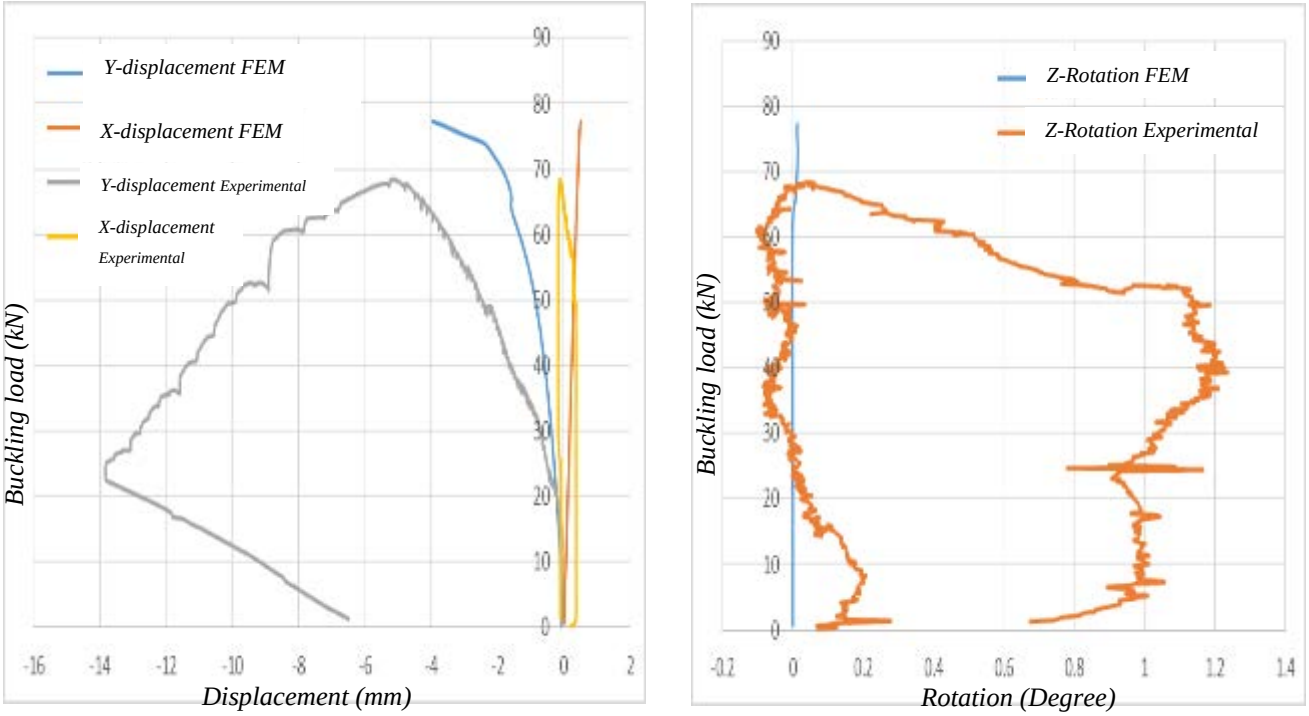

Figure (7-26) FEM and experimental load-deformation relations for 1.0 m length at the mid web of 0.5L of the C-section with pinned end.

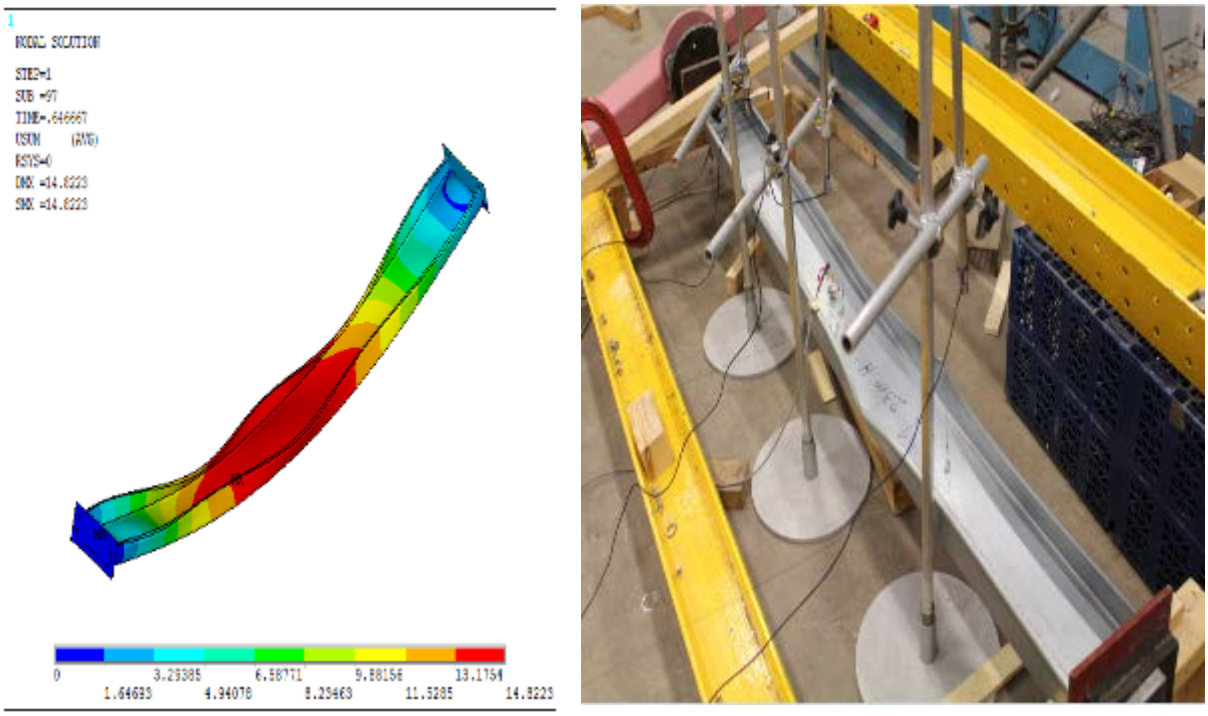

Figure (7-27) FEM and experimental buckling mode shape of 2.3 m length of C-section with pinned end conditions.

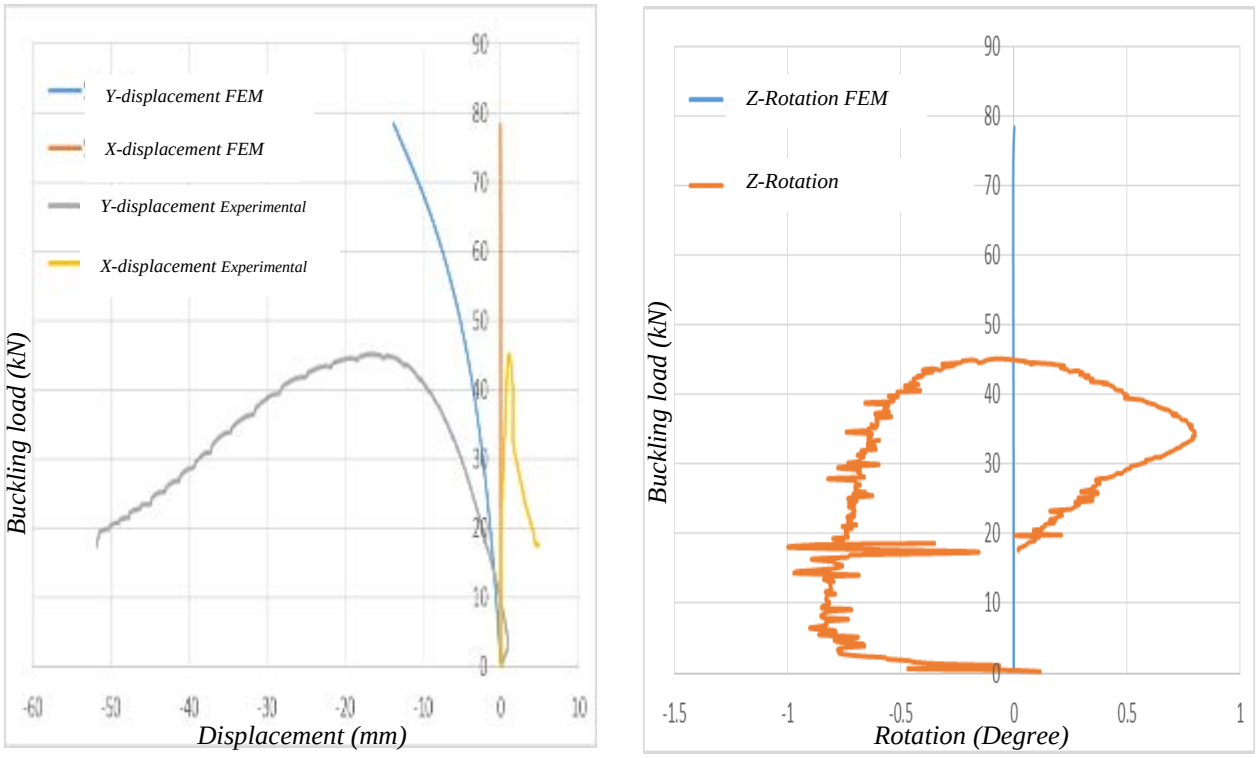

Figure (7-28) FEM and experimental load-deformation relations for 2.3 m length at the mid web of 0.5L of the C-section with pinned end conditions.

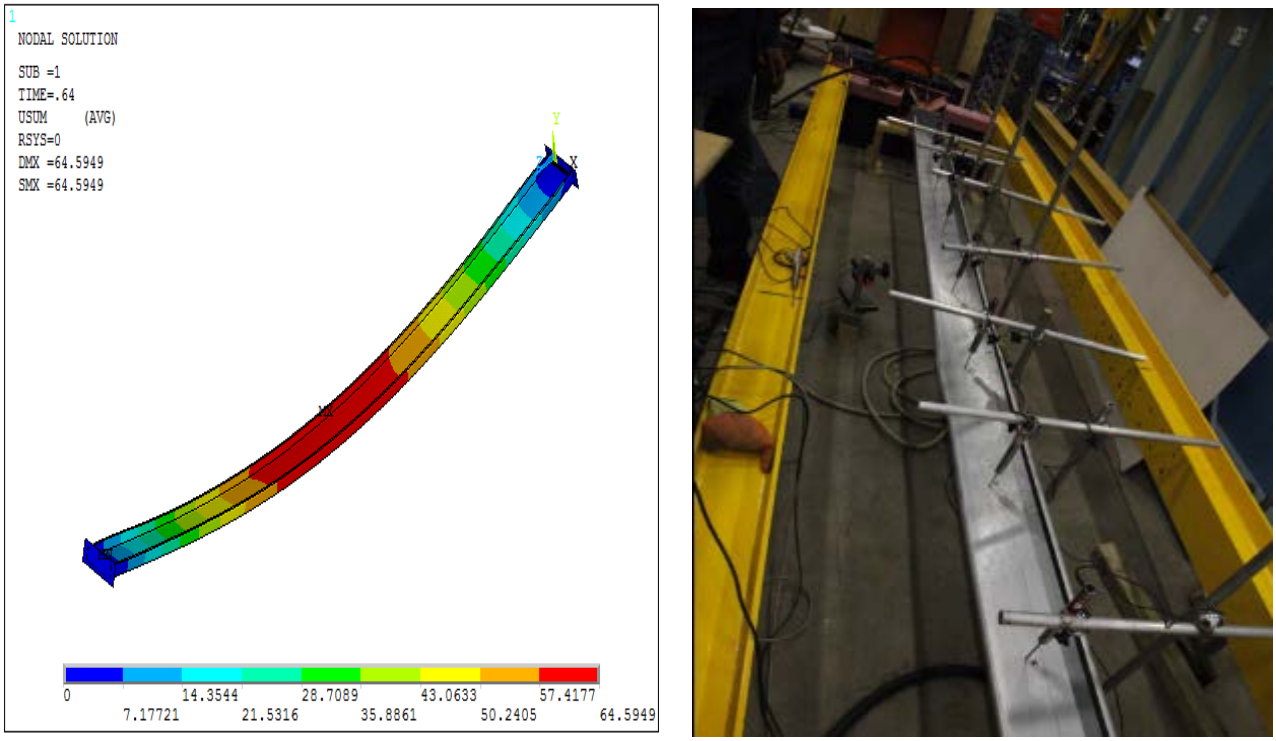

Figure (7-29) FEM and experimental buckling mode shape of 4.0 m length of C-section with pinned end conditions.

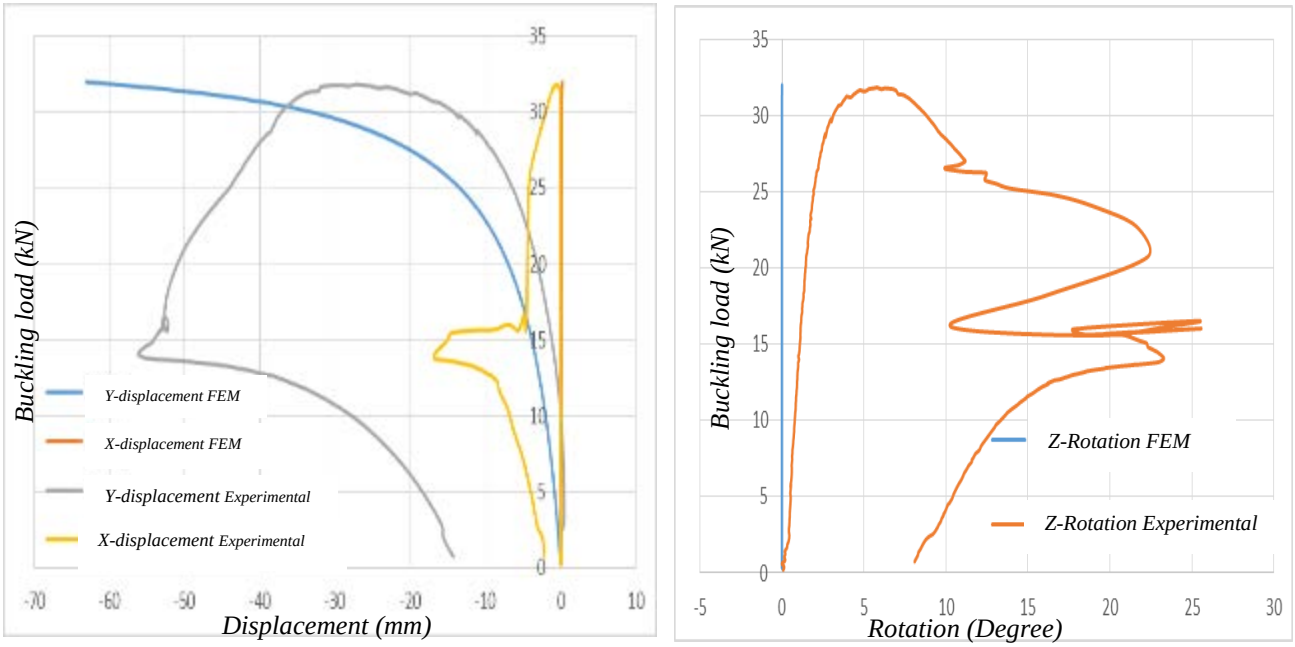

Figure (7-30) FEM and experimental load-deformation relations for 4.0 m length at the mid web of 0.5L of the C-section with pinned end conditions.

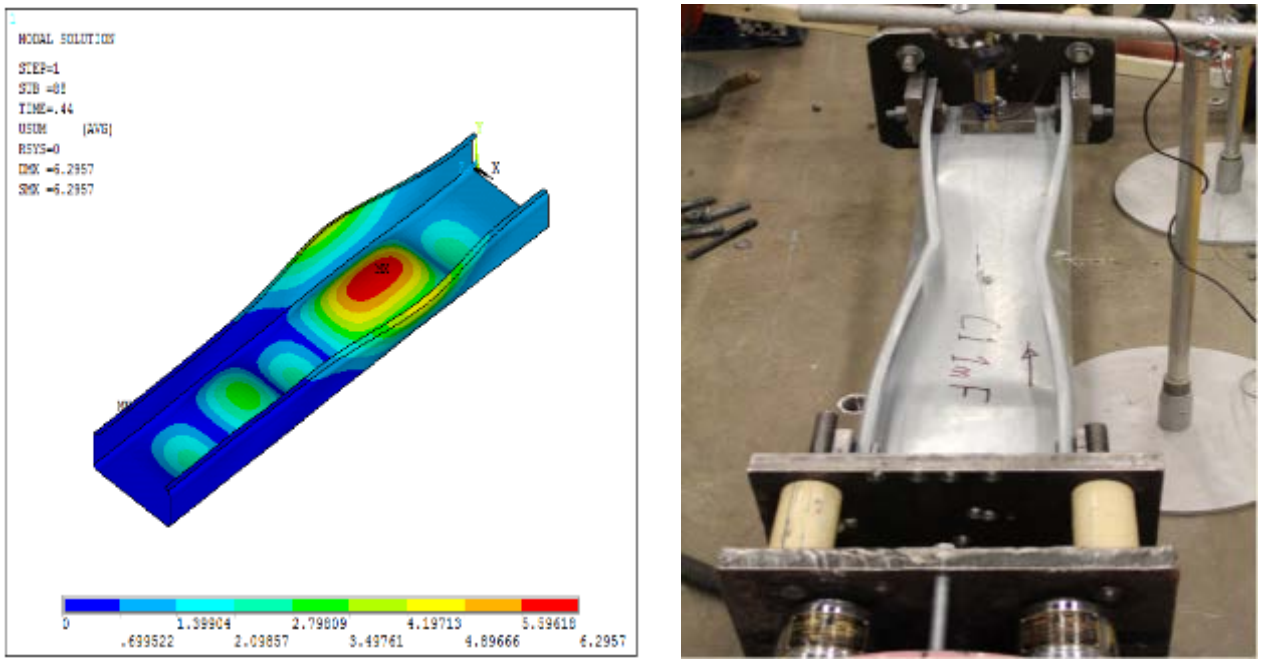

Figure (7-31) FEM and experimental buckling mode shape of 1.0 m length of C-section with fixed end conditions.

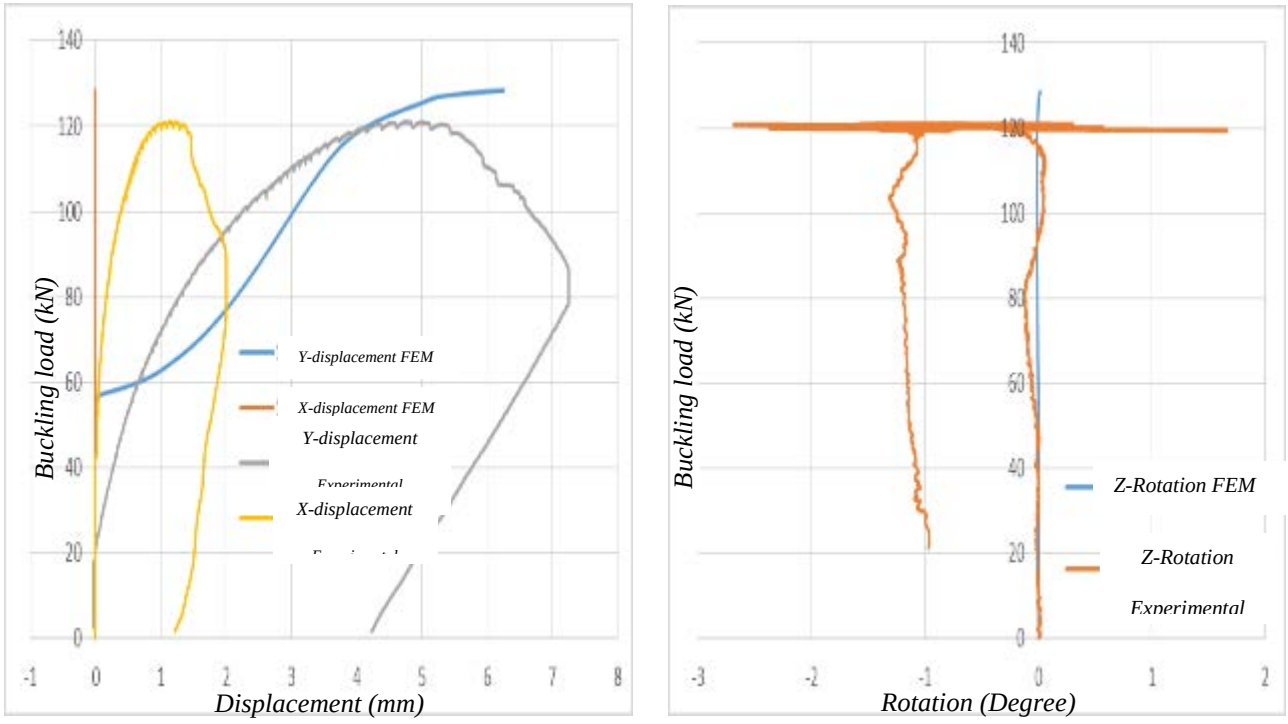

Figure (7-32) FEM and experimental load-deformation relations for 1.0 m length at the mid web of 0.5L of the C-section with fixed end conditions.

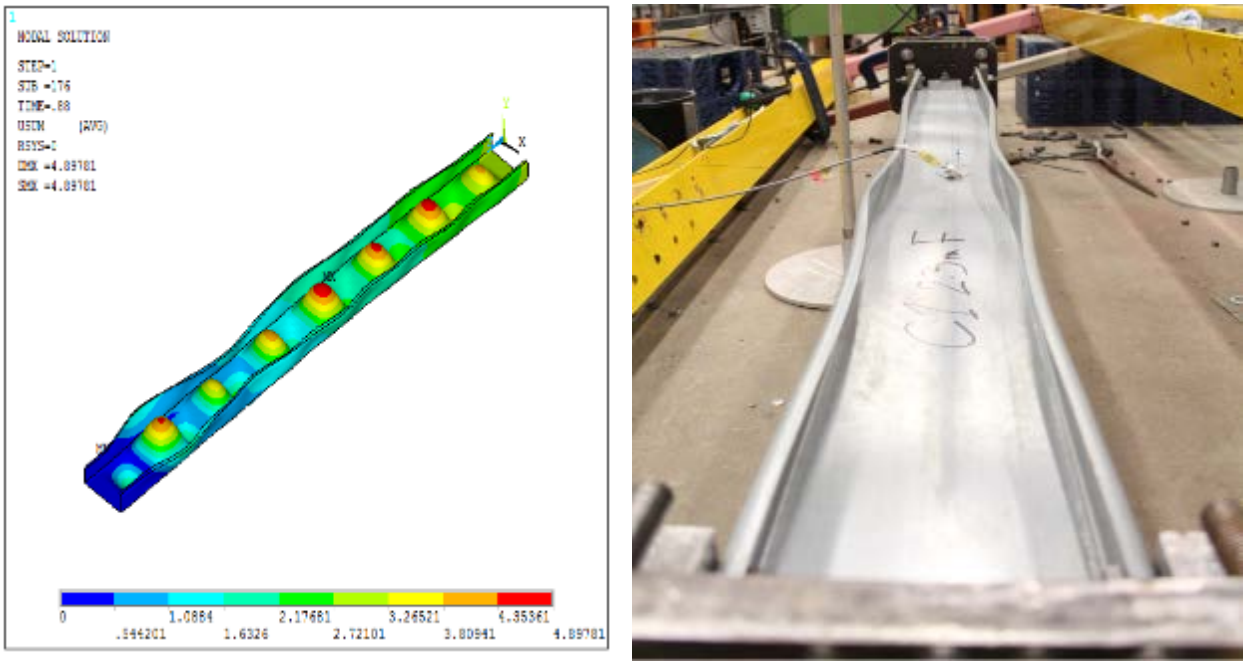

Figure (7-33) FEM and experimental buckling mode shape of 2.3 m length of C-section with fixed end conditions.

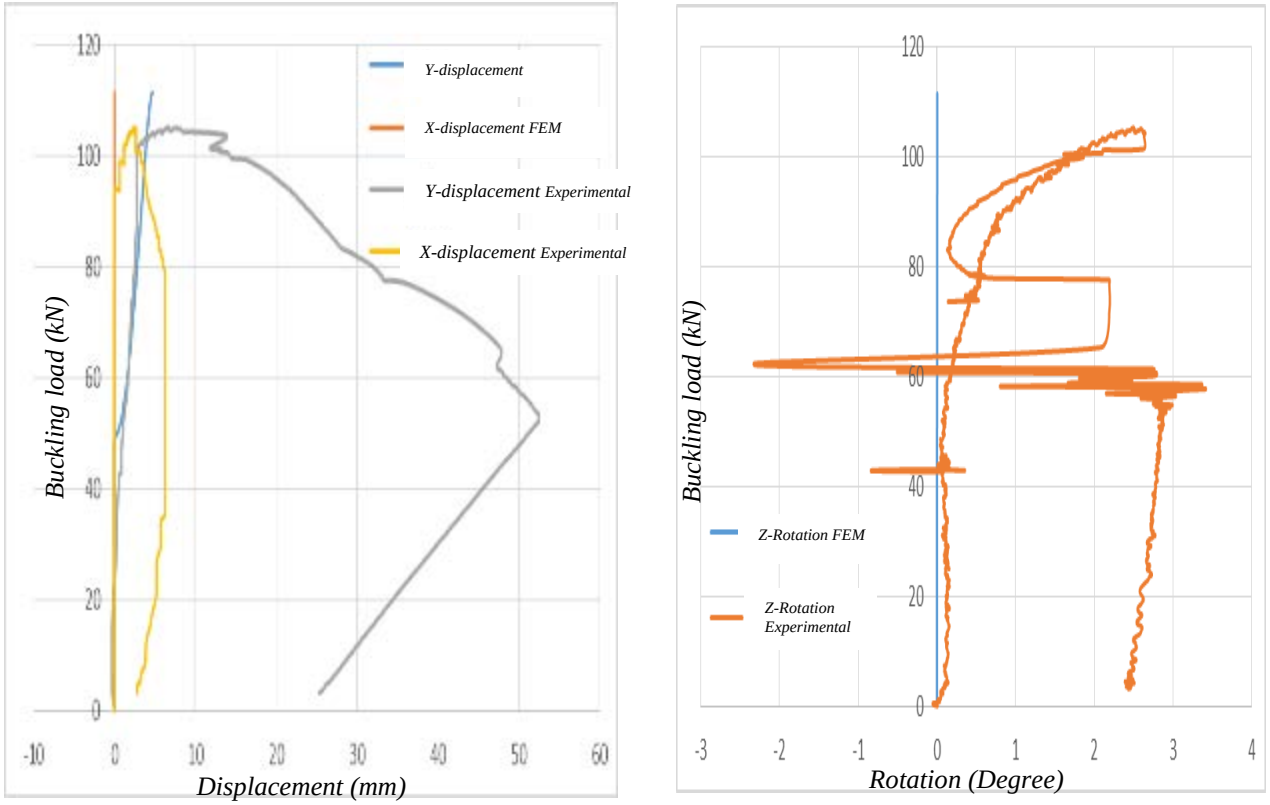

Figure (7-34) FEM and experimental load-deformation relations for 2.3 m length at the mid web of 0.5L of the C-section with fixed end conditions.

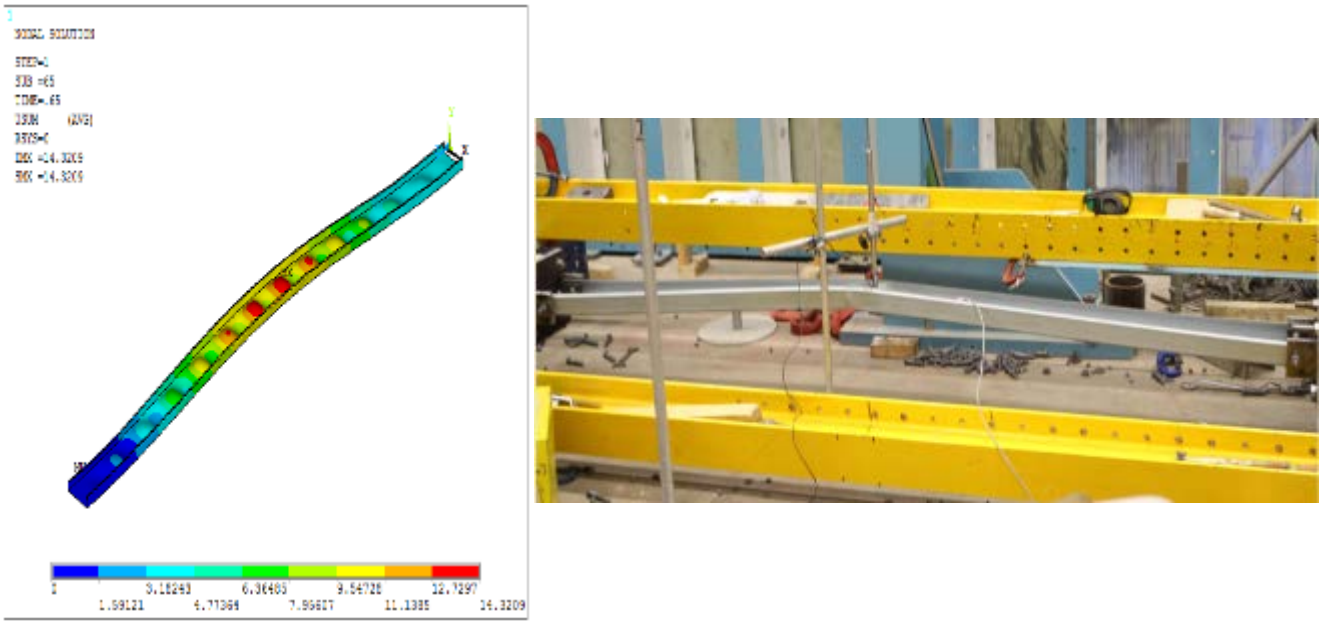

Figure (7-35) FEM and experimental buckling mode shape of 4.0 m length of C-section with fixed end conditions.

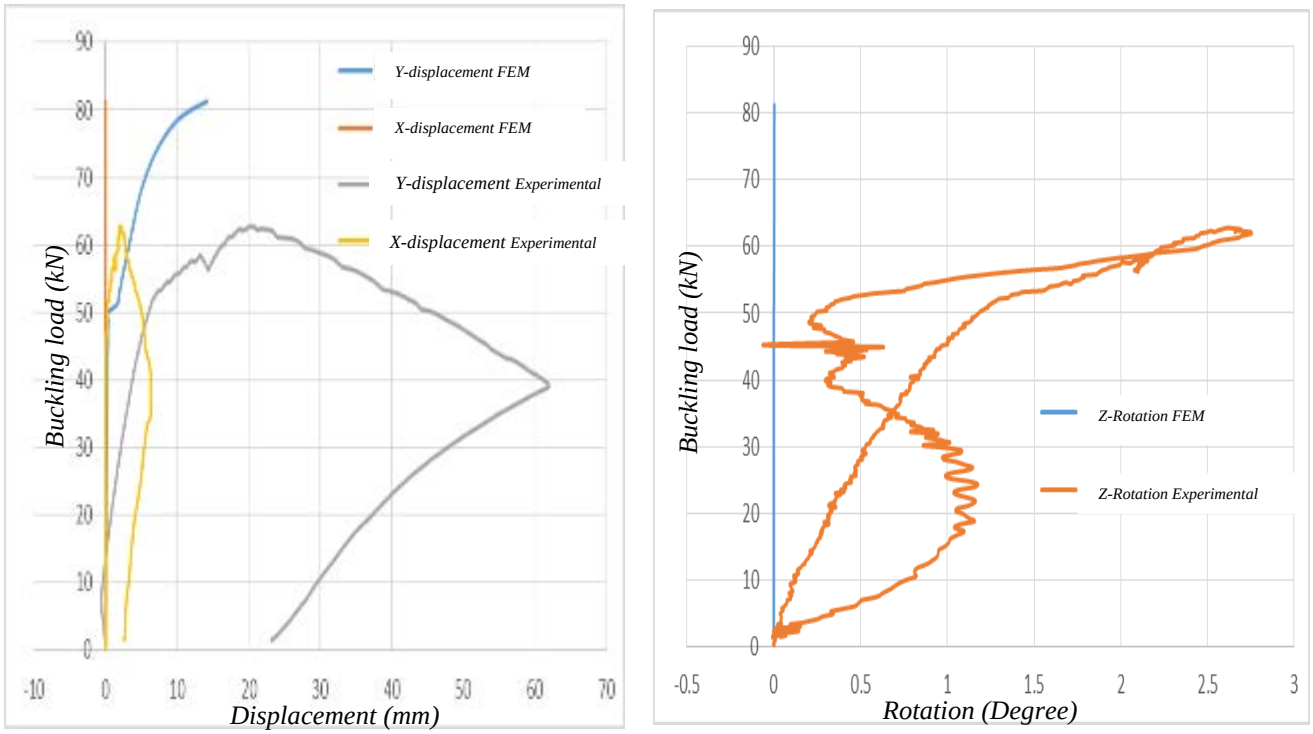

Figure (7-36) FEM and experimental load-deformation relations for 4.0 m length at the mid web of 0.5L of the C-section with fixed end conditions.

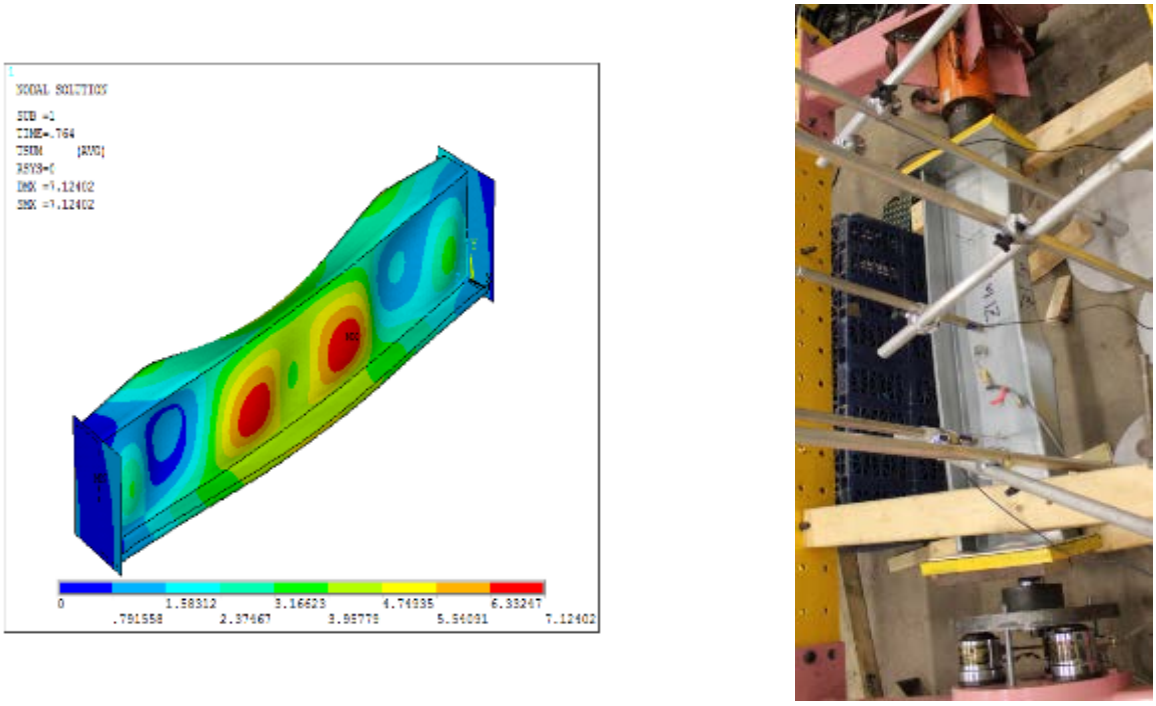

Figure (7-37) FEM and experimental buckling mode shape of 1.0 m length of Z-section with pinned end conditions.

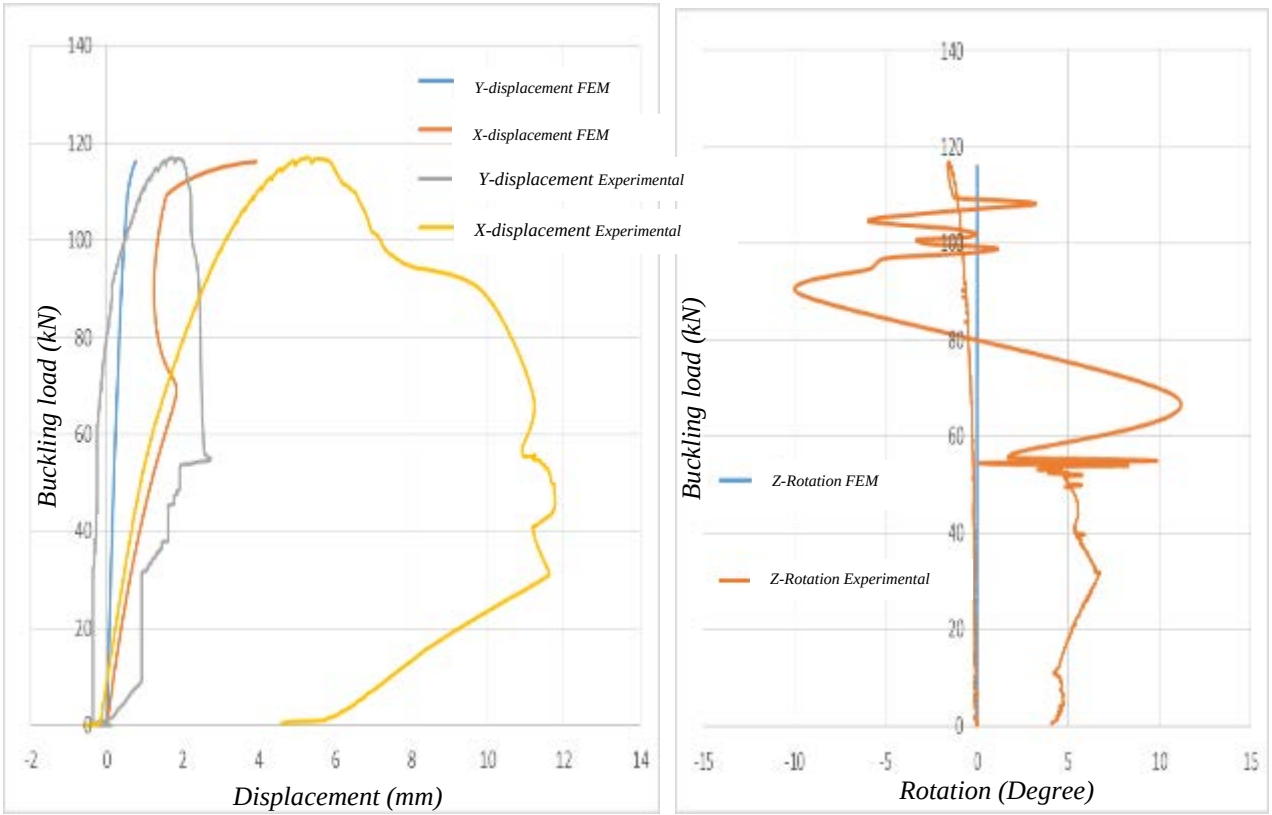

Figure (7-38) FEM and experimental load-deformation relations for 1.0 m length at the mid web of 0.5L of the Z-section with pinned end conditions.

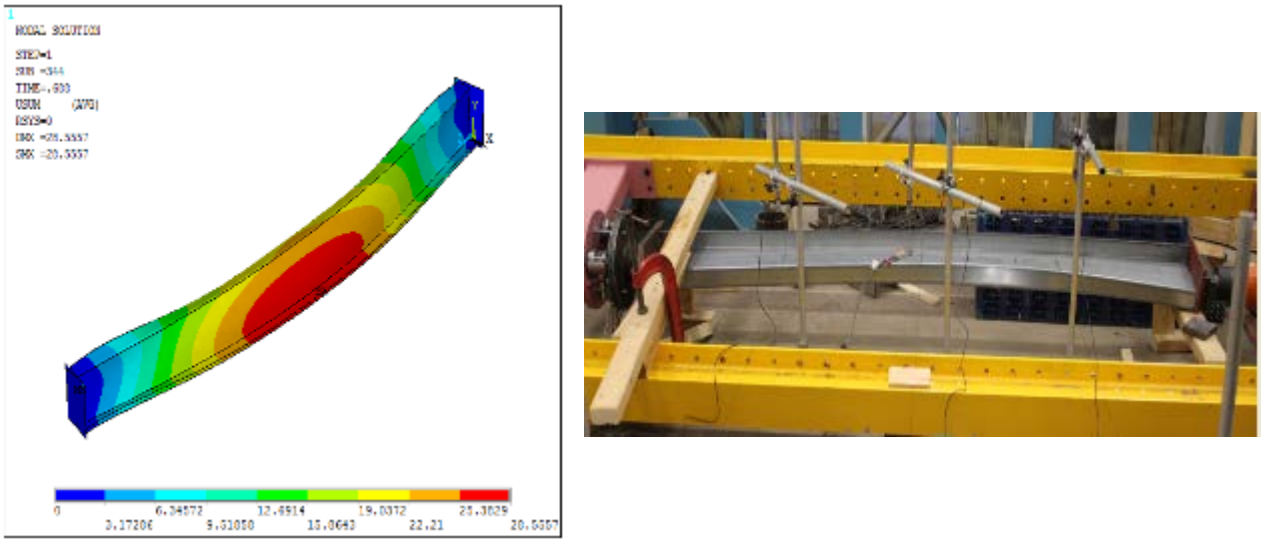

Figure (7-39) FEM and experimental buckling mode shape of 2.3 m length of Z-section with pinned end conditions.

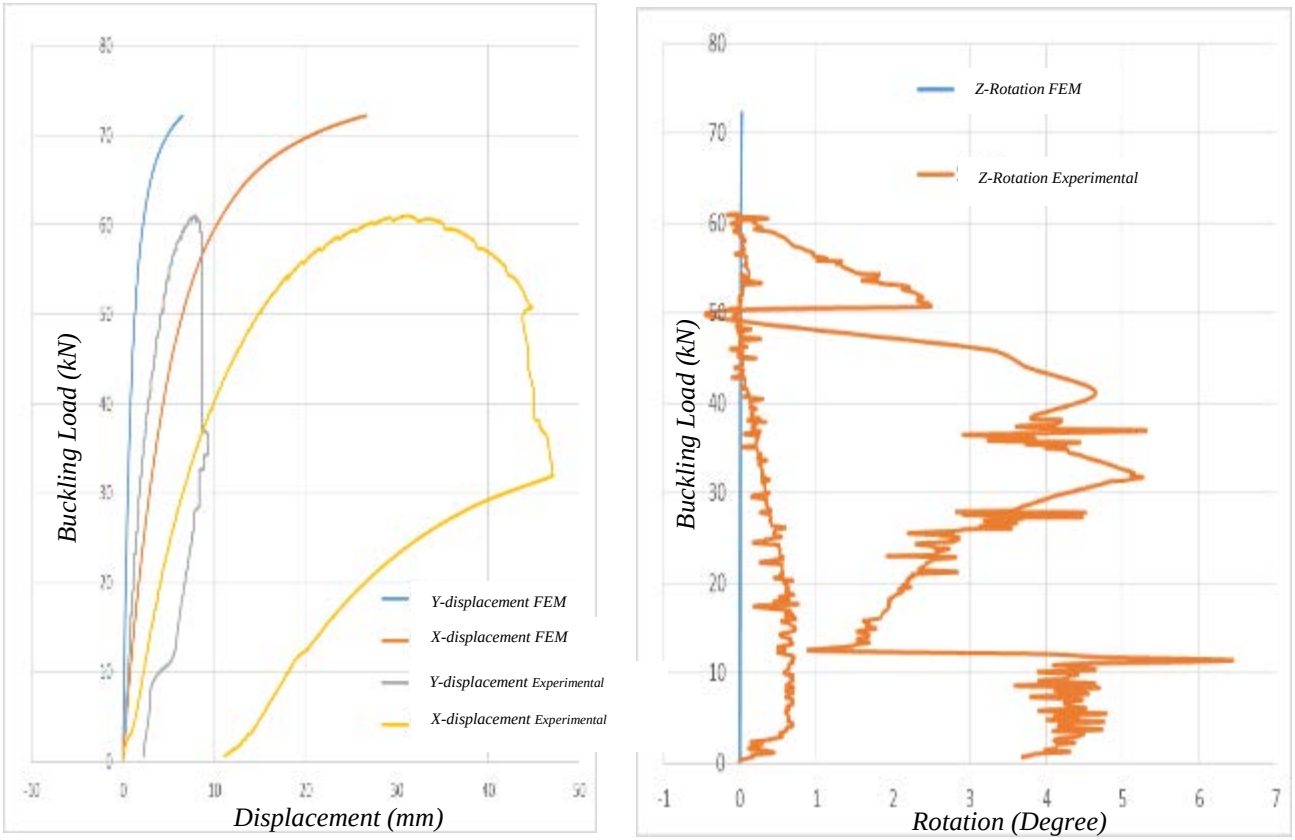

Figure (7-40) FEM and experimental load-deformation relations for 2.3 m length at the mid web of 0.5L of the Z-section with pinned end conditions.

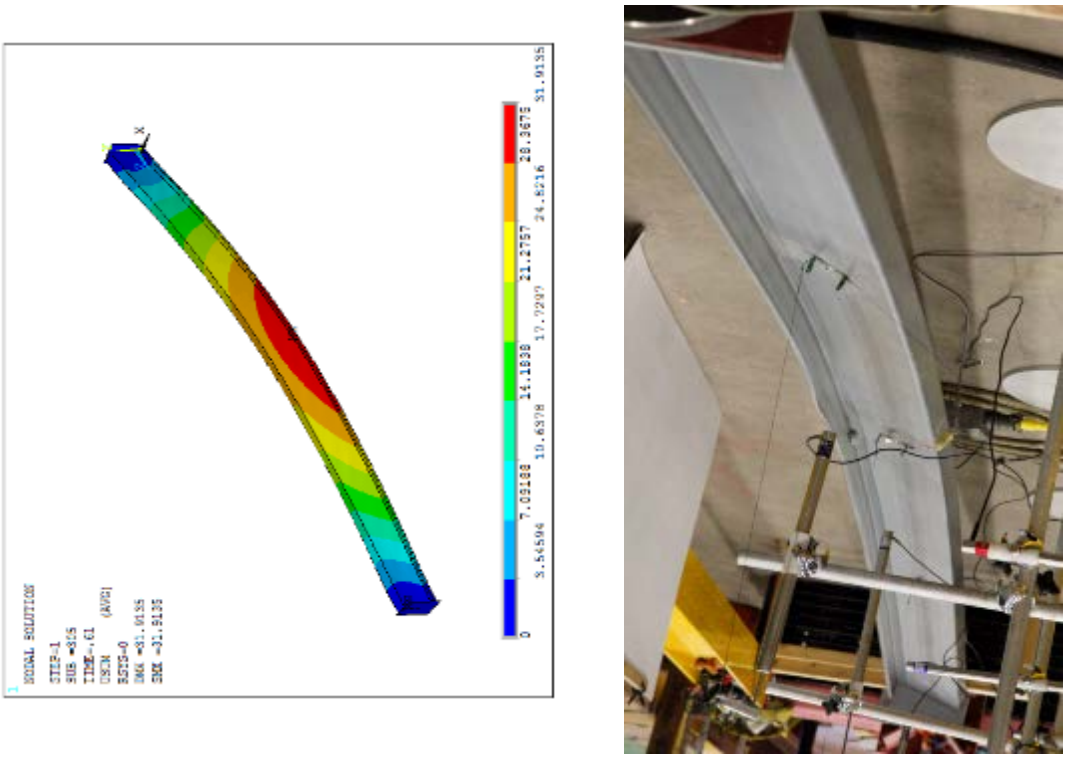

Figure (7-41) FEM and experimental buckling mode shape of 4.0 m length of Z-section with pinned end conditions.

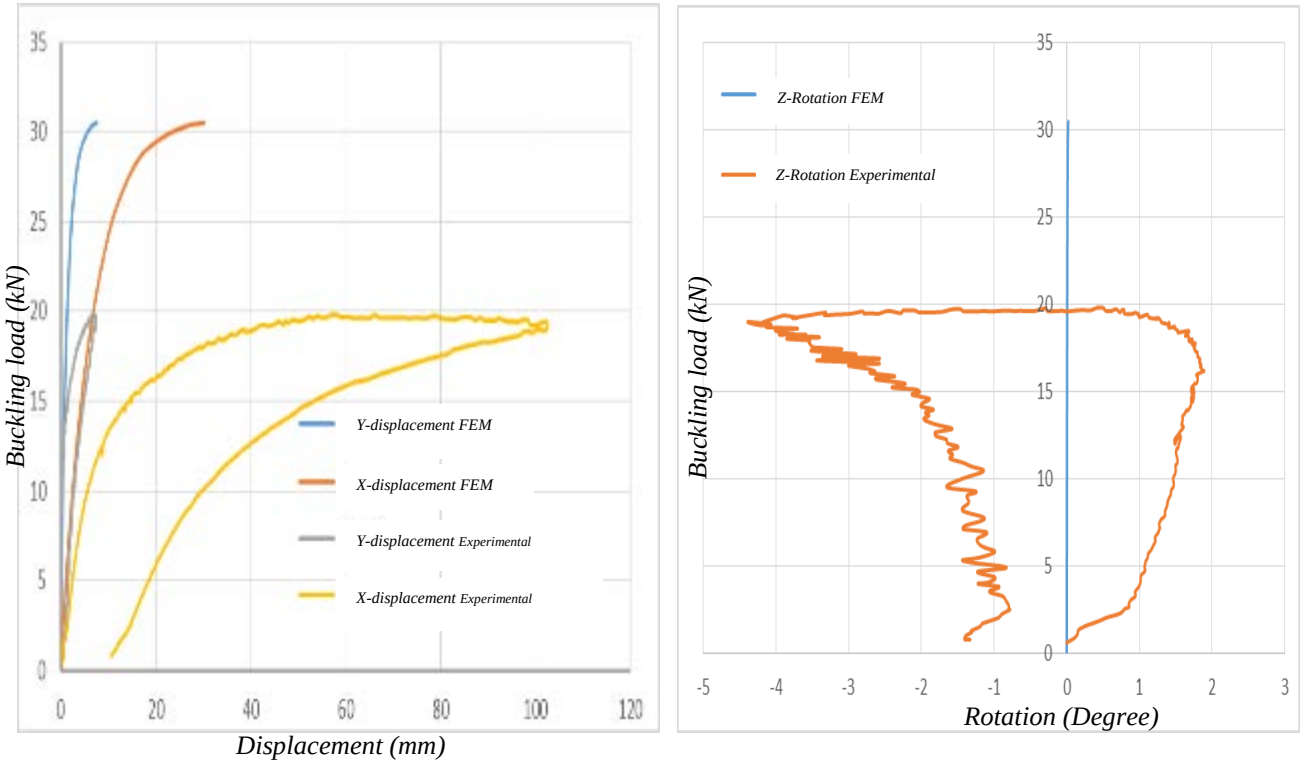

Figure (7-42) FEM and experimental load-deformation relations for 4.0 m length at the mid web of 0.5L of the Z-section with pinned end conditions.

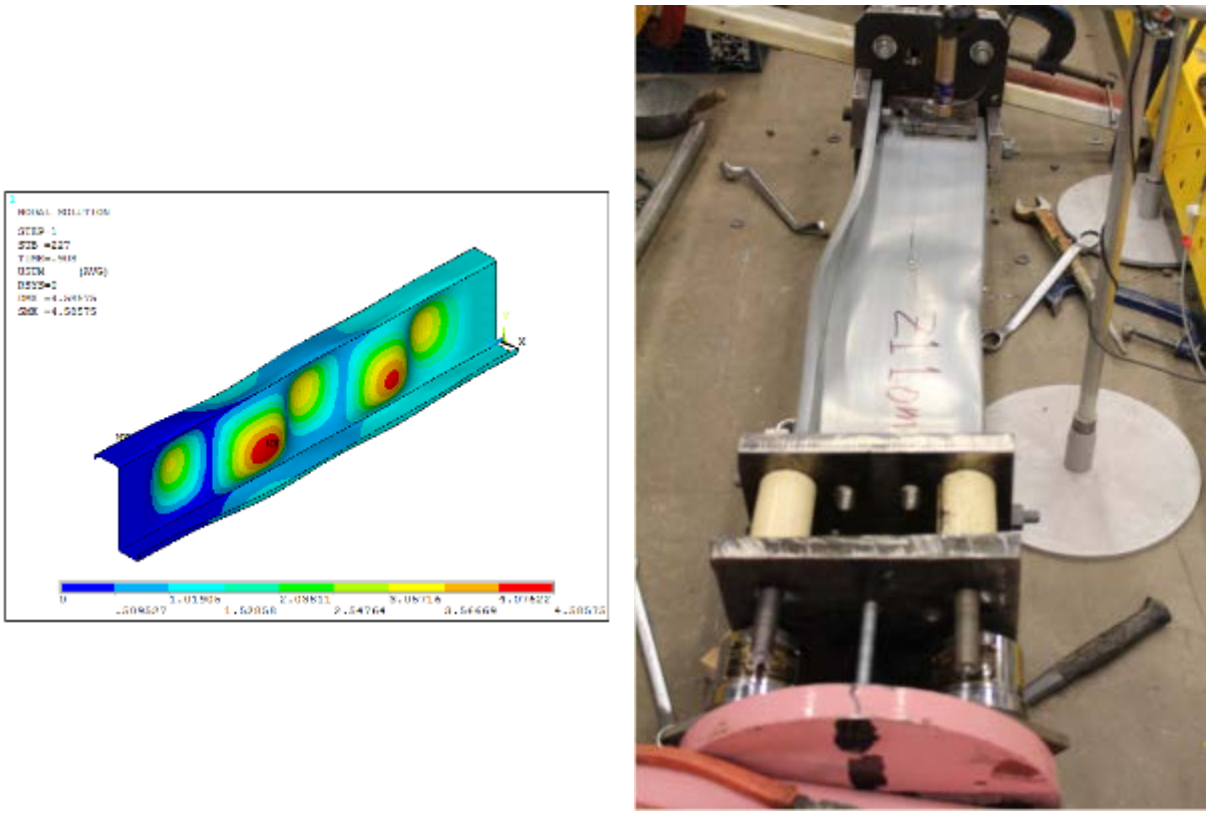

Figure (7-43) FEM and experimental buckling mode shape of 1.0 m length of Z-section with fixed end conditions.

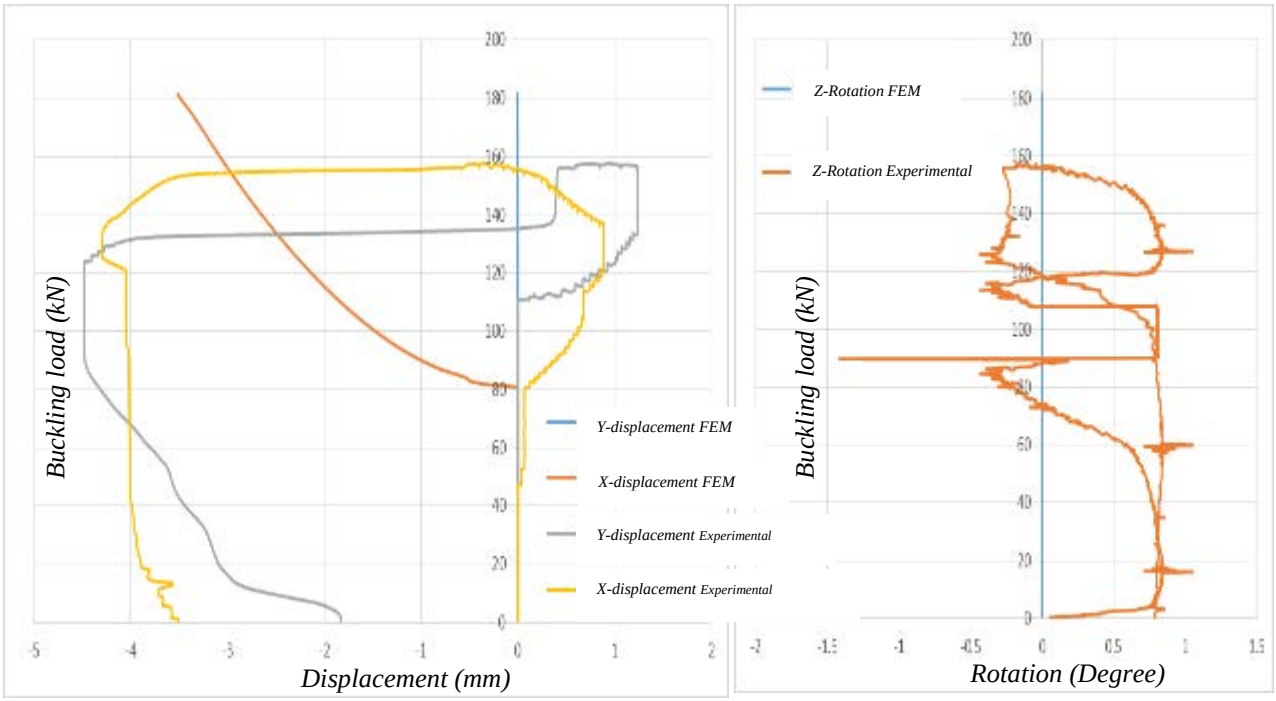

Figure (7-44) FEM and experimental load-deformation relations for 1.0 m length at the mid web of 0.5L of the Z-section with fixed ends conditions.

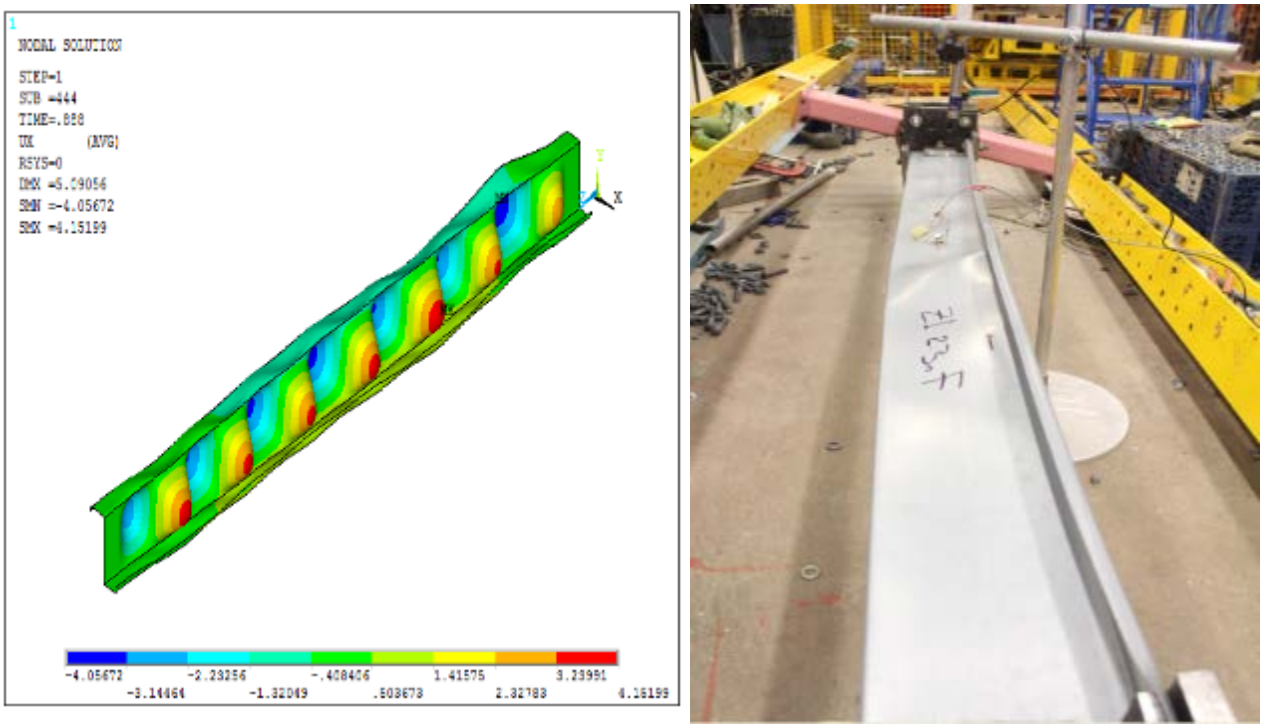

Figure (7-45) FEM and experimental buckling mode shape of 2.3 m length of Z-section with fixed end conditions.

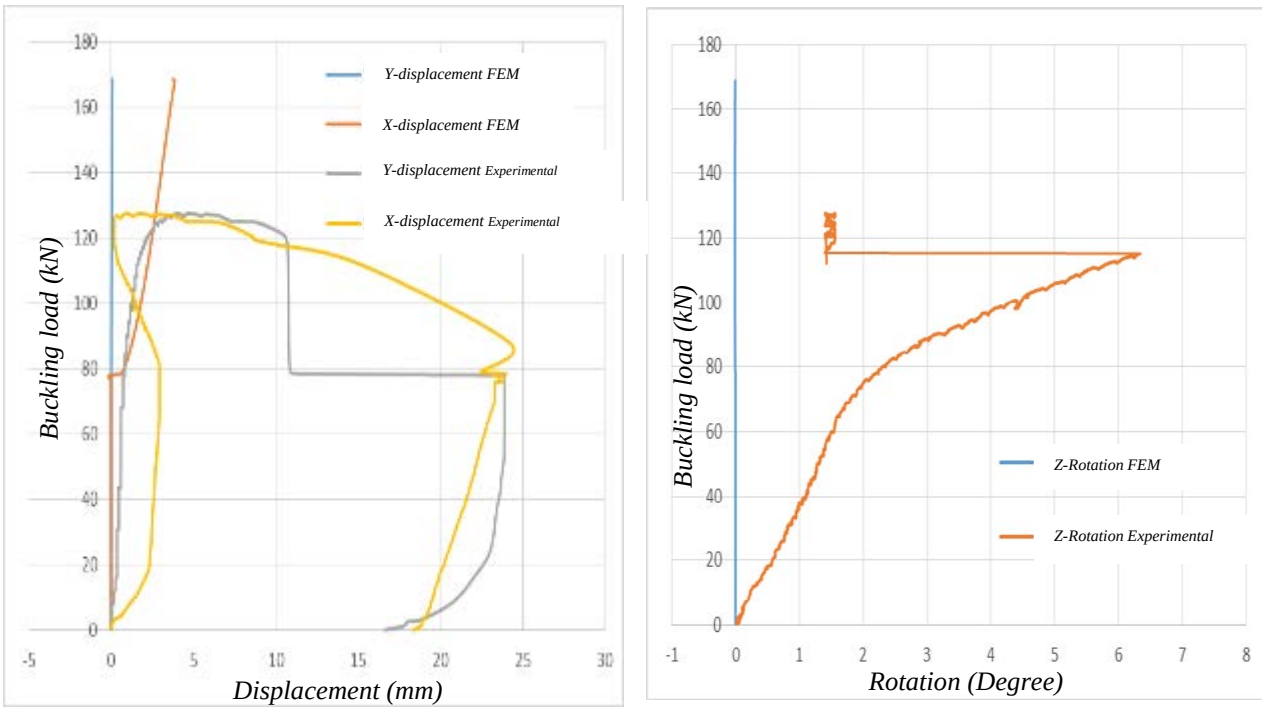

Figure (7-46) FEM and experimental load-deformation relations for 2.3 m length at the mid web of 0.5L of the Z-section with fixed end conditions.

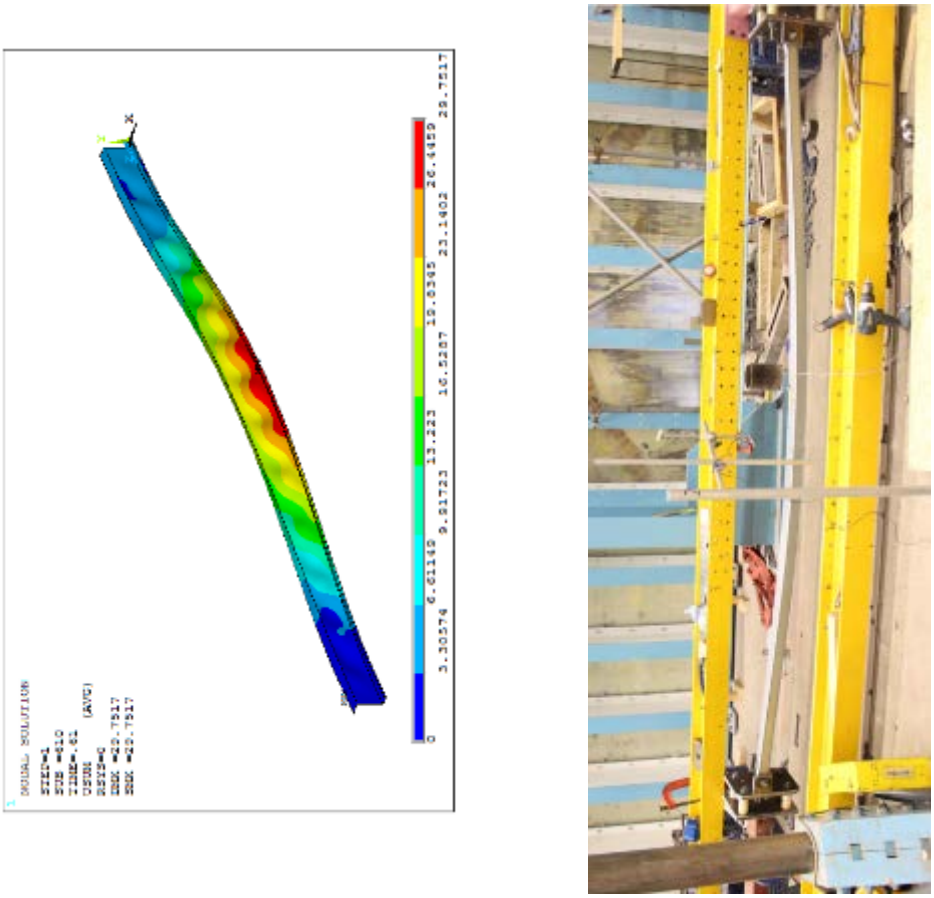

Figure (7-47) FEM and experimental buckling mode shape of 4.0 m length of Z-section with fixed end conditions.

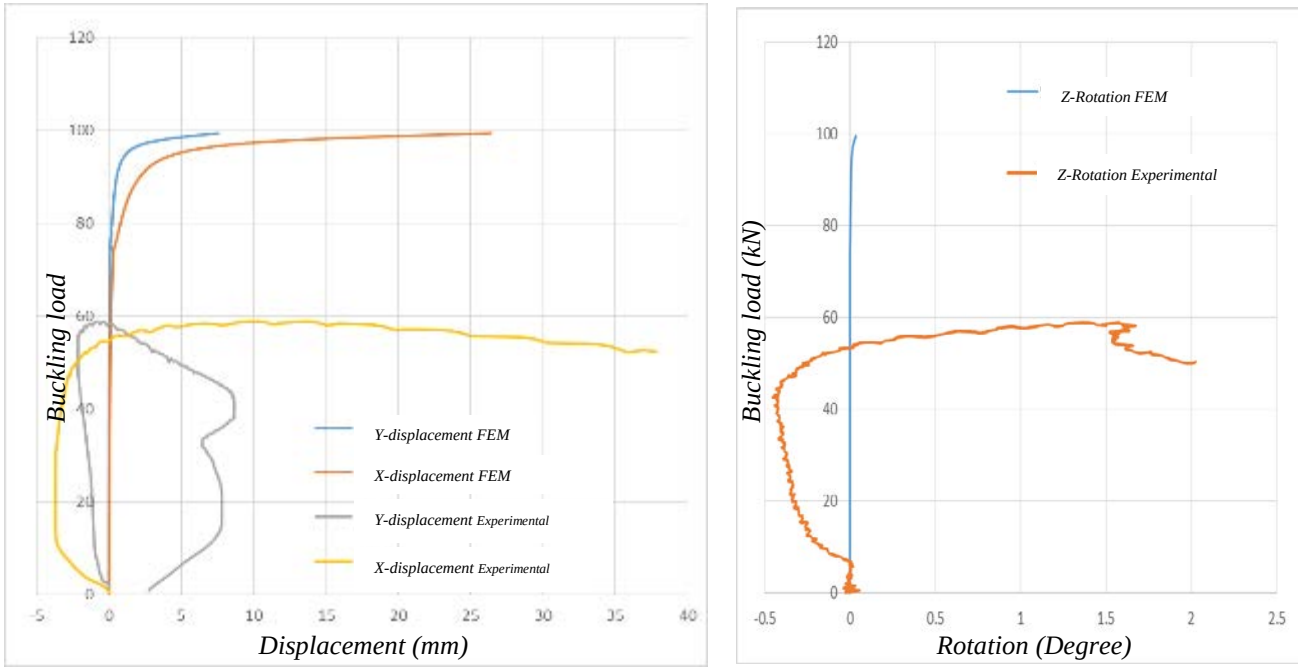

Figure (7-48) FEM and experimental load-deformation relations for 4.0 m length at the mid web of 0.5L of the Z-section with fixed end conditions.

CHAPTER EIGHT

GENERAL CONCLUSIONS

AND FURTHER WORK

CHAPTER EIGHT

GENERAL CONCLUSIONS AND FURTHER WORK

8.1 Summary

This thesis has presented a detailed investigation into the buckling behaviour of cold-formed steel lipped C and Z sections subject to axial load using the finite element method and the generalized beam theory. Models which examined both linear critical buckling analyses and non-linear geometric and material analysis with the effects of boundary conditions (pinned and fixed end conditions) were produced. These results were verified by experimental tests comprising two types of cross-sections (lipped C & Z sections).

In the first chapter, an introductory review of cold-formed steel processing methods was presented. Chapter two presented a literature review of current research into the analysis of buckling, including experimental testing of cold-formed steel members. Chapter three addresses the derivation of Schardt's GBT and establishes a unified energy formulation for it (applicable to open non-branched cross sections only, since it follows Schardt's basic assumptions. Chapter four presented further applications of GBT theory where the generation of eigen-buckling loads were obtained using the finite difference method to solve the differential equations. This was achieved through a computer code written in Matlab. The Matlab code was then extended to address nonlinear geometry incorporating an initial imperfection and a load stepping procedure. Linear problems (member subjected to axial load), linear analysis of buckling problems (Eigenvalue problem) in both single and combined modes and non-linear geometric analysis problems were solved for different types of boundary conditions (pinned-pinned, pinned-fixed and fixed-fixed boundary conditions). All of these analyses were verified through illustrative examples.

For the second phase of this research, Chapter five presents the evaluation of buckling behaviour using the finite element method (ANSYS). Linear and nonlinear analyses were carried out, examining the effects of the element type, element size, element aspect ratio and the local and global boundary conditions. Also, these analyses were explained by the demonstrative examples of cold-formed cladding section with pinned and fixed end conditions.

In the third phase of this research, Chapter six, the experimental test program was presented. All of the samples were subject to axial loading and these were used to verify the results from the numerical analysis methods (incorporating different cross-sections of cold-formed steel and variable lengths and boundary condition types). Preparation of the loading rig, the applied load, instrumentation, and an extensive investigation of the representation of the boundary conditions was presented. The representation of the boundary conditions as either pinned or fixed was carefully examined in the laboratory using three different arrangements, followed by the selection of the appropriate one for use in the main load testing program. In addition to the load tests, appropriate coupon tests provided material properties for use in the numerical analyses.

8.2 Conclusions

The most significant conclusions and developments obtained from this research are as follows:

- Improved knowledge and understanding of the GBT and the development of a new Matlab code program to calculate the GBT section properties of thin-walled open sections. This program was able to calculate the section properties with the higher order modes (local buckling) in the presence of intermediate nodes or without them. Intermediate nodes would only be required should higher order modes be necessary for extraction.
- Significantly improved knowledge and understanding of the buckling behaviour of cold-formed steel sections subjected to an axial load using the GBT by taking the advantage of its separation of mode failures. The new Matlab code was extended to calculate the linear buckling load in both cases of single and combined modes.
- The most significant development in the Matlab code was to extend it further to predict the failure load of cold-formed steel sections subject to axial load with the effects of the initial imperfection, using the unique characteristics of GBT. This development was only extended as far as attempting to predict failure initiated by global buckling modes (classical Euler type buckling).
- The use of GBT is easier to program than the conventional theories (rod-theory, Euler-Bernoulli beam theory and non-uniform torsion of Vlasov torsion theory) because it uses one general equation rather than many equations with different parameters as for conventional theories.

- The GBT analysis provides a clearer understanding of higher order modes local buckling of general beam behaviour (5^{th} and more) which is difficult to visualise in conventional theories.
- The use of first order GBT equations to solve linear problems (beam subjected to axial load) gives a more useful illustration of the effect of each mode individually, i.e. it can deal with each mode's characteristic behaviour (deflection, stresses etc.) individually for design purposes.
- In buckling analysis, GBT provides information as to the mode shapes along the length of the beam; therefore, it will be easy to examine each mode in the design process.
- In general buckling analysis, the distortional buckling modes occur in lengths which are among the more commonly used lengths in the design of cold-form steel structures. So distortional buckling modes may be critical modes from the design point of view.
- The linear buckling loads obtained from GBT and the finite element analyses provide a good comparison, thereby providing confidence in the use GBT for design purposes.
- It was seen that the number of half sine waves associated with local plate buckling mode shapes in the local zone for both cross-section shapes with different boundary condition types was exactly the same for both linear analysis methods of the finite element analysis (ANSYS) and the finite difference analysis of GBT. Again this provided substantiation that both linear analysis methods are predicting the correct eigen-buckling mode shape. Also both linear analysis methods predicted one-half sine wave for each of the cross-section shapes with different boundary condition types, comparable to the Euler buckling mode shapes (lateral and torsional buckling mode shapes).
- It can be concluded that the results of both the buckling loads and buckling mode shapes show a good comparison in each of the linear analyses of the finite element and GBT. The finite element method (ANSYS) requires a longer time to process and develop than GBT. This is true for both the modelling and the solution processes of each separate length. So GBT was the ideal analysis method to get a quick prediction of linear buckling loads and mode shapes of thin-walled steel structures due to the relative accuracy of results and time saved.

- For the GBT non-linear failure analysis, the non-linear buckling loads always less than the linear buckling loads which is as expected because of the geometrical effect of the initial imperfection. However, the non-linear GBT analysis could not produce the effects of post-buckling which appears clearly in the short and medium lengths, because it does not take into account the material non-linearity and cross sectional geometry effects. So, future development of GBT to predict post buckling effects for members exhibiting local buckling will need to addressed this.
- For the finite element method, post-buckling effects are evident as ANSYS will capture the 3D geometric local behaviour of the plates which form the member, and also the material nonlinearity. Hence the failure load was significantly larger than the linear eigen-buckling load for both the local and distortional mode shape zones, solely due to post-buckling effects. On the other hand, the non-linear load was less than the linear buckling load due to the effects of initial imperfection for the global buckling modes.
- The experimental test results corroborated both the non-linear finite element (ANSYS) and the non-linear GBT analyses in the global buckling zone for both the pinned and fixed end boundary conditions. In the local and distortional buckling zones, the experimental test results were enveloped by the non-linear finite element analysis (ANSYS). This is expected as the non-linear finite element analysis models the boundaries as perfect restraints i.e. pinned or fixed end conditions. In the laboratory simulations, it is impossible to achieve these end conditions. The extent to which the boundary conditions can be represented accurately is much more uncertain with shorter members and higher axial loading.
- It can be observed that the effect of boundary conditions is small on the buckling load but the zones of local and distortional mode shape for the fixed end condition were much wider than the zones for pinned end condition. This means the member will carry more buckling load by extending the local plate buckling zone (due to the boundary condition change from pinned end conditions to fixed end conditions).

8.3 Further work

Evidently, there is much to be investigated with regards the structural stability of thin-walled prismatic members. Several of the tasks presented below are recommended to be

addressed by future work hopefully providing a broader application of the GBT theory and finite element method, to the behaviour of thin-walled members in general. There is much to be done to develop GBT to address other cross section shapes, other load cases, and examine various supporting conditions such as introducing rotational and translational stiffness. Some further suggestions are listed below.

- Improve and develop new (and existing) software programs to calculate the GBT section properties of closed sections of thin-walled structures by adding the shear terms for the second order generalized beam theory formulation and evaluate its effects on the buckling behaviour for both the buckling load and the buckling mode shape types.
- Improve and develop a new software programs to calculate the GBT section properties of branched sections of thin-walled structures and take the bifurcation effects into consideration.
- Improve and develop the GBT analysis methods to carry out the effects of post-buckling in the cold-formed steel sections which was more sensitive especially for shorter column lengths.
- Continue the research to predict the effects of the manufactural cross-section imperfections on buckling load and its mode shape by using the unique advantages of mode separation for the GBT and the finite analysis method. The Matlab program developed in this research was able to evaluate these manufacturing cross-sectional imperfections for different member cross-sections and end conditions, but this was outside the scope of work intended to be presented in this thesis.
- Use the unique characterises of GBT to evaluate the actual behaviour of cold-formed steel sections subjected to concentrated or uniform bending moment, including torque, accounting for the effects of both the global and cross-section initial imperfections which more commonly occur in the intermediate (bending moment) and edge (torsion) purlins of structures.
- Develop GBT to be more user friendly (output the cross sectional displacements on a plot).
- Formulate an automatic procedure for ANSYS which will allow a scripted file to undertake instant pre-processing. In fact, all of the solution could then be batched and left to run for a range of sections.

- FEA can obviously deal with post buckling effects, so simpler plate member models can be developed (closed sections, branched sections) to examine the range of uncertainty in post-buckling prediction.
- More laboratory tests should be undertaken to examine the effects of different boundary conditions in the cases of axial, bending and torsion individually and interaction effects.

References

Abambres, M., Camotim, D., & Silvestre, N. (2013). GBT-based first-order analysis of elastic-plastic thin-walled steel members exhibiting strain-hardening. *The IES Journal Part A: Civil & Structural Engineering*. Volume 6, 119-134.

Abambres, M., Camotim, D., & Silvestre, N. (2014). GBT-based elastic–plastic post-buckling analysis of stainless steel thin-walled members. *Thin-Walled Structures*, 83, 85-102.

Akin, J. E. (2009). *FEA-Buckling Analysis. (pp. 182-188).* Houston, Texas : Rice University.

Ali, B. A., Saad, S., Osman, M. H., & Ahmad, Y. (2011). Finite element analysis of cold-formed steel connections. *International Journal of Engineering (IJE), 5(2), 55-61.*

Ananthi, G., Palani, G., & Iyer, N. R. (2015). Numerical and theoretical studies on cold-formed steel unlipped channels subjected to axial compression. *Latin American Journal of Solids and Structures, 12(1), 1-17.*

Ansys, I. (2007). *ANSYS advanced analysis techniques guide. Ansys Help*. published in the USA.

Bailey, C., Burgess, I., & Plank, R. (1996). The lateral-torsional buckling of unrestrained steel beams in fire. *Journal of Constructional Steel Research, 36(2), 101-119.*

Basaglia, C., Camotim, D., & Silvestre, N. (2015). Buckling and vibration analysis of cold-formed steel CHS members and frames using Generalized Beam Theory. *International Journal of Structural Stability and Dynamics, 15(08), 1540021.*

Bebiano, R., Silvestre, N., & Camotim, D. (2008). GBTUL-a code for the buckling analysis of cold-formed steel members. *Nineteenth International Specialty Conference on Cold-Formed Steel Structures.* St. Louis, Missouri, U.S.A: Missouri University of Science and Technology.

Bleich, F. (1952). *Buckling strength of metal structures*. USA: McGraw-Hill.

Brune, B., & Ungermann, D. (2008). Coupled instabilities of cold-formed steel members in minor axis bending. *Fifth International Conference on Coupled Instabilities in Metal Structures CIMS2008.*

BSI (2007). Eurocode 3: Design of Steel Structures-Part 1-2: General Rules-Structural Fire Design. *European Committee for Standardisation*. London.

BSI (2014). Eurocode 3: Design of Steel Structures Part 1-3 – Design of Cold-formed Steel Structures. European Committee for Standardisation. London.

Bulson. (1970). *The Stability of Flat Plates*. London: Chatto and Windus Ltd.

Bulson, & Allen, H. (1980). *Background to buckling*. US :McGraw-Hill Inc.

Casafont, M., Pastor, M. M., Roure, F., & Peköz, T. (2011). An experimental investigation of distortional buckling of steel storage rack columns. *Thin-Walled Structures, 49(8), 933-946.*

Cava, D., Camotim, D., Dinis, P., & Madeo, A. (2016). Numerical investigation and direct strength design of cold-formed steel lipped channel columns experiencing local–distortional–global interaction. *Thin-Walled Structures, 105, 231-247.*

Celebi, N. M., Winter, G., & Pekoz, T. (1972). Diaphraghm Braced Channel and Z-section Beams: Cornell University. *Center for Cold-Formed Steel Structures Library*. St. Louis, Missouri, U.S.A: Missouri University of Science and Technology.

Chu, X.-t., Kettle, R., & Li, L.-y. (2004). Lateral-torsion buckling analysis of partial-laterally restrained thin-walled channel-section beams. *Journal of Constructional Steel Research, 60(8), 1159-1175.*

Code, P. (2007). Eurocode 3: Design of Steel Structures-Part 1-2: General Rules-Structural Fire Design. London: European Committee for Standardisation.

Craveiro, H. D., Paulo, J., Rodrigues, C., & Laím, L. (2016). Buckling resistance of axially loaded cold-formed steel columns. *Thin-Walled Structures, 106, 358-375.*

Davies, J. (2000). Recent research advances in cold-formed steel structures. *Journal of Constructional Steel Research, 55(1), 267-288.*

Davies, J., & Jiang, C. (1996a). Design of thin-walled beams for distortional buckling. *the Thirteenth International Specialty Conference on Cold-Formed Steel Structures.* St. Louis, Missouri, U.S.A: Missouri University of Science and Technology.

Davies, J., & Jiang, C. (1996b). Non-linear buckling analysis of thin-walled metal columns. *the 13th International Specialty Conference on Cold-Formed Steel Structures.* St. Louis, Missouri, U.S.A: Missouri University of Science and Technology.

Davies, J., & Jiang, C. (1998). Design for distortional buckling. *Journal of Constructional Steel Research, 1(46), 174-175.*

Davies, J. M., & Bryan, E. R. (1982). *Manual of stressed skin diaphragm design*. London: Wiley.

Dawe, D. (2002). Use of the finite strip method in predicting the behaviour of composite laminated structures. *Composite Structures, 57(1), 11-36.*

de Barros Chodraui, G. M., Neto, J. M., Gonçalves, R. M., & Malite, M. (2006). Distortional Buckling of Cold-Formed Steel Members 1. *Journal of Structural Engineering, 132(4), 636-639.*

Dinis, P. B., Camotim, D., & Silvestre, N. (2007). FEM-based analysis of the local-plate/distortional mode interaction in cold-formed steel lipped channel columns. *Computers & Structures, 85(19), 1461-1474.*

dos Santos, E. S., Batista, E. M., & Camotim, D. (2012). Experimental investigation concerning lipped channel columns undergoing local–distortional–global buckling mode interaction. *Thin-Walled Structures, 54, 19-34.*

El-Zanaty, M. H., & Murray, D. W. (1983). Nonlinear finite element analysis of steel frames. *Journal of Structural Engineering, 109(2), 353-368.*

Ellifrit, D., Sputo, T., & Haynes, J. (1991). *Flexural strength and deflections of discretely braced cold formed steel channel and zee sections.* USA: American Iron and Steel Institute.

Galambos, T. V. (1998). *Guide to stability design criteria for metal structures*. New York: John Wiley & Sons. 5th ed.

Godat, A., Legeron, F., & Bazonga, D. (2012). Stability investigation of local buckling behavior of tubular polygon columns under concentric compression. *Thin-Walled Structures, 53, 131-140.*

Gonçalves, R., Dinis, P., & Camotim, D. (2009). GBT formulation to analyse the first-order and buckling behaviour of thin-walled members with arbitrary cross-sections. *Thin-Walled Structures, 47(5), 583-600.*

Gotluru, B. P., Schafer, B., & Peköz, T. (2000). Torsion in thin-walled cold-formed steel beams. *Thin-Walled Structures, 37(2), 127-145.*

Hakim, B. L., Soepriyanto, S., Korda, A. A., Sunendar, B., Purqon, A., Hidayat, T., Arimura, H. (2015). The ceramic brittleness of the pressed and sintered yttria zirconia-mullite-magnesia system. *the AIP Conference Proceedings Volume 1677, Issue 1 > 10.1063/1.4930730.* AIP Publishing LLC.

Hancock, & Rogers, C. (1998). Design of cold-formed steel structures of high strength steel. *Journal of Constructional Steel Research, 1(46), 167-168.*

Hancock, G. J. (2003). Cold-formed steel structures. *Journal of Constructional Steel Research, 59(4), 473-487.*

Hancock, G. J., Kwon, Y. B., & Bernard, E. S. (1994). Strength design curves for thin-walled sections undergoing distortional buckling. *Journal of Constructional Steel Research, 31(2-3), 169-186.*

Hansapinyo, C. (2015). Buckling Performance of Irregular Section Cold-Formed Steel Columns under Axially Concentric Loading. World Academy of Science, Engineering and Technology, *International Journal of Civil, Environmental, Structural, Construction and Architectural Engineering, 9(5), 542-548.* World Academy of Science, Engineering and Technology.

Hill, H.N., Lateral Buckling of Channels and Z Beams, *Transactions of the ASCE, Vol.119, 1954, pp.829-841*.

Institution, B. S. (1990). *The physical testing required for preferential uses*. London: European Committee for Standardisation.

Kavanagh, K., & Ellifritt, D. (1994). Design strengths of cold-formed channels in bending and torsion. *Journal of Structural Engineering, 120(5), 1599-1607.*

Kesti, J., & Davies, J. M. (1999). Local and distortional buckling of thin-walled short columns. *Thin-Walled Structures, 34(2), 115-134.*

Key, P. W., & Hancock, G. J. (1988). Nonlinear analysis of cold-formed sections using the finite strip method. *the 9th International Specialty Conference on ColdFormed Steel Structures.* St. Louis, Missouri, U.S.A: Missouri University of Science and Technology.

Khong, P. W. (1994). Behaviour of axially loaded lipped channel. *Journal of Constructional Steel Research, 28(3), 243-255.*

Kitipornchai, S., & Trahair, N. S. (1900). Inelastic buckling of simply supported steel I-beams. *Journal of the Structural Division*.

Kurowski, P. M. (2011). Teaching Finite Element Analysis for Design Engineers. the *Canadian Design Engineering Network (CDEN) Conference*. Toronto, Canada: The University of Western Ontario.

Kwon, & Hancock, G. J. (1992). Tests of cold-formed channels with local and distortional buckling. *Journal of Structural Engineering, 118(7), 1786-1803.*

Kwon, Y. B., Kim, B. S., & Hancock, G. J. (2009). Compression tests of high strength cold-formed steel channels with buckling interaction. *Journal of Constructional Steel Research, 65(2), 278-289.*

Lau, S. C. W., & Hancock, G. J. (1986). Buckling of thin flat-walled structures by a spline finite strip method. *Thin-Walled Structures, 4(4), 269-294.*

Leach, P. (1989). The generalised beam theory with finite difference applications. *11th International Specialty Conference on ColdFormed Steel Structures*. St. Louis, Missouri, U.S.A: Missouri University of Science and Technology.

Leach, P., & Davies, J. (1996). An experimental verification of the generalized beam theory applied to interactive buckling problems. *Thin-Walled Structures, 25(1), 61-79.*

Lecce, M., & Rasmussen, K. (2006). Distortional buckling of cold-formed stainless steel sections: Finite-element modeling and design. *Journal of Structural Engineering, 132(4), 505-514.*

Lengyel, P., & Cusens, A. (1983). A finite strip method for the geometrically nonlinear analysis of plate structures. *International Journal for Numerical Methods in Engineering, 19(3), 331-340.*

Macdonald, M., & Rhodes, J. (2005). Finite element modelling of cold formed stainless steel columns. *Acta Polytechnica, 45(3)*. Prague: Czech Technical University

Mahaarachchi, D., & Mahendran, M. (2005). Lateral buckling tests of LiteSteel beam sections. *Thin-Walled Structures, 47(1). pp. 109-119.*

McCann, F., Fang, C., Gardner, L., & Silvestre, N (2016). Postbuckling strength of slender elliptical hollow sections in compression. *Insights and Innovations in Structural Engineering, Mechanics and Computation.*

Megson, T. H. G. (2005). *Structural and stress analysis*. Oxford: Butterworth-Heinemann.

Najjar, S., & Burgess, I. (1996). A nonlinear analysis for three-dimensional steel frames in fire conditions. *Engineering Structures, 18(1), 77-89.*

Najjar, S. R. (1994). *Three-dimensional analysis of steel frames and subframes in fire*. Sheffield: University of Sheffield .

Narayanan, S., & Mahendran, M. (2003). Ultimate capacity of innovative cold-formed steel columns. *Journal of Constructional Steel Research, 59(4), 489-508.*

Pi, Y.-L., Put, B., & Trahair, N. S. (1998). Lateral buckling strengths of cold-formed channel section beams. *Journal of Structural Engineering, 124(10), 1182-1191*.

Pi, Y. L., & Trahair, N. (1995). Lateral buckling strengths of cold-formed rectangular hollow sections. *Thin-Walled Structures, 22(2), 71-95.*

Put, B. M., Pi, Y.-L., & Trahair, N. S. (1999). Bending and torsion of cold-formed channel beams. *Journal of Structural Engineering, 125(5), 540-546.*

Rondal, J. (2000). Cold formed steel members and structures: general report. J*ournal of Constructional Steel Research, 55(1), 155-158.*

Saab, H., & Nethercot, D. (1991). Modelling steel frame behaviour under fire conditions. *Engineering Structures, 13(4), 371-382.*

Schafer, B. (2002). Local, distortional, and Euler buckling of thin-walled columns. *Journal of Structural Engineering, 128(3), 289-299.*

Schafer, B. (2006). *CUFSM: Elastic buckling analysis of thin-walled members by finite strip analysis. CUFSM v4, 5.* USA.

Schafer, B., & Peköz, T. (1999). Laterally braced cold-formed steel flexural members with edge stiffened flanges. *Journal of Structural Engineering, 125(2), 118-127.*

Schardt, R. (1966). *Eine erweiterung der technischen biegetheorie zur berechnung prismatischer faltwerke. Der Stahlbau, 35, 161-171.* Germany.

Silva, N., Camotim, D., & Silvestre, N. (2008). Generalized beam theory formulation able to capture load application and localized web buckling effects. *the 19th international specialty conference on cold-formed steel structures.* USA: Missouri University of Science and Technology.

Silvestre, N. (2007). Generalised beam theory to analyse the buckling behaviour of circular cylindrical shells and tubes. *Thin-Walled Structures, 45(2), 185-198.*

Silvestre, N., & Camotim, D. (2003). Nonlinear generalized beam theory for cold-formed steel members. *International Journal of Structural Stability and Dynamics, 3(04), 461-490.*

Silvestre, N., & Camotim, D. (2006). GBT-based local and global vibration analysis of loaded composite open-section thin-walled members. *International Journal of Structural Stability and Dynamics, 6(01), 1-29.*

Silvestre, N., Camotim, D., & Dinis, P. B. (2012). Post-buckling behaviour and direct strength design of lipped channel columns experiencing local/distortional interaction. *Journal of Constructional Steel Research, 73, 12-30.*

Silvestre , Abambres, M., & Camotim, D. (2013). Physically non-linear GBT analysis of thin-walled members. *Computers & Structures, 129, 148-165.*

Simão, F. P. S. d. S. (2007). *Post-buckling bifurcational analysis of thin-walled prismatic members in the context of the generalized beam theory*. Coimbra : University of Coimbra.

Sivakumaran, K., & Abdel-Rahman, N. (1998). A finite element analysis model for the behaviour of cold-formed steel members. *Thin-Walled Structures, 31(4), 305-324.*

Taig, G., & Ranzi, G. (2014). Generalised beam theory (GBT) for stiffened sections. *International Journal of Steel Structures, 14(2), 381-397.*

Thombare, C. N., Sangle, K. K., & Mohitkar, V. M. (2016). Nonlinear buckling analysis of 2-D cold-formed steel simple cross-aisle storage rack frames. *Journal of Building Engineering, 7, 12-22.*

Timoshenko, S., & Gere, J. (1961). *Theory of elastic stability.* New York: McGraw-Hill.

Tomà, T., & Wittemann, K. (1994). Design of cold-formed purlins and rails restrained by sheeting. *Journal of Constructional Steel Research, 31(2-3), 149-168.*

Ungermann, D., & Kalameya J (2006). *Realistic determination of the ultimate load of thin-walled steel sections susceptible to coupled instabilities.* Dortmund, Germany: University of Dortmund, Institute of steel construction.

Valarinho, L., Correia, J. R., Machado-e-Costa, M., Branco, F. A., & Silvestre, N. (2016). Lateral-torsional buckling behaviour of long-span laminated glass beams: Analytical, experimental and numerical study. *Materials & Design, 102, 264-275.*

Winter, G., Lansing, W., & McCalley, R. (1949). *Performance of laterally loaded channel beams*. London: Research, Engineering, Structures Supplement (Colston papers, vol. II), 49.

Young, B., & Ellobody, E. (2007). Design of cold-formed steel unequal angle compression members. *Thin-Walled Structures, 45(3), 330-338.*

Young, B., & Rasmussen, K. (1997). Bifurcation of singly symmetric columns. *Thin-Walled Structures, 28(2), 155-177.*

Young, B., Silvestre, N., & Camotim, D. (2012). Cold-formed steel lipped channel columns influenced by local-distortional interaction: strength and DSM design. *Journal of Structural Engineering, 139(6), 1059-1074.*

Young, B., & Yan, J. (2000). Finite element analysis of cold-formed channel columns. 15th International Specialty Conference on ColdFormed Steel Structures. St. Louis, Missouri, U.S.A: Missouri University of Science and Technology.

Yu, C., & Schafer, B. W. (2006). Finite element modeling of cold-formed steel beams validation and application. 1*8th International Specialty Conference on ColdFormed Steel Structures*. St. Louis, Missouri, U.S.A: Missouri University of Science and Technology.

Yu, W.-W. (2000). *Cold-formed steel design*. USA: John Wiley & Sons.

(2014, March 27th). Cold Forming C-section Sequences. In sheet-metal-forming (Ed.), JPG. www.Custompartnet.Com.

(2017 August 16th). Inclinometer for inclination measurement in the range of ±10 degrees. Retrieved from (http://www.seika.net/english/index.htm).

(2014 March 27th). machinery-machining-tools/thread-producing-profile-rolling-machines. Retrieved from (http://www.news.thomasnet.com).

Appendices

Appendix A : GBT section properties

```
% Routine to calculate the GBT section properties

clear all

E=205;  % kN/mm2
Nu=0.3;


% Nodal Co-ordinates (mm)

x(1)=14;  y(1)=60;
x(2)=0;  y(2)=60;
x(3)=0; y(3)=30;
x(4)=0;  y(4)=0;
x(5)=100;  y(5)=0;
x(6)=200;  y(6)=0;
x(7)=200;  y(7)=30;
x(8)=200;  y(8)=60;
x(9)=186;  y(9)=60;

Nnode=length(x);

% Thickness  (mm)
t=1.77;
G=E/(2*(1+Nu));

for i=1:Nnode-1
    Length(i)= ((x(i+1)-x(i))^2 + (y(i+1)-y(i))^2)^0.5;
    Alpha(i)=acos((x(i+1)-x(i))/(y(i+1)-y(i)));
    if (y(i+1)-y(i))>=0;
        Alpha(i)=acos((x(i+1)-x(i))/Length(i));
    else
        Alpha(i)=-acos((x(i+1)-x(i))/Length(i));
    end
end


for i=1:Nnode-2;
    dAlpha(i+1)=Alpha(i)-Alpha(i+1);
end
dAlpha(Nnode)=0;

% Identify Intermediate Nodes

MainNode=ones(1,Nnode);

for i=2:Nnode-1;
if (dAlpha(i))==0;
    MainNode(i)=0;
else end
end

% Map Main Nodes to all Nodes

MainNodeNum(1,1)=1;
```

```
MainNodeNum(1,2)=1;

for i=2:Nnode;
    MainNodeNum(i,1)=i;
    MainNodeNum(i,2)=MainNodeNum(i-1,2)+MainNode(i);
end

% Calculate flat plate lengths - Mlength

SumMainNodes=MainNodeNum(Nnode,2);

 MLength=zeros(1,SumMainNodes-1);

for j=1:SumMainNodes-1;
    for i=1:Nnode-1;
        if MainNodeNum(i,2)==j
    MLength(j)=MLength(j)+Length(i);
        end
    end
end

% Recalcculate dAlpha for main nodes only MdAlpha

MdAlpha=zeros(1,SumMainNodes);

j=2;
for i=2:Nnode
    if MainNode(i)==1;
        MdAlpha(j)=dAlpha(i);
        j=j+1;
    end
end


% Create matrices Ai and Bi for main nodes

SNodes=SumMainNodes;

Ai=zeros(SNodes-1,SNodes);
Bi=zeros(SNodes-1,SNodes);

for i=2:SNodes-1
  Ai(i,i-1)=-1/(MLength(i-1)*sin(MdAlpha(i)));
  Ai(i,i)=1/(MLength(i)*tan(MdAlpha(i)))+1/(MLength(i-1)*sin(MdAlpha(i)));
  Ai(i,i+1)=-1/(MLength(i)*tan(MdAlpha(i)));

  Bi(i-1,i-1)=-1/(MLength(i-1)*tan(MdAlpha(i)));
  Bi(i-1,i)=1/(MLength(i-
1)*tan(MdAlpha(i)))+1/(MLength(i)*sin(MdAlpha(i)));
  Bi(i-1,i+1)=-1/(MLength(i)*sin(MdAlpha(i)));
end

% Expand the matrices to original size

for i=1:Nnode
    for j=1:Nnode-1
```

```
AAi(MainNodeNum(j,1),MainNodeNum(i,1))=Ai(MainNodeNum(j,2),MainNodeNum(i,2)
);

BBi(MainNodeNum(j,1),MainNodeNum(i,1))=Bi(MainNodeNum(j,2),MainNodeNum(i,2)
);

    end
end

%Insert blank columns where required
for i=1:Nnode
    for j=1:Nnode-1
        if MainNode(i)<1
           AAi(j,i)=0;
           BBi(j,i)=0;
        end
    end
end

    %Insert blank rows where require


for i=1:Nnode
     for j=1:Nnode-1
          if MainNode(j)<1
            AAi(j,i)=0;
          end
          if MainNode(j+1)<1
            BBi(j,i)=0;
          end
    end
end

       %Insert unity of leading diagonal

    for i=1:Nnode
       for j=1:Nnode-1
         if MainNode(j)<1
            AAi(j,j)=1;
         end
         if MainNode(j+1)<1
            BBi(j,j+1)=1;
         end
       end
    end

% Flexibility Matrix

for i=1:Nnode-1
EI(i)=E*t^3/(12*(1-Nu^2));
end

% Create an identity matrix

f=eye(Nnode);

% populate internal nodes
```

```
for i=4:Nnode-3
if Nnode>6
 f(i,i-1)=Length(i-1)/(6*EI(i-1)) ;
 f(i,i)=Length(i-1)/(3*EI(i-1)) + Length(i)/(3*EI(i));
 f(i,i+1)=Length(i)/(6*EI(i)) ;
end
end

% End Nodes

f(3,3)=Length(3)/(3*EI(3)) + Length(2)/(3*EI(2));
f(3,4)=Length(3)/(6*EI(3));

f(Nnode-2,Nnode-2)=Length(Nnode-2)/(3*EI(Nnode-2)) + Length(Nnode-
3)/(3*EI(Nnode-3));
f(Nnode-2,Nnode-3)=Length(Nnode-3)/(6*EI(Nnode-3));

% Stiffness Matrix

Stiff=inv(f);

% Plate Rotations

for i=2:Nnode-2
    for j=1:Nnode
        Theta(i,j)=(BBi(i,j)-AAi(i,j))/Length(i);
    end
end

Ang=zeros(Nnode,Nnode);
for i=3:Nnode-2
    for j=1:Nnode
        Ang(i,j)=(Theta(i,j)-Theta(i-1,j));
    end
end


% Calculate moment at each plate intersection using moment distribution
% (needed for boundary conditions of end plates)

Mom=Stiff*Ang;

for j=1:Nnode
Theta(1,j)=Theta(2,j)-Length(2)/(6*EI(3))*Mom(3,j);
Theta(Nnode-1,j)=Theta(Nnode-2,j)+Length(Nnode-2)/(6*EI(Nnode-
2))*Mom(Nnode-2,j);
end

ThetaStart=Theta;

% Matrices relating node rotations to plate rotations

A=eye(Nnode);

for i=3:Nnode-2
    A(i,i-1)=2*EI(i-1)/Length(i-1);
    A(i,i)=4*EI(i-1)/Length(i-1)+4*EI(i)/Length(i);
    A(i,i+1)=2*EI(i)/Length(i);
```

```
end

A;

B=zeros(Nnode,Nnode-1);
B(1,1)=1;
B(2,1)=1;
B(Nnode-1,Nnode-1)=1;
B(Nnode,Nnode-1)=1;

for i=3:Nnode-2
    B(i,i-1)=6*EI(i-1)/Length(i-1);
    B(i,i)=6*EI(i)/Length(i);
end

% Matrix relating plate and node rotations

C=inv(A)*B;

% Node Rotations

Phi=C*Theta;

PhiStart=Phi;

% Calculate Matrix Fij

w=eye(Nnode);

f0(Nnode-1,Nnode)=0;

for j=1:Nnode
AAi(1,j)=BBi(1,j)-Theta(1,j)*Length(1);
end

% Calculate function F and derivatives

[F0, F1,F2,F3,FD0,FD1,FD2,FDD0,FDD1 ] = CalculateF(
AAi,w,Nnode,Phi,Length,Theta );

% Calculate Matrix B using a function

[ jkB ] = CalculateB( Nnode,EI,Length,FDD0,FDD1 );

% Calculate Matrix jkC1 using a function

[ jkEC1,jkEC11, jkEC12 ] = CalculateEC( w,Nnode,MainNode,E,EI,
t,F0,F1,F2,F3,Length );


% Calculate eigen vectors relating to higher modes 5-N. Each eigen vector
% has a non zero eigen value associated with it. These non zero eigen
% values can be used to identify the eigen vectors relating to modes 5-N.

[Eigenvecs,Eigenvalues]=(eig(jkB,jkEC1,'chol'));

for i=1:Nnode
```

```
Eigenvals1(i)=abs(Eigenvalues(i,i));
end

w=Eigenvecs;

[ w ] = NormalizeAndSort( w,Nnode,Eigenvals1,Nnode );


% Modes 5 - N complete. We now carry out a very similar process for mode 4,
% using the calculated values of w. At this stage modes 5 - N
% are ortohogonalized, but not modes 1-4.

Theta=ThetaStart*w;
Phi=PhiStart*w;

% recalculate F and derivatives using a function

[F0, F1,F2,F3,FD0,FD1,FD2,FDD0,FDD1 ] = CalculateF(
AAi,w,Nnode,Phi,Length,Theta );

% Calculate Matrix jkC2 using a function

[ jkEC2,jkEC21, jkEC22 ] = CalculateEC( w,Nnode,MainNode,E,EI,
t,F0,F1,F2,F3,Length );

% Calculate Matrix jkD using a function

[ jkD,jkD1,jkD2] = CalculatejkD( w,Nu,Nnode,MainNode,E,EI,
t,F0,F1,F2,F3,FD0,FD1,FD2,FDD0,FDD1,Length );

% Zeroise columns 5-N and rows 5-N in matrices EC and D
for i=1:Nnode;
    for j=5:Nnode;
        jkD(i,j)=0;
        jkEC2(i,j)=0;
    end
end
for i=5:Nnode;
    for j=1:Nnode;
    jkD(i,j)=0;
    jkEC2(i,j)=0;
    end
end

jkD/71.4;

%[Eigenvecs2,Eigenvals]=convergent(eig(D,EC2));
%[Eigenvecs2]=(eig(D,EC2));
[Eigenvecs2,Eigenvalues]=(eig(jkD,jkEC2,'chol'));

for i=1:4
Eigenvals2(i)=abs(Eigenvalues(i,i));
end

w2=w*Eigenvecs2;
w=w2;

% Normalize and sort the Eigenvectors using a function
```

```
[ w2 ] = NormalizeAndSort( w2,Nnode,Eigenvals2,4);

% Add modes 5 - Nnode

for i=1:Nnode
    for j=5:Nnode
        w2(i,j)=w(i,j);
    end
end

w=w2;

% Mode 4-N complete. We now carry out a very similar process for modes 1-3,
% using the calculated values of w.At this stage mode 4-N are
% orthognalized,but not modes 1-3.

Theta=ThetaStart*w;
Phi=PhiStart*w;

% recalculate F and derivatives using a function

[F0, F1,F2,F3,FD0,FD1,FD2,FDD0,FDD1 ] = CalculateF(
AAi,w,Nnode,Phi,Length,Theta );

% Calculate Matrix jkC1 using a function

[ jkEC3,jkEC31, jkEC32 ] = CalculateEC( w,Nnode,MainNode,E,EI,
t,F0,F1,F2,F3,Length );

% % Calculate FL- the displacement at the centre of the plate parallel to
the
% % plate
%
% % interpolate w between main nodes
%
% ww=w;
% for j=1:Nnode
%     for i=2:Nnode-2
%         if MainNode(i)==0;
%         ww(i,j)=(w(i-1,j)+w(i+1,j))/2;
%         end
%     end
% end
%
% FL=zeros(Nnode-1,Nnode);
% for i=1:Nnode-1
%         FL(i,:)=(ww(i+1,:)-ww(i,:))/Length(i);
% end

% Calculate Matrix Kappa1 using a function

[ Kappa,FL ] = CalculateKappaijk( w,Nnode,MainNode,E,EI,
t,F0,F1,F2,F3,Length );

% Zeroise columns 4-N rows 4-N matrices EC and kappa
for i=1:Nnode
    for j=4:Nnode
```

```
        Kappa(i,j)=0;
        jkEC3(i,j)=0;
    end
end
for i=4:Nnode
    for j=1:Nnode
        Kappa(i,j)=0;
        jkEC3(i,j)=0;
    end
end

[Eigenvecs3,Eigenvalues]=(eig(Kappa,jkEC3));

for i=1:3
Eigenvals3(i)=abs(Eigenvalues(i,i));
end

w3=w*Eigenvecs3;

w=w3;

% Normalize and sort the Eigenvectors using a function

[ w3 ] = NormalizeAndSort( w3,Nnode,Eigenvals3,3 );


% Add modes 5 - Nnode

for i=1:Nnode
    for j=4:Nnode
        w3(i,j)=w(i,j);
    end
end
w=w3;

% recalculate Theta and Phi

Theta=ThetaStart*w;
Phi=PhiStart*w;

% Recalculate function F and derivatives

[F0, F1,F2,F3,FD0,FD1,FD2,FDD0,FDD1 ] = CalculateF(
AAi,w,Nnode,Phi,Length,Theta );

% Write warping function to a file

%dlmwrite ('C:\Data Files\Temp.txt',w);

% Warping function now calculated correctly for all modes.
% Next step is to calculate section properties.
% for this, w must be modified in modes 1-4 for unit displacement

% Mode 4 is torsion - so adjust w for a unit twist (theta)

Factor(4)=abs(Theta(1,4));
```

```
% Calculate FL and FQ using a function

[ FL,FQ ] = CalculateFLFQ( w,Nnode,Length,F0,F1,F2,F3,Theta,MainNode);


% Calculate vertical and horizontal displacements of each plate

for i=1:Nnode-1
    for j=1:Nnode
        Vert(i,j)=(FL(i,j)*sin(Alpha(i)))-(FQ(i,j)*cos(Alpha(i)));
        Horiz(i,j)=(FL(i,j)*cos(Alpha(i)))+(FQ(i,j)*sin(Alpha(i)));
    end
end


Factor(2)=(Horiz(1,2)^2+Vert(1,2)^2)^0.5;
Factor(3)=(Horiz(1,3)^2+Vert(1,3)^2)^0.5;

% Modify w in modes 2-4 for unit displacement

for i=1:Nnode
    for j=2:4
        w(i,j)=w(i,j)/Factor(j);
    end
end

% recalculate Theta and Phi

Theta=ThetaStart*w;
Phi=PhiStart*w;

% Recalculate function F and derivatives

[F0, F1,F2,F3,FD0,FD1,FD2,FDD0,FDD1 ] = CalculateF(
AAi,w,Nnode,Phi,Length,Theta );

% Recalculate FL and FQ using a function

[ FL,FQ ] = CalculateFLFQ( w,Nnode,Length,F0,F1,F2,F3,Theta,MainNode);

% Recalculate vertical and horizontal displacements of each plate


for i=1:Nnode-1
    for j=1:Nnode
        Vert(i,j)=(FL(i,j)*sin(Alpha(i)))-(FQ(i,j)*cos(Alpha(i)));
        Horiz(i,j)=(FL(i,j)*cos(Alpha(i)))+(FQ(i,j)*sin(Alpha(i)));
    end
end


% Calculate Matrix B using a function

[ jkB ] = CalculateB( Nnode,EI,Length,FDD0,FDD1 );

for i=1:Nnode
Bjk(i)=jkB(i,i);
```

```
end
B=Bjk';

% Calculate Matrix jkC1 using a function

[ jkEC4,jkEC41, jkEC42 ] = CalculateEC( w,Nnode,MainNode,E,EI,
t,F0,F1,F2,F3,Length );


for i=1:Nnode
Cjk(i)=jkEC4(i,i)/E;
end
C=Cjk';

% Calculate Matrix jkD using a function

[ jkD,jkD1,jkD2] = CalculatejkD( w,Nu,Nnode,MainNode,E,EI,
t,F0,F1,F2,F3,FD0,FD1,FD2,FDD0,FDD1,Length );


for i=1:Nnode
Djk(i)=jkD(i,i)/(G);
end
D=Djk';

% Calculate Matrix Kappa1 using a function

[ Kappa,FL ] = CalculateKappaijk( w,Nnode,MainNode,E,EI,
t,F0,F1,F2,F3,Length );

kappa=Kappa/jkEC4(1,1);

%=======================================
n_n=Nnode;
n_p=n_n-1;
Section='C:\Users\user\Documents\MATLAB\C Section\C-section Lab.xls';
xlswrite(Section,C,3,'A1')
xlswrite(Section,D,3,'B1')
xlswrite(Section,B,3,'C1')
```

A.1. Function file of C calculations

```
function [ EC,EC1, EC2 ] = CalculateEC( w,Nnode,MainNode,E,EI,
t,F0,F1,F2,F3,Length )

% Function to calculate EC

% Calculate Matrix jkC1

% interpolate w between main nodes

ww=w;
for j=1:Nnode
    for i=2:Nnode-2
        if MainNode(i)==0;
        ww(i,j)=(w(i-1,j)+w(i+1,j))/2;
        end
    end
end

% put w into a suitable 'linear' form

syms s;

for i=1:Nnode-1
    for j=1:Nnode
        w0(i,j)=ww(i,j);
        w1(i,j)=ww(i+1,j)-ww(i,j);
    end
end

EC1=zeros(Nnode,Nnode);
for j=1:Nnode
    for k=1:Nnode
        for i=1:Nnode-1
EC1(j,k)=EC1(j,k)+(E*t*Length(i))*int((w0(i,j)+w1(i,j)*s)*(w0(i,k)+w1(i,k).
..
*s),s,0,1);
        end
    end
end

% Calculate Matrix EC2(j,k)

EC2=zeros(Nnode);
for j=1:Nnode
    for k=1:Nnode
        for i=1:Nnode-1
EC2(j,k)=EC2(j,k)+(EI(i)*Length(i))*int((F0(i,j)+F1(i,j)*s+F2(i,j)*s^2+...
F3(i,j)*s^3)*(F0(i,k)+F1(i,k)*s+F2(i,k)*s^2+F3(i,k)*s^3),s,0,1);
        end
    end
end
EC=EC1+EC2;

end
```

A.2. Function file of D calculations

```
function [D,D1,D2] = CalculatejkD( w,Nu,Nnode,MainNode,E,EI,
t,F0,F1,F2,F3,FD0,FD1,FD2,FDD0,FDD1,Length )

 %Calculate Matrix D1(j,k)
 syms s;
D1=zeros(Nnode);
for j=1:Nnode
    for k=1:Nnode
        for i=1:Nnode-1
D1(j,k)=D1(j,k)+(EI(i)*Length(i))*int((FD0(i,j)+FD1(i,j)*s+FD2(i,j)*s^2)*..
.
(FD0(i,k)+FD1(i,k)*s+FD2(i,k)*s^2),s,0,1);
        end
    end
end
% Calculate Matrix D2(j,k)
D2=zeros(Nnode);
for j=1:Nnode;
    for k=1:Nnode;
        for i=1:Nnode-1;
D2(j,k)=D2(j,k)+(EI(i)*Length(i))*int((F0(i,j)+F1(i,j)*s+F2(i,j)*s^2+...
F3(i,j)*s^3)*(FDD0(i,k)+FDD1(i,k)*s),s,0,1);
        end
    end
end
%ERROR IN MATHCAD HERE - does not seem to affect section without
%intermediate nodes!!!
for i=1:Nnode
    for j=1:Nnode
        D(i,j)=2*(1-Nu)*D1(i,j)-Nu*(D2(i,j)+D2(j,i));
    end
end
end
```

A.3. Function file of B calculations

```
function [ jkB ] = CalculatejkB( Nnode,EI,Length,FDD0,FDD1 )

% Calculate Matrix jkB

syms s;

jkB=zeros(Nnode,Nnode);
for j=1:Nnode
    for k=1:Nnode
        for i=1:Nnode-1

jkB(j,k)=jkB(j,k)+(EI(i)*Length(i))*int((FDD0(i,j)+FDD1(i,j)*s)*...
            (FDD0(i,k)+FDD1(i,k)*s),s,0,1);
        end
    end
end

end
```

A.4. Function file of Kappa calculations

```
function [ Kappa,FL ] = CalculateKappaijk( w,Nnode,MainNode,E,EI,
t,F0,F1,F2,F3,Length )
% Calculate Matrix Kappa1 using a function

% Calculate FL- the displacement at the centre of the plate parallel to the
% plate

% interpolate w between main nodes

ww=w;
for j=1:Nnode
    for i=2:Nnode-2
        if MainNode(i)==0;
        ww(i,j)=(w(i-1,j)+w(i+1,j))/2;
        end
    end
end

FL=zeros(Nnode-1,Nnode);
for i=1:Nnode-1
        FL(i,:)=(ww(i+1,:)-ww(i,:))/Length(i);
end

syms s;

Kappa=zeros(Nnode);
for j=1:Nnode
    for k=1:Nnode
        for i=1:Nnode-1
Kappa(j,k)=Kappa(j,k)+(E*t*Length(i))*int((F0(i,k)+F1(i,k)*s+F2(i,k)*s^2+..
.
F3(i,k)*s^3)*(F0(i,j)+F1(i,j)*s+F2(i,j)*s^2+F3(i,j)*s^3),s,0,1)+...
E*t*Length(i)*int((FL(i,j)*FL(i,k)),s,0,1);
        end
    end
end

end
```

A.5. Function file of FL-FQ calculations

```
function [ FL,FQ ] =CalculateFLFQ(w,Nnode,Length,F0,F1,F2,F3,Theta,MainNode
)
% Calculate FL and FQ

ww=w;
for j=1:Nnode
    for i=2:Nnode-2
        if MainNode(i)==0;
        ww(i,j)=(w(i-1,j)+w(i+1,j))/2;
        end
    end
end
FL=zeros(Nnode-1,Nnode);
for i=1:Nnode-1
        FL(i,:)=(ww(i+1,:)-ww(i,:))/Length(i);
```

```
end
for i=1:Nnode-1
    for j=1:Nnode
        FF(i,j)=F0(i,j);
        FP(i,j)=F0(i,j)+F1(i,j)+F2(i,j)+F3(i,j);
    end
end

% For internal nodes
for i=2:Nnode-2
    for j=1:Nnode
        FQ(i,j)=(FF(i,j)+FP(i,j))/2;
    end
end

% For external nodes
    for j=1:Nnode
        FQ(1,j)=FP(1,j)-Length(1)*Theta(1,j)/2;
    end
       for j=1:Nnode
        FQ(Nnode-1,j)=FP(Nnode-1,j)+Length(Nnode-1)*Theta(Nnode-1,j)/2;
       end


end
```

A.6. Function file of F calculations

```
function [ F0,F1,F2,F3,FD0,FD1,FD2,FDD0,FDD1 ] = CalculateF(
AAi,w,Nnode,Phi,Length,Theta )

% Function to calculate F0

F0=AAi*w;

for i=1:Nnode-1
    for j=1:Nnode
        F1(i,j)=Length(i)*Phi(i,j);
        F2(i,j)=Length(i)*(3*Theta(i,j)-2*Phi(i,j)-Phi(i+1,j));
        F3(i,j)=Length(i)*(-2*Theta(i,j)+1*Phi(i,j)+Phi(i+1,j));
    end
end

% Calculate derivatives of F

for i=1:Nnode-1
    for j=1:Nnode
        FD0(i,j)=F1(i,j)/Length(i);
        FD1(i,j)=F2(i,j)*2/Length(i);
        FD2(i,j)=F3(i,j)*3/Length(i);
        FDD0(i,j)=F2(i,j)*2/Length(i)^2;
        FDD1(i,j)=F3(i,j)*6/Length(i)^2;
    end
end

fprintf('Function f completed')

end
```

A.7. Function file of normalize (w) calculations

```
function [ w ] = Normalize( w,Nnode )

% Function to normalize the eigen vectors

    Factor=max(abs(w));

for j=1:Nnode
    for i=1:Nnode
   w(i,j)=w(i,j)/Factor(j);
    end
end

end
```

A.8. Function file of normalize and sort calculations

```
function [ NewW ] = NormalizeAndSort( w,Nnode,Eval,Modes )

% Function to normalize and sort the eigen vectors

% Order vector

% Allow for zero Eigen values - give each zero EV a very small, different,
% value

Modes;

for i=1:Modes
if Eval(i)==0;
    Eval(i)=i*1E-25;
end
end

for i=1:Modes
OldPos(i)=i;
end
OldPos;
Eval;

% Normalize

% Normalize the Eigenvectors

    Factor=max(abs(w));

for j=1:Nnode
    for i=1:Nnode
   w(i,j)=w(i,j)/Factor(j);
    end
end

w;

% Order the Eigenvectors from column Start to column Finish
```

```
NewOrder=(sort(Eval));

NewOrder;

% Find new position of Eval(i)
for i=1:Modes;
for j=1:Modes;
if Eval(i)==NewOrder(j);
    NewPos(i)=j;

end
end
end

OldPos;
NewPos;
Eval;

for i=1:Nnode
    for j=1:1: Modes
        NewW(i,NewPos)=w(i,OldPos);
    end
end

NewW;


end
```

Appendix B: GBT linear analysis

```
% ======================================================
% Linear Analysis of GBT Using Finite Diffrence Method
% ======================================================
% Divide lenght of beam to small lengths
dx=5;
L_B=300;
Py=-0.25;
Nodes_B=(L_B/dx)+1;
% Set up the load for the GBT equation
L_pos=200;
Nodes_L=(L_pos/dx)+1;
Q=zeros(n_n,Nodes_B);
P_load=zeros(n_p,Nodes_B);
% load case
P_load(4,Nodes_L)=Py;
for j=1:Nodes_B;
Q(:,j)=(P_load(:,j)'*FL)/dx;
end
% Finite Diffrence Analysis
Q=Q(:,2:Nodes_B-1);
for k=1:n_n
K1(k)=(6*E*C(k)/dx^4+2*G*D(k)/dx^2+B(k));
K2(k)=(-G*D(k)/dx^2-4*E*C(k)/dx^4);
K3(k)=(E*C(k)/dx^4);
KG=diag(K1(k)*ones(Nodes_B,1))+diag(K2(k)*ones(Nodes_B-1,1),1)+...
diag(K2(k)*ones(Nodes_B-1,1),-1)+diag(K3(k)*ones(Nodes_B-2,1),2)+...
diag(K3(k)*ones(Nodes_B-2,1),-2);
% Apply boundary condtions (pin ends)
KG(2,2)=KG(2,2)-K3(k);
KG(Nodes_B-1,Nodes_B-1)=KG(Nodes_B-1,Nodes_B-1)-K3(k);
KG=KG(2:Nodes_B-1,2:Nodes_B-1);
Vt(k,:)=inv(KG)*Q(k,:)';
end
V=zeros(n_n,Nodes_B);
V(:,2:Nodes_B-1)=Vt;
% Calculate Stress Resultants
W=zeros(n_n,Nodes_B);
for i=1:n_n
    for j=2:Nodes_B-1
     W(i,j)=E/dx^2*C(i)*(-V(i,j-1)+2*V(i,j)-V(i,j+1));
    end
end
for i=1:n_n
V_max(i)=max(abs(V(i,:)));
W_max(i)=max(abs(W(i,:)));
end
% Calculate Nodal Stress
St=0;
for i=1:n_n
    st=W(i,:)'*w(:,i)'/C(i);
    St=St+st;
end
% Calculate Plate Deflections (NPD & PPD)
NPD=0;
PPD=0;
for i=1:n_n
    nPD=V(i,:)'*FQ(:,i)';
    NPD=NPD+nPD;
```

```
    pPD=V(i,:)'*FL(:,i)';
    PPD=PPD+pPD;
end
Section='Z-Section3.xls';
xlswrite(Section,V(:,30:50),1,'A1')
xlswrite(Section,W(:,30:50),2,'A1')
xlswrite(Section,V_max,3,'A1')
xlswrite(Section,W_max,3,'A10')
xlswrite(Section,St(30:50,:),4,'A1')
xlswrite(Section,C,5,'A1')
xlswrite(Section,D,5,'B1')
xlswrite(Section,B,5,'C1')
```

Appendix C: GBT linear buckling analysis (single mode)

```
%=========================================================================
% Calculations of Buckling loads and its mode shapes Using FDM along beam
%=========================================================================
%Section='C:\Users\user\Documents\MATLAB\C Section\Z1-section Lab F.xls';
Nodes_B=100;
for k=1:n_n
r=1;
for L_B=10:10:10000
dx=L_B/(Nodes_B+1);
S1=diag(6*ones(Nodes_B,1))+diag(-4*ones(Nodes_B-1,1),1)+...
diag(-4*ones(Nodes_B-1,1),-1)+diag(1*ones(Nodes_B-2,1),2)+...
diag(1*ones(Nodes_B-2,1),-2);
S2=diag(-2*ones(Nodes_B,1))+diag(1*ones(Nodes_B-1,1),1)+...
diag(1*ones(Nodes_B-1,1),-1);
S3=eye(Nodes_B,Nodes_B);
% applied Boundery Conditions
S1(1,1)=5;
S1(Nodes_B,Nodes_B)=5;
A=E*C(k)/dx^4*S1-G*D(k)/dx^2*S2+B(k)*S3;
Z=-kappa(k,k,1)*S2/dx^2;
[A1,Z1]=(eig(A,Z));
Z2=zeros(Nodes_B,1);
for i=1:Nodes_B
    Z2(i)=Z1(i,i);
end
Z3(r)=min(abs(Z2));
L(r)=L_B;
r=r+1;
%Plot Critical Mode along beam length
%====================================
if L_B==7500
    if k==4
    L1=zeros(Nodes_B,1);
    t1=1;
    t2=dx;
    L_B1=L_B-dx;
   for i=dx:dx:L_B1
       L1(t1)=t2;
       t1=t1+1;
       t2=t2+dx;
   end
A1(Nodes_B+1,:)=Z2.';
A1=A1';
A1=sortrows(A1,Nodes_B+1);
A1=A1';
A1=A1(1:Nodes_B,:);
L11=L1/10;
figure(2)
plot(L11,A1(:,1))
hold on
    end
end
end
figure(1)
Lc=L/10;
plot(Lc,Z3)
hold on
 end
```

Appendix D: GBT linear buckling analysis (combined modes)

```
%=========================================================================
% Calculations of Buckling loads and its mode shapes Using FDM along beam
%=========================================================================
Nodes_B=59;
r=1;
for L_B=100:100:10000
dx=L_B/(Nodes_B+1);
y1=Nodes_B*n_n;
A1=zeros(y1);
Z1=zeros(y1);
y2=1;
y3=Nodes_B;
for k=1:n_n
S1=diag(6*ones(Nodes_B,1))+diag(-4*ones(Nodes_B-1,1),1)+...
diag(-4*ones(Nodes_B-1,1),-1)+diag(1*ones(Nodes_B-2,1),2)+...
diag(1*ones(Nodes_B-2,1),-2);
S2=diag(-2*ones(Nodes_B,1))+diag(1*ones(Nodes_B-1,1),1)+...
diag(1*ones(Nodes_B-1,1),-1);
S3=eye(Nodes_B,Nodes_B);
% applied Boundery Conditions
S1(1,1)=7;
S1(Nodes_B,Nodes_B)=7;
%**********************
A=E*C(k)/dx^4*S1-G*D(k)/dx^2*S2+B(k)*S3;
A1(y2:y3,y2:y3)=A;
Z=kappa(k,k,1)*S2/dx^2;
Z1(y2:y3,y2:y3)=Z;
y2=y3+1;
y3=y3+Nodes_B;
end
[A2,Z2]=(eig(A1,Z1));
for i=1:n_n*Nodes_B
    Z3(i)=Z2(i,i);
end
Z4(r)=(min(abs(Z3)));
Lc(r)=L_B;
r=r+1;
end
figure(1)
plot(Lc,Z4)


Section='C:\Users\user\Documents\MATLAB\C Section\Z-section Lab F.xls';
xlswrite(Section,Lc',2,'H1')
xlswrite(Section,Z4',2,'I1')
```

Appendix E: GBT non-linear analysis

```
%=========================================================================
% Calculations of Non-linear loads and its mode shapes Using FDM
%=========================================================================
Nodes_B=59;
xd=1
for L_B=50:50:10000
    %if L_B==6000
%=======================
% intial imperfection
%=======================
Py=0.024*C(3)*E/(L_B^2);
dx=L_B/(Nodes_B-1);
% Set up the load for the GBT equation
Nodes_L=Nodes_B/2+0.5;
Q=zeros(n_n,Nodes_B);
P_load=zeros(n_p,Nodes_B);
% load case
P_load(3,Nodes_L)=Py;
P_load(5,Nodes_L)=-Py;
for j=1:Nodes_B;
Q(:,j)=(P_load(:,j)'*FL)/dx;
end
% Finite Diffrence Analysis
%Q=Q(:,2:Nodes_B-1);
for k=1:n_n
S1=diag(6*ones(Nodes_B,1))+diag(-4*ones(Nodes_B-1,1),1)+...
diag(-4*ones(Nodes_B-1,1),-1)+diag(1*ones(Nodes_B-2,1),2)+...
diag(1*ones(Nodes_B-2,1),-2);
S2=diag(-2*ones(Nodes_B,1))+diag(1*ones(Nodes_B-1,1),1)+...
diag(1*ones(Nodes_B-1,1),-1);
S3=eye(Nodes_B,Nodes_B);
% applied Boundery Conditions
S1(1,1)=5;
S1(Nodes_B,Nodes_B)=5;
At=E*C(k)/dx^4*S1-G*D(k)/dx^2*S2+B(k)*S3;
Vt(k,:)=inv(At)*Q(k,:)';
end
Vj=Vt;
%=======================================
% imperfect member
%=======================================
Px=0.1;
 for n=1:1000000000
     Vg=0;
 for r=1:1000000000
 for k=1:n_n
A1=E*C(k)/dx^4*S1-G*D(k)/dx^2*S2+B(k)*S3;
A2=(kappa(k,k,1)*Px*S2/dx^2);
A=A1+A2;
%Sdr=inv(A)
Z(k,:)=(kappa(k,k,1)*Px*S2*Vt(k,:)'/dx^2);
V(k,:)=inv(A)*Z(k,:)';
 end
 ert=Z';
 Vd=abs(max(max(V)));
 if (Vd-Vg) <1e-8,break,end
 Vg=Vd;
 Vt=Vt+V;
```

```
 end
 % Calculate Stress Resultants
W=zeros(n_n,Nodes_B);
for i=1:n_n
    for j=2:Nodes_B-1
     W(i,j)=E/dx^2*C(i)*(-V(i,j-1)+2*V(i,j)-V(i,j+1));
    end
end
% Calculate Nodal Stress
St1=0;
for i=1:n_n
    st=W(i,:)'*w(:,i)'/C(i);
    St1=St1+st;
end
St2=-ones(Nodes_B,n_n)*Px/C(1);
St=St1+St2;
if sum(sum(isnan(V)))==Nodes_B,break,end
if abs(min(min(St)))> 430,break,end
if abs(max(max(St)))> 430,break,end
Pt(n)=Px;
Vm(n)=V(7,30);

Px=Px+0.1;
 end
 Rx(xd)=L_B;
 Ry(xd)=Px;
% Critical Buckling load
%=========================
y1=Nodes_B*n_n;
Ac1=zeros(y1);
Zc1=zeros(y1);
y2=1;
y3=Nodes_B;
for k=1:n_n
Ac=E*C(k)/dx^4*S1-G*D(k)/dx^2*S2+B(k)*S3;
Ac1(y2:y3,y2:y3)=Ac;
Zc=kappa(k,k,1)*S2/dx^2;
Zc1(y2:y3,y2:y3)=Zc;
y2=y3+1;
y3=y3+Nodes_B;
end
[Ac2,Zc2]=(eig(Ac1,Zc1));
for i=1:n_n*Nodes_B
    Zc3(i)=Zc2(i,i);
end
Pe(xd)=(min(abs(Zc3)));
 xd=xd+1
end
Rx1=Rx/10;
figure(1)
plot(Rx1,Pe)
hold on
plot(Rx1,Ry)
hold off
%figure(2)
%plot(Vm,Pt)
Section='C:\Users\user\Documents\MATLAB\C Section\C-section Lab.xls';
xlswrite(Section,Rx1',2,'A1')
xlswrite(Section,Pe',2,'B1')
xlswrite(Section,Ry',2,'C1')
```

Appendix F: Tension control bolt (*TCB) details*

Dimensions of standard HRC Bolts to EN 14399-10

All dimensions in millimetres

Thread d		M12	M16	M20	M22	M24	M27	M30	M36
p		1.75	2	2.5	2.5	3	3	3.5	4
b	≤ 125mm	30	38	46	50	54	60	66	78
	> 125 ≤200mm	-	44	52	56	60	66	72	84
	> 200mm	-	-	65	69	73	79	85	97
d_s	max	12.70	16.70	20.84	22.84	24.84	27.84	30.84	37.00
	min	11.30	15.30	19.16	21.16	23.16	26.16	29.16	35.00
d_w	min	20	26	33	37	41	46	50	61
d_k	min	21	27	34	38	43	48	52	66
k	nom	8	10	13	14	15	17	19	23
	max	8.8	10.8	13.9	14.9	15.9	17.9	20.0	24.0
	min	7.2	9.2	12.1	13.1	14.1	16.1	18.0	22.0
r	min	1.2	1.2	1.5	1.5	1.5	2.0	2.0	2.0
R	nom	18	20	22	23	25	27	30	36
$F1$	min	11	13	15	15.5	16	19	21	25
$F2$	max	16	18	20	21	21.5	24	26	31
Spline a/f S_b	max	8.0	11.6	14.4	15.7	17.1	19.3	21.4	25.7
	min	7.4	11.0	13.8	15.1	16.5	18.7	20.8	25.1
Spline a/c e_b	min	8.36	12.43	15.60	17.06	18.65	21.13	23.50	28.50
U a				Incomplete thread $u \leq 2$ p					

Dimensions of HRD Nuts to EN 14399-10

All dimensions in millimetres

Nominal diameter		M12	M16	M20	M22	M24	M27	M30	M36
p		1.75	2	2.5	2.5	3	3	3.5	4
d_w	max	= 's' actual							
	min	20.1	24.9	29.5	33.3	38.0	42.8	46.6	55.9
e	min	23.91	29.56	35.03	39.55	45.20	50.85	55.37	66.44
m	max	12.35	16.35	20.65	22.65	24.65	27.65	30.65	36.65
	min	11.65	15.65	19.35	21.35	23.35	26.35	29.35	35.35
c	max	0.8	0.8	0.8	0.8	0.8	0.8	0.8	0.8
	min	0.4	0.4	0.4	0.4	0.4	0.4	0.4	0.4
s	max	22	27	32	36	41	46	50	60
	min	21.16	26.16	31	35	40	45	49	58.8

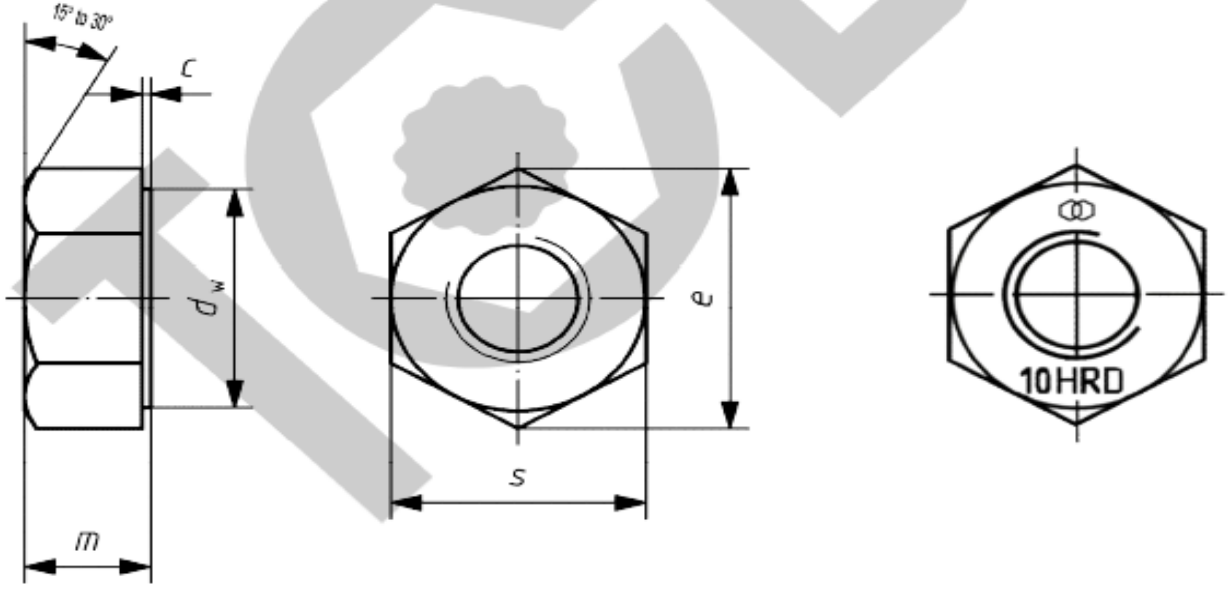

Bolt lengths and tolerances for standard TCBs to EN 14399-10

Length *(l)*			M12		M16		M20		M22		M24		M27		M30		M36	
			l_s	l_g	l_s	l_g	l_s	l_g	l_s	l_g	l_s	l_g	l_s	l_g	l_s	l_g	l_s	l_g
nom	*min*	*max*	*min*	*max*	*min*	*max*	*min*	*max*	*min*	*max*	*min*	*max*	*min*	*max*	*min*	*max*	*min*	*Max*
30	*28.75*	*31.25*	6	11.25														
35	*33.75*	*36.25*	6	11.25														
40	*38.75*	*41.25*	6	11.25	8	14												
45	*43.75*	*46.25*	6.25	15	8	14												
50	*48.75*	*51.25*	11.25	20	8	14	10	17.5	11	18.5								
55	*53.50*	*56.5*	16.25	25	8	14	10	17.5	11	18.5								
60	*58.50*	*61.5*	21.25	30	12	22	10	17.5	11	18.5	12	21						
65	*63.50*	*66.5*	26.25	35	17	27	10	17.5	11	18.5	12	21						
70	*68.50*	*71.5*	31.25	40	22	32	11.5	24	11	18.5	12	21						
75	*73.50*	*76.5*	36.25	45	27	37	16.5	29	12.5	25	12	21						
80	*78.50*	*81.5*	41.25	50	32	42	21.5	34	17.5	30	12	21	13.5	22.5	15	25.5		
85	*83.25*	*86.75*	46.25	55	37	47	26.5	39	22.5	35	16	31	13.5	22.5	15	25.5		
90	*88.25*	*91.75*	51.25	60	42	52	31.5	44	27.5	40	21	36	15	30	15	25.5		
95	*93.25*	*96.75*	56.25	65	47	57	36.5	49	32.5	45	26	41	20	35	15	25.5		
100	*98.25*	*101.75*	61.25	70	52	62	41.5	54	37.5	50	31	46	25	40	16.5	34	18	30
105	*103.25*	*106.75*			57	67	46.5	59	42.5	55	36	51	30	45	21.5	39	18	30
110	*108.25*	*111.75*			62	72	51.5	64	47.5	60	41	56	35	50	26.5	44	18	30
115	*113.25*	*116.75*			67	77	56.5	69	52.5	65	46	61	40	55	31.5	49	23	35
120	*118.25*	*121.75*			72	82	61.5	74	57.5	70	51	66	45	60	36.5	54	22	42
125	*123.0*	*127.0*			77	87	66.5	79	62.5	75	56	71	50	65	41.5	59	27	47
130	*128.0*	*132.0*			76	86	65.5	78	61.5	80	55	70	49	64	40.5	58	26	46
135	*133.0*	*137.0*			81	91	70.5	83	66.5	85	60	75	54	69	45.5	63	31	51

Appendix G: Eurocode Calculations

- This appendix presents capacity calculations for C and Z section presented in Chapter 7, an accordauce with provisios of Eurocode for structural steelwork design:

- C-Section

1-Design Against Local and Distortional Buckling (EN1993-1-3)

Calculation of effective section properties for a cold-formed lipped channel section in compression

Total height of web	h=	200	mm
Total width of flange	b=	60	mm
Total width of edge fold	c=	20	mm
Internal radius	r=	3	mm
Nominal thickness	t_{nom}=	1.77	mm
Steel core thickness	t=	1.43	mm
Yield strength	fy=	430	N/mm^2
Modulus of elasticity	E=	205000	N/mm^2
Poisson's ratio	ν=	0.3	
Partial factor	γ_m=	1	

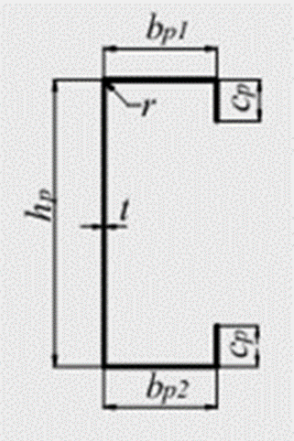

Figure (G-1) C-section

The dimensions of the section centre line are:

h_p=h-t	h_p=	198.23	mm
b_p=b-t	b_p=	58.23	mm
c_p=c-t/2	c_p=	19.12	mm

Checking of geometrical proportions

b/t ≤ 60	b/t=	33.90	<60	OK
c/t ≤ 50	c/t =	11.30	<50	OK
h/t<500	h/t=	112.99	<500	OK
0.2 ≤c/b ≤0.6	c/b=	0.33		OK

The influence of rounding of corners is neglected if:

$r/t \leq 5$ $r/t=$ 1.69 <5 OK

$r/b_p \leq 0.1$ $r/b_p=$ 0.05 <0.1 OK

Gross cross-section properties

$A_{br}= t(2c_p+2b_p+h_b)$ $A_{br}=$ 504.68 mm^2

Position of the natural axis with respect to the top flange is:

$Z_{bi}= t\,[c_p(h_p-c_p/2)+b_p*h_p+h_p^2/2+c_b^2/2]/A_{br}$ $Z_{bi}=$ 99.12 mm

The stress ratio $\Psi=1$ Uniform compression

$K_\sigma =$ 4 For internal compression element

$\varepsilon=\sqrt{235/f_y}$ $\varepsilon=$ 0.739

$\lambda_{p,b}=b_p/(28.4\varepsilon t\sqrt{k_\sigma})$ $\lambda_{p,b}=$ 0.970

The reduction factor is :

$\rho_1= (\lambda_{p,b}-0.055(3+\Psi))/\lambda_{p,b}^2$ $\rho_1=$ 0.797

The effective width is:

$b_{eff,p}=\rho_1*b_p$ $b_{eff,p}=$ 46.42 mm

$b_{e1,u}=0.5*b_{eff,p}$ $b_{e1,u}=$ 23.21 mm

$b_{e2,u}= b_{e1,u}$ $b_{e2,u}=$ 23.75 mm

- Effective width of edge fold (Cl. 3.7.3.2.2. eqn (3.47))

The buckling factor is:

$c_p/b_p=$ 0.328 <0.35 → $K_\sigma =$ 0.5

$\lambda_{p,c}=c_p/(28.4\varepsilon t\sqrt{k_\sigma})$ $\lambda_{p,c}=$ 0.9

The width reduction factor is:

$\rho_1= (\lambda_{p,b}-0.188)/\lambda_{p,b}^2$ $\rho_1=$ 0.879

$c_{eff,u}=\rho_1*c_p$ $c_{eff,u}=$ 16.80 mm

The effective area of edge stiffener is:

$A_{s,u}= t*(b_{e1,1}+c_{eff})$ $A_{s,u}=$ 57.21 mm^2

Use the initial cross section of the stiffener to determine the reduction factor, allowing for effects of the continuous spring restraint

-The elastic critical buckling stress for the edge stiffener

$$\sigma_{cr} = 2\sqrt{KEI_s}/A_s$$

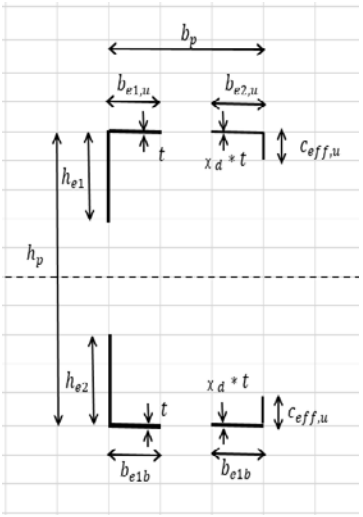

Figure (G-1) Effective area of C-section

For the upper edge stiffener (Cl. 3.7.3.1 eqn 3.44)

The spring stiffness is:

$K=Et^3/((4(1-\nu^2)(b_1^2*h_p+b_1^3+0.5*b_1*b_2*h_p*k_{f1}))$

b_1=distance from the web to the centre of the effective area of stiffener (upper flange)

b_2=distance from the web to the centre of the effective area of stiffener (lower flange)

$b_1=b_p-(b_{e1,u}*t*(b_{e1,u}/2))/((b_{e1,u}+c_{eff,u})*t)$ $b_1=$ 51.50

$b_1=b_2$ → $b_2=$ 51.50

$k_{f1}=A_{s,u}/A_{s,l}$ $k_{f1}=$ 1.0 For a member in axial compression

K= 0.178

For upper edge stiffener (Cl.3.7.3.1 eqn 2.44)

The effective second moment of area is:

$I_{su}=b_{e1,1}*t^3/12+c_{eff}*t/12+b_{e1,1}*t[c_{eff}^2/2(b_{e1,1}+c_{eff})]^2+c_{eff}*t[c_{eff}/2-[c_{eff}^2/2(b_{e1,1}+c_{eff})]^2$

$I_{su=}$ 886.15 mm^4

For upper edge :

$\sigma_{cr,u}=$ 198.80 N/mm^2

Thickness reduction factor χ_d for the edge stiffener is:

if $\lambda_d \leq 0.65$ $\chi_d=1.0$

if $0.65 < \lambda_d < 1.38$ $\chi_d=1.47-0.723\lambda_d$

if $\lambda_d \geq 1.38$ $\chi_d=0.66/\lambda_d$

The relative slenderness λ_d

$\lambda_d=\sqrt{fy/\sigma_{cr,s}}$ $\lambda_d=$ 1.471

$\chi_d=0.66/\lambda_d$ $\chi_d=$ 0.449

Effective section properties of web

the stress ratio : $\Psi=1$ (uniform compression)

The buckling factor k_σ = 4 for internal compression element

The relative slenderness:

$\lambda_{p,b}=h_p/(28.4\xi t\sqrt{k_\sigma})$ $\lambda_{p,b}=$ 3.301

The width reduction factor is

$\rho=(\lambda_{p,b}-0.055(3+\Psi))/\lambda_{p,b}^2$ $\rho=$ 0.283

The effective width of web is:

$h_{eff}=\rho*h_p$ $h_{eff}=$ 56.04 mm

$h_{e1}=0.5*heff$ $h_{e1}=$ 28.02 mm

The cross section is summitry in x-axis

$h_{e2}=$ 28.88 mm

For bottom flange

$b_{e1,b}= b_{e1,u}$ $b_{e1,b}=$ 23.75 mm

$b_{e2,b}= b_{e2,u}$ $b_{e2,b}=$ 23.75 mm

$c_{eff,b}=c_{eff,u}$ $c_{eff,b}=$ 17.20 mm

Effective section properties of the flange and lip in compression

$A_{eff}= t [b_{e1,u}+b_{e1,b}+h_{e1}+h_{e2}+(b_{e2,u}+b_{e2,b}+c_{eff,u}+c_{eff,b})*\chi_d]$

$A_{eff}=$ 200.55 mm^2

$N_{ed}=f_y/\gamma_m*A_{eff}$ Ned= 86.24 kN

2-Design Against Global Buckling (EN1993-1-5)

- For stiffened plate $\sigma_{cr,c}$ may be determined from the elastic critical column buckling

stress $\sigma_{cr,sl}$ of the stiffener closest to the panel edge with the highest compressive stress as follows:

$\sigma_{cr,sl}= \pi^2EI_{sl,1}/A_{sl,1}a^2$

$Ned=\pi^2EI_{sl,1}/a^2$

$I_{sl,1}=$ 291616E4 mm^4

- Z-Section

1-Design Against Local and Distortional Buckling (EN1993-1-3)

-Calculation of effective section properties for a cold-formed lipped channel section in compression

Total height of web	h=	200	mm
Total width of flange	b_1=	64	mm
	b_2=	54	mm
Total width of edge fold	c_1=	18	mm
	c_2=	15	mm
Internal radius	r=	3	mm
Nominal thickness	t_{nom}=	2.05	mm
Steel core thickness	t=	2.00	mm
Yield strength	fy=	500	N/mm^2
Modulus of elasticity	E=	207000	N/mm^2
Poisson's ratio	ν=	0.3	
Partial factor	γ_m	1	

The dimensions of the section centre line are:

$h_p=h-t$	h_p=	197.95	mm
$b_{p1}=b_1-t$	b_{p1}=	61.95	mm
$b_{p2}=b_2-t$	b_{p2}=	52.00	mm
$c_{p1}=c_1-t/2$	c_{p1}=	16.98	mm
$c_{p2}=c_2-t/2$	c_{p2}=	14.00	mm

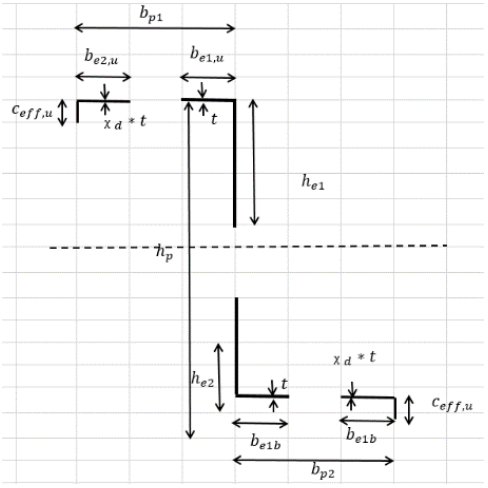

Figure (G-1) Effective area of Z-section

Checking of geometrical proportions

$b/t \leq 60$	b_1/t=	31.2	<60	OK
	b_2/t=	26.3	<60	OK
$c/t \leq 50$	c_1/t =	8.78	<50	OK
	c_2/t =	7.32	<50	OK
h/t<500	h/t=	97.5	<500	OK

$0.2 \leq c/b \leq 0.6$ c_1/b_1= 0.28 OK

c_2/b_2= 0.28 OK

The influence of rounding of corners is neglected if:

$r/t \leq 5$ r/t= 1.46 <5 OK

$r/b_p \leq 0.1$ r/b_{p1}= 0.05 <0.1 OK

r/b_{p2}= 0.06 <0.1 OK

Gross cross-section properties

$A_{br}= t(c_{p1}+c_{p2}+b_{p1+}b_{p2}+h_b)$ 685.75 mm^2

Position of the natural axis with respect to the top flange is:

$Z_{bi}= t [c_{p2}(h_p-c_{p2}/2)+b_{p2}*h_p+h_p^2/2+c_{b1}^2/2]/A_{br}$ Z_{bi}= 95.38 mm

The stress ratio Ψ=1 Uniform compression

K_σ = 4 For internal compression element

$\varepsilon=\sqrt{235/f_y}$ ε= 0.686

For upper flange stiffener:

$\lambda_{p,b}=b_{p1}/(28.4\varepsilon t\sqrt{k_\sigma})$ $\lambda_{p,b}$= 0.795

The reduction factor is :

$\rho_1= (\lambda_{p,b}-0.055(3+\Psi))/\lambda_{p,b}^2$ ρ_1= 0.909

The effective width is:

$b_{eff,p}=\rho_1*b_p$ $b_{eff,p}$= 56.341 mm

$b_{e1,u}=0.5*b_{eff,p}$ $b_{e1,u}$= 28.170 mm

$b_{e2,u}= b_{e1,u}$ $b_{e2,u}$= 28.170 mm

Effective width of edge fold (Cl. 3.7.3.2.2. eqn(3.47))

The buckling factor is:

c_{p1}/b_{p1}= 0.274 <0.35 → K_σ = 0.5

$\lambda_{p,c1}=c_{p1}/(28.4\varepsilon t\sqrt{k_\sigma})$ $\lambda_{p,c1}$= 0.616

The width reduction factor is:

$\rho_1= (\lambda_{p,c1}-0.188)/\lambda_{p,c1}^2$ ρ_1= 1.13 >1 → ρ_1= 1.0

$c_{eff,u}=\rho_1*c_p$ $c_{eff,u}$= 16.98 mm

The effective area of edge stiffener is:

$A_{s,u}= t*(b_{e1,1}+c_{eff})$ $A_{s,u}=$ 90.29 mm^2

Use the initial cross section of the stiffener to determine the reduction factor,

allowing for effects of the continuous spring restraint

The elastic critical buckling stress for the edge stiffener

$\sigma_{cr} = 2\sqrt{KEI_s}/A_s$

For the upper edge stiffener (Cl. 3.7.3.1 eqn 3.44)

The spring stiffness is:

$K=Et^3/((4(1-v^2)(b_1^2*h_p+b_1^3+0.5*b_1*b_2*h_p*k_{f1}))$

b_1=distance from the web to the centre of the effective area of stiffener (upper flange)

b_2=distance from the web to the centre of the effective area of stiffener (lower flange)

$b_1=b_{p1}-(b_{e1,u}*t*(b_{e1,u}/2))/((b_{e1,u}+c_{eff,u})*t)$ $b_1=$ 53.16

$b_1=b_2$ → $b_2=$ 53.16

$k_{f1}=A_{s,u}/A_{s,l}$ $k_{f1}=$ 1.0 For a member in axial compression

K= 0.460

For upper edge stiffener (Cl.3.7.3.1 eqn 2.44)

The effective second moment of area is:

$I_{su}=b_{e1,1}*t^3/12+c_{eff}*t/12+b_{e1,1}*t[c_{eff}^2/2(b_{e1,1}+c_{eff})]^2+c_{eff}*t[c_{eff}/2-[c_{eff}^2/2(b_{e1,1}+c_{eff})]^2$

$I_{su=}$ 1350 mm^4

For upper egde :

$\sigma_{cr,u}=$ 251.11 N/mm^2

Thickness reduction factor χ_d for the edge stiffener is:

if $\lambda_d \leq 0.65$ $\chi_d = 1.0$

if $0.65 < \lambda_d < 1.38$ $\chi_d = 1.47-0.723\lambda_d$

if $\lambda_d \geq 1.38$ $\chi_d = 0.66/\lambda_d$

The relative slenderness λ_d

$\lambda_d = \sqrt{fy}/\sigma_{cr,s}$ $\lambda_{d.u}=$ 1.411

$\chi_d = 0.66/\lambda_d$ $\chi_{d,u} =$ 0.468

Effective section properties of web

the stress ratio : $\Psi=1$ (uniform compression)

The buckling factor $k_\sigma = 4$ for internal compression element

The relative slenderness:

$\lambda_{p,b}=h_p/(28.4\varepsilon t\sqrt{k_\sigma})$ $\lambda_{p,b}=$ 2.542

The width reduction factor is

$\rho= (\lambda_{p,b}-0.055(3+\Psi))/\lambda_{p,b}^2$ $\rho=$ 0.359

The effective width of web is:

$h_{eff}=\rho*h_p$ $h_{eff}=$ 71.14 mm

$h_{e1}=0.5*heff$ $h_{e1}=$ 35.57 mm

The cross section is summitry in x-axis

$h_{e2}=$ 28.88 mm

For bottom flange stiffener:

$\lambda_{p,b}=b_{p2}/(28.4\varepsilon t\sqrt{k_\sigma})$ $\lambda_{p,b}=$ 0.668

The reduction factor is :

$\rho_1= (\lambda_{p,b}-0.055(3+\Psi))/\lambda_{p,b}^2$ $\rho_1=$ 1.004 → $\rho_1=$ 1

The effective width is:

$b_{eff,p,b}=\rho_1*b_{p2}$ $b_{eff,p,b}=$ 52.00 mm

$b_{e1,b}=0.5*b_{eff,p,u}$ $b_{e1,b}=$ 26.00 mm

$b_{e2,b}= b_{e1,b}$ $b_{e2,b}=$ 26.00 mm

Effective width of edge fold (Cl. 3.7.3.2.2. eqn(3.47))

The buckling factor is:

$c_{p2}/b_{p2}=$ 0.269 <0.35 → $K_\sigma =$ 0.5

$\lambda_{p,c2}=c_{p2}/(28.4\varepsilon t\sqrt{k_\sigma})$ $\lambda_{p,c2}=$ 0.508

The width reduction factor is:

$\rho_1= (\lambda_{p,c2}-0.188)/\lambda_{p,c2}^2$ $\rho_1=$ 1.24 >1 → $\rho_1=$ 1.0

$c_{eff,u}=\rho_1*c_p$ $c_{eff,u}=$ 14.0 mm

The effective area of edge stiffener is:

$A_{s,b}= t*(b_{e1,1}+c_{eff})$ $A_{s,b}=$ 80 mm^2

Use the initial cross section of the stiffener to determine the reduction factor,

allowing for effects of the continuous spring restraint

The elastic critical buckling stress for the edge stiffener

$\sigma_{cr} = 2\sqrt{KEI_s}/A_s$

For the upper edge stiffener (Cl. 3.7.3.1 eqn 3.44)

The spring stiffness is:

$K=Et^3/((4(1-v^2)(b_1^2*h_p+b_1^3+0.5*b_1*b_2*h_p*k_{f1}))$

b_1=distance from the web to the centre of the effective area of stiffener (upper flange)

b_2=distance from the web to the centre of the effective area of stiffener (lower flange)

$b_1=b_{p1}-(b_{e1,u}*t*(b_{e1,u}/2))/((b_{e1,u}+c_{eff,u})*t)$ $b_1=$ 53.5

$b_1=b_2$ → $b_2=$ 53.5

$k_{f1}=A_{s,u}/A_{s,l}$ $k_{f1}=$ 1.0 For a member in axial compression

K= 0.454

For lower edge stiffener (Cl.3.7.3.1 eqn 2.44)

The effective second moment of area is:

$I_{su}=b_{e1,1}*t^3/12+c_{eff}*t/12+b_{e1,1}*t[c_{eff}^2/2(b_{e1,1}+c_{eff})]^2+c_{eff}*t[c_{eff}/2-[c_{eff}^2/2(b_{e1,1}+c_{eff})]^2$

$I_{su=}$ 357.4 mm^4

For upper egde :

$\sigma_{cr,u}=$ 144.82 N/mm^2

Thickness reduction factor χ_d for the edge stiffener is:

if $\lambda_d \leq 0.65$ $\chi_d=1.0$

if $0.65 < \lambda_d < 1.38$ $\chi_d=1.47-0.723\lambda_d$

if $\lambda_d \geq 1.38$ $\chi_d=0.66/\lambda_d$

The relative slenderness λ_d

$\lambda_d=\sqrt{fy/\sigma_{cr,s}}$ $\lambda_{d,b}=$ 1.858

$\chi_d=0.66/\lambda_d$ $\chi_{d,b}=$ 0.355

Effective section properties of the flange and lip in compression

$A_{eff}= t\,[b_{e1,u}+b_{e1,b}+h_{e1}+h_{e2}+(b_{e2,u}+b_{e2,b})\chi_{d,u}+(c_{eff,b}+c_{eff,b})\chi_{d,b}\,]$

$A_{eff}=$ 307.9 mm^2

$N_{ed}=f_y/\gamma_m*A_{eff}$ Ned= 153.9 kN

1-Design Against Global Buckling (EN1993-1-5)

For stiffened plate $\sigma_{cr,c}$ may be determined from the elastic critical column buckling

stress $\sigma_{cr,sl}$ of the stiffener closest to the panel edge with the highest compressive stress as follows:

$\sigma_{cr,sl}= \pi^2EI_{sl,1}/A_{sl,1}a^2$

$Ned=\pi^2KEI_{sl,1}/a^2$

$I_{sl,1}=$ 232693E4 mm^4

For pinned end K= 1.0

For fixed end K= 4.0

Appendix H: Experimental results

C-section / pinned end / 1.0 m length

Figure (H-1) Experimental buckling mode shape of 1.0 m length of C-section for pinned ends conditions

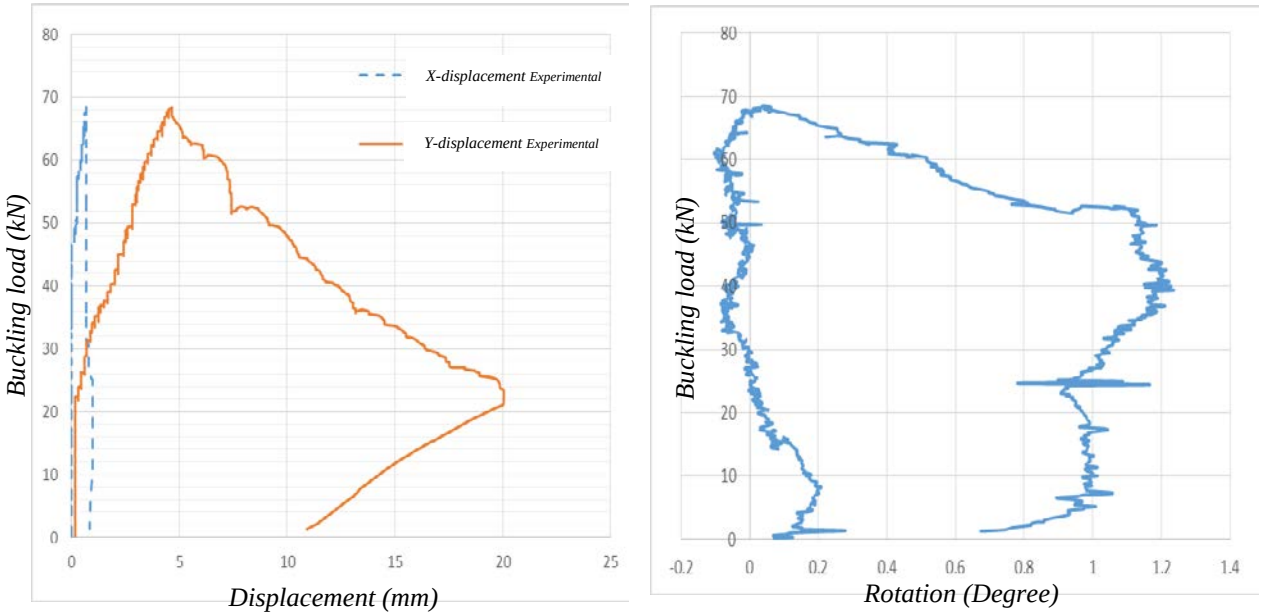

Figure (H-2) Experimental load-deformation relations of 1.0 m length at mid web of 0.5L of C-section for pinned ends conditions

C-section / pinned end / 1.3 m length

Figure (H-3) Experimental buckling mode shape of 1.3 m length of C-section for pinned ends conditions

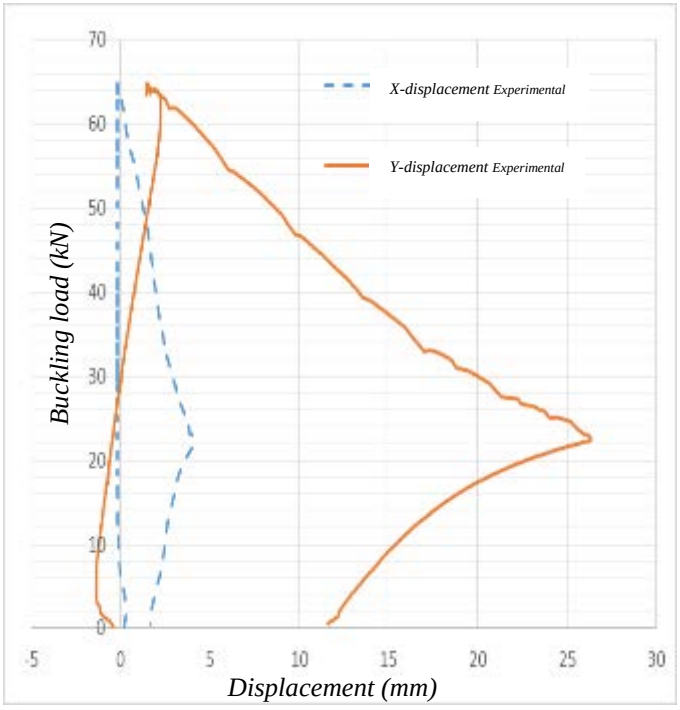

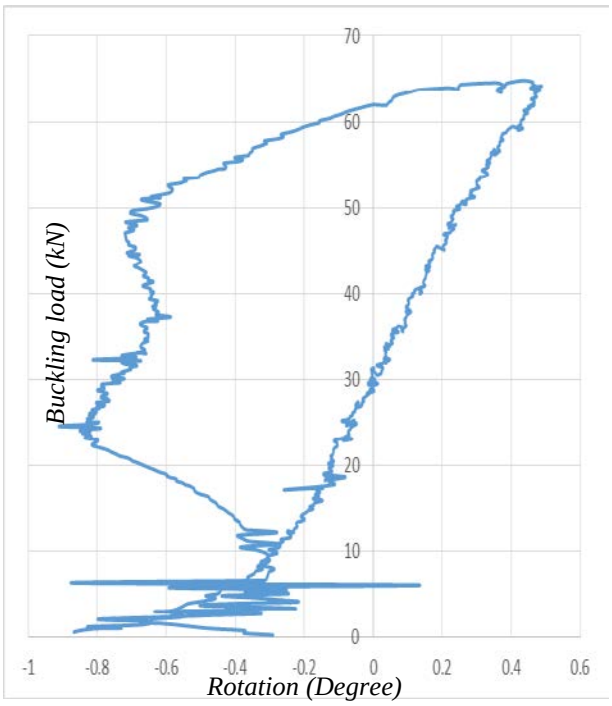

Figure (H-4) Experimental load-deformation relations of 1.3 m length at mid web of 0.5L of C-section for pinned ends conditions

C-section / pinned end / 1.7 m length

Figure (H-5) Experimental buckling mode shape of 1.7 m length of C-section for pinned ends conditions

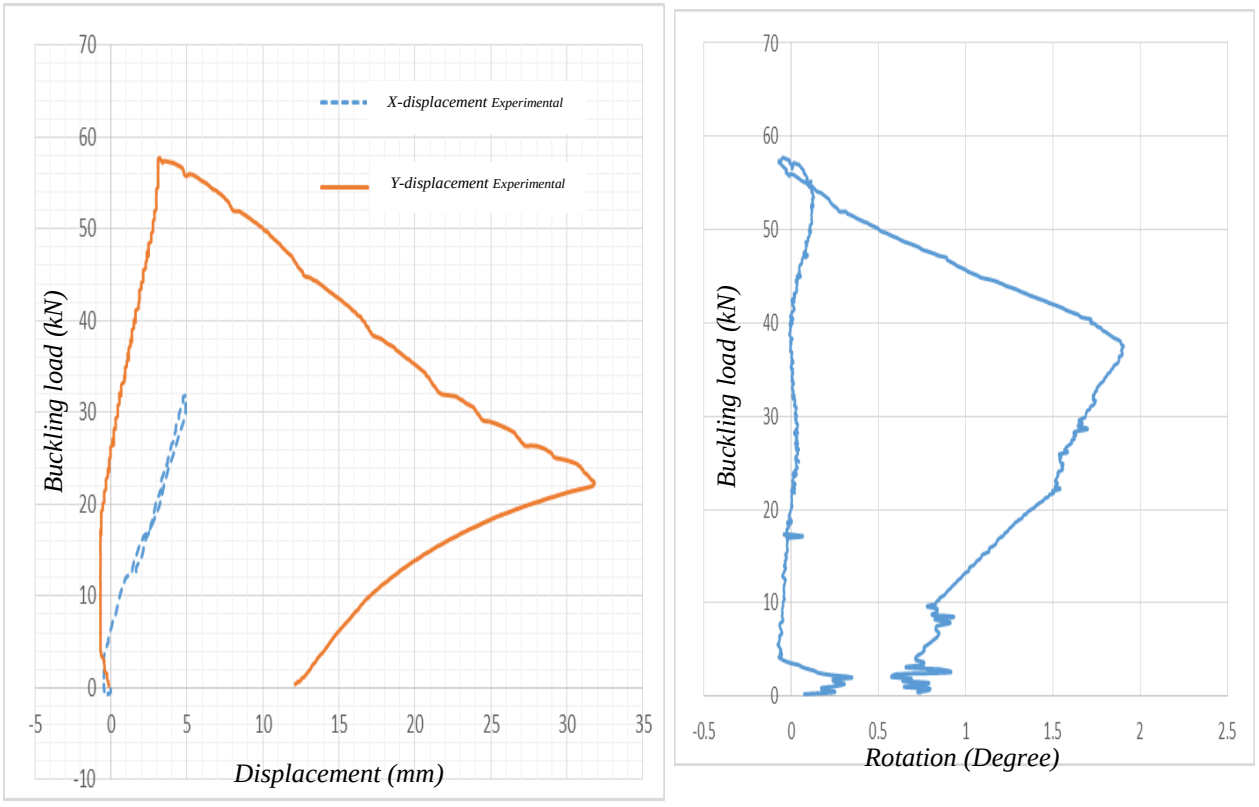

Figure (H-6) Experimental load-deformation relations of 1.7 m length at mid web of 0.5L of C-section for pinned ends conditions

C-section / pinned end / 2.0 m length

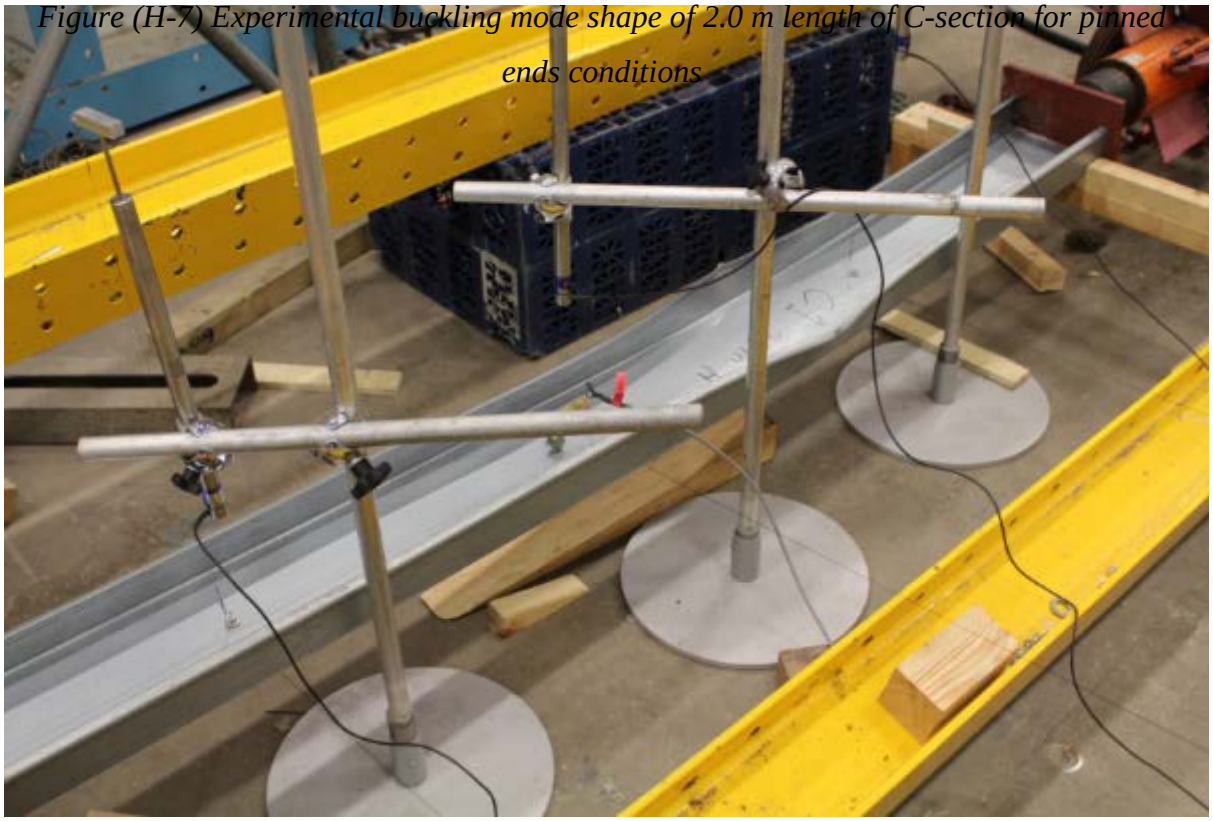

Figure (H-7) Experimental buckling mode shape of 2.0 m length of C-section for pinned ends conditions

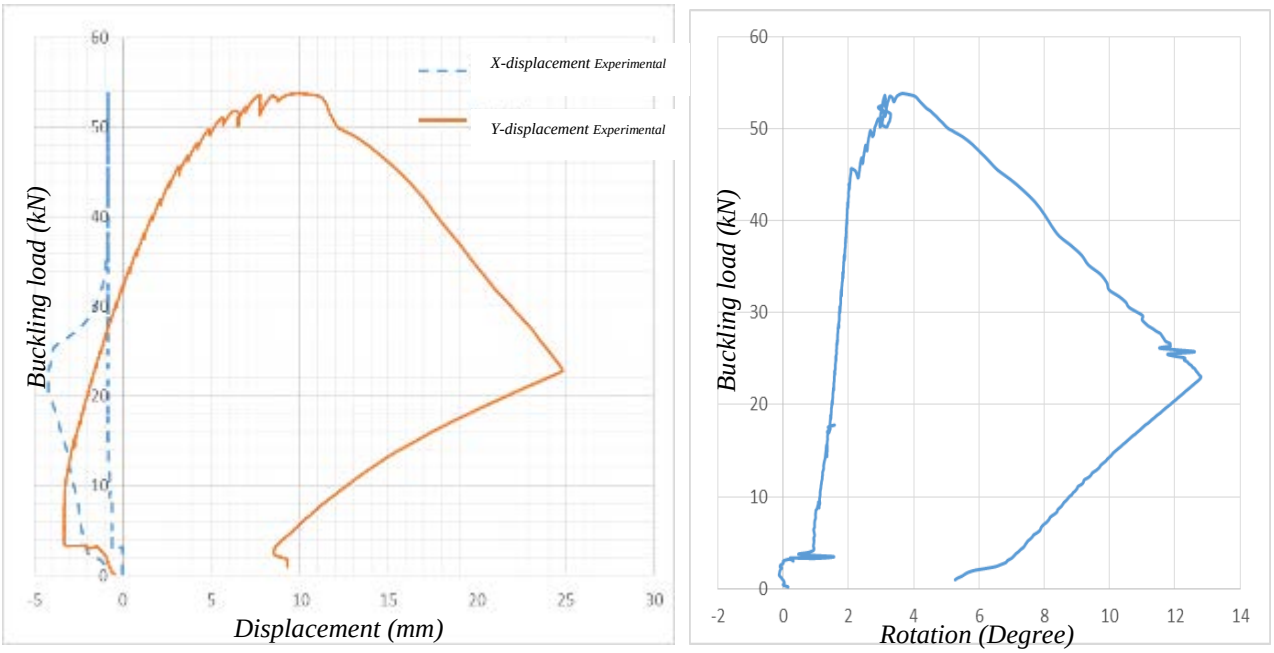

Figure (H-8) Experimental load-deformation relations of 2.0 m length at mid web of 0.5L of C-section for pinned ends conditions

C-section / pinned end / 2.3 m length

Figure (H-9) Experimental buckling mode shape of 2.3 m length of C-section for pinned ends conditions

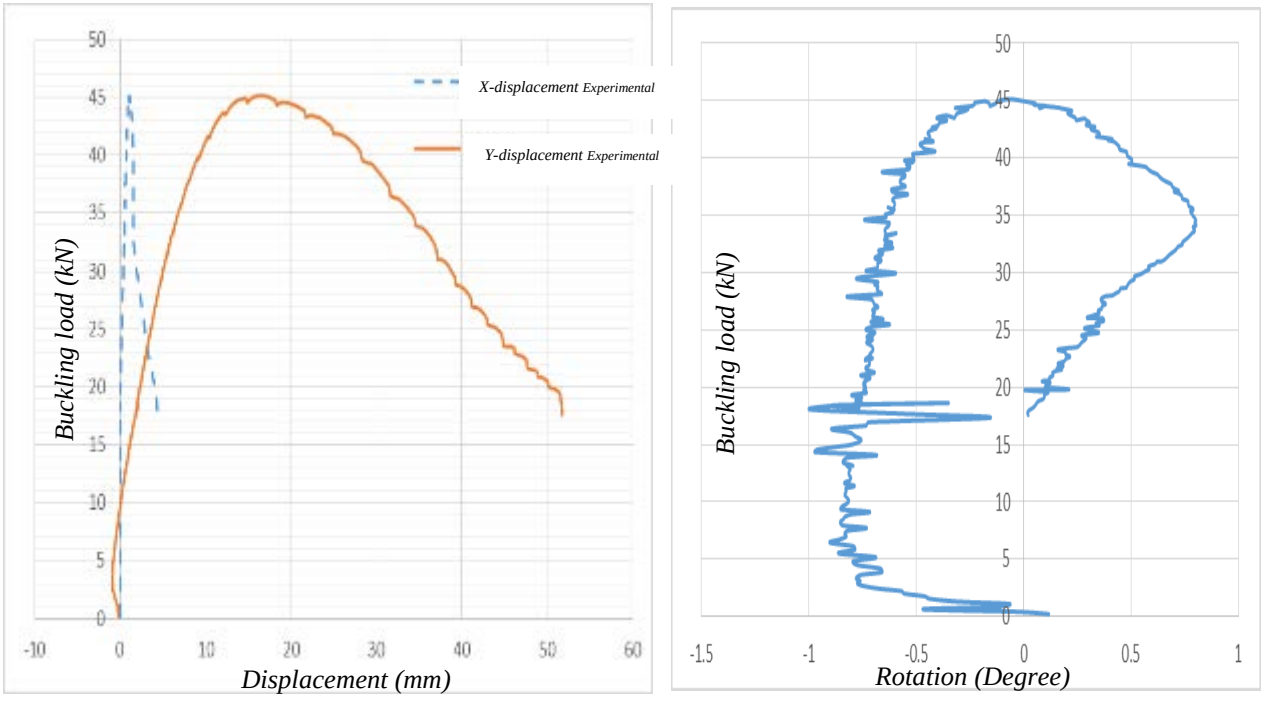

Figure (H-10) Experimental load-deformation relations of 2.3 m length at mid web of 0.5L of C-section for pinned ends conditions

C-section / pinned end / 2.7 m length

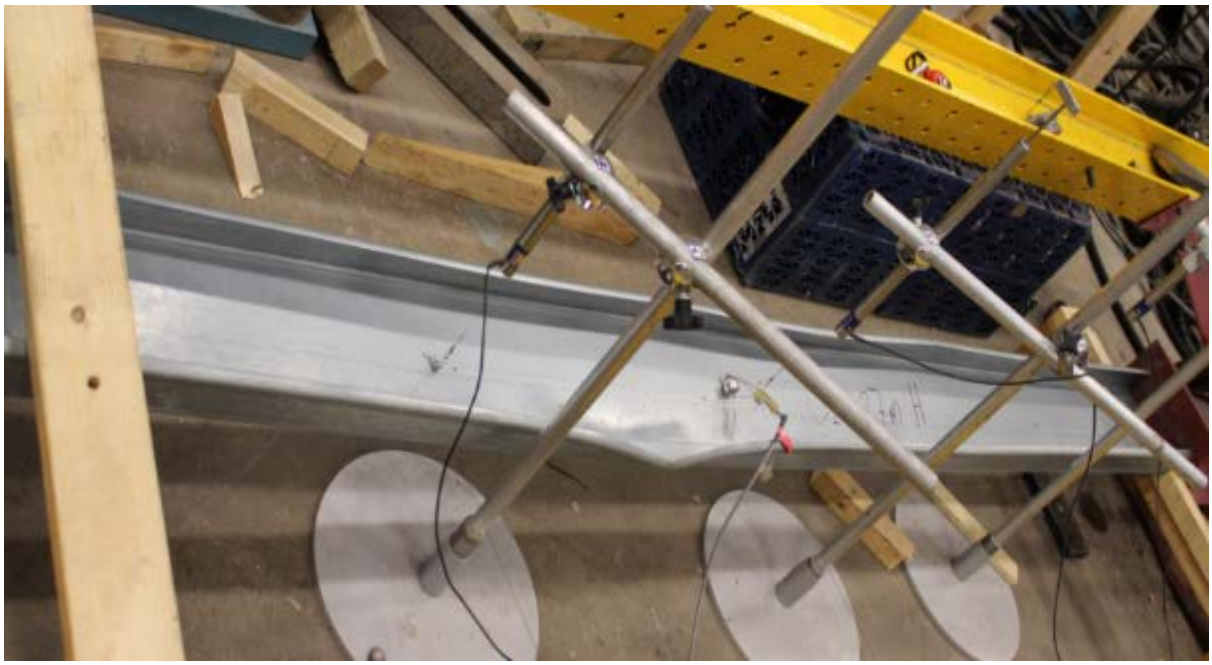

Figure (H-11) Experimental buckling mode shape of 2.7 m length of C-section for pinned ends conditions

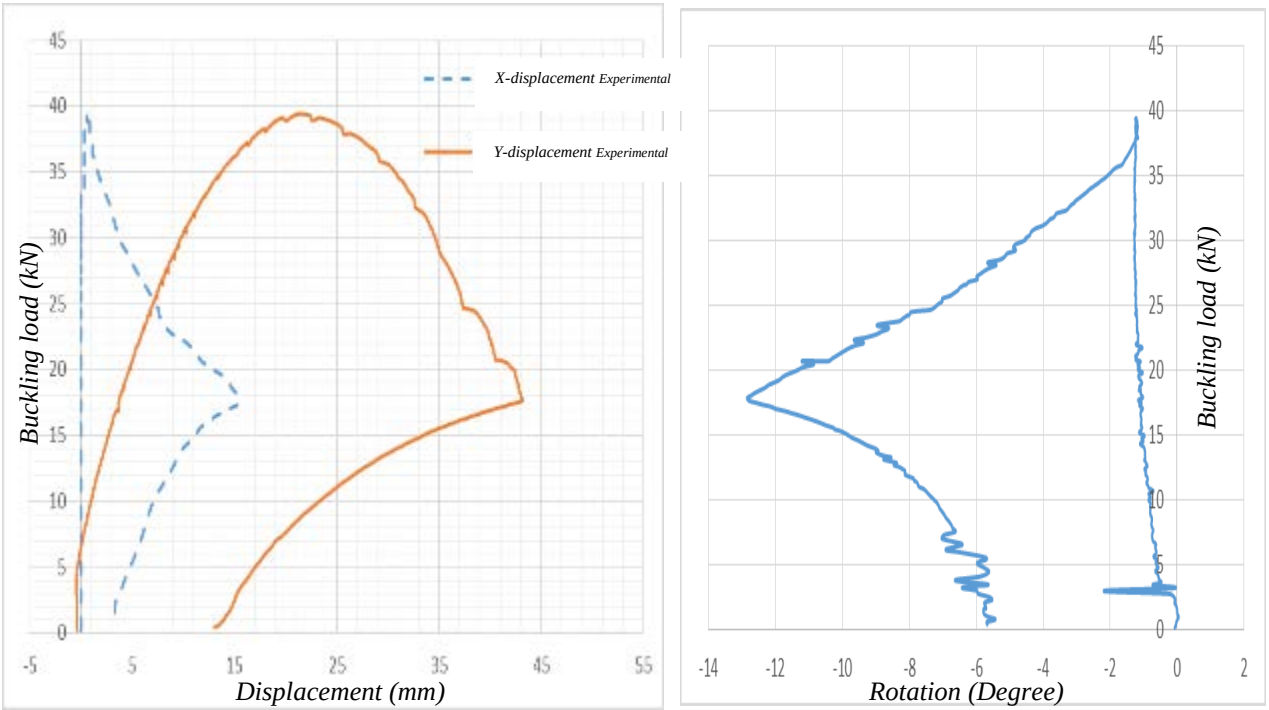

Figure (H-12) Experimental load-deformation relations of 2.7 m length at mid web of 0.5L of C-section for pinned ends conditions

C-section / pinned end / 3.0 m length

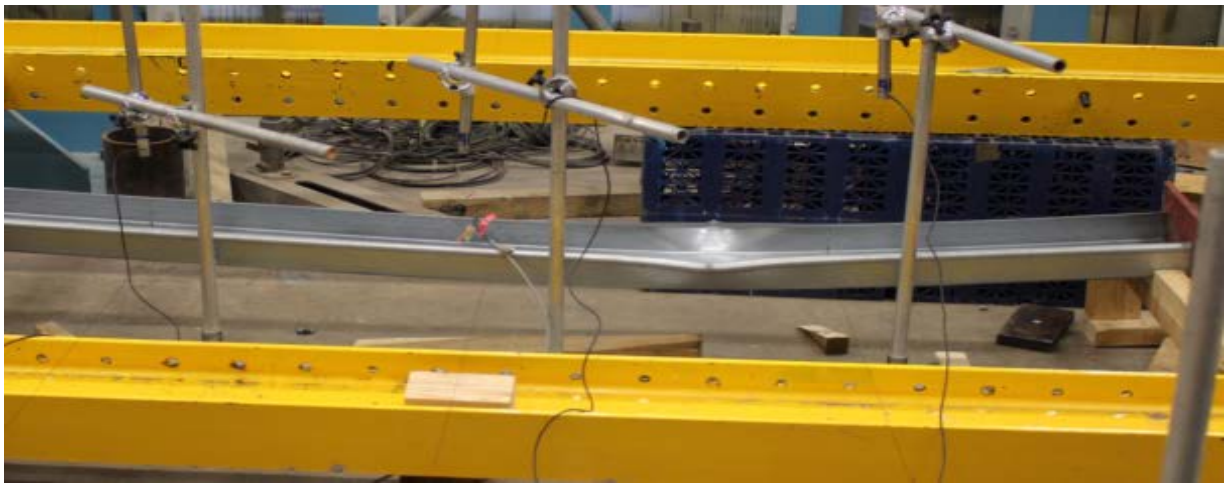

Figure (H-13) Experimental buckling mode shape of 3.0 m length of C-section for pinned ends conditions

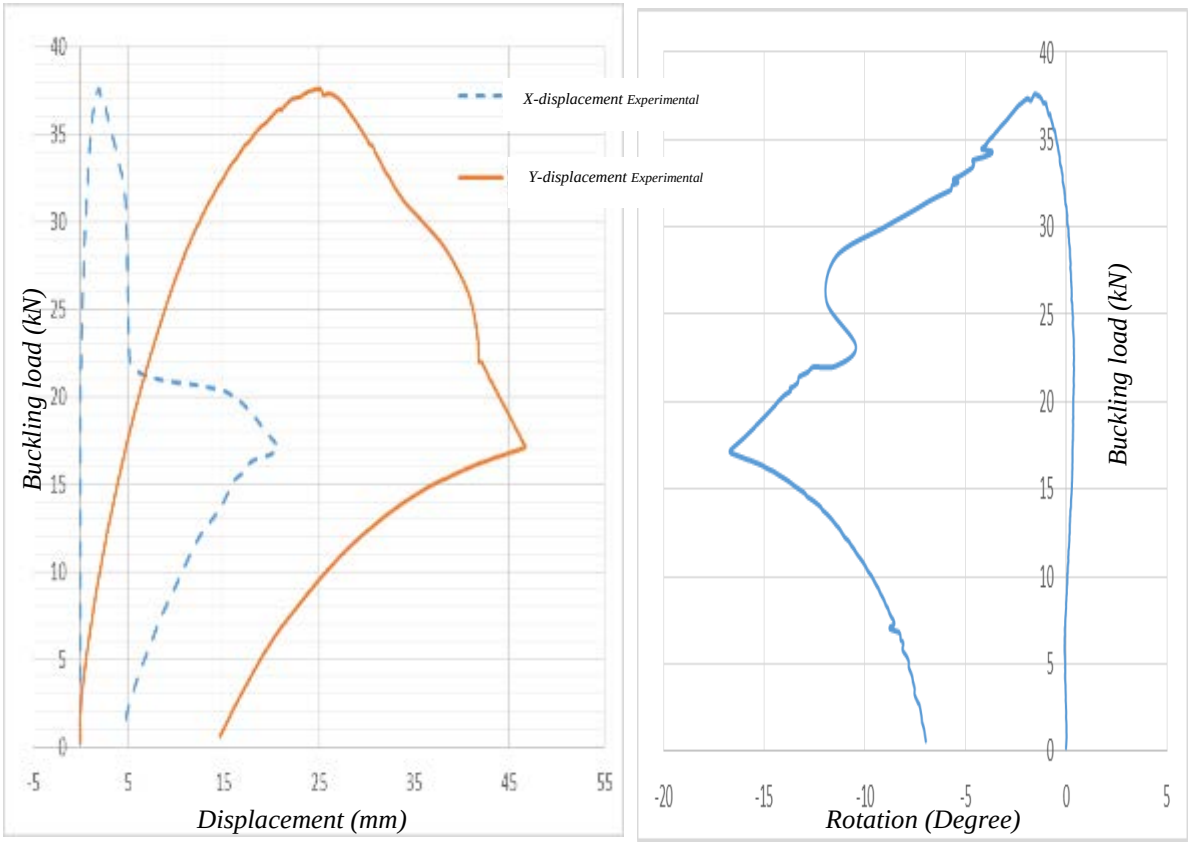

Figure (H-14) Experimental load-deformation relations of 3.0 m length at mid web of 0.5L of C-section for pinned ends conditions

C-section / pinned end / 4.0 m length

Figure (H-15) Experimental buckling mode shape of 4.0 m length of C-section for pinned ends conditions

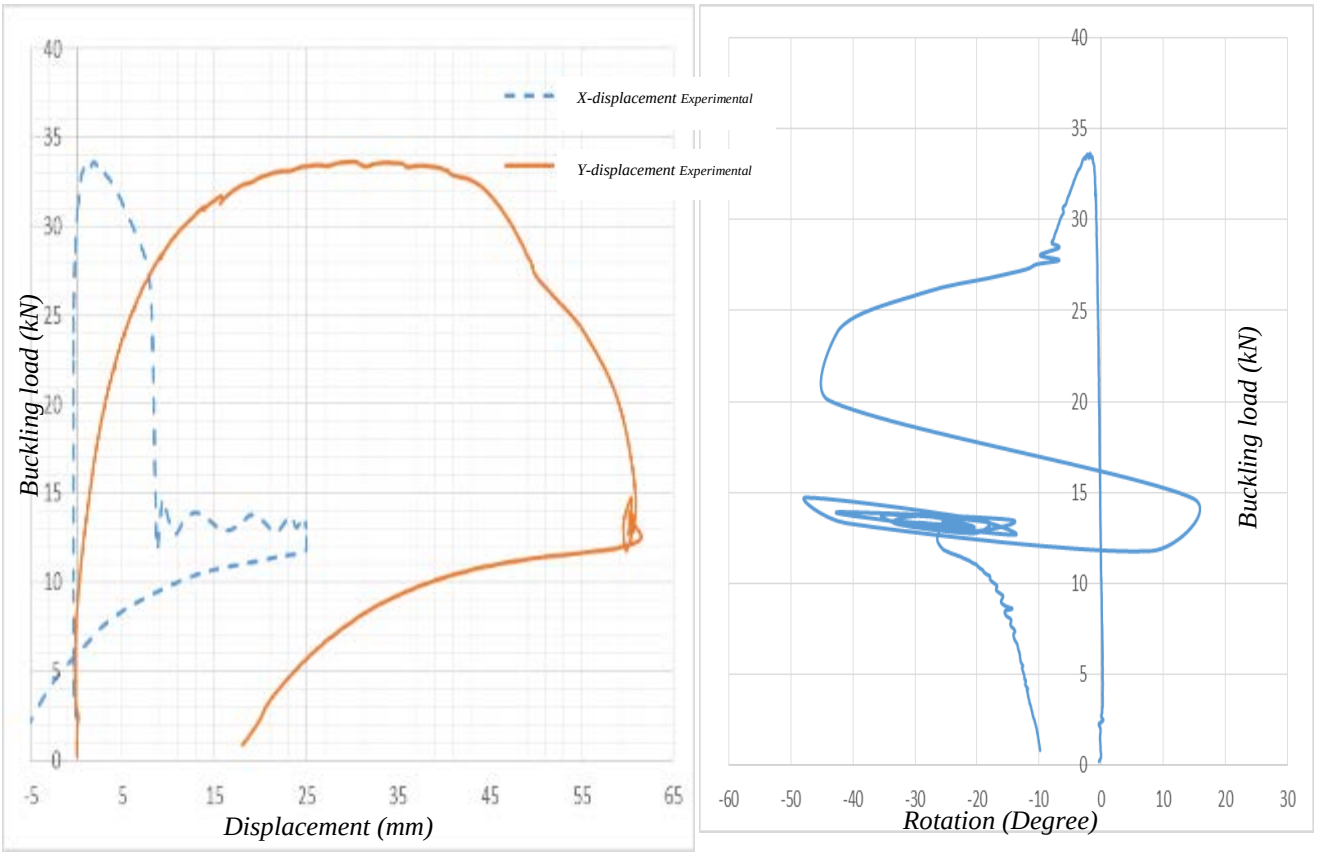

Figure (H-16) Experimental load-deformation relations of 4.0 m length at mid web of 0.5L of C-section for pinned ends conditions

C-section / pinned end / 5.0 m length

Figure (H-17) Experimental buckling mode shape of 5.0 m length of C-section for pinned ends conditions

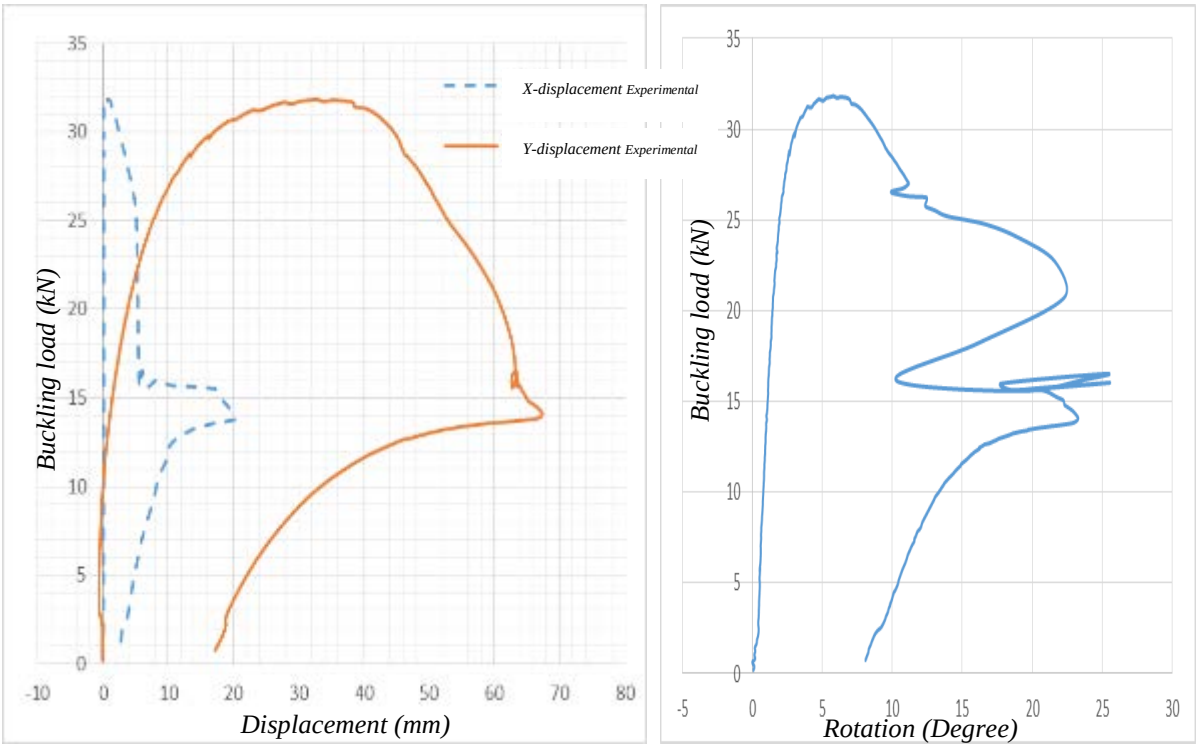

Figure (H-18) Experimental load-deformation relations of 5.0 m length at mid web of 0.5L of C-section for pinned ends conditions

Z-section / pinned end / 1.0 m length

Figure (H-19) Experimental buckling mode shape of 1.0 m length of Z-section for pinned ends conditions

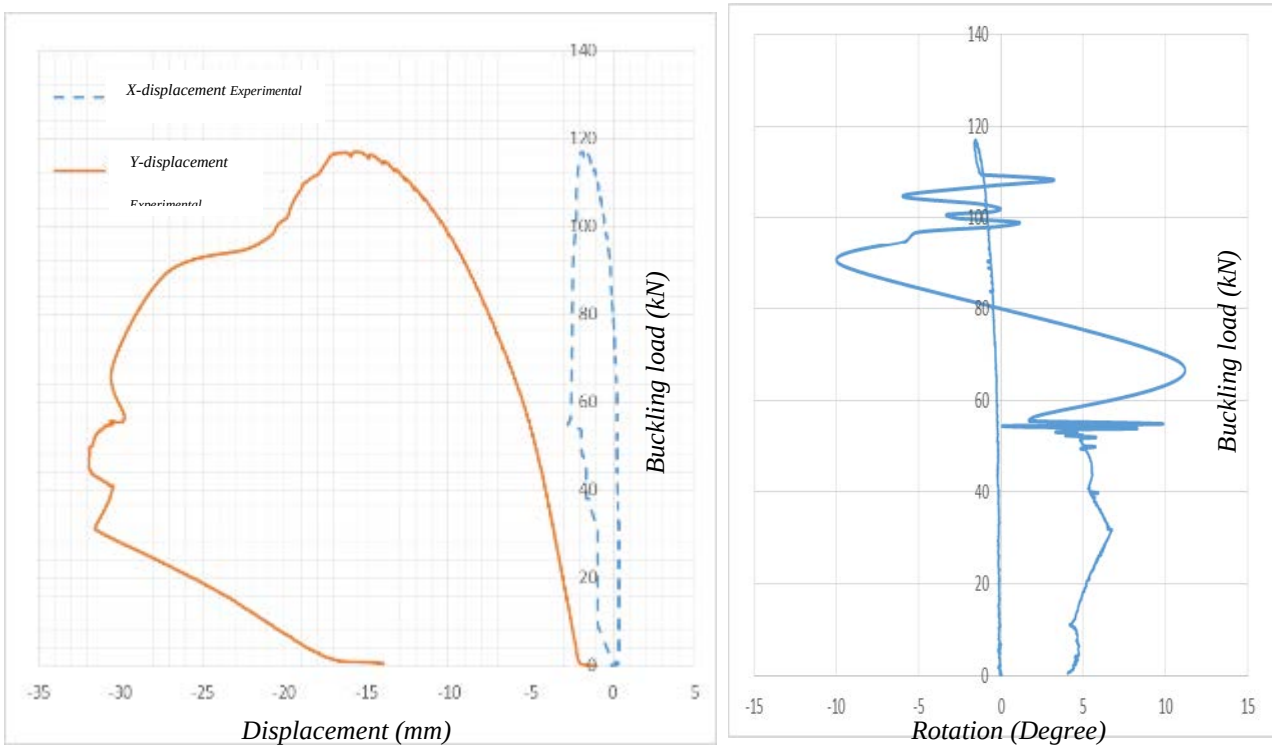

Figure (H-20) Experimental load-deformation relations of 1.0 m length at mid web of 0.5L of Z-section for pinned ends conditions

Z-section / pinned end / 1.3 m length

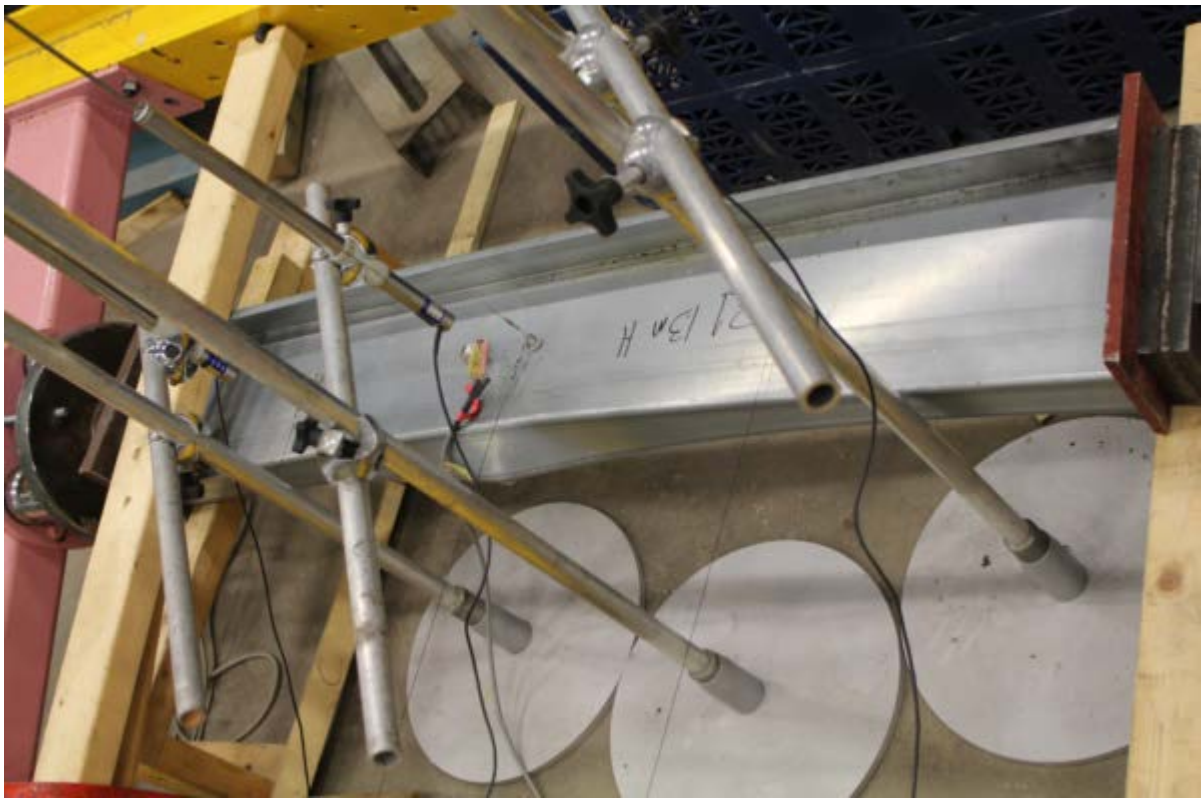

Figure (H-21) Experimental buckling mode shape of 1.3 m length of Z-section for pinned ends conditions

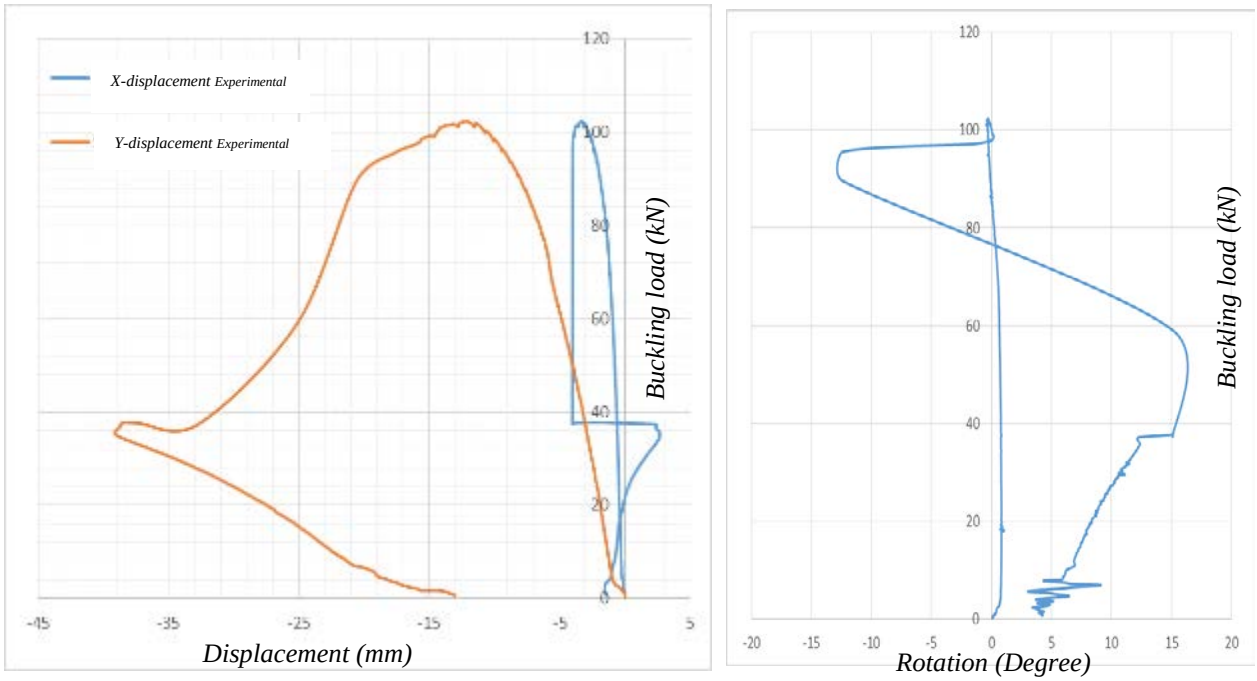

Figure (H-22) Experimental load-deformation relations of 1.3 m length at mid web of 0.5L of Z-section for pinned ends conditions

Z-section / pinned end / 1.7 m length

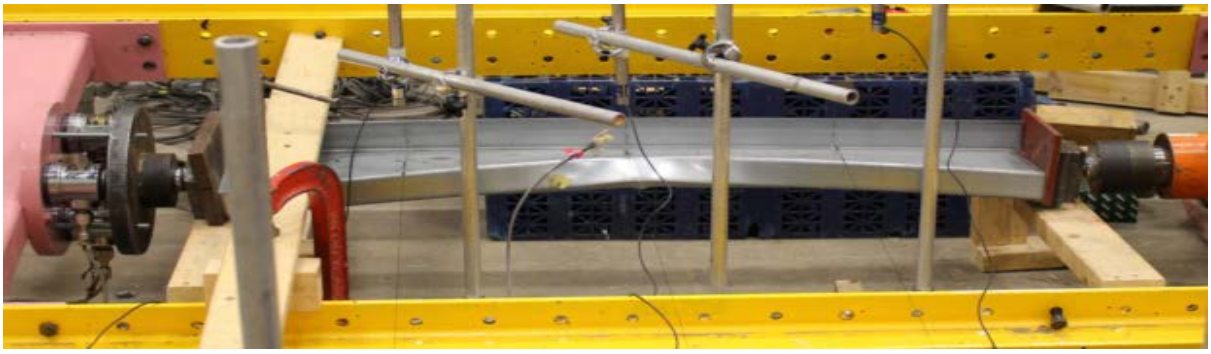

Figure (H-23) Experimental buckling mode shape of 1.7 m length of Z-section for pinned ends conditions

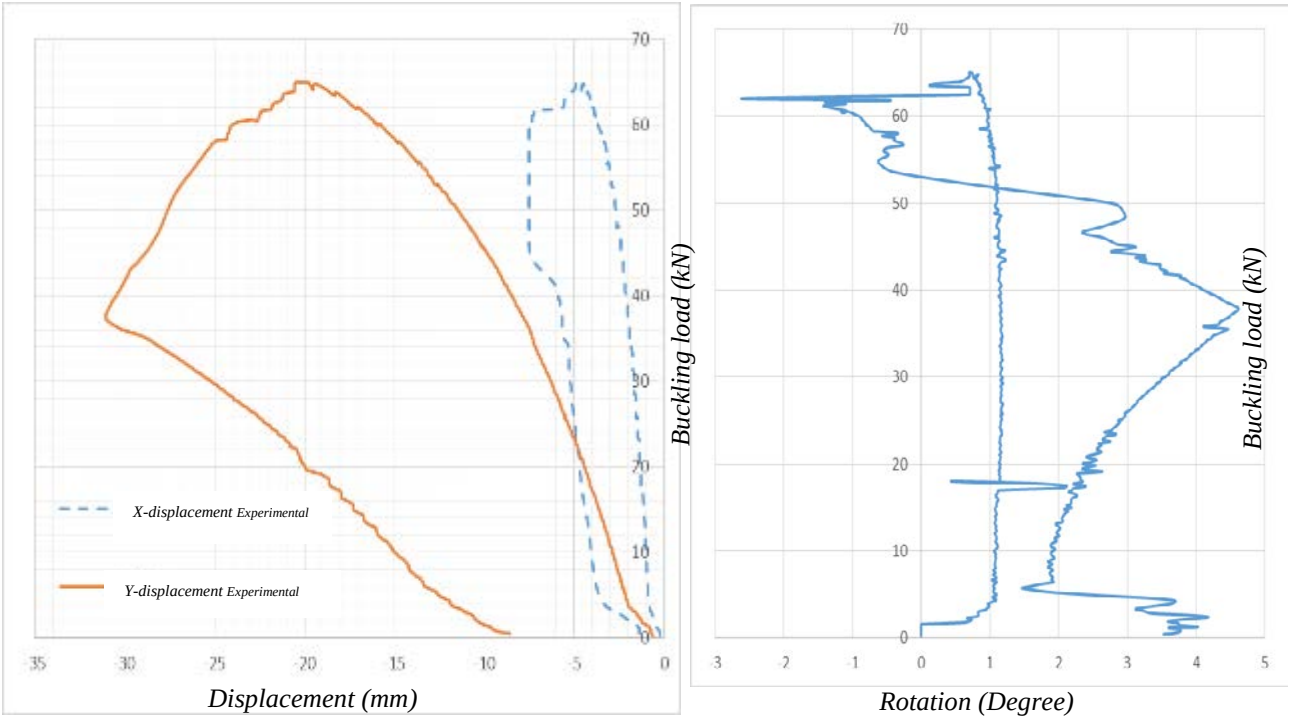

Figure (H-24) Experimental load-deformation relations of 1.7 m length at mid web of 0.5L of Z-section for pinned ends conditions

Z-section / pinned end / 2.0 m length

Figure (H-25) Experimental buckling mode shape of 2.0 m length of Z-section for pinned ends conditions

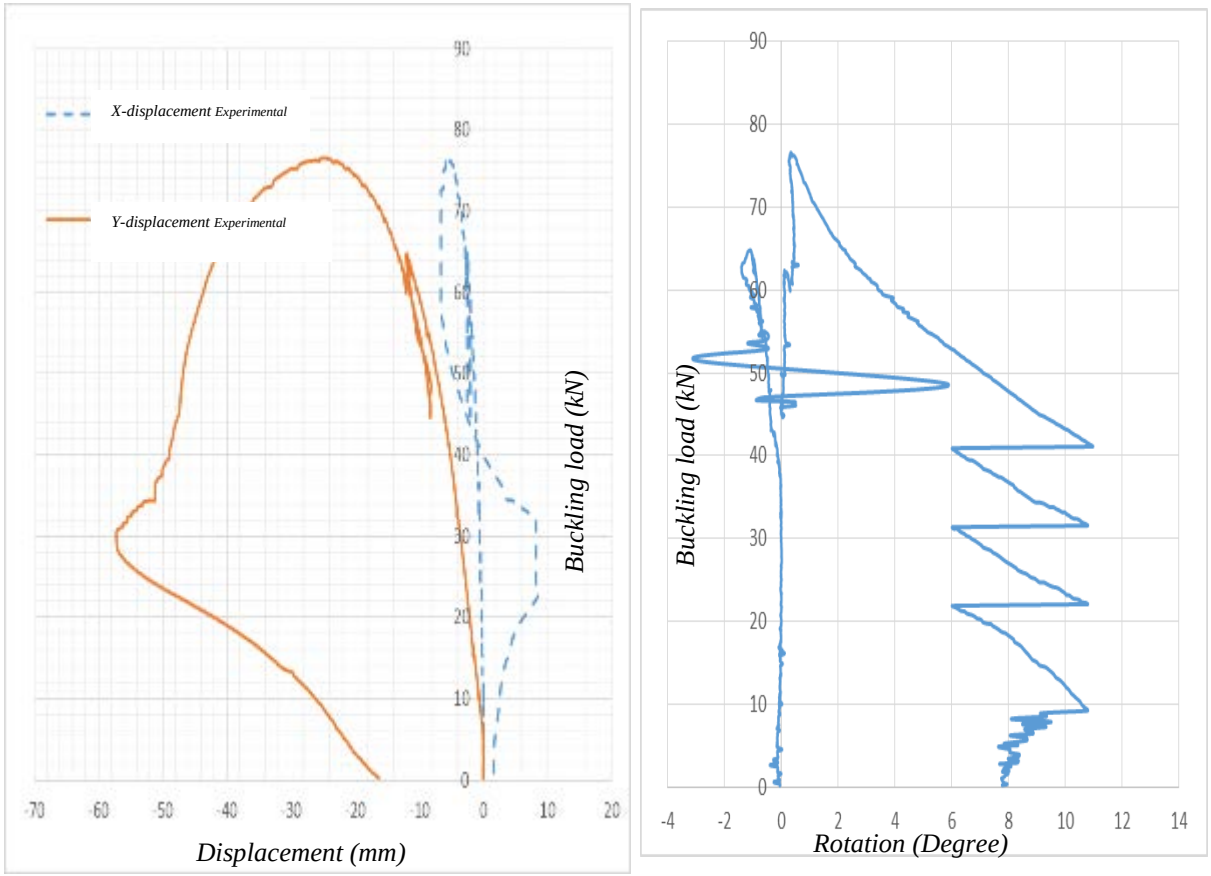

Figure (H-26) Experimental load-deformation relations of 2.0 m length at mid web of 0.5L of Z-section for pinned ends conditions

Z-section / pinned end / 2.3 m length

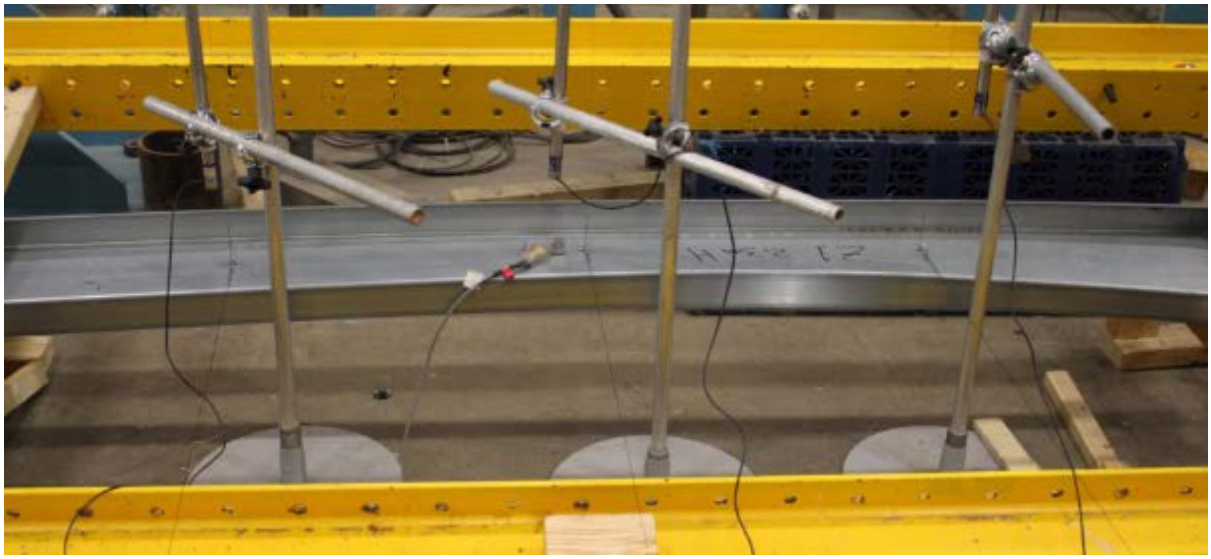

Figure (H-27) Experimental buckling mode shape of 2.3 m length of Z-section for pinned ends conditions

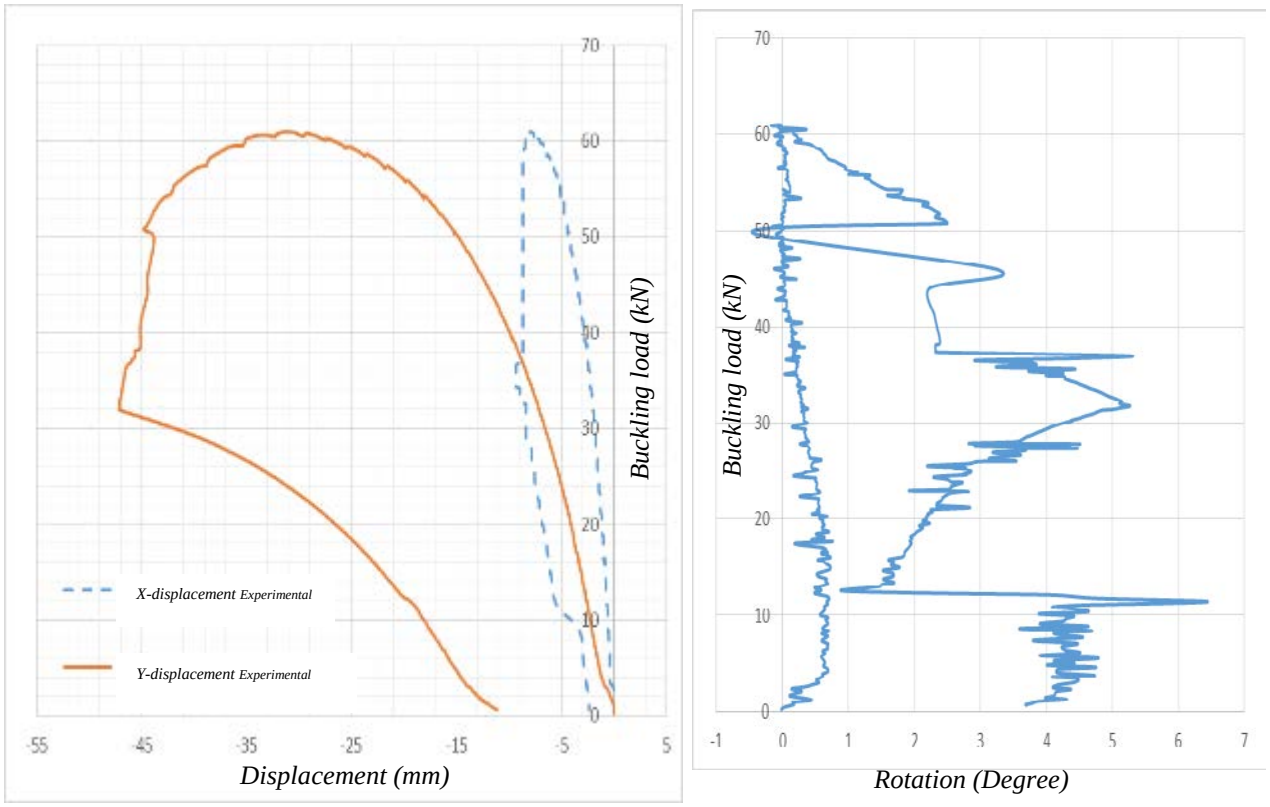

Figure (H-28) Experimental load-deformation relations of 2.3 m length at mid web of 0.5L of Z-section for pinned ends conditions

Z-section / pinned end / 2.7 m length

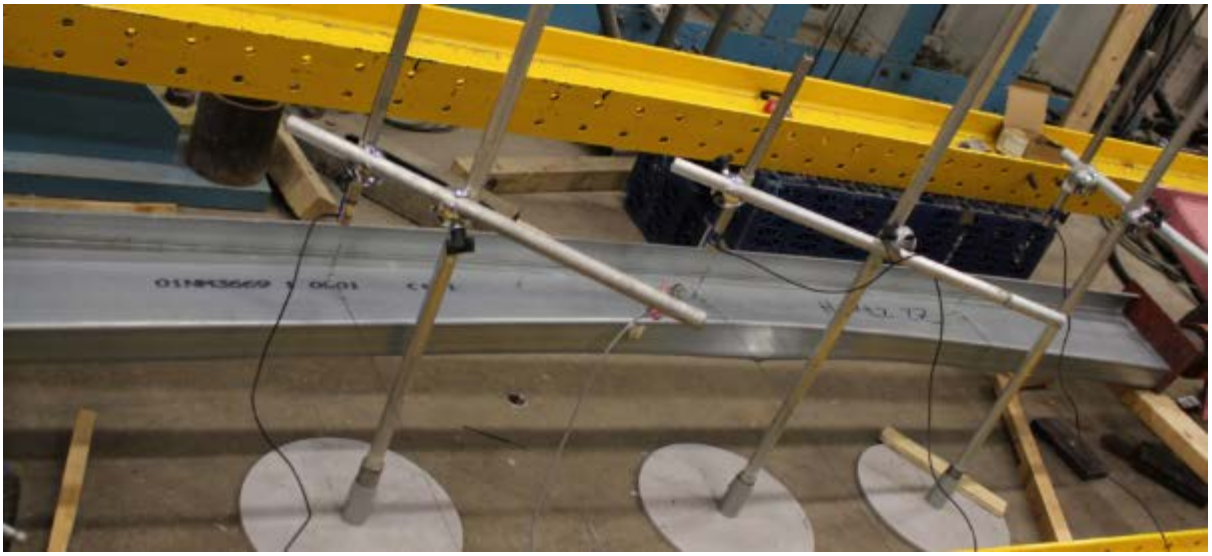

Figure (H-29) Experimental buckling mode shape of 2.7 m length of Z-section for pinned ends conditions

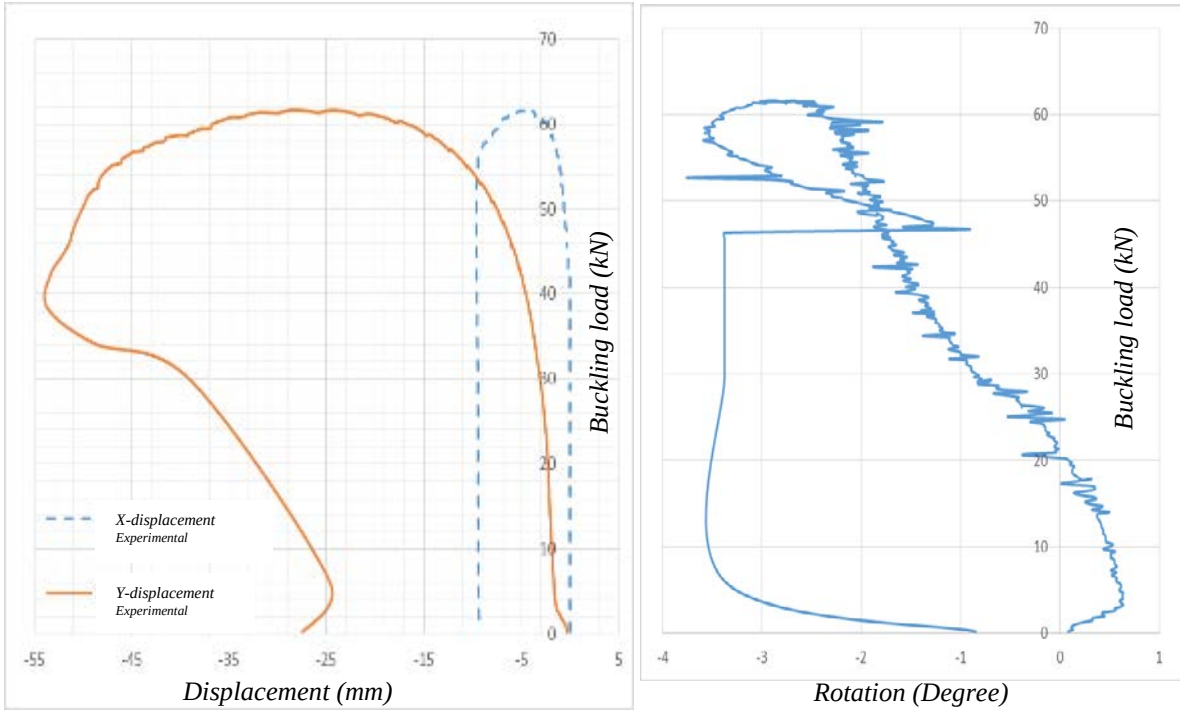

Figure (H-30) Experimental load-deformation relations of 2.7 m length at mid web of 0.5L of Z-section for pinned ends conditions

Z-section / pinned end / 3.0 m length

Figure (H-31) Experimental buckling mode shape of 3.0 m length of Z-section for pinned ends conditions

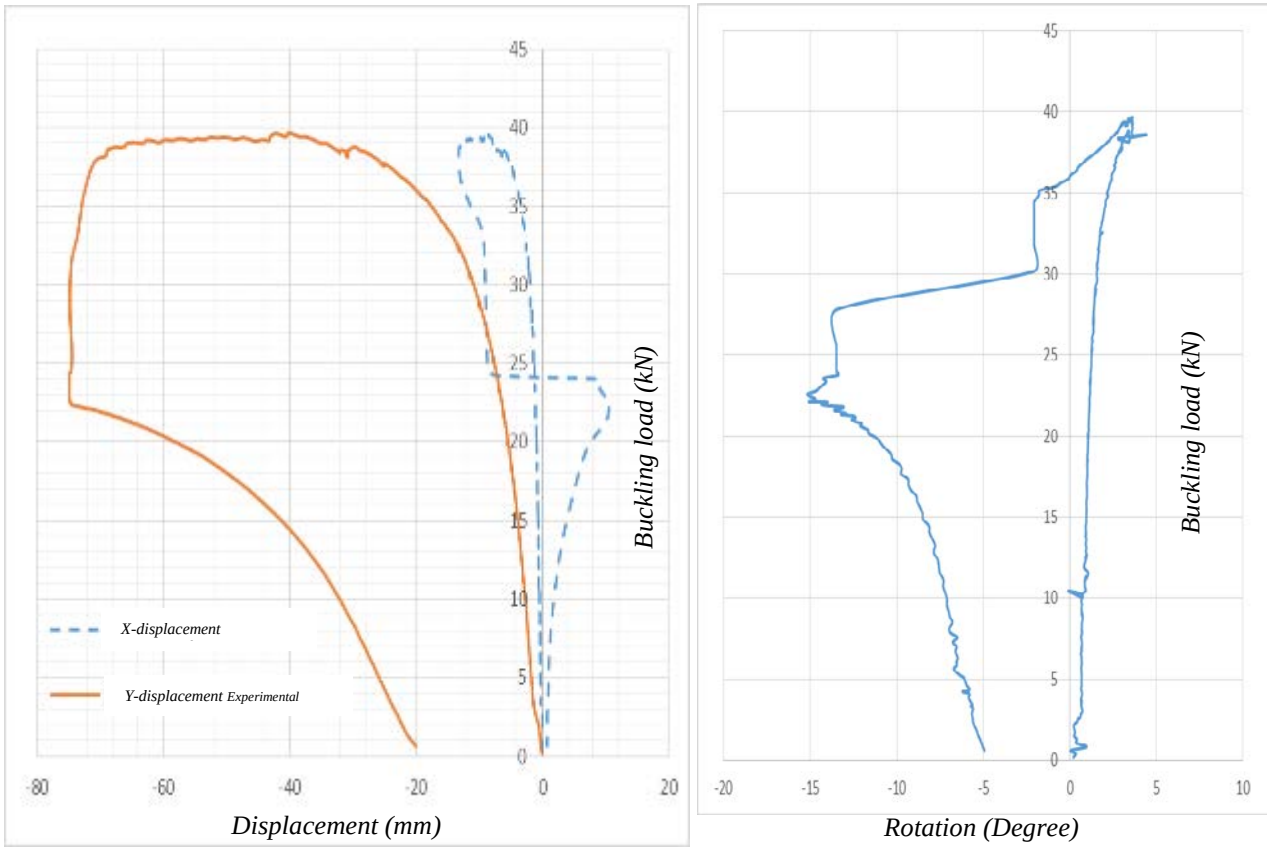

Figure (H-32) Experimental load-deformation relations of 3.0 m length at mid web of 0.5L of Z-section for pinned ends conditions

Z-section / pinned end / 4.0 m length

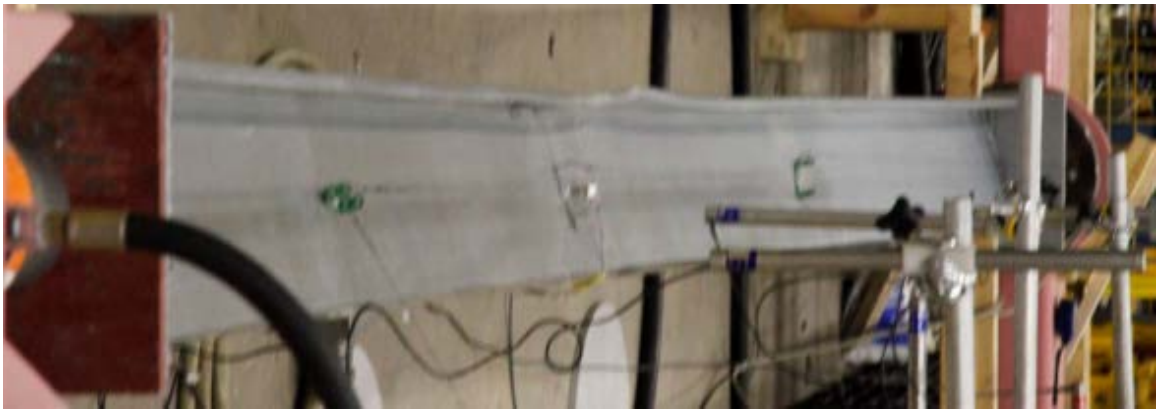

Figure (H-33) Experimental buckling mode shape of 4.0 m length of Z-section for pinned ends conditions

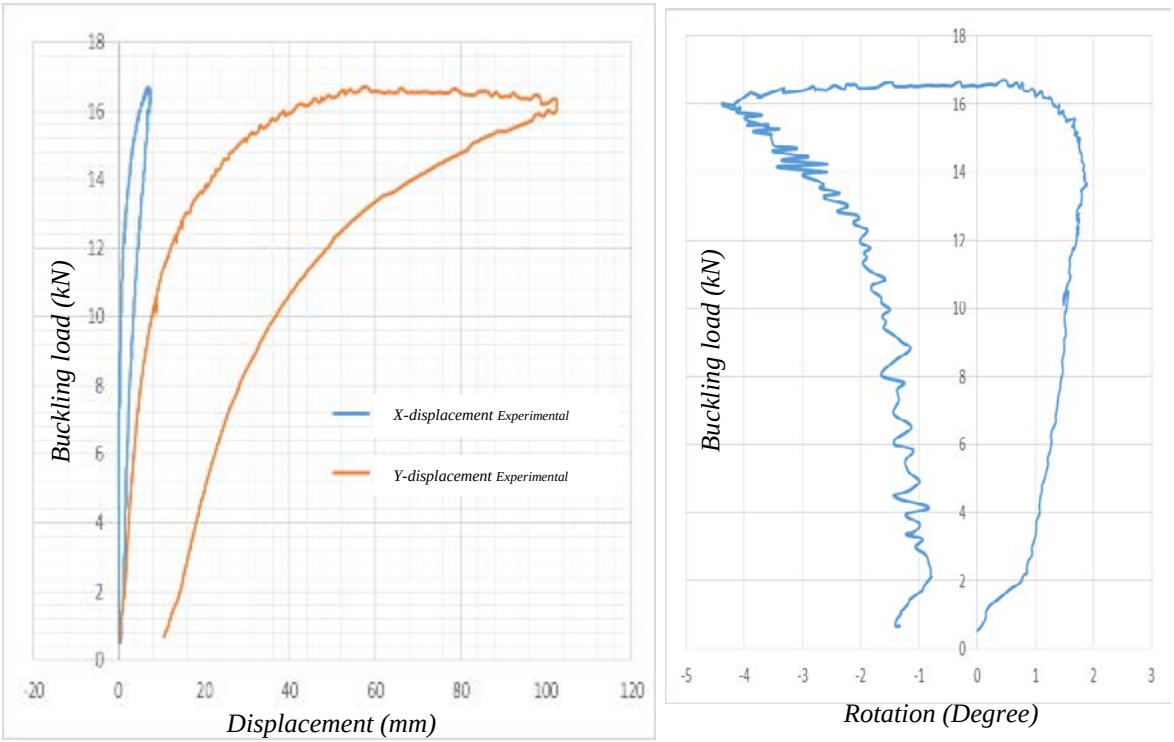

Figure (H-34) Experimental load-deformation relations of 4.0 m length at mid web of 0.5L of Z-section for pinned ends conditions

Z-section / pinned end / 5.0 m length

Figure (H-35) Experimental buckling mode shape of 5.0 m length of Z-section for pinned ends conditions

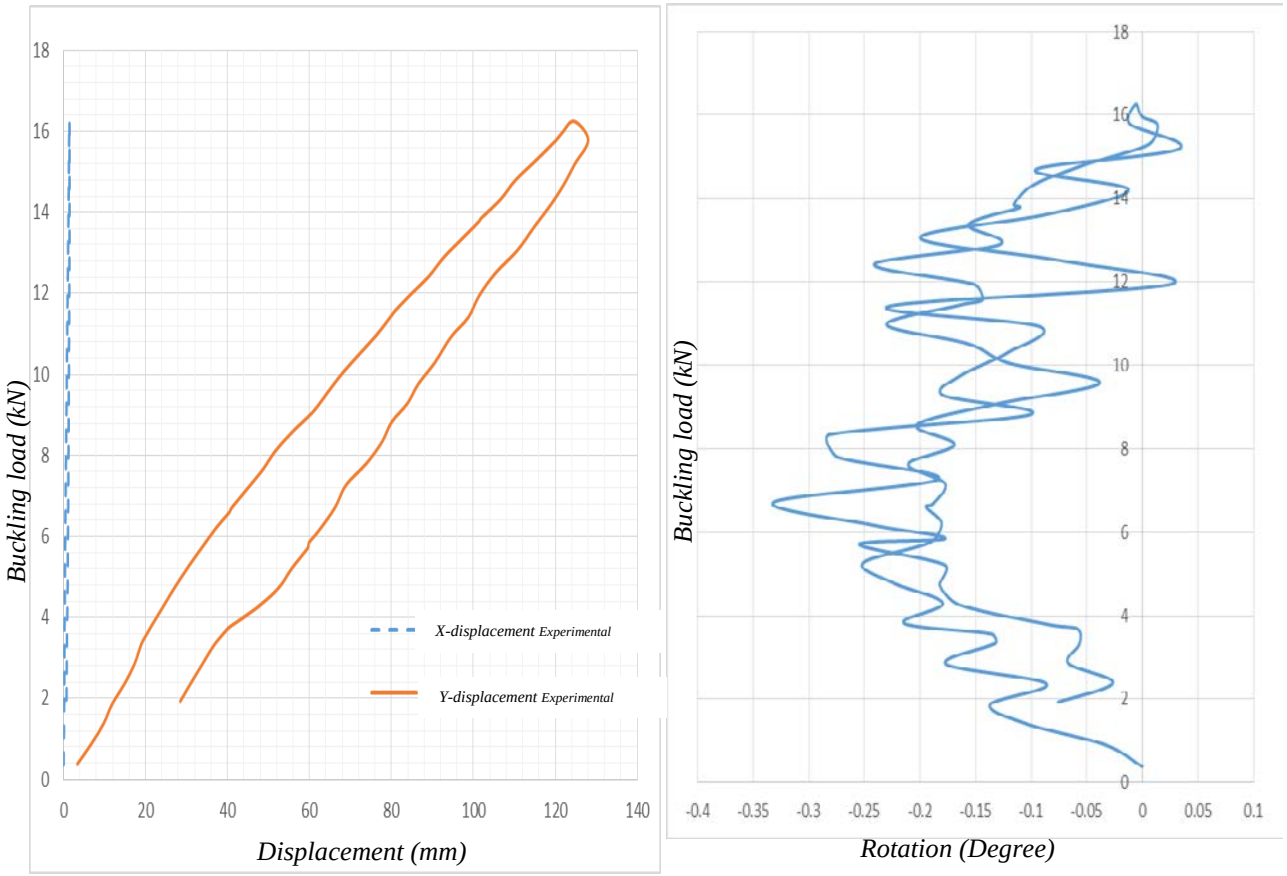

Figure (H-36) Experimental load-deformation relations of 5.0 m length at mid web of 0.5L of Z-section for pinned ends conditions

C-section / fixed end / 1.0 m length

Figure (H-37) Experimental buckling mode shape of 1.0 m length of C-section for fixed ends conditions

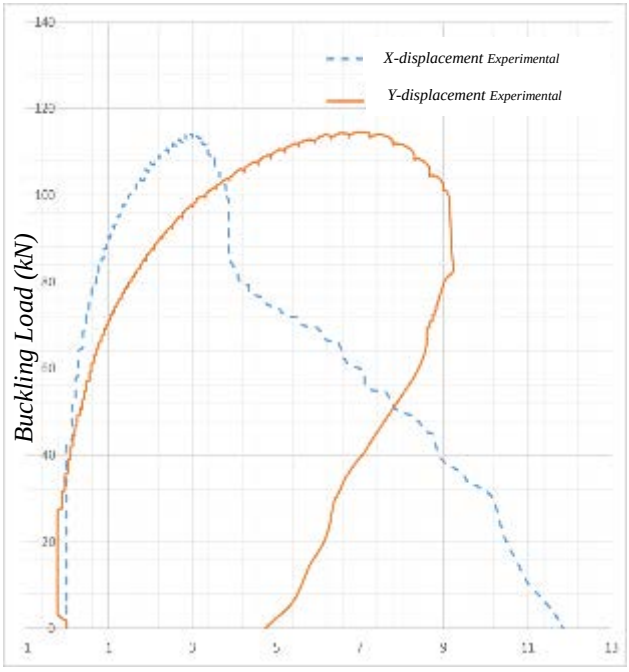

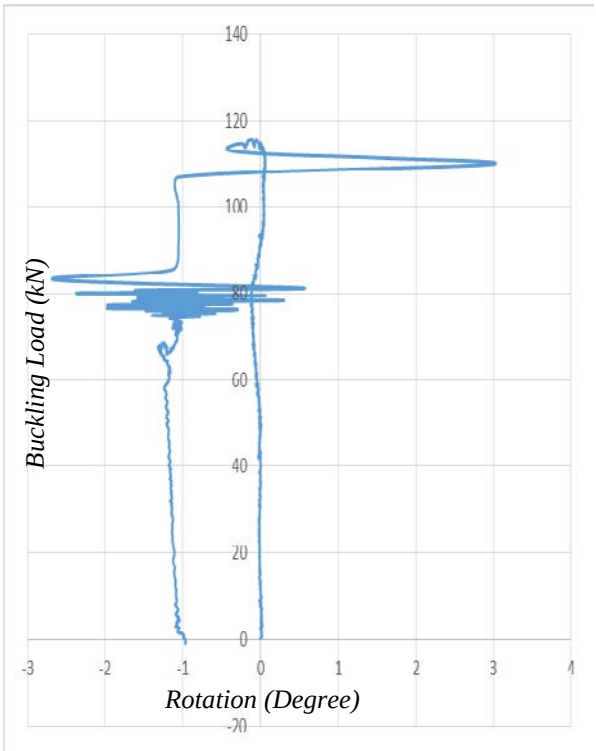

Figure (H-38) Experimental load-deformation relations of 1.0 m length at mid web of 0.5L of C-section for fixed ends conditions

C-section / fixed end / 1.3 m length

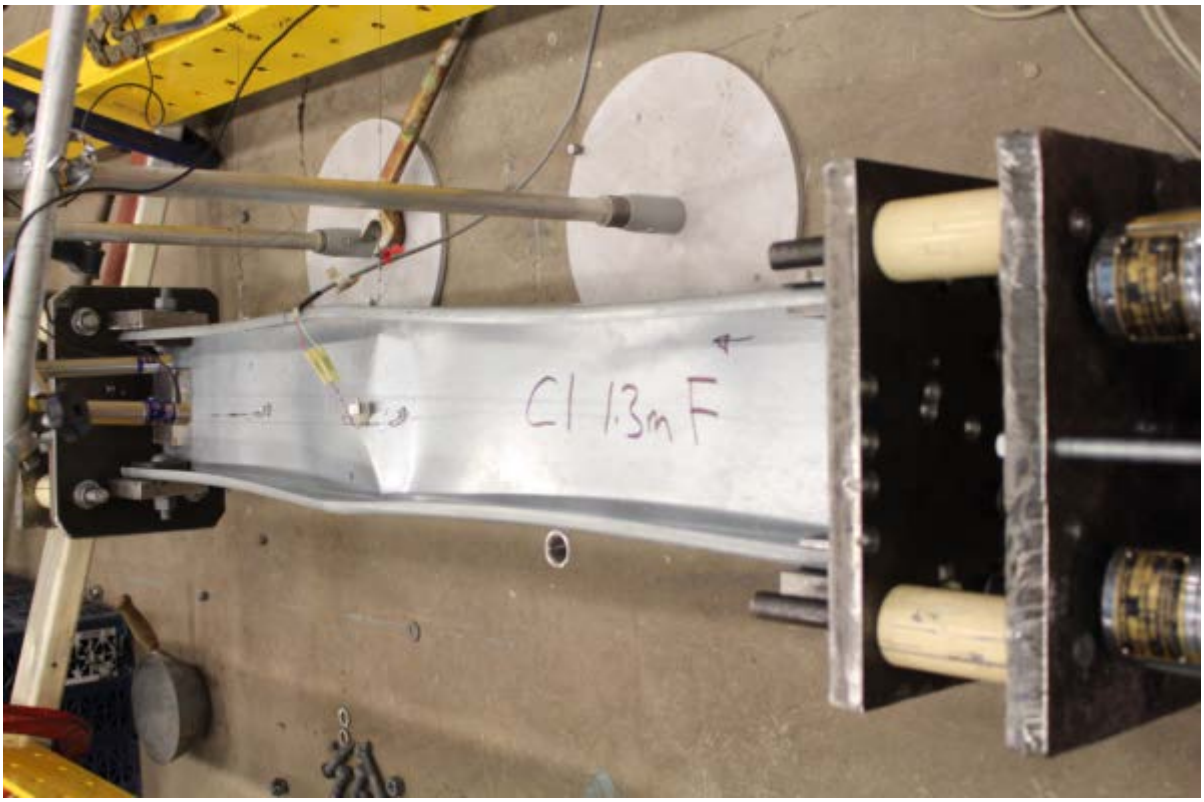

Figure (H-39) Experimental buckling mode shape of 1.3 m length of C-section for fixed ends conditions

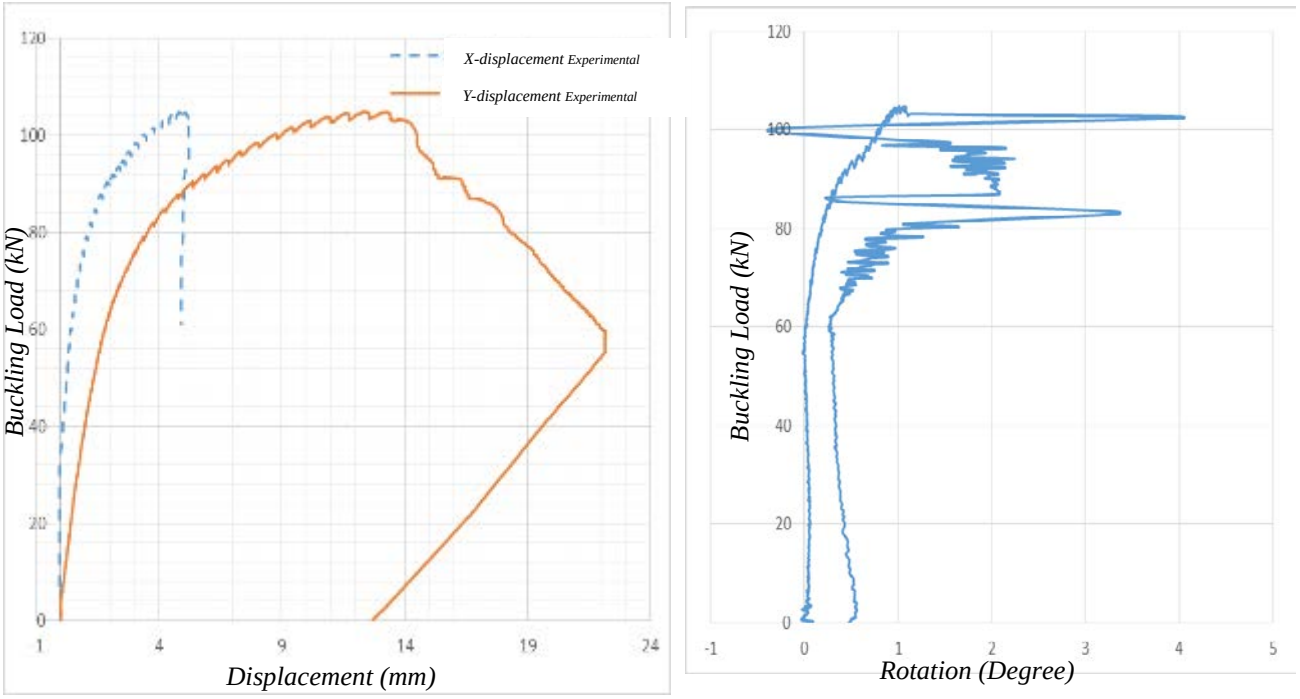

Figure (H-40) Experimental load-deformation relations of 1.3 m length at mid web of 0.5L of C-section for fixed ends conditions

C-section / fixed end / 1.7 m length

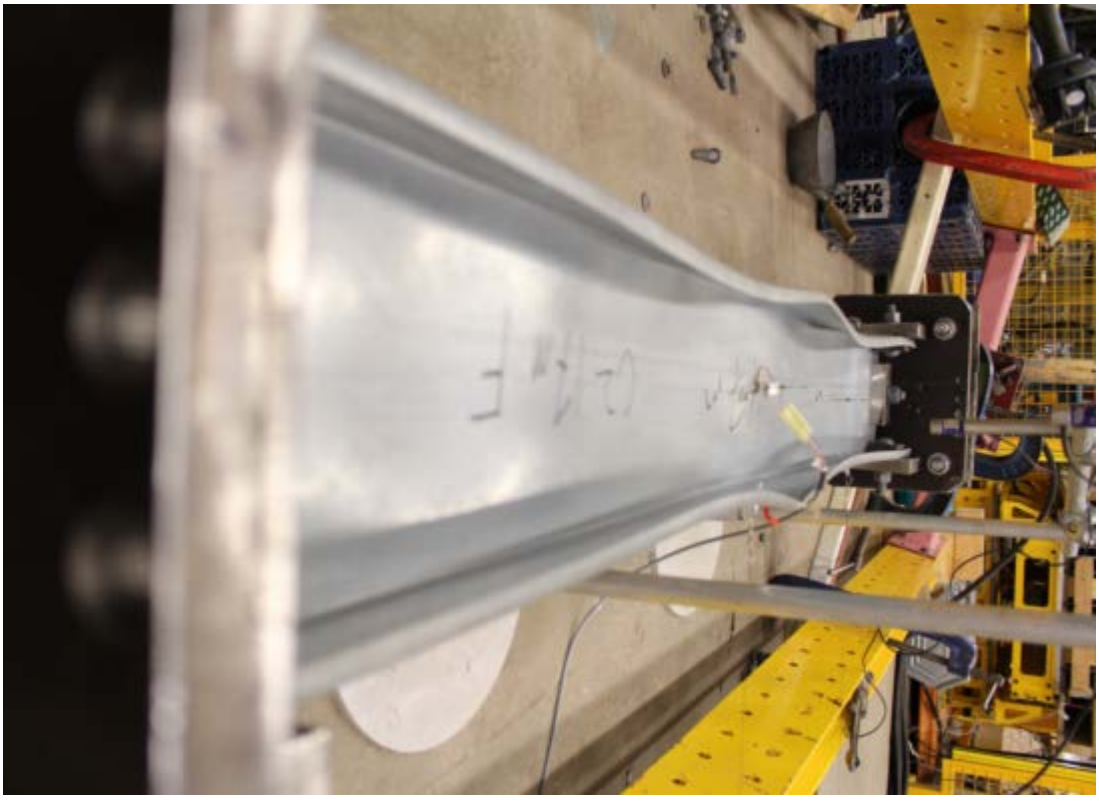

Figure (H-41) Experimental buckling mode shape of 1.7 m length of C-section for fixed ends conditions

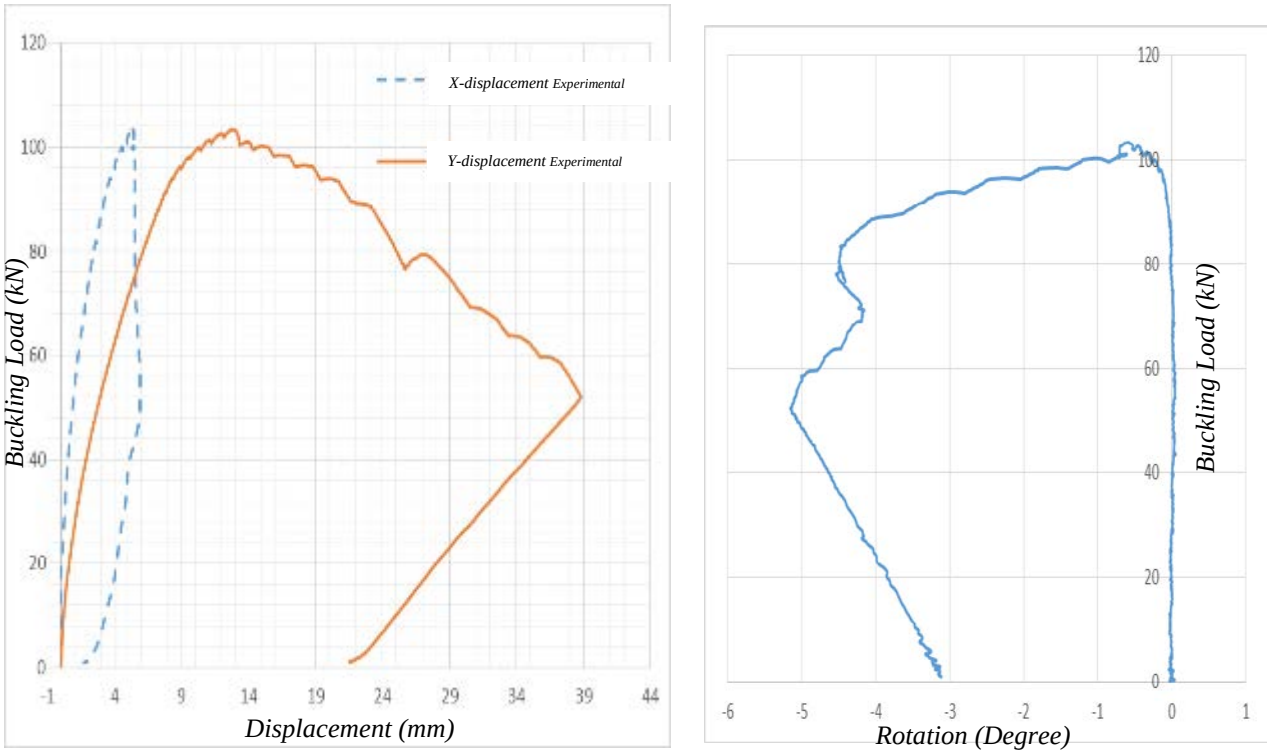

Figure (H-42) Experimental load-deformation relations of 1.7 m length at mid web of 0.5L of C-section for fixed ends conditions

C-section / fixed end / 2.0 m length

Figure (H-43) Experimental buckling mode shape of 2.0 m length of C-section for fixed ends conditions

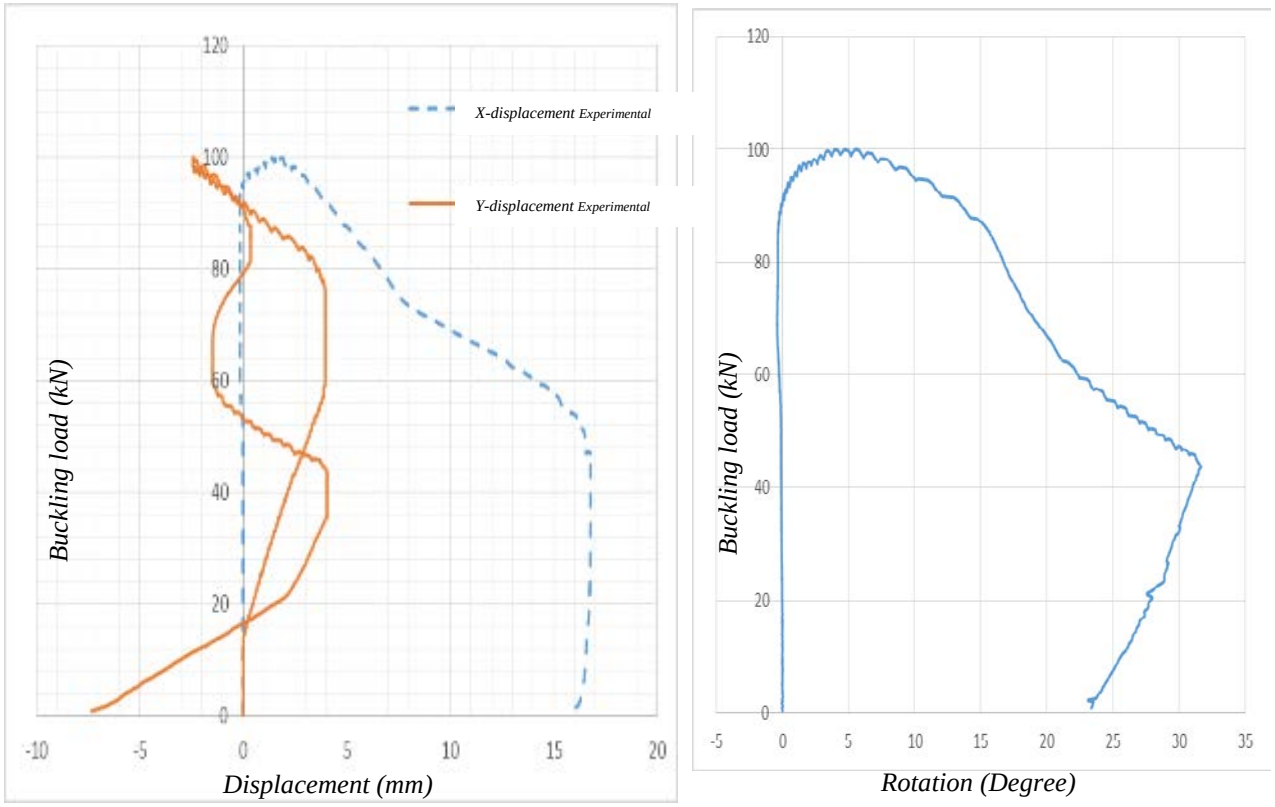

Figure (H-44) Experimental load-deformation relations of 2.0 m length at mid web of 0.5L of C-section for fixed ends conditions

C-section / fixed end / 2.3 m length

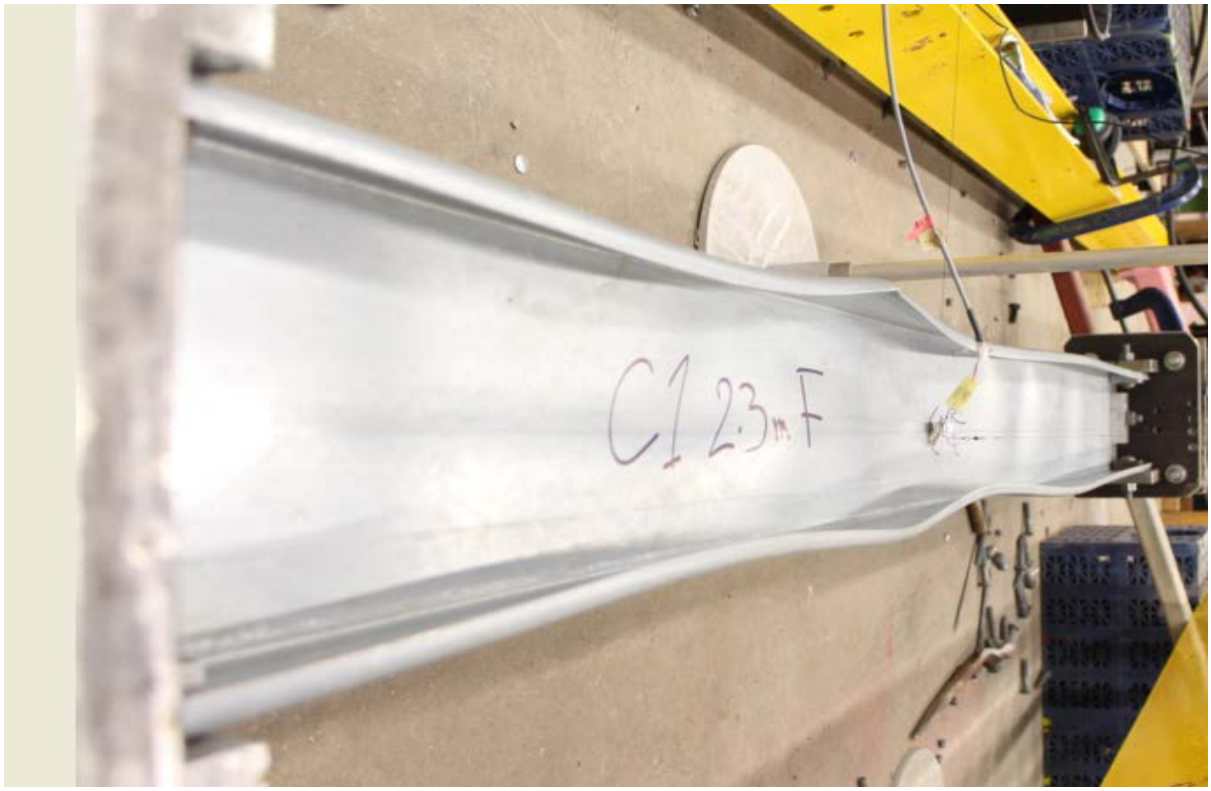

Figure (H-45) Experimental buckling mode shape of 2.3 m length of C-section for fixed ends conditions

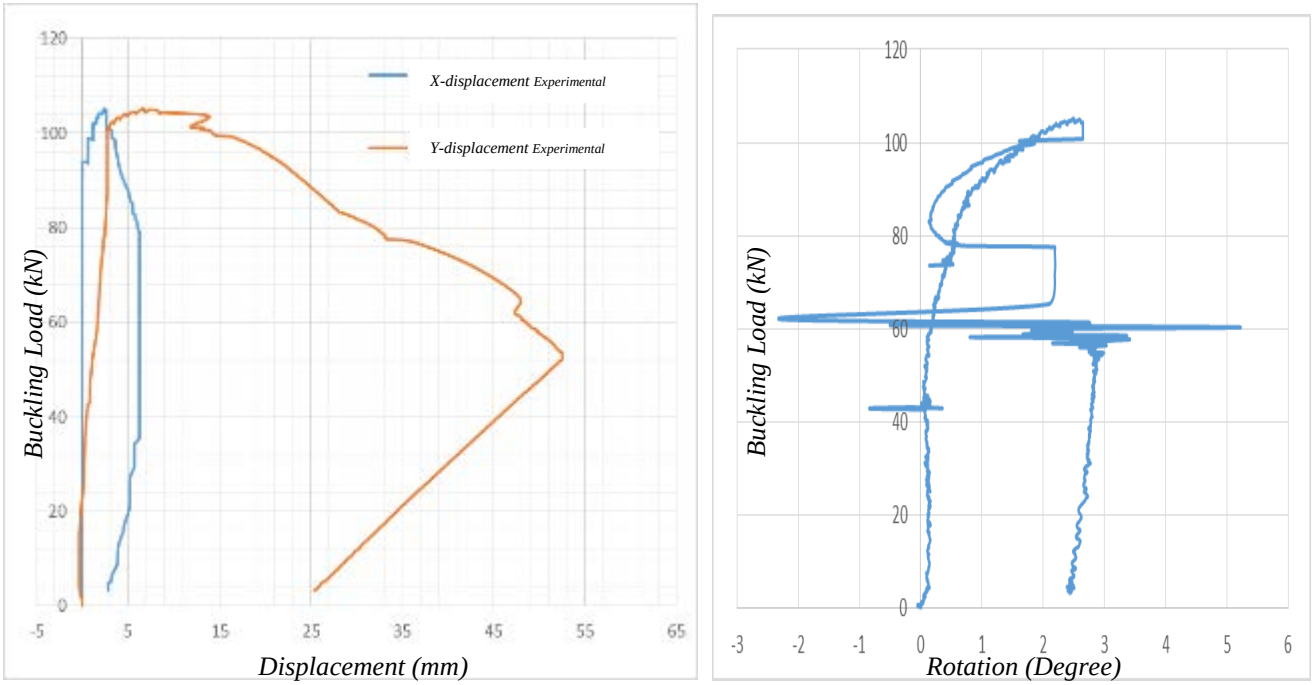

Figure (H-46) Experimental load-deformation relations of 2.3 m length at mid web of 0.5L of C-section for fixed ends conditions

C-section / fixed end / 2.7 m length

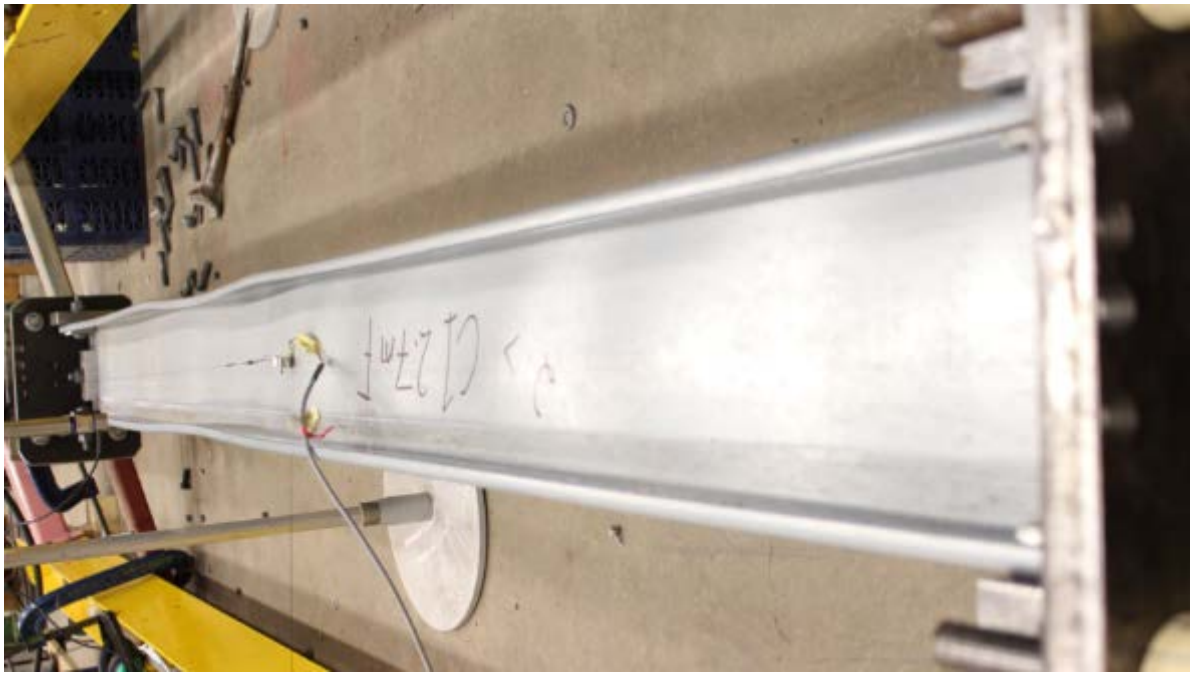

Figure (H-47) Experimental buckling mode shape of 2.7 m length of C-section for fixed ends conditions

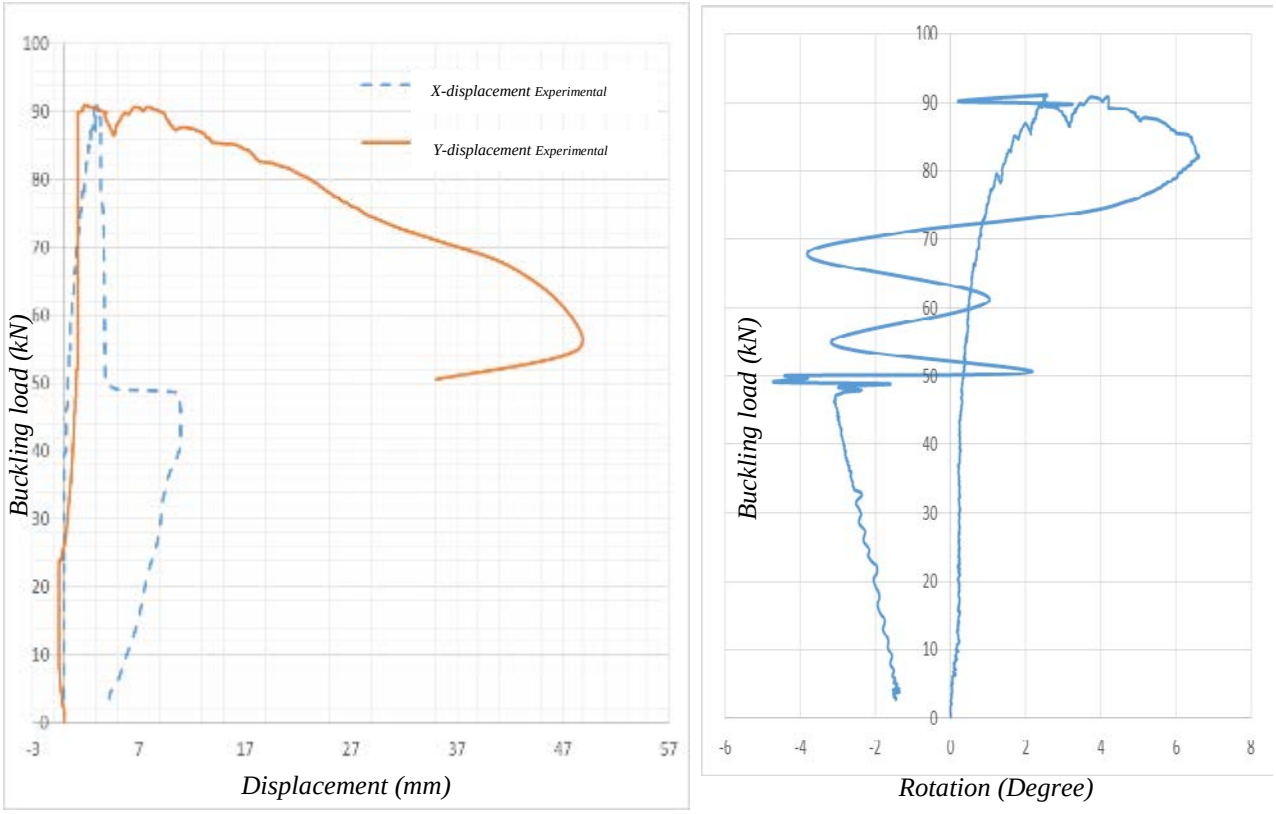

Figure (H-48) Experimental load-deformation relations of 2.7 m length at mid web of 0.5L of C-section for fixed ends conditions

C-section / fixed end / 3.0 m length

Figure (H-49) Experimental buckling mode shape of 3.0 m length of C-section for fixed ends conditions

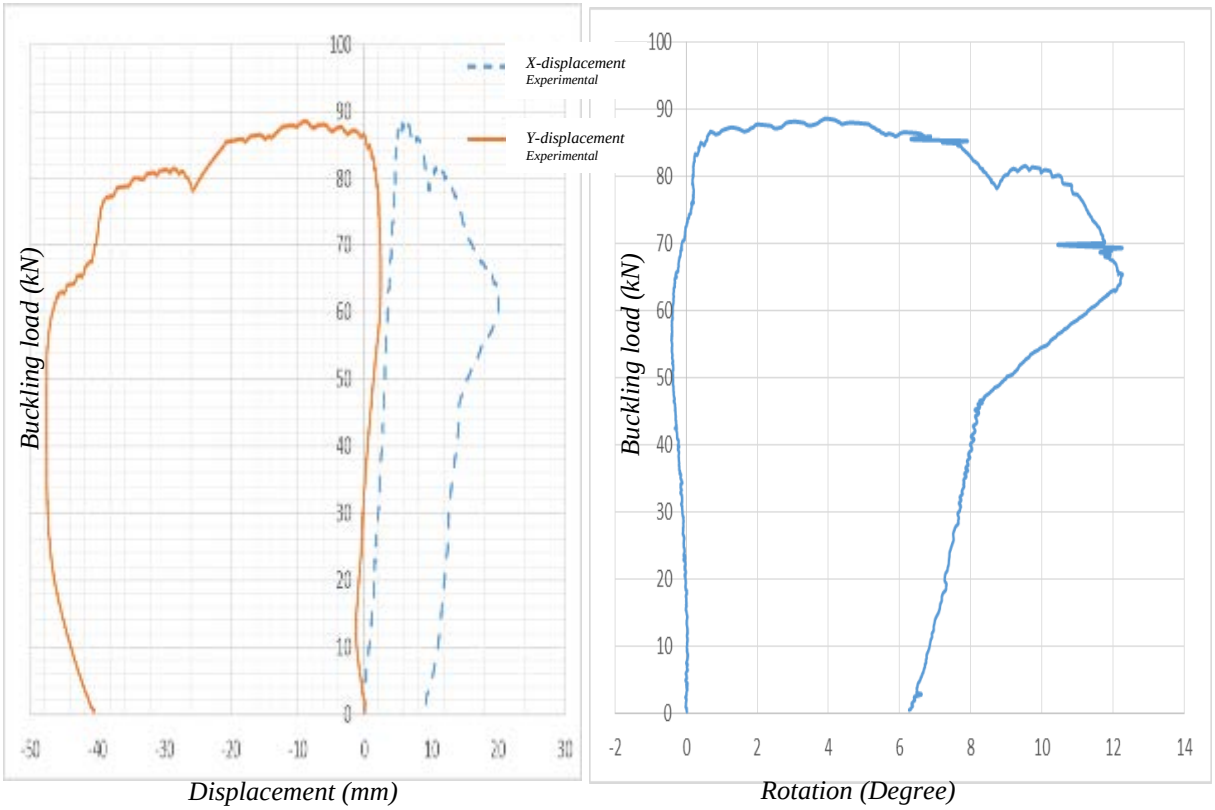

Figure (H-50) Experimental load-deformation relations of 3.0 m length at mid web of 0.5L of C-section for fixed ends conditions

C-section / fixed end / 3.5 m length

Figure (H-51) Experimental buckling mode shape of 3.5 m length of C-section for fixed ends conditions

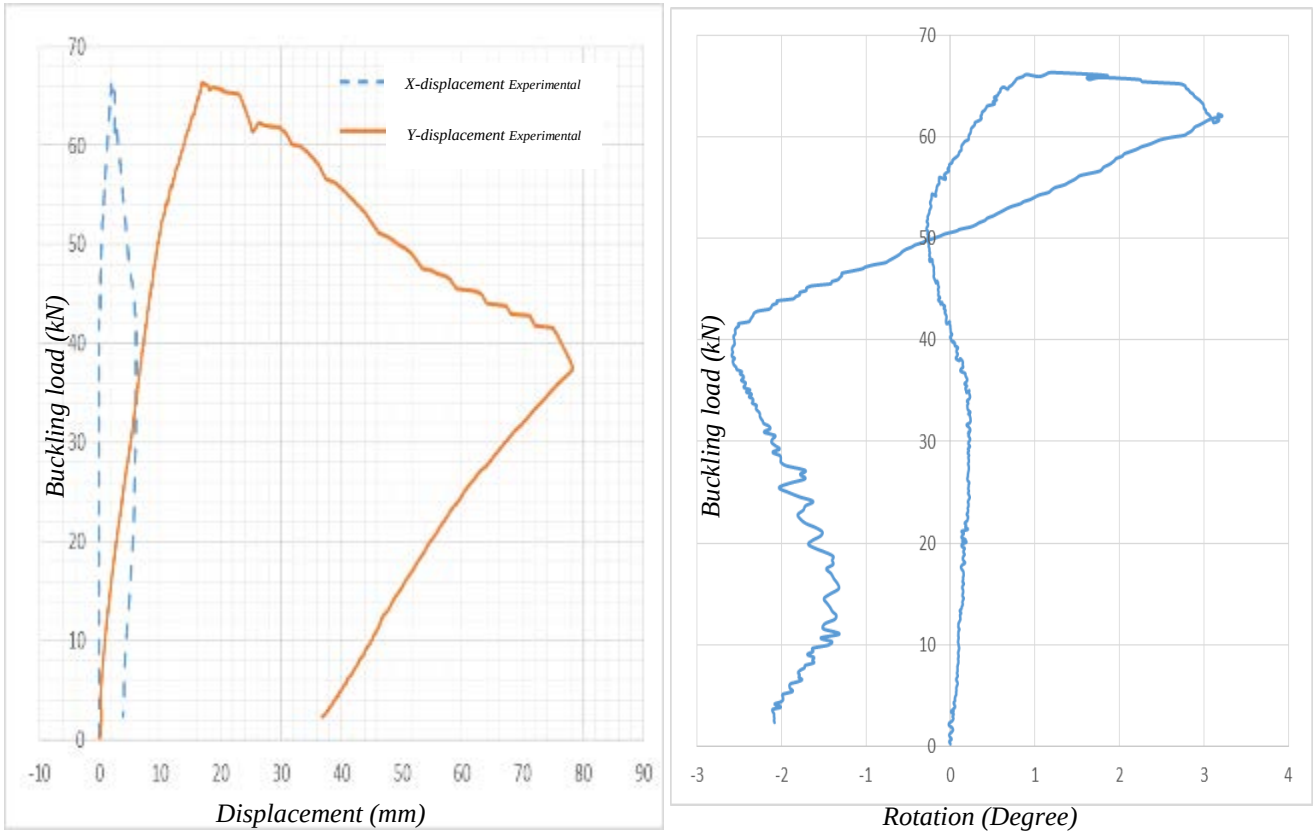

Figure (H-52) Experimental load-deformation relations of 3.5 m length at mid web of 0.5L of C-section for fixed ends conditions

C-section / fixed end / 4.0 m length

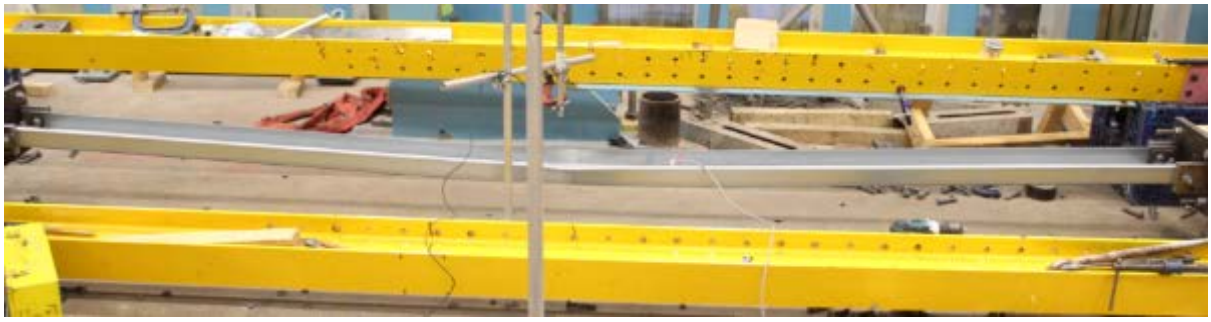

Figure (H-53) Experimental buckling mode shape of 4.0 m length of C-section for fixed ends conditions

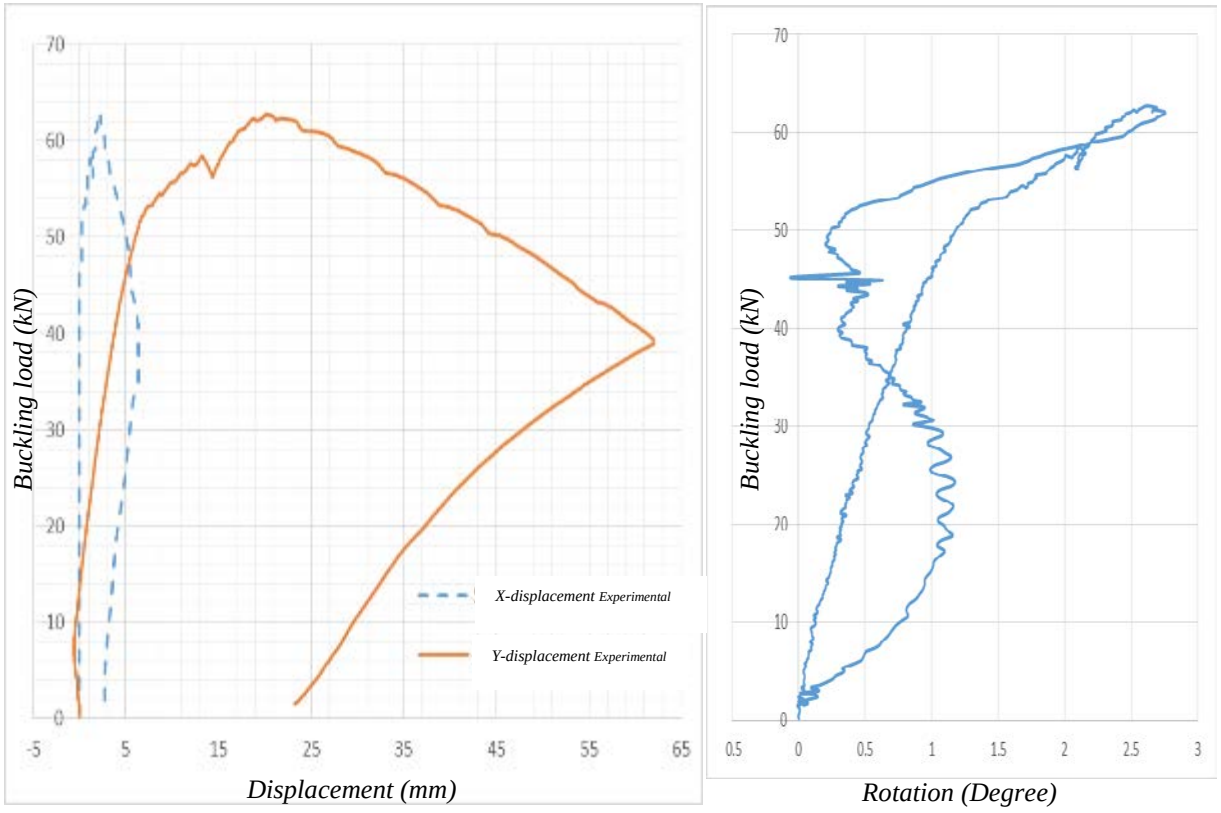

Figure (H-54) Experimental load-deformation relations of 4.0 m length at mid web of 0.5L of C-section for fixed ends conditions

Z-section / fixed end / 1.0 m length

Figure (H-55) Experimental buckling mode shape of 1.0 m length of Z-section for fixed ends conditions

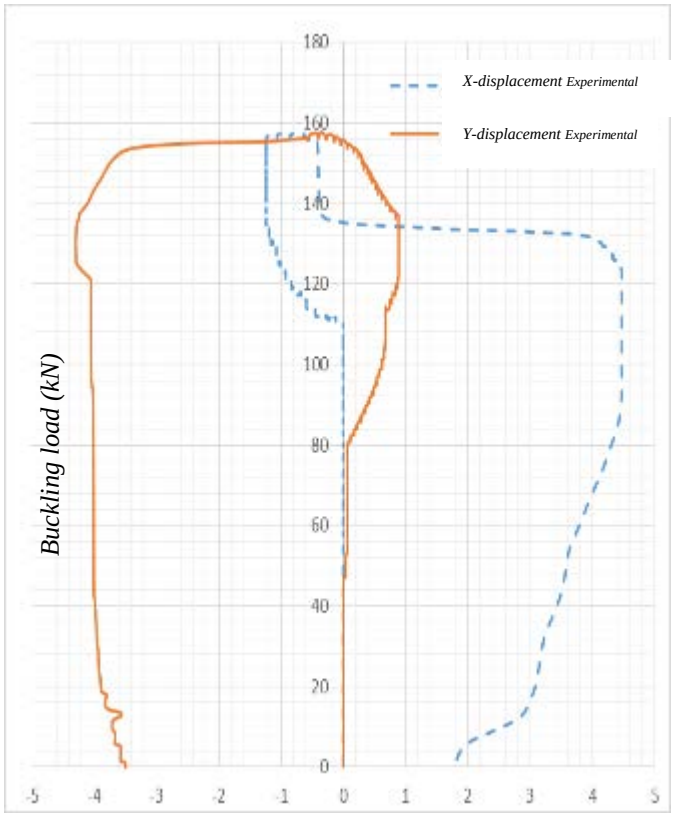

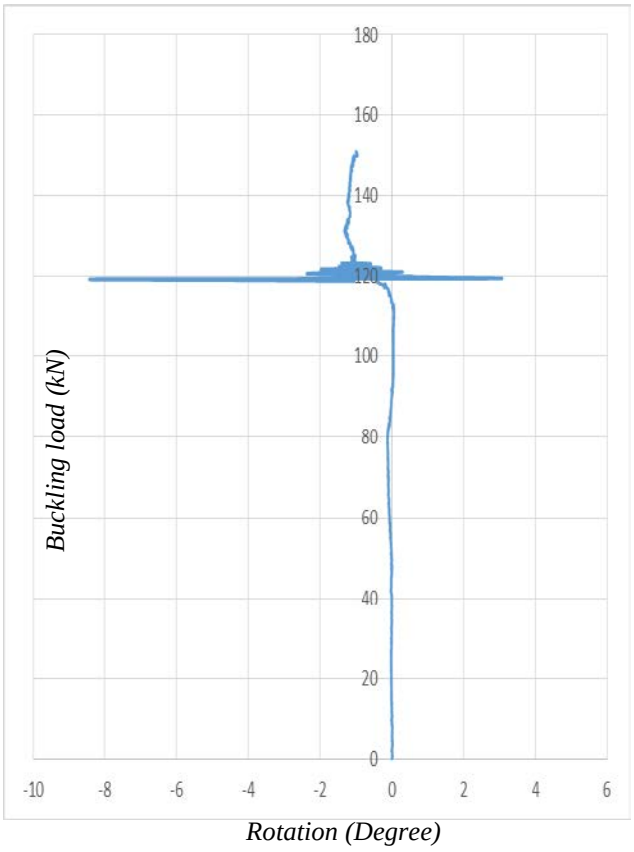

Figure (H-56) Experimental load-deformation relations of 1.0 m length at mid web of 0.5L of Z-section for fixed ends conditions

Z-section / fixed end / 1.3 m length

Figure (H-57) Experimental buckling mode shape of 1.3 m length of Z-section for fixed ends conditions

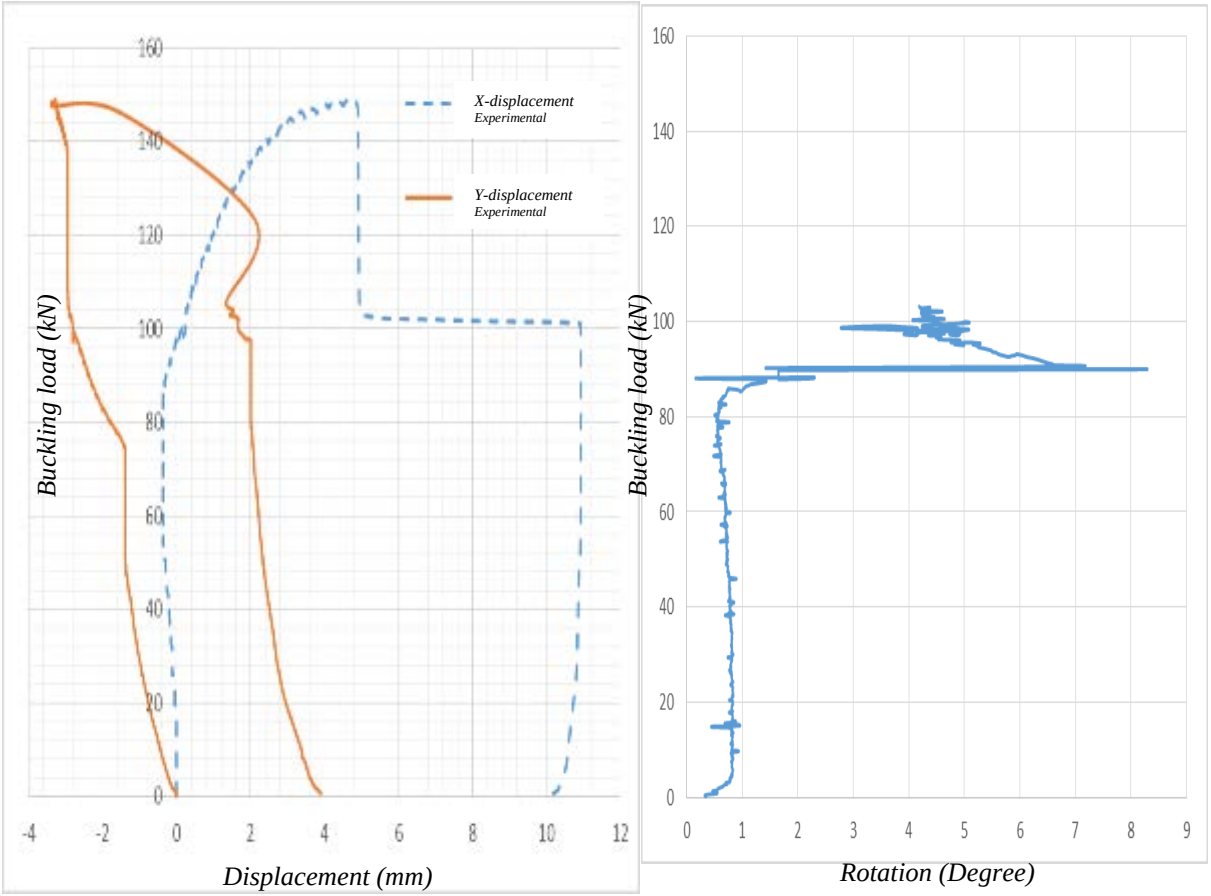

Figure (H-58) Experimental load-deformation relations of 1.3 m length at mid web of 0.5L of Z-section for fixed ends conditions

Z-section / fixed end / 1.7 m length

Figure (H-59) Experimental buckling mode shape of 1.7 m length of Z-section for fixed ends conditions

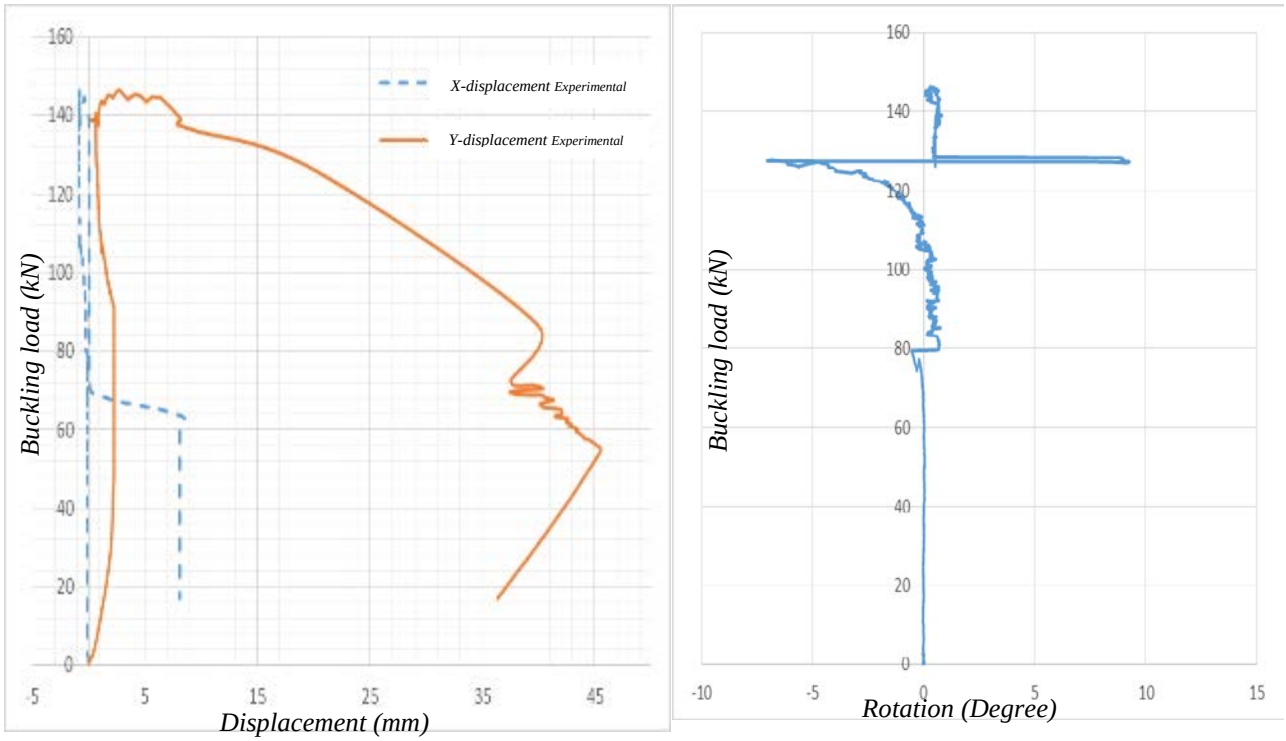

Figure (H-60) Experimental load-deformation relations of 1.7 m length at mid web of 0.5L of Z-section for fixed ends conditions

Z-section / fixed end / 2.0 m length

Figure (H-61) Experimental buckling mode shape of 2.0 m length of Z-section for fixed ends conditions

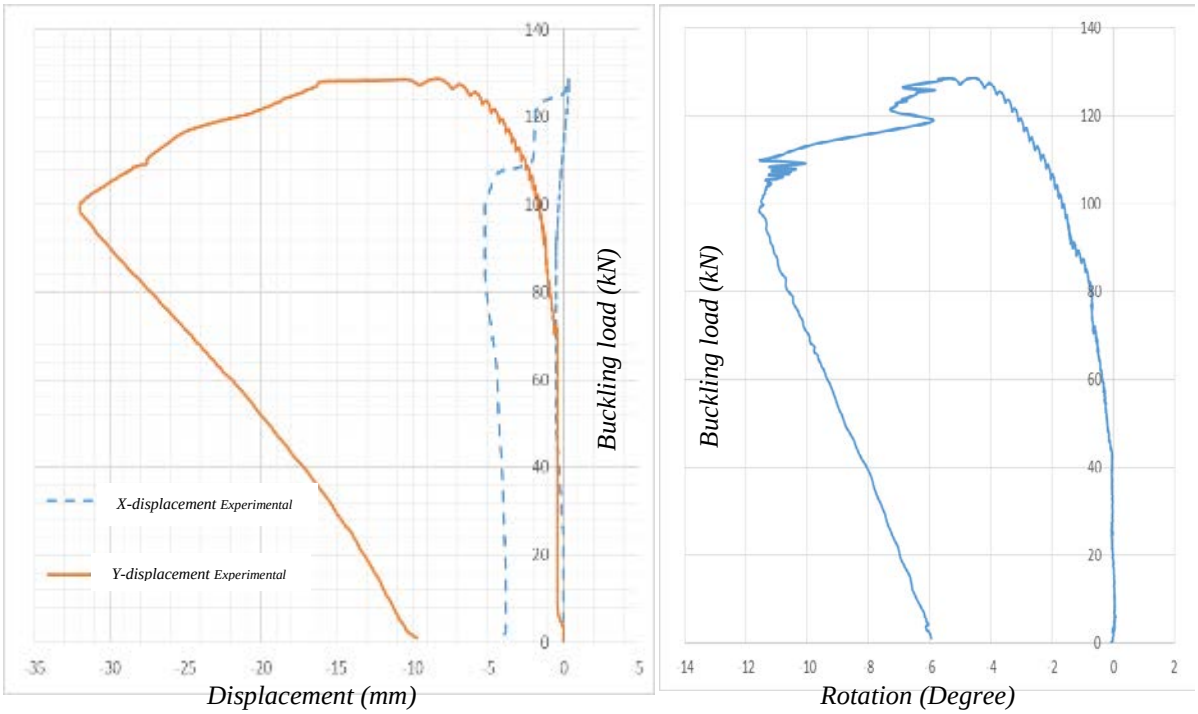

Figure (H-62) Experimental load-deformation relations of 2.0 m length at mid web of 0.5L of Z-section for fixed ends conditions

Z-section / fixed end / 2.3 m length

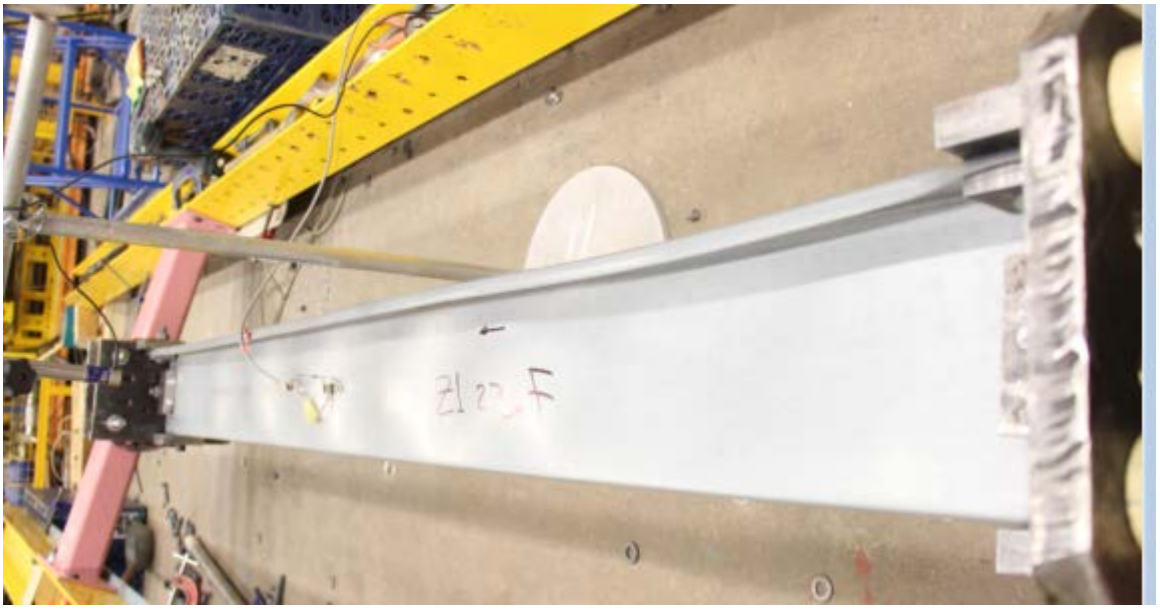

Figure (H-63) Experimental buckling mode shape of 2.3 m length of Z-section for fixed ends conditions

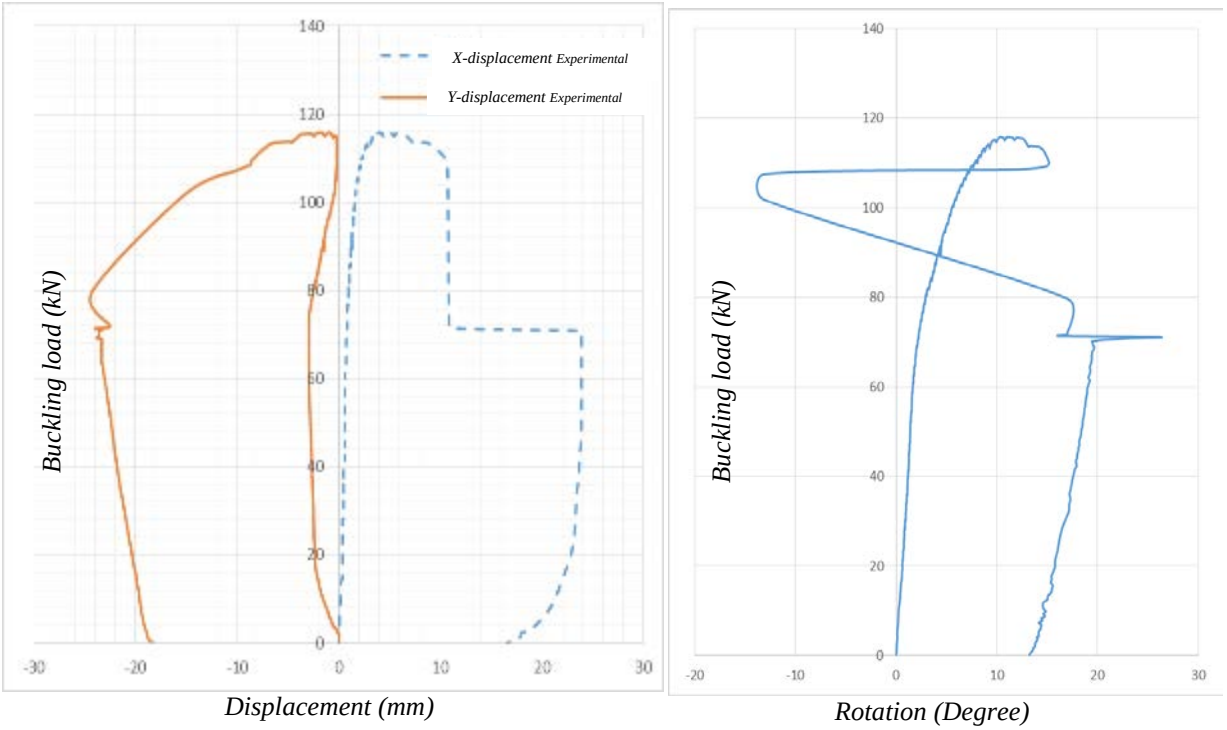

Figure (H-64) Experimental load-deformation relations of 2.3 m length at mid web of 0.5L of Z-section for fixed ends conditions

Z-section / fixed end / 2.7 m length

Figure (H-65) Experimental buckling mode shape of 2.7 m length of Z-section for fixed ends conditions

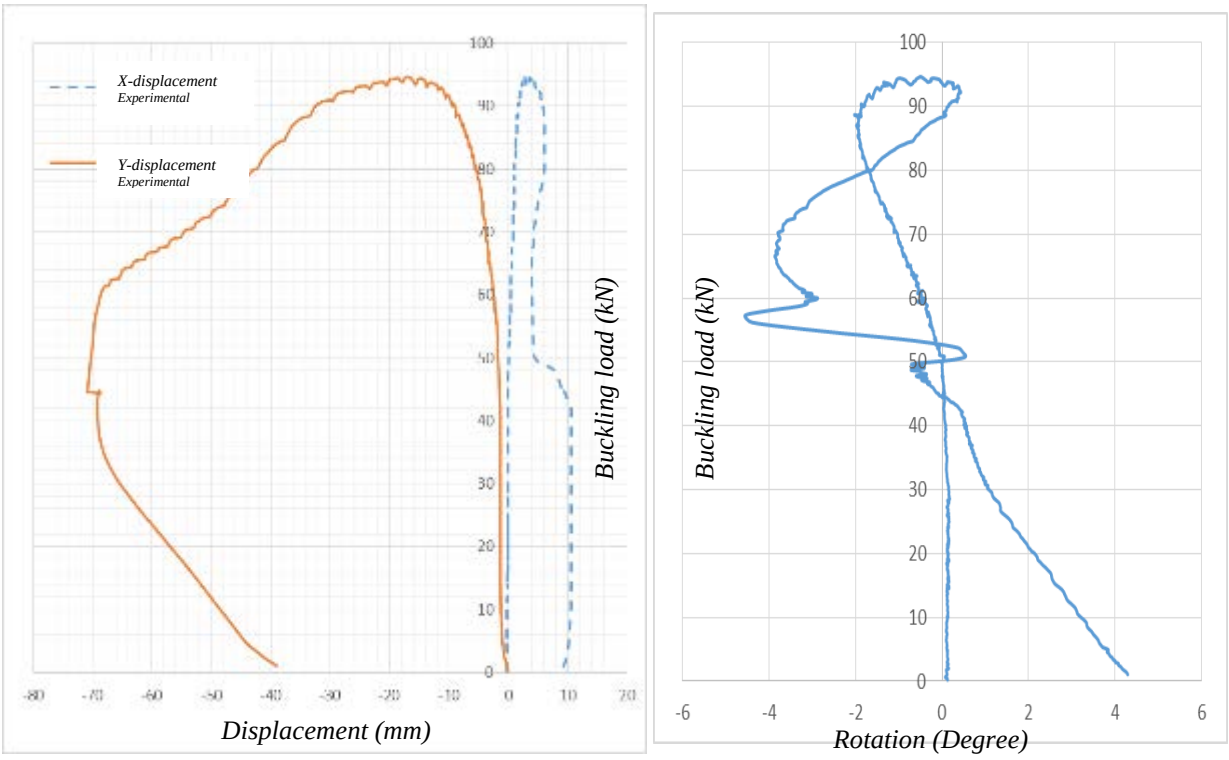

Figure (H-66) Experimental load-deformation relations of 2.7 m length at mid web of 0.5L of Z-section for fixed ends conditions

Z-section / fixed end / 3.0 m length

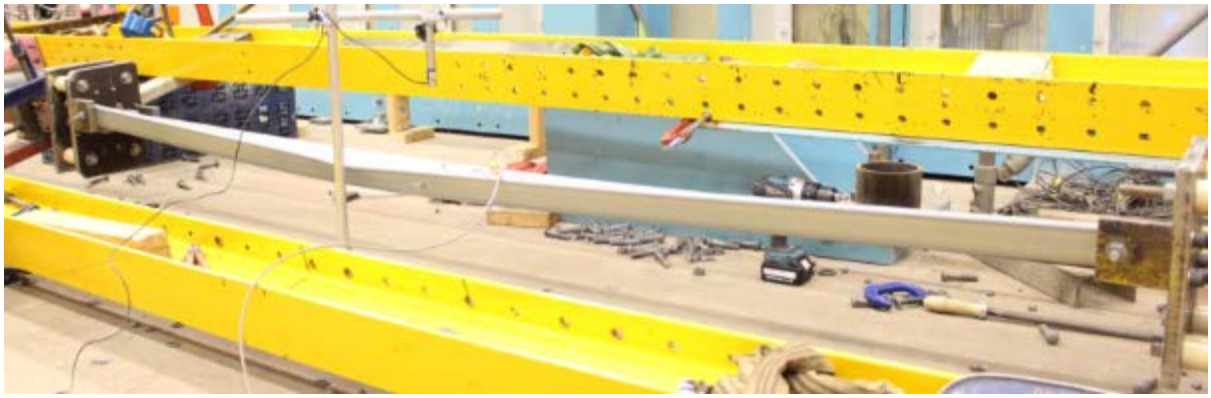

Figure (H-67) Experimental buckling mode shape of 3.0 m length of Z-section for fixed ends conditions

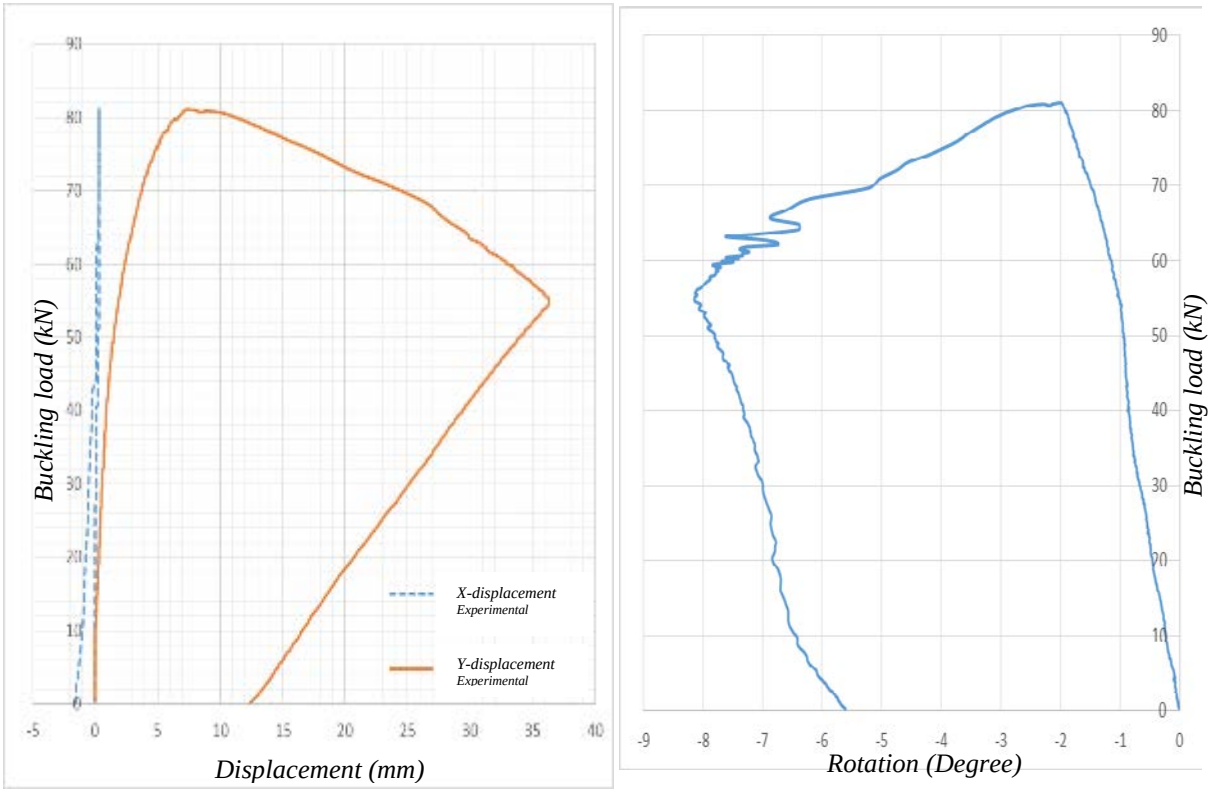

Figure (H-68) Experimental load-deformation relations of 3.0 m length at mid web of 0.5L of Z-section for fixed ends conditions

Z-section / fixed end / 3.5 m length

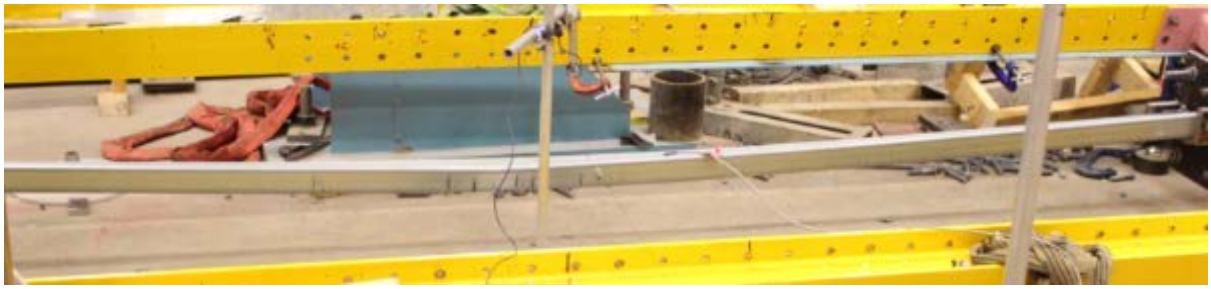

Figure (H-69) Experimental buckling mode shape of 3.5 m length of Z-section for fixed ends conditions

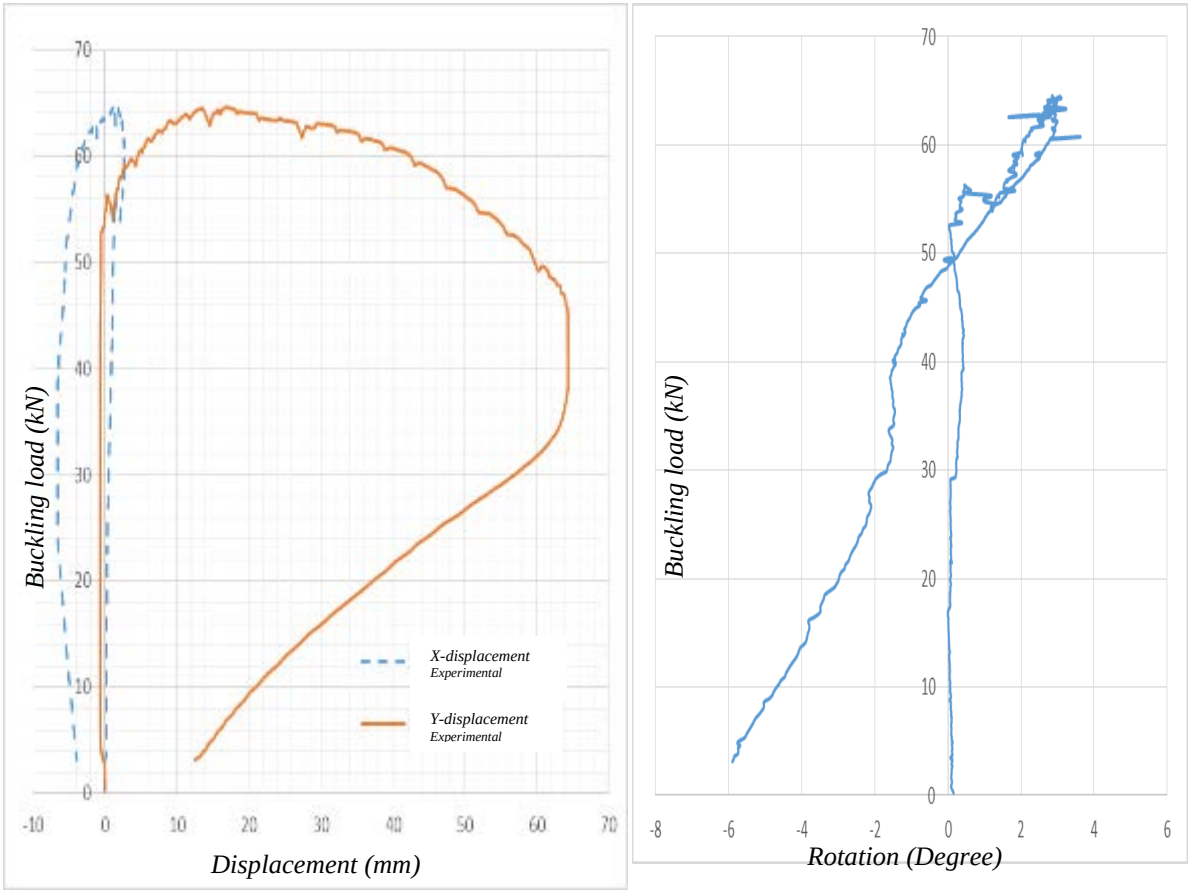

Figure (H-70) Experimental load-deformation relations of 3.5 m length at mid web of 0.5L of Z-section for fixed ends conditions

Z-section / fixed end / 4.0 m length

Figure (H-71) Experimental buckling mode shape of 4.0 m length of Z-section for fixed ends conditions

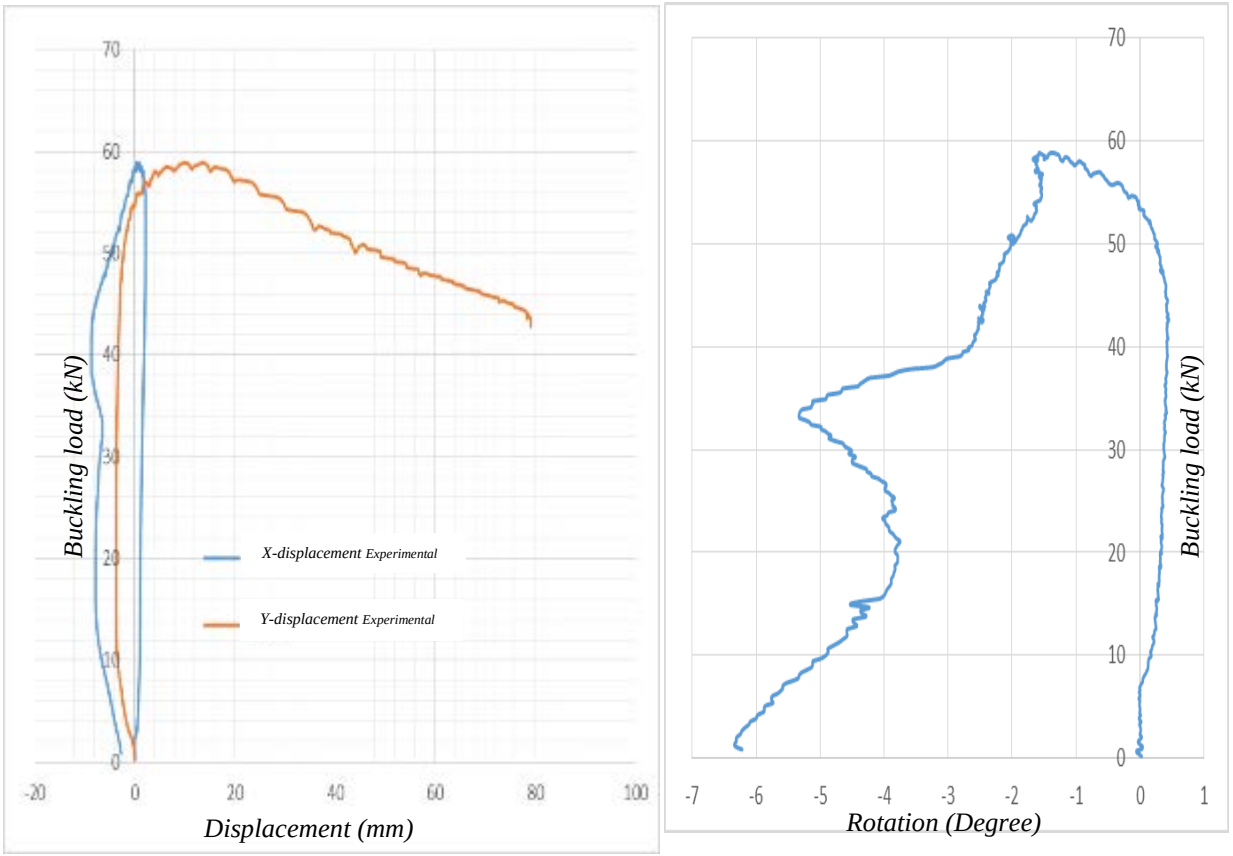

Figure (H-72) Experimental load-deformation relations of 4.0 m length at mid web of 0.5L of Z-section for fixed ends conditions